CELEBRATING THE INTERNATIONAL YEAR OF THE PERIODIC TABLE: BEYOND MENDELEEV 150

EDITED BY: Mikhail V. Kurushkin, W. H. Eugen Schwarz and Eugene A. Goodilin
PUBLISHED IN: Frontiers in Chemistry

frontiers Research Topics

ISSN 1664-8714
ISBN 978-2-88966-319-4
DOI 10.3389/978-2-88966-319-4

About Frontiers

Frontiers is more than just an open-access publisher of scholarly articles: it is a pioneering approach to the world of academia, radically improving the way scholarly research is managed. The grand vision of Frontiers is a world where all people have an equal opportunity to seek, share and generate knowledge. Frontiers provides immediate and permanent online open access to all its publications, but this alone is not enough to realize our grand goals.

Frontiers Journal Series

The Frontiers Journal Series is a multi-tier and interdisciplinary set of open-access, online journals, promising a paradigm shift from the current review, selection and dissemination processes in academic publishing. All Frontiers journals are driven by researchers for researchers; therefore, they constitute a service to the scholarly community. At the same time, the Frontiers Journal Series operates on a revolutionary invention, the tiered publishing system, initially addressing specific communities of scholars, and gradually climbing up to broader public understanding, thus serving the interests of the lay society, too.

Dedication to Quality

Each Frontiers article is a landmark of the highest quality, thanks to genuinely collaborative interactions between authors and review editors, who include some of the world's best academicians. Research must be certified by peers before entering a stream of knowledge that may eventually reach the public - and shape society; therefore, Frontiers only applies the most rigorous and unbiased reviews.
Frontiers revolutionizes research publishing by freely delivering the most outstanding research, evaluated with no bias from both the academic and social point of view.
By applying the most advanced information technologies, Frontiers is catapulting scholarly publishing into a new generation.

What are Frontiers Research Topics?

Frontiers Research Topics are very popular trademarks of the Frontiers Journals Series: they are collections of at least ten articles, all centered on a particular subject. With their unique mix of varied contributions from Original Research to Review Articles, Frontiers Research Topics unify the most influential researchers, the latest key findings and historical advances in a hot research area! Find out more on how to host your own Frontiers Research Topic or contribute to one as an author by contacting the Frontiers Editorial Office: researchtopics@frontiersin.org

CELEBRATING THE INTERNATIONAL YEAR OF THE PERIODIC TABLE: BEYOND MENDELEEV 150

Topic Editors:
Mikhail V. Kurushkin, ITMO University, Russia
W. H. Eugen Schwarz, University of Siegen, Germany
Eugene A. Goodilin, Lomonosov Moscow State University, Russia

Citation: Kurushkin, M. V., Schwarz, W. H. E., Goodilin, E. A., eds. (2021). Celebrating the International Year of the Periodic Table: Beyond Mendeleev 150. Lausanne: Frontiers Media SA. doi: 10.3389/978-2-88966-319-4

Table of Contents

frontiers in Chemistry

EDITORIAL
published: 05 November 2020
doi: 10.3389/fchem.2020.610869

Editorial: Celebrating the International Year of the Periodic Table: Beyond Mendeleev 150

Mikhail V. Kurushkin[1]*, *W. H. Eugen Schwarz*[2] *and Eugene Goodilin*[3]

[1] *Chemistry Education Research and Practice Laboratory, SCAMT Institute, ITMO University, Saint Petersburg, Russia,* [2] *Chemistry Department, University of Siegen, Siegen, Germany,* [3] *Lomonosov Moscow State University, Moscow, Russia*

Keywords: Iypt 2019, periodic table, Mendeleev 150, periodic system, chemical elements

Editorial on the Research Topic

Celebrating the International Year of the Periodic Table: Beyond Mendeleev 150

The Periodic Table of all Chemical Elements has been, for the first time, designed and graphically displayed as a pervasive natural law by the Russian scientist Dmitri Mendeleev in March 1869, followed immediately by a large jump in pure and applied chemistry, physics and other natural sciences, and in education. The Periodic Table of Elements covers most of preceding efforts of other researches on the same subject; it was convincingly supported by the famous quantitative graphs of various elemental properties by Julius Lothar Meyer. During the past one and a half centuries, the Periodic Table has undoubtedly become the true icon of chemistry, having inspired numerous scientists of various specialities, philosophical thinkers, bel-esprits and bread-and-butter scholars as well. Thereby it has opened up new exciting horizons for innovative sustainable developments and improved advances of humankind. Periodic Tables have become an integral part of basic natural sciences, of all chemical classrooms, and even of popular culture and arts across the globe (Ball, 2019; Chapman, 2019; Düllmann, 2019; Goodilin et al., 2019; Gorbunova et al., 2019; Liddle, 2019; Poliakoff et al., 2019; Radford, 2019; Rahm et al., 2019; Rampling, 2019; Scerri, 2019; Shaik et al., 2019).

On this background, the United Nations General Assembly proclaimed the International Year of the Periodic Table of Chemical Elements (IYPT 2019) to commemorate the 150th anniversary of the discovery of the Natural System of Chemical Elements as one of the most important and influential achievements in modern sciences. This provided an unparalleled opportunity to highlight the continuous nature of scientific discovery in a peaceful and enlightened world. Advances in research in many different contexts were triggered by the discovery of the Natural System, yielding good ground for recognizing the importance of chemistry in cooperation with other basic disciplines in a world endangered by climate change and unlimited population increase.

The present collection of Research Topics is dedicated to the Natural System of Elements and its various representations in the form of Periodic Tables, its scientific chemical and physical foundations, its innovative applications in laboratory research, its cutting-edge findings in chemical periodicity and elemental groups, in advanced chemical research, physics, chemical engineering, material science, catalysis, environmental science, photovoltaics, and memristors.

Cao et al. discuss the chemical elements in their review as the "kernel" that is conserved when substances are altered. Graphical displays of the chemical properties of the elements, in the form of Periodic Tables, have been designed with the aim of either classifying real chemical substances or emphasizing formal and aesthetic concepts. The former tables usually incorporate typical valence electron configurations of bonded atoms in chemical compounds, instead of the common but chemically atypical ground states of free atoms in physical vacuum; basic chemical

Edited and reviewed by:
Valeria Conte,
University of Rome Tor Vergata, Italy

****Correspondence:***
Mikhail V. Kurushkin
kurushkin@scamt-itmo.ru

Specialty section:
This article was submitted to Green and Sustainable Chemistry, a section of the journal Frontiers in Chemistry

Received: *27 September 2020*
Accepted: *08 October 2020*
Published: *05 November 2020*

Citation:
Kurushkin MV, Schwarz WHE and Goodilin E (2020) Editorial: Celebrating the International Year of the Periodic Table: Beyond Mendeleev 150. Front. Chem. 8:610869. doi: 10.3389/fchem.2020.610869

properties like valence numbers, size and energy of the valence shells with their joint variation over the elements showing principal and secondary periodicity; peculiar elements at the top and at the bottom of the Periodic Table. While it is essential that Periodic Tables display important trends in element chemistry we might expect unusual chemical behavior in ambient, near ambient, or unusual conditions. The combination of experimental data and theoretical insight supports a more nuanced understanding of the complex periodic trends and the non-periodic phenomena.

As an example of the rich chemistry of elements and its pronounced influence on fundamental properties and structural correlations for modern materials, Belich et al. compare several revolutionary materials based on the perovskite type of crystal lattices including the legendary families of high-temperature superconductive cuprates, of colossal magnetoresistive manganites and of hybrid lead halides for a new generation of solar cells. The authors demonstrate that the widely spread crystal lattices of perovskites represent a natural flexible platform for chemical design of various advanced functional materials with unique features. An interplay between chemical bonding, defects and crystal chemistry peculiarities makes the perovskite structure a "lego designer" utilizing the natural features of the chemical elements.

Several authors presented their ideas advancing important classes of materials and nanomaterials from the C, Si, Ti, Sn, Pb family of group IV elements of the classical form of the Periodic Table. Navrotskaya et al. describes deeply modified 1D carbon nanomaterials, focusing on hybrid nanomaterials with unique mechanical, electrical, thermal, and optical characteristics. Among them, hybrids based on filamentous forms of carbon, such as carbon nanotubes and carbon nanofibers, in combination with inorganic nanoparticles attract particular attention. Due to the structure and morphology, charge, and energy transfer processes lead to synergistic effects that allow the use of less material with higher productivity including their ecological applications.

Morozova et al. discuss an important class of silicon nanomaterials—quantum dots. The authors noted that widely known silicon quantum dots (SiQDs), semiconductor Si nanoparticles ranging from 1 to 10 nm, still hold a great applicative potential for optoelectronic devices and fluorescent bio-marking agents. Their much higher biocompatibility, as compared to conventional toxic Group II-VI and III-V metal-based quantum dots, makes their practical applications even more attractive to prevent environmental pollution and to avoid damage of living organisms.

Oxide derivatives of silicon composes a special class of glass materials. In particular, Shakhgildyan et al. shared a perspective of how glass is the only material that could represent almost all elements of the Periodic Table inside itself, showing the effect of the Periodic Law on properties of the final material. The authors reproduced for the first time the Periodic Table in birefringence colors in the bulk of silica glass using a direct laser writing technique.

Highly important and technologically relevant oligosiloxanes are discussed by Rabanzo-Castillo et al.. In particular, the utility of $(C_6F_5)_3B(OH_2)$ as a catalyst for the simple and environmentally benign synthesis of oligosiloxanes directly from hydrosilanes, is discussed. The authors note that this protocol offers several advantages compared to other methods of synthesizing siloxanes, such as mild reaction conditions, low catalyst loading, and a short reaction time with high yields and purity, although such reactions have a rather complicated mechanism. With the hydrosilane (R_3SiH) as the sole starting material, the fate of the reaction largely depends on the creation of silanol (R_3SiOH) from R_3SiH as these two undergo dehydrocoupling to yield a disiloxane product. Generation of the silanol is based on a modified Piers-Rubinsztajn reaction. Once the silanol has been produced, the mechanism involves a series of competitive reactions with multiple catalytically relevant species involving water, silane, and silanol interacting with the Lewis acid, and the favored reaction cycle depends on the concentration of various species in solution.

Rodionov et al. describe improved access to expected applications of titania and its derivatives for photocatalytic systems. The authors present new preparation routes, final structural and functional properties of layered hybrid derivatives of titania as an efficient photocatalyst for hydrogen production from aqueous alcohol solution. The hybrid photocatalyst $H_2Nd_2Ti_3O_{10} \times BuNH_2$ was synthesized by a solid-state ceramic method followed by protonation, intercalation of methylamine and subsequent substitution by n-butylamine. While the non-intercalated Pt-loaded $H_2Nd_2Ti_3O_{10}$ showed a maximum quantum efficiency of only 2% in the 220–340 nm range, the efficiency for hybrid samples reached 23–52%. This effect may be associated with the significant expansion of the interlayer space, which is considered as a separate reaction zone.

In addition, Voytovich et al. compare titanates and their role as photocatalytic splitting systems with a similar series of hybrid niobates $HCa_2Nb_3O_{10} \times RNH_2$, containing intercalated n-alkylamines (R = Me, Et, Pr, Bu, Hx, Oc). Special attention was also paid to the feasible improvement of the photocatalytic activity of the samples via their modification with Pt nanoparticles as a cocatalyst. Thus, modification of layered perovskite-like oxides by organic substances appears to be an effective strategy to manage their photocatalytic activity, which may be applied to other related photocatalytic materials.

Illarionov et al. review state-of-the-art memristive titania as one of the most widely used materials in resistive switching applications, including random-access memory, neuromorphic computing, biohybrid interfaces, and sensors. The functional memristive properties of titanium dioxide thin films are drastically dependent on their processing methods, including synthesis, fabrication, and post-fabrication treatment, and thus the authors provide an overview of the major application domains of TiO_2-based memristive devices.

In their mini-review, Petrov and Tarasov summarize the existing data on the unique properties of reactionary polyiodide melts (RPM) used for the development of the novel type of technologies of scalable production of a new generation of solar cells based on hybrid halloplumbate perovskites. The authors discuss the potential of RPM for the fabrication of hybrid perovskite films and describe the role of polyhalides the degradation of perovskite solar cells.

Another potential candidate for photovoltaics based of halostannates is presented in the article of Umedov et al.. Structure and properties of inorganic perovskite Cs_2SnI_6 demonstrate its potential as a light-harvester or electron-hole transport material. The authors report the way of light tuning of absorption and transport properties of cesium iodostannate(IV) Cs_2SnI_6 via partial heterovalent substitution of tin for indium. Light absorption and optical bandgaps of such materials have been investigated by UV-VIS absorption and photoluminescent spectroscopies. Low-temperature electron paramagnetic resonance spectroscopy was used to study the kind of the paramagnetic centers in these materials.

A further domain of articles in this Collection is closely connected with f-elements. A quite original mini-review of radiochemistry experts Romanchuk et al. disclose some most important mainstream problems in radio-ecology. The review briefly but comprehensively analyzes the highly complicated chemistry of the actinides and their applications and utilization. Among them, uranium and plutonium are the most important, as they are used in the nuclear fuel cycle and nuclear weapon production, and thus the review is focused on the latest experimental, modeling and case study achievements in the investigation of plutonium and uranium migration in the environment, which include the speciation of these elements and the chemical reactions that control their migration pathways.

Visentin et al. presented the current status of gaseous transport studies of singly-charged lanthanide and actinide ions in the light of potential applications to superheavy ions. The correlation of the ion-neutral interaction potential and mobility variations with the spatial parameters of the electron distributions in the bare ions is explored through the ionic radii concept. While the qualitative trends found for interaction potentials and mobilities render them appealing for superheavy ion research, lack of experimental data and limitations of the scalar relativistic ab initio approaches in use make further efforts necessary to bring the transport measurements into the inventory of techniques operating in the "one atom at a time" mode.

Finally, Elkina and Kurushkin authored a comprehensive mini-review on the history, the different syntheses, and possibly all known applications of artificial element promethium. The mini-review is expected to be the definitive starting point for anyone interested in learning about the only chemical element in the lanthanide series that has no stable isotopes.

Overall, the Collection summarizes various new achievements and trends in the chemistry of elements over the Periodic System and is certainly useful for chemists and practical researchers in materials science as well as sustainable chemistry.

AUTHOR CONTRIBUTIONS

All authors listed have made a substantial, direct and intellectual contribution to the work, and approved it for publication.

ACKNOWLEDGMENTS

We thank all authors who participated in this collection of articles, as well as all the reviewers for their relevant contributions to the Research Topics.

REFERENCES

Ball, P. (2019). Extreme chemistry: experiments at the edge of the periodic table. *Nature* 565, 552–555. doi: 10.1038/d41586-019-00285-9

Chapman, K. (2019). Superheavy: making and breaking the periodic table. *Science* 365, 974–975.

Düllmann, C. E. (2019). 118 and Counting … The Periodic Table on its 150th Anniversary. *Angew. Chem. Int. Ed.* 58, 4070–4072. doi: 10.1002/anie.201901617

Goodilin, E. A., Weiss, P. S., and Gogotsi, Y. (2019). Nanotechnology facets of the periodic table of elements. *ACS Nano* 13, 12206–12218. doi: 10.1021/acsnano.9b06998

Gorbunova, Y., Oro, L., Trzeciak, A., and Trifonov, A. (2019). Celebrating the 150th anniversary of the periodic table of chemical elements: 5th EuChemS inorganic chemistry conference. *Eur. J. Inorg. Chem.* 2019, 4166–4169. doi: 10.1002/ejic.201901104

Liddle, S. T. (2019). International year of the periodic table: lanthanide and actinide chemistry. *Angew. Chem. Int. Ed.* 58, 5140–5141. doi: 10.1002/anie.201901578

Poliakoff, M., Makin, A. D. J., Tang, S. L. Y., and Poliakoff, E. (2019). Turning the periodic table upside down. *Nat. Chem.* 11, 391–393. doi: 10.1038/s41557-019-0253-6

Radford, T. (2019). In his element: looking back on Primo Levi's The Periodic Table. *Nature* 565, 564–565. doi: 10.1038/d41586-019-00288-6

Rahm, M., Cammi, R., Ashcroft, N. W., and Hoffmann, R. (2019). Squeezing all elements in the periodic table: electron configuration and electronegativity of the atoms under compression. *J. Am. Chem. Soc.* 141, 10253–10271. doi: 10.1021/jacs.9b02634

Rampling, J. (2019). More than 2,000 years of elements: a prehistory of the periodic table. *Nature* 565, 563–564. doi: 10.1038/d41586-019-00289-5

Scerri, E. R. (2019). Happy 150th Birthday to the Periodic Table. *Chem. A Eur. J.* 25, 7410–7415. doi: 10.1002/chem.201900460

Shaik, S., Cremades, E., and Alvarez, S. (2019). The periodic-table—a universal icon: its birth 150 years ago, and its popularization through literature art and music. *Angew. Chem. Int. Ed.* 58, 13194–13206. doi: 10.1002/anie.201904584

Conflict of Interest: The authors declare that the research was conducted in the absence of any commercial or financial relationships that could be construed as a potential conflict of interest.

ORIGINAL RESEARCH
published: 12 December 2019
doi: 10.3389/fchem.2019.00863

Layered Titanate $H_2Nd_2Ti_3O_{10}$ Intercalated With *n*-Butylamine: A New Highly Efficient Hybrid Photocatalyst for Hydrogen Production From Aqueous Solutions of Alcohols

Ivan A. Rodionov*, Elizaveta A. Maksimova, Artem Y. Pozhidaev, Sergey A. Kurnosenko, Oleg I. Silyukov and Irina A. Zvereva

Institute of Chemistry, Saint-Petersburg State University, Saint-Petersburg, Russia

Edited by:
Eugene A. Goodilin,
Lomonosov Moscow State University, Russia

Reviewed by:
Van-Huy Nguyen,
Duy Tan University, Vietnam
Fernando Fresno,
IMDEA Energy Institute, Spain
Kirill Sergeevich Napolskii,
Lomonosov Moscow State University, Russia

***Correspondence:**
Ivan A. Rodionov
i.rodionov@spbu.ru

Specialty section:
This article was submitted to Catalysis and Photocatalysis, a section of the journal Frontiers in Chemistry

Received: 10 October 2019
Accepted: 28 November 2019
Published: 12 December 2019

Citation:
Rodionov IA, Maksimova EA, Pozhidaev AY, Kurnosenko SA, Silyukov OI and Zvereva IA (2019) Layered Titanate $H_2Nd_2Ti_3O_{10}$ Intercalated With n-Butylamine: A New Highly Efficient Hybrid Photocatalyst for Hydrogen Production From Aqueous Solutions of Alcohols. Front. Chem. 7:863. doi: 10.3389/fchem.2019.00863

A layered perovskite-type oxide intercalated with *n*-butylamine is reported as an efficient photocatalyst for hydrogen production from aqueous solutions of alcohols for the first time. The hybrid photocatalyst $H_2Nd_2Ti_3O_{10}\times BuNH_2$ was synthesized by solid-state ceramic method followed by protonation, intercalation of methylamine and subsequent substitution by *n*-butylamine. The product was characterized by powder XRD, TGA, STA-MS, DRS, IR, and Raman spectroscopy, CHN analysis, SEM. Intercalation of *n*-butylamine caused a dramatic increase in photocatalytic activity of $H_2Nd_2Ti_3O_{10}$ in the reaction of hydrogen evolution from aqueous solutions of methanol, ethanol, and *n*-butanol under UV radiation. While the non-intercalated Pt-loaded $H_2Nd_2Ti_3O_{10}$ showed a maximum quantum efficiency of only 2% in the 220–340 nm range, the efficiency for hybrid samples reached 23% under the same conditions and after variation of experimental parameters even 52% efficiency was achieved. This effect may be associated with the significant expansion of the interlayer space, which is considered as a separate reaction zone.

Keywords: photocatalysis, hydrogen production, layered titanate, perovskite-type structure, intercalation, amine, hybrid compounds

INTRODUCTION

Excessive consumption of fuel resources and related environmental problems, which together could lead to an energy crisis, forces scientists to look for alternative energy sources, more attractive from the environmental point of view. One of the solutions to this problem is the environmentally friendly production of hydrogen fuel by splitting of water or available organic substrates using photocatalysts (Maeda, 2011). In this regard, semiconductor photocatalysts with a layered structure, especially layered perovskite-like oxides, have been intensively studied (Rodionov and Zvereva, 2016). In particular, compounds related to the Dion–Jacobson (DJ), Aurivillius (AV), and Ruddlesden–Popper (RP) phases consisting of negatively charged perovskite layers and interlayer cations with general formula $A'[A_{n-1}B_nO_{3n+1}]$ and $A'_2[A_{n-1}B_nO_{3n+1}]$ were most actively investigated as photocatalysts (Machida et al., 2005; Compton et al., 2007; Huang et al., 2011; Chen et al., 2012; Rodionov et al., 2012, 2017a,d; Sabio et al., 2012; Zvereva and Rodionov, 2013). These materials exhibit unique photocatalytic properties derived from their layered structure, including ion-exchange and intercalation (Zvereva et al., 2011; Silyukov et al., 2015; Rodionov et al., 2017c; Shelyapina et al., 2019).

Since photocatalysts should be capable of absorbing visible light, have a large number of active catalytic sites and also support mechanisms for the efficient charge separation, different attempts have been made to modify layered oxides by cationic and anionic substitution and doping (Zou et al., 2001; Reddy et al., 2003; Kumar et al., 2011; Zhou et al., 2016; Kawashima et al., 2017a), sensitization with dyes (Youngblood et al., 2009), intercalation of metals or other inorganic particles (Huang et al., 2006, 2009) and also the creation of composites with other materials (Cui et al., 2012, 2013, 2014; Liu et al., 2018).

Hybrid organic-inorganic compounds are of great importance for modern materials science, since they allow combining the already known organic and inorganic materials and compounds with completely different properties in one composite (Gómez-Romero and Sanchez, 2006; Kickelbick, 2007). Such hybrids are interesting because the combination of components leads to improved or even new properties that were not observed in the individual components. Particularly the organic-inorganic hybrids of perovskite-like oxides can be prepared by introducing organic guests into the interlayer space while maintaining the structural features of the inorganic host. These modifications of the perovskite hosts do not require extreme conditions and lead to organic-inorganic hybrids that are stable to moderate chemical and physical impacts.

Perovskite-based hybrids are usually the result of either grafting reaction, where organic compounds are bonded to terminal interlayer oxygen atoms through strong ion-valence bonds (Tahara et al., 2007; Boykin and Smith, 2015; Shori et al., 2015), or intercalation, where organic amines form ammonium ions and interact with negatively charged perovskite layers (Tsunoda et al., 2003; Shimizu et al., 2006; Wang et al., 2007). Organic modification of layered oxide perovskites was first performed by intercalation of amines (Jacobson et al., 1987), and then expanded by covalent grafting of alcohols (Takahashi et al., 1995). Since then, the spectrum of organic compounds introduced into various protonated derivatives of the DJ, RP and AV phases has been significantly expanded (including amino alcohols, carboxylic acids, amino acids, etc.) (Hong and Kim, 1996; Han et al., 2001; Tsunoda et al., 2003; Tong et al., 2005; Takeda et al., 2006, 2008; Tahara, 2007; Wang et al., 2012, 2018; Boykin and Smith, 2015; Shori et al., 2015; Sato et al., 2017; Silyukov et al., 2018).

Despite the rather large number of currently synthesized hybrid compounds based on layered oxides, little attention has been paid to the study of the photocatalytic activity of such compounds. Perhaps this is due to concerns about the photodegradation of embedded organics during the photocatalytic process. For example, Machida et al. studied the photocatalytic activity of the layered tantalate $HCa_2Ta_3O_{10}$ intercalated with $C_6H_{13}NH_2$ in the reaction of water splitting under UV-light and noted a significantly higher activity of the hybrid in hydrogen evolution compared to $MCa_2Ta_3O_{10}$ (M = Cs, Na, and H) (Machida et al., 2005). At the same time, the studied hybrid turned out to be unstable to oxidation during the photocatalytic process, which was confirmed by the collapse of the interlayer gallery and insignificant oxygen evolution, followed by a dramatic decrease in activity after the first 8 h of irradiation. More optimistic results were obtained by Wang et al. (2014) who used derivatives of the double-layered perovskite $H_2CaTa_2O_7$ with n-alcohols as photocatalyst for the decomposition of rhodamine B and methyl orange under UV-visible light irradiation. Grafting of long-chain *n*-alcohols ($n > 3$) into the perovskite layers of $H_2CaTa_2O_7$ improved the photocatalytic activity drastically. One can also note interesting results obtained for layered oxides intercalated by polyaniline. Such hybrids have shown themselves to be effective photocatalysts in the visible spectral region, having been tested on the model decomposition reaction of methylene blue dye (Guo et al., 2010; Zhu et al., 2013; Liu et al., 2014). Although aniline-intercalated compounds have also been obtained for layered perovskite-like oxides (Uma and Gopalakrishnan, 1994, 1995; Tong et al., 2005), the photocatalytic activity of such hybrids has not yet been studied.

$A_2Ln_2Ti_3O_{10}$ (A = Li, Na, K, Rb; Ln = La, Nd, Gd, Sm, Dy, Eu) are layered RP perovskite-type compounds with alkali cations in the interlayer space. These compounds are known to exhibit ion exchange and intercalation properties (Gopalakrishnan and Bhat, 1987; Richard et al., 1994; Rodionov et al., 2017d) and are one of the most extensively studied photocatalytic materials (Takata et al., 1997a,b; Rodionov et al., 2012; Kawashima et al., 2017b). Ni-loaded $Rb_2La_2Ti_3O_{10}$ was one of the first highly active photocatalysts for water splitting with a quantum efficiency estimated around 5% (Takata et al., 1997a). $H_2Ln_2Ti_3O_{10}$ are protonated forms of $A_2Ln_2Ti_3O_{10}$ compounds that can be obtained by acid leaching of interlayer alkali cations (Gopalakrishnan and Bhat, 1987; Richard et al., 1994). They can be used to develop new materials by intercalating organic molecules into the interlayer space (Tong et al., 2005; Tahara et al., 2007; Akbarian-Tefaghi and Wiley, 2018) as well as by exfoliation and self-assembly processes (Huang et al., 2006; Wu et al., 2006; Ida et al., 2008). However, to our best knowledge, amine-intercalated titanites of such structure have never been investigated as photocatalysts for hydrogen production. Particularly, it is unclear, if the intercalated organic molecules always undergo photodegradation, or, at some conditions, they might be stable and promote the photocatalytic process. Therefore, our work focuses on the photocatalytic properties of the *n*-butylamine intercalated titanate $H_2Nd_2Ti_3O_{10}$ as an example of a hybrid organic-inorganic layered material obtained by intercalation reaction. Its photocatalytic activity was investigated in the reaction of hydrogen evolution from aqueous alcohol solutions (methanol, ethanol and *n*-butanol) under UV radiation and compared with the initial $H_2Nd_2Ti_3O_{10}$ oxide.

MATERIALS AND METHODS

Synthesis

$K_2Nd_2Ti_3O_{10}$

The initial layered oxide $K_2Nd_2Ti_3O_{10}$ was synthesized by conventional solid-state reaction (1) using K_2CO_3, Nd_2O_3 and TiO_2 as reagents (Vecton, 99.9%).

$$Nd_2O_3 + 3TiO_2 + K_2CO_3 \rightarrow K_2Nd_2Ti_3O_{10} + CO_2\uparrow \quad (1)$$

The stoichiometric amounts of oxides needed to yield 20 g of the final product (7.1497 g TiO_2, 10.0401 g Nd_2O_3) with 50% excess of potassium carbonate (5.7736 g), were weighted with an accuracy of 10^{-4} g (Ohaus Pioneer PA214C balance), mixed together and ground on a Fritsch Pulverisette 7 planetary micro mill with silicon nitride accessories at a speed of 600 rpm using a program of 10 repetitions of 10 min each with 5 min interval. Hexane was also added to the bowl to prevent any hydration of the reactants and provide more uniform grinding. The obtained mixture was dried at 50°C for 1 h, then at 150°C for 30 min to remove the hexane, and finally pressed into tablets of ca. 1.5 g at 50 bar using a PI 88.00 Omec hydraulic press. The tablets were placed into corundum crucibles and heated at 700°C for 2 h in a Nabertherm L-011K2RN furnace in air atmosphere. After cooling down, the tablets were ground in an agate mortar, re-pelletized and heated at 1,000°C for 10 h as the final synthesis step. The obtained tablets were again ground in an agate mortar to prepare for XRD analysis and for the next synthesis step.

$H_2Nd_2Ti_3O_{10}$

Prior to protonation, the $K_2Nd_2Ti_3O_{10}$ oxide was transformed into its hydrated form $K_2Nd_2Ti_3O_{10}\times H_2O$ by exposition to humid air (RH = 75%) for 24 h (Utkina et al., 2018). After the XRD analysis ensured complete hydration, the sample (15 g) was dispersed in 3 L of 0.1 M hydrochloric acid and stirred for 7 days at room temperature. Then the product was separated from the solution by centrifugation (Elmi CM-6MT centrifuge), dried in a desiccator over CaO and analyzed by XRD and TGA.

$H_2Nd_2Ti_3O_{10}\times MeNH_2$

To intercalate methylamine into the interlayer space of $H_2Nd_2Ti_3O_{10}$, the sample (12 g) was dispersed in 120 ml of 38% aqueous $MeNH_2$ solution, sealed in a flask and stirred for 10 days at 60°C. Afterwards, the solid was separated by centrifugation, dried in air atmosphere for 2 days and analyzed by XRD, TGA, and CHN.

$H_2Nd_2Ti_3O_{10}\times BuNH_2$

n-Butylamine was introduced into the interlayer space by substitution of methylamine, because the attempts of direct intercalation into $H_2Nd_2Ti_3O_{10}$ led only to non-singe phase products. The methylamine-intercalated sample was dispersed in 80 ml of $BuNH_2$ with the addition of 10 ml of water, sealed in a flask and stirred for 4 days at room temperature. The final product was separated by centrifugation, dried in air atmosphere for 2 days, characterized by the further described methods and subsequently used for photocatalytic experiments.

Characterization

XRD Analysis

Powder XRD analysis was performed on every step of synthesis using a Rigaku Miniflex II diffractometer (CuKα radiation, 2θ range 3–60°, scan speed 10°/min). The obtained XRD patterns were indexed and the unit cell parameters were determined with an accuracy of 0.05% using Bruker Topas software.

TGA

Thermogravimetric analysis was carried out on the Netzsch TG 209 F1 Libra microbalance. In the case of $H_2Nd_2Ti_3O_{10}$, the measurement was performed in an argon atmosphere with a heating rate of 10 K/min from room temperature to 900°C. Typically, two steps of mass loss are observed on the TG curve of the protonated layered oxide $H_2Nd_2Ti_3O_{10}$ (Rodionov et al., 2017b). The first low-temperature step (RT−250°C) corresponds to the liberation of intercalated/adsorbed water (2) and the second step (300–400°C) refers to the decomposition of the protonated layered oxide with the liberation of water (3):

$$H_xK_{2-x}Nd_2Ti_3O_{10}\cdot yH_2O = H_xK_{2-x}Nd_2Ti_3O_{10} + yH_2O \quad (2)$$

$$H_xK_{2-x}Nd_2Ti_3O_{10} = K_{2-x}Nd_2Ti_3O_{10-x/2} + x/2H_2O \quad (3)$$

The protonation degree (x/2) was calculated from the mass loss at the second step using the formula

$$x = \frac{M_{K_2Nd_2Ti_3O_{10}}\,(m_1 - m_2)}{m_1\left(M_K + \frac{1}{2}M_O\right) - m_2\left(M_K - M_H\right)} \quad (4)$$

which can be easily derived from Equation (3). Here m_1 stands for the sample mass before reaction (3) starts, m_2 stands for the final mass after decomposition. M_i represents the molar mass of corresponding species i ($K_2Nd_2Ti_3O_{10}$, K, O, and H).

The TGA of amine-intercalated samples was performed in a synthetic dry air atmosphere (flow rate 100 ml/min) in order to ensure complete oxidation of organics as well as titanium, which might become partially reduced by organics at high temperature if the experiment is conducted in an inert atmosphere. The temperature program consisted of two steps: heating at a rate of 10 K/min from room temperature to 950°C followed by an isothermal step for 20 min.

STA-MS

Simultaneous thermal analysis coupled with the mass spectrometric detection of evolved gases (STA-MS) was carried out on a Netzsch STA 409 CD-QMS 403/5 Skimmer system using air-containing (oxidative) atmosphere (50 ml/min) at a heating rate of 20°/min.

CHN Analysis

The amounts of carbon, hydrogen and nitrogen in the hybrids were determined by the elemental CHN-analysis on a Euro EA3028-HT analyzer.

Raman Spectroscopy

Raman spectra were obtained on a Bruker Senterra spectrometer (spectral range 100–4,000 cm^{-1}, laser 488 nm, 20 mW, spectrum accumulation time 10 s).

IR Spectroscopy

Fourier-transformed infrared (IR) absorption spectra were recorded on a Shimadzu IRAffinity-1 spectrometer (spectral range 400–4,000 cm^{-1}, step 1 cm^{-1}) using KBr tabletting technique.

DRS

Diffuse reflectance spectroscopy (DRS) was performed using a Shimadzu UV-2550 spectrophotometer with ISR-2200 integrating sphere attachment. The Kubelka-Munk function (F) was calculated by the formula

$$F = \frac{(1-R)^2}{2R} \tag{5}$$

where R is the reflection of the sample. If the reflectance coefficient is considered to be constant, F is proportional to the absorption coefficient of the sample. The optical band gap was determined from the Tauc plot, i.e., from the cross point of linear plot sections in the coordinates $(F \cdot h\nu)^{1/2} = f(h\nu)$ corresponding to an allowed indirect transition.

SEM

The morphology of the samples was investigated by scanning electron microscopy (SEM) on the Zeiss Merlin scanning electron microscope with field emission cathode, electron optics column GEMINI-II and oil-free vacuum system. Energy-dispersive X-ray microanalysis (Oxford Instruments INCAx-act) was also carried out in order to detect the platinum co-catalyst.

BET

The specific surface area of the samples was determined using the Brunauer-Emmett-Teller (BET) method (Quadosorb SI) by measuring the amount of adsorbed nitrogen.

Photocatalytic Experiments

Experimental Technique

The photocatalyst suspension (50 mL) was placed in an external-irradiation reaction cell (**Figure 1**), equipped with a magnetic stirrer, a liquid cut-off filter and connected to a closed gas circulation system (120 mL dead volume). A medium-pressure mercury lamp DRT-125 (125W) was used as a radiation source. Light reaches the reaction cell only after passing through a thermostated at 15°C light filter solution (KCl + NaBr, 6 g/L each, 2 cm optical path), which cuts off radiation with $\lambda <$ 220 nm (**Figure 2**). During the photocatalytic reaction, hydrogen accumulates in the gas phase, which composition was analyzed by an on-line gas chromatograph at certain time intervals (Shimadzu GC-2014, Rt-Msieve 5A Column, TCD, Ar carrier). At the beginning of each experiment, the system was deaerated and argon gas was introduced at atmospheric pressure.

To prepare the suspension for the photocatalytic experiment, 30 mg of the photocatalyst sample were added to 60 mL of aqueous alcohol solution of desired concentration (the standard concentration was 1 mol.%). The suspension was shaken and left for 1 h to establish equilibrium between the photocatalyst and the solution. Straight before the experiment, each suspension was sonicated for 10 min (Elmasonic S10H ultrasound bath) to disaggregate the photocatalyst particles.

Platinum co-catalyst nanoparticles were loaded on the photocatalyst by the common method of photocatalytic platinization *in situ*. During the first experimental series, 1 ml of 2.56 $mmol \cdot L^{-1}$ H_2PtCl_6 aqueous solution was injected into the reaction suspension after the kinetic curve of hydrogen evolution for the bare sample was collected during 2 h. The concentration corresponds to 1 wt.% of Pt with respect to the catalyst, which was chosen as a standard amount. After H_2PtCl_6 was introduced into the reaction cell, the system was flushed with argon for 15 min under UV-irradiation, then the system was closed and the kinetic data were collected. Since hydrogen already evolves during these 15 min at quite a high rate, its amount at the starting point of measurement is non-zero. In the second experimental series, platinization was carried out at the beginning of the experiment without the 2 h pre-radiation period. In some experiments, the platinum content was varied in the range of 0.1–5 wt.% by the corresponding adjustment of the H_2PtCl_6 concentration.

Determination of the Apparent Quantum Efficiency

The apparent quantum efficiency of hydrogen generation ϕ was calculated by the formula

$$\varphi = \frac{\omega}{\omega_0} \tag{6}$$

where ω is the observed hydrogen evolution rate measured in $mol \cdot h^{-1}$ and ω_0 is the theoretical maximum hydrogen evolution rate, if we assume that all incident photons with energy greater than E_g are absorbed with the generation of electron-hole pairs, which subsequently lead to hydrogen reduction and alcohol oxidation with a 100% yield without recombination and other side-reactions. According to the half-reaction

$$2H^+ + 2e^- = H_2 \tag{7}$$

two electrons and thus two photons are needed to produce one hydrogen molecule. Therefore, ω_0 equals half of the incident photon flux with $\lambda < 340$ nm (I_1), which can be absorbed by the catalyst according to its bandgap. The required photon flux I_1 was determined by a differential ferrioxalate actinometry method.

At the first step, we determined the photon flux with $\lambda < 550$ nm (I_2) which corresponds to the absorption edge of ferrioxalate. For this aim we prepared the light-sensitive solution of potassium ferrioxalate (5 g) in 1 L of 0.1 M H_2SO_4, introduced 50 ml into the reaction cell and performed irradiation at the same conditions, as during photocatalytic experiments, but for shorter periods of time (10 and 20 s). The amount of generated Fe^{2+} ions was determined by the standard photometric method with the addition of 1,10-phenanthroline and acetate buffer. The calculated photon flux I_2 was 32 $mE \cdot h^{-1}$.

At the second step, we replaced the usual light filter solution (NaBr + KCl) with a 1 M solution of KNO_3, which completely cuts off light with $\lambda < 340$ nm (**Figure 2**). Then we performed the actinometric experiment again and thus determined the photon flux with $340 < \lambda < 550$ nm (I_3) which was found to be 17

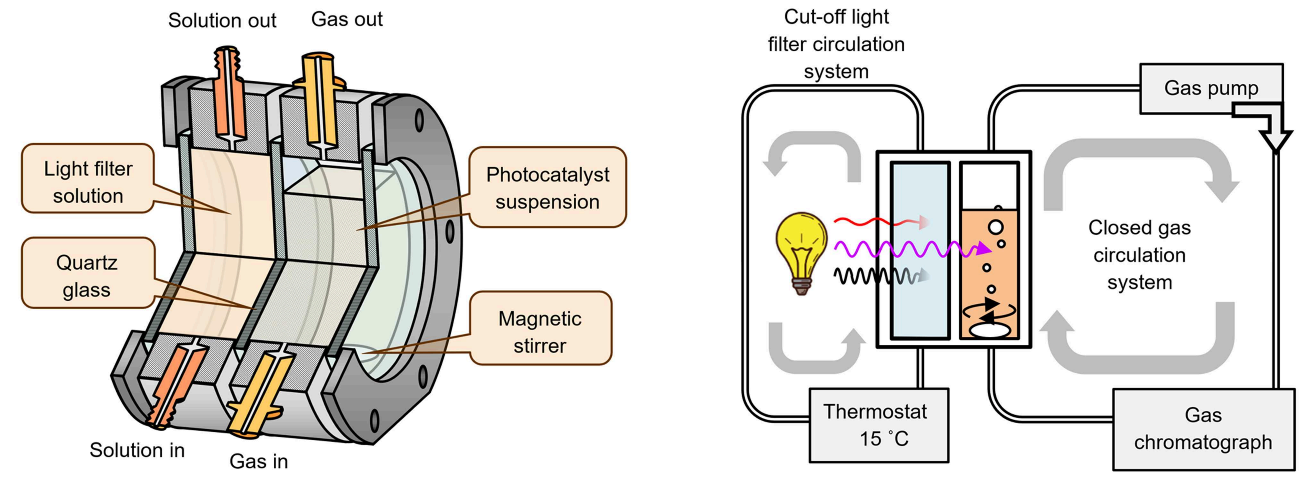

FIGURE 1 | Photocatalytic reaction cell and scheme of the photocatalytic experimental set-up.

mE·h^{-1}. Finally, we calculated the required photon flux I_1 by the difference between I_2 and I_3: 15 mE·h^{-1}. This corresponds to a theoretical hydrogen evolution rate ω_0 of 7.5 mmol·h^{-1}.

Two remarks should be made about apparent quantum efficiency ϕ, determined by this approach. On the one hand, it is the lower estimate of the true quantum efficiency, because we assume 100% light absorption by the catalyst and do not take into account any scattering. On the other hand, the ϕ value is not limited by 100% because of the possible current doubling effect (Schneider and Bahnemann, 2013).

RESULTS AND DISCUSSION

Characterization of Samples

According to powder XRD analysis (**Figure 3**), the layered oxide $K_2Nd_2Ti_3O_{10}$ was obtained as an almost single-phase product with a minor impurity of the hydrated form $K_2Nd_2Ti_3O_{10}\times H_2O$ which is a result of its contact with atmospheric moisture. After prolonged contact with 75% humid air the sample completely transformed into the hydrated phase with enlarged interlayer distance *d* (**Figure 4**). The anhydrous form was indexed in the I4/mmm space group with $a = 3.847$ Å, $c = 29.56$ Å, which is close to the literature data (ICDD #01-087-0479). The hydrated form was indexed in P4/mmm with $a = 3.834$ Å, $c = 16.65$ Å.

The ion exchange reaction in diluted hydrochloric acid led to a single-phase protonated compound $H_2Nd_2Ti_3O_{10}$ which was indexed in a C222 space group with $a = 27.18$ Å, $b = c = 3.783$ Å. The interlayer distance *d*, which in this case equals *a*/2, desreased in comparison to the initial alkaline form due to the exchange of potassium cations for more compact protons. Thermogravimetric analysis (**Figure 5**) revealed that the degree of protonation is 100% meaning that all potassium ions were successively substituted with protons. Also, the sample contained about 0.2 intercalated water molecules per formula unit, which are irreversible liberated at T > 150°C. Thus, its true composition can be expressed as $H_2Nd_2Ti_3O_{10}\cdot 0.2H_2O$.

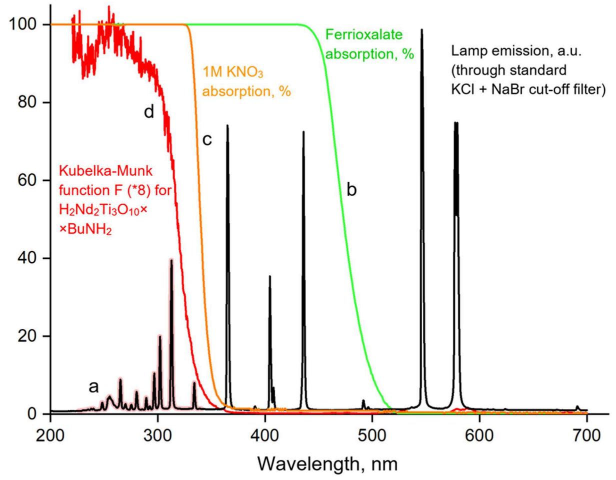

FIGURE 2 | Emission spectrum for the DRT-125 lamp used for photocatalytic experiments (a), absorption of the light-sensitive potassium ferrioxalate solution used for light intensity measurements (b), absorption of the additional KNO_3 cut-off filter (c), absorption of the $H_2Nd_2Ti_3O_{10}\times BuNH_2$ photocatalyst expressed by the Kubelka-Munk function (d).

The treatment of the $H_2Nd_2Ti_3O_{10}$ sample with methylamine solution led to a significant increase in the interlayer distance, indicating the intercalation of methylamine molecules into the interlayer space, and further exchange reaction with *n*-butylamine led to even greater expansion of the interlayer gallery (**Figure 4**). The final product $H_2Nd_2Ti_3O_{10}\times BuNH_2$ was obtained as a single phase with tetragonal symmetry, which is perfectly indexed in the simple P4/mmm space group with parameters $a = 3.802$ Å, $c = 24.70$ Å.

Thermogravimetric analysis was carried out in order to determine the content of *n*-butylamine in the sample. The TG curve (**Figure 5**) demonstrates a significant mass loss from room temperature to 400°C followed by a mass increase up to 700°C and finally the loss of mass at higher temperatures. In order

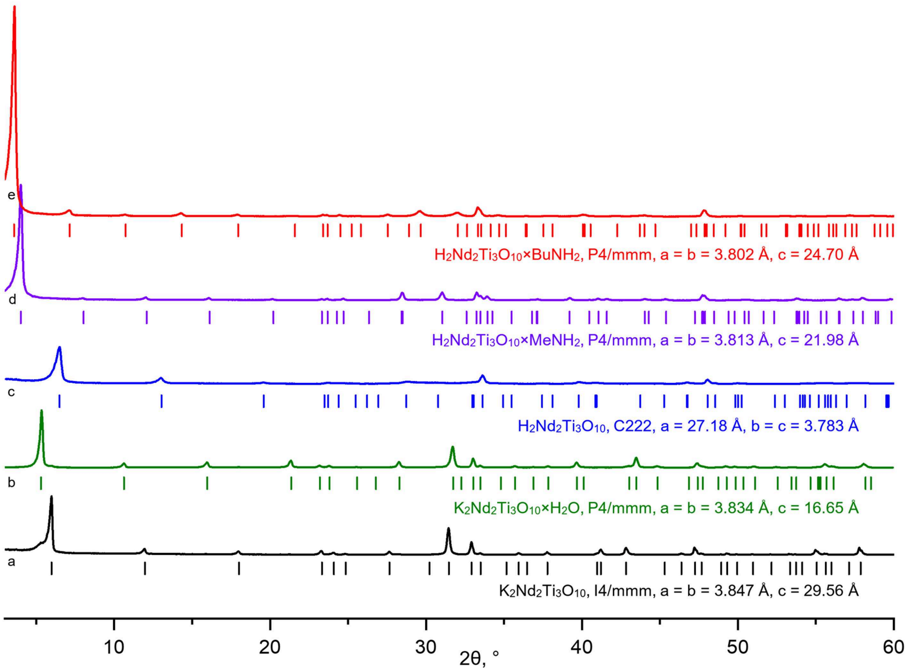

FIGURE 3 | X-ray diffraction patterns and unit cell parameters of synthesized layered titanates $K_2Nd_2Ti_3O_{10}$ (a), $K_2Nd_2Ti_3O_{10} \times H_2O$ (b), $H_2Nd_2Ti_3O_{10}$ (c) and amine-intercalated hybrid compounds $H_2Nd_2Ti_3O_{10} \times MeNH_2$ (d), $H_2Nd_2Ti_3O_{10} \times BuNH_2$ (e).

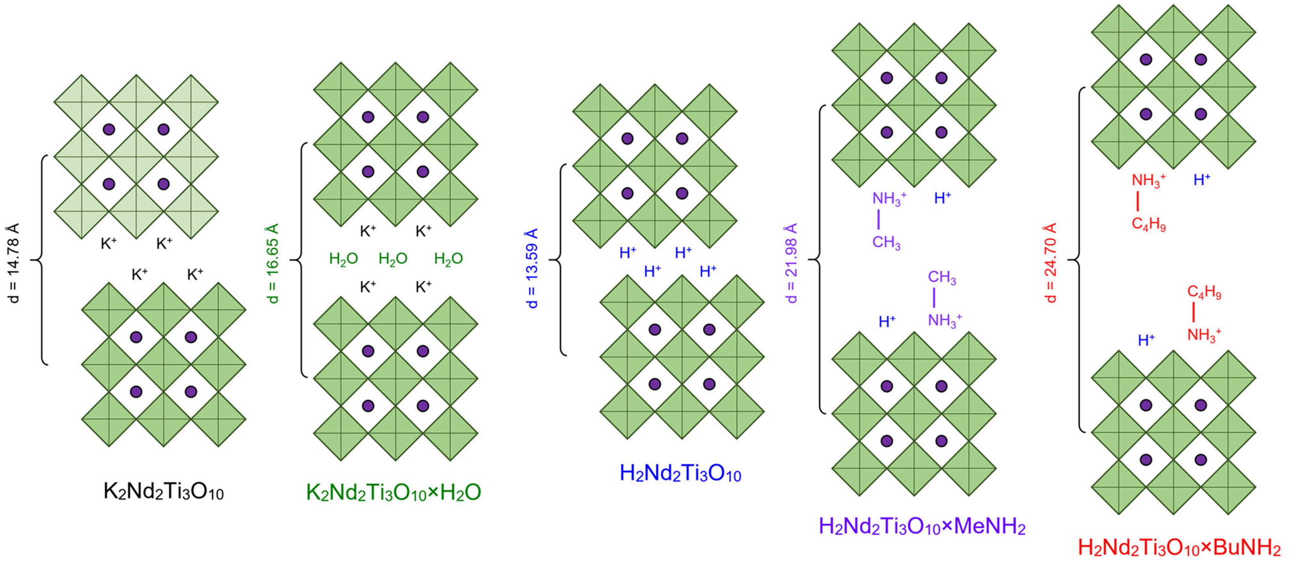

FIGURE 4 | Schematic representation of the interlayer distance change at different synthetic steps.

to explain such complex behavior, STA-MS was carried out. Mass spectrometry showed that at the first step (T < 200°C) butylamine and water are the main components which are liberated into the gas phase. Apparently, at this step we observe only the deintercalation of both compounds. At the second step (200°C < T < 500°C) not only water but also carbon dioxide is liberated, whereas the *n*-butylamine content in the gas phase gradually decreases. This may be associated with the beginning of the *n*-butylamine burning accompanied by the subsequent decomposition of the protonated $H_2Nd_2Ti_3O_{10}$ compound. At temperature about 500°C the mass of the sample begins to rise, that may be explained by the oxidation of either the remained carbon-containing species or the titanium cations, which might be reduced at lower temperatures by the reaction with organics. However, subsequent liberation of CO_2 during the mass loss after 700°C clearly indicates, that some carbon species still remain in the sample after 500°C, when all butylamine is apparently gone. After an isotherm segment at 950°C for 20 min the mass of the sample stabilizes and an overall mass loss of 12.66% is reached. If we reasonably assume, that the final composition of the sample is described by the formula $Nd_2Ti_3O_9$, then this mass loss gives us the upper estimate of the *n*-butylamine content in the sample, which is 0.9 per formula unit. While calculating this value, we also take into account the amount of H_2O formed during $H_2Nd_2Ti_3O_{10}$ decomposition. However, the sample may also contain some unknown amount of intercalated water, which contributes to the mass loss at the first step. Thus, another independent method is needed to determine the composition of the sample more precisely. The use of CHN analysis data allowed to calculate the content of the organic component in the sample, which, together with thermogravimetric data, gave us following formula of the sample: $H_2Nd_2Ti_3O_{10}\cdot 0.8BuNH_2\cdot 0.4H_2O$. Also, CHN analysis showed that the molar ratio of C/N in this sample is close to 4, which indicates complete substitution of methylamine by *n*-butylamine.

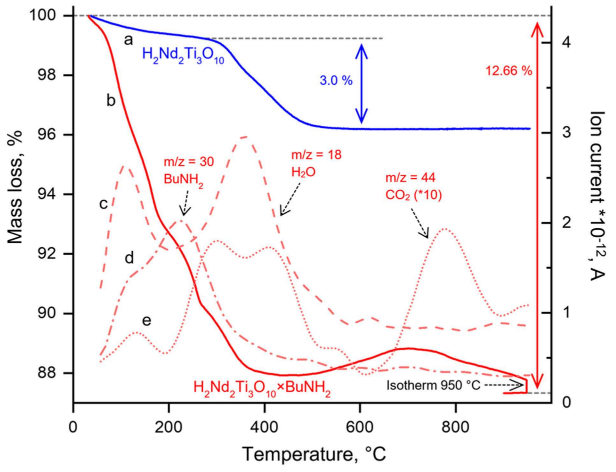

FIGURE 5 | Thermogravimetric curves for $H_2Nd_2Ti_3O_{10}$ (a), $H_2Nd_2Ti_3O_{10}\times BuNH_2$ (b) and ion currents recorded during simultaneous thermal analysis coupled with mass spectrometry at m/z = 18 (c), m/z = 30 (d), m/z = 44 (e).

Raman spectra of the protonated form and its *n*-butylamine derivative are presented in **Figure 6**. The hybrids formation is indicated by appearance of characteristic bands relating to latitudinal vibrations of C–C–H/C–N–H (1,100, 1,330 cm^{-1}), methylene (1,460 cm^{-1}) and amino fragments (1,575 cm^{-1}) as well as stretching of C–N (1,055 cm^{-1}) and C–H fragments (2,860–3,000 cm^{-1}). Intercalation of *n*-butylamine is accompanied by redistribution of some bands' intensities (265–280 and 320 cm^{-1}) and suppression of vibrations at 160–250 cm^{-1}. The band relating to the symmetric stretching mode (ν_1) of axial Ti–O bonds (810 cm^{-1} for the protonated forms) splits into two bands (765, 895 cm^{-1}) during *n*-butylamine intercalation that points at the existence of two types of octahedra with unequal axial Ti–O distances.

IR spectra of the samples **Figure 6** also indicate successful *n*-butylamine intercalation, the presence of water in the interlayer space (1,625 cm^{-1}) and stretching of its O–H

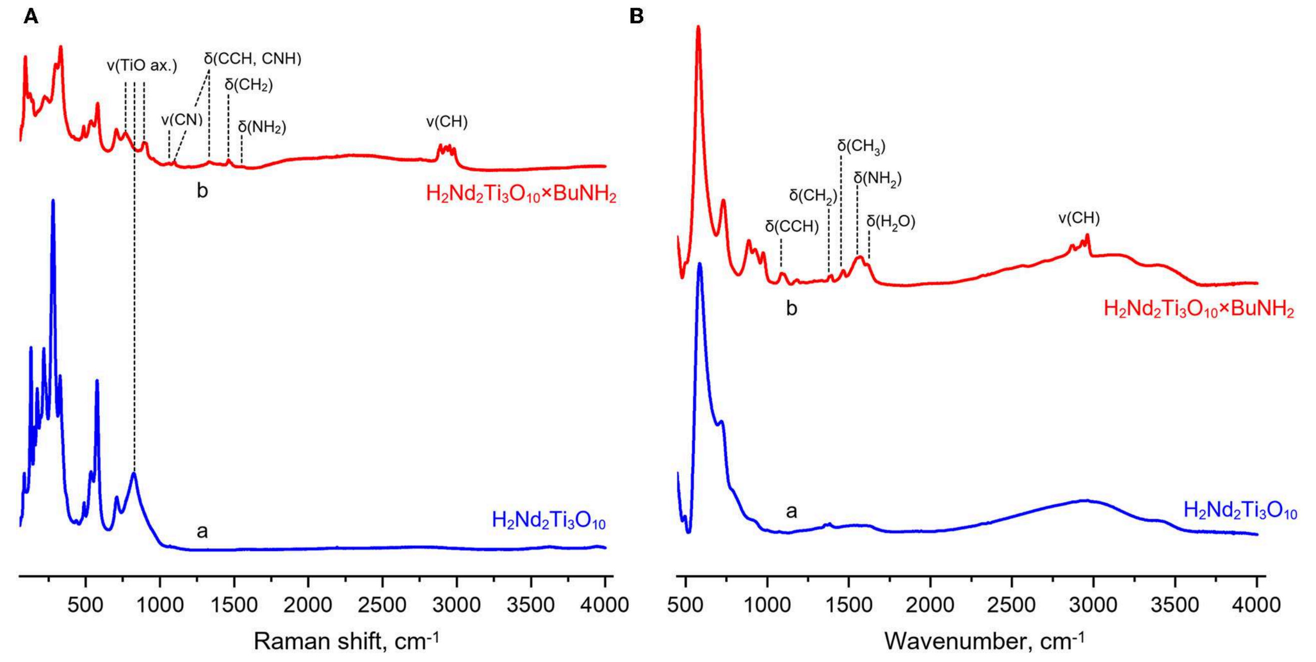

FIGURE 6 | Raman **(A)** and infrared **(B)** spectra of the protonated titanate $H_2Nd_2Ti_3O_{10}$ (a) and its butylamine-intercalated form $H_2Nd_2Ti_3O_{10}\times BuNH_2$ (b).

fragments (wide band at 2,800–3,500 cm^{-1}). Thereby, IR spectroscopy indicates joint intercalation of *n*-butylamine and water. The absence of characteristic bands at 3,500–3,300 cm^{-1} relating to unprotonated amino groups –NH_2 shows that *n*-butylamine is presented in the interlayer space in the form of *n*-butylammonium ions. This fact is well consistent with data from the earlier report (Tahara et al., 2007) where the presence of interlayer *n*-butylamine in the cationic form was confirmed using NMR spectroscopy.

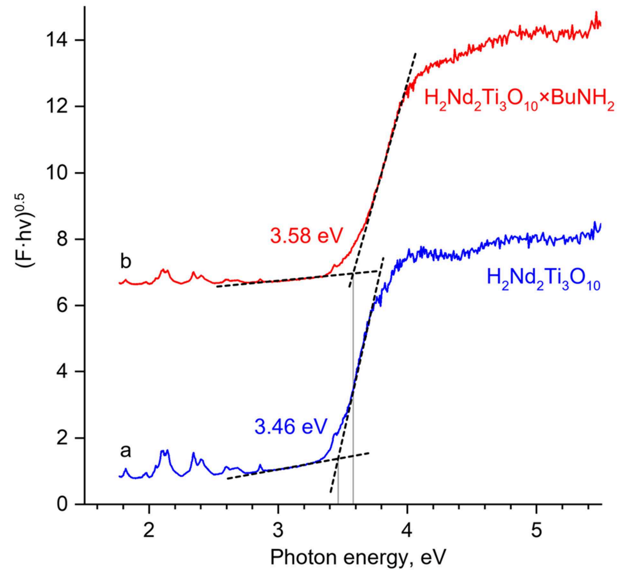

FIGURE 7 | The Tauc plots for $H_2Nd_2Ti_3O_{10}$ (a) and $H_2Nd_2Ti_3O_{10}$ × $BuNH_2$ (b) based on diffuse reflectance measurements. The Kubelka-Munk function F is plot against the photon energy hν in the coordinates (F·hν)$^{0.5}$ – hν. The bandgap energy is determined from the cross point of linear sections.

The bandgap energy of the butylamine-intercalated titanate (3.58 eV) slightly exceeds that of the initial $H_2Nd_2Ti_3O_{10}$ (3.46 eV) as can be seen from the Tauc plot of the Kubelka-Munk function (**Figure 7**). This is quite expected, because the bandgap usually increases with the increase of the interlayer distance in the absence of additional factors (Rodionov et al., 2017d). It is important, that due to the close values of band gap energy, both catalysts absorb the same peaks in the lamp emission spectrum (**Figure 2**), and thus there is no factor of different amount of available light, which could otherwise contribute to the difference in observed photocatalytic activity.

SEM investigation showed that the particle morphology of $H_2Nd_2Ti_3O_{10}$ × $BuNH_2$ is almost the same as for the initial $H_2Nd_2Ti_3O_{10}$ (**Figure 8**). We observe plate-like particles with an irregular size in the range of 100–1,000 nm that is typical for layered oxides prepared by the solid-state method. The morphology also does not considerably change after the photocatalytic experiment with platinization. The platinum nanoparticles can be observed at the SEM image as light dots with an average diameter of 4–6 nm. The EDX analysis also confirms the presence of 1 ± 0.4 wt.% platinum in this sample, which is consistent with the expected value.

The BET surface area of the $H_2Nd_2Ti_3O_{10}$ sample was found to be 21 m^2/g. Unfortunately, we were unable to measure the surface area for amine-intercalated samples due to the fact that they are unstable under vacuum conditions. However, the preservation of the particle morphology allows to assume that

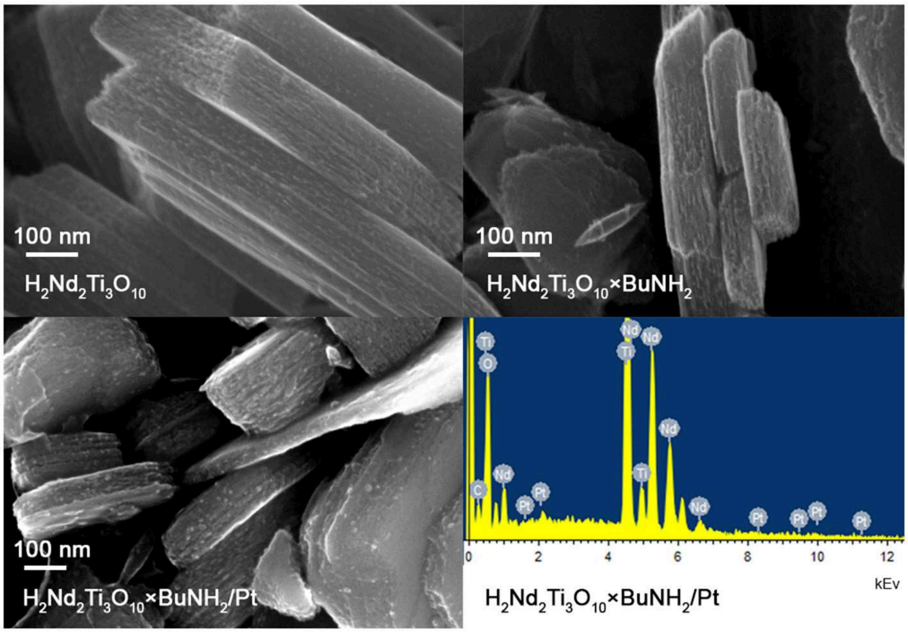

FIGURE 8 | SEM images of initial $H_2Nd_2Ti_3O_{10}$ and $H_2Nd_2Ti_3O_{10}$ × $BuNH_2$ samples, SEM image and EDX spectrum for $H_2Nd_2Ti_3O_{10}$ × $BuNH_2$/Pt sample after the photocatalytic experiment in 1% methanol solution.

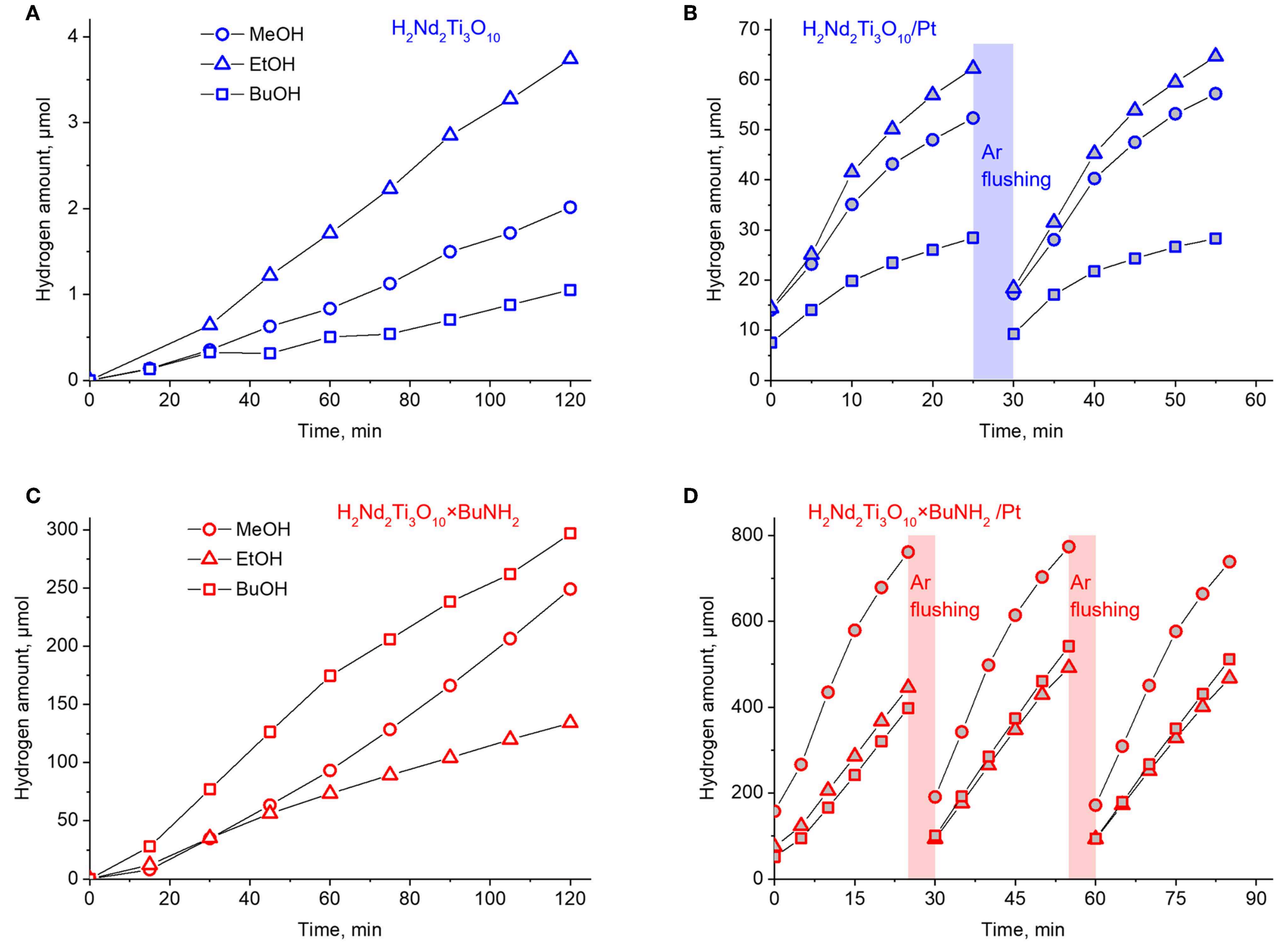

FIGURE 9 | Kinetic curves of photocatalytic hydrogen evolution over $H_2Nd_2Ti_3O_{10}$ **(A)**, $H_2Nd_2Ti_3O_{10}$/Pt **(B)**, $H_2Nd_2Ti_3O_{10}\times BuNH_2$ **(C)**, and $H_2Nd_2Ti_3O_{10}\times BuNH_2$/Pt **(D)**.

TABLE 1 | Rate of photocatalytic hydrogen evolution (ω) and its apparent quantum efficiency at 220–340 nm (ϕ) from 1 mol.% aqueous methanol, ethanol and *n*-butanol solutions over $H_2Nd_2Ti_3O_{10}$, $H_2Nd_2Ti_3O_{10}$/Pt, $H_2Nd_2Ti_3O_{10}\times BuNH_2$ and $H_2Nd_2Ti_3O_{10}\times BuNH_2$/Pt.

Photocatalyst	**Methanol**		**Ethanol**		***n*-Butanol**	
	ω, mmol/h	**ϕ, %**	**ω, mmol/h**	**ϕ, %**	**ω, mmol/h**	**ϕ, %**
$H_2Nd_2Ti_3O_{10}$	0.0011	0.015	0.0020	0.027	0.00057	0.0076
$H_2Nd_2Ti_3O_{10}$/Pt	0.12	1.6	0.15	2.0	0.064	0.86
$H_2Nd_2Ti_3O_{10}\times BuNH_2$	0.12	1.7	0.077	1.0	0.20	2.6
$H_2Nd_2Ti_3O_{10}\times BuNH_2$/Pt	1.7	23	1.0	14	1.1	15

at least the outside surface area of the samples does not change much as a result of intercalation.

Photocatalytic Activity

The results of photocatalytic experiments are presented in **Figure 9**. In each case the hydrogen evolution rate *ω* was calculated from the slope of the kinetic curve. In case when the curve is not linear, the initial rate was calculated from the first points by linear approximation. These data, as well as the calculated values of apparent quantum efficiency *ϕ*, are summarized in **Table 1**. The standard error of hydrogen evolution rate determined in this way is estimated as 7%.

The protonated titanate $H_2Nd_2Ti_3O_{10}$ demonstrates a very low photocatalytic activity with a quantum efficiency of hydrogen generation in the range of 0.01–0.03% depending on the alcohol nature. After 1 wt.% platinum was loaded on it as a co-catalyst, the hydrogen evolution rate significantly increased and the quantum efficiency reached 2% in the case of ethanol. This is quite expected because platinum nanoparticles serve both for the improved charge separation and as active hydrogen evolution sites. Note that both the platinized and non-platinized $H_2Nd_2Ti_3O_{10}$ showed the maximum hydrogen evolution rate for ethanol rather than methanol. Probably, this is due to the fact that ethanol is a slightly stronger reducing agent.

For the platinized sample the hydrogen evolution rate decreases with time, but restores its original value after flushing the gas system with argon. Thus, we can conclude that the

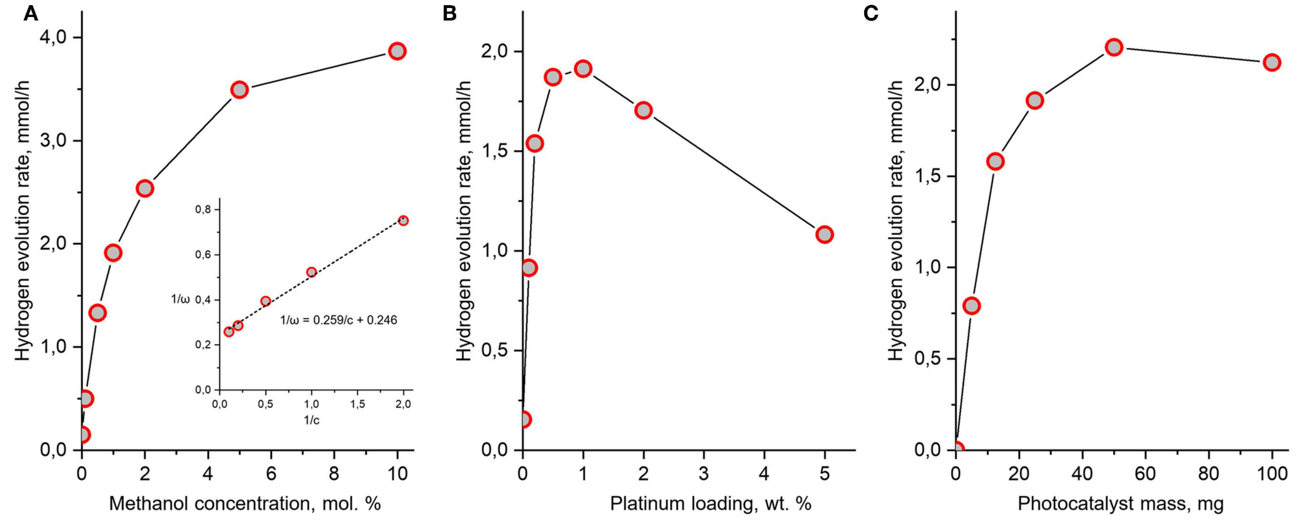

FIGURE 10 | Dependence of hydrogen evolution rate over $H_2Nd_2Ti_3O_{10} \times BuNH_2/Pt$ on methanol concentration **(A)**, platinum loading **(B)**, and photocatalyst mass **(C)**. Unless varied, the methanol concentration is 1 mol.%, the platinum content is 1 wt.% and the mass of photocatalyst is 25 mg in every experiment.

deceleration is associated with the accumulation of hydrogen in the gas phase which may give rise to some backward reactions involving hydrogen and alcohol oxidation products (i.e., aldehydes) as reactants.

After *n*-butylamine was introduced into the interlayer space, the photocatalytic activity of the bare titanate increased to almost the same level as for the platinized non-intercalated sample in the case of methanol. It is known, that the interlayer space plays an important role in the reaction of water splitting by alkaline forms of triple-layered titanates $A_2Ln_2Ti_3O_{10}$ (A = alkaline metal, Ln = La, Nd). Remarkable activity is observed only for K- and Rb-containing compounds, which are capable of spontaneous water intercalation, whereas Li- and Na-containing compounds do not undergo water intercalation and show almost no activity. A similar relationship is also noticed for triple-layered Dion-Jacobson phases. Thus, the increased photocatalytic activity may be explained by the expansion of the interlayer space by *n*-butylamine, which allows the alcohol substrate molecules to intercalate and undergo oxidation between the perovskite layers. Surprisingly, in this case the maximum quantum efficiency of 2.6% was observed for *n*-butanol, which showed the worst performance for initial $H_2Nd_2Ti_3O_{10}$. The reason is not quite clear yet, but it may be due to the similarity of *n*-butanol and *n*-butylamine molecules, which facilitates the incorporation of alcohol molecules in the interlayer space during the reaction.

Finally, after platinization *in situ* the photocatalytic activity of $H_2Nd_2Ti_3O_{10} \times BuNH_2$ increased by one order of magnitude. This time the best quantum efficiency (23%) was achieved in the case of methanol, whereas ethanol and *n*-butanol gave 14–15%. The effect of reaction rate decay with time is also noted here, but it is not as significant as in the previous case. Thus, the effects of *n*-butylamine intercalation and platinization together gave rise to a much higher efficiency, than any of them separately. The reason is probably that these two modification methods affect different parts of the photocatalytic system and thus different reaction steps. While *n*-butylamine is likely to promote the alcohol oxidation in the interlayer space, the platinum co-catalyst particles facilitate the hydrogen reduction on the surface. Since during photocatalysis the oxidation and reduction reactions should proceed at the same rate, if only one of them is promoted, then the other may become rate-limiting. But if both are promoted, the rate of the whole process increases much more efficiently.

During the photocatalytic experiment with $H_2Nd_2Ti_3O_{10} \times BuNH_2/Pt$ in 1 mol.% methanol solution hydrogen was formed with a total amount of ca. 2.5 mmol. The mass of photocatalyst in each experiment was 25 mg. Thus, even if we assume the content of *n*-butylamine in the sample to be equal to its upper limit according to TGA data (0.9 per formula unit), the total amount of *n*-butylamine in the reaction system is only 0.034 mmol. That means a more than 70-fold excess of hydrogen was generated without significant loss of reaction rate. Therefore, we can conclude that the reaction proceeds catalytically and that hydrogen is formed from the reaction solution rather than from the intercalated amine.

Since the maximum efficiency was observed for $H_2Nd_2Ti_3O_{10} \times BuNH_2/Pt$ in methanol solution, we decided to investigate this photocatalytic system more extensive. Particularly, we studied the effect of different operating conditions, such as methanol concentration, amount of platinum loaded and the catalyst amount on the hydrogen evolution rate. We stated 1 mol.% methanol concentration, 1 wt.% platinum loading and 25 mg photocatalyst mass as standard conditions and varied one of these parameters in each experiment series. Unlike in previous cases, this time we added H_2PtCl_6 straight at the beginning of the experiment to obtain the platinized photocatalyst immediately. The results are presented at **Figure 10**.

Usually, the dependence of photocatalytic reaction rate ω on the substrate concentration c is described by the Langmuir-Hinshelwood equation

$$\omega = \frac{kKc}{Kc + 1} \quad (8)$$

where k is the apparent rate constant, K is the adsorption constant of the substrate by the catalyst. If this is the case, a linear relation between ω^{-1} and c^{-1} should be present. As can be seen from **Figure 10**, such a relation between the hydrogen evolution rate and methanol concentration is indeed observed. Like usual, the reaction order with respect to methanol gradually decreases with the increase of its concentration. However, in our case the Langmuir-Hinshelwood equation is obeyed only at methanol concentrations higher than 0.5 mol.%. At lower concentrations there are deviations caused by the fact that the hydrogen evolution rate from water without methanol is not zero, but has a significant value of 0.15 mmol/h ($\phi = 2\%$). Since methanol is not the only reactant which can act as a source of hydrogen, but there is also water, the kinetics of the overall reaction cannot be fully described by the simple Equation (8).

At standard conditions (1 mol.% methanol) the measured hydrogen evolution rate was 1.9 mmol/h that is somewhat greater, than in the first experimental series (1.7 mmol/h). This is due to the fact that the platinization was performed immediately at the start of the experiment thus preventing any possible undesired processes, which may occur with the bare catalyst during the first 2 h of experiment, such as partial degradation *n*-butylamine or sedimentation.

The maximum hydrogen evolution rate (3.9 mmol/h) was observed at the maximum methanol concentration (10 mol.%) and corresponds to an apparent quantum efficiency as high as 52%.

The dependence of photocatalytic activity on the amount of loaded platinum co-catalyst represents a curve with a maximum around 1 wt.%. Such type of dependence has been reported earlier for many photocatalytic systems, including layered oxides (Kudo et al., 1988; Cui et al., 2006; Rodionov et al., 2014), but the position of the maximum always depends on the nature of the photocatalyst and co-catalyst. Thus, our standard platinum content of 1 wt.% was found to be optimal accidentally. The slow decay of hydrogen evolution rate at higher platinum content is explained by the increased light shielding of the catalyst by the platinum particles.

Finally, the observed dependence of the hydrogen evolution rate on the catalyst amount is also consistent with known examples (Minero and Vione, 2006). At low catalyst concentrations a linear dependence is observed due to the light absorption being proportional to the suspension turbidity. When the catalyst concentration is so high that almost no light transmits through the suspension, the dependence reaches saturation and the change of catalyst amount does not considerably affect the reaction rate. If the catalyst concentration is set even higher, a slow decay of reaction rate is observed due to increased light scattering. In the conditions of our experiment, the maximum efficiency is observed around 50 mg of catalyst and it is only 15% higher than at the standard amount of 25 mg. The optimal catalyst concentration is therefore 1 g/L, which is consistent with literature data for other systems.

CONCLUSIONS

We have discovered, that the intercalation of *n*-butylamine is an efficient method to improve the photocatalytic activity of the protonated triple-layered titanate $H_2Nd_2Ti_3O_{10}$ in the reaction of hydrogen production from aqueous solutions of methanol, ethanol and *n*-butanol. The obtained hybrid photocatalyst $H_2Nd_2Ti_3O_{10} \times BuNH_2/Pt$ demonstrated an apparent quantum efficiency of 52% in the wavelength range of 220–340 nm. The hydrogen evolution rate was stable with time and the amount of generated hydrogen exceeded the amount of intercalated *n*-butylamine more than 70 times, indicating that hydrogen is produced from the alcohol solution rather than from the intercalated amine. The dependences of photocatalytic activity on operating conditions, such as alcohol concentration, platinum co-catalyst content and catalyst loading are well-described by the usual theoretical approaches for heterogeneous photocatalysis. We propose that the intercalation of amines is an effective strategy to improve photocatalytic properties of protonated layered oxides that can be applied to other related compounds as well. At the present moment we investigate carefully the composition, structure and properties of the samples which are obtained after photocatalytic experiments, including the platinized samples. It is important to explore what changes occur in the interlayer space during the reaction. Also, further studies involving different amines and different layered oxides are in progress.

DATA AVAILABILITY STATEMENT

The datasets generated for this study are available on request to the corresponding author.

AUTHOR CONTRIBUTIONS

IR, OS, and IZ contributed the conception and design of the study. Experimental work was carried out by EM (photocatalytic experiments, quantum efficiency), SK and AP (synthesis, characterization) under supervision of IR and OS. IR wrote the manuscript and prepared images with contributions of OS, EM, and IZ in certain sections. All authors participated in the analysis and discussion of obtained results.

FUNDING

This study was financially supported by the Russian Science Foundation (Project No. 19-13-00184).

ACKNOWLEDGMENTS

The study was technically supported by the Saint Petersburg State University Research Park. The authors were grateful to the Center of Thermal Analysis and Calorimetry (TG and STA studies), Research Centre for X-ray Diffraction Studies (XRD studies), Chemistry Educational Centre (GC for photocatalytic experiments, DRS), Centre for Chemical Analysis and Materials Research (IR spectroscopy, CHN analysis), Interdisciplinary Resource Centre for Nanotechnology (SEM), Centre for Optical and Laser Materials Research (Raman spectroscopy), Centre for Diagnostics of Functional Materials for Medicine, Pharmacology and Nanoelectronics (BET).

REFERENCES

Akbarian-Tefaghi, S., and Wiley, J. B. (2018). Microwave-assisted routes for rapid and efficient modification of layered perovskites. *Dalt. Trans.* 47, 2917–2924. doi: 10.1039/C7DT03865H

Boykin, J. R., and Smith, L. J. (2015). Rapid microwave-assisted grafting of layered perovskites with n-alcohols. *Inorg. Chem.* 54, 4177–4179. doi: 10.1021/ic503001w

Chen, W., Li, C., Gao, H., Yuan, J., Shangguan, W., Su, J., et al. (2012). Photocatalytic water splitting on protonated form of layered perovskites $K_{0.5}La_{0.5}Bi_2M_2O_9$ (M = Ta; Nb) by ion-exchange. *Int. J. Hydrogen Energy* 37, 12846–12851. doi: 10.1016/j.ijhydene.2012.05.090

Compton, O. C., Carroll, E. C., Kim, J. Y., Larsen, D. S., and Osterloh, F. E. (2007). Calcium niobate semiconductor nanosheets as catalysts for photochemical hydrogen evolution from water. *J. Phys. Chem. C* 111, 14589–14592. doi: 10.1021/jp0751155

Cui, W., Guo, D., Liu, L., Hu, J., Rana, D., and Liang, Y. (2014). Preparation of $ZnIn_2S_4/K_2La_2Ti_3O_{10}$ composites and their photocatalytic H_2 evolution from aqueous Na_2S/Na_2SO_3 under visible light irradiation. *Catal. Commun.* 48, 55–59. doi: 10.1016/j.catcom.2014.01.026

Cui, W., Liu, L., Feng, L., Xu, C., Li, Z., Lü, S., et al. (2006). Preparation of $Pt/K_2La_2Ti_3O_{10}$ and its photo-catalytic activity for hydrogen evolution from methanol water solution. *Sci. China Ser. B Chem.* 49, 162–168. doi: 10.1007/s11426-006-0162-6

Cui, W., Liu, L., Ma, S., Liang, Y., and Zhang, Z. (2013). CdS-sensitized $K_2La_2Ti_3O_{10}$ composite: a new photocatalyst for hydrogen evolution under visible light irradiation. *Catal. Today* 207, 44–49. doi: 10.1016/j.cattod.2012.05.009

Cui, W., Qi, Y., Liu, L., Rana, D., Hu, J., and Liang, Y. (2012). Synthesis of $PbS–K_2La_2Ti_3O_{10}$ composite and its photocatalytic activity for hydrogen production. *Prog. Nat. Sci. Mater. Int.* 22, 120–125. doi: 10.1016/j.pnsc.2012.03.002

Gómez-Romero, P., and Sanchez, C. (2006). *Functional Hybrid Materials*. Weinheim: Wiley-VCH Verlag GmbH & Co. KGaA.

Gopalakrishnan, J., and Bhat, V. (1987). $A_2Ln_2Ti_3O_{10}$ (A = potassium or rubidium; Ln = lanthanum or rare earth): a new series of layered perovskites exhibiting ion exchange. *Inorg. Chem.* 26, 4299–4301. doi: 10.1021/ic00273a001

Guo, T., Wang, L., Evans, D. G., and Yang, W. (2010). Synthesis and photocatalytic properties of a polyaniline-intercalated layered protonic titanate nanocomposite with a p–n heterojunction structure. *J. Phys. Chem. C* 114, 4765–4772. doi: 10.1021/jp9055413

Han, Y.-S., Park, I., and Choy, J.-H. (2001). Exfoliation of layered perovskite, $KCa_2Nb_3O_{10}$, into colloidal nanosheets by a novel chemical process. *J. Mater. Chem.* 11, 1277–1282. doi: 10.1039/b006045n

Hong, Y., and Kim, S.-J. (1996). Intercalation of primary diamines in the layered perovskite oxides, $HSr_2Nb_3O_{10}$. *Bull. Korean Chem. Soc.* 17, 730–735.

Huang, Y., Li, J., Wei, Y., Li, Y., Lin, J., and Wu, J. (2009). Fabrication and photocatalytic property of Pt-intercalated layered perovskite niobates $H_{1-x}LaNb_{2-x}MoxO_7$ (x=0–0.15). *J. Hazard. Mater.* 166, 103–108. doi: 10.1016/j.jhazmat.2008.11.040

Huang, Y., Li, Y., Wei, Y., Huang, M., and Wu, J. (2011). Photocatalytic property of partially substituted Pt-intercalated layered perovskite, $ASr_2TaxNb_{3-x}O_{10}$ (A=K, H; x = 0, 1, 1.5, 2 and 3). *Sol. Energy Mater. Sol. Cells* 95, 1019–1027. doi: 10.1016/j.solmat.2010.12.017

Huang, Y., Wu, J., Li, T., Hao, S., and Lin, J. (2006). Synthesis and photocatalytic properties of $H_2La_2Ti_3O_{10}/TiO_2$ intercalated nanomaterial. *J. Porous Mater.* 13, 55–59. doi: 10.1007/s10934-006-5490-6

Ida, S., Ogata, C., Eguchi, M., Youngblood, W. J., Mallouk, T. E., Matsumoto, Y., et al. (2008). Photoluminescence of perovskite nanosheets prepared by exfoliation of layered oxides, $K_2Ln_2Ti_3O_{10}$, $KLnNb_2O_7$, and $RbLnTa_2O_7$ (Ln: lanthanide ion). *J. Am. Chem. Soc.* 130, 7052–7059. doi: 10.1021/ja7114772

Jacobson, A. J., Johnson, J. W., and Lewandowski, J. (1987). Intercalation of the layered solid acid $HCa_2Nb_3O_{10}$ by organic amines. *Mater. Res. Bull.* 22, 45–51. doi: 10.1016/0025-5408(87)90148-6

Kawashima, K., Hojamberdiev, M., Chen, S., Yubuta, K., Wagata, H., Domen, K., et al. (2017a). Understanding the effect of partial N^{3-}-to-O^{2-} substitution and H^+-to-K^+ exchange on photocatalytic water reduction activity of Ruddlesden-Popper layered perovskite $KLaTiO_4$. *Mol. Catal.* 432, 250–258. doi: 10.1016/j.mcat.2017.01.004

Kawashima, K., Hojamberdiev, M., Wagata, H., Yubuta, K., Domen, K., and Teshima, K. (2017b). Protonated oxide, nitrided, and reoxidized $K_2La_2Ti_3O_{10}$ crystals: visible-light-induced photocatalytic water oxidation and fabrication of their nanosheets. *ACS Sustain. Chem. Eng.* 5, 232–240. doi: 10.1021/acssuschemeng.6b01344

Kickelbick, G. (2007). *Hybrid Materials: Synthesis, Characterization, and Applications*. Weinheim: Wiley-VCH Verlag GmbH & Co. KGaA.

Kudo, A., Tanaka, A., Domen, K., Maruya, K., Aika, K., and Onishi, T. (1988). Photocatalytic decomposition of water over $NiO-K_4Nb_6O_{17}$ catalyst. *J. Catal.* 111, 67–76. doi: 10.1016/0021-9517(88)90066-8

Kumar, V., Govind, and Uma, S. (2011). Investigation of cation (Sn^{2+}) and anion (N^{3-}) substitution in favor of visible light photocatalytic activity in the layered perovskite $K_2La_2Ti_3O_{10}$. *J. Hazard. Mater.* 189, 502–508. doi: 10.1016/j.jhazmat.2011.02.064

Liu, C., Wu, L., Chen, J., Liang, J. Y., Li, C. S., Ji, H. M., et al. (2014). The nanocomposite of polyaniline and nitrogen-doped layered $HTiNbO_5$with excellent visible-light photocatalytic performance. *Phys. Chem. Chem. Phys.* 16, 13409–13417. doi: 10.1039/C4CP01423E

Liu, Y., Zhou, Y., Lv, C., Zhang, C., Jin, X., Meng, Q., et al. (2018). Construction of 2D-composite $HCa_2Nb_3O_{10}/CaNb_2O_6$ heterostructured photocatalysts with enhanced hydrogen production performance. *New J. Chem.* 42, 681–687. doi: 10.1039/C7NJ03707D

Machida, M., Mitsuyama, T., Ikeue, K., Matsushima, S., and Arai, M. (2005). Photocatalytic property and electronic structure of triple-layered perovskite tantalates, $MCa_2Ta_3O_{10}$ (M = Cs, Na, H, and $C_6H_{13}NH_3$). *J. Phys. Chem. B* 109, 7801–7806. doi: 10.1021/jp044833d

Maeda, K. (2011). Photocatalytic water splitting using semiconductor particles: history and recent developments. *J. Photochem. Photobiol. C Photochem. Rev.* 12, 237–268. doi: 10.1016/j.jphotochemrev.2011.07.001

Minero, C., and Vione, D. (2006). A quantitative evalution of the photocatalytic performance of TiO_2 slurries. *Appl. Catal. B Environ.* 67, 257–269. doi: 10.1016/j.apcatb.2006.05.011

Reddy, V., Hwang, D., and Lee, J. (2003). Effect of Zr substitution for Ti in $KLaTiO_4$ for photocatalytic water splitting. *Catal. Lett.* 90, 39–44. doi: 10.1023/A:1025812125852

Richard, M., Brohan, L., and Tournoux, M. (1994). Synthesis, characterization, and acid exchange of the layered perovskites: $A_2Nd_2Ti_3O_{10}$ (A–Na, K). *J. Solid State Chem.* 112, 345–354. doi: 10.1006/jssc.1994.1315

Rodionov, I. A., Fateev, S. A., and Zvereva, I. A. (2017a). Effect of protonation on the photocatalytic activity of the layered titanate $Rb_2Nd_2Ti_3O_{10}$. *Russ. J. Gen. Chem.* 87, 2728–2729. doi: 10.1134/S1070363217110317

Rodionov, I. A., Fateev, S. A., and Zvereva, I. A. (2017b). Synthesis of a new layered $Rb_2Nd_2Ti_3O_{10}$ oxide, its hydration and protonation. *Glas. Phys. Chem.* 43, 593–596. doi: 10.1134/S1087659617060128

Rodionov, I. A., Mechtaeva, E. V., Burovikhina, A. A., Silyukov, O. I., Toikka, M. A., and Zvereva, I. A. (2017c). Effect of protonation on the photocatalytic activity of the $K_2La_2Ti_3O_{10}$ layered oxide in the reaction of hydrogen production. *Mon. Chem.* 149, 475–482. doi: 10.1007/s00706-017-2105-7

Rodionov, I. A., Mechtaeva, E. V., and Zvereva, I. A. (2014). Photocatalytic activity of TiO_2-MO_x composites in the reaction of hydrogen generation from aqueous isopropanol solution. *Russ. J. Gen. Chem.* 84, 611–616. doi: 10.1134/S107036321404001X

Rodionov, I. A., Silyukov, O. I., Utkina, T. D., Chislov, M. V., Sokolova, Y. P., and Zvereva, I. A. (2012). Photocatalytic properties and hydration of perovskite-type layered titanates $A_2Ln_2Ti_3O_{10}$ (A = Li, Na, K; Ln = La, Nd). *Russ. J. Gen. Chem.* 82, 1191–1196. doi: 10.1134/S1070363212070018

Rodionov, I. A., Sokolova, I. P., Silyukov, O. I., Burovikhina, A. A., Fateev, S. A., and Zvereva, I. A. (2017d). Protonation and photocatalytic activity of the $Rb_2La_2Ti_3O_{10}$ layered oxide in the reaction of hydrogen production. *Int. J. Photoenergy* 2017, 1–8. doi: 10.1155/2017/9628146

Rodionov, I. A., and Zvereva, I. A. (2016). Photocatalytic activity of layered perovskite-like oxides in practically valuable chemical reactions. *Russ. Chem. Rev.* 85, 248–279. doi: 10.1070/RCR4547

Sabio, E. M., Chamousis, R. L., Browning, N. D., and Osterloh, F. E. (2012). Photocatalytic water splitting with suspended calcium niobium oxides: why nanoscale is better than bulk–a kinetic analysis. *J. Phys. Chem. C* 116, 3161–3170. doi: 10.1021/jp209006n

Sato, S., Shintani, K., Idota, N., Nishino, T., and Sugahara, Y. (2017). Effect of the graft density of cellulose diacetate-modified layered perovskite nanosheets on mechanical properties of the transparent organic–inorganic hybrids bearing covalent bonds at the interface. *Cellulose* 24, 5463–5473. doi: 10.1007/s10570-017-1475-7

Schneider, J., and Bahnemann, D. W. (2013). Undesired role of sacrificial reagents in photocatalysis. *J. Phys. Chem. Lett.* 4, 3479–3483. doi: 10.1021/jz4018199

Shelyapina, M. G., Nefedov, D. Y., Kostromin, A. V., Silyukov, O. I., and Zvereva, I. A. (2019). Proton mobility in Ruddlesden–Popper phase H2La2Ti3O10 studied by 1H NMR. *Ceram. Int.* 45, 5788–5795. doi: 10.1016/j.ceramint.2018.12.045

Shimizu, K., Itoh, S., Hatamachi, T., Kitayama, Y., and Kodama, T. (2006). Pillaring of Ruddlesden–Popper perovskite tantalates, $H_2ATa_2O_7$ (A = Sr or $La_2/_3$), with n-alkylamines and oxide nanoparticles. *J. Mater. Chem.* 16:773–779. doi: 10.1039/B514066H

Shori, S., Pellechia, P. J., zur Loye, H.-C., and Ploehn, H. J. (2015). Covalent grafting of phenylphosphonate on calcium niobate platelets. *J. Colloid Interface Sci.* 437, 97–110. doi: 10.1016/j.jcis.2014.09.024

Silyukov, O. I., Abdulaeva, L. D., Burovikhina, A. A., Rodionov, I. A., and Zvereva, I. A. (2015). Phase transformations during $HLnTiO_4$ (Ln=La, Nd) thermolysis and photocatalytic activity of obtained compounds. *J. Solid State Chem.* 226, 101–106. doi: 10.1016/j.jssc.2015.02.008

Silyukov, O. I., Kurnosenko, S. A., and Zvereva, I. A. (2018). Intercalation of methylamine into the protonated forms of layered perovskite-like oxides $HLnTiO_4$ (Ln = La and Nd). *Glas. Phys. Chem.* 44, 428–432. doi: 10.1134/S1087659618050176

Tahara, S. (2007). *Preparation of inorganic-organic hybrids via intercalation and grafting reactions of protonated forms of ion-exchangeable layered perovskites* (Dissertation thesis), Waseda University, Tokyo, Japan.

Tahara, S., Ichikawa, T., Kajiwara, G., and Sugahara, Y. (2007). Reactivity of the Ruddlesden–Popper phase H2La2Ti3O10 with organic compounds: intercalation and grafting reactions. *Chem. Mater.* 19, 2352–2358. doi: 10.1021/cm0623662

Takahashi, S., Nakato, T., Hayashi, S., Sugahara, Y., and Kuroda, K. (1995). Formation of a methoxy-modified interlayer surface via the reaction between methanol and layered perovskite $HLaNb_2O_{7x}H_2O$. *Inorg. Chem.* 34, 5065–5069. doi: 10.1021/ic00124a023

Takata, T., Furumi, Y., Shinohara, K., Tanaka, A., Hara, M., Kondo, J. N., et al. (1997a). Photocatalytic decomposition of water on spontaneously hydrated layered perovskites. *Chem. Mater.* 9, 1063–1064. doi: 10.1021/cm960612b

Takata, T., Shinohara, K., Tanaka, A., Hara, M., Kondo, J. N., and Domen, K. (1997b). A highly active photocatalyst for overall water splitting with a hydrated layered perovskite structure. *J. Photochem. Photobiol. A Chem.* 106, 45–49. doi: 10.1016/S1010-6030(97)00037-3

Takeda, Y., Momma, T., Osaka, T., Kuroda, K., and Sugahara, Y. (2008). Organic derivatives of the layered perovskite $HLaNb_2O_7 \cdot xH_2O$ with polyether chains on the interlayer surface: characterization, intercalation of $LiClO_4$, and ionic conductivity. *J. Mater. Chem.* 18:3581–3587. doi: 10.1039/b802003e

Takeda, Y., Suzuki, H., Notsu, K., Sugimoto, W., and Sugahara, Y. (2006). Preparation of a novel organic derivative of the layered perovskite bearing $HLaNb_2O_7 \cdot nH_2O$ interlayer surface trifluoroacetate groups. *Mater. Res. Bull.* 41, 834–841. doi: 10.1016/j.materresbull.2005.10.004

Tong, Z., Zhang, G., Takagi, S., Shimada, T., Tachibana, H., and Inoue, H. (2005). Preparation and characterization of a transparent thin film of the layered perovskite, $K_2La_2Ti_3O_{10}$, intercalated with an ionic porphyrin. *Chem. Lett.* 34, 632–633. doi: 10.1246/cl.2005.632

Tsunoda, Y., Sugimoto, W., and Sugahara, Y. (2003). Intercalation behavior of n-alkylamines into a protonated form of a layered perovskite derived from aurivillius phase $Bi_2SrTa_2O_9$. *Chem. Mater.* 15, 632–635. doi: 10.1021/cm0200893

Uma, S., and Gopalakrishnan, J. (1994). Synthesis of anion-deficient layered perovskites, $ACa_2Nb_{3-x}M_xO_{10-x}$ (A = Rb, Cs; M = Al, Fe), exhibiting ion-exchange and intercalation. evidence for the formation of layered brownmillerites, $ACa_2Nb_2AlO_9$ (A = Cs, H). *Chem. Mater.* 6, 907–912. doi: 10.1021/cm00043a008

Uma, S., and Gopalakrishnan, J. (1995). Polymerization of aniline in layered perovskites. *Mater. Sci.* 34, 175–179. doi: 10.1016/0921-5107(95)01235-4

Utkina, T., Chislov, M., Myshenkov, M., Rodionov, I., and Zvereva, I. (2018). Water sorption by the perovskite-like layered titanate $K_2Nd_2Ti_3O_{10}$ in humid atmosphere. *J. Therm. Anal. Calorim.* 134, 323–331. doi: 10.1007/s10973-018-7017-1

Wang, B., Dong, X., Pan, Q., Cheng, Z., and Yang, Y. (2007). Intercalation behavior of n-alkylamines into an A-site defective layered perovskite $H_2W_2O_7$. *J. Solid State Chem.* 180, 1125–1129. doi: 10.1016/j.jssc.2007.01.009

Wang, C., Tang, K., Wang, D., Liu, Z., Wang, L., Zhu, Y., et al. (2012). A new carbon intercalated compound of Dion–Jacobson phase $HLaNb_2O_7$. *J. Mater. Chem.* 22:11086. doi: 10.1039/c2jm14902h

Wang, Y., Nikolopoulou, M., Delahaye, E., Leuvrey, C., Leroux, F., Rabu, P., et al. (2018). Microwave-assisted functionalization of the Aurivillius phase $Bi_2SrTa_2O_9$: diol grafting and amine insertion vs. alcohol grafting. *Chem. Sci.* 9, 7104–7114. doi: 10.1039/C8SC01754A

Wang, Y., Wang, C., Wang, L., Hao, Q., Zhu, X., Chen, X., et al. (2014). Preparation of interlayer surface tailored protonated double-layered perovskite $H_2CaTa_2O_7$ with n-alcohols, and their photocatalytic activity. *RSC Adv.* 4, 4047–4054. doi: 10.1039/C3RA44623A

Wu, J., Huang, Y., Li, T., Lin, J., Huang, M., and Wei, Y. (2006). Synthesis and photocatalytic properties of layered nanocomposite $H_2La_2Ti_3O_{10}/Fe_2O_3$. *Scr. Mater.* 54, 1357–1362. doi: 10.1016/j.scriptamat.2005.12.008

Youngblood, W. J., Lee, S.-H. A., Maeda, K., and Mallouk, T. E. (2009). Visible light water splitting using dye-sensitized oxide semiconductors. *Acc. Chem. Res.* 42, 1966–1973. doi: 10.1021/ar9002398

Zhou, Y., Wen, T., Guo, Y., Yang, B., and Wang, Y. (2016). Controllable doping of nitrogen and tetravalent niobium affords yellow and black calcium niobate nanosheets for enhanced photocatalytic hydrogen evolution. *RSC Adv.* 6, 64930–64936. doi: 10.1039/C6RA11407E

Zhu, H., Yao, X., and Hua, S. (2013). Nanocomposite of polyaniline and a layered niobate acid host: synthesis, electrochemical studies, and photocatalytic properties. *Polym. Compos.* 34, 834–841. doi: 10.1002/pc.22485

Zou, Z., Ye, J., and Arakawa, H. (2001). Substitution effects of In^{3+} by Fe^{3+} on photocatalytic and structural properties of Bi_2InNbO_7 photocatalysts. *J. Mol. Catal.* 168, 289–297. doi: 10.1016/S1381-1169(00)00545-8

Zvereva, I., and Rodionov, I. (2013). "Photocatalytic properties of perovskite-type layered oxides," in *Perovskite: Crystallography, Chemistry and Catalytic Performance*, eds J. Zhang and H. Li (New York, NY: Nova Science Publishers), 181–198.

Zvereva, I. A., Silyukov, O. I., and Chislov, M. V. (2011). Ion-exchange reactions in the structure of perovskite-like layered oxides: I. protonation of $NaNdTiO_4$ complex oxide. *Russ. J. Gen. Chem.* 81, 1434–1441. doi: 10.1134/S1070363211070061

Conflict of Interest: The authors declare that the research was conducted in the absence of any commercial or financial relationships that could be construed as a potential conflict of interest.

frontiers in Chemistry

MINI REVIEW
published: 07 April 2020
doi: 10.3389/fchem.2020.00191

Silicon Quantum Dots: Synthesis, Encapsulation, and Application in Light-Emitting Diodes

Sofia Morozova[1]*, **Mariya Alikina**[1], **Aleksandr Vinogradov**[1] **and Mario Pagliaro**[2]

[1] *Laboratory of Inkjet Printing of Functional Materials, SCAMT Institute, ITMO University, Saint-Petersburg, Russia,* [2] *Istituto per lo Studio dei Materiali Nanostrutturati, CNR, Palermo, Italy*

Silicon quantum dots (SiQDs) are semiconductor Si nanoparticles ranging from 1 to 10 nm that hold great applicative potential as optoelectronic devices and fluorescent bio-marking agents due to their ability to fluoresce blue and red light. Their biocompatibility compared to conventional toxic Group II-VI and III-V metal-based quantum dots makes their practical utilization even more attractive to prevent environmental pollution and harm to living organisms. This work focuses on their possible use for light-emitting diode (LED) manufacturing. Summarizing the main achievements over the past few years concerning different Si quantum dot synthetic methods, LED formation and characteristics, and strategies for their stabilization by microencapsulation and modification of their surface by specific ligands, this work aims to provide guidance *en route* to the development of the first stable Si-based light-emitting diodes.

Keywords: silicon quantum dots, synthesis method, fluorescence, quantum yield, microencapsulation, light-emitting diodes

OPEN ACCESS

Edited by:
Eugene A. Goodilin,
Lomonosov Moscow State University, Russia

Reviewed by:
Clara S. B. Gomes,
New University of Lisbon, Portugal
Liubov A. Osminkina,
Lomonosov Moscow State University, Russia

***Correspondence:**
Sofia Morozova
morozova@scamt-itmo.ru

Specialty section:
This article was submitted to Inorganic Chemistry, a section of the journal Frontiers in Chemistry

Received: *13 November 2019*
Accepted: *02 March 2020*
Published: *07 April 2020*

Citation:
Morozova S, Alikina M, Vinogradov A and Pagliaro M (2020) Silicon Quantum Dots: Synthesis, Encapsulation, and Application in Light-Emitting Diodes. Front. Chem. 8:191. doi: 10.3389/fchem.2020.00191

INTRODUCTION

Silicon quantum dots are nanometer-sized particles of crystalline silicon with properties of great interest in light of photonics, microelectronics, and biotechnological applications: high quantum yield (QY, the ratio between the number of photons emitted by a fluorophore and the number of absorbed photons), high lifetime of photoluminescence (PL), wide range of wavelength emission, and non-toxicity (Pavesi and Turan, 2010). Affecting the efficient emission and absorption of light, silicon in the bulk state is a semiconductor with an indirect bandgap. Yet, a decrease in particle size to $<$5 nm (the excitonic Bohr radius of silicon) allows the conversion of Si particles from indirect to direct bandgap materials with a high quantum yield (QY) of photoluminescence to up to 90% (Li et al., 2016; Gelloz et al., 2019).

In silicon SiQDs of $<$ 5 nm in size, the photoluminescence intensity dramatically increases and blue shifts with further decreasing particle size (Sychugov et al., 2016). As happens with other QDs, the optical and electrical properties of SiQDs can be controlled by varying the particle size, the crystallinity, the nature of the surface groups and the surrounding matrix, and by doping with transition metals (Sychugov et al., 2016).

The methods for producing nanosized silicon particles are rather well-studied and can be divided into chemical and physical approaches. The first include laser ablation (Li et al., 2004; Beard et al., 2007; Vendamani et al., 2015; Xin et al., 2017) and non-thermal plasma synthesis (Cheng et al., 2010; Yasar-Inceoglu et al., 2012; Liu et al., 2016). The second include electrochemical etching (Sato et al., 2009; Castaldo et al., 2014; Chen et al., 2019), reduction of silicon halides

(Tilley and Yamamoto, 2006; Cheng et al., 2012; Choi et al., 2014; Sacarescu et al., 2016), thermal destruction of silicon-rich oxides (Hessel et al., 2007, 2011), hydrothermal decomposition of different Si-contained organic precursors (Lopez-Delgado et al., 2017; Liu et al., 2018b; Phan et al., 2018; Yi et al., 2019), oxidation of sodium silicide or Zintl monoclinic phase (Na_4Si_4) (Neiner et al., 2006; Atkins et al., 2011; Beekman et al., 2019), mechanochemistry (Chaudhary et al., 2014), processing porous silicon (Gongalsky M. et al., 2019), and others (Holmes et al., 2001; Dasog et al., 2012).

Recent reviews on the utilization of SiQDs in bioimaging and biosensing (Cheng et al., 2014; McVey and Tilley, 2014; Cheng and Guan, 2017; Ji et al., 2018), solar cells (Chen and Yang, 2015), nonlinear optics (Bisadi et al., 2015), and photonics (Priolo et al., 2014; Zhao et al., 2018) show the broad interest and scope of the research concerning these nanomaterials. Less attention has been paid to the features of Si quantum dot-based light-emitting diodes (LEDs), even though in principle one of the most valuable applications of said quantum dots would be in making new LEDs based on abundant silicon in place of current commercial LEDs, which are based on rare earths or on organic phosphors (Buckley et al., 2017).

Compared to organic phosphors, LEDs based on Si QDs are color-pure and photostable and have a narrow emission peak and a wide spectrum of emission controlled by particle size (Cheng et al., 2014). Unfortunately, Si-based LEDs have a very short lifetime. Moreover, the quantum yield is generally low. In general, the monodispersity of silicon QDs is improving lifetime of LED, but quick degradation of LEDs based on nanosized Si occurs due to diffusion and migration of Si atoms to the outer surface of the Si nanoparticle (Maier-Flaig et al., 2013a). Two possible solutions for improving stability have been investigated: microencapsulation of SiQDs or functionalization of their surface. The presence of a shell in encapsulated silicon QDs in which the shell material consists of particles with a larger bandgap, compatible with the lattice of Si QDs, makes it possible to increase the probability of radiative recombination by isolating excitons from surface states (Gong et al., 2015). Another stabilization factor for SiQDs may be encapsulation, the variants of which are considered in the examples of solid dielectric matrices for solar cell applications (Chen and Yang, 2015) and biocompatible polymer matrices for bioimaging (Dasog et al., 2016). Aiming to provide guidelines *en route* to the development of the first stable Si-based light-emitting diodes, in the following, we summarize recent advances in the field of Si-based LEDs, focusing on SiQD synthesis methods affording high (45–90%) QY of photoluminescence, strategies of encapsulation, and recent progress in the formation of LEDs using Si quantum dots.

SiQD PREPARATION

Techniques for SiQD synthesis are divided into physical and chemical methods. Most physical routes are top-down (laser generation, plasma synthesis), with bottom-up methods consisting only of plasma synthesis. Chemical methods include both top-down (decomposition of Si-based precursors, electrochemical etching) and bottom-up approaches (reduction of silicon halides, Zintl phases oxidation). **Scheme 1** illustrates the main routes divided into the two main methods.

Physical Routes to Synthesizing SiQDs

Laser Generation

Irradiation of a Si plate with the light of a laser of sufficient power (number of monochromatic photons) results in the formation of QDs of high purity and crystallinity (Li et al., 2004; Beard et al., 2007; Vendamani et al., 2015; Xin et al., 2017). The low monodispersity and low stability of the resulting quantum dots are the main limitations of the method. Nevertheless, it was recently shown that, when extending the femtosecond laser ablation time from 30 to 120 min, the size of the SiQDs formed in 1-octene varied from 4.2 to 1.4 nm, with measured PL quantum yield going from 23.6 to 55.8% (Zhang et al., 2018).

Plasma Synthesis

The non-thermal plasma method is used both to obtain Si nanoparticles embedded in thin films and to synthesize free-standing silicon nanoparticles. Hot electrons in a plasma during a microwave discharge lead to the dissociation of precursor molecules such as SiX_4 ($X = H$, Cl, Br) (Liu et al., 2016). The advantage of the method is a wide choice of fluorescent color of the nanoparticles obtained. Unlike most bottom-up methods, where only blue-green colors are available, red to orange fluorescence can be obtained using non-thermal plasma synthesis (Cheng et al., 2010; Yasar-Inceoglu et al., 2012). The method requires the utilization of special equipment. Yet, it affords nanocrystals reaching very high luminescence efficiency (QY up to 90%), as lately shown for Si/SiO_2 core-shell QDs obtained via non-thermal plasma synthesis followed by formation of a thin (∼1 nm) oxide shell via high-pressure water vapor annealing (Gelloz et al., 2019).

Chemical Routes to SiQDs

Electrochemical Etching

The electrochemical generation of Si quantum dots makes use of a Si wafer as the cathode and graphite as the anode. The electrolyte generally consists of aqueous HF with H_2O_2 or HNO_3 and different additives (polyoxometalates, for example) (Kang et al., 2007). The technique allows the rapid creation of SiQDs with a range of light of fluorescence from blue to red and with rather narrow size dispersion (Sato et al., 2009; Castaldo et al., 2014; Chen et al., 2019). Originally, the Si QDs thereby obtained were characterized by low QY, but recent advances devoted to surface modification of SiQDs resulted in enhanced QY, up to 55% (Tu et al., 2016).

Zintl Salt Oxidation

The reaction of Zintl salts (Me_ySi_x, $Me = Na$, K, Mg, etc.) with silicon halides, gaseous bromine, or ammonium bromide in a boiling solution of glyme or under microwave irradiation affords SiQDs (Neiner et al., 2006; Atkins et al., 2011; Beekman et al., 2019). The advantages of the method are accessibility and scalability, thanks to the use of conventional reagents and equipment that is characteristic of conventional colloidal

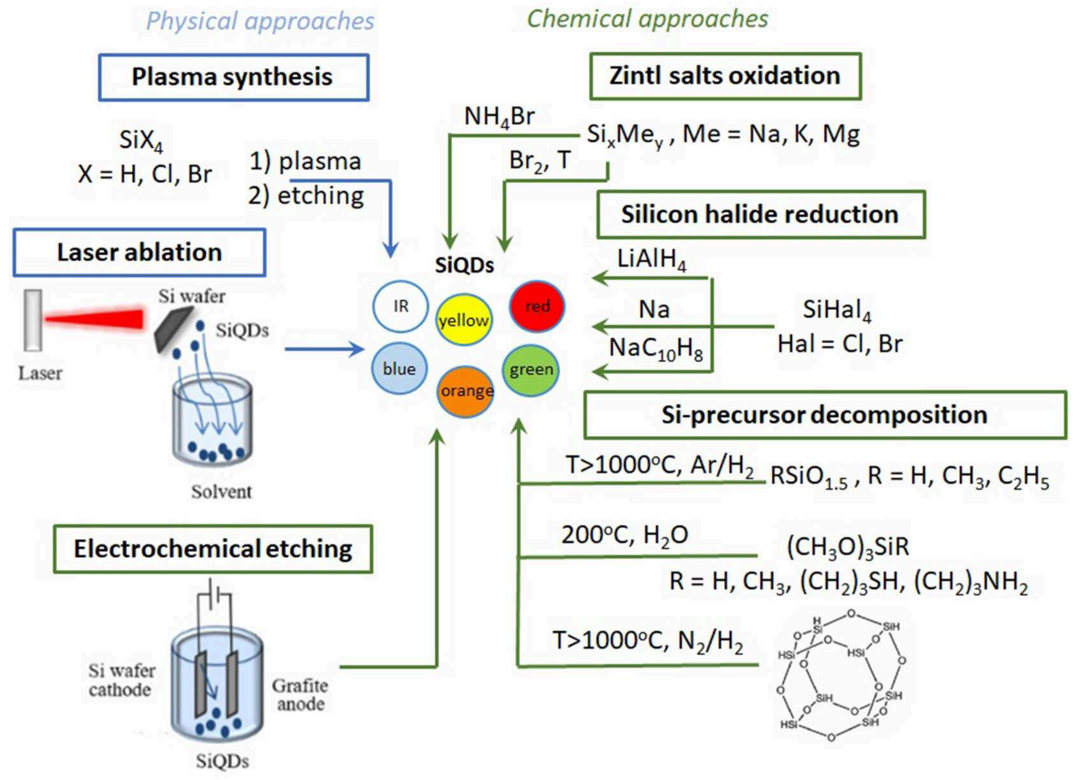

SCHEME 1 | Different approaches to SiQDs synthesis. Blue lines correspond to the physical approaches for SiQD synthesis; green lines correspond to the chemical approaches.

benchtop chemistry. However, the technique only affords Si nanocrystals fluorescing in the blue-green range of the light spectrum. The luminescence efficiency achieved, in terms of QY, is up to 50% (Bart van Dam et al., 2018).

Reduction of Silicon Halides

The reduction of $SiCl_4$ using sodium naphthalenide, sodium, lithium aluminum hydride, or tetraethylorthosilicate as a reducing agent quickly produces Si nanocrystals (Cheng et al., 2012; Choi et al., 2014; Sacarescu et al., 2016). As expected, however, the particle size distribution is very wide. The addition of surfactant molecules to create micelle "nanoreactors" gives some control over the size (Tilley and Yamamoto, 2006). Usually, this method only gives blue luminescent nanocrystals of colloidal silicon, but high QY up to 90% can be obtained (Li et al., 2016).

Decomposition of Si-Containing Precursors

The hydrothermal decomposition of organosilicates such as N-[3-(trimethoxysilyl)propyl]-ethylenediamine (DAMO), 3-aminopropyl triethoxysilane (APTES), or 3-aminopropyl trimethoxysilane (APTMS), in the presence of reducing agents such as $LiAlH_4$, sodium citrate, $NaBH_4$, and thiourea affords Si QDs (Dasog et al., 2012; Lopez-Delgado et al., 2017; Liu et al., 2018b; Phan et al., 2018; Yi et al., 2019). By varying the reaction time, temperature, and the nature of reducing agent and of the precursor, nanocrystals with QY 65–85% can be synthesized (Ma et al., 2018; Abdelhameed et al., 2019). It is also possible to synthesize SiQDs by the thermal decomposition either of silicon monoxide (SiO) powder heated to 1,350°C (Lu et al., 2017) or of other precursors, such as silsequioxanes, followed by etching and hydrosilylation (Yu et al., 2017).

Template Synthesis

SiQDs could be obtained in gram-scale quantity by metallothermal reduction. In one approach, mesoporous SiO_2 obtained via template-assisted sol-gel synthesis is reduced using magnesium powder at 500°C to yield silicon nanocrystals that are reacted with trioctylphosphine oxide to yield hydroxyl-terminated, encapsulated Si QDs exhibiting red luminescence (Dasog et al., 2012). Free-standing NCs liberated using HF acid and further functionalized with alkyl groups yield NCs that are dispersible in organic solvents with QY up to 48% (Kirshenbaum et al., 2018).

Data concerning the state of the art in SiQDs synthesis with respect to luminescence efficiency (QY of PL 45–90%), wavelength of emission, average nanoparticle size, and surface group are summarized in **Table 1A**.

SIZE SEPARATION OF SiQDs

Size separation methods of SiQDs are important because precise monodispersity is required in many applications, including LED

TABLE 1 | Main features of SiQDs obtained via different synthetic routes and the main recent advances in SiQD LEDs.

Synthesis technique		PL wavelength, nm	Particle size, nm (size distribution, %)	Surface group	QY, %	References
(A) MAIN FEATURES OF SiQDs OBTAINED VIA DIFFERENT SYNTHETIC ROUTES						
Physical	Laser generation	430	1–2 (80%)	1-octene	55.8	Zhang et al., 2018
	Non-thermal plasma synthesis	825	4	Si/SiO$_2$	90	Gelloz et al., 2019
Chemical methods	Electrochemical etching	621	5-8	Complex shell*	55	Tu et al., 2016
	Zintl salt oxidation	650	2.2	n-butyl	50**	Bart van Dam et al., 2018
	Reduction of silicon halides	520	4.5–6 (60%)	1,2,3,4-tetrahydrocarbazol-4-one	90	Li et al., 2016
	Hydrothermal decomposition DAMO***	445	4–5	Citrate/thiourea	73.3	Ma et al., 2018
	Hydrothermal decomposition DAPTMS***	445	4.1	Citrate/thiourea	84.9	Ma et al., 2018
	Hydrothermal decomposition APTES***	515	1–3 (97%)	Fluorescein isothiocyanate	64.7	Abdelhameed et al., 2019
	Decomposition of silsesquioxane	400	6.1	Dodecene and SiO$_2$ matrice	45	Yu et al., 2017
	Template synthesis	645-712	2.9–3.6	dodecyl	48	Kirshenbaum et al., 2018

SiQD synthesis technique	PL, wl****, nm (QY, %)	EQE*****, %	L******, Cd/m^2	$V_T^{*******}$, V	LED structure ********	References
(B) The MAIN RECENT ADVANCES IN SiQD LEDs						
TES decomposition and encapsulation in SiO$_2$	620	0.033	4,200	2.8	ITO/ZnO/SiQDs/CBP/MoO$_3$/Al	Yamada and Shirahata, 2019
TES decomposition	710 (25)	0.035	–	3.5	ITO/PEDOT:PSS/polyTPD/SiQDs/ZnO/Al	Ghosh et al., 2014
(HSiO$_{1.5}$)$_n$ thermal decomposition	625–680 (43)	0.09–0.074	22.6	1.8	glass/TPBi/SiQDs/polyTPD/PEDOT/ITO/glass	Maier-Flaig et al., 2013b
TES decomposition	720–840 (44–56)	0.20–0.23	4.4–5.5	2.5–2.1	ITO/PEDOT:PSS/SiQDs/TPBi/Al	Ghosh et al., 2018a
Non-thermal plasma synthesis	740 (31)	2.4	–	6.4	ITO/PEDOT:PSS/polyTPD/SiQDs/ZnO/Ag	Gu et al., 2017
Non-thermal plasma synthesis	700 (40)	2.7	–	6.0	glass/ITO/PEI/ZnO/SiQDs/TAPC/MoO$_3$/Al	Yao et al., 2016
TES decomposition	720 (40)	3.1	5,000	3.5	ITO/PEDOT:PSS/polyTPD/SiQDs/TPBi/Al	Ghosh et al., 2018b
Non-thermal plasma synthesis	735 (47)	6.2	–	–	ITO/PEDOT:PSS/polyTPD/PVK/SiQDs/ZnO/Ag	Liu et al., 2018a
Non-thermal plasma synthesis	777 (43)	8.6	–	1.3	ITO/PEDOT:PSS/polyTPD/SiQDs/CPB/LiF,Al	Cheng et al., 2011

*SiQDs - (ethylenedioxy)diethanethiol-1-(2-isothiocyanatoethyl)-1H-pyrrole-2,5-dion/bovine serum albumin/ isothiocyanate–PEG–isothiocyanate/antibode; **-internal quantum efficiency; ***DAMO – N-[3-(trimethoxysilyl)propyl]ethylenediamine; DAPTMS – [3-(2-aminoethylamino)propyl]trimethoxysilane; APTES – 3-aminopropyl triethoxysilane; ****PL-photoluminescence, wl-wavelength; *****EQE-external quantum efficiency; ******L-luminance; *******V_T_-turn-on voltage; ********TES is triethoxysilane; CBP is 4,4′-Bis(N-carbazolyl)-1,1′-biphenyl; TPBi is 2,2′,2″-(1,3,5-benzinetriyl)-tris(1-phenyl-1-H-benzimidazole); polyTPD is poly(bis-4-butylphenyl-N,N-bisphenyl) benzidine; PEDOT:PSS is poly(3,4-ethylenedioxythiophene) polystyrene sulfonate; PEI is polyethyleneimine; TAPC is 1,1-bis[(di-4-tolylamino)phenyl]cyclohexane; PVK is poly(9-vinylcarbazole)._

devices (Maier-Flaig et al., 2013a), due to the dependence of luminescence on the nanocrystal size and size distribution, influencing the purity of the emitted color and the quantum yield. Several techniques can be applied for size-separation of QDs: field flow fractionation, membrane methods, and size exclusion chromatography (Mori, 2015). Field flow fractionation is directed by variant force fields: crossflow stream, temperature gradient, electrical potential gradient, centrifugal, dielectrophoretic, and magnetic forces. However, the application of an electric or magnetic field imposes restrictions on the particles used, since they must contain ionic/dipole fragments or have magnetic properties (Mastronardi et al., 2012). Ultracentrifugation and size-selective precipitation are the most common and scalable approaches to produce SiQDs with polydispersity index <1.01 (Rinck et al., 2015; Brown et al., 2017).

MICROENCAPSULATION OF SiQDs

The application of SiQDs requires their chemical and physical stabilization (Maier-Flaig et al., 2013a; Buckley et al., 2017). Modern stabilization techniques include ligand exchange (Purkait et al., 2016) and microencapsulation in inorganic (Chen and Yang, 2015) or organic (polymer) (Dasog et al., 2016) matrixes. Organosilicon polymers, in particular, are promising candidates for encapsulation due to their affinity to SiQDs, high transparency in the visible region, and high thermal and photostability (Pagliaro, 2009; Vinogradov and Vinogradov, 2014).

Hydrolysis and Polycondensation of Trichlorosilane and Methyl Trichlorosilane

The first attempt at the encapsulation of SiQDs involved thermal processing of hydrogen silsesquioxane SiQD precursor in 5% H_2/95%Ar in the presence of a silica matrix $(HSiO_{1.5})_n$ or of a methyl-modified silica matrix $[(HSiO_{1.5})_n(CH_3SiO_{1.5})_m]$, in turn obtained from hydrolytic polycondensation of $HSiCl_3$ or of $HSiCl_3$ and $(CH_3)_3SiCl$ (Henderson et al., 2009). An important finding was that greater networking and cross-linking density of $(HSiO_{1.5})_n$, resulted in the formation of smaller SiQDs in comparison to HSQ, whereas increasing the amount of methyl groups in the organically modified silica (ORMOSIL) produced larger Si nanocrystals (Palmisano et al., 2006).

Encapsulation in Mesoporous Silica

A straightforward approach lately demonstrated to increase the water dispersibility and photostability of SiQDs requires encapsulation into mesoporous silica through a simple condensation reaction in which mesoporous silica dispersed in toluene is mixed with a SiQD solution in C_2H_5OH, followed by heating to 110°C for reflux for 3 h. The resulting encapsulated SiQD has excellent hydrophilicity, good biocompatibility, low cytotoxicity, retains a high surface area, and exhibits better fluorescence stability in acidic solutions, making it ideally suited for biological applications (Huang et al., 2018; Phatvej et al., 2019). A procedure for obtaining SiQDs capped with an Si–C bonded alkyl layer by heating in an ultrahigh vacuum at 200°C has been reported (Chao et al., 2007). This type of encapsulation may be useful for the controlled preparation of new quantum-confined silicon structures and could facilitate their mass spectroscopic study (Gongalsky M. B. et al., 2019).

APPLICATION OF SiQDs IN LED DEVICES

The main characteristics of LEDs are the turn-on voltage (V_T), which characterizes the beginning of working of the device, luminance (L), which describes the brightness of the device, and external quantum efficiency (EQE, Equation 1), which is associated with the efficiency of the diode (Ghosh et al., 2018a):

$$EQE\ (\%) = \frac{q \times P}{J \times E} \times 100\% \tag{1}$$

where q is the electron charge, P is the optical power density, J is the current density, and E is the energy of a photon emitted by the LED. **Table 1B** summarizes recent advances in SiQD LEDs producing light-emitting diodes with the highest EQEs. **Table 1** also includes a description of the LED design. We briefly remind the reader that design generally involves one electrode being made from indium tin oxide (ITO) glass and the other from aluminum or silver. The multilayer structure of a typical LED consists of an electron injection layer, an electron transfer layer, an optically active layer, a hole transfer layer, and a hole injection layer (Khriachtchev, 2016). Nanoparticles of ZnO are usually used as the material for the electron transfer layer (Yang et al., 2016; Kim and Park, 2017), whereas MoO_3, WO_3 are often used in the hole transfer layer due to the simplicity of their synthesis (Son et al., 2009; Wang et al., 2014). The best values of EQE for SiLED are 8.6% for near-infrared emission (Cheng et al., 2011), while for white, red, and orange emissions, values of EQE are less than 0.1% (Maier-Flaig et al., 2013b; Yamada and Shirahata, 2019). There are several ways of improving LED characteristics, including using a device with an inverted structure of instead of a direct one (Yao et al., 2016; Ghosh et al., 2018b; Yamada and Shirahata, 2019), the control of the thickness of the SiQDs and polyTPD layers (Ghosh et al., 2014), the control of the size-dependence of SiQDs (Maier-Flaig et al., 2013a), and using aromatic ligands on SiQD surfaces instead of aliphatic ones (Liu et al., 2018a).

CONCLUSIONS AND PERSPECTIVES

Significant progress has been made in the synthesis of Si quantum dots with high quantum yield. The development of light-emitting diodes based on SiQDs has so far been limited by their short lifetime, ranging from several hours (Gu et al., 2017; Liu et al., 2018a) to several days (Maier-Flaig et al., 2013b). Fundamental recent works aimed at investigating the origins of such low lifetimes have shown that the destruction of the diode is associated with the migration and diffusion of nanoparticles, as well as with the appearance of macro- and microscopic surface defects on the layers (Maier-Flaig et al., 2013a). Monodisperse SiQDs, in any case, are less prone to migration, allowing for a considerably longer lifetime of the device. Furthermore, significant progress in nanomaterial synthesis, translating into photoluminescence quantum yield of up to 90%, has not been matched in electroluminescence, as Si-based LEDs generally achieve QY of up to 47%. Intense research efforts are currently being aimed at developing SiQDs with high QY and external quantum efficiency and long lifetime. Along with the use of monodisperse Si nanoparticles, their microencapsulation holds promise for the first practical applications. While, for certain photonics technologies such as photoluminescence-based sensing in biology, encapsulation of SiQDs in mesoporous silica particles is already suitable for practical uses, this is not yet the case for LEDs. Due to the low cost, large abundance, and excellent health and environmental profile of silicon, when and if the issue of their poor stability will be solved, the use of silicon quantum dots will develop to become the dominant technology in photonics.

AUTHOR CONTRIBUTIONS

MA and SM organized and wrote the manuscript. AV and MP discussed the results. All authors approved this manuscript.

FUNDING

This work was financially supported by the Russian Science Foundation (project No 16-19-10346).

REFERENCES

Abdelhameed, M., Aly, S., Maity, P., Manni, E., Mohammed, O. F., and Charpentier, P. A. (2019). Impact of the chemical nature and position of spacers on controlling the optical properties of silicon quantum dots. *Phys. Chem. Chem. Phys.* 21, 17096–17108. doi: 10.1039/C9CP03537K

Atkins, T. M., Thibert, A., Larsen, D. S., Dey, S., Browning, N. D., and Kauzlarich, S. M. (2011). Femtosecond ligand/core dynamics of microwave-assisted synthesized silicon quantum dots in aqueous solution. *J. Am. Chem. Soc.* 133, 20664–20667. doi: 10.1021/ja207344u

Bart van Dam, B., Osorio, C. I., Hink, M. A., Muller, R., Koenderink, A. F., and Dohnalova, K. (2018). High internal emission efficiency of silicon nanoparticles emitting in the visible range. *ACS photonics* 5, 2129–2136. doi: 10.1021/acsphotonics.7b01624

Beard, M. C., Knutsen, K. P., Yu, P., Luther, J. M., Song, Q., Metzger, W. K., et al. (2007). Multiple exciton generation in colloidal silicon nanocrystals. *Nano Lett.* 7, 2506–2512. doi: 10.1021/nl071486l

Beekman, M., Kauzlarich, S. M., Doherty, L., and Nolas, G. S. (2019). Zintl phases as reactive precursors for synthesis of novel silicon and germanium-based materials. *Materials* 12:1139. doi: 10.3390/ma12071139

Bisadi, Z., Mancinelli, M., Manna, S., Tondini, S., Bernard, M., Samusenko, A., et al. (2015). Silicon nanocrystals for nonlinear optics and secure communications. *Appl. Mater. Sci.* 212, 2659–2671. doi: 10.1002/pssa.201532528

Brown, S. L., Miller, J. B., Anthony, R. J., Kortshagen, U. R., Kryjevski, A., and Hobbie, E. K. (2017). Abrupt size partitioning of multimodal photoluminescence relaxation in monodisperse silicon nanocrystals. *ACS nano* 11, 1597–1603. doi: 10.1021/acsnano.6b07285

Buckley, S., Chiles, J., McCaughan, A. N., Moody, G., Silverman, K. L., Stevens, M. J., et al. (2017). All-silicon light-emitting diodes waveguide-integrated with superconducting single-photon detectors. *Appl. Phys. Lett.* 111:141101. doi: 10.1063/1.4994692

Castaldo, A., Antonaia, A., and Addonizio, M. L. (2014). Synthesis of silicon quantum dots in zinc silicate matrix by low-temperature process: optical, structural and electrical characterization. *Thin Solid Films* 562, 172–180. doi: 10.1016/j.tsf.2014.04.044

Chao, Y., Šiller, L., Krishnamurthy, S., Coxon, P. R., Bangert, U., Gass, M., et al. (2007). Evaporation and deposition of alkyl-capped silicon nanocrystals in ultrahigh vacuum. *Nat Nanotechnol.* 2, 486–489. doi: 10.1038/nnano.2007.224

Chaudhary, A. L., Sheppard, D. A., Paskevicius, M., Saunders, M., and Buckley, C. E. (2014). Mechanochemical synthesis of amorphous silicon nanoparticles. *RSC Advances*, 4, 21979–21983. doi: 10.1039/C3RA47431C

Chen, X., and Yang, P. (2015). Preparation and photovoltaic properties of silicon quantum dots embedded in a dielectric matrix: a review. *J. Mater. Sci. Mater. Electr*, 26, 4604–4617. doi: 10.1007/s10854-015-3147-4

Chen, Y., Sun, L., Liao, F., Dang, Q., and Shao, M. (2019). Fluorescent-stable and water-soluble two-component-modified silicon quantum dots and their application for bioimaging. *J. Lumin.* 215:116644. doi: 10.1016/j.jlumin.2019.116644

Cheng, K. Y., Anthony, R., Kortshagen, U. R., and Holmes, R. J. (2010). Hybrid silicon nanocrystal–organic light-emitting devices for infrared electroluminescence. *Nano Lett.*, 10, 1154–1157. doi: 10.1021/nl903212y

Cheng, K. Y., Anthony, R., Kortshagen, U. R., and Holmes, R. J. (2011). High-efficiency silicon nanocrystal light-emitting devices. *Nano lett.* 11, 1952–1956. doi: 10.1021/nl2001692

Cheng, X., Gondosiswanto, R., Ciampi, S., Reece, P. J., and Gooding, J. J. (2012). One-pot synthesis of colloidal silicon quantum dots and surface functionalization via thiolene click chemistry. *Chem. Commun.* 48:11874–11876. doi: 10.1039/c2cc35954e

Cheng, X., and Guan, B. (2017). Optical biosensing and bioimaging with porous silicon and silicon quantum dots (Invited Review). *Prog. Electromagn. Res.* 160, 103–121. doi: 10.2528/PIER17120504

Cheng, X., Lowe, S. B., Reece, P. J., and Gooding, J. J. (2014). Colloidal silicon quantum dots: from preparation to the modification of self-assembled monolayers (SAMs) for bio-applications. *Chem. Soc. Rev.* 43, 2680–2700. doi: 10.1039/c3cs60353a

Choi, J.-H., Dung, M. X., and Jeong, H. D. (2014). Novel synthesis of covalently linked silicon quantum dote polystyrene hybrid materials: silicon quantum dote polystyrene polymers of tunable refractive index. *Mater. Chem. Phys.* 148, 463–472. doi: 10.1016/j.matchemphys.2014.08.016

Dasog, M., Kehrle, J., Rieger, B., and Veinot, J. G. (2016). Silicon nanocrystals and silicon-polymer hybrids: synthesis, surface engineering, and applications. *Angew. Chem. Int. Ed.* 55, 2322–2339. doi: 10.1002/anie.201506065

Dasog, M., Yang, Z., and Veinot, J. G. (2012). Size-controlled solid state synthesis of luminescent silicon nanocrystals using Stöber silica particles. *CrystEngComm.* 14, 7576–7578. doi: 10.1039/C2CE25950H

Gelloz, B., Juangs, F. B., Nozaki, T., Koji, A., Koshida, N., and Jin, L. (2019). Si/SiO_2 core/shell luminescent silicon nanocrystals and porous silicon powders with high quantum yield, long lifetime and good stability. *Front. Phys.* 7:47. doi: 10.3389/fphy.2019.00047

Ghosh, B., Hamaoka, T., Nemoto, Y., Takeguchi, M., and Shirahata, N. (2018a). Impact of anchoring monolayers on the enhancement of radiative recombination in light-emitting diodes based on silicon nanocrystals. *J. Phys. Chem. C* 122, 6422–6430. doi: 10.1021/acs.jpcc.7b12812

Ghosh, B., Masuda, Y., Wakayama, Y., Imanaka, Y., Inoue, J. I., Hashi, K., et al. (2014). Hybrid white light emitting diode based on silicon nanocrystals. *Adv. Funct. Mater.* 24, 7151–7160. doi: 10.1002/adfm.201401795

Ghosh, B., Yamada, H., Chinnathambi, S., Özbilgin, I. N. G., and Shirahata, N. (2018b). Inverted device architecture for enhanced performance of flexible silicon quantum dot light-emitting diode. *J. Phys. Chem. Lett.* 9, 5400–5407. doi: 10.1021/acs.jpclett.8b02278

Gong, K., Martin, J. E., Shea-Rohwer, L. E., Lu, P., and Kelley, D. F. (2015). Radiative lifetimes of zincblende CdSe/CdS quantum dots. *J. Phys. Chem. C*, 119, 2231–2238. doi: 10.1021/jp5118932

Gongalsky, M., Tsurikova, U. A., Storey, C. J., Evstratova, Y. V., Kudryavtsev, A., Canham, L. T., et al. (2019). The effects of drying technique and surface pre-treatment on the cytotoxicity and dissolution rate of luminescent porous silicon quantum dots in model fluids and living cells. *Faraday Discuss*. doi: 10.1039/C9FD00107G

Gongalsky, M. B., Kargina, J. V., Cruz, J. F., Sanchez-Royo, J. F., Chirvony, V., Osminkina, L. A., et al. (2019). Formation of Si/SiO$_2$ luminescent quantum dots from mesoporous silicon by sodium tetraborate/citric acid oxidation treatment. *Front. Chem.* 7:165. doi: 10.3389/fchem.2019.00165

Gu, W., Liu, X., Pi, X., Dai, X., Zhao, S., Yao, L., et al. (2017). Silicon-quantum-dot light-emitting diodes with interlayer-enhanced hole transport. *IEEE Photonics J.* 9, 1–10. doi: 10.1109/JPHOT.2017.2671023

Henderson, E. J., Kelly, J. A., and Veinot, J. G. C. (2009). Influence of HSiO$_{1.5}$ Sol–Gel polymer structure and composition on the size and luminescent properties of silicon nanocrystals. *Chem. Mater.* 21, 5426–5434. doi: 10.1021/cm902028q

Hessel, C. M., Reid, D., Panthani, M. G., Rasch, M. R., Goodfellow, B. W., Wei, J., et al. (2011). Synthesis of ligand-stabilized silicon nanocrystals with size-dependent photoluminescence spanning visible to near-infrared wavelengths. *Chem. Mater.* 24, 393–401. doi: 10.1021/cm2032866

Hessel, C. M., Summers, M. A., Meldrum, A., Malac, M., and Veinot, J. G. (2007). Direct patterning, conformal coating, and erbium doping of luminescent nc-Si/SiO$_2$ thin films from solution processable hydrogen silsesquioxane. *Adv. Mater.* 19, 3513–3516. doi: 10.1002/adma.200700731

Holmes, J. D., Ziegler, K. J., Doty, R. C., Pell, L. E., Johnston, K. P., and Korgel, B. A. (2001). Highly luminescent silicon nanocrystals with discrete optical transitions. *J. Am. Chem. Soc.* 123, 3743–3748. doi: 10.1021/ja002956f

Huang, L., Mu, Y., Chen, J., Tian, J., Huang, Q., Huang, H., et al. (2018). One-pot ultrafast preparation of silica quantum dots and their utilization for fabrication of luminescent mesoporous silica nanoparticles. *Mater. Sci. Eng. C* 93, 679–685. doi: 10.1016/j.msec.2018.08.035

Ji, X., Wang, H., Song, B., Chu, B., and He, Y. (2018). Silicon nanomaterials for biosensing and bioimaging analysis. *Front. Chem.* 6:38. doi: 10.3389/fchem.2018.00038

Kang, Z., Tsang, C. H. A., Zhang, Z., Zhang, M., Wong, N. B., Zapien, J. A., et al. (2007). A polyoxometalate-assisted electrochemical method for silicon nanostructures preparation: from quantum dots to nanowires. *J. Am. Chem. Soc.* 129, 5326–5327. doi: 10.1021/ja068894w

Khriachtchev, L. (2016). *Silicon Nanophotonics: Basic Principles, Current Status and Perspectives*. New York, NY: Jenny Stanford Publishing. ISBN: 13: 978-981-4241-13-7

Kim, J. H., and Park, J. W. (2017). Designing an electron-transport layer for highly efficient, reliable, and solution-processed organic light-emitting diodes. *J. Mater. Chem. C* 5, 3097–3106. doi: 10.1039/C7TC00488E

Kirshenbaum, M. J., Boebinger, M. G., Katz, M. J., McDowell, M. T., and Dasog, M. (2018). Solid-state route for the synthesis of scalable, luminescent silicon and germanium nanocrystals. *ChemNanoMat*. 4, 423–429. doi: 10.1002/cnma.201800059

Li, Q., Luo, T.-Y., Zhou, M., Abroshan, H., Huang, J., Kim, H. J., et al. (2016). Silicon nanoparticles with surface nitrogen: 90% quantum yield with narrow luminescence bandwidth and the ligand structure based energy law. *ACS Nano*. 10, 8385–8393. doi: 10.1021/acsnano.6b03113

Li, X., He, Y., and Swihart, M. T. (2004). Surface functionalization of silicon nanoparticles produced by laser-driven pyrolysis of silane followed by HF-HNO3Etching. *Langmuir* 20, 4720–4727. doi: 10.1021/la036219j

Liu, X., Zhang, Y., Yu, T., Qiao, X., Gresback, R., Pi, X., et al. (2016). Optimum quantum yield of the light emission from 2 to 10 nm hydrosilylated silicon quantum dots. *Part. Part. Syst. Char.* 33, 44–52. doi: 10.1002/ppsc.20150014

Liu, X., Zhao, S., Gu, W., Zhang, Y., Qiao, X., Ni, Z., et al. (2018a). Light-emitting diodes based on colloidal silicon quantum dots with octyl and phenylpropyl ligands. *ACS Appl. Mater. Interfaces* 10, 5959–5966. doi: 10.1021/acsami.7b16980

Liu, Y., Wang, Q., Guo, S., Jia, P., Shui, Y., Yao, S., et al. (2018b). Highly selective and sensitive fluorescence detection of hydroquinone using novel silicon quantum dots. *Sens. Actuat. B Chem.* 275, 415–421. doi: 10.1016/j.snb.2018.08.073

Lopez-Delgado, R., Higuera-Valenzuela, H. J., Zazueta-Raynaud, A., Ramos-Carrazco, A., Pelayo, J. E., Berman-Mendoza, D., et al. (2017). Solar cell efficiency improvement employing down-shifting silicon quantum dots. *Microsyst. Tech.* 24, 495–502. doi: 10.1007/s00542-017-3405-x

Lu, S., Wu, B., Sun, Y., Cheng, Y., Liao, F., and Shao, M. (2017). Photoluminescence of pure silicon quantum dots embedded in an amorphous silica wire array. *J. Mater. Chem. C* 5, 6713–6717. doi: 10.1039/c7tc01117b

Ma, S., Yue, T., Xiao, X., Cheng, H., and Zhao, D. (2018). A proof of concept study of preparing ultra bright silicon quantum dots based on synergistic effect of reductants. *J. Lumin.* 201, 77–84. doi: 10.1016/j.jlumin.2018.04.006

Maier-Flaig, F., KÃbel, C., Rinck, J., Bocksrocker, T., Scherer, T., Prang, R., et al. (2013a). Looking inside a working SiLED. *Nano Lett.* 13, 3539–3545. doi: 10.1021/nl400975u

Maier-Flaig, F., Rinck, J., Stephan, M., Bocksrocker, T., Bruns, M., KÃbel, C., et al. (2013b). Multicolor silicon light-emitting diodes (SiLEDs). *Nano Lett.* 13, 475–480. doi: 10.1021/nl3038689

Mastronardi, M. L., Henderson, E. J., Puzzo, D. P., and Ozin, G. A. (2012). Small silicon, big opportunities: the development and future of colloidally-stable monodisperse silicon nanocrystals. *Adv. Mater.* 24, 5890–5898. doi: 10.1002/adma.201202846

McVey, B. F., and Tilley, R. D. (2014). Solution synthesis, optical properties, and bioimaging applications of silicon nanocrystals. *Acc. Chem. Res.* 47, 3045–3051. doi: 10.1021/ar500215v

Mori, Y. (2015). Size-selective separation techniques for nanoparticles in liquid. *KONA Powder Particie J.* 32, 102–114. doi: 10.14356/kona.2015023

Neiner, D., Chiu, H. W., and Kauzlarich, S. M. (2006). Low-Temperature solution route to macroscopic amounts of hydrogen terminated silicon nanoparticles. *J. Am. Chem. Soc.* 128, 11016–11017. doi: 10.1021/ja064177q

Pagliaro, M. (2009). *Silica-Based Materials for Advanced Chemical Applications*. Cambridge: Royal Society of Chemistry.

Palmisano, G., Le Bourhis, E., Ciriminna, R., Tranchida, D., and Pagliaro, M. (2006). ORMOSIL thin films: tuning mechanical properties via a nanochemistry approach. *Langmuir* 22, 11158–11162. doi: 10.1021/la061520w

Pavesi, L., and Turan, R. (eds.). (2010). *Silicon Nanocrystals: Fundamentals, Synthesis and Applications.* Weinheim: John Wiley & Sons.

Phan, L. M. T., Baek, S. H., Nguyen, T. P., Park, K. Y., Ha, S., Rafique, R., et al. (2018). Synthesis of fluorescent silicon quantum dots for ultra-rapid and selective sensing of Cr(VI) ion and biomonitoring of cancer cells. *Mater. Sci. Eng. C* 93, 429–436. doi: 10.1016/j.msec.2018.08.024

Phatvej, W., Datta, H. K., Wilkinson, S. C., Mutch, E., Daly, A. K., and Horrocks, B. R. (2019). Endocytosis and lack of cytotoxicity of alkyl-capped silicon quantum dots prepared from porous silicon. *Materials* 12:1702. doi: 10.3390/ma12101702

Priolo, F., Gregorkiewicz, T., Galli, M., and Krauss, T. F. (2014). Silicon nanostructures for photonics and photovoltaics. *Nat. Nanotechnol.* 9, 19–32. doi: 10.1038/NNANO.2013.271

Purkait, T. K., Iqbal, M., Islam, M. A., Mobarok, M. H., Gonzalez, C. M., Hadidi, L., et al. (2016). Alkoxy-terminated si surfaces: a new reactive platform for the functionalization and derivatization of silicon quantum dots. *J. Am. Chem. Soc.* 138, 7114–7120. doi: 10.1021/jacs.6b03155

Rinck, J., Schray, D., Kübel, C., Powell, A. K., and Ozin, G. A. (2015). Size-dependent oxidation of monodisperse silicon nanocrystals with allylphenylsulfide surfaces. *Small* 11, 335–340. doi: 10.1002/smll.201401965

Sacarescu, L., Roman, G., Sacarescu, G., and Simionescu, M. (2016). Fluorescence detection system based on silicon quantum dots–polysilane nanocomposites. *Express Polym. Lett.* 10, 990–1002. doi: 10.3144/expresspolymlett.2016.92

Sato, K., Tsuji, H., Hirakuri, K., Fukata, N., and Yamauchi, Y. (2009). Controlled chemical etching for silicon nanocrystals with wavelength-tunable photoluminescence. *Chem. Commun.* 25, 3759–3761. doi: 10.1039/B903313K

Son, M. J., Kim, S., Kwon, S., and Kim, J. W. (2009). Interface electronic structures of organic light-emitting diodes with WO$_3$ interlayer: a study by photoelectron spectroscopy. *Org. Electron.* 10, 637–642. doi: 10.1016/j.orgel.2009.02.017

Sychugov, I., Pevere, F., Luo, J. W., Zunger, A., and Linnros, J. (2016). Single-dot absorption spectroscopy and theory of silicon nanocrystals. *Phy. Rev. B* 93:161413. doi: 10.1103/PhysRevB.93.161413

Tilley, R. D., and Yamamoto, K. (2006). The microemulsion synthesis of hydrophobic and hydrophilic silicon nanocrystals. *Adv. Mater.* 18, 2053–2056.doi: 10.1002/adma.200600118

Tu, C.-C., Chen, K.-P., Yang, T.-A., Chou, M.-Y., Lin, L. Y., and Li, Y.-K. (2016). Silicon quantum dot nanoparticles with antifouling coatings for immunostaining on live cancer cells. *ACS Appl. Mater. Interfaces* 8, 13714–13723. doi: 10.1021/acsami.6b02318

Vendamani, V. S., Hamad, S., Saikiran, V., Pathak, A. P., Rao, S. V., Kumar, V. R. K., et al. (2015). Synthesis of ultra-small silicon nanoparticles by femtosecond laser ablation of porous silicon. *J. Mater. Sci.* 50, 1666–1672. doi: 10.1007/s10853-014-8727-9

Vinogradov, A. V., and Vinogradov, V. V. (2014). Low-temperature sol–gel synthesis of crystalline materials. *RSC Adv.* 4, 45903–45919. doi: 10.1021/cr300399c

Wang, G., Jiu, T., Li, P., Li, J., Sun, C., Lu, F., et al. (2014). Preparation and characterization of MoO_3 hole-injection layer for organic solar cell fabrication and optimization. *Sol. Energy Mater. Sol. Cells* 120, 603–609. doi: 10.1016/j.solmat.2013.10.002

Xin, Y., Kitasako, T., Maeda, M., and Saitow, K. I. (2017). Solvent dependence of laser-synthesized blue-emitting Si nanoparticles: size, quantum yield, and aging performance. *Chem. Phys. Lett.* 674, 90–97. doi: 10.1016/j.cplett.2017.02.060

Yamada, H., and Shirahata, N. (2019). Silicon quantum dot light emitting diode at 620 nm. *Micromachines* 10, 318. doi: 10.3390/mi10050318

Yang, G., Tao, H., Qin, P., Ke, W., and Fang, G. (2016). Recent progress in electron transport layers for efficient perovskite solar cells. *J. Mater. Chem. A* 4, 3970–3990. doi: 10.1039/C5TA09011C

Yao, L., Yu, T., Ba, L., Meng, H., Fang, X., Wang, Y., et al. (2016). Efficient silicon quantum dots light emitting diodes with an inverted device structure. *J. Mater. Chem. C* 4, 673–677. doi: 10.1039/c5tc03064a

Yasar-Inceoglu, O., Lopez, T., Farshihagro, E., and Mangolini, L. (2012). Silicon nanocrystal production through non-thermal plasma synthesis: a comparative study between silicon tetrachloride and silane precursors. *Nanotechnology* 23:255604.

Yi, Y., Liu, L., Zeng, W., Lv, B., and Zhu, G. (2019). Bifunctional silicon quantum dots sensing platform for selective and sensitive detection of p-dihydroxybenzene with double signals. *Microchem. J.* 147, 245–252. doi: 10.1016/j.microc.2019.03.018

Yu, Y., Fan, G., Fermi, A., Mazzaro, R., Morandi, V., Ceroni, P., et al. (2017). Size-dependent photoluminescence efficiency of silicon nanocrystal quantum dots. *J. Phys. Chem. C* 121, 23240–23248. doi: 10.1021/acs.jpcc.7b08054

Zhang, Y. X., Wu, W. S., Hao, H. L., and Shen, W. Z. (2018). Femtosecond laser-induced size reduction and emission quantum yield enhancement of colloidal silicon nanocrystals: effect of laser ablation time. *Nanotechnology* 29:365706. doi: 10.1088/1361-6528/aacd75

Zhao, S., Liu, X., Pi, X., and Yang, D. (2018). Light-emitting diodes based on colloidal silicon quantum dots. *J. Semicond.* 39:061008. doi: 10.1088/1674-4926/39/6/061008ji

Conflict of Interest: The authors declare that the research was conducted in the absence of any commercial or financial relationships that could be construed as a potential conflict of interest.

frontiers in Chemistry

ORIGINAL RESEARCH
published: 23 April 2020
doi: 10.3389/fchem.2020.00300

Study of *n*-alkylamine Intercalated Layered Perovskite-Like Niobates $HCa_2Nb_3O_{10}$ as Photocatalysts for Hydrogen Production From an Aqueous Solution of Methanol

Vladimir V. Voytovich, Sergei A. Kurnosenko, Oleg I. Silyukov*, Ivan A. Rodionov, Iana A. Minich and Irina A. Zvereva

Institute of Chemistry, Saint Petersburg State University, Saint Petersburg, Russia

Edited by:
Eugene A. Goodilin,
Lomonosov Moscow State
University, Russia

Reviewed by:
Andrei Baranov,
Lomonosov Moscow State
University, Russia
Vitaly V. Kuznetsov,
D. Mendeleyev University of Chemical
Technology of Russia, Russia

***Correspondence:**
Oleg I. Silyukov
oleg.silyukov@spbu.ru

Specialty section:
This article was submitted to
Catalysis and Photocatalysis,
a section of the journal
Frontiers in Chemistry

Received: *16 February 2020*
Accepted: *26 March 2020*
Published: *23 April 2020*

Citation:
Voytovich VV, Kurnosenko SA, Silyukov OI, Rodionov IA, Minich IA and Zvereva IA (2020) Study of n-alkylamine Intercalated Layered Perovskite-Like Niobates $HCa_2Nb_3O_{10}$ as Photocatalysts for Hydrogen Production From an Aqueous Solution of Methanol. Front. Chem. 8:300. doi: 10.3389/fchem.2020.00300

A series of hybrid niobates $HCa_2Nb_3O_{10} \times RNH_2$, containing *n*-alkylamines (R = Me, Et, Pr, Bu, Hx, Oc) intercalated into the interlayer space, has been thoroughly studied concerning the photocatalytic hydrogen production from a model aqueous solution of methanol for the first time. All the hybrid photocatalysts were synthesized by the conventional ceramic technique followed by protonation and intercalation of *n*-alkylamines. The products were characterized using XRD, Raman, IR and diffuse reflectance spectroscopy, TGA, CHN-analysis and SEM. Photocatalytic measurements were conducted according to an advanced scheme taking into account possible changes in the photocatalyst concentration because of sedimentation, pH shifts and exfoliation of the samples into nanoplatelets. Special attention was also paid to the feasible improvement of the photocatalytic activity of the samples via their modification with Pt nanoparticles as a cocatalyst. In the series of amine derivatives, the highest rate of hydrogen generation was demonstrated by the Pt-loaded $HCa_2Nb_3O_{10} \times BuNH_2$ reaching apparent quantum efficiency of 13% in the 220–340 nm range. The initial $HCa_2Nb_3O_{10}$ showed comparable efficiency of 8.3% that is greater than for other amine derivatives. It was demonstrated that for the investigated samples the photocatalytic activity correlates with their ability of water intercalation.

Keywords: photocatalysis, hydrogen, layered, perovskite, niobate, intercalation, amine, hybrid compounds

INTRODUCTION

The intensive consumption of energy resources such as petroleum and coal for the last decades is presently assumed as a reason for environmental degradation and the energy crisis, which forces the development of new renewable and more attractive from the environmental point of view alternative energy sources. The use of solar light as a renewable energy source has been lately intensified and, in particular, the photocatalytic water and organic substrates splitting are considered as an effective and ecologically friendly way of the hydrogen fuel production (Maeda, 2011). The most widely studied catalysts for photocatalytic water splitting are TiO_2 and TiO_2-based materials. Their activity, however, is often limited by a number of factors including the surface area and charge separation efficiency that justifies the research on new promising materials. Therefore, the class of layered materials with a perovskite-like structure including Dion–Jacobson (DJ) and Ruddlesden–Popper (RP) phases has been actively studied. Their structure may be presented as an alteration of perovskite blocks and interlayer cations with the general formulae $A'[A_{n-1}B_nO_{3n+1}]$ (for DJ) and $A'_2[A_{n-1}B_nO_{3n+1}]$ (for RP) (Machida et al., 2005; Compton et al., 2007; Huang et al., 2011; Chen et al., 2012; Rodionov et al., 2012, 2017; Sabio et al., 2012; Zvereva and Rodionov, 2013). These compounds are amenable to reactions involving their interlayer space, such as intercalation and ion exchange, which provide their unique photocatalytic properties (Zvereva et al., 2011; Silyukov et al., 2015; Rodionov et al., 2018; Shelyapina et al., 2019).

The main factors determining high efficiency of modern photocatalysts include narrowing of the bandgap into the visible light region, achieving high surface areas, crystallinity, a large number of catalytic sites and in addition realization of efficient charge separation. In accordance with these objectives, different approaches in preparation and modification of the catalysts have been applied, including cationic and anionic substitution and doping (Zou et al., 2001; Reddy et al., 2003; Kumar et al., 2011; Zhou et al., 2016; Kawashima et al., 2017), sensitization with dyes (Youngblood et al., 2009), intercalation of metals and other inorganic particles (Huang et al., 2006, 2009) as well as preparation of composites with other materials (Cui et al., 2012, 2013, 2014; Saito et al., 2016; Liu et al., 2018).

The hybrid inorganic-organic compounds form a promising class of materials which allows combining properties of preliminarily investigated inorganic and organic parts in order to prepare materials with new often unique properties which often differ from their original hosts (Sanchez, 2006; Kickelbick, 2007). Fabrication of these materials includes various strategies such as sol-gel and solvothermal bottom-up synthesis, dispersion self-assembly methods and intercalation chemistry approaches (Mir et al., 2018).

Practically, perovskite-like inorganic-organic hybrids may be prepared by insertion of organic molecules into their interlayer space while the hard structure of perovskite blocks remains unchanged. Such reactions are shown to proceed under soft chemistry conditions and usually require conventional or solvothermal/microwave-assisted heating and lead to the formation of inorganic-organic hybrids being stable to moderate physical and chemical impacts. The two main approaches to modify the interlayer space of perovskite-like oxides are presently known. The intercalation reactions with organic bases (usually amines) proceed through the acid-base mechanism, where positively charged ammonium ions interact with negatively charged perovskite blocks (Tsunoda et al., 2003; Shimizu et al., 2006; Wang et al., 2007). The grafting reactions involve the formation of strong ion-valence bonds between terminal interlayer oxygen atoms and organic molecules and may be described by the esterification-like mechanism (Tsunoda et al., 2003; Shimizu et al., 2006; Wang et al., 2007). The first example of the preparation of inorganic-organic amine intercalated compounds based on layered perovskite like oxide was presented for the DJ niobates (Jacobson et al., 1985, 1987) and later broadened by grafting reactions with methanol (Takahashi et al., 1995). By now, the number of various inorganic hosts with both DJ and RP type of structure has been applied for preparation of inorganic-organic derivatives with a row of aliphatic and bulky amines and alcohols, amino alcohols, carboxylic acids, amino acids, carbohydrates, etc. (Hong and Kim, 1996; Han et al., 2001; Tsunoda et al., 2003; Tong et al., 2005; Takeda et al., 2006, 2008; Seiichi and Tahara, 2007; Tahara et al., 2007; Wang et al., 2012, 2018; Boykin and Smith, 2015; Shori et al., 2015; Sato et al., 2017; Silyukov et al., 2018).

However, despite the wide range of obtained inorganic-organic hybrids, lower attention has been paid to their functional properties, for instance, to the investigation of their photocatalytic activity. One of the possible reasons is the assumption of their low stability due to the photodegradation of inserted organic parts during the photocatalytic process. For example, the study on photocatalytic activity of the *n*-hexylamine-intercalated DJ tantalate $HCa_2Ta_3O_{10}$ has shown that modification of the interlayer space definitely leads to the enhancement of hydrogen evolution in the water-splitting reaction under ultraviolet light compared to the initial unmodified forms $MCa_2Ta_3O_{10}$ ($M =$ Na, Cs, and H) but the dramatic decrease in activity after the 8 h cycle was detected. This fact was explained by the degradation of the sample due to oxidation of the organic component which was confirmed by the decreased interlayer space and the insignificant oxygen evolution rate (Machida et al., 2005). The better results were achieved for *n*-alcohols grafted samples obtained from the RP type tantalate $H_2CaTa_2O_7$ in reactions of rhodamine B and methyl orange decomposition under ultraviolet-visible irradiation (Wang et al., 2014). A series of *n*-alkoxy hybrids with organic chains containing $n = 1, 3, 6, 10, 18$ carbon atoms has been tested and it was shown that, unlike short-chain alcohols, modification by long-chain alcohols ($n = 10, 18$) significantly improves the photocatalytic activity of the samples. Another example of the preparation of hybrid catalysts based on niobates and titanates is polyaniline-intercalated compounds which proved themselves as effective catalysts in the visible light region in the decomposition of methylene blue reaction (Guo et al., 2010; Zhu et al., 2013; Liu et al., 2014). Such hybrids have also been obtained from some other layered perovskite-like oxides, though their photocatalytic activity has not been studied (Uma and Gopalakrishnan, 1994; Uma et al., 1995; Tong et al., 2005). One more approach for the preparation of visible-light catalysts was shown by Wang et al. who prepared carbon-intercalated composite by thermolysis of D-glucopyranose derivative of $HLaNb_2O_7$ which showed a narrowed bandgap comparing to the parent compound (Wang et al., 2012).

This study presents the results of the systematic investigation of the photocatalytic activity of a series of intercalated by *n*-amines niobates $HCa_2Nb_3O_{10}\times RNH_2$. $KCa_2Nb_3O_{10}$ is a triple-layered niobate belonging to the DJ structural type with general formula $A'[A_{n-1}B_nO_{3n+1}]$ which was firstly prepared by Dion et al. (1981). The hydrated protonated form $HCa_2Nb_3O_{10}\cdot yH_2O$ (usually presented as $HCa_2Nb_3O_{10}\cdot 1.5H_2O$ in the literature) is typically obtained by the ion-exchange reaction in acid solutions from the initial alkali form $KCa_2Nb_3O_{10}$ (Jacobson et al., 1986). The structure of KCN_3 may be described as an alternation of two-dimensional perovskite slabs, formed by the cubic array of corner-sharing NbO_6 octahedra and Ca^{2+} ions in 12-coordinated sites in the center of each cube, whose structure remains upon protonation, and K^+ ions, which form so-called interlayer space and undergo substitution by protons (Fukuoka et al., 2000). As it was shown, the ion-exchanged phase $HCa_2Nb_3O_{10} \cdot 1.5H_2O$ undergoes further modification of the interlayer space by intercalation of amines (Jacobson et al., 1987) and may be exfoliated into nanoplatelets by intercalation of bulky organic bases with subsequent physical treatment such as shaking or sonication (Schaak and Mallouk, 2000; Ebina et al., 2002). In addition, the alkali form $KCa_2Nb_3O_{10}$, its protonated form $HCa_2Nb_3O_{10} \cdot 1.5H_2O$ and their exfoliated and restacked composites have been studied as promising highly efficient photocatalytic materials (Domen et al., 1993; Sabio et al., 2012; Oshima et al., 2014).

Although this triple-layered DJ niobate has been widely studied as a starting material for the preparation of inorganic-organic hybrids, the investigations on their photocatalytic properties are not presented in the literature. Based on the limited works performed for other compounds, several important points remain unclear. In particular, it should be further clarified whether the obtained inorganic-organic hybrids may be stable under special conditions during the photocatalytic process and lead to its promotion, or the intercalated organic components, in any case, undergo the photodegradation. Therefore, our work focuses on the synthesis and photocatalytic properties of the *n*-alkylamine modified niobates $HCa_2Nb_3O_{10} \times RNH_2$ as examples of hybrid inorganic-organic layered materials obtained via the intercalation reaction. Their photocatalytic activity was investigated in the reaction of hydrogen evolution from an aqueous methanol solution under ultraviolet radiation and compared with the initial oxide $HCa_2Nb_3O_{10} \cdot yH_2O$.

MATERIALS AND METHODS

Synthesis

$KCa_2Nb_3O_{10}$ (KCN_3)

The initial perovskite-like niobate KCN_3 was synthesized by the standard ceramic method in the air atmosphere at atmospheric pressure using CaO, Nb_2O_5, and K_2CO_3 as reactants:

$4CaO + 3Nb_2O_5 + K_2CO_3 = 2KCa_2Nb_3O_{10} + CO_2\uparrow$

Amounts of oxides CaO and Nb_2O_5 were taken according to the stoichiometry of the reaction, potassium carbonate K_2CO_3- with a 30% excess. All components were mixed and ground in the planetary-ball mill under a layer of *n*-heptane. The powder obtained was pelletized into ∼2 g tablets. The tablets were calcined at 800°C for 12 h, ground in an agate mortar, pelletized again and calcined at 1,100°C for 24 h.

$HCa_2Nb_3O_{10} \cdot yH_2O$ ($HCN_3 \cdot yH_2O$)

The protonated form of the niobate was prepared by acid treatment of KCN_3 with an excess of 12 M HNO_3 (50 ml per 2.5 g of the oxide) at room temperature for 24 h. After this, the product was centrifuged, washed with 50 ml of water three times to remove acid residues and dried under ambient pressure. Subsequent storage of $HCN_3 \cdot yH_2O$ was carried out in an atmosphere of humid air to prevent dehydration.

TABLE 1 | Conditions of the $HCN_3 \times RNH_2$ preparation.

R	Amine concentration, %	Temperature, °C	Duration, d
Me	38 (in water)	25	1
Et	70 (in water)		
Pr	90 (in water)		
Bu			
Hx	100	60	7
Oc	30 (in *n*-heptane)		

$HCa_2Nb_3O_{10} \times RNH_2$ ($HCN_3 \times RNH_2$)

For the synthesis of *n*-alkylamine derivatives $HCN_3 \times RNH_2$ (R= Me, Et, Pr, Bu, Hx, and Oc), in each case, 0.25 g of the protonated form $HCN_3 \cdot yH_2O$ was stirred with 10 ml of the amine solution in a sealed glass tube in accordance with the conditions shown in **Table 1**. Afterwards, each product was filtered, rinsed with acetone to remove residual adsorbed amines, dried under ambient pressure and analyzed via the following methods.

Characterization

XRD Analysis

Powder X-ray diffraction (XRD) patterns were obtained on the Rigaku Miniflex II diffractometer (CuK_α radiation, angle range $2\theta = 3–60°$, scanning rate 10 °/min, step 0.02°). The lattice parameters were calculated in the tetragonal system on the basis of all the reflections observed using DiffracPlus Topas software. During indexing, estimated space groups were also determined.

Raman Spectroscopy

Raman scattering spectra were collected on the Bruker Senterra spectrometer (spectral range 100–4,000 cm^{-1}, incident laser 488 nm 20 mW, spectrum accumulation time 10 s).

IR Spectroscopy

Fourier-transformed infrared (IR) absorption spectra were recorded on the Shimadzu IRAffinity-1 spectrometer (spectral range 400–4,000 cm^{-1}, tableting in KBr).

TG Analysis

Thermogravimetric (TG) analysis of the samples was carried out on the Netzsch TG 209 F1 Libra thermobalance in an oxidative atmosphere (temperature range 30–950°C, heating rate 10°C/min).

CHN Analysis

The amounts of carbon, hydrogen, and nitrogen in *n*-alkylamine derivatives were determined using the Euro EA3028-HT analyzer.

Diffuse Reflectance Spectroscopy

Diffuse reflectance spectroscopy (DRS) of the samples was performed on the Shimadzu UV-2550 spectrophotometer with the ISR-2200 integrating sphere attachment. Optical bandgap energies of the samples were found via transformation of reflectance spectra into coordinates $(F \cdot h\nu)^{1/2} = f(h\nu)$, where F is the Kubelka-Munk function, and further determination of abscissas of the intersection points of linear sections of the graphs.

SEM

The morphology of the samples was investigated on the Zeiss Merlin scanning electron microscope (SEM) with a field emission cathode, an electron optics column GEMINI-II and an oil-free vacuum system.

Vacuum Stability

To investigate the stability of *n*-alkylamine derivatives at reduced pressure, their hitches of 50 mg were placed in a desiccator with the oil vacuum pump Edwards E2M1.5 and held under residual pressure of 10^{-4} atm for 5 and 10 d. Compositions of the resulting samples were determined via the CHN-analysis.

Specific Surface Area

Specific surface areas of the samples were measured by the BET method on the Micromeritics ASAP 2020MP system with the previous vacuum degassing at room temperature using N_2 and Kr as adsorbates.

Stability in Water

To investigate the resistance of *n*-alkylamine derivatives to hydrolysis, their hitches of 50 mg were placed into sealed glass tubes with 10 ml of water and stirred for 1 and 10 d at room temperature. After this, samples were filtered and analyzed by XRD and, in some cases, Raman spectroscopy.

Photocatalytic Experiments

Study of the Hydrogen Generation Kinetics

Photocatalytic activity of the samples was measured in the reaction of light-driven hydrogen evolution from an aqueous solution of methanol. The photocatalytic equipment, as well as the experimental conditions, were the same as in our previous work (Rodionov et al., 2019).

To prepare the suspension for the photocatalytic experiment, 30 mg of the sample was added to 60 ml of 1 mol. % methanol. The mixture was shaken and left for 10 min to establish equilibrium between the photocatalyst and the solution. Then it was sonicated for 10 min in the Elmasonic S10H ultrasound bath to disaggregate the photocatalyst particles.

The suspension obtained (50 ml) was placed in the external irradiation reaction cell, equipped with a magnetic stirrer and a liquid cut-off-filter and connected to a closed gas circulation system (120 ml dead volume). A medium-pressure mercury lamp DRT-125 (125 W) was used as a radiation source. The light was reaching the reaction cell only after passing through a light filter solution (KCl+NaBr, 6 g/L of each salt, 2 cm optical path) thermostated at 15°C, which cuts off radiation with $\lambda < 220$ nm. During the photocatalytic reaction, hydrogen was accumulating in the gas phase, the composition of which was analyzed by the online gas chromatograph (Shimadzu GC-2014, Rt-Msieve 5A Column, TCD, Ar carrier) at certain time intervals. At the beginning of the experiment, the system was deaerated and argon was introduced at atmospheric pressure.

The pH of the suspension and its concentration c (mg/l) determined from its ultraviolet-visible (UV-vis) transmission spectra were measured at the beginning of the photocatalytic experiment (pH_1, c_1), in the ending (pH_2, c_2) and after centrifuging of the suspension at 1000 RCF for 1 h (pH_3, c_3) to take into account a possible change of the suspension concentration during the photocatalytic experiment and potential exfoliation of the sample into nanoplatelets.

The apparent quantum efficiency of hydrogen generation ϕ was calculated by the formula $\phi = \omega/\omega_0$, where ω is the observed hydrogen evolution rate and ω_0 is the theoretical maximum hydrogen evolution rate if we assume that all incident photons with energy greater than bandgap E_g are absorbed with generation of electron-hole pairs, which subsequently lead to hydrogen reduction and alcohol oxidation with a 100% yield without recombination and other side-reactions. For the experimental setup used, $\omega_0 = 7.5$ mmol/h was previously determined via the ferrioxalate actinometry technique (Rodionov et al., 2019).

All the photocatalytic measurements were performed both without a cocatalyst addition and with loading 1 mass. % Pt cocatalyst via *in situ* photocatalytic platinization. In the latter case 1.1 ml of 2.56 mmol/L H_2PtCl_6 aqueous solution was added to 54 ml of the reaction mixture before the experiment. After 15 min of irradiation under argon flushing conditions, a suspension sample of 4 ml was taken to photometrically measure the concentration of platinized particles in the suspension. Additional argon flushing was performed for 15 min to exclude air components from the system and then the system was closed and the measurement was started.

Suspension Concentration and pH Measurements

In order to determine the concentration of photocatalytic suspensions before, after the experiment and after their centrifuging, their UV-vis spectra were recorded on the Thermo Scientific Genesys 10S UV-Vis spectrophotometer at the spectral range of 190–1,100 nm. If necessary, suspensions were diluted to achieve optical density $A < 1$ at the maximum of the most intense band. To determine their concentrations (mg/l) from UV-vis spectra, spectrophotometric calibration plots for suspensions of non-exfoliated (bulk) and exfoliated into nanoplatelets niobate were previously built as it is described in the **Supporting Information S1**.

pH values of the photocatalytic suspensions were determined using the Mettler Toledo S220 SevenCompact pH-meter equipped with the InLabExpert Pro-ISM before, after the experiment and also after their centrifuging after the experiment.

RESULTS AND DISCUSSION

Characterization of the Samples

According to data of the powder XRD analysis (**Figure 1**), protonated layered perovskite-like niobate $HCN_3 \cdot yH_2O$ was successfully obtained in a single-phase form and its lattice parameters were found to be in good consistency with the literature values (Jacobson et al., 1986; Tahara and Sugahara, 2003). Reactions of $HCN_3 \cdot yH_2O$ with *n*-alkylamines lead to a series of single-phase amine derivatives with greater *c* parameters because of intercalation of amines into the interlayer space. In

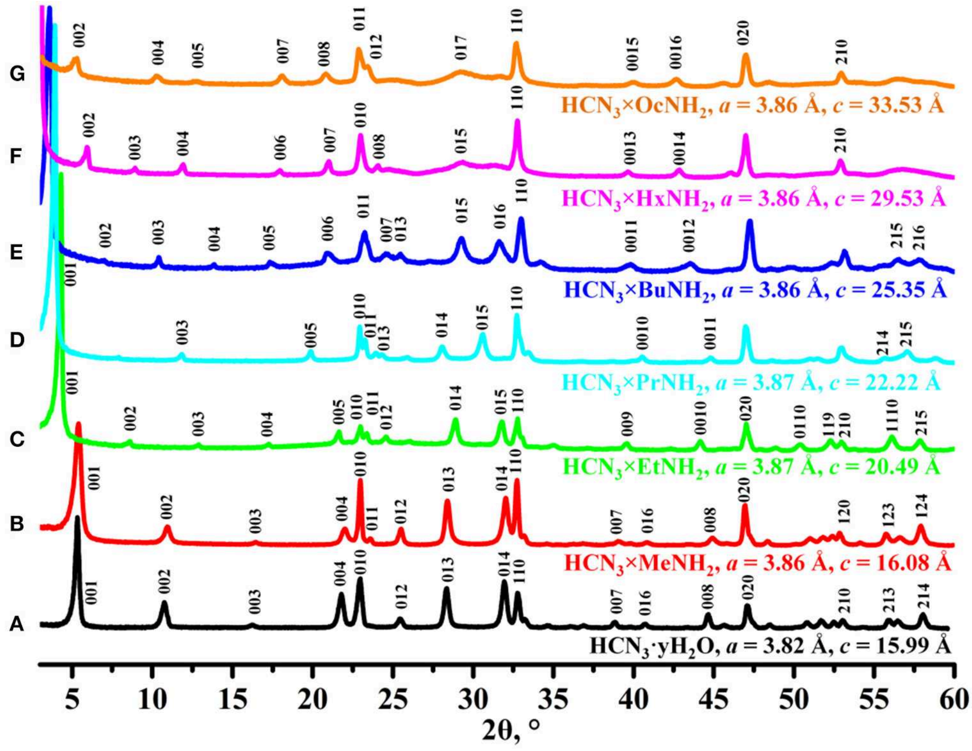

FIGURE 1 | X-ray diffraction patterns and unit cell parameters indexed in tetragonal system (P4/mmm) of **(A)** $HCN_3 \cdot yH_2O$, **(B)** $HCN_3 \times MeNH_2$, **(C)** $HCN_3 \times EtNH_2$, **(D)** $HCN_3 \times PrNH_2$, **(E)** $HCN_3 \times BuNH_2$, **(F)** $HCN_3 \times HxNH_2$, **(G)** $HCN_3 \times OcNH_2$.

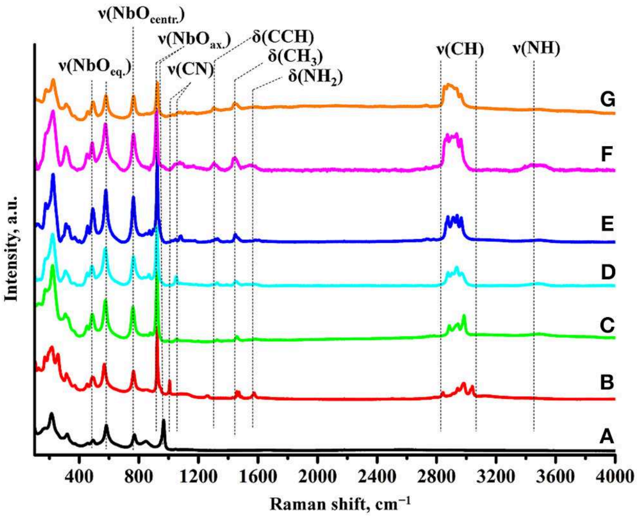

FIGURE 2 | Raman spectra of **(A)** $HCN_3 \cdot yH_2O$, **(B)** $HCN_3 \times MeNH_2$, **(C)** $HCN_3 \times EtNH_2$, **(D)** $HCN_3 \times PrNH_2$, **(E)** $HCN_3 \times BuNH_2$, **(F)** $HCN_3 \times HxNH_2$, **(G)** $HCN_3 \times OcNH_2$.

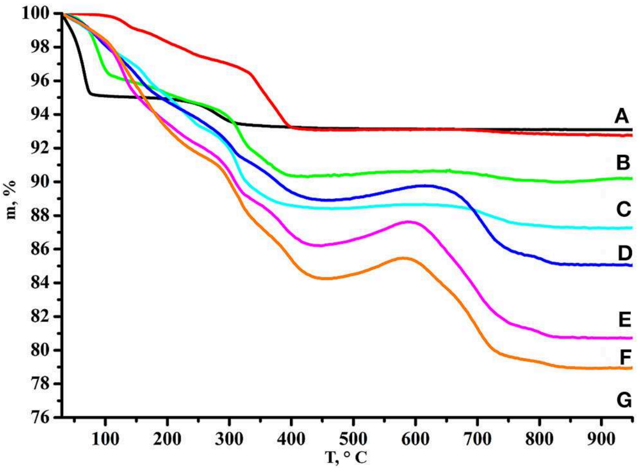

FIGURE 3 | TG curves of **(A)** $HCN_3 \cdot yH_2O$, **(B)** $HCN_3 \times MeNH_2$, **(C)** $HCN_3 \times EtNH_2$, **(D)** $HCN_3 \times PrNH_2$, **(E)** $HCN_3 \times BuNH_2$, **(F)** $HCN_3 \times HxNH_2$, **(G)** $HCN_3 \times OcNH_2$.

general, the *c* lattice parameter, which is known to correspond to the interlayer distance of the sample (Silyukov et al., 2018; Kurnosenko et al., 2019), was found to be proportional to the length of the *n*-alkylamine chain that consists with earlier reports (Jacobson et al., 1986; Tahara and Sugahara, 2003; Kurnosenko et al., 2019; Rodionov et al., 2019). Since all the samples were successfully indexed in the P4/mmm group without doubling of the *c* lattice parameter, we suppose that intercalation of amines did not cause a relative shift of adjacent perovskite slabs which is absent in the case of the initial protonated niobate $HCN_3 \cdot yH_2O$.

Formation of the amine derivatives is clearly seen from their Raman spectra (**Figure 2**). It is accompanied by appearance of characteristic bands relating to latitudinal vibrations of C–C–H (1,310 cm^{-1}), methyl (1,445 cm^{-1}), and amino (1,575 cm^{-1}) fragments as well as stretching of C–N (1,010–1,080 cm^{-1}), C–H (2,820–3,060 cm^{-1}), and N–H (3,430–3,530 cm^{-1}) bonds. Intercalation of amines also results in the shift of the axial Nb–O stretching mode from 965 to 925 cm^{-1}. Unlike the Ruddlesden-Popper titanates (Rodionov et al., 2019), this band does not undergo noticeable splitting into two new bands indicating that all niobium-oxygen octahedra adjacent to the interlayer space possess equal axial Nb–O distances, i.e., almost all the interlayer protons of the initial niobate are associated with molecules of amines. At the same time, stretching modes of equatorial (490, 580 cm^{-1}) and located in central octahedra (765 cm^{-1}) Nb–O fragments are seen not to be influenced by the amines introduction into the inorganic matrix. IR spectra (**Supporting Information S2**) also confirm the formation of the derivatives and point at the presence of water molecules in the interlayer space (1,625 cm^{-1}) that is typical of other amine-modified compounds (Silyukov et al., 2018; Kurnosenko et al., 2019; Rodionov et al., 2019) due to formation of strong hydrogen bonds.

TABLE 2 | Quantitative compositions of the samples ($HCN_3{\cdot}xRNH_2{\cdot}yH_2O$) and their light absorption characteristics.

Sample	x (RNH_2)	y (H_2O)	Total mass loss, %	E_g, eV	λ_{max}, nm
$HCN_3{\cdot}yH_2O$	–	1.5	6.86	3.49	355
$HCN_3 \times MeNH_2$	0.94	0.09	7.23	3.56	348
$HCN_3 \times EtNH_2$	0.97	0.23	9.98	3.60	344
$HCN_3 \times PrNH_2$	0.99	0.40	12.75	3.55	349
$HCN_3 \times BuNH_2$	1.00	0.45	14.95	3.62	343
$HCN_3 \times HxNH_2$	1.06	0.33	19.27	3.55	349
$HCN_3 \times OcNH_2$	0.94	0.31	21.06	3.60	344

Processing of the TG curve (Rodionov et al., 2017, 2019) corresponding to the initial protonated niobate (**Figure 3**) confirmed that $HCN_3{\cdot}yH_2O$ does not contain residual potassium cations from the alkali precursor KCN_3 and exists in the hydrated form $HCN_3{\cdot}1.5H_2O$. Thus, its thermal decomposition proceeds in two steps: deintercalation of the interlayer water (30–70°C) and topochemical condensation of the inorganic matrix (250–350°C) with the formation of $Ca_2Nb_3O_{9.5}$. Mass losses of the *n*-alkylamine derivatives are proportional to molecular masses of intercalated amines and their TG curves demonstrate much more complex behavior. At the first stage (50–400°C) deintercalation of amines and water takes place giving significant mass loss. After a temperature of ∼450°C is reached, mass begins to rise that is more pronounced in the case of heavier amines. This mass gain points out that even at such a high temperature some carbon-containing species are still remaining and that at 450–600°C they undergo partial oxidation. Further heating, apparently, leads to their burning which explains the consequent mass decrease.

Compositions of the derivatives calculated on the basis of TG and CHN-analysis data are presented in **Table 2** in the form $HCN_3{\cdot}xRNH_2{\cdot}yH_2O$. As one can see from the table, the amount of each intercalated amine is approximately equal to the number of protons from the initial protonated form (∼1:1) that conforms to the absence of the axial Nb–O band splitting in the Raman spectra (**Figure 2**).

Table 2 contains optical bandgap energies E_g of the samples calculated from their transformed diffuse reflectance spectra (**Supporting Information S3**) and corresponding maximum wavelengths λ_{max} of absorbed light. According to the presented data, all the samples mainly absorb the radiation of the near-ultraviolet region and intercalation of amines slightly increases the E_g value because of the interlayer space expansion (Rodionov et al., 2017). Thus, there is no factor of different amounts of available light that could otherwise explain the difference in observed photocatalytic activity of the samples.

According to SEM images of the samples (**Supporting Information S4**), their particles are presented as intergrown lamellar polycrystals possessing linear sizes of

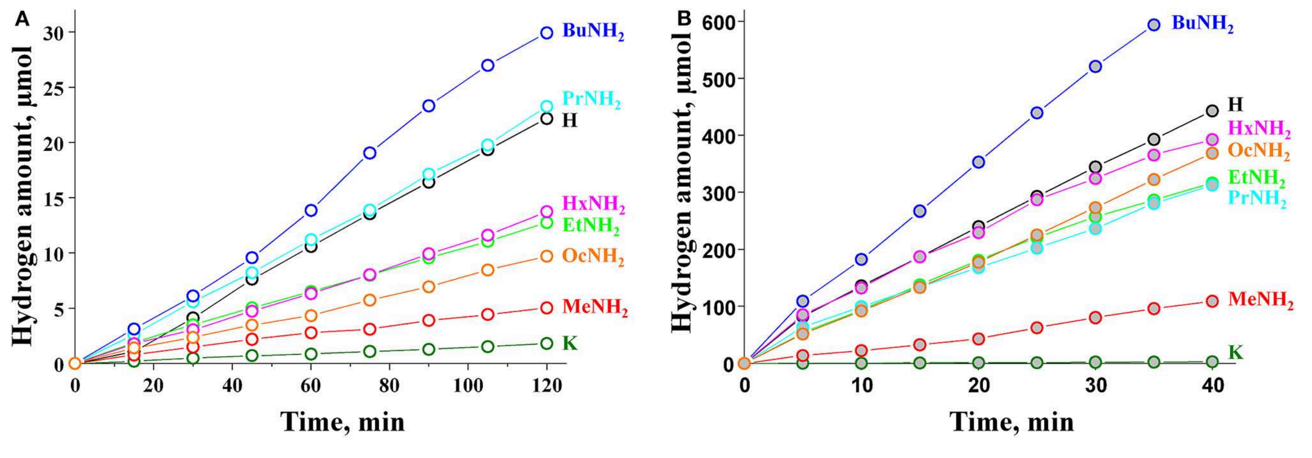

FIGURE 4 | Kinetic curves of photocatalytic hydrogen evolution over **(A)** bare and **(B)** platinized KCN_3, $HCN_3{\cdot}yH_2O$, and $HCN_3 \times RNH_2$.

0.5–2.5 μm and thickness of 150–500 nm that is typical of ceramic layered oxides. Moreover, intercalation of amines does not greatly affect the morphology of particles that is due to the topochemical mechanism of the aforementioned reaction.

Prior to the measurement of specific surface areas by BET, the stability of the amine derivatives under vacuum conditions was studied. **Supporting Information S5** summarizes amounts of intercalated amines per formula unit in the initial derivatives as well as in the samples kept for 5 and 10 d under residual pressure of 10^{-4} atm. As one can see from the table, the amine content in most cases remains virtually unchanged. It means *n*-alkylamine derivatives $HCN_3 \times RNH_2$ are stable under reduced pressure and may be investigated by BET and other methods requiring previous degassing at room temperature. High stability of the compounds is, apparently, connected with strong ionic bonding between interlayer amines and the inorganic matrix.

All the samples studied by BET ($HCN_3 \cdot yH_2O$, $HCN_3 \times MeNH_2$, $HCN_3 \times OcNH_2$) possess a small specific surface area that is typical of ceramic oxide materials. Since BET measurements in this range are carried out with a relatively high error, we present data obtained with two different adsorbates (**Supporting Information S6**). According to the results, protonation and formation of the *n*-alkylamine derivatives are not accompanied by a noticeable change in the specific surface area (that is consistent with minor changes in the morphology of the samples noted by the results of SEM) and, consequently, this factor should not be the main reason for differences in their photocatalytic properties.

TABLE 3 | Rate of photocatalytic hydrogen evolution (ω) and its apparent quantum efficiency at 220–340 nm (ϕ) from 1 mol. % aqueous methanol solution.

Photocatalyst	Bare photocatalyst		Pt-loaded photocatalyst	
	ω, mmol/h	**ϕ, %**	**ω, mmol/h**	**ϕ, %**
KCN_3	0.0009	0.012	0.005	0.072
HCN_3	0.012	0.16	0.62	8.3
$HCN_3 \times MeNH_2$	0.0024	0.032	0.17	2.3
$HCN_3 \times EtNH_2$	0.0061	0.082	0.46	6.1
$HCN_3 \times PrNH_2$	0.012	0.16	0.43	5.7
$HCN_3 \times BuNH_2$	0.016	0.22	0.99	13
$HCN_3 \times HxNH_2$	0.0069	0.091	0.54	7.2
$HCN_3 \times OcNH_2$	0.0048	0.064	0.55	7.3

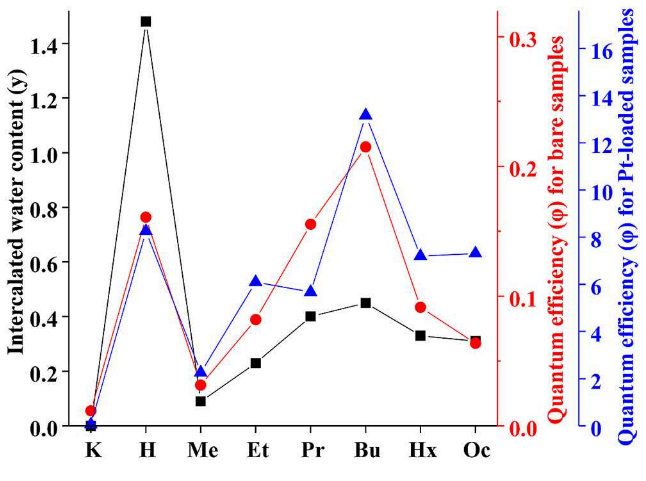

FIGURE 5 | Correlation between apparent quantum efficiency of photocatalytic hydrogen evolution over KCN_3, $HCN_3 \cdot yH_2O$, and $HCN_3 \times RNH_2$ and intercalated water content (y).

Comparison of XRD patterns of initial amine derivatives and products obtained via their water treatment (**Supporting Information S7**) showed that methylamine- and ethylamine-containing samples do not undergo any noticeable changes in the interlayer distance since their (00x) reflections preserve initial positions indicating maintaining the *c* lattice parameter. Preservation of organic components in these samples was also confirmed by characteristic bands in their Raman spectra (not shown). However, water treatment of the *n*-propylamine derivative lead to the formation of new by-phases that may be explained by partial leaching of *n*-propylamine or additional hydration of the interlayer space. Keeping of the *n*-butylamine derivative in water for 10 d gave a new phase with significantly increased interlayer distance. Such expansion of the interlayer space should be due to its strong hydration. In the case of *n*-hexylamine and *n*-octylamine derivatives, structural changes during water treatment are practically absent. This fact may be connected with the low polarity of long-chain *n*-alkylamines which makes intercalation of polar water molecules a thermodynamically unprofitable process.

Photocatalytic Activity

The results of photocatalytic experiments are presented in **Figure 4**. The kinetic curves demonstrate almost linear behavior during the time of measurement (120 min for bare samples and 40 min for Pt-loaded samples). The hydrogen evolution rate ω was calculated for each sample from the slope of the kinetic curve. These data, together with the calculated values of apparent quantum efficiency ϕ, are collected in **Table 3**. The standard error of the hydrogen evolution rate determined is estimated at 7%.

The initial potassium niobate KCN_3 showed poor photocatalytic activity with a quantum efficiency of hydrogen evolution as low as 0.012%. However, after protonation, this value increased ca. 14-fold and reached 0.16% for the HCN_3 sample. This effect is already known from the literature (Domen et al., 1993) and is explained by the capability of the protonated form to reversibly intercalate water into the interlayer space, which is considered a separate reaction zone for the oxidation half-reaction. Our study supports this data, showing that the HCN_3 sample contains 1.5 water molecules per formula unit (**Table 2**). KCN_3, however, does not intercalate water at ambient conditions.

By analogy with the triple-layered titanate $H_2Nd_2Ti_3O_{10}$ (Rodionov et al., 2019), we expected the photocatalytic activity to rise significantly after the *n*-alkylamines intercalation. However, it was not quite the case. We see that the methylamine sample $HCN_3 \times MeNH_2$ shows 4 times lower

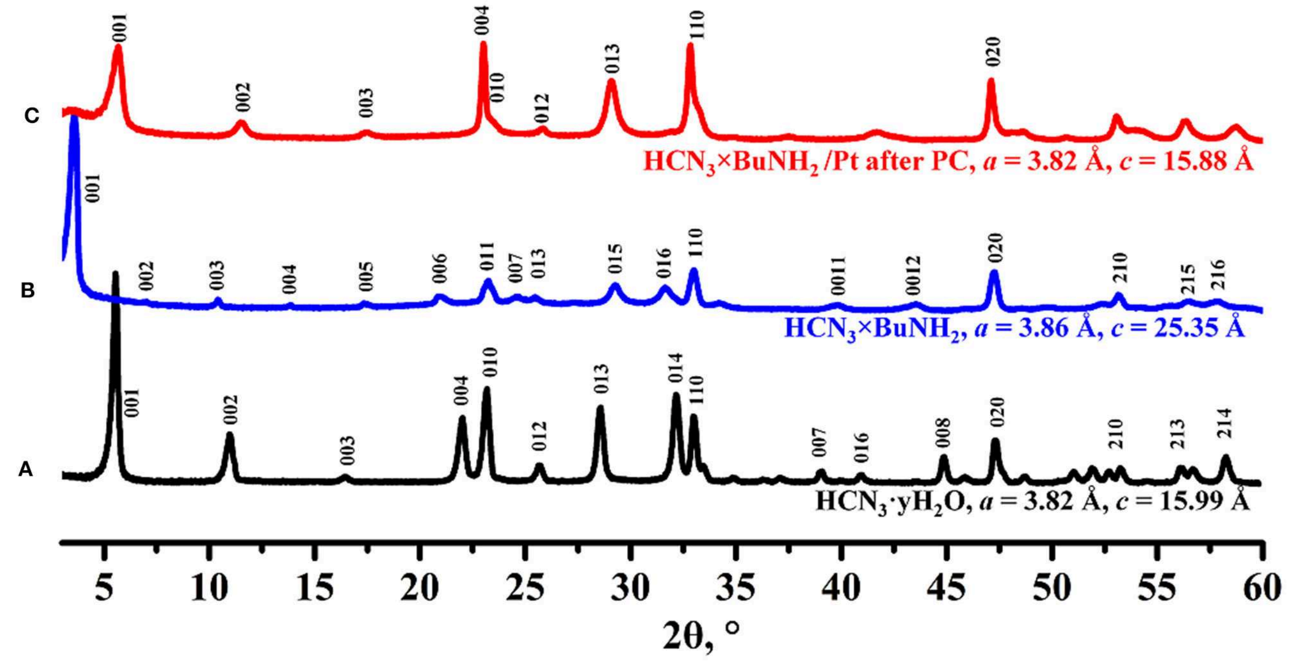

FIGURE 6 | XRD patterns of **(A)** HCN_3·yH_2O, **(B)** HCN_3×$BuNH_2$ before photocatalysis, **(C)** HCN_3×$BuNH_2$/Pt after photocatalysis.

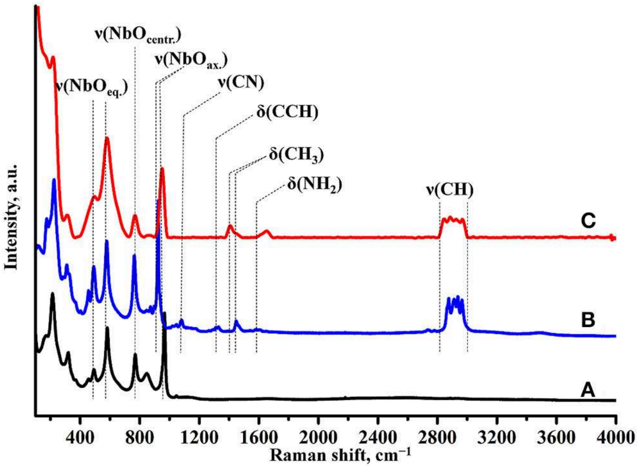

FIGURE 7 | Raman spectra of **(A)** HCN_3·yH_2O, **(B)** HCN_3×$BuNH_2$ before photocatalysis, **(C)** HCN_3×$BuNH_2$/Pt after photocatalysis.

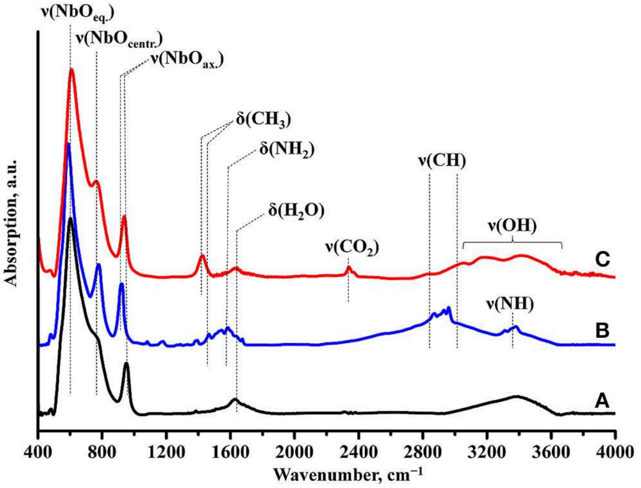

FIGURE 8 | IR spectra of **(A)** HCN_3·yH_2O, **(B)** HCN_3×$BuNH_2$ before photocatalysis, **(C)** HCN_3×$BuNH_2$/Pt after photocatalysis.

activity compared to the protonated form. Subsequently, the efficiency rises with the increase of the carbon chain length of the amine reaching a maximum value of 0.22% for HCN_3×$BuNH_2$. This value exceeds that for HCN_3 only by a factor of 1.4. For HCN_3×$HxNH_2$ and HCN_3×$OcNH_2$ the hydrogen production rate decreases. Although there is no strict explanation for such behavior, we noticed, that the hydrogen evolution efficiency strongly correlates with the amount of water contained in the amine-intercalated samples (**Figure 5**). Moreover, the highest photocatalytic activity was demonstrated by precisely those samples (HCN_3×$PrNH_2$ and HCN_3×$BuNH_2$) for which the greatest tendency to hydrolysis was revealed (**Supporting Information S7**). We can, therefore, assume that it is the intercalated water that mainly contributes to the photocatalytic activity rather than the amine itself. The amine molecules may create transport channels for the water molecules by the expansion of the interlayer space and thus increase their mobility. However, in the case of compact methylamine molecules, there is almost no expansion compared with the hydrated protonated form (**Figure 1**). Methylamine just substitutes water in the interlayer space and thus the photocatalytic activity decreases. The results obtained are in contrast with the study of the triple-layered titanate $H_2Nd_2Ti_3O_{10}$ because its initial protonated form is not capable of reversible water intercalation. After loading of 1 mass. % platinum, activities of all the samples increased 50–100 times except for the low active KCN_3. The general dependence of the hydrogen evolution rate on the nature of intercalated amine remains the same after platinization (**Figure 5**). The $HCN_3 \times BuNH_2$ sample demonstrates the maximum quantum efficiency of 13%, which is 1.6 times higher than for the protonated sample $HCN_3 \cdot yH_2O$, but 1.9 times lower than for the *n*-butylamine-intercalated $H_2Nd_2Ti_3O_{10}$ under the same conditions (Rodionov et al., 2019). During the photocatalytic experiment, a 14-fold excess of hydrogen (0.6 mmol) compared to *n*-butylamine (0.04 mmol) was formed without significant loss of the reaction rate. Therefore, we can conclude that hydrogen is mainly formed from the reaction solution rather than from the intercalated amine. In most cases, there were no significant differences in the pH and suspension concentrations which could affect the results of photocatalytic experiments (**Supporting Information S8**).

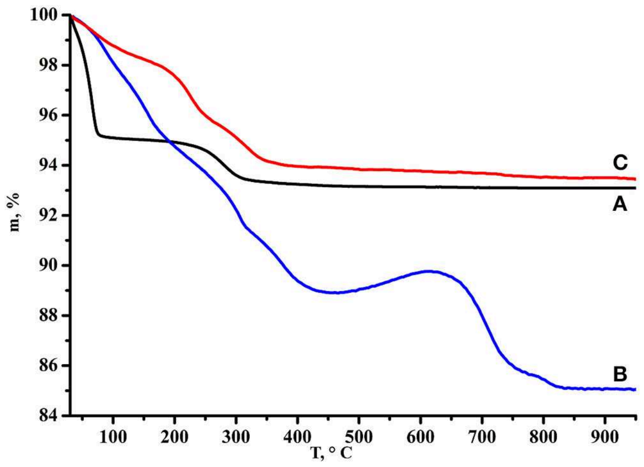

FIGURE 9 | TG curves of **(A)** $HCN_3 \cdot yH_2O$, **(B)** $HCN_3 \times BuNH_2$ before photocatalysis, **(C)** $HCN_3 \times BuNH_2/Pt$ after photocatalysis.

Analysis of $HCN_3 \times BuNH_2/Pt$ After the Photocatalytic Measurement

To investigate possible changes in the structure and composition of the derivatives during the photocatalytic process, the most photocatalytically active sample $HCN_3 \times BuNH_2/Pt$ was collected after the measurement via filtering and thoroughly analyzed.

Powder XRD analysis (**Figure 6**) reveals that the crystal structure of the initial compound $HCN_3 \times BuNH_2$ changed after the photocatalytic experiment. Despite the broadened reflections, the obtained compound can be indexed in the tetragonal system with lattice parameters $a = 3.86$ Å, $c = 15.88$ Å. This indicates a significant narrowing of the interlayer distance compared to the initial *n*-butylamine derivative $HCN_3 \times BuNH_2$

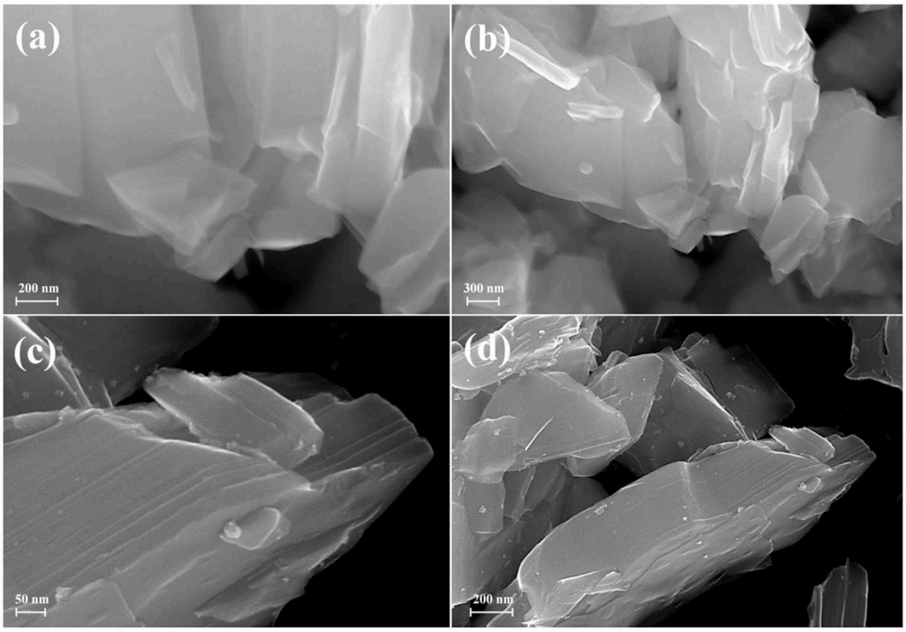

FIGURE 10 | SEM images of **(a,b)** $HCa_2Nb_3O_{10} \times BuNH_2$ before photocatalysis, **(c,d)** $HCa_2Nb_3O_{10} \times BuNH_2/Pt$ after photocatalysis.

and is comparable to the interlayer distance of the protonated form $HCN_3 \cdot yH_2O$.

Raman spectroscopy (**Figure 7**) indicates the presence of the organic component in the sample after photocatalysis. However, the band, relating to latitudinal vibrations of the methyl group in the initial compound shifts from 1,445 to 1,415 cm^{-1}, a new band at 1,650 cm^{-1} appears and intensity of the C–H stretching bands (2,820–3,060 cm^{-1}) decreases. These facts clearly show that the interlayer organic component inevitably undergoes some changes during the photocatalytic experiment. IR spectroscopy data (**Figure 8**) are fully consistent with this assumption and point at the high degree of hydration of $HCN_3 \times BuNH_2/Pt$ (wide intense band of O–H stretching at 3,000–3,600 cm^{-1}).

The TG curve of $HCN_3 \times BuNH_2/Pt$ (**Figure 9**) demonstrates smaller total mass loss (6.5%) and no mass gain as compared with initial $HCN_3 \times BuNH_2$ that points at the reduced organics fraction in the sample. Additionally, results of the CHN-analysis (0.77% N, 0.96% C and 0.75% H of the total sample mass) allow suggesting that organic content in the sample is low and no more than ∼2.5% of the total mass loss on the TG curve may be related to the organic component; the rest mass loss should correspond to the high amount of water in the sample. Moreover, the C:N ratio changes to 1.5:1, i.e., the carbon skeleton of the organic component does not remain unchanged.

SEM investigation (**Figure 10**) showed that the morphology of the sample does not considerably change during the photocatalytic measurement with platinization. Platinum nanoparticles are observed at the SEM images as light dots with linear sizes of 4–6 nm.

CONCLUSIONS

In the presented work we have tested the photocatalytic activity of a series of *n*-alkylamine derivatives $HCN_3 \times RNH_2$ (R = Me, Et, Pr, Bu, Hx, and Oc) of the layered niobate $HCa_2Nb_3O_{10}$ (HCN_3). The change of the hydrogen production rate after *n*-alkylamine intercalation strongly depended on the nature of the amine. The platinized *n*-butylamine sample $HCN_3 \times BuNH_2/Pt$ showed the greatest efficiency of $\phi = 13\%$, that is 1.6 times higher compared to the initial protonated form $HCN_3 \cdot yH_2O/Pt$ ($\phi = 8.3\%$), while the methylamine sample $HCN_3 \times MeNH_2/Pt$ demonstrated the least efficiency of $\phi = 2.3\%$. The photocatalytic activity correlates with the amount of water in the interlayer space as well as the reactivity of the samples with respect to hydrolysis. Thus, we assume that it is the intercalated water that mainly contributes to the photocatalytic activity. The role of the amine may be associated with the expansion of the interlayer space that creates transport channels for water molecules and increases their mobility. On the example of the most active sample $HCN_3 \times BuNH_2$ it was shown that the amine in the interlayer space undergoes chemical changes during the photocatalytic experiment, resulting in a decrease of the interlayer distance, a decrease of the total organic content and also a decrease of the C:N molar ratio. However, there still remains a significant amount of organic molecules in the interlayer space that was proven by Raman spectroscopy and CHN-analysis, and the hydrogen evolution rate remains stable during the time of the measurement. The obtained results can be used to develop relevant methods for producing hydrogen fuel using bio alcohols, the representative of which is the methanol used in the work. Despite the fact that the *n*-butylamine sample turned out to be the most active under the conditions of the experiments, a more detailed study is necessary to maximize the observed effect of intercalation of organic amines, which includes variation of experimental conditions and testing of a wider range of introduced compounds. Also, further studies will be performed to investigate carefully the composition, structure and properties of the samples obtained after photocatalytic measurements.

DATA AVAILABILITY STATEMENT

The datasets generated for this study are available on request to the corresponding author.

AUTHOR CONTRIBUTIONS

IR, OS, and IZ contributed conception and design of the study. Experimental work was carried out by VV and SK (photocatalytic experiments), VV, SK, and IM (synthesis, characterization) under supervision of IR, OS, and IZ. All authors participated in the analysis and discussion of the obtained results. SK and OS wrote the manuscript and prepared images with contributions of IR and VV in certain sections.

FUNDING

This study was financially supported by the Russian Science Foundation (project No 19-13-00184).

ACKNOWLEDGMENTS

The study was technically supported by the Saint Petersburg State University Research Park. Authors are grateful to the Centre for X-ray Diffraction Studies (XRD analysis), Centre for Optical and Laser Materials Research (Raman spectroscopy), Centre for Chemical Analysis and Materials Research (IR spectroscopy, DRS, CHN analysis), Centre for Thermal Analysis and Calorimetry (TG analysis), Interdisciplinary Centre for Nanotechnology (SEM), Centre for Innovative Technologies of Composite Nanomaterials (BET).

SUPPLEMENTARY MATERIAL

The Supplementary Material for this article can be found online at: https://www.frontiersin.org/articles/10.3389/fchem.2020.00300/full#supplementary-material

REFERENCES

Boykin, J. R., and Smith, L. J. (2015). Rapid microwave-assisted grafting of layered perovskites with n-alcohols. *Inorg. Chem.* 54, 4177–4179. doi: 10.1021/ic503001w

Chen, W., Li, C., Gao, H., Yuan, J., Shangguan, W., Su, J., et al. (2012). Photocatalytic water splitting on protonated form of layered perovskites $K_{0.5}La_{0.5}Bi_2M_2O_9$ (M = Ta; Nb) by ion-exchange. *Int. J. Hydrogen Energy* 37, 12846–12851. doi: 10.1016/j.ijhydene.2012.05.090

Compton, O. C., Carroll, E. C., Kim, J. Y., Larsen, D. S., and Osterloh, F. E. (2007). Calcium niobate semiconductor nanosheets as catalysts for photochemical hydrogen evolution from water. *J. Phys. Chem. C* 111, 14589–14592. doi: 10.1021/jp0751155

Cui, W., Guo, D., Liu, L., Hu, J., Rana, D., and Liang, Y. (2014). Preparation of $ZnIn_2S_4/K_2La_2Ti_3O_{10}$ composites and their photocatalytic H_2 evolution from aqueous Na_2S/Na_2SO_3 under visible light irradiation. *Catal. Commun.* 48, 55–59. doi: 10.1016/j.catcom.2014.01.026

Cui, W., Liu, L., Ma, S., Liang, Y., and Zhang, Z. (2013). CdS-sensitized $K_2La_2Ti_3O_{10}$ composite: a new photocatalyst for hydrogen evolution under visible light irradiation. *Catal. Today* 207, 44–49. doi: 10.1016/j.cattod.2012.05.009

Cui, W., Qi, Y., Liu, L., Rana, D., Hu, J., and Liang, Y. (2012). Synthesis of PbS–$K_2La_2Ti_3O_{10}$ composite and its photocatalytic activity for hydrogen production. *Prog. Nat. Sci. Mater. Int.* 22, 120–125. doi: 10.1016/j.pnsc.2012.03.002

Dion, M., Ganne, M., and Tournoux, M. (1981). Nouvelles familles de phases $M^IM^{II}_2Nb_3O_{10}$ a feuillets "perovskites." *Mater. Res. Bull.* 16, 1429–1435. doi: 10.1016/0025-5408(81)90063-5

Domen, K., Yoshimura, J., Sekine, T., Kondo, J., Tanaka, A., Maruya, K., et al. (1993). A novel series of photocatalysts with an ion-exchangeable layered structure of niobate. *Stud. Surf. Sci. Catal.* 2159–2162. doi: 10.1016/S0167-2991(08)64250-0

Ebina, Y., Sasaki, T., and Watanabe, M. (2002). Study on exfoliation of layered perovskite-type niobates. *Solid State Ionics* 151, 177–182. doi: 10.1016/S0167-2738(02)00707-5

Fukuoka, H., Isami, T., and Yamanaka, S. (2000). Crystal structure of a layered perovskite niobate $KCa_2Nb_3O_{10}$. *J. Solid State Chem.* 151, 40–45. doi: 10.1006/jssc.2000.8619

Guo, T., Wang, L., Evans, D. G., and Yang, W. (2010). Synthesis and photocatalytic properties of a polyaniline-intercalated layered protonic titanate nanocomposite with a p–n heterojunction structure. *J. Phys. Chem. C* 114, 4765–4772. doi: 10.1021/jp9055413

Han, Y.-S., Park, I., and Choy, J.-H. (2001). Exfoliation of layered perovskite, $KCa_2Nb_3O_{10}$, into colloidal nanosheets by a novel chemical process. *J. Mater. Chem.* 11, 1277–1282. doi: 10.1039/b006045n

Hong, Y., and Kim, S.-J. (1996). Intercalation of primary diamines in the layered perovskite oxides, $HSr_2Nb_3O_{10}$. *Bull. Korean Chem. Soc.* 17, 730–735.

Huang, Y., Li, J., Wei, Y., Li, Y., Lin, J., and Wu, J. (2009). Fabrication and photocatalytic property of Pt-intercalated layered perovskite niobates $H_{1-x}LaNb_{2-x}Mo_xO_7$ (x = 0–0.15). *J. Hazard. Mater.* 166, 103–108. doi: 10.1016/j.jhazmat.2008.11.040

Huang, Y., Li, Y., Wei, Y., Huang, M., and Wu, J. (2011). Photocatalytic property of partially substituted Pt-intercalated layered perovskite, $ASr_2Ta_xNb_{3-x}O_{10}$ (A=K, H; x=0, 1, 1.5, 2 and 3). *Sol. Energy Mater. Sol. Cells* 95, 1019–1027. doi: 10.1016/j.solmat.2010.12.017

Huang, Y., Wu, J., Li, T., Hao, S., and Lin, J. (2006). Synthesis and photocatalytic properties of $H_2La_2Ti_3O_{10}/TiO_2$ intercalated nanomaterial. *J. Porous Mater.* 13, 55–59. doi: 10.1007/s10934-006-5490-6

Jacobson, A. J., Johnson, J. W., and Lewandowski, J. (1987). Intercalation of the layered solid acid $HCa_2Nb_3O_{10}$ by organic amines. *Mater. Res. Bull.* 22, 45–51. doi: 10.1016/0025-5408(87)90148-6

Jacobson, A. J., Johnson, J. W., and Lewandowski, J. T. (1985). Interlayer chemistry between thick transition-metal oxide layers: synthesis and intercalation reactions of $K[Ca_2Na_{n-3}Nb_nO_{3n+1}]$ (3.ltoreq. n.ltoreq. 7). *Inorg. Chem.* 24, 3727–3729. doi: 10.1021/ic00217a006

Jacobson, A. J., Lewandowski, J. T., and Johnson, J. W. (1986). Ion exchange of the layered perovskite $KCa_2Nb_3O_{10}$ by protons. *J. Less Common Met.* 116, 137–146. doi: 10.1016/0022-5088(86)90224-9

Kawashima, K., Hojamberdiev, M., Chen, S., Yubuta, K., Wagata, H., Domen, K., et al. (2017). Understanding the effect of partial N^{3-} to O^{2-} substitution and H^+ to K^+ exchange on photocatalytic water reduction activity of Ruddlesden–Popper layered perovskite $KLaTiO_4$. *Mol. Catal.* 432, 250–258. doi: 10.1016/j.mcat.2017.01.004

Kickelbick, G. (2007). *Hybrid Materials: Synthesis, Characterization, and Applications*. Weinheim: Wiley-VCH Verlag GmbH & Co. KGaA.

Kumar, V., Govind., and Uma, S. (2011). Investigation of cation (Sn^{2+}) and anion (N^{3-}) substitution in favor of visible light photocatalytic activity in the layered perovskite $K_2La_2Ti_3O_{10}$. *J. Hazard. Mater.* 189, 502–508. doi: 10.1016/j.jhazmat.2011.02.064

Kurnosenko, S. A., Silyukov, O. I., Mazur, A. S., and Zvereva, I. A. (2019). Synthesis and thermal stability of new inorganic-organic perovskite-like hybrids based on layered titanates $HLnTiO_4$ (Ln = La, Nd). *Ceram. Int.* 46, 5058–5068. doi: 10.1016/j.ceramint.2019.10.249

Liu, C., Wu, L., Chen, J., Liang, J. Y., Li, C. S., Ji, H. M., et al. (2014). The nanocomposite of polyaniline and nitrogen-doped layered $HTiNbO_5$ with excellent visible-light photocatalytic performance. *Phys. Chem. Chem. Phys.* 16, 13409–13417. doi: 10.1039/c4cp01423e

Liu, Y., Zhou, Y., Lv, C., Zhang, C., Jin, X., Meng, Q., et al. (2018). Construction of 2D-composite $HCa_2Nb_3O_{10}$ /$CaNb_2O_6$ heterostructured photocatalysts with enhanced hydrogen production performance. *New J. Chem.* 42, 681–687. doi: 10.1039/C7NJ03707D

Machida, M., Mitsuyama, T., Ikeue, K., Matsushima, S., and Arai, M. (2005). Photocatalytic property and electronic structure of triple-layered perovskite tantalates, $MCa_2Ta_3O_{10}$ (M = Cs, Na, H, and $C_6H_{13}NH_3$). *J. Phys. Chem. B* 109, 7801–7806. doi: 10.1021/jp044833d

Maeda, K. (2011). Photocatalytic water splitting using semiconductor particles: history and recent developments. *J. Photochem. Photobiol. C Photochem. Rev.* 12, 237–268. doi: 10.1016/j.jphotochemrev.2011.07.001

Mir, S. H., Nagahara, L. A., Thundat, T., Mokarian-Tabari, P., Furukawa, H., and Khosla, A. (2018). Review—organic-inorganic hybrid functional materials: an integrated platform for applied technologies. *J. Electrochem. Soc.* 165, B3137–B3156. doi: 10.1149/2.0191808jes

Oshima, T., Ishitani, O., and Maeda, K. (2014). Non-sacrificial water photo-oxidation activity of lamellar calcium niobate induced by exfoliation. *Adv. Mater. Interfaces* 1:1400131. doi: 10.1002/admi.201400131

Reddy, V., Hwang, D., and Lee, J. (2003). Effect of Zr substitution for Ti in $KLaTiO_4$ for photocatalytic water splitting. *Catal. Lett.* 90, 39–44. doi: 10.1023/A:1025812125852

Rodionov, I., Maksimova, E., Pozhidaev, A., Kurnosenko, S., Silyukov, O., and Zvereva, I. (2019). Layered Titanate $H_2Nd_2Ti_3O_{10}$ intercalated with n-Butylamine: a new highly efficient hybrid photocatalyst for hydrogen production from Aqueous solutions of Alcohols. *Front. Chem.* 7:863. doi: 10.3389/fchem.2019.00863

Rodionov, I. A., Mechtaeva, E. V., Burovikhina, A. A., Silyukov, O. I., Toikka, M. A., and Zvereva, I. A. (2018). Effect of protonation on the photocatalytic activity of the $K_2La_2Ti_3O_{10}$ layered oxide in the reaction of hydrogen production. *Chem. Mon.* 149, 475–482. doi: 10.1007/s00706-017-2105-7

Rodionov, I. A., Silyukov, O. I., Utkina, T. D., Chislov, M. V., Sokolova, Y. P., and Zvereva, I. A. (2012). Photocatalytic properties and hydration of perovskite-type layered titanates $A_2Ln_2Ti_3O_{10}$ (A = Li, Na, K; Ln = La, Nd). *Russ. J. Gen. Chem.* 82, 1191–1196. doi: 10.1134/S1070363212070018

Rodionov, I. A., Sokolova, I. P., Silyukov, O. I., Burovikhina, A. A., Fateev, S. A., and Zvereva, I. A. (2017). Protonation and photocatalytic activity of the $Rb_2La_2Ti_3O_{10}$ layered oxide in the reaction of hydrogen production. *Int. J. Photoenergy* 2017:9628146. doi: 10.1155/2017/9628146

Sabio, E. M., Chamousis, R. L., Browning, N. D., and Osterloh, F. E. (2012). Photocatalytic water splitting with suspended calcium Niobium oxides: why nanoscale is better than bulk–a kinetic analysis. *J. Phys. Chem. C* 116, 3161–3170. doi: 10.1021/jp209006n

Saito, K., Kozeni, M., Sohmiya, M., Komaguchi, K., Ogawa, M., Sugahara, Y., et al. (2016). Unprecedentedly enhanced solar photocatalytic activity of a layered titanate simply integrated with TiO_2 nanoparticles. *Phys. Chem. Chem. Phys.* 18, 30920–30925. doi: 10.1039/c6cp05635k

Sanchez, P. G.-R. C. (2006). *Functional Hybrid Materials*. Weinheim: Wiley-VCH Verlag GmbH & Co. KGaA.

Sato, S., Shintani, K., Idota, N., Nishino, T., and Sugahara, Y. (2017). Effect of the graft density of cellulose diacetate-modified layered perovskite nanosheets on mechanical properties of the transparent organic–inorganic hybrids bearing covalent bonds at the interface. *Cellulose* 24, 5463–5473. doi: 10.1007/s10570-017-1475-7

Schaak, R. E., and Mallouk, T. E. (2000). Prying apart ruddlesden–popper phases: exfoliation into sheets and nanotubes for assembly of perovskite thin films. *Chem. Mater.* 12, 3427–3434. doi: 10.1021/cm000495r

Seiichi, T., and Tahara, S. (2007). *Preparation of Inorganic-Organic Hybrids via Intercalation and Grafting Reactions of Protonated Forms of Ion-Exchangeable Layered Perovskites Thesis Submitted To Waseda University Seiichi Tahara.* Available online at: https://dspace.wul.waseda.ac.jp/dspace/handle/2065/28481 (accessed December 23, 2012).

Shelyapina, M. G., Nefedov, D. Y., Kostromin, A. V., Silyukov, O. I., and Zvereva, I. A. (2019). Proton mobility in Ruddlesden–Popper phase $H_2La_2Ti_3O_{10}$ studied by 1H NMR. *Ceram. Int.* 45, 5788–5795. doi: 10.1016/j.ceramint.2018.12.045

Shimizu, K., Itoh, S., Hatamachi, T., Kitayama, Y., and Kodama, T. (2006). Pillaring of Ruddlesden–Popper perovskite tantalates, $H_2ATa_2O_7$ (A = Sr or $La_{2/3}$), with n-alkylamines and oxide nanoparticles. *J. Mater. Chem.* 16, 773-779. doi: 10.1039/b514066h

Shori, S., Pellechia, P. J., Zur Loye, H.-C., and Ploehn, H. J. (2015). Covalent grafting of phenylphosphonate on calcium niobate platelets. *J. Colloid Interface Sci.* 437, 97–110. doi: 10.1016/j.jcis.2014.09.024

Silyukov, O. I., Abdulaeva, L. D., Burovikhina, A. A., Rodionov, I. A., and Zvereva, I. A. (2015). Phase transformations during $HLnTiO_4$ (Ln=La, Nd) thermolysis and photocatalytic activity of obtained compounds. *J. Solid State Chem.* 226, 101–106. doi: 10.1016/j.jssc.2015.02.008

Silyukov, O. I., Kurnosenko, S. A., and Zvereva, I. A. (2018). Intercalation of Methylamine into the protonated forms of layered Perovskite-like oxides $HLnTiO_4$ (Ln = La and Nd). *Glas. Phys. Chem.* 44, 428–432. doi: 10.1134/S1087659618050176

Tahara, S., Ichikawa, T., Kajiwara, G., and Sugahara, Y. (2007). Reactivity of the Ruddlesden–Popper phase $H_2La_2Ti_3O_{10}$ with organic compounds: intercalation and grafting reactions. *Chem. Mater.* 19, 2352–2358. doi: 10.1021/cm0623662

Tahara, S., and Sugahara, Y. (2003). Interlayer surface modification of the protonated triple-layered perovskite $HCa_2Nb_3O_{10}\cdot xH_2O$ with n -Alcohols. *Langmuir* 19, 9473–9478. doi: 10.1021/la0343876

Takahashi, S., Nakato, T., Hayashi, S., Sugahara, Y., and Kuroda, K. (1995). Formation of Methoxy-modified interlayer surface via the reaction between methanol and layered perovskite HLaNb2O7.cntdot.xH2O. *Inorg. Chem.* 34, 5065–5069. doi: 10.1021/ic00124a023

Takeda, Y., Momma, T., Osaka, T., Kuroda, K., and Sugahara, Y. (2008). Organic derivatives of the layered perovskite $HLaNb_2O_7\cdot xH_2O$ with polyether chains on the interlayer surface: characterization, intercalation of $LiClO_4$, and ionic conductivity. *J. Mater. Chem.* 18, 3581–3587. doi: 10.1039/b802003e

Takeda, Y., Suzuki, H., Notsu, K., Sugimoto, W., and Sugahara, Y. (2006). Preparation of a novel organic derivative of the layered perovskite bearing $HLaNb_2O_7\cdot nH_2O$ interlayer surface trifluoroacetate groups. *Mater. Res. Bull.* 41, 834–841. doi: 10.1016/j.materresbull.2005.10.004

Tong, Z., Zhang, G., Takagi, S., Shimada, T., Tachibana, H., and Inoue, H. (2005). Preparation and characterization of a transparent thin film of the layered perovskite, $K_2La_2Ti_3O_{10}$, intercalated with an ionic porphyrin. *Chem. Lett.* 34, 632–633. doi: 10.1246/cl.2005.632

Tsunoda, Y., Sugimoto, W., and Sugahara, Y. (2003). Intercalation behavior of n-alkylamines into a protonated form of a layered perovskite derived from aurivillius phase $Bi_2SrTa_2O_9$. *Chem. Mater.* 15, 632–635. doi: 10.1021/cm0200893

Uma, S., and Gopalakrishnan, J. (1994). Synthesis of anion-deficient layered perovskites, $ACa_2Nb_{3-x}M_xO_{10-x}$ (A = Rb, Cs; M = Al, Fe), exhibiting ion-exchange and intercalation. evidence for the formation of layered brownmillerites, $ACa_2Nb_2AlO_9$ (A = Cs, H). *Chem. Mater.* 6, 907–912. doi: 10.1021/cm00043a008

Uma, S., Gopalakrishnan, J., State, S., and Unit, S. C. (1995). Polymerization of aniline in layered perovskites. *Mater. Sci.* 34, 175–179. doi: 10.1016/0921-5107(95)01235-4

Wang, B., Dong, X., Pan, Q., Cheng, Z., and Yang, Y. (2007). Intercalation behavior of n-alkylamines into an A-site defective layered perovskite $H_2W_2O_7$. *J. Solid State Chem.* 180, 1125–1129. doi: 10.1016/j.jssc.2007.01.009

Wang, C., Tang, K., Wang, D., Liu, Z., Wang, L., Zhu, Y., et al. (2012). A new carbon intercalated compound of Dion-Jacobson phase $HLaNb_2O_7$. *J. Mater. Chem.* 22, 11086–11092. doi: 10.1039/c2jm14902h

Wang, Y., Nikolopoulou, M., Delahaye, E., Leuvrey, C., Leroux, F., Rabu, P., et al. (2018). Microwave-assisted functionalization of the Aurivillius phase $Bi_2SrTa_2O_9$: diol grafting and amine insertion *vs.* alcohol grafting. *Chem. Sci.* 9, 7104–7114. doi: 10.1039/C8SC01754A

Wang, Y., Wang, C., Wang, L., Hao, Q., Zhu, X., Chen, X., et al. (2014). Preparation of interlayer surface tailored protonated double-layered perovskite $H_2CaTa_2O_7$ with n-alcohols, and their photocatalytic activity. *RSC Adv.* 4, 4047–4054. doi: 10.1039/C3RA44623A

Youngblood, W. J., Lee, S.-H. A., Maeda, K., and Mallouk, T. E. (2009). Visible light water splitting using dye-sensitized oxide semiconductors. *Acc. Chem. Res.* 42, 1966–1973. doi: 10.1021/ar9002398

Zhou, Y., Wen, T., Guo, Y., Yang, B., and Wang, Y. (2016). Controllable doping of nitrogen and tetravalent niobium affords yellow and black calcium niobate nanosheets for enhanced photocatalytic hydrogen evolution. *RSC Adv.* 6, 64930–64936. doi: 10.1039/C6RA11407E

Zhu, H., Yao, X., and Hua, S. (2013). Nanocomposite of polyaniline and a layered niobate acid host: synthesis, electrochemical studies, and photocatalytic properties. *Polym. Compos.* 34, 834–841. doi: 10.1002/pc.22485

Zou, Z., Ye, J., and Arakawa, H. (2001). Substitution effects of In^{3+} by Fe^{3+} on photocatalytic and structural properties of Bi_2InNbO_7 photocatalysts. *J. Mol. Catal.* 168, 289–297. doi: 10.1016/S1381-1169(00)00545-8

Zvereva, I., and Rodionov, I. (2013). "Photocatalytic properties of perovskite-type layered oxides," in *Perovskite: Crystallography, Chemistry and Catalytic Performance*, eds J. Zhang and H. Li (New York, NY: Nova Science Publishers), 181–198. Available online at: https://www.novapublishers.com/catalog/product_info.php?products_id=35898

Zvereva, I. A., Silyukov, O. I., and Chislov, M. V. (2011). Ion-exchange reactions in the structure of perovskite-like layered oxides: I. Protonation of $NaNdTiO_4$ complex oxide. *Russ. J. Gen. Chem.* 81, 1434–1441. doi: 10.1134/S1070363211070061

Conflict of Interest: The authors declare that the research was conducted in the absence of any commercial or financial relationships that could be construed as a potential conflict of interest.

PERSPECTIVE
published: 30 April 2020
doi: 10.3389/fchem.2020.00384

Glass: Home of the Periodic Table

Georgiy Shakhgildyan*, Alexey Lipatiev, Sergey Lotarev, Sergey Fedotov and Vladimir Sigaev

Department of Glass and Glass-Ceramics, Mendeleev University, Moscow, Russia

Glass is the most common material around us, and humankind uses it every day for more than 5000 years. However, from the chemical point of view, glass is the only material that could represent almost all elements of the Periodic Table inside itself, showing the effect of the Periodic Law on properties of the final material. In this paper, we show the most remarkable examples demonstrating that glass can rightfully be called "home" for all chemical elements providing different properties depending on its composition. We gave a new look at the Periodic Table and described how a small number of glass-forming components creates unique glass structure which could enclose almost all remaining elements including transition and noble metals, lanthanides and actinides as modifying components providing an inconceivable number of discoveries in material science. Moreover, we reviewed a series of studies on the direct femtosecond laser writing in glasses which paves the way for a redistribution of chemical elements in the spatially confined nanosized zone in glass volume providing unique properties of laser-induced structures. Finally, for the first time, we reproduce the Periodic Table in birefringence colors in the bulk of silica glass using a direct laser writing technique. This image of 3.6 × 2.4 mm size can withstand temperature up to 900°C, humidity, electromagnetic fields, powerful cosmic and reactor radiation and other environmental factors and demonstrates both the art of direct laser writing and symbolic role of glass as the safest and eternal home for the Periodic Table.

Keywords: Periodic Table, glass, glass-ceramics, glass formation, direct laser writing

Edited by:
Mikhail V. Kurushkin,
ITMO University, Russia

Reviewed by:
Alexander Tolstoguzov,
Ryazan State Radiotechnical University, Russia
Viktor Andreevich Markov,
Peter the Great St.Petersburg Polytechnic University, Russia

****Correspondence:***
Georgiy Shakhgildyan
georgiy.shahgildyan@gmail.com

Specialty section:
This article was submitted to Inorganic Chemistry, a section of the journal Frontiers in Chemistry

Received: *15 March 2020*
Accepted: *14 April 2020*
Published: *30 April 2020*

Citation:
Shakhgildyan G, Lipatiev A, Lotarev S, Fedotov S and Sigaev V (2020) Glass: Home of the Periodic Table. Front. Chem. 8:384. doi: 10.3389/fchem.2020.00384

INTRODUCTION

Glass has been known to mankind for more than 5000 years, and it is one of the most common materials in modern life. Despite its long history, glass remains one of the most interesting objects to study in the field of inorganic materials science. Thanks to the work of researchers around the world and the variety of chemical elements collected in the Periodic Table, new glass compositions and processing methods are produced every year, creating new materials for the development of vital and sustainable technologies. According to theoretical calculations, the number of possible compositions of glasses is so large that the synthesis of all compositions would require the number of atoms close to the maximum theoretical content of atoms in the whole Universe (Zanotto and Coutinho, 2004). Understanding the importance of glass science and technology, D. I. Mendeleev himself was actively engaged in the development of new glass-based materials, his main results were reflected in his 1864s book "Glass Production" (Mendeleev, 1864).

In this paper, in honor of the recent anniversary of the Periodic Table of chemical elements, we briefly describe how a large class of glasses can be classified into groups of chemical elements of the Periodic Table and give a look on the perspective developments in the field of glass which make it one of the most promising materials of our time.

GLASS FAMILIES AND THEIR PLACE IN THE PERIODIC TABLE

As mentioned above, almost all elements of the Periodic Table can be used for the production of glass, which makes it a kind of "home" for all elements. Depending on the type of chemical compounds that form glasses, they are divided into classes, each of which has a unique structure and properties that determine their application.

The most common class of glasses is oxide glasses. They are formed by structural units that are compounds of various elements with oxygen. These elements primarily include Si, Ge, B, P, As, their oxides are easily obtained in a glassy state and most glasses are produced on their basis. Also, oxides of Te, Ti, Se, Sb, Mo, W, Bi, Al, Ga, V, and other elements can act as glass-forming agents, either individually or in a mixture with other oxides. Depending on the type of the main glass-forming oxide, the name of the group of glasses is derived—silicate, phosphate, tellurite, etc.

A special place among oxide glasses is occupied by fused silica or silica glass (SiO_2). It is the most refractory glass, it has a wide transparency window in the optical region and an abnormally low coefficient of thermal expansion (CTE) equal to $5.5{\cdot}10^{-7}/K^{-1}$(LeLosq et al., 2019). These determine its wide range of applications—from UV lamps to optical elements. It is thanks to the development of silica glass technology and the production of optical fibers that the worldwide implementation of broadband Internet access has become possible (Ballato and Dragic, 2016).

Silicate glasses which include oxides of various chemical elements from groups 1 to 17 are the most extensive group of glasses. In addition to Si and O, the most important elements of silicate glasses are alkaline (Li, Na, K) and alkaline earth (Mg, Ca, Sr, Ba) metals, as well as elements Al and B. Due to high transparency, acceptable strength and relatively low cost of production, products made of silicate glasses are present in all areas of human life: construction and transport, storage of products, machinery and much more. Ion exchange technology which includes replacement of small metal ions with larger ones in the surface layer of silicate glasses allows to significantly increase glass strength, which is used to create flexible mobile devices (Mauro and Morten, 2016). Using silicate glasses and different thin-film layers smart glasses are developed. Smart glass technology enables the fabrication of glass-based devices to control passing light. This can considerably decrease the building's energy demands with improving the indoor environment (Rezaei et al., 2017). The introduction of various chemical elements into the glass composition (mainly transition, rare earth, and noble metals), leads to the coloring of glasses. Even elements of the actinide group can be used for the production of glasses. Thus, U_2O_3 has long been used for the production of tableware, jewelry and optical filters, since U ions give a bright green color to the glass (Strahan, 2001). Currently, the ability of silicate glasses to contain radioactive elements (U, Pu) is used for the disposal of radioactive waste in vitrification technology (Gin et al., 2013). If it is necessary, some elements can be even converted to a radioactive state in glasses, thereby creating radiopharmaceuticals. Thus, glass microspheres with the Y^{90} isotope for liver cancer treatment are produced using Y_2O_3-Al_2O_3-SiO_2 glass (Ehrhardt and Day, 1987; Sigaev et al., 2012). Moreover, utilizing silicate glasses containing oxides of Al, Li, Mg, Ca, Ti, Zr, P, and other elements, glass-ceramics can be made by the bulk nucleated crystallization routine. Glass-ceramics demonstrate different combinations of properties [high strength, zero porosity, precision-regulated coefficient of thermal expansion (CTE), including near-zero values, biocompatibility, etc.] and find applications in various fields from medicine to astronomy (Zanotto, 2010).

The industrial production of non-silica oxide glasses is less widespread. Meanwhile, new challenges in science and technology lead to the development of such glasses. TeO_2-based glasses have an increased refractive index (>2.0) and are used in complex optical devices in the visible and near-IR range. GeO_2-based glasses are actively being studied to create new optical and laser components (Sigaev et al., 2011; Starobor et al., 2016). Borate glasses (based on B_2O_3) with additives of different oxides are used in medicine for the restoration of soft tissues, in optics and photonics (Lorenzi et al., 2018; Feller, 2019). Phosphate glasses (based on P_2O_5) containing oxides of rare earth elements (Nd, Eu, Tb, Er, Yb) are used in industry for the production of active elements of high-power lasers (Campbell and Suratwala, 2000). Phosphate and borate glasses with additives of Zn, Sn, B, Al, Na, K oxides are widely used for: sealing materials with a variety of CTE values, biomedical applications and the development of solid electrolytes for the new generation of batteries (Muñoz et al., 2019).

Glasses formed by the elements of group 16 (S, Se, Te) together with elements of group 14 and 15 (Ge, Sn, P, As, Sb) belong to the class of chalcogenide glasses. These glasses have ultrahigh transparency in the IR range (up to 25 microns), which determines their use as IR imaging devices in new generation thermal imagers, optical sensors for IR spectroscopy and active elements of fiber CO_2 lasers (Hubert et al., 2011).

The class of halide glasses includes materials based on elements of group 17 (primarily F, also Cl, Br, I) in the combination with metals (Be, Zr, Hf, Ba, La, Al, Y). The most widely studied glass composition is ZBLAN (in the ZrF_4-BaF_2-LaF_3-AlF_3-NaF system). Production of such glasses is complicated by their high tendency to crystallization and extremely high requirements for the degree of purity of raw materials. However, research in this area is justified by the possibility of obtaining optical fibers with minimal optical losses which could provide a significant (up to 100 times) increase in data transfer speed compared to current fiber cables and open the way for a new generation of near-IR fiber lasers (Wetenkamp et al., 1992; Clare et al., 2019). It is worth noting that the researchers have established the possibility of obtaining a defect-free fiber from ZBLAN glass in the absence of gravity and are currently conducting experiments to obtain such a fiber on the International space station (Starodubov et al., 2014).

Metal glasses are the general name of a wide class of amorphous materials consisting of metals or alloys of metals and metalloids, including elements of groups 2–15 (the most common are Zr, Ti, Cu, Ni, Be, Mg, Fe, Co, etc.). Metal glasses have high crystallization tendency which could be overcome by unusually high melt cooling rates (from 10^5 to 10^{12} °C/s). The advantages of metal glasses over metals and metal alloys are high values of mechanical strength, corrosion resistance, magnetic properties and electrical resistance. Currently, it is possible to produce not only metal glasses in the form of thin plates but bulk products with complex surface morphology (Greer, 1995; Schroers, 2013).

Thus, almost all elements of the Periodic Table in various ratios and compounds can be part of the glass, changing its structure and giving unique properties to the material. The abundance of variations in the composition and methods of glass production opens up new directions for its use in the promising fields of optics, medicine, photonics, energy and many others.

DIRECT LASER WRITING IN GLASS AND REDISTRIBUTION OF ELEMENTS

In addition to changing the chemical composition of glass, post-processing methods are important technologies for creating materials with specified properties. Using methods of ion exchange and surface coatings, it is possible to create high-strength and energy-efficient materials with specified optical properties. At once, the possibility of micro- and even nanoscale control of glass properties opens up previously impossible ways for the development of new materials and devices. Due to the intensive evolution of femtosecond laser technology, a wide field of research has emerged into the interaction of ultrashort laser pulses with glasses. Through a multiphoton mechanism, the energy of focused ultrashort laser pulses is absorbed by glass in the focus area. In this area, laser intensity exceeds the values of 10^{13} W/cm^2, resulting in modification of the glass structure. The non-linear nature of the absorption of ultrashort pulses makes it possible to control the spatial position of modified regions in the volume of glass, which opens up prospects for their three-dimensional (3D) modification at the micro- and nanoscale by so-called direct laser writing (DLW) technique (Osellame et al., 2012; Sugioka and Cheng, 2014; Phillips et al., 2015).

In recent years, studies on DLW of various structures in glasses have revealed a wide range of phenomena that occur when the material absorbs ultrashort pulses. These include local changes in the refractive index and writing of optical waveguides (Phillips et al., 2015), the formation of surface and bulk birefringent nanoperiodic structures (nanogratings) (Shimotsuma et al., 2003; Lotarev et al., 2019a), formation of micro-and nanobubbles (Bellouard and Hongler, 2011), local crystallization of non-linear phases in glass (Lipatiev et al., 2018b, 2020; Lotarev et al., 2019b), precipitation of metal clusters, nanoparticles, and semiconductor quantum dots (Marquestaut et al., 2014; Shakhgildyan et al., 2018; Vetchinnikov et al., 2018; Hu et al., 2019). Despite the physical nature of the processes, involved in the interaction of laser pulses with glass, they lead to a local change in the chemical composition of glass by ions migrations to different areas of the laser affected zone. According to the latest studies, glass-modifier ions (Na, K, Mg, Ca, Sr, Ba, Zr) are most susceptible to migration. When observed in a plane perpendicular to the laser beam, such ions migrate to the periphery of the laser affected zone, while glass-forming ions tend to concentrate in the center (Fernandez et al., 2018; Lotarev et al., 2018). The most promising application of DLW in glasses is multidimensional optical data storage with a high capacity and almost unlimited lifetime. This method is based on the periodic nanostructures (nanogratings) laser-written in silica glass (Shimotsuma et al., 2003). Nanogratings are formed by periodic nanoporous regions interlaced with solid glass. They are oriented perpendicular to the plane of polarization of the writing beam and exhibiting form birefringence which can be used for the data encoding (Zhang et al., 2014). In order to increase data writing speed, it was proposed to use nanoporous SiO_2 glass as storage media instead of silica glass (Fedotov et al., 2018; Lipatiev et al., 2018a). In this case, birefringent sub-micron hollow cavities were formed under the action of ultrafast laser pulses. The above-mentioned promising results served as the basis for launching applied research projects aimed at creating glass-based optical memory technology. The first project of this kind was launched in the Mendeleev University in Russia (Project "Quartz") Lotarev (2017), next in the Microsoft laboratories (Project "Silica") Project Silica (2017).

Thus, using various combinations of chemical elements for glass production and laser processing methods, it is possible to create new materials and devices for a wide range of applications. First of all, they include secure data storage, as well as elements of integrated photonic circuits (waveguides, interferometers, switches), optical sensors, microfluidic devices, and much more. The processes occurring during the interaction of femtosecond laser radiation with glass, in most cases, lead to a local change in its chemical composition and migration of chemical elements to certain zones limited by the laser spot, which largely determines the changed properties of the resulting region. At the same time, the ability of a fine-tuning of glass composition at the production stage allows to ensure the most efficient flow of DLW processes.

ETERNAL AND MINIATURE PERIODIC TABLE

To symbolically mark the possibility of using almost all elements of the Periodic Table in glass, we inscribed a color image in polarized light of the Periodic Table in the volume of commercially available KU-1 type silica glass (TechnoQuartz Ltd., Russia) using the DLW method. This writing technology is based on the birefringent properties of laser-induced

TABLE 1 | Writing conditions for the DLW of the Periodic Table in the sample of silica glass.

Group of elements	Number of layers	Shift between layers, μm	Pulse energy, μJ
Alkali and alkali earth metals	1	–	4.8
Transition metals	2	100	4.2
Non-metals	3	130	4.2
Lanthanides and Actinides	2	175	4.2
Post-transition metals	2	290	4.2
Noble gases	2	44	4.2

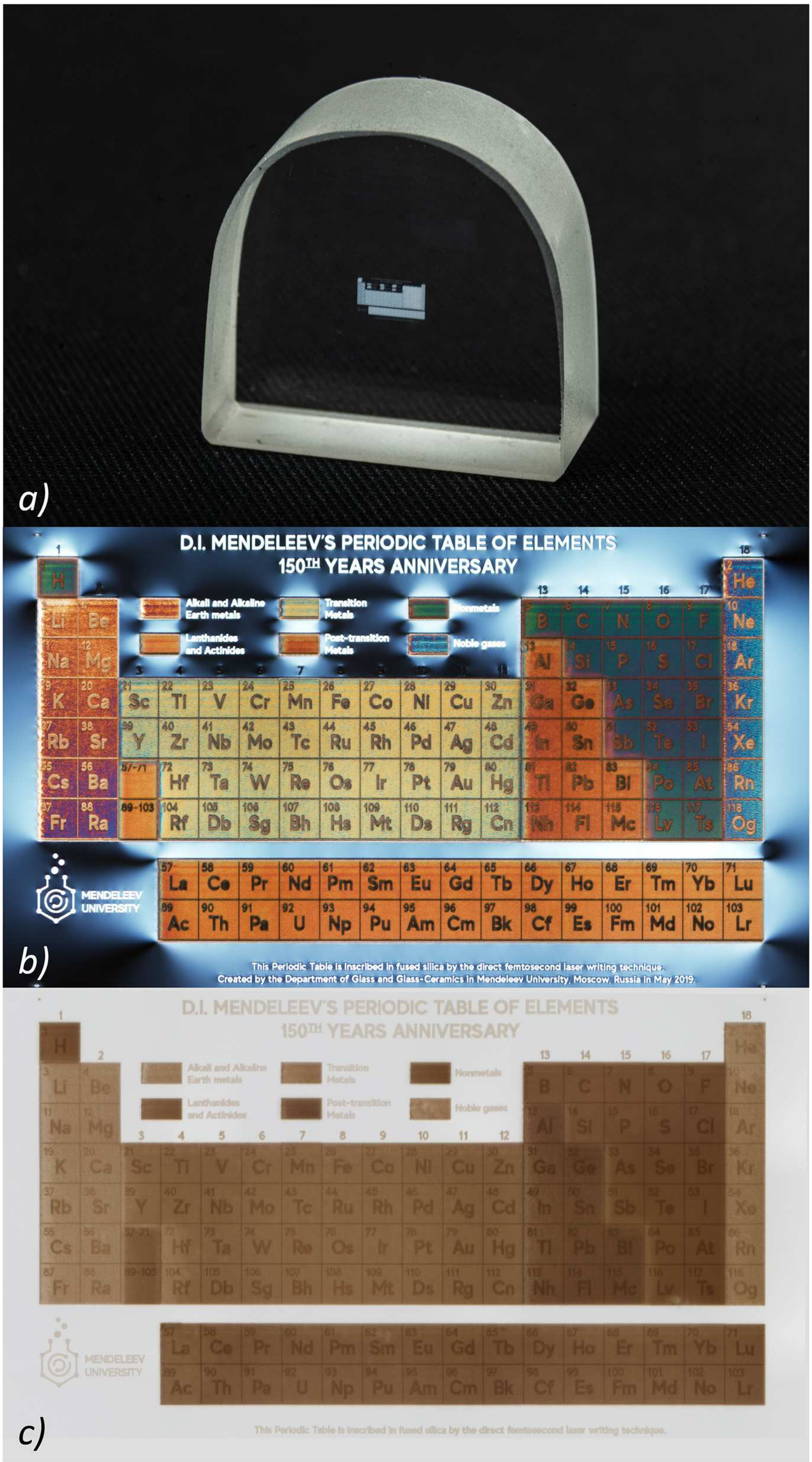

FIGURE 1 | (a) Real-size image of the silica glass sample with the laser written Periodic Table; **(b,c)** Optical microscopy image of the Periodic Table laser written in the silica glass sample captured with and without crossed polarizers, respectively. The length of the one cell is 200 μm.

nanogratings and stress, due to which it is possible to vary the wavelength of light passing through the polarizer and light analyzer (Spring et al., 2010; Sun et al., 2020).

In this work, the Periodic Table was written in a 10 mm thick silica glass sample at a depth of 900 microns from the surface by a laser beam focused with a Mitutoyo MPlan APO 5X lens (N. A. = 0.14). We used Pharos 6 W femtosecond laser (Light Conversion Dev.) with a 1,030 nm central wavelength. To control the color of cells via their birefringence in the Periodic Table, the energy of laser pulses, the number of layers, and the distance between them were varied. The scanning speed of the laser beam was 2 mm/s. The writing conditions of certain groups of elements are shown in **Table 1**. It should be mentioned that **Table 1** represents the actual interlayer shift whereas the corresponding shift of the sample during writing of the Periodic Table was equal to these values divided by 1.45 taking the refraction into account because the refractive index of silica glass is 1.45 at 1030 nm wavelength. The names of the elements were written using tighter focusing of the laser beam by means of an Olympus LCPLNIR 20X lens (N. A. = 0.45) and with the relative rotation of the laser beam polarization plane by 45°.

The photo of the glass sample with the written Table is shown in **Figure 1a**. The total size of the Table is 3.6 × 2.4 mm. To see the Table in color, it is necessary to observe it through a microscope with crossed polarizers (**Figure 1b**), while the image of the Table without crossed polarizers is shown in **Figure 1c**. The size of each Table cell is 200 × 200 microns. Annealing of a glass sample with a written Table at 900°C for 1 h does not lead to noticeable degradation of the image nevertheless its color was slightly changed due to the relaxation of laser-induced stress. After repeated thermal shocks (rapid cooling from 900°C to cold water) of the glass sample with the written Table completely retains its integrity. Due to the high chemical and radiation stability of silica glass, written image is also not subjected to degradation under the influence of moisture, acids, alkalis and radiation exposure (within the stability of silica glass). Thus, on the one hand, glass can be produced using almost all elements of the Periodic Table, and on the other, thanks to the DLW method, glass becomes the eternal storage of the Periodic Table.

DISCUSSION AND CONCLUSION

Despite the long history, today glass is the most important class of materials that is in demand in various industries. The variety of properties and applications of glass is associated with an unimaginably large number of possible compositions—combinations of various chemical elements. New opportunities for creating materials based on glass with unique properties are introduced by laser modification methods, which allow to create various multifunctional structures and objects in the glass volume.

In honor of the 150th anniversary of the Periodic Table of chemical elements, we showed the possibility of creating a color image of the Periodic Table in silica glass using direct laser writing technology. This image covers an area of 3.6 × 2.4 mm, while the size of each Table cell is 200 × 200 microns. Annealing of a glass sample with a written Table at 900°C for 1 h does not lead to noticeable degradation of the image. After repeated thermal shocks of the glass sample with the Table it completely retains its integrity. Due to the high chemical and radiation stability of silica glass, the written image is also not subjected to degradation under the influence of moisture, acids, alkalis and radiation exposure (within the stability of silica glass). Therefore, the created Table image can be considered eternal.

Thus, we want to show that on the one hand, glass can be produced using almost all elements of the Periodic Table, and on the other, that thanks to the DLW method, glass becomes the eternal storage of the Periodic Table. With these conclusions, we want to emphasize the importance of developing research in the field of glassy materials, which, thanks to the variety of elements of the Periodic Table and the use of new technologies, ensure the ever-accelerating development of the material science, instrumentation and information base of mankind.

DATA AVAILABILITY STATEMENT

The datasets generated for this study are available on request to the corresponding author.

AUTHOR CONTRIBUTIONS

GS, AL, SL, and VS contributed the conception and design of the study. Experimental work was carried out by AL and SF (programming, modeling, and laser writing) under supervision of SL and VS. GS wrote the manuscript and prepared images with contributions of AL, SL, and VS in certain sections. All authors participated in the analysis and discussion of obtained results.

FUNDING

This work was supported by the grant of Mendeleev University, Project No. 2020-020.

REFERENCES

Ballato, J., and Dragic, P. (2016). Glass: the carrier of light - a brief history of optical fiber. *Int. J. Appl. Glass Sci.* 7, 413–422. doi: 10.1111/ijag.12239

Bellouard, Y., and Hongler, M.-O. (2011). Femtosecond-laser generation of self-organized bubble patterns in fused silica. *Opt. Express* 19, 6807–6821. doi: 10.1364/oe.19.006807

Campbell, J. H., and Suratwala, T. I. (2000). Nd-doped phosphate glasses for high-energy/high-peak-power lasers. *J. Non Cryst. Solids* 263–264, 318–341. doi: 10.1016/S0022-3093(99)00645-6

Clare, A. G., Wachtel, P. F., and Musgraves, J. D. (2019). "Halide glasses," in *Springer Handbook of Glass*, eds J. D. Musgraves, J. Hu, L. Calvez (Springer International Publishing), 595–616. doi: 10.1007/978-3-319-93728-1_17

Ehrhardt, G. J., and Day, D. E. (1987). Therapeutic use of ^{90}Y microspheres. *Int. J. Rad. Appl. Instrum. B* 14, 233–242. doi: 10.1016/0883-2897(87)90047-x

Fedotov, S. S., Okhrimchuk, A. G., Lipatiev, A. S., Stepko, A. A., Piyanzina, K. I., Shakhgildyan, G. Y., et al. (2018). 3-bit writing of information in nanoporous glass by a single sub-microsecond burst of femtosecond pulses. *Opt. Lett.* 43:851. doi: 10.1364/ol.43.000851

Feller, S. (2019). "Borate glasses," in *Springer Handbook of Glass,* eds J. D. Musgraves, J. Hu, L. Calvez. 505–524. doi: 10.1007/978-3-319-93728-1_14

Fernandez, T. T., Sakakura, M., Eaton, S. M., Sotillo, B., Siegel, J., Solis, J., et al. (2018). Bespoke photonic devices using ultrafast laser driven ion migration in glasses. *Progr. Mater. Sci.* 94, 68–113. doi: 10.1016/j.pmatsci.2017.12.002

Gin, S., Abdelouas, A., Criscenti, L. J., Ebert, W. L., Ferrand, K., Geisler, T., et al. (2013). An international initiative on long-term behavior of high-level nuclear waste glass. *Mater. Today* 16, 243–248. doi: 10.1016/j.mattod.2013.06.008

Greer, A. L. (1995). Metallic glasses. *Science* 267, 1947–1953. doi: 10.1126/science.267.5206.1947

Hu, Y., Zhang, W., Ye, Y., Zhao, Z., and Liu, C. (2019). Femtosecond-laser-induced precipitation of CsPbBr3 perovskite nanocrystals in glasses for solar spectral conversion. *ACS Appl. Nano Mater.* 3, 850–857. doi: 10.1021/acsanm.9b02362

Hubert, M., Delaizir, G., Monnier, J., Godart, C., Ma, H. L., Zhang, X. H., et al. (2011). An innovative approach to develop highly performant chalcogenide glasses and glass-ceramics transparent in the infrared range. *Opticsexpress* 19, 23513–23522. doi: 10.1364/OE.19.023513

LeLosq, C., Cicconi, M. R., Greaves, G. N., and Neuville, D. R. (2019). "Silicate glasses," in *Springer Handbook of Glass*, eds J. D. Musgraves, J. Hu, L. Calvez. 441–503. doi: 10.1007/978-3-319-93728-1_13

Lipatiev, A. S., Fedotov, S. S., Okhrimchuk, A. G., Lotarev, S. V., Vasetsky, A. M., Stepko, A. A., et al. (2018a). Multilevel data writing in nanoporous glass by a few femtosecond laser pulses. *Appl. Opt.* 57, 978–982. doi: 10.1364/ao.57.000978

Lipatiev, A. S., Lotarev, S. V., Smayev, M. P., Lipateva, T. O., Karateev, I. A., Presnyakov, M. Y., et al. (2020). Space-selective crystallization of glass by an optical vortex beam. *CrystEngComm* 22, 430–434. doi: 10.1039/c9ce01869g

Lipatiev, A. S., Moiseev, I. A., Lotarev, S. V., Lipateva, T. O., Presnyakov, M. Y., Fedotov, S. S., et al. (2018b). Growth of fresnoite single crystal tracks inside glass using femtosecond laser beam followed by heat treatment. *Cryst. Growth Des.* 18, 7183–7190. doi: 10.1021/acs.cgd.8b01358

Lorenzi, R., Golubev, N. V., Ziaytdinova, M. Z., Jar,ý, V., Babin, V., Malashkevich, G. E., et al. (2018). Radio- and photoluminescence properties of Ce/Tb co-doped glasses with huntite-like composition. *Opt. Mater.* 78, 247–252. doi: 10.1016/j.optmat.2018.02.016

Lotarev, S. (2017). *In Search of Permanent Memory: From Cuneiform on Clay to Nanostructures in Glass*.Available online at: https://www.kommersant.uk/articles/in-search-of-permanent-memory-from-cuneiform-on-clay-to-nanostructures-in-glass (accessed March 15, 2020).

Lotarev, S., Fedotov, S., Lipatiev, A., Presnyakov, M., Kazansky, P., and Sigaev, V. (2018). Light-driven nanoperiodical modulation of alkaline cation distribution inside sodium silicate glass. *J. Non Cryst. Solids* 479, 49–54. doi: 10.1016/j.jnoncrysol.2017.10.008

Lotarev, S. V., Fedotov, S. S., Kurina, A. I., Lipatiev, A. S., and Sigaev, V. N. (2019a). Ultrafast laser-induced nanogratings in sodium germanate glasses. *Opt. Lett.* 44, 1564–1567. doi: 10.1364/ol.44.001564

Lotarev, S. V., Lipatiev, A. S., Lipateva, T. O., Fedotov, S. S., Naumov, A. S., Moiseev, I. A., et al. (2019b). Ultrafast-laser vitrification of laser-written crystalline tracks in oxide glasses. *J. Non Cryst. Solids* 516, 1–8. doi: 10.1016/j.jnoncrysol.2019.04.027

Marquestaut, N., Petit, Y., Royon, A., Mounaix, P., Cardinal, T., and Canioni, L. (2014). Three-dimensional silver nanoparticle formation using femtosecond laser irradiation in phosphate glasses: analogy with photography. *Adv. Funct. Mater.* 24, 5824–5832. doi: 10.1002/adfm.201401103

Mauro, J. C., and Morten, M. S. (2014). *Ultra-Thin Strengthened Glasses*. U.S. Patent Application No. 13/961, 211.

Mendeleev, D. I. (1864). *Glass Production*. Saint Petersburg: Public benefit.

Muñoz, F., Rocherullé, J., Ahmed, I., and Hu, L. (2019). "Phosphate glasses," in *Springer Handbook of Glass*, eds J. D. Musgraves, J. Hu, L. Calvez. 553–594. doi: 10.1007/978-3-319-93728-1_16

Osellame, R., Cerullo, G., and Ramponi, R. (Eds.). (2012). "Femtosecond laser micromachining," in *Topics in Applied Physics* (Berlin; Heidelberg: Springer). doi: 10.1007/978-3-642-23366-1

Phillips, K. C., Gandhi, H. H., Mazur, E., and Sundaram, S. K. (2015). Ultrafast laser processing of materials: a review. *Adv. Opt. Photonics* 7:684. doi: 10.1364/aop.7.000684

Project Silica, (2017). *Microsoft Research*. Available online at: https://www.microsoft.com/en-us/research/project/project-silica/c (accessed March 15, 2020).

Rezaei, S. D., Shannigrahi, S., and Ramakrishna, S. (2017). A review of conventional, advanced, and smart glazing technologies and materials for improving indoor environment. *Solar Energy Mater. Solar Cells* 159, 26–51. doi: 10.1016/j.solmat.2016.08.026

Schroers, J. (2013). Bulk metallic glasses. *Phys. Today* 66, 32–37. doi: 10.1063/pt.3.1885

Shakhgildyan, G. Y., Lipatiev, A. S., Vetchinnikov, M. P., Popova, V. V., Lotarev, S. V., Golubev, N. V., et al. (2018). One-step micro-modification of optical properties in silver-doped zinc phosphate glasses by femtosecond direct laser writing. *J. Non Cryst. Solids* 481, 634–642. doi: 10.1016/j.jnoncrysol.2017.12.011

Shimotsuma, Y., Kazansky, P. G., Qiu, J., and Hirao, K. (2003). Self-organized nanogratings in glass irradiated by ultrashort light pulses. *Phys. Rev. Lett.* 91:247405. doi: 10.1103/physrevlett.91.247405

Sigaev, V. N., Atroschenko, G. N., Savinkov, V. I., Sarkisova, P. D., Babajewb, G., Lingel, K., et al. (2012). Structural rearrangement at the yttrium-depleted surface of HCl-processed yttrium aluminosilicate glass for ^{90}Y-microsphere brachytherapy. *Mater. Chem. Phys.* 133, 24–28. doi: 10.1016/j.matchemphys. 2011.12.079

Sigaev, V. N., Golubev, N. V., Ignat'eva, E. S., Savinkov, V. I., Campione, M., Lorenzi, R., et al. (2011). Nickel-assisted growth and selective doping of spinel-like gallium oxide nanocrystals in germano-silicate glasses for infrared broadband light emission. *Nanotechnology* 23:15708. doi: 10.1088/0957-4484/23/1/015708

Spring, K. R., Parry-Hill, M. J., and Davidson, M. W. (2010). *Michel-Levy Birefringence Chart*. Olympus Microscopy Resource Center. Available online at: http://olympus.magnet.fsu.edu/primer/java/polarizedlight/michellevy/index.html

Starobor, A. V., Zheleznov, D. S., Palashov, O. V., Savinkov, V. I., and Sigaev, V. N. (2016). Borogermanate glasses for Faraday isolators at high average power. *Opt. Commun.* 358, 176–179. doi: 10.1016/j.optcom.2015.09.047

Starodubov, D., Mechery, S., Miller, D., Ulmer, C., Willems, P., Ganley, J., et al. (2014). ZBLAN fibers: from zero gravity tests to orbital manufacturing. *Appl. Ind. Optics.* doi: 10.1364/aio.2014.am4a.2

Strahan, D. (2001). Uranium in glass, glazes and enamels: history, identification and handling. *Stud. Conserv.* 46, 181–195. doi: 10.1179/sic.2001.46.3.181

Sugioka, K., and Cheng, Y. (2014). Ultrafast lasers—reliable tools for advanced materials processing. *Light Sci. Appl.* 3:e149. doi: 10.1038/lsa.2014.30

Sun, Q., Lee, T., Beresna, M., and Brambilla, G. (2020). Control of laser induced cumulative stress for efficient processing of fused silica. *Sci. Rep.* 10:3819. doi: 10.1038/s41598-020-60828-3

Vetchinnikov, M. P., Lipatiev, A. S., Shakhgildyan, G. Y., Golubev, N. V., Ignat'eva, E. S., Fedotov, S. S., et al. (2018). Direct femtosecond laser-induced formation of CdS quantum dots inside silicate glass. *Opt. Lett.* 43, 2519–2522. doi: 10.1364/ol.43.002519

Wetenkamp, L., West, G. F., and Többen, H. (1992). Optical properties of rare earth-doped ZBLAN glasses. *J. Non Cryst. Solids* 140, 35–40. doi: 10.1016/s0022-3093(05)80737-9

Zanotto, E. D. (2010). Bright future for glass-ceramics. *Am. Ceramics Soc. Bull.* 89, 19–27.

Zanotto, E. D., and Coutinho, F. A. B. (2004). How many non-crystalline solids can be made from all the elements of the periodic table? *J. Non Cryst. Solids* 347, 285–288. doi: 10.1016/j.jnoncrysol.2004.07.081

Zhang, J., Gecevičius, M., Beresna, M., and Kazansky, P. G. (2014). Seemingly unlimited lifetime data storage in nanostructured glass. *Phys. Rev. Lett.* 112:033901. doi: 10.1103/PhysRevLett.112.033901

Conflict of Interest: The authors declare that the research was conducted in the absence of any commercial or financial relationships that could be construed as a potential conflict of interest.

frontiers
in Chemistry

MINI REVIEW
published: 13 May 2020
doi: 10.3389/fchem.2020.00418

Methylammonium Polyiodides in Perovskite Photovoltaics: From Fundamentals to Applications

Andrey A. Petrov[1] *and Alexey B. Tarasov*[1,2]*

[1] *Laboratory of New Materials for Solar Energetics, Department of Materials Science, Lomonosov Moscow State University, Moscow, Russia,* [2] *Department of Chemistry, Lomonosov Moscow State University, Moscow, Russia*

Discovered in 2017, methylammonium polyiodides were proposed as a facile precursor for synthesis of hybrid perovskites by means of their interaction with metallic lead, which initiated further active exploration of their potential applications. Investigation of their unusual properties such as liquid state, unprecedented phase diversity and high reactivity revealed that methylammonium polyiodides are the first representatives of a new class of compounds—reactive polyhalide melts (RPM). In this review, we summarize the reported data on the unique properties of these compounds, discuss their potential for fabrication of hybrid perovskite films and describe the role of polyhalides in degradation of perovskite solar cells.

Keywords: methylammonium polyiodides, reactive polyiodide melts, RPM, hybrid perovskites, lead halide perovskites, perovskite solar cells

Edited by:
Mikhail V. Kurushkin,
ITMO University, Russia

Reviewed by:
Sergey Makarov,
ITMO University, Russia
Vitaliy E. Gasumyants,
Peter the Great St. Petersburg
Polytechnic University, Russia

****Correspondence:***
Alexey B. Tarasov
alexey.bor.tarasov@yandex.ru

Specialty section:
This article was submitted to
Inorganic Chemistry,
a section of the journal
Frontiers in Chemistry

Received: *23 March 2020*
Accepted: *21 April 2020*
Published: *13 May 2020*

Citation:
Petrov AA and Tarasov AB (2020)
Methylammonium Polyiodides in
Perovskite Photovoltaics: From
Fundamentals to Applications.
Front. Chem. 8:418.
doi: 10.3389/fchem.2020.00418

INTRODUCTION

Hybrid organic-inorganic perovskites with a general formula $APbX_3$ [$A = CH_3NH_3^+$ (MA^+), $CH(NH_2)_2^+$ (FA^+); $X = I^-$, Br^-] represent a new perspective class of materials used for optoelectronic devices (LEDs, lasers, sensors, etc.) and solar cells of new generation, so called perovskite solar cells. For the last decade, unprecedented interest to these materials has arouse because of the unique combination of their properties such as strong light absorption (Lin et al., 2015), large electron and hole diffusion lengths (Dong et al., 2015), wide tunability of their properties through the selection of the composition and facile fabrication using solution-processing methods (Gao et al., 2014; Zhao and Zhu, 2016). The efforts applied to the development of perovskite solar cells lead to an outstanding growth of their efficiency from ∼4% in 2009 to 25.2% in 2019 (NREL, 2020) thus overcoming record efficiencies for silicon solar cells.

Almost all proposed methods for fabrication of perovskite films rely on one of two processes: crystallization of hybrid perovskites from polar aprotic solvents (Saliba et al., 2016; Kim et al., 2019) or addition reaction between lead salt and organic salt (e.g., PbI_2 and MAI) (Yang et al., 2017). While deposition from solutions remains the most common method for obtaining high-quality perovskite films due to its simplicity, the crystallization of perovskites goes through formation of solvate intermediate phases such as $(MA)_2(S)_2Pb_3I_8$ (S = DMSO, DMF, GBL) which tend to grow in a form of needle-like crystals resulting in inhomogeneous morphology and pinholes of perovskite films (Cao et al., 2016; Petrov et al., 2017b,c; Fateev et al., 2018). The process is further exacerbated with the shrinkage of film volume upon decomposition of the intermediate phases into perovskite leading to the formation of cracks. The approaches based on reaction between lead and organic salts can be implemented in two ways: either by (co-)evaporation in vacuum or using successive solution deposition. The former needs a complex vacuum equipment whereas the latter suffers from the incomplete reaction (Hsieh et al., 2017). The abovementioned issues provoked search and development of alternative synthesis methods.

The recent discovery of a new group of low-melting methylammonium and formamidinium polyiodides (Petrov et al., 2017a) opened a new branch of strategies for hybrid perovskite synthesis through a redox reaction with metallic lead. Because of their liquid state and high reactivity toward metallic lead, the name of such polyiodides were coined as reactive polyiodide melts (RPM). In present review, we give a generalized vision on methylammonium polyiodides and related compounds known so far in terms of their fundamental features and technological applications.

LIQUID STATE

RPM can be easily obtained by simple mixing of crystalline methylammonium iodide (MAI)/formamidinium iodide (FAI) and iodine (I_2) (Petrov et al., 2017a). If the two solid compounds are brought into contact, a liquid RPM immediately forms even at room temperature (**Figure 1a**). Similarly, a crystal of organic salts transforms into RPM droplet in the atmosphere containing I_2 vapors (Turkevych et al., 2019).

According to Raman spectroscopy, methylammonium polyiodides have three characteristic vibrations near 110 cm^{-1}, 145 cm^{-1} and 170 cm^{-1} that correspond to an I_3^- symmetrical stretch vibrations, I_3^- asymmetrical stretch vibrations and vibrations of solvating I_2 molecular units, respectively (Petrov et al., 2017a; Turkevych et al., 2019; Udalova et al., 2020).

Liquid state of the RPM is a distinctive feature, making it a special precursor for hybrid perovskites because it does not require any organic solvents and therefore exempts the fabrication process from concomitant problems. In fact, a liquid state of RPM at room temperature is not unique itself if considering the whole class of plolyiodides. However, it was previously thought that only polyiodides with large organic cations such as aromatic (e.g., imidazolium) (Thorsmølle et al., 2012; Fei et al., 2015), trialkylsulfonium [e.g., $(Et)_3S^+$] (Bengtsson et al., 1991), or tetraalkylammonium [e.g., $(Oc)_4N^+$] (Stegemann et al., 1992; Wang et al., 2014; Yushina et al., 2014) are able to generate liquid phases of such polyiodides at room temperature (Bengtsson et al., 1991; Stegemann et al., 1992; Thorsmølle et al., 2012). Conversely, CsI_3 has a melting point over 130°C (Topol, 1968).

The melting points of methylammonium and formamidinium polyiodides were found to be unexpectedly low. Detailed physicochemical analysis of the RPM revealed a complex phase diagram of the MAI-I_2 system with 3 eutectics and 4 polyiodide phases MAI_2, $MAI_{2.67}$, MAI_4, $MAI_{5.5}$ (**Figure 1b**). While MAI_2 and $MAI_{2.67}$ phases were found to undergo peritectic and peritectoid decompositions at 23°C and 14°C, the melting temperatures of MAI_4 and $MAI_{5.5}$ phases were determined at 35°C (Petrov et al., 2019).

To estimate thermodynamic stability of the crystalline polyiodides, DFT calculations were performed. The selected approach to calculate formation enthalpy and entropy values of the compounds from isolated particles (I^-, MA^+, I_2) demonstrated excellent agreement with experimental data for MAI and I_2 and was therefore used to calculate thermodynamic state-functions of the polyiodides. The performed DFT calculations revealed that MAI_2 forms due to major enthalpy contribution whereas in the case of higher methylammonium polyiodides entropy plays a crucial role in their formation (Petrov et al., 2019).

The low melting points of methylammonium polyiodides were explained by high energy of cation solvation and increase in conformational entropy upon melting. The former arises from high dipole moment of methylammonium cation along with its ability to form numerous H-bonds therefore ensuring strong interaction with anions in a liquid state. The latter follows from the low energy barriers to rotation of the cations and their amphiphility leading to the realization of all possible cation-anion conformations in the melt (Petrov et al., 2019).

According to the phase diagram, there are two compositional regions with a liquid homogeneous state of MAI_x at room temperature ($3.0 < x < 3.3$; $4.3 < x < 4.4$), whereas at 40°C a liquid state of MAI_x is observed in the wide range of compositions ($2.9 < x < 9.0$), which opens up great opportunities for technological application of RPM.

HIGH REACTIVITY

The RPM demonstrate high reactivity toward various metals. In particular, the reaction of RPM with metallic lead manifests an amazingly simple redox process of perovskite synthesis:

$MAI_{3(liquid)} + Pb_{(solid)} \text{ -> } MAPbI_{3\ (solid)}$

The process can be implemented by spin-coating or spraying of RPM onto Pb films. If such treatment is followed by rinsing of the specimen with isopropanol to eliminate the unreacted RPM, large cuboid morphology of the film can be observed (**Figure 1c**). In case of the incomplete conversion there is PbI_2 layer between the layer of unreacted Pb and grown perovskite layer according to XRD and SEM data. On the other hand, long contact of RPM with perovskite film leads to its recrystallization and dissolution. For instance, it was shown, that 50 nm thickness film of lead treated with RPM completely disappear within 15 s indicating that some amount of lead can be dissolved in RPM. Later experiment showed that the solubility of Pb is rather small and does not exceed 1 mol.% at room temperature and slightly increases at elevated temperatures.

The conversion of Pb into $MAPbI_3$ is accompanied by volume increase in 8.4 times thus ensuring the formation of pinhole free perovskite films. This feature was successfully utilized for perovskite growth in confined space. Thin patterned perovskite films were obtained by pressing the die with a given relief containing RPM deposited onto it against the metallic lead film (**Figure 1d**). Because the sum of molar volumes of Pb and RPM is almost equal to that for $MAPbI_3$, the proposed method allows to dose the exact amount of RPM and fabricate perovskite films with any particular relief (Grishko et al., 2019), which can improve the efficiency of the devices due to optimization of light-scattering (Wang et al., 2012). The other way to dose RPM can be the use of

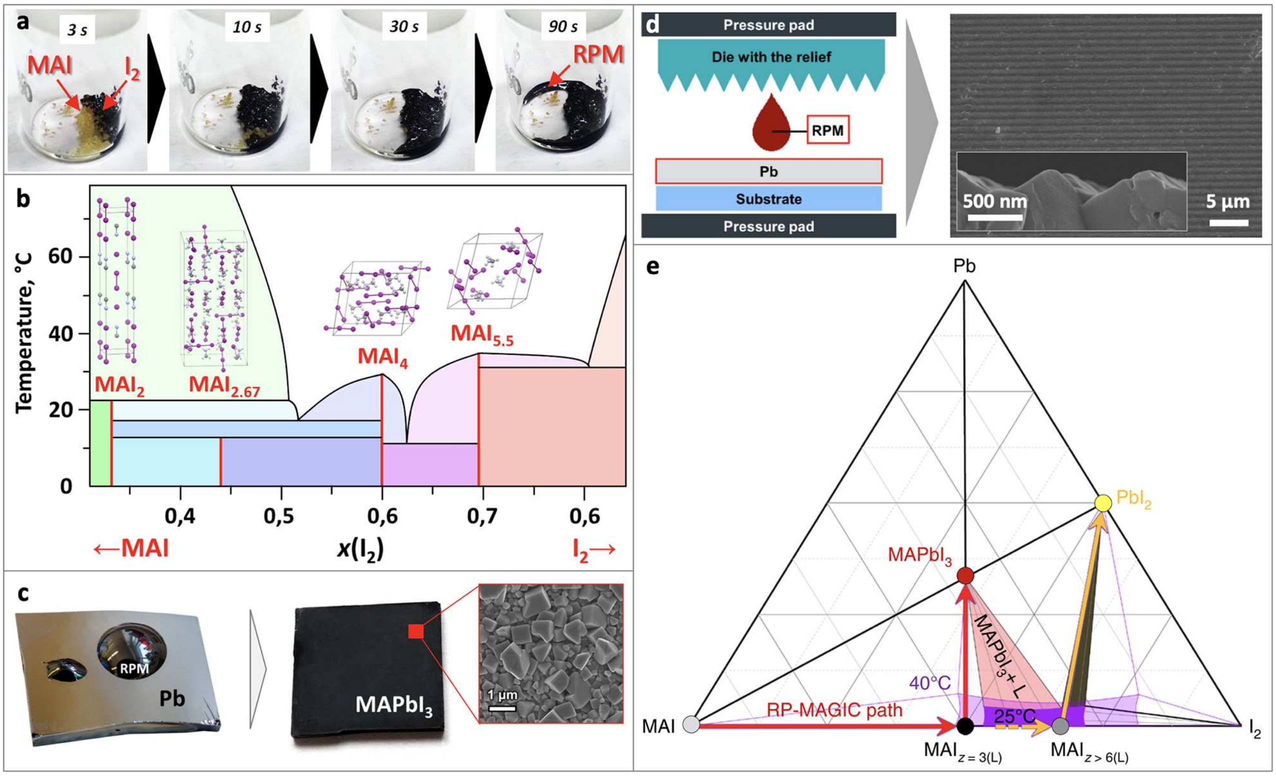

FIGURE 1 | (a) Formation of RPM from MAI and I_2, **(b)** Phase diagram of MAI-I_2, **(c)** perovskite film obtained by spin-coating of RPM onto Pb film, **(d)** scheme of a method for fabrication textured perovskite films, **(e)** Ternary Pb-MAI-I_2 diagram. Adapted from Petrov et al. (2017a) with permission from the Royal Society of Chemistry. Adapted with permission from Petrov et al. (2019). Copyright (2019) American Chemical Society. Adapted from Grishko et al. (2019) with permission from the Royal Society of Chemistry. Material from: "Ivan Turkevych et al. Strategic advantages of reactive polyiodide melts for scalable perovskite photovoltaics. Nature Nanotechnology, published 2018, Springer Nature".

starch to eliminate its excess through formation of RPM-starch complex (Shlenskaya et al., 2018b).

Other metals such as Cu and Au are also subject to the reaction with RPM resulting in formation of $MACu_2I_3$ and $(MA)_2Au_2I_6$, respectively (Petrov et al., 2018; Shlenskaya et al., 2018a). Likewise, RPM easily oxidize spiro-MeOTAD which is the most popular material for hole-transporting layer in perovskite solar cells (Shlenskaya et al., 2018a). The formation of these products is particularly important when one considers stability of perovskite solar cells and formation of RPM under operational conditions in the perovskite-based devices, which is discussed in the last section.

PHASE RELATIONS IN THE PB-MAI-I_2 TERNARY SYSTEM

Phase diagram of the Pb-MAI-I_2 system (**Figure 1e**) shows the technologically relevant area, where RPM coexist with $MAPbI_3$ (light-red triangle), which enlarges with the temperature increase. On the right side of it there is an unfavorable area in which iodine-rich RPM coexist with PbI_2. A reaction between Pb and RPM corresponds to a linear pathway on the phase diagram from the point corresponding to a particular composition of RPM toward Pb apex. In order to obtain pure perovskite phase, one should develop a synthetic process which does not go beyond the light-red area. Therefore, RPM should have the composition MAI_X, where $x < 5.5$ to avoid PbI_2 formation and $x > 3$ (for the case of $T = 40°C$) to be liquid for ensuring effective lead conversion (Petrov et al., 2017a; Turkevych et al., 2019).

PEROVSKITE SOLAR CELLS

Although it is tricky to dose RPM precisely onto metallic lead due to its extremely high reactivity, two approaches were proposed to solve this task. The first is based on addition of a reagent which initiates RPM formation and further reaction, whereas the second is based on withdrawal of a compound which inhibits the reaction.

The first approach is named RP-MAGIC (Reactive Polyiodide Melt-Assisted Growth through *in-situ* Conversion), in which a stoichiometric Pb/MAI bilayer on a substrate obtained by subsequent thermal evaporation of Pb and MAI is treated with iodine vapors at 40°C (**Figure 2a**). Upon the reaction of $MAI_{(solid)}$ and $I_{2(gas)}$ the RPM is formed and instantly reacts with a Pb underlayer:

$$Pb_{(solid)} + MAI_{(solid)} + I_{2(gas)} \text{ -> } MAPbI_{3\ (solid)}$$

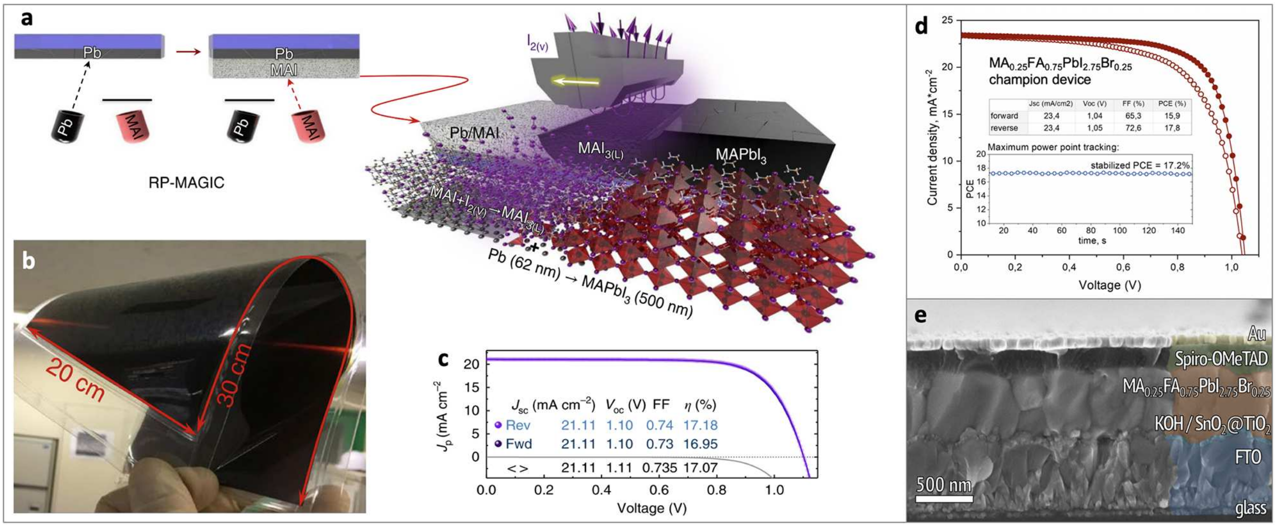

FIGURE 2 | **(a)** Scheme of the RP-MAGIC approach, **(b)** $MAPbI_3$ film on a 20 × 30 cm^2 flexible PET/ITO substrate obtained by RP-MAGIC approach, **(c)** PCE of the device obtained by RP-MAGIC approach, **(d,e)** PCE and cross-section of the device obtained by spin-coating of RPM solution onto Pb film. Material from: "Ivan Turkevych et al. Strategic advantages of reactive polyiodide melts for scalable perovskite photovoltaics. Nature Nanotechnology, published 2018, Springer Nature". Adapted with permission from Belich et al. (2020). Copyright (2020) American Chemical Society.

Authors demonstrated highly uniform perovskite films on relatively large area such as 100 cm^2 on glass/FTO and 600 cm^2 on flexible PET/ITO substrates therefore showing high scalability potential of the method (**Figure 2b**). The solar cells fabricated using RP-MAGIC approach demonstrated power conversion efficiencies (PCE) up to 17.2% (reverse scan) in the standard FTO/m-TiO_2/Perovskite/Spiro-OMeTAD/Au architecture (**Figure 2c**) (Turkevych et al., 2019).

Another approach is a spin-coating onto Pb film a certain amount of RPM dissolved in isopropanol. The reactivity of RPM in such solution was shown to be inhibited by the presence of solvent molecules. Upon evaporation of isopropanol, pure RPM is formed starting to react with the lead film. Using this method high-quality perovskite films were obtained and perovskite solar cells with PCE = 17.8% (reverse scan) were demonstrated (**Figures 2d,e**) (Belich et al., 2020).

Although the obtained efficiency of solar cells obtained using RPM is less than that achieved by conventional solution based spin-coating approach with record values up to 21% for $MAPbI_3$ (Chiang and Wu, 2018; Liu et al., 2019b), the first proof-of-concept results obtained without advanced optimization of charge transporting layers are fair enough and comparable with other alternative approaches such as crystallization from methylamine/acetonitrile mixture (19.0%) (Noel et al., 2017) methylamine based technology (19.3%) (Chen et al., 2017).

To achieve the efficiencies over 22%, mixed-cation and mixed-halide perovskites should be used (Yang et al., 2017; Jiang et al., 2019; Jung et al., 2019; Kim et al., 2019; Liu et al., 2019a). Such technologically attractive perovskites with mixed compositions were also successfully obtained using the proposed methods as the corresponding polyiodides have melting points below 65°C (Petrov et al., 2019; Turkevych et al., 2019). In particular, $Cs_{0.05}MA_{0.2}FA_{0.75}PbI_3$ perovskite films and corresponding devices were obtained by RP-MAGIC approach [$T_m(Cs_{0.05}MA_{0.2}FA_{0.75}I_3) = 38°C$] (Turkevych et al., 2019). Mixed compositions [$MA_{0.5}FA_{0.5}PbI_3$, $MA_{0.25}FA_{0.75}PbI_3$, $MA_{0.25}FA_{0.75}PbI_{2.75}Br_{0.25}$, $(FAPbI_3)_{0.83}(MAPbBr_3)_{0.17}$] were obtained by spin-coating of the RPM solutions onto Pb films (T_m of all corresponding polyhalides $< 5°C$) (Petrov et al., 2019; Belich et al., 2020). Further optimization of polyhalide compositions as well as their application techniques is therefore a vital scientific task which can further improve the efficiency of the devices obtained using RPM.

FORMATION OF RPM UNDER ILLUMINATION

It is known that intensive irradiation of hybrid perovskites leads to the release of degradation products I_2, Br_2, MAI, and MABr (Abdelmageed et al., 2016; Pistor et al., 2016; Wang et al., 2016; Ceratti et al., 2018). It was shown recently, that the accumulation of these compounds leads to the formation of RPM in perovskite films (Shlenskaya et al., 2018a; Udalova et al., 2020). Particularly, the fast formation of RPM under laser beam was confirmed for the six most relevant perovskite compositions: $MAPbI_3$, $MA_{0.15}FA_{0.85}PbI_3$, $FAPbI_3$, $FA_{0.85}Cs_{0.15}PbI_3$, $MA_{0.25}FA_{0.75}PbI_{2.25}Br_{0.75}$, and $Cs_{0.05}MA_{0.15}FA_{0.8}PbI_{2.5}Br_{0.5}$ (Udalova et al., 2020).

Slow formation of RPM was observed under intense UV irradiation of a perovskite solar cell causing the degradation of the gold electrode through formation of $[AuI_2]^-$ and $[AuI_4]^-$ complexes and subsequent precipitation of the $(MA)_2Au_2I_6$ phase on the Au/perovskite interface (Shlenskaya et al., 2018a). Ironically, methylammonium polybromides were also found to be responsible for perovskite self-healing under illumination

(Ceratti et al., 2018) indicating a critical role of polyhalides in the photochemistry of hybrid perovskites.

CONCLUSION AND OUTLOOK

To sum up, RPM are a new class of highly reactive polyhalide compounds with a general formula $RHal_x$ (R = MA, FA, Cs; Hal = I, Br) attracting great interest in the view of their unusual physicochemical properties and potential applications. Demonstrating low melting temperatures and unprecedented phase diversity, these compounds can serve as facile precursors for perovskite solar cells fabrication and be responsible for their degradation and self-healing.

We believe that the RPM can promote the development of solvent-free methods of obtaining hybrid perovskites which is free from potential sources of contamination as the reaction between RPM and Pb proceeds without formation of any by-products. Hybrid perovskites obtained using RPM demonstrate excellent optoelectronic properties and have a large range of potential applications including solar cells, photodetectors, light-emitting diodes and photonic devices.

Today, further detailed physicochemical investigation of the RPM is needed to reveal the influence of various polyhalides on the functional properties of the perovskite and other accompanying materials in the devices. The objects of particular interest are RPM with mixed compositions and RPM with other cations including those which are able to form 2D perovskites and compounds with perovskite-like structure.

AUTHOR CONTRIBUTIONS

All authors listed have made a substantial, direct and intellectual contribution to the work, and approved it for publication.

FUNDING

This research was financially supported by the Russian Science Foundation (Project No. 18-73-10224).

ACKNOWLEDGMENTS

Authors are grateful to the team of the Laboratory of New Materials for Solar Energetics.

REFERENCES

Abdelmageed, G., Jewell, L., Hellier, K., Seymour, L., Luo, B., Bridges, F., et al. (2016). Mechanisms for light induced degradation in MAPbI3 perovskite thin films and solar cells. *Appl. Phys. Lett.* 109:233905. doi: 10.1063/1.4967840

Belich, N. A., Petrov, A. A., Rudnev, P. O., Stepanov, N. M., Turkevych, I., Goodilin, E. A., et al. (2020). From metallic lead films to perovskite solar cells through lead conversion with polyhalides solutions. *ACS Appl. Mater. Interfaces*. 12, 20456–20461. doi: 10.1021/acsami.0c02492. [Epub ahead of print].

Bengtsson, L. A., Stegemann, H., Holmberg, B., and Füllbier, H. (1991). The structure of room temperature molten polyiodides. *Mol. Phys.* 73, 283–296. doi: 10.1080/00268979100101201

Cao, J., Jing, X., Yan, J., Hu, C., Chen, R., Yin, J., et al. (2016). Identifying the molecular structures of intermediates for optimizing the fabrication of high-quality perovskite films. *J. Am. Chem. Soc.* 138, 9919–9926. doi: 10.1021/jacs.6b04924

Ceratti, D. R., Rakita, Y., Cremonesi, L., Tenne, R., Kalchenko, V., Elbaum, M., et al. (2018). Self-healing inside APbBr3 halide perovskite crystals. *Adv. Mater.* 30, 1–7. doi: 10.1002/adma.201706273

Chen, H., Ye, F., Tang, W., He, J., Yin, M., Wang, Y., et al. (2017). A solvent- and vacuum-free route to large-area perovskite films for efficient solar modules. *Nature* 550, 92–95. doi: 10.1038/nature23877

Chiang, C.-H., and Wu, C.-G. (2018). A method for the preparation of highly oriented MAPbI 3 crystallites for high-efficiency perovskite solar cells to achieve an 86% fill factor. *ACS Nano* 12, 10355–10364. doi: 10.1021/acsnano.8b05731

Dong, Q., Fang, Y., Shao, Y., Mulligan, P., Qiu, J., Cao, L., et al. (2015). Electron-hole diffusion lengths > 175 um in solution-grown CH 3 NH 3 PbI 3 single crystals. *Science* 347, 967–970. doi: 10.1126/science.aaa5760

Fateev, S. A., Petrov, A. A., Khrustalev, V. N., Dorovatovskii, P. V., Zubavichus, Y. V., Goodilin, E. A., et al. (2018). Solution processing of methylammonium lead iodide perovskite from γ-butyrolactone: crystallization mediated by solvation equilibrium. *Chem. Mater.* 30, 5237–5244. doi: 10.1021/acs.chemmater.8b01906

Fei, Z., Bobbink, F. D., Păunescu, E., Scopelliti, R., and Dyson, P. J. (2015). Influence of elemental iodine on imidazolium-based ionic liquids: solution and solid-state effects. *Inorg. Chem.* 54, 10504–10512. doi: 10.1021/acs.inorgchem.5b02021

Gao, P., Grätzel, M., and Nazeeruddin, M. K. (2014). Organohalide lead perovskites for photovoltaic applications. *Energy Environ. Sci.* 7, 2448–2463. doi: 10.1039/C4EE00942H

Grishko, A. Y., Petrov, A. A., Goodilin, E. A., and Tarasov, A. B. (2019). Patterned films of a hybrid lead halide perovskite grown using space-confined conversion of metallic lead by reactive polyiodide melts. *RSC Adv.* 9, 37079–37081. doi: 10.1039/C9RA07613A

Hsieh, T. Y., Huang, C. K., Su, T.-S., Hong, C.-Y., and Wei, T.-C. (2017). Crystal growth and dissolution of methylammonium lead iodide perovskite in sequential deposition: correlation between morphology evolution and photovoltaic performance. *ACS Appl. Mater. Interfaces* 9, 8623–8633. doi: 10.1021/acsami.6b12303

Jiang, Q., Zhao, Y., Zhang, X., Yang, X., Chen, Y., Chu, Z., et al. (2019). Surface passivation of perovskite film for efficient solar cells. *Nat. Photon.* 13, 460–466. doi: 10.1038/s41566-019-0398-2

Jung, E. H., Jeon, N. J., Park, E. Y., Moon, C. S., Shin, T. J., Yang, T.-Y., et al. (2019). Efficient, stable and scalable perovskite solar cells using poly(3-hexylthiophene). *Nature* 567, 511–515. doi: 10.1038/s41586-019-1036-3

Kim, M., Kim, G. H., Lee, T. K., Choi, I. W., Choi, H. W., Jo, Y., et al. (2019). Methylammonium chloride induces intermediate phase stabilization for efficient perovskite solar cells. *Joule* 3, 2179–2192. doi: 10.1016/j.joule.2019.06.014

Lin, Q., Armin, A., Nagiri, R. C. R., Burn, P. L., and Meredith, P. (2015). Electro-optics of perovskite solar cells. *Nat. Photon.* 9, 106–112. doi: 10.1038/nphoton.2014.284

Liu, Y., Akin, S., Pan, L., Uchida, R., Arora, N., Milić, J. V., et al. (2019a). Ultrahydrophobic 3D/2D fluoroarene bilayer-based water-resistant perovskite solar cells with efficiencies exceeding 22%. *Sci. Adv.* 5, 1–9. doi: 10.1126/sciadv.aaw2543

Liu, Z., Krückemeier, L., Krogmeier, B., Klingebiel, B., Márquez, J. A., Levcenko, S., et al. (2019b). Open-circuit voltages exceeding 1.26 V in planar methylammonium lead iodide perovskite solar cells. *ACS Energy Lett.* 4, 110–117. doi: 10.1021/acsenergylett.8b01906

Noel, N. K., Habisreutinger, S. N., Wenger, B., Klug, M. T., Hörantner, M. T., Johnston, M. B., et al. (2017). A low viscosity, low boiling point, clean solvent system for the rapid crystallisation of highly specular perovskite films. *Energy Environ. Sci.* 10, 145–152. doi: 10.1039/C6EE02373H

NREL (2020). *Best Research-Cell Efficiencies*.

Petrov, A. A., Belich, N. A., Grishko, A. Y., Stepanov, N. M., Dorofeev, S. G., Maksimov, E. G., et al. (2017a). A new formation strategy of hybrid perovskites via room temperature reactive polyiodide melts. *Mater. Horiz.* 4, 625–632. doi: 10.1039/C7MH00201G

Petrov, A. A., Fateev, S. A., Zubavichus, Y. V., Dorovatovskii, P. V., Victor, N., Zvereva, I. A., et al. (2019). Methylammonium polyiodides: remarkable phase diversity of the simplest and low-melting alkylammonium polyiodide system. *J. Phys. Chem. Lett.* 10, 5776–5780. doi: 10.1021/acs.jpclett.9b02360

Petrov, A. A., Khrustalev, V. N., Zubavichus, Y. V., Dorovatovskii, P. V., Goodilin, E. A., and Tarasov, A. B. (2018). Synthesis and crystal structure of a new hybrid methylammonium iodocuprate. *Mendeleev Commun.* 28, 245–247. doi: 10.1016/j.mencom.2018.05.005

Petrov, A. A., Pellet, N., Seo, J.-Y., Belich, N. A., Kovalev, D. Y., Shevelkov, A. V., et al. (2017b). New insight into the formation of hybrid perovskite nanowires via structure directing adducts. *Chem. Mater.* 29, 587–594. doi: 10.1021/acs.chemmater.6b03965

Petrov, A. A., Sokolova, I. P., Belich, N. A., Peters, G. S., Dorovatovskii, P. V., Zubavichus, Y. V., et al. (2017c). Crystal structure of DMF-intermediate phases uncovers the link between CH 3 NH 3 PbI 3 morphology and precursor stoichiometry. *J. Phys. Chem. C* 121, 20739–20743. doi: 10.1021/acs.jpcc.7b08468

Pistor, P., Ruiz, A., Cabot, A., and Izquierdo-Roca, V. (2016). Advanced Raman spectroscopy of methylammonium lead iodide: development of a non-destructive characterisation methodology. *Sci. Rep.* 6, 1–8. doi: 10.1038/srep35973

Saliba, M., Matsui, T., Seo, J.-Y. Y., Domanski, K., Correa-Baena, J.-P. P., Nazeeruddin, M. K., et al. (2016). Cesium-containing triple cation perovskite solar cells: improved stability, reproducibility and high efficiency. *Energy Environ. Sci.* 9, 1989–1997. doi: 10.1039/C5EE03874J

Shlenskaya, N. N., Belich, N. A., Grätzel, M., Goodilin, E. A., and Tarasov, A. B. (2018a). Light-induced reactivity of gold and hybrid perovskite as a new possible degradation mechanism in perovskite solar cells. *J. Mater. Chem. A* 6, 1780–1786. doi: 10.1039/C7TA10217H

Shlenskaya, N. N., Goodilin, E. A., and Tarasov, A. B. (2018b). Isolation of methylammonium room temperature reactive polyiodide melt into a new starch complex. *Mendeleev Commun.* 28, 242–244. doi: 10.1016/j.mencom.2018.05.004

Stegemann, H., Rohde, A., Reiche, A., Schnittke, A., and Füllbier, H. (1992). Room temperature molten polyiodides. *Electrochim. Acta* 37, 379–383. doi: 10.1016/0013-4686(92)87025-U

Thorsmølle, V. K., Brauer, J. C., Zakeeruddin, S. M., Grätzel, M., and Moser, J. E. (2012). Temperature-dependent ordering phenomena of a polyiodide system in a redox-active ionic liquid. *J. Phys. Chem. C* 116, 7989–7992. doi: 10.1021/jp300105h

Topol, L. E. (1968). Thermodynamic studies in the polyiodide systems, rubidium iodide-rubidium triiodide, ammonium iodide-ammonium triiodide, cesium iodide-cesium triiodide, and cesium triiodide-cesium tetraiodide. *Inorg. Chem.* 7, 451–454. doi: 10.1021/ic50061a013

Turkevych, I., Kazaoui, S., Belich, N. A., Grishko, A. Y., Fateev, S. A., Petrov, A. A., et al. (2019). Strategic advantages of reactive polyiodide melts for scalable perovskite photovoltaics. *Nat. Nanotechnol.* 14, 57–63. doi: 10.1038/s41565-018-0304-y

Udalova, N. N., Tutantsev, A. S., Chen, Q., Kraskov, A., Goodilin, E. A., and Tarasov, A. B. (2020). New features of photochemical decomposition of hybrid lead halide perovskites by laser irradiation. *ACS Appl. Mater. Interfaces* 12, 12755–12762. doi: 10.1021/acsami.9b21689

Wang, K. X., Yu, Z., Liu, V., Cui, Y., and Fan, S. (2012). Absorption enhancement in ultrathin crystalline silicon solar cells with antireflection and light-trapping nanocone gratings. *Nano Lett.* 12, 1616–1619. doi: 10.1021/nl204550q

Wang, S., Jiang, Y., Juarez-Perez, E. J., Ono, L. K., and Qi, Y. (2016). Accelerated degradation of methylammonium lead iodide perovskites induced by exposure to iodine vapour. *Nat. Energy* 2:16195. doi: 10.1038/nenergy.2016.195

Wang, Y., Xue, Y., Wang, X., Cui, Z., and Wang, L. (2014). The stable polyiodides: experimental and theoretical studies of formation mechanism. *J. Mol. Struct.* 1074, 231–239. doi: 10.1016/j.molstruc.2014.05.062

Yang, W. S., Park, B.-W., Jung, E. H., Jeon, N. J., Kim, Y. C., Lee, D. U., et al. (2017). Iodide management in formamidinium-lead-halide–based perovskite layers for efficient solar cells. *Science* 356, 1376–1379. doi: 10.1126/science.aan2301

Yushina, I., Rudakov, B., Krivtsov, I., and Bartashevich, E. (2014). Thermal decomposition of tetraalkylammonium iodides. *J. Therm. Anal. Calorim.* 118, 425–429. doi: 10.1007/s10973-014-3944-7

Zhao, Y., and Zhu, K. (2016). Organic–inorganic hybrid lead halide perovskites for optoelectronic and electronic applications. *Chem. Soc. Rev.* 45, 655–689. doi: 10.1039/C4CS00458B

Conflict of Interest: The authors declare that the research was conducted in the absence of any commercial or financial relationships that could be construed as a potential conflict of interest.

ORIGINAL RESEARCH
published: 25 May 2020
doi: 10.3389/fchem.2020.00438

Mobility of the Singly-Charged Lanthanide and Actinide Cations: Trends and Perspectives

Giorgio Visentin[1], **Mustapha Laatiaoui**[2,3], **Larry A. Viehland**[4] **and Alexei A. Buchachenko**[1,5]*

[1] Center for Energy Science and Technology, Skolkovo Institute of Science and Technology, Moscow, Russia, [2] Department Chemie, Johannes Gutenberg-Universität, Mainz, Germany, [3] Helmholtz-Institut Mainz, Mainz, Germany, [4] Science Department, Chatham University, Pittsburgh, PA, United States, [5] Theoretical Department, Institute of Problems of Chemical Physics, Russian Academy of Sciences, Chernogolovka, Russia

The current status of gaseous transport studies of the singly-charged lanthanide and actinide ions is reviewed in light of potential applications to superheavy ions. The measurements and calculations for the mobility of lanthanide ions in He and Ar agree well, and they are remarkably sensitive to the electronic configuration of the ion, namely, whether the outer electronic shells are 6s, 5d6s or $6s^2$. The previous theoretical work is extended here to ions of the actinide family with zero electron orbital momentum: Ac^+ ($7s^2$, ^1S), Am^+ ($5f^77s$ $^9S^\circ$), Cm^+ ($5f^77s^2$ $^8S^\circ$), No^+ ($5f^{14}7s$ ^2S), and Lr^+ ($5f^{14}7s^2$ ^1S). The calculations reveal large systematic differences in the mobilities of the 7s and $7s^2$ groups of ions and other similarities with their lanthanide analogs. The correlation of ion-neutral interaction potentials and mobility variations with spatial parameters of the electron distributions in the bare ions is explored through the ionic radii concept. While the qualitative trends found for interaction potentials and mobilities render them appealing for superheavy ion research, lack of experimental data and limitations of the scalar relativistic *ab initio* approaches in use make further efforts necessary to bring the transport measurements into the inventory of techniques operating in "one atom at a time" mode.

Keywords: ion mobility, interaction potential, lanthanides, actinides, electronic configuration, superheavy ions

OPEN ACCESS

Edited by:
Eugene A. Goodilin,
Lomonosov Moscow State University,
Russia

Reviewed by:
Tetsuya K. Sato,
Japan Atomic Energy Agency, Japan
Andery Vladislavovich Stolyarov,
Lomonosov Moscow State University,
Russia

***Correspondence:**
Alexei A. Buchachenko
a.buchachenko@skoltech.ru

Specialty section:
This article was submitted to
Physical Chemistry and Chemical
Physics,
a section of the journal
Frontiers in Chemistry

Received: *11 February 2020*
Accepted: *27 April 2020*
Published: *25 May 2020*

Citation:
Visentin G, Laatiaoui M, Viehland LA
and Buchachenko AA (2020) Mobility
of the Singly-Charged Lanthanide and
Actinide Cations: Trends and
Perspectives. Front. Chem. 8:438.
doi: 10.3389/fchem.2020.00438

1. INTRODUCTION

While celebrating 1869 as the year of the Periodic Table's discovery, one may also recall other important milestones of its shaping toward the present form (Karol et al., 2016a,b). The last element found in nature was francium $Z = 87$ in 1939 (Perey, 1939), although a few more have been confirmed after being produced artificially. The synthetic era started in 1937 with technetium $Z = 43$ (Perrier and Segrè, 1947). The transuranium elements up to fermium $Z = 100$, discovered in 1952 (Ghiorso et al., 1955a), are produced in nuclear reactors by neutron capture reactions. About the same time, mendelevium $Z = 101$ was synthesized (Ghiorso et al., 1955b) by a new recoil technique in "one atom at a time" mode. This technique has opened the modern era of heavy ion fusion synthesis that is still being used in high power accelerators (Türler and Pershina, 2013; Haba, 2019).

Although recent discoveries have been driven by physical methods, it is essentially chemistry that fit them into the Periodic Table. Even the actinides had not found their proper placement until the chemical analysis of neptunium $Z = 93$ and plutonium $Z = 94$ in the 1940's (Seaborg, 1945; Seaborg and Loveland, 1990). Since then, the chemical isolation of an element marks its discovery (Wallmann, 1959). Sophisticated techniques of production, isolation and characterization of simple chemical compounds in both gas and liquid phases are in use (Türler and Pershina, 2013; Schädel and Shaughnessy, 2014; Oganessian and Dmitriev, 2016; Eichler, 2017, 2019; Düllmann, 2019) for superheavy elements to determine their volatility, adsorption enthalpies and bonding parameters.

Information on the electronic structure and properties of bare heavy atoms and ions is no less valuable. In particular, spectroscopic data enables firm assignments of ground state configurations, irrespective of the chemical behavior. In addition, it provides fingerprint spectral lines for use in the search for heavy and superheavy elements in the universe (Ter-Akopian and Dmitriev, 2015) and benchmark data for *ab initio* methods of atomic and nuclear structure theory (Pershina, 1996; Pyykkö, 2012, 2016; Eliav et al., 2015; Dzuba et al., 2017; Liu, 2017; Giuliani et al., 2019). The recent review by Backe et al. (2015) relates the progress in spectroscopic measurements to the use of ion or buffer gas traps to collect a few atomic species emerging one by one from a recoil separator. It acknowledges that "quite good spectroscopic information is available up to the element einsteinium ($Z = 99$)…up to the year 2003." Since then, the bound has been gradually pushed upward (Sewtz et al., 2003; Laatiaoui et al., 2016; Chhetri et al., 2018) to nobelium ($Z = 102$) owing to resonance ionization spectroscopy of the neutral atoms inside buffer gas cells.

The extension of these technique to heavier elements is certainly challenging, mostly due to decreasing production yield with increasing atomic number. Classical methods based on fluorescence detection suffer from low sensitivity, which renders them incompatible with one atom at a time experiments (Campbell et al., 2016). Not surprisingly, studies of the gaseous transport properties are currently being considered as prospective means for probing the superheavy ions (Rickert et al., 2020), not least for their compatibility with in-flight separators that provide recoil ions (Backe et al., 2015).

From many measurements across the Periodic Table, gaseous ion mobility is known to be sensitive to the electronic configuration of open-shell ions (Kemper and Bowers, 1991; Bowers et al., 1993; Taylor et al., 1999; Iceman et al., 2007; Ibrahim et al., 2008; Manard and Kemper, 2016a,b). It is a fundamental property of an ion that defines, macroscopically, the rate of its steady-state drift through a neutral buffer gas and reflects its microscopic interactions with the buffer-gas particles (Mason and McDaniel, 1988; Viehland, 2018). In a sense, characterization of an ion through its gas-phase interaction with other species is equivalent to chemical characterization by chromatography. By choosing monoatomic inert gases as the buffers, one reduces the complexity of covalent chemical bonding to the (relative) simplicity of the physical ion-atom polarization forces.

The theory of intermolecular forces tells us that the properties of a weakly bound dimer can be reliably described by the properties of the constituting monomers (Kaplan, 2006; Stone, 2013). Thus, ion-atom interaction potentials are very sensitive to the electronic structure of an ion, to its electronic configuration, electronic state symmetry, electric momenta, and static and dynamic polarizabilities. Exemplary confirmation of this for the main-group and transition-metal ions has been provided by Bellert and Breckenridge (2002) and Wright and Breckenridge (2010). Ion mobility inherits this sensitivity. The field-induced drift discrimination of the ions in ground and excited electronic states (Kemper and Bowers, 1991; Bowers et al., 1993; Taylor et al., 1999; Iceman et al., 2007; Ibrahim et al., 2008; Manard and Kemper, 2016a,b), known as the electronic-state chromatography effect, is a direct consequence of the mobility variation with electronic configuration. It has been proposed recently (Laatiaoui, 2019) that this effect can be used for spectroscopic investigation of heavy and superheavy ions.

Measurements of ion mobility (equivalently, the drift time through a fixed distance) are indeed compatible with the separation and buffer gas trapping techniques. They are well-controlled by operating temperature, pressure and external field strength. Potentially, they can enrich our knowledge of electronic structure of ions produced in one atom at a time mode.

The present paper addresses the current state-of-the-art in the studies of gaseous transport of singly-charged lanthanide and actinide ions. Though far from being complete, experimental and theoretical data for the lanthanide ions still permit us to analyze the relation between the electronic structure of an ion and its mobility determined by the *ab initio* ion-atom interaction potential. In particular, mobility trends for distinct electronic configurations and effective sizes of an ion are established. To step into the actinide period, we extend the scalar relativistic *ab initio* approaches tested for lanthanides to compute ion-atom interaction potentials for selected actinide ions. We show that the trends found for the lanthanides largely persist for the actinide family and thus can underlie experimental exploration of their transport and, in turn, electronic structure properties. This also sheds light on potential use of transport properties for exploration of superheavy ions.

In section 2 we briefly review the theoretical concepts and computational methods of ion mobility in rare gases. Section 3 presents the review and analysis of the lanthanide results, while ions of the actinide family are discussed in section 4. Conclusions and outlook follow.

2. ION MOBILITY AND INTERACTION POTENTIALS

Experimental techniques, general theoretical concepts and computational approaches relevant to gaseous ion transport are described in detail in two monographs by Mason and McDaniel (1988) and by Viehland (2018). The macroscopic definition of the mobility, K, for trace amounts of drifting ions is given by the equation

$$\mathbf{v}_d = K\mathbf{E}, \tag{1}$$

where the vector, $\mathbf{v}_d$, is the ion drift velocity and $\mathbf{E}$ is the electric field vector. Throughout this paper, only the monoatomic rare gases He and Ar (collectively, RG) are considered as the buffer gases. The ion mobility can be deduced with good accuracy from the measured arrival time distribution of the ions drifting through the tube of length l. In particular, the mean drift time t_d is

$$t_d = l/KE. \tag{2}$$

It is convenient to consider the standard mobility, K_0, by the equation

$$K_0 = n_0 K/N_0, \tag{3}$$

where n_0 and $N_0 = 2.6867805\ \mathrm{m}^{-3}$ are the buffer gas number density and the Loschmidt number, respectively. The standard mobility depends on the reduced electric field strength, E/n_0, and the temperature of the gas, T_0.

From a rigorous theoretical standpoint, the ion mobility is a transport coefficient determined by the solution of the Boltzmann equation, which accounts for anisotropic diffusion and equilibration of the dragging electrostatic force by the momentum transfer that determines the stationary velocity of an ion through the buffer gas. The Boltzmann equation is parameterized by collision integrals, which are expressed through the binary collision cross sections (Mason and McDaniel, 1988; Viehland, 2018). The cross sections are, in turn, fully determined by the ion-atom interaction potential(s). Vice versa, knowledge of the zero-field mobility over a reasonably wide range of E/n_0 or T_0 is enough for direct reconstruction of the interaction potential (Viehland et al., 1976; Viehland, 1983; Mason and McDaniel, 1988).

The Gram-Charlier expansion of the ion distribution function provides the most sophisticated approach for solving the Boltzmann equation for atomic ions drifting in atomic gases (Viehland, 1994, 2018). Its accuracy has been shown to be limited solely by the accuracy of the underlying ion-atom potential (Viehland, 2012; Viehland et al., 2017). The Gram-Charlier method is used for all mobility calculations considered in this paper. The results of these calculations have been placed in the on-line database (Viehland, 2009–2020) within the LXCat project, that already has about 5,000 tables of theoretical and experimental results.

In the low-field limit, which is the only situation considered here, K_0 has only a slight dependence on the gas temperature, as indicated by writing it as $K_0(T_0)$. The Gram-Charlier theory reduces in this situation to the one-temperature theory (Mason and McDaniel, 1988; Viehland, 2018) and the so-called zero-field mobility, $K_0(T_0)$, obeys the fundamental low-field ion mobility equation (Viehland, 2018), which contains the momentum-transfer collision integral, $\bar{\Omega}^{(1,1)}(T_0)$. According to Mason and McDaniel (1988) and Viehland (2018), this equation is

$$K_0(T_0) = \left(\frac{2\pi}{\mu_0 k_B T_0}\right)^{1/2} \frac{3q}{16N_0} \frac{1+\alpha_c(T_0)}{\bar{\Omega}^{(1,1)}(T_0)}, \tag{4}$$

where μ_0 is the reduced mass of the ion-atom system, k_B is the Boltzmann constant, q is the ion charge (always +1 in electron charge units here), and $\alpha_c(T_0)$ is a temperature-dependent correction term that is small enough to be neglected for heavy ions (Viehland, 2018). Note that $\bar{\Omega}^{(1,1)}(T_0)$ has the standard definition (Hirschfelder et al., 1954) as the temperature average of the energy-dependent momentum-transfer cross section. Throughout this paper, the classical-mechanical cross sections were computed using the program PC (Viehland and Chang, 2010).

A complication arises when an ion has an open-shell electronic structure, as is the case for the majority of singly-charged lanthanides and actinides. Non-zero electronic orbital angular momentum, L, makes the ion-atom interaction anisotropic (Aquilanti and Grossi, 1980; Krems et al., 2004). The ion-atom collisions controlling the ion transport may involve multiple underlying interaction potentials and the respective cross sections depend on Λ, the projection of L onto the collision axis. If, in addition, an ion bears non-vanishing electronic spin, S, vectorial spin-orbit (SO) interaction couples L and S into the total electronic angular momentum, J. The interaction remains anisotropic in Ω, the projection of J onto the collision axis, if $J \geq 1$. Moreover, if the SO splitting is small, inelastic fine-structure transitions can affect the transport at elevated T_0.

As the present paper primarily explores the relation between the ion electronic structure and the ion mobility, through the ion-atom interaction potential, we will mostly consider scalar relativistic approaches. Vectorial SO coupling can be used in subsequent work for accurate comparisons with experimental data.

Consideration of interaction anisotropy gives rise to some ambiguity. A transparent one-to-one relation between the interaction potential and transport properties holds within the so-called "isotropic scalar relativistic" (ISR) approximation that was first introduced by Aquilanti and Vecchiocattivi (1989) for diffusion of neutral atoms. It assumes that the collisions changing Λ are very efficient, so that an atom "feels" an ion through average isotropic potential V_0. For ions in the states of D symmetry ($L = 2$), like Gd^+ ($4f^7 5d6s$, $^{10}\mathrm{D}^{\circ}$) and metastable Lu^+ ($4f^{14} 5d6s$, $^3\mathrm{D}$) of relevance here, the isotropic potential has the form

$$V_0(R) = [V_\Sigma(R) + 2V_\Pi(R) + 2V_\Delta(R)]/5, \tag{5}$$

where Σ, Π and Δ correspond to projections $|\Lambda| = 0, 1$, and 2, respectively, and R is the ion-atom internuclear distance. Alas, the ISR approximation can be rather poor (Buchachenko and Viehland, 2019). More accurate is the "anisotropic" approximation (ASR), which assumes the conservation of Λ during each ion-atom collision. The ASR implies that the transport cross sections should be computed for each V_Λ potential separately and then averaged with the same degeneracy factors as appeared in Equation (5).

The sensitivity of the ion mobility to the interaction potential is well-known (Mason and McDaniel, 1988; Viehland, 2018). Extensive comparisons by Viehland et al. (2017) for ions lighter than caesium $Z = 55$ indicates that the potentials calculated using an accurate single-reference *ab initio* technique, such as the CCSD(T) (coupled cluster with singles, doubles and non-iterative triples) method, normally provide the zero-field mobilities accurate within 0.05%. By contrast, multireference methods of the configuration interaction type (like MRCI, multireference configuration interaction) are not well-suited for interaction potentials involving heavy ions. Accounting for the static electron correlation in a bare ion requires long expansions over configurations with multiple high-angular momentum shell occupancies, while the recovery of the dynamic correlation necessary to reproduce the polarization forces makes the problem intractable. As a result, *ab initio* interaction potential calculations fitting the accuracy required for transport properties are presently possible only for ions whose electron configurations are well-described in the single-reference approximation. This limits the variety of ions studied using the CCDS(T) method and considered below. Another concern is the strong relativistic effects inherent to heavy ions. Ion-atom interactions predominantly depend on the density of outermost electrons and could be less sensitive to relativity than, say, electronic energy levels or chemical bonding. Indeed, as we show below, scalar relativistic effective core potentials for lanthanide ions permit one to reproduce the measured mobility quantitatively. The same level of accuracy cannot be guaranteed for actinide ions and no direct comparison between the measured and calculated mobilities is currently possible. However, we believe that scalar relativistic CCSD(T) method is still able to capture qualitative trends in interaction potential and mobility variations along the family, while the applications of the more elaborate relativistic method should be reserved for quantitative analysis to come.

Throughout this paper, we will use the following notations for ions. Complete specification for Eu$^+$, for instance, $^{151}_{63}\mathrm{Eu}^+(4f^7 6s, {}^9S^\circ)$, includes the nuclear charge Z, the number of neutrons in the nuclei, the electronic configuration of outer shells and the term symbol in the scalar relativistic approximation. Particular isotopes are specified mostly for measured or calculated mobility data. In transparent cases, some of these symbols will be omitted. When the SO splitting is considered explicitly, the J subscript is added to the term symbol.

3. LANTHANIDE IONS

3.1. Overview

Lanthanide ions provide a useful test case for assessments of the theoretical approaches to heavy ion mobility and analysis of information about an ion's electronic structure that can be derived from the limited measurements. The first relevant experimental study performed by Laatiaoui et al. (2012) provided the zero-field mobilities in Ar at 300 K for the $^{151}_{63}\mathrm{Eu}^+$ ($4f^7 6s$, $^9S^\circ$), $^{156}_{64}\mathrm{Gd}^+$ ($4f^7 5d6s$, $^{10}D^\circ$), $^{159}_{65}\mathrm{Tb}^+$ ($4f^9 6s$, $^7H^\circ$), $^{165}_{67}\mathrm{Ho}^+$ ($4f^{11} 6s$, $^5I^\circ$), $^{168}_{68}\mathrm{Er}^+$ ($4f^{12} 6s$, ^4H), and $^{174}_{70}\mathrm{Yb}^+$ ($4f^{14} 6s$, ^2S) ions. Shortly after, two of us reported the *ab initio* CCSD(T) interaction potentials and transport properties for the ground S-state ions Eu$^+$, Yb$^+$, and $^{175}_{71}\mathrm{Lu}^+(4f^{14} 6s^2, {}^1S)$ in He, Ne, Ar, Kr, and Xe for wide ranges of T_0 and E/n_0 [data available from the LXCat database (Viehland, 2009–2020)]. For the Gd$^+$ ion in the rare gases, a combination of the CCSD(T) and MRCI methods was applied together with an asymptotic model for SO coupling. Simultaneously, the Eu$^+$ ($4f^7 6s$) interactions with the rare gases were calculated by Lee and Wright (2011–2013) using the CCSD(T) method combined with the large-core effective core potentials (ECP), see also Buchachenko and Viehland (2014). Manard and Kemper (2017a,b) measured the zero-field mobilities in He at 295 K, first for the same four ions and then for the rest of the lanthanide family from $^{140}_{58}\mathrm{Ce}^+$ ($4f5d^2$, $^4H^\circ$) to $^{175}_{71}\mathrm{Lu}^+$ ($4f^{14} 6s^2$) except for $_{61}\mathrm{Pm}^+$ ($4f^5 6s$, $^7H^\circ$). More sophisticated *ab initio* calculations have allowed us to bring the Gd$^+$ ion mobilities in He and Ar into agreement with the measurements (Buchachenko and Viehland, 2019) and to evaluate the interaction potentials for the metastable $^{175}_{71}\mathrm{Lu}^+$ ($4f^{14} 5d6s$, ^3D), as presented here.

Figure 1 provides an overview of the room-temperature zero-field mobilities available for lanthanide ions. Most of the ions have the $4f^m 6s$ ground-state configuration and their mobilities follow well-defined trend lines. Remarkable deviations take place for a few ions with different outer shell occupancies: Ce$^+$ ($5d^2$), Gd$^+$ ($5d6s$), and Lu$^+$ ($6s^2$). Noteworthy, theory predicts quite similar mobilities for Gd$^+$ and Lu$^+$ in the metastable ^3D state of the same 5d6s configuration, whereas the difference in the ground- and metastable-state Lu$^+$ mobilities is huge comparing to the trend line variation. This clearly confirms the sensitivity of the ion transport to the ion electronic configuration that underlies the electronic state chromatography effect (Kemper and Bowers, 1991; Bowers et al., 1993; Taylor et al., 1999; Iceman et al., 2007; Ibrahim et al., 2008; Manard and Kemper, 2016a,b). On the other hand, the striking difference between the mobilities in He and Ar gases looks surprising, not because of the magnitudes of the K_0 values (which arise due to the ion-neutral reduced masses and interaction strengths), but because the trends with atomic number are so different. While the mobility of the $4f^m 6s$ ions in He generally increases with Z, that in Ar remains almost constant. Moreover, the change of electronic configuration causes opposite mobility variations in the two gases. This behavior can only be understood by analyzing the features of the ion-atom interactions and their manifestations in the transport properties. To justify such an analysis, we should emphasize the very good agreement between the experimental and theoretical data shown in **Figure 1**. The most remarkable exception of the $^{156}_{64}\mathrm{Gd}^+$ ($4f^7 5d6s$) ion originates in fact from the vectorial SO coupling effect (Buchachenko and Viehland, 2019). Compared to the small-core CCSD(T) results, the potentials obtained by the MRCI method lack the accuracy required for transport calculations (Buchachenko and Viehland, 2014). Consideration of $^{151}_{63}\mathrm{Eu}^+$ ($4f^7 6s$) revealed worse performance of the large-core description of lanthanide ions within the CCSD(T) framework (Lee and Wright, 2011–2013; Buchachenko and Viehland, 2014).

3.2. Interaction Potentials

Here, we provide a brief presentation of the *ab initio* approach that was successfully applied for the lanthanide ions to help understanding its extension to the actinide ions, where no direct comparison with experiment is possible so far (see below). It relies on the small-core (28 electron) ECPs adjusted at the quasi-relativistic, Wood-Boring, Hartree-Fock level of theory, ECP28MWB (Dolg et al., 1989). The supplementary atomic natural orbital basis sets (Cao and Dolg, 2001) suffer from the lack of diffuse functions. The optimized s2pdfg diffuse augmentation (Buchachenko et al., 2007) was therefore used together with the segmented basis contraction (Cao and

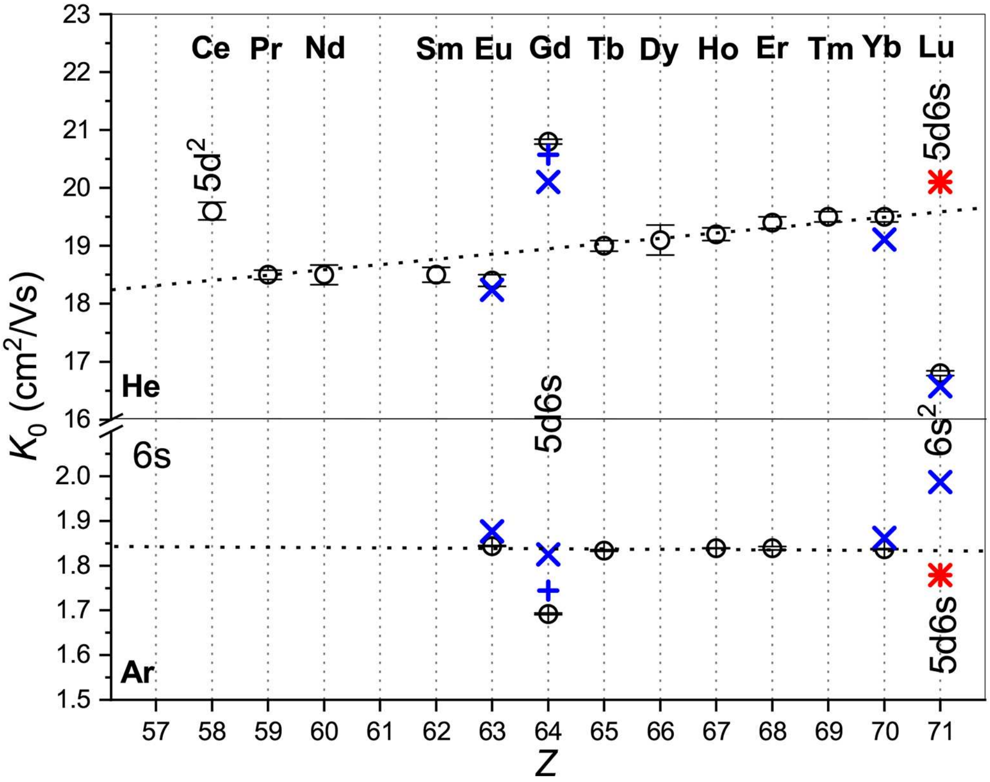

FIGURE 1 | Comparison of the zero-field mobilities of the lanthanide ions in He (top panel) and Ar (bottom panel) near or at 300 K. Circles indicate experimental data by Laatiaoui et al. (2012) and Manard and Kemper (2017a); crosses the scalar relativistic theoretical calculations from Buchachenko and Viehland (2014, 2019). Results that include SO coupling (Buchachenko and Viehland, 2019) are shown by pluses. Asterisks present the ASR theoretical results for $^{175}_{71}$Lu$^+$ (4f^{14}5d6s, ^{3}D). The labels mark electronic configurations of ions that differ from the most common 4f^{m}6s.

Dolg, 2002). He and Ar atoms were described using the augmented, correlation-consistent, polarized basis sets aug-cc-pV5Z (Woon and Dunning, 1994) and the 3s3p2d2f1g bond function set (Cybulski and Toczyłowski, 1999) was placed at the midpoint of the ion-atom distance. The CCSD(T) calculations were performed using the Hartree-Fock references and kept the 4s^{2}4p^{6}4d^{10} shells of the ion and the 1s^{2}2s^{2}2p^6 shells of the Ar atom in core. For the states of D symmetry (Gd$^+$ and Lu$^+$ ions) Hartree-Fock reference wave functions were obtained for each Λ separately, using either different symmetry representations or enforcing an electron population of the 5d$_\sigma$ or 5d$_\delta$ orbital as described by Buchachenko and Viehland (2019). The CCSD(T) potentials were obtained on fine grids of internuclear distances extending up to 25–40 Å and corrected for basis set superposition error by means of the counterpoise procedure by Boys and Bernardi (1970). The MOLPRO program package (Werner et al., 2015) was used for all calculations.

The obtained interaction potentials are plotted in the left column of **Figure 2**, while the parameters of their minima, equilibrium distances R_e and binding energies D_e, are presented in **Table 1**. Tabulated potential functions are given in the LXCat database (Viehland, 2009–2020). Note that for the Gd$^+$ (^{10}D$^\circ$) and Lu$^+$ (^{3}D) ions, only the isotropic potentials $V_0(R)$, Equation (5), are discussed hereafter. The lowest-order induction interaction, $V_{\text{ind}}(R) = -\alpha_{\text{RG}}/2R^4$, where α_{RG} is the static dipole polarizability of the rare gas atom (RG), does not depend on the nature of the ion and determines the common features of interaction potentials at large separations. Indeed, the deviations of D_e from $V_{\text{ind}}(R_e)$ do not exceed 20%, being generally positive (more attraction) for He and negative (more repulsion) for Ar. The equilibrium distance generally decreases with Z for ions with the same valence electronic configurations. In contrast, population of the 5d shell enhances the interaction energy and shrinks the equilibrium distance.

It is instructive to compare the overall shapes of the potentials by introducing the reduced functions, $V(R/R_e)/D_e$, as depicted in the right column of **Figure 2**. In the case of He, the reduced potentials are hardly distinguishable from each other except that for the Lu$^+$ ion with its unique closed-shell, 6s^2 configuration. The reduced potentials show an exception for Lu$^+$ with Ar too, but now with a softer repulsive wall. In contrast to He case, repulsive interaction of the Eu$^+$, Gd$^+$, and Yb$^+$, Lu$^+$(^{3}D) ions with Ar differ slightly from each other. This reflects the effect of the 4f^7 and 4f^{14} occupancies.

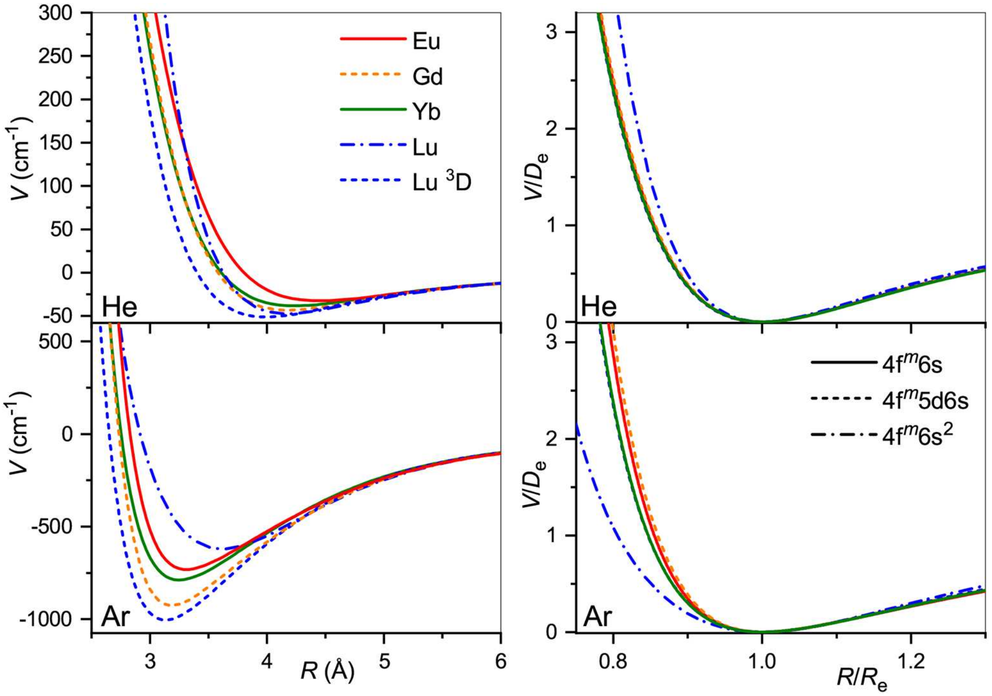

FIGURE 2 | Interaction potentials of the lanthanide ions with He (top panels) and Ar (bottom panels). True and reduced potentials are shown on the left and on the right, respectively.

TABLE 1 | Equilibrium parameters of the ion-atom interaction potentials for lanthanide ions, R_e (Å) and D_e (cm^{-1}).

Ion	**He**		**Ar**	
	R_e	D_e	R_e	D_e
Eu^+ $4f^7 6s$ $^9S^\circ$	4.45	33	3.31	732
Gd^+ $4f^7 5d6s$ $^{10}D^{\circ a}$	4.18	43	3.18	925
Yb^+ $4f^{14} 6s$ ^2S	4.23	38	3.25	789
Lu^+ $4f^{14} 6s^2$ ^1S	4.17	47	3.62	620
Lu^+ $4f^{14} 5d6s$ $^3D^a$	3.99	51	3.13	1005

[a] *Parameters of the isotropic potential* V_0.

3.3. Ion Mobility

While the good agreement between the experimental and theoretical mobilities at room temperature demonstrated in **Figure 1** indicates reasonable accuracy of the scalar relativistic *ab initio* interaction potentials, only a wide temperature dependence of the mobility can fully uncover the features pertinent to a particular ion-neutral interaction (Mason and McDaniel, 1988; Viehland, 2018). Unfortunately, no such measurements have been performed so far for the lanthanide ions, so only theoretical dependences are available (see **Figure 3**).

Our first comment is that the ISR approximation does not work well for the $^{156}_{64}$Gd$^+$ ($4f^7 5d6s$) ion (Buchachenko and Viehland, 2019). In other words, its transport properties are not reproduced quantitatively by a single isotropic V_0 potential. By contrast, the ISR and ASR (not shown) approximations agree with each other well for the $^{175}_{71}$Lu$^+$ ($4f^{14}5d6s$) ion. The second comment is that the main features of the interaction potentials discussed above are clearly reflected in $K_0(T_0)$. Those for $^{151}_{63}$Eu$^+$ ($4f^7 6s$) and $^{174}_{70}$Yb$^+$ ($4f^{14}6s$), and for $^{156}_{64}$Gd$^+$ ($4f^7 5d6s$) (ISR approximation) and $^{175}_{71}$Lu$^+$ ($4f^{14}5d6s$), pair with each other, whereas the results for $^{175}_{71}$Lu$^+$ ($4f^{14}6s^2$) differ, like the underlying potentials do. Third, it is evident that room temperature corresponds to different regions of the mobility functions for He and Ar. In the former case, it falls beyond the mobility maximum, while in the latter it falls in the region of the shallow mobility minimum. A rich early-days experience with model potential functions and direct potential inversion (Viehland et al., 1976; Viehland, 1983), summarized by Mason and McDaniel (1988, chap.7) and Viehland (2018, chapter 9), helps to connect, qualitatively, the radial dependence of the potential and temperature dependence of the mobility. The low-temperature trend toward the polarization limit reflects the dominant interaction term, V_{ind}, the mobility minimum features an intermediate interaction range where attractive van der Waals forces of higher order are also operative, the maximum is predominantly connected to the potential well, and the decreasing high-temperature branch reflects the repulsive interactions. Note that flipping a $K_0(T_0)$ plot upside down and right to left, one sees a cartoon of an interaction potential. An immediate conclusion is that the room temperature measurements in different buffer gases do not equally attest the properties of the ion. These and the ion-neutral reduced masses provide a good but partial explanation for why the variations of the room-temperature mobility with the nature of ion are so strikingly different for He and Ar (see **Figure 3**). However,

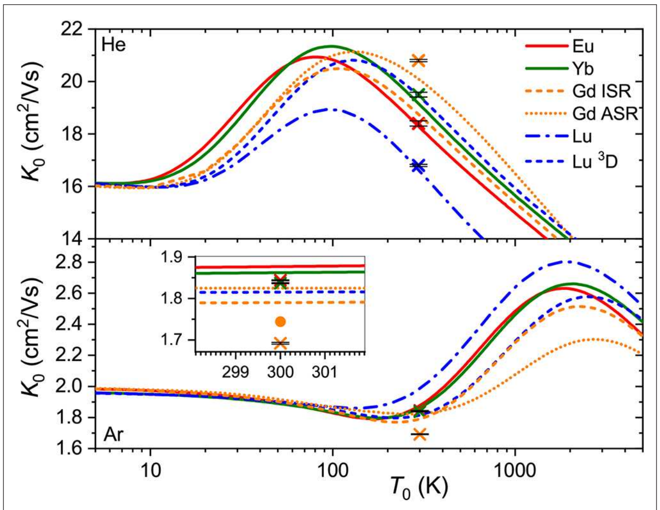

FIGURE 3 | Zero-field mobilities of the lanthanide ions in He (top panel) and Ar (bottom panel) calculated as functions of temperature. Crosses with tiny error bars indicate experimental data by Laatiaoui et al. (2012) and Manard and Kemper (2017a). The inset for Ar provides an enlarged view of the room-temperature region. The dot represents an accurate calculation (Buchachenko and Viehland, 2019) for the $^{156}_{64}$Gd$^+$ (4f^{7}5d6s, ^{10}D$^\circ_{5/2}$) ion that includes the vectorial SO coupling and hence emphasizes the error of the scalar relativistic approach. The same example is used to illustrate the difference between ISR and ASR approximations.

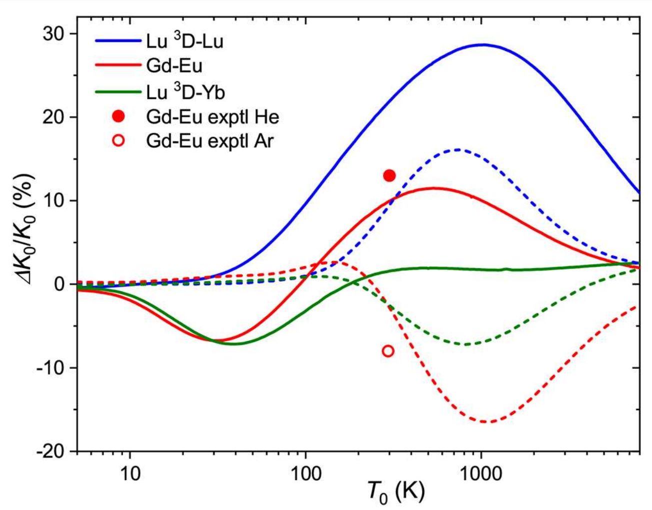

FIGURE 4 | Relative changes in the ion mobilities upon 6s^2 → 5d6s excitation of the Lu$^+$ ion and upon "adding" d electron to Eu$^+$ and Yb$^+$ ions. Solid and dashed lines are used for He and Ar buffer gases, respectively. Experimental room-temperature values are derived from Laatiaoui et al. (2012) and Manard and Kemper (2017b).

the electronic state difference also contributes substantially (**Figure 2**). As a side note, the slightly deeper mobility minimum in Ar can be mentioned for the reduced potentials of Gd$^+$ and Lu$^+$ (4f^{14}5d6s); these may reflect an interaction of the ion permanent quadrupole moment with the induced dipole moment of an atom, which is obviously absent for the S-state ions (Bellert and Breckenridge, 2002).

3.4. Sensitivity to Electronic Configuration

One way to quantify the mobility variations with the electronic configuration of the ion can be closely related to so-called electronic state chromatography effect, or the discrimination of the ground- and metastable-state ions by distinct mean drift times. Although well-studied experimentally for the transition metal ions (Kemper and Bowers, 1991; Bowers et al., 1993; Taylor et al., 1999; Iceman et al., 2007; Ibrahim et al., 2008; Manard and Kemper, 2016a,b), this effect has not been investigated for other ions. Theoretical results for Lu$^+$ (4f^{14}5d6s) allow us to demonstrate this effect for the lanthanide family.

It is convenient to consider the drift time of the ion given by Equation (2). Marking the quantities related to metastable ions by an asterisk and using Equation (3), one gets

$$\Delta t_d^* = t_d^* - t_d = \frac{1}{E/n_0}\frac{l}{N_L}\frac{K_0 - K_0^*}{K_0^* K_0} \tag{6}$$

for the absolute drift time difference and

$$\Delta t_d^*/t_d^* = (K_0 - K_0^*)/K_0 = -\Delta K_0/K_0 \tag{7}$$

for the relative one, where $\Delta K_0/K_0$ is the relative deviation of the mobility of the metastable state ion from that of the ground-state ion. Note that it depends on temperature (and E/n_0) through the individual mobilities. **Figure 4** shows the zero-field $\Delta K_0/K_0$ ratios for $^{175}_{71}$Lu$^+$ (4f^{14}6s^2, ^{1}S) and $^{175}_{71}$Lu$^+$ (4f^{14}5d6s, ^{3}D) ions as a function of temperature. The maximum difference in drift times in He and Ar amounts 30 and 15% at 750 and 1000 K, respectively. The room-temperature difference in He, 22%, is comparable to those measured (Ibrahim et al., 2008) for the coinage metal ions (50, 25, and 13% for copper, silver and gold). These values attest the discrimination between the ground nd^{10} and metastable $nd^9(n+1)$s configurations. Comparison for the third-row transition metal ions that have 6s and 6s^2 ground and metastable configurations, like Hf$^+$, Re$^+$, or Hg$^+$, would be more relevant to Lu$^+$ ion, but to our knowledge none of these ions has been detected in metastable states in mobility experiments (Taylor et al., 1999).

The same pictorial approach can be used for the mobilities of distinct ions in similar configurations. From the present data, the effect of "adding" a 5d electron to the 6s one can be viewed for the Gd$^+$-Eu$^+$ and Lu$^+$(^{3}D)-Yb$^+$ pairs. The corresponding $\Delta K_0/K_0$ ratios (5d6s ion is taken as the "metastable" state) are also plotted in **Figure 4**. In general, they follow a similar trend for each buffer gas, but the two trends are almost opposite. Interestingly, the calculated mobilities demonstrate that higher sensitivity to electronic configuration can sometimes be achieved in Ar rather than He.

3.5. Ionic Radii

Effective ionic radii are important parameters in crystallography, electronic structure theory and molecular modeling. For heavy ions, their dependence on Z should reveal the effect of relativistic contraction. Though the effective size of an ion can be extracted from the *ab initio* interaction potentials themselves, it is important to understand whether or not the transport measurements can provide a systematic means to probe the ionic radii, taking into account exploratory experiments for the actinide ions (Sewtz et al., 2003; Backe et al., 2005) and speculating to the superheavy ions.

The ionic radius can be defined simply as

$$R_{\mathrm{ion}}(R) = R_e - R_{\mathrm{RG}}, \tag{8}$$

where R_e is the equilibrium distance of the ion-RG interaction potential and R_{RG} is the atomic radius of the RG atom, here He or Ar. This definition was analyzed by Wright and Breckenridge (2010) (WB), who recommended the systematics based on He interactions (with the van der Waals radius of 1.49 Å) and noticed that significant distortions of an ion electron density by Ar ($R_{\mathrm{Ar}} = 1.88$ Å) make the definition (8) inconsistent for that RG.

To deduce R_{ion} (or, equivalently, R_e) from the zero-field mobility, one should use Equation (4) and somehow relate $\bar{\Omega}^{(1,1)}(T_0)$ to the ion-neutral interaction potential. Within the hard sphere (HS) model

$$\bar{\Omega}^{(1,1)}(T_0) = \pi R_e^2. \tag{9}$$

Combining Equations (4) and (9), one finds that

$$R_e = \left(\frac{2}{\pi \mu_0 k_B T_0}\right)^{1/4} \left(\frac{3q}{16 N_0 K_0(T_0)}\right)^{1/2}. \tag{10}$$

Then one can easily obtain R_{ion} from Equation (8).

In **Figure 5** radii obtained this way are compared with the parameters of the radial electron distributions calculated by Indelicato et al. (2007) for bare ions, namely, the mean radii of the 6s orbitals, $<r_s>$, and (if any) the 5d orbitals, $<r_d>$, and with the maximum of the density of the outermost orbital, r_{max}. The case of He provides a quite consistent picture. The WB radii correlate well (within 15%) with the electronic parameters, being 1 and 0.8 Å larger than r_{max} and $<r_s>$, respectively, due to the presence of the He atom.

Effective contraction of the bare ion radius in He when going from Eu$^+$ to Yb$^+$ amounts to 0.15 Å, whereas the WB radius shrinks by 0.22 Å. In contrast, the HS model applied to both experimental and calculated room-temperature mobility data gives smaller radii and underestimates their contraction (0.09 Å for the Yb$^+$-Eu$^+$ pair). When applied to the theoretical mobilities at their maxima, the HS model gives a more consistent trend; results become closer to the WB definition and the Yb$^+$-Eu$^+$ contraction becomes 0.26 Å. Still, the HS model works reasonably only for potentials of very similar shape. Even a minor deviation

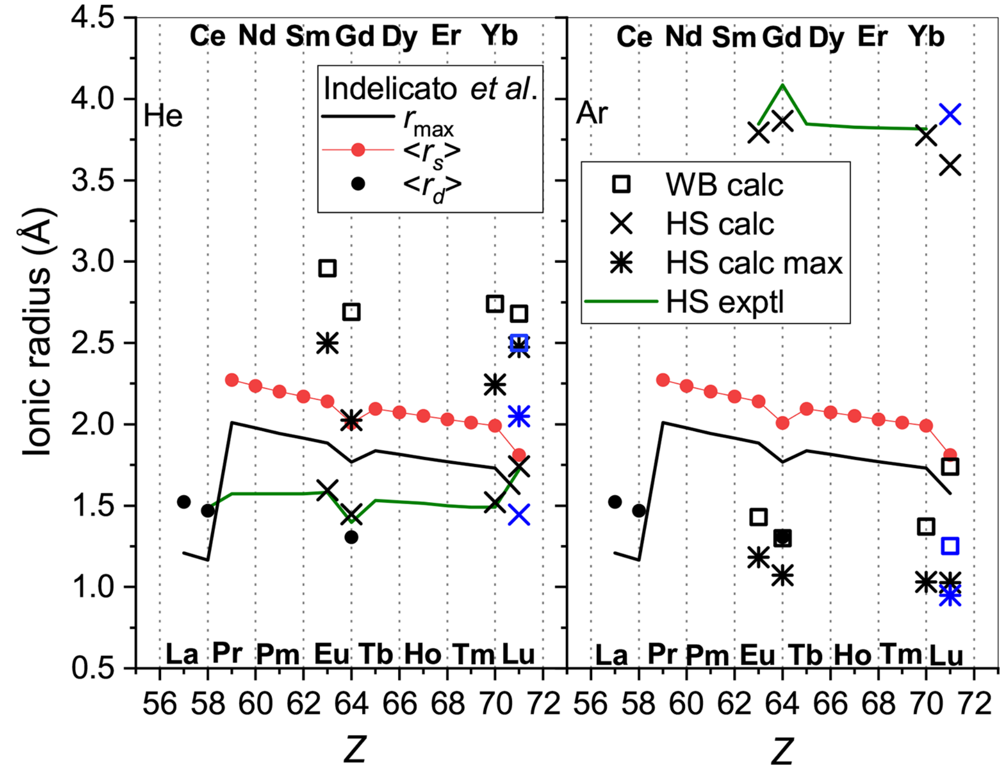

FIGURE 5 | The radii of the lanthanide ions determined from He (left panel) and Ar (right panel) data. Presented are the WB radii from *ab initio* calculations and the results of the HS model applied to experimental and calculated room-temperature mobilities "HS exptl" and "HS calc," respectively and to the calculated mobility at its maximum ("HS calc max"). Blue color is used for $^{175}_{71}$Lu$^+$ (4f^{14}5d6s). Parameters of the ion electron distributions calculated by Indelicato et al. (2007) are also shown; see text for explanation.

TABLE 2 | Equilibrium parameters of the ion-atom interaction potentials for actinide ions, R_e (Å) and D_e (cm^{-1}).

Ion	He		Ar	
	R_e	D_e	R_e	D_e
Ac$^+$ 7s^2 ^{1}S	4.82	30	4.07	426
Ac$^+$ 7s^2 ^{1}S^a	4.80	30	4.04	434
U$^+$ [5f^3]7s^{2b}	4.62	33	3.96	454
U$^+$ [5f^3]7s^{2a}	4.59	34	3.96	470
Am$^+$ 5f^{7}7s ^{9}S$^\circ$	4.27	39	3.45	698
Cm$^+$ 5f^{7}7s^2 ^{8}S$^\circ$	4.36	42	3.82	538
Cm$^+$ [5f^7]7s^{2a}	4.39	40	3.88	509
No$^+$ 5f^{14}7s ^{2}S	4.03	48	3.38	763
Lr$^+$ 5f^{14}7s^2 ^{1}S	4.08	52	3.71	598
Lr$^+$ [5f^{14}]7s^{2a}	4.11	50	3.78	565

[a] *Large-core calculations, this work.*

[b] *Large-core calculations by Lee et al. (2011).*

at the repulsive wall in the case of Lu$^+$-He interaction (see **Figure 2**) causes an artificial increase of the effective radius.

In the case of Ar as the buffer gas, there is a much larger mismatch between the electronic parameters and models based on ion-atom interactions and transport. The effective ionic radii derived from interaction potentials are too small in comparison to $<r_s>$ and even $r_{\max}$, show weaker Z-dependence and opposite variation for the "soft" Lu$^+$-Ar interaction. This is in line with the analysis by Wright and Breckenridge (2010) for lighter ions. The HS model works reasonably for mobilities at their maxima but gives meaningless results mobilities near room temperature.

4. ACTINIDE IONS

The data on actinide ion mobility are very scarce. In fact, the only dedicated experiment is that of Johnsen and Biondi (1972) who measured the mobility of $^{238}_{92}$U$^+$ (5f^{3}7s^2) in He as a function of E/n_0 and pressure near room temperature. Smoothed data are tabulated by Ellis et al. (1976) and are also available in the LXCat database (Viehland, 2009–2020). A few relative drift time measurements were carried out (Sewtz et al., 2003; Backe et al., 2005) in Ar for the $^{255}_{100}$Fm$^+$ (5f^{12}7s):$^{251}_{98}$Cf$^+$ (5f^{10}7s) and $^{243}_{95}$Am$^+$ (5f^{7}7s):$^{239}_{94}$Pu$^+$ (5f^{6}7s) ion pairs to assess their effective radii. Mobilities of U$^+$ ion in all rare gases from He to Xe were also calculated using *ab initio* interaction potentials (Lee et al., 2011).

4.1. Interaction Potentials

Accepting the scalar relativistic approximation for actinide ions, one can straightforwardly extend the *ab initio* approach described above for the lanthanide family. Instead of the small-core 28-electron ECP28MWB effective core potentials, compatible 60-electron ECP60MWB ones (Küchle et al., 1994) with analogous segmented atomic natural orbital basis sets (Cao and Dolg, 2004) have to be used. The exponents of the spdfg set of the diffuse primitives (0.01, 0.008, 0.03, 0.07, and 0.05, respectively) have been optimized for the polarizabilities of the neutral Am, No, and Lr atoms. The basis sets for He and Ar and other features of the CCSD(T) calculations remain the same. The single-reference restriction limits the application of this approach to the ground states of the $^{227}_{89}$Ac$^+$ (7s^2, ^{1}S), $^{241}_{95}$Am$^+$ (5f^{7}7s, ^{9}S$^\circ$), $^{247}_{96}$Cm$^+$ (5f^{7}7s^2, ^{8}S$^\circ$), $^{254}_{102}$No$^+$ (5f^{14}7s, ^{2}S), and $^{255}_{103}$Lr$^+$ (5f^{14}7s^2, ^{1}S) ions.

An alternative approach was suggested by Lee et al. (2011). It exploits large-core ECPs ("5f-in-core") that absorb 5s5p5d5f shells leaving for explicit consideration the outer 6s, 6p, 6d, 7s,…electrons only (Moritz et al., 2007). With this approach, electronic angular momenta and configuration mixing effects due to incomplete 5f shell occupancies are hidden in the ECPs and the ground electronic states of the ions acquire ^{1}S or ^{2}S effective symmetry, except for ^{232}Th$^+$ (6d^{2}7s). To test the difference with the small-core approach in a systematic way, we calculated the CCSD(T) interaction potentials for the ground-state Ac$^+$, U$^+$, Cm$^+$, and Lr$^+$ ions with He and Ar using the same large-core ECPs. In contrast to Lee et al. (2011), we used the supplementary basis sets of aug-cc-pVQZ quality without further modification but augmented by the 3s3p2d2f1g bond function set (Cybulski and Toczyłowski, 1999) placed in the middle of the ion-atom distance. The results are shown in **Table 2**.

For the Ac$^+$ ion without 5f electrons, the comparison apparently favors the large-core description that gives slightly stronger ion-atom interactions. However, the opposite is seen for the 5f^7 and 5f^{14} configurations of Cm$^+$ and Lr$^+$ ions. The interaction strengths differ by 4–5% for He and by 5–6% in Ar, whereas the equilibrium distances differ by 0.03–0.06 Å. A reason for caution with the large-core approach is its modest accuracy for mobility calculations of U$^+$ in He (Lee et al., 2011) and for Eu$^+$ in He (Buchachenko and Viehland, 2014) (with analogous "4f-in-core" ECP); these were low by 8 and 4%, respectively, compared to the experimental values. Also, for open-shell ions it permits only the simplest ISR calculation for collision cross sections and transport properties. In what follows we will consider only the small-core approach, since it is consistent with the lanthanide results summarized above.

The true and reduced interaction potentials for the actinide ions are shown in **Figure 6**. As in the lanthanide case shown in **Figure 2**, interactions of the actinide ions with 7s and 7s^2 outer shells differ significantly from each other. They exhibit weaker bonding and repulsion that is stronger for He and softer for Ar. The dependence on the inner f-shell occupancy is more pronounced than in lanthanides, in accord with the facts known from chemical interactions. Actinide ions with the 7s configuration interact with He more strongly than their lanthanide counterparts, with R_e reduced by almost 0.2 Å and D_e increased by more than 20%. In contrast, R_e increases when switching from Lu$^+$ to Lr$^+$ ion with the ns^2 configuration being accompanied by a marginal 2% increase of the binding energy. Interactions with Ar are weaker for actinide ions regardless of the outer configuration. Overall, the two ion families demonstrate impressive similarity in their interaction potentials. This is illustrated in **Figure 7** that presents the potentials for various analogs. Especially telling are the reduced potentials showing that the difference due to outer ns occupancy decreases from the lanthanides to the actinides. Note that reduced potentials for the No$^+$ and Yb$^+$ are

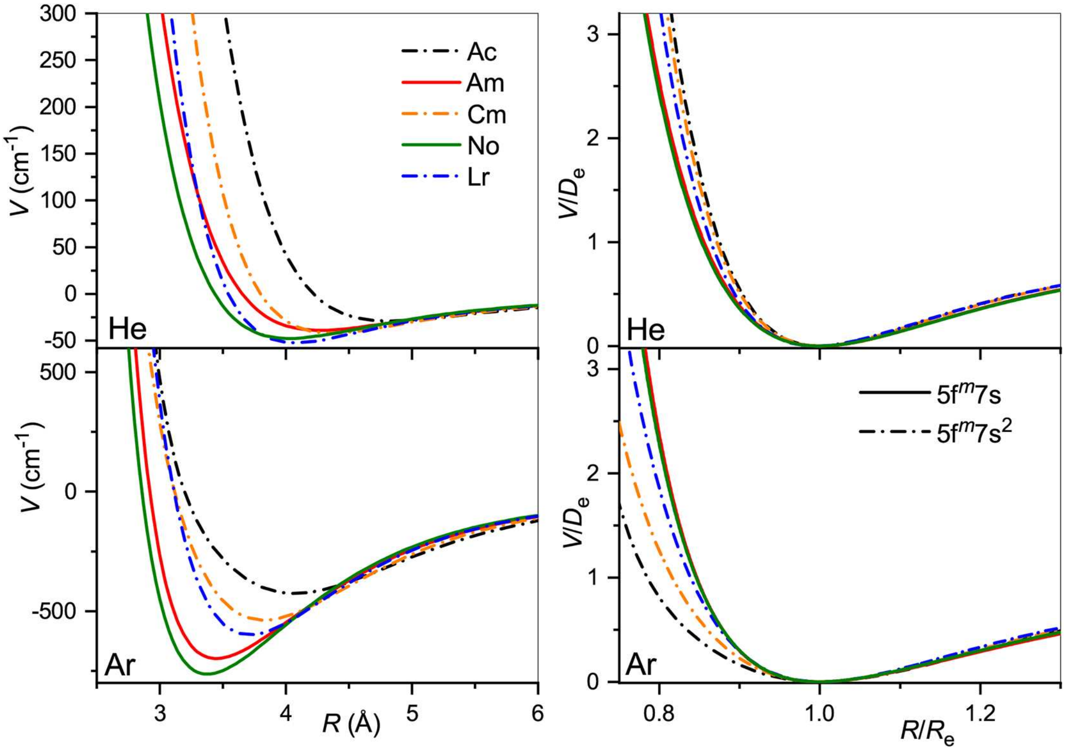

FIGURE 6 | Interaction potentials of the actinide ions with He (top panels) and Ar (bottom panels). True and reduced potentials are shown on the left and on the right, respectively.

indistinguishable from those of Am$^+$ and Eu$^+$ at the scale of the figure.

4.2. Ion Mobility

The interaction potentials described above were used to compute the mobilities of $^{227}_{89}\mathrm{Ac}^+$ ($7s^2$), $^{241}_{95}\mathrm{Am}^+$ ($5f^7 7s$), $^{247}_{96}\mathrm{Cm}^+$ ($5f^7 7s^2$), $^{254}_{102}\mathrm{No}^+$ ($5f^{14} 7s$) and $^{255}_{103}\mathrm{Lr}^+$ ($5f^{14} 7s^2$) in He and Ar. The calculated temperature dependences shown in **Figure 8** exhibit trends similar to those found in lanthanides. The mobility maxima in He for ions with both 7s and 7s^2 configurations are slightly reduced and shifted toward higher temperatures. The trend of increasing mobility with Z is visible for ions of both groups, Am$^+$-No$^+$ and Ac$^+$-Cm$^+$-Lr$^+$. Experimental data by Johnsen and Biondi (1972) for U$^+$ in He, though somewhat uncertain, does not support the latter trend, but fits to the theoretical results for 7s^2 group. In Ar, the mobility of the ions with 7s^2 configuration follows the reverse trend, decreasing along the Ac$^+$-Cm$^+$-Lr$^+$ sequence, while the difference in Am$^+$ and No$^+$ mobilities becomes marginal. As discussed above, such a reversal also takes place for lanthanide ions of the 5d6s configuration and, similarly, mirrors the short-range behavior of ion-atom interaction potentials.

4.3. Sensitivity to Electronic Configuration

In **Figure 9** are plotted the relative mobility differences, $\Delta K_0/K_0$, for the Cm$^+$-Am$^+$ and Lr$^+$-No$^+$ pairs of ions that differ by their 7s occupancies in comparison with that for lanthanide analog Lu$^+$-Yb$^+$. In He, all three pairs behave similarly, giving room-temperature drift time difference of 10-15%. As has been already mentioned, the difference in the mobility of 7s and 7s^2 ions in Ar has the opposite sign. Interestingly, the difference due to 5f shell occupancy between Cm$^+$-Am$^+$ and Lr$^+$-No$^+$ is larger than that between the lanthanide and actinide families.

Overall, the effect on the mobility in both buffer gases of outer *n*s shell occupancy in the lanthanide and actinide ions is smaller than the effect of 5d occupancy considered above for the lanthanides. The ground-state calculations do not allow us to estimate the sensitivity of actinide mobility to the 5d configuration responsible for the electronic state chromatography effect for the metastable states. This would require interaction potential calculations for the excited metastable states. Experience with the lanthanide family shows that the present *ab initio* methods are likely applicable only for Ac$^+$ and Lr$^+$ ions in their 6d7s metastable states.

4.4. Ionic Radii

The models used in section 3.5 for lanthanide ionic radii can also be tested for actinide ions. The results are summarized in **Figure 10** that follows the format of **Figure 5**. Parameters of the electron distributions of the bare ions taken from the same source (Indelicato et al., 2007) split into two parallel trend lines for ions with the 7s^2 (lower) and 7s (upper) outer shell configurations. The WB radii for ion-He interactions available from the present calculations follow the opposite order. The

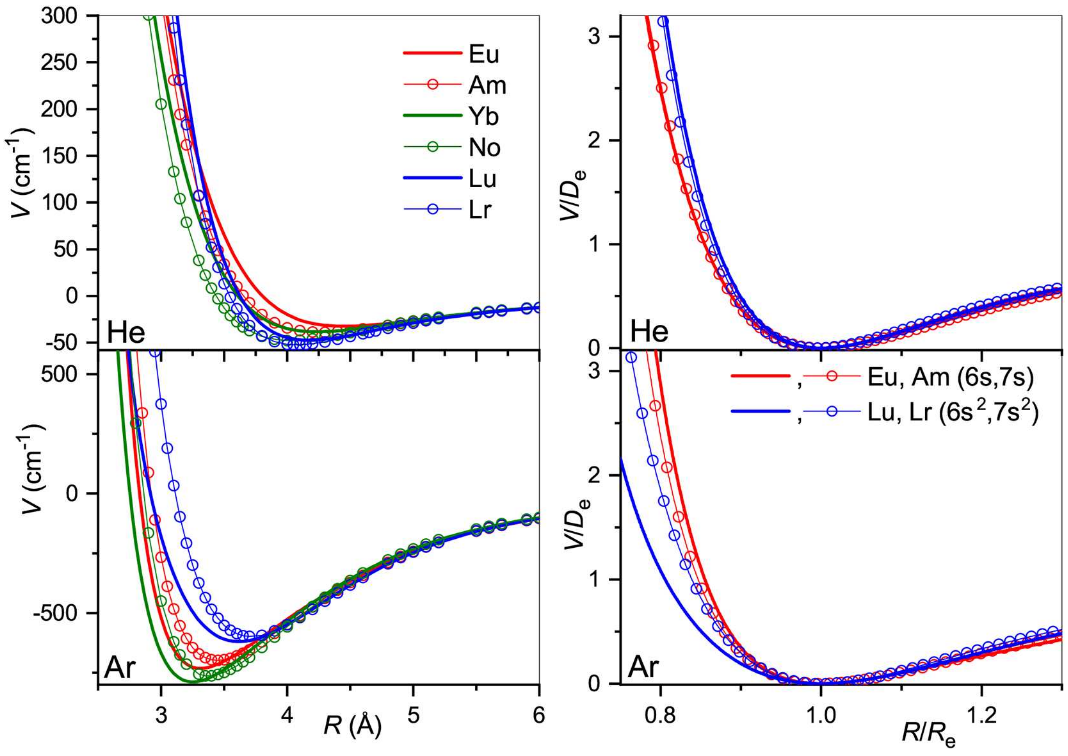

FIGURE 7 | Interaction potentials of the analogous actinide and lanthanide ions with He (top panels) and Ar (bottom panels). True and reduced potentials are shown on the left and on the right, respectively.

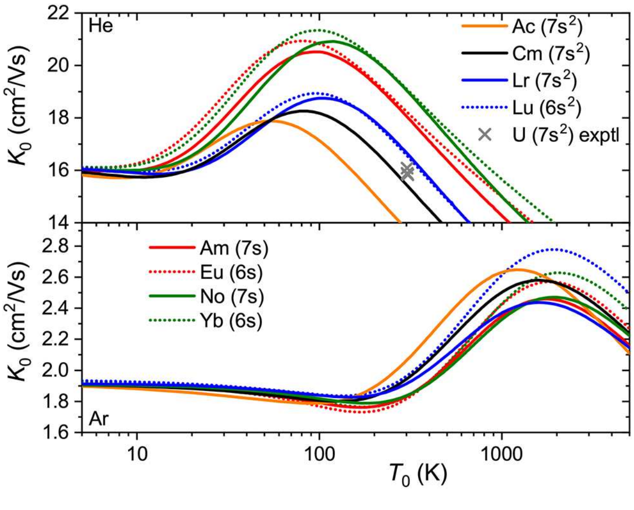

FIGURE 8 | Zero-field mobilities of some actinide ions in He (top panel) and Ar (bottom panel) calculated as functions of temperature. For comparison, mobilities of the lanthanide analogs are also shown. Crosses indicate experimental data (Johnsen and Biondi, 1972) for the U$^+$ ion in He.

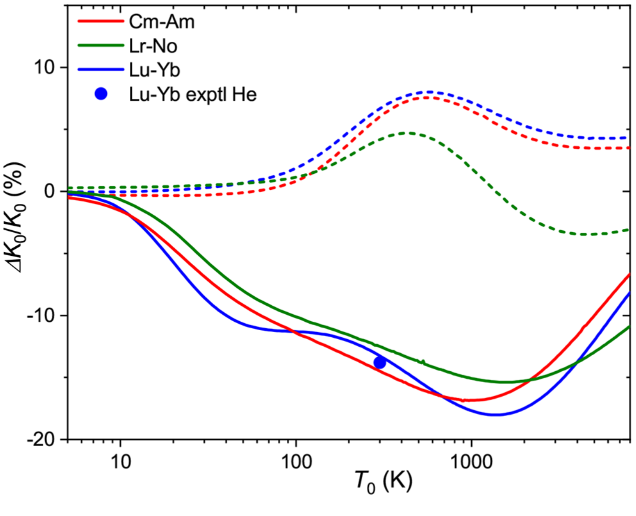

FIGURE 9 | Relative changes in the ion mobilities between 7s^2 and 7s ions Cm$^+$-Am$^+$ and Lr$^+$-No$^+$. The lanthanide analog of the latter pair, Lu$^+$-Yb$^+$, is also shown. Solid and dashed lines are used for He and Ar buffer gases, respectively. The experimental room-temperature value is from Manard and Kemper (2017b).

obvious reason already discussed is the enhancement of repulsive electronic interactions for the filled outer s shell. The radii extracted from the mobility analysis within the HS model show qualitatively similar variations and agree well in magnitude with the results for the lanthanide ions. **Figure 10** confirms that the results of HS model are much less consistent and informative in the case of Ar. The 7s and 7s^2 trends are less evident for the

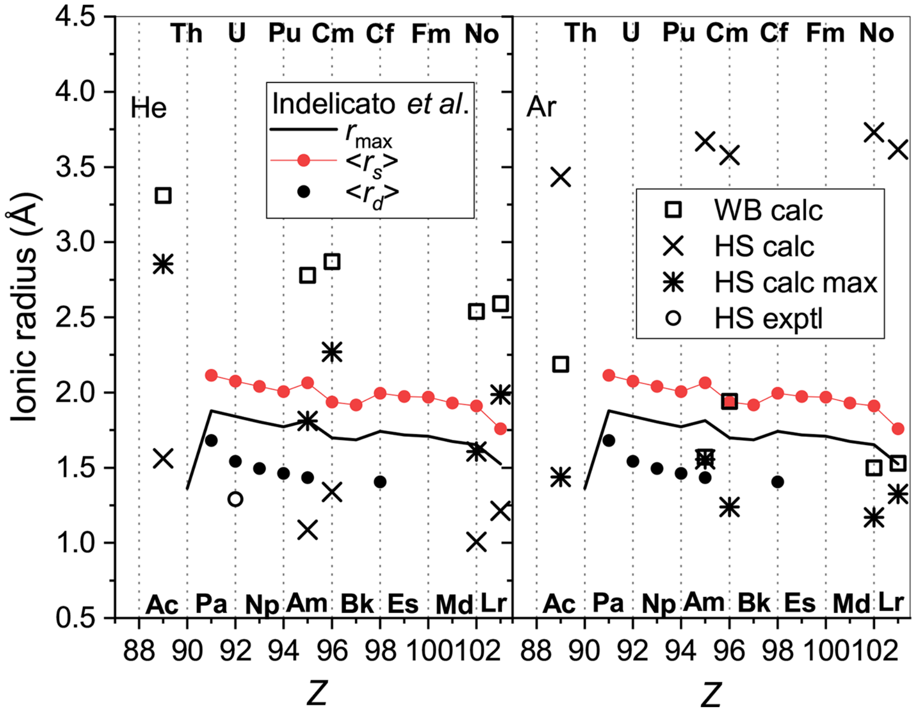

FIGURE 10 | The radii of the actinide ions determined from He (left panel) and Ar (right panel) data. Presented are WB radii from *ab initio* calculations and the results of the HS model applied to experimental and calculated room-temperature mobilities "HS exptl" and "HS calc," respectively and to the calculated mobility at the maximum ("HS calc max"). Parameters of the ion electron distribution calculated by Indelicato et al. (2007) are also shown; see section 3.5 for explanation.

parameters derived from interaction potentials and mobilities, except for the room-temperature HS result. The latter, however, wrongly predicts a general increase of ionic radii with *Z*. It is important to mention in this regard the relative measurements of the drift times for the Pu^+-Am^+ and Cf^+-Fm^+ pairs of ions in Ar (Sewtz et al., 2003; Backe et al., 2005). The HS model estimated the relative contraction of the ionic radii in these pairs as 3.1 ± 1.3 and 2%, respectively. Indelicato et al. (2007) have already discussed these variations in terms of electronic structure parameters of the bare ions. The present analysis indicates that the drift times in Ar at room temperature correspond to the mobility minimum and may not be sensitive to the effective size of an ion. Quantitative interpretation of such data within the oversimplified HS model requires caution, as pointed out by Backe et al. (2015).

5. CONCLUSIONS AND OUTLOOK

Progress in the one atom at a time production of the heavy and superheavy elements calls for new experimental techniques capable of characterizing the electronic structure of nascent or neutralized fusion products. Measurements of transport properties of the ions, in particular their gaseous mobilities, have already been counted among the most likely approaches, at least from the technical standpoint (Backe et al., 2015; Rickert et al., 2020). The lanthanide and actinide families serve as a natural example for interpretation of such measurements in terms of electronic structure parameters. They can also provide solid grounds for assessing the accuracy of *ab initio* calculations of ion-atom interaction potentials and transport properties, which are invaluable for guiding complicated and expensive on-line experiments in one atom at a time mode.

The conclusion of the present analysis is that the mobility is very sensitive to the electronic configuration of the ion. Both room-temperature measurements and *ab initio* theoretical calculations for the lanthanide ions reveal sharp deviations in the mobilities of the 5d6s and $6s^2$ ions from the trend line for the 6s ions, and slowly varying changes with 4f shell occupancy (equivalently, atomic number). Comparison between experiment and theory shows that the latter is presently able to predict the mobility differences for lanthanide ions in the ground and metastable states and to determine the conditions (buffer gas temperature, reduced electric field strength, pressure, etc.) for achieving the best discrimination of the ions by their drift times. Here, we have extended this conclusion to the actinides, which are virtually unexplored experimentally. We found significant difference in the mobility of 7s and $7s^2$ ions, which finds qualitative confirmations in the spatial electron density distributions of the bare ions (Indelicato et al., 2007). Supplementing the profound effect of the $nd^m \leftrightarrow nd^{m-1}(n+1)s$ electron promotion on the mobility already known for transition metal ions (Kemper and Bowers, 1991; Bowers et al., 1993; Taylor et al., 1999; Iceman et al., 2007; Ibrahim et al., 2008;

Manard and Kemper, 2016a,b), discrimination of the ns, $(n-1)dns$ and ns^2 configurations have direct implications for probing the electronic configurations of the superheavy elements with $Z = 104 - 112$. Another important application is the so-called laser resonance chromatography proposal for indirect detection of the spectroscopic transitions by discrimination of the ions in metastable states (Laatiaoui, 2019), which is currently being explored for the Lu^+ and Lr^+ ions.

The present overview demonstrates that the current theoretical state of the art allows one to interpret and predict trends in the mobility of heavy ions. Standard (and relatively cheap) scalar relativistic, single-reference, *ab initio* methods are able to link the electronic structure of selected ions and their transport properties by means of the ion-atom interaction potentials. Predicted changes in the mobility upon the electronic excitations are useful for advancing experimental methods of ion discrimination. At the same time, the lack of experimental data strongly limits the quantitative assessment of the *ab initio* results and further development of the theory. Measurements of the mobility as function of temperature or E/n_0 are absent for most of the elements above Ba. Indeed, only two room-temperature mobility values for lanthanide ions, i.e., for $Gd^+(^{10}D)$ ion in He and Ar (Laatiaoui et al., 2012; Manard and Kemper, 2017b), are available to compare the performance of the single- and multi-reference methods, to assess the role of vectorial spin-orbit coupling and to establish the uncertainty of the transport calculations for heavy, open-shell ions. Careful analysis reported here roughly estimated the respective variances as 20, 10, and 5% (Buchachenko and Viehland, 2019). This indicates the need for testing multi-reference coupled cluster techniques (Evangelista, 2018) in combination with SO configuration interaction methods. Such a demanding approach, however, will probably need to be customized for each particular lanthanide ion for which experimental data exists. Experimental mobilities for the actinides and even more difficult theoretical calculations remain for the future. Only by means of aligned experimental and theoretical efforts can the frontier of ion transport studies be pushed from the present scattered reconnaissance to a legitimate inventory of heavy- and superheavy ion research.

DATA AVAILABILITY STATEMENT

Interaction potentials, ion mobilities and other transport data are available in the Viehland (2009–2020) database within the LXCat Plasma Data Exchange Project (http://www.lxcat.net/Viehland, last accessed February 11, 2020). The transport data for various isotopes was obtained from the present results using the aliasing technique of Viehland (2016).

AUTHOR CONTRIBUTIONS

GV and AB carried out the *ab initio* calculations and data analysis. LV performed the calculations of ion mobilities and other transport properties. ML made a problem statement and assessment of the results and their implications to heavy and superheavy ion research. All authors contributed to the manuscript preparation.

FUNDING

This work was supported by the Russian Foundation for Basic Research under the project No. 19-03-00144. ML acknowledges funding from the European Research Council (ERC) under the European Union's Horizon 2020 research and innovation programme (grant agreement No. 819957).

ACKNOWLEDGMENTS

We thank Ms. Nika Buchachenko for her help with the manuscript formatting. Calculations were performed at Pardus and Arkuda Skoltech HPC clusters (*ab initio*) and at Chatham University (transport).

REFERENCES

Aquilanti, V., and Grossi, G. (1980). Angular momentum coupling schemes in the quantum mechanical treatment of P-state atom collisions. *J. Chem. Phys*. 73, 1165–1172. doi: 10.1063/1.440270

Aquilanti, V., and Vecchiocattivi, F. (1989). Transport properties of open-shell systems: fine structure effects on collision integrals for oxygen and fluorine atoms with rare gases. *Chem. Phys. Lett*. 156, 109–114. doi: 10.1016/0009-2614(89)87091-5

Backe, H., Dretzke, A., Horn, R., Kolb, T., Lauth, W., Repnow, R., et al. (2005). Ion mobility measurements and ion chemical reaction studies at heavy elements in a buffer gas cell. *Hyperf. Int*. 162, 77–84. doi: 10.1007/s10751-005-9210-4

Backe, H., Lauth, W., Block, M., and Laatiaoui, M. (2015). Prospects for laser spectroscopy, ion chemistry and mobility measurements of superheavy elements in buffer-gas traps. *Nucl. Phys. A* 944, 492–517. doi: 10.1016/j.nuclphysa.2015.07.002

Bellert, D., and Breckenridge, W. H. (2002). Bonding in ground-state and excited-state $A^+ \cdot Rg$ van der waals ions (A = atom, Rg = rare-gas atom): a model-potential analysis. *Chem. Rev*. 102, 1595–1622. doi: 10.1021/cr980090e

Bowers, M. T., Kemper, P. R., von Helden, G., and van Koppen, P. A. M. (1993). Gas-phase ion chromatography: transition metal state selection and carbon cluster formation. *Science* 260, 1446–1451. doi: 10.1126/science.260.5113.1446

Boys, S. F., and Bernardi, F. (1970). The calculation of small molecular interactions by the differences of separate total energies. Some procedures with reduced errors. *Mol. Phys*. 19, 553–566. doi: 10.1080/00268977000101561

Buchachenko, A. A., Chałasiński, G., and Szczęśniak, M. M. (2007). Diffuse basis functions for small-core relativistic pseudopotential basis sets and static dipole polarizabilities of selected lanthanides La, Sm, Eu, Tm and Yb. *Struct. Chem*. 18, 769–772. doi: 10.1007/s11224-007-9243-1

Buchachenko, A. A., and Viehland, L. A. (2014). Mobility of singly-charged lanthanide cations in rare gases: theoretical assessment of the state specificity. *J. Chem. Phys*. 140:114309. doi: 10.1063/1.4868102

Buchachenko, A. A., and Viehland, L. A. (2019). Ab initio study of the mobility of Gd^+ ions in He and Ar gases. *Int. J. Mass Spectrom*. 443, 86–92. doi: 10.1016/j.ijms.2019.06.005

Campbell, P., Moore, I. D., and Pearson, M. R. (2016). Laser spectroscopy for nuclear structure physics. *Progr. Part. Nucl. Phys*. 86, 127–180. doi: 10.1016/j.ppnp.2015.09.003

Cao, X., and Dolg, M. (2001). Valence basis sets for relativistic energy-consistent small-core lanthanide pseudopotentials. *J. Chem. Phys*. 115, 7348–7355. doi: 10.1063/1.1406535

Cao, X., and Dolg, M. (2002). Segmented contraction scheme for small-core lanthanide pseudopotential basis sets. *J. Mol. Struct*. 581, 139–147. doi: 10.1016/S0166-1280(01)00751-5

Cao, X., and Dolg, M. (2004). Segmented contraction scheme for small-core actinide pseudopotential basis sets. *J. Mol. Struct*. 673, 203–209. doi: 10.1016/j.theochem.2003.12.015

Chhetri, P., Ackermann, D., Backe, H., Block, M., Cheal, B., Droese, C., et al. (2018). Precision measurement of the first ionization potential of nobelium. *Phys. Rev. Lett*. 120:263003. doi: 10.1103/PhysRevLett.120.263003

Cybulski, S. M., and Toczyłowski, R. R. (1999). Ground state potential energy curves for He_2, Ne_2, Ar_2, $He - Ne$, $He - Ar$, and $Ne - Ar$: a coupled-cluster study. *J. Chem. Phys*. 111, 10520–10528. doi: 10.1063/1.480430

Dolg, M., Stoll, H., and Preuss, H. (1989). Energy-adjusted ab initio pseudopotentials for the rare earth elements. *J. Chem. Phys*. 90, 1730–1734. doi: 10.1063/1.456066

Düllmann, C. E. (2019). Production and study of chemical properties of superheavy elements. *Radiochim. Acta* 107, 587–602. doi: 10.1515/ract-2019-0012

Dzuba, V. A., Flambaum, V. V., and Webb, J. K. (2017). Isotope shift and search for metastable superheavy elements in astrophysical data. *Phys. Rev. A* 95:062515. doi: 10.1103/PhysRevA.95.062515

Eichler, R. (2017). "Superheavy element chemistry-new experimental results challenge theoretical understanding," in *New Horizons in Fundamental Physics, FIAS Interdisciplinary Science Series*, eds S. Schramm and M. Schafer (Cham: Springer), 41–53. doi: 10.1007/978-3-319-44165-8_4

Eichler, R. (2019). The periodic table–an experimenter's guide to transactinide chemistry. *Radiochim. Acta* 107, 865–877. doi: 10.1515/ract-2018-3080

Eliav, E., Fritzsche, S., and Kaldor, U. (2015). Electronic structure theory of the superheavy elements. *Nucl. Phys. A* 944, 518–550. doi: 10.1016/j.nuclphysa.2015.06.017

Ellis, H. W., Pai, R. Y., McDaniel, E. W., Mason, E. A., and Viehland, L. A. (1976). Transport properties of gaseous ions over a wide energy range. *At. Data Nucl. Data Tables* 17, 177–210. doi: 10.1016/0092-640X(76)90001-2

Evangelista, F. A. (2018). Perspective: Multireference coupled cluster theories of dynamical electron correlation. *J. Chem. Phys*. 149:030901. doi: 10.1063/1.5039496

Ghiorso, A., Harvey, B. G., Choppin, G. R., Thompson, S. G., and Seaborg, G. T. (1955a). New element mendelevium, atomic number 101. *Phys. Rev*. 98, 1518–1519. doi: 10.1103/PhysRev.98.1518

Ghiorso, A., Thompson, S. G., Higgins, G. H., Seaborg, G. T., Studier, M. H., Fields, P. R., et al. (1955b). New elements einsteinium and fermium, atomic numbers 99 and 100. *Phys. Rev*. 99, 1048–1049. doi: 10.1103/PhysRev.99.1048

Giuliani, S. A., Matheson, Z., Nazarewicz, W., Olsen, E., Reinhard, P. G., Sadhukhan, J., et al. (2019). Colloquium: superheavy elements: Oganesson and beyond. *Rev. Mod. Phys*. 91:011001. doi: 10.1103/RevModPhys.91.011001

Haba, H. (2019). A new period in superheavy-element hunting. *Nat. Chem*. 11, 10–13. doi: 10.1038/s41557-018-0191-8

Hirschfelder, J. O., Curtiss, C. F., and Bird, R. B. (1954). *Molecular Theory of Gases and Liquids*. New York, NY: John Wiley and Sons.

Ibrahim, Y., Alsharaeh, E., Mabrouki, R., Momoh, P., Xie, E., and El-Shall, M. S. (2008). Ion mobility of ground and excited states of laser-generated transition metal cations. *J. Phys. Chem. A* 112, 1112–1124. doi: 10.1021/jp077477i

Iceman, C., Rue, C., Moision, R. M., Chatterjee, B. K., and Armentrout, P. B. (2007). Ion mobility studies of electronically excited states of atomic transition metal cations: development of an ion mobility source for guided ion beam experiments. *J. Am. Soc. Mass Spectrom*. 18, 1196–1205. doi: 10.1016/j.jasms.2007.02.012

Indelicato, P., Santos, J. P., Boucard, S., and Desclaux, J.-P. (2007). QED and relativistic corrections in superheavy elements. *Eur. Phys. J. D* 45, 155–170. doi: 10.1140/epjd/e2007-00229-y

Johnsen, R., and Biondi, M. A. (1972). Mobilities of uranium and mercury ions in helium. *J. Chem. Phys*. 57, 5292–5294. doi: 10.1063/1.1678220

Kaplan, I. G. (2006). Intermolecular interactions: physical picture, computational methods and model potentials. New York, NY: John Wiley and Sons. doi: 10.1002/047086334X

Karol, P. J., Barber, R. C., Sherrill, B. M., Vardaci, E., and Yamazaki, T. (2016a). Discovery of the element with atomic number $z = 118$ completing the 7th row of the periodic table (IUPAC technical report). *Pure Appl. Chem*. 88, 155–160. doi: 10.1515/pac-2015-0501

Karol, P. J., Barber, R. C., Sherrill, B. M., Vardaci, E., and Yamazaki, T. (2016b). Discovery of the elements with atomic numbers $z = 113$, 115 and 117 (IUPAC technical report). *Pure Appl. Chem*. 88, 139–153. doi: 10.1515/pac-2015-0502

Kemper, P. R., and Bowers, M. T. (1991). Electronic-state chromatography: application to first-row transition-metal ions. *J. Phys. Chem*. 95, 5134–5146. doi: 10.1021/j100166a042

Krems, R. V., Groenenboom, G. C., and Dalgarno, A. (2004). Electronic interaction anisotropy between atoms in arbitrary angular momentum states. *J. Phys. Chem. A* 108, 8941–8948. doi: 10.1021/jp0488416

Küchle, W., Dolg, M., Stoll, H., and Preuss, H. (1994). Energy-adjusted pseudopotentials for the actinides. Parameter sets and test calculations for thorium and thorium monoxide. *J. Chem. Phys*. 100, 7535–7542. doi: 10.1063/1.466847

Laatiaoui, M. (2019). "Laser resonance chromatography (LRC): a new methodology in superheavy element research," in *The 13th International Conference on Stopping and Manipulation of Ions and Related Topics (SMI-2019)*, *Book of Abstracts*, 8 (Montreal, QC).

Laatiaoui, M., Backe, H., Habs, D., Kunz, P., Lauth, W., and Sewtz, M. (2012). Low-field mobilities of rare-earth metals. *Eur. Phys. J. D* 66:232. doi: 10.1140/epjd/e2012-30221-3

Laatiaoui, M., Lauth, W., Backe, H., Block, M., Ackermann, D., Cheal, B., et al. (2016). Atom-at-a-time laser resonance ionization spectroscopy of nobelium. *Nature* 538, 495–498. doi: 10.1038/nature19345

Lee, E. P. F., Viehland, L. A., Johnsen, R., Breckenridge, W. H., and Wright, T. G. (2011). Interaction potentials of uranium cations with rare gases (RG) and transport of U^+ in RG ($RG = He, Ne, Ar, Kr,$ and Xe). *J. Phys. Chem. A* 115, 12126–12131. doi: 10.1021/jp2076879

Lee, E. P. F., and Wright, T. G. (2011–2013). Personal communications to LAV.

Liu, W., and (Ed.). (2017). *Handbook of Relativistic Quantum Chemistry*. Berlin: Springer.

Manard, M. J., and Kemper, P. R. (2016a). Characterizing the electronic states of the second-row transition metal cations using high-resolution ion mobility mass spectrometry. *Int. J. Mass Spectrom*. 407, 69–76. doi: 10.1016/j.ijms.2016.07.006

Manard, M. J., and Kemper, P. R. (2016b). Ion mobility mass spectrometry: the design of a new high-resolution ion mobility instrument with applications toward electronic-state characterization of first-row transition metal cations. *Int. J. Mass Spectrom*. 402, 1–11. doi: 10.1016/j.ijms.2016.02.014

Manard, M. J., and Kemper, P. R. (2017a). An experimental investigation into the reduced mobilities of lanthanide cations using high-resolution ion mobility mass spectrometry. *Int. J. Mass Spectrom*. 423, 54–58. doi: 10.1016/j.ijms.2017.10.010

Manard, M. J., and Kemper, P. R. (2017b). Reduced mobilities of lanthanide cations measured using high-resolution ion mobility mass spectrometry with comparisons between experiment and theory. *Int. J. Mass Spectrom*. 412, 14–19. doi: 10.1016/j.ijms.2016.11.015

Mason, E., and McDaniel, E. (1988). *Transport Properties of Ions in Gases*. New York, NY: John Wiley and Sons. doi: 10.1002/3527602852

Moritz, A., Cao, X., and Dolg, M. (2007). Quasirelativistic energy-consistent 5f-in-core pseudopotentials for trivalent actinide elements. *Theor. Chem. Acc*. 117, 473–481. doi: 10.1007/s00214-006-0180-7

Oganessian, Y. T., and Dmitriev, S. N. (2016). Synthesis and study of properties of superheavy atoms. Factory of superheavy elements. *Russ. Chem. Rev*. 85, 901–916. doi: 10.1070/RCR4607

Perey, M. (1939). L'élément 87: AcK, dérivé de l'actinium. *J. Phys. Radium* 10, 435–438. doi: 10.1051/jphysrad:019390010010043500

Perrier, C., and Segré, E. (1947). Technetium: the element of atomic number 43. *Nature* 159:24. doi: 10.1038/159024a0

Pershina, V. G. (1996). Electronic structure and properties of the transactinides and their compounds. *Chem. Rev*. 96, 1977–2010. doi: 10.1021/cr941182g

Pyykkö, P. (2012). The physics behind chemistry and the periodic table. *Chem. Rev*. 112, 371–384. doi: 10.1021/cr200042e

Pyykkö, P. (2016). Is the periodic table all right ("PTOK")? *Eur. Phys. J. Web Conf.* 131:01001. doi: 10.1051/epjconf/201613101001

Rickert, E., Backe, H., Block, M., Laatiaoui, M., Lauth, W., Schneider, J., et al. (2020). Ion mobilities for heaviest element identification. *Hyper. Int.* 241:49. doi: 10.1007/s10751-019-1691-7

Schädel, M., and Shaughnessy, D. (Eds.). (2014). *The Chemistry of Superheavy Elements*. Berlin; Heidelberg: Springer.

Seaborg, G. T. (1945). The chemical and radioactive properties of the heavy elements. *Chem. Eng. News* 23, 2190–2193. doi: 10.1021/cen-v023n023.p2190

Seaborg, G. T., and Loveland, W. D. (1990). *The Elements Beyond Uranium*. New York, NY: John Wiley and Sons.

Sewtz, M., Backe, H., Dretzke, A., Kube, G., Lauth, W., Schwamb, P., et al. (2003). First observation of atomic levels for the element fermium ($z = 100$). *Phys. Rev. Lett.* 90:163002. doi: 10.1103/PhysRevLett.90.163002

Stone, A. J. (2013). *The Theory of Intermolecular Forces*. Oxford: Oxford University Press. doi: 10.1093/acprof:oso/9780199672394.001.0001

Taylor, W. S., Spicer, E. M., and Barnas, D. F. (1999). Metastable metal ion production in sputtering DC glow discharge plasmas: characterization by electronic state chromatography. *J. Phys. Chem. A* 103, 643–650. doi: 10.1021/jp983887i

Ter-Akopian, G. M., and Dmitriev, S. N. (2015). Searches for superheavy elements in nature: cosmic-ray nuclei; spontaneous fission. *Nucl. Phys. A* 944, 177–189. doi: 10.1016/j.nuclphysa.2015.09.004

Türler, A., and Pershina, V. G. (2013). Advances in the production and chemistry of the heaviest elements. *Chem. Rev.* 113, 1237–1312. doi: 10.1021/cr3002438

Viehland, L. A. (1983). Interaction potentials for Li^+-rare gas systems. *Chem. Phys.* 78, 279–294. doi: 10.1016/0301-0104(83)85114-3

Viehland, L. A. (1994). Velocity distribution functions and transport coefficients of atomic ions in atomic gases by a Gram-Charlier approach. *Chem. Phys.* 179, 71–92. doi: 10.1016/0301-0104(93)E0337-U

Viehland, L. A. (2009–2020). *Viehland Database,* LXCat *Plasma Data Exchange Project*.

Viehland, L. A. (2012). Zero-field mobilities in helium: highly accurate values for use in ion mobility spectrometry. *Int. J. Ion Mobility Spectrom.* 15, 21–29. doi: 10.1007/s12127-011-0079-4

Viehland, L. A. (2016). Mobilities of mixtures of ion isotopes in gas mixtures. *Int. J. Ion Mobility Spectrom.* 19, 1–10. doi: 10.1007/s12127-015-0186-8

Viehland, L. A. (2018). *Gaseous Ion Mobility, Diffusion, and Reaction*. Cham: Springer. doi: 10.1007/978-3-030-04494-7

Viehland, L. A., and Chang, Y. (2010). Transport cross sections for collisions between particles. *Comput. Phys. Commun.* 181, 1687–1696. doi: 10.1016/j.cpc.2010.06.008

Viehland, L. A., Harrington, M. M., and Mason, E. A. (1976). Direct determination of ion-neutral molecule interaction potentials from gaseous ion mobility measurements. *Chem. Phys.* 17, 433–441. doi: 10.1016/S0301-0104(76)80007-9

Viehland, L. A., Skaist, T., Adhikari, C., and Siems, W. F. (2017). Accurate zero-field mobilities of atomic ions in the rare gases for calibration of ion mobility spectrometers. *Int. J. Ion Mobility Spectrom.* 20, 1–9. doi: 10.1007/s12127-016-0212-5

Wallmann, J. C. (1959). The first isolations of the transuranium elements: a historical survey. *J. Chem. Educ.* 36, 340–343. doi: 10.1021/ed036p340

Werner, H.-J., Knowles, P. J., Knizia, G., Manby, F. R., Schütz, M., Celani, P. et al. (2015). *Molpro, Version 2015.1, A Package of ab initio Programs*. Available online at: http://www.molpro.net/.

Woon, D. E., and Dunning, T. H. Jr. (1994). Gaussian basis sets for use in correlated molecular calculations. iv. calculation of static electrical response properties. *J. Chem. Phys.* 100, 2975–2988. doi: 10.1063/1.466439

Wright, T. G., and Breckenridge, W. H. (2010). Radii of atomic ions determined from diatomic ion-He bond lengths. *J. Phys. Chem. A* 114, 3182–3189. doi: 10.1021/jp9091927

Conflict of Interest: The authors declare that the research was conducted in the absence of any commercial or financial relationships that could be construed as a potential conflict of interest.

frontiers in Chemistry

ORIGINAL RESEARCH
published: 23 June 2020
doi: 10.3389/fchem.2020.00477

Catalytic Synthesis of Oligosiloxanes Mediated by an Air Stable Catalyst, $(C_6F_5)_3B(OH_2)$

Kristel M. Rabanzo-Castillo [1,2], ***Vipin B. Kumar*** [1,2], ***Tilo Söhnel*** [1,2] ***and Erin M. Leitao*** [1,2]*

[1] School of Chemical Sciences, University of Auckland, Auckland, New Zealand, [2] The MacDiarmid Institute for Advanced Materials and Nanotechnology, Auckland, New Zealand

The utility of $(C_6F_5)_3B(OH_2)$ as catalyst for the simple and environmentally benign synthesis of oligosiloxanes directly from hydrosilanes, is reported. This protocol offers several advantages compared to other methods of synthesizing siloxanes, such as mild reaction conditions, low catalyst loading, and a short reaction time with high yields and purity. The considerable H_2O-tolerance of $(C_6F_5)_3B(OH_2)$ promoted a catalytic route to disiloxanes which showed >99% conversion of three tertiary silanes, Et_3SiH, $PhMe_2SiH$, and Ph_3SiH. Preliminary data on the synthesis of unsymmetrical disiloxanes (Si-O-Si') suggests that by modifying the reaction conditions and/or using a 1:1 combination of silane to silanol the cross-product can be favored. Intramolecular reactions of disilyl compounds with catalytic $(C_6F_5)_3B(OH_2)$ led to the formation of novel bridged siloxanes, containing a Si-O-Si linkage within a cyclic structure, as the major product. Moreover, the reaction conditions enabled recovery and recycling of the catalyst. The catalyst was re-used 5 times and demonstrated excellent conversion for each substrate at 1.0 mol% catalyst loading. This seemingly simple reaction has a rather complicated mechanism. With the hydrosilane (R_3SiH) as the sole starting material, the fate of the reaction largely depends on the creation of silanol (R_3SiOH) from R_3SiH as these two undergo dehydrocoupling to yield a disiloxane product. Generation of the silanol is based on a modified Piers-Rubinsztajn reaction. Once the silanol has been produced, the mechanism involves a series of competitive reactions with multiple catalytically relevant species involving water, silane, and silanol interacting with the Lewis acid and the favored reaction cycle depends on the concentration of various species in solution.

Keywords: siloxane, lewis acid catalysis, dehydrocoupling, catalyst recycling, silane, competing mechanisms

Edited by:
Eugene A. Goodilin,
Lomonosov Moscow State
University, Russia

Reviewed by:
Grzegorz Hreczycho,
Adam Mickiewicz University, Poland
Aziz M. Muzafarov,
A. N. Nesmeyanov Institute of
Organoelement Compounds
(RAS), Russia

****Correspondence:***
Erin M. Leitao
erin.leitao@auckland.ac.nz

Specialty section:
This article was submitted to
Green and Sustainable Chemistry,
a section of the journal
Frontiers in Chemistry

Received: *14 March 2020*
Accepted: *08 May 2020*
Published: *23 June 2020*

Citation:
Rabanzo-Castillo KM, Kumar VB,
Söhnel T and Leitao EM (2020)
Catalytic Synthesis of Oligosiloxanes
Mediated by an Air Stable Catalyst,
$(C_6F_5)_3B(OH_2)$. Front. Chem. 8:477.
doi: 10.3389/fchem.2020.00477

INTRODUCTION

Organo(poly)siloxanes (silicones), bearing the repeating Si-O bond motif, are considered one of the most important classes of functional materials that have influenced many technological industries (Sawama et al., 2016; Wang et al., 2017). Industrially, polysiloxanes are generated by acid- or base-catalyzed ring opening polymerization of cyclic siloxanes, or by hydrolysis of chlorosilanes (Grubb, 1954; Brinker and Scherer, 1990). However, these methods have limited control over the oligomeric or polymeric siloxane sequence being formed. The substitution process is catalyzed either by an acid or a base under equilibrium in which the polysiloxanes can also be degraded (Brinker and Scherer, 1990). Although a step-wise synthesis of oligosiloxane has been reported, it is still based on conventional condensation of silanols with chlorosilanes (Uchida et al., 1990; Matsumoto et al., 2018, 2019). Other methods available in literature for the preparation of oligosiloxanes involve catalytic cross-coupling reactions of oxygen nucleophiles (e.g., alkoxysilanes, silanols, phenols, and ethers) with hydrosilanes (Brook, 2018; Zhang et al., 2020). The synthesis of symmetrical disiloxanes directly from hydrosilanes have been reported using $InBr_3$, a reaction which involves Lewis acid-catalyzed air oxidation of hydrosilanes (**Scheme 1**, **A**, conditions **I**) (Sridhar et al., 2009). Reduction of CO_2 with hydrosilanes and a zirconium complex/$B(C_6F_5)_3$ as the catalyst have also been reported to produce methane and oligosiloxanes as products (Matsuo and Kawaguchi, 2006). Other direct syntheses reported the use of H_2O as the solvent and oxidant, however, generally these involved expensive transition metal catalysts and are conducted at elevated temperature (**Scheme 1**, **A**, conditions **II–IV**) (Lee et al., 2000, 2004; Ison et al., 2005; Mitsudome et al., 2008, 2009; Chauhan et al., 2009; Asao et al., 2010; John et al., 2011; Tan et al., 2011; Jeon et al., 2012; Shimizu et al., 2012a,b; Liu et al., 2014; Sawama et al., 2016; Tsuchido et al., 2020). The development of synthetic methods catalyzed by abundant and cheap base-metal complexes then emerged to form symmetrical and unsymmetrical disiloxanes and other oligosiloxanes (Pattanaik and Gunanathan, 2019) (**Scheme 1**, **B**, conditions **V**). Catalytic routes toward unsymmetrical siloxanes (Si-O-Si') have also been demonstrated (**Scheme 1**, **B**, conditions **VI–VIII**) using $Sc(OTf)_3$ (Hreczycho et al., 2013; Hreczycho, 2015), Nafion (Kaźmierczak and Hreczycho, 2018), or Amberlyst-15 (Kuciński and Hreczycho, 2019a) with silanols and alkylsilanes at room temperature. Transition metal catalyzed routes to unsymmetrical disiloxanes have been achieved through Pd-catalyzed arylation of hydroxysiloxanes (Kurihara et al., 2013), nonhydrolytic Pd/C-catalyzed cross-coupling reactions (Igarashi et al., 2014), Ba-mediated dehydrocoupling of hydrosilanes and silanols (Le Coz et al., 2019) and silylation of silanols catalyzed by a ruthenium complex (Marciniec et al., 2008). Other routes to form Si-O-Si' bonds include the use of fluoride and azidosilanes (Abele et al., 2003) as well as a catalyst-free, chlorine-free option using disilazanes (Kuciński and Hreczycho, 2019b) (**Scheme 1**, **B**, conditions **IX–X**).

Main group (and metal-free) catalysts such as $B(C_6F_5)_3$ have gained great interest as a catalyst activator and as strong Lewis acid for many purposes (Piers, 2004; Lawson and Melen, 2017; Brook, 2018). Several studies have been published for the

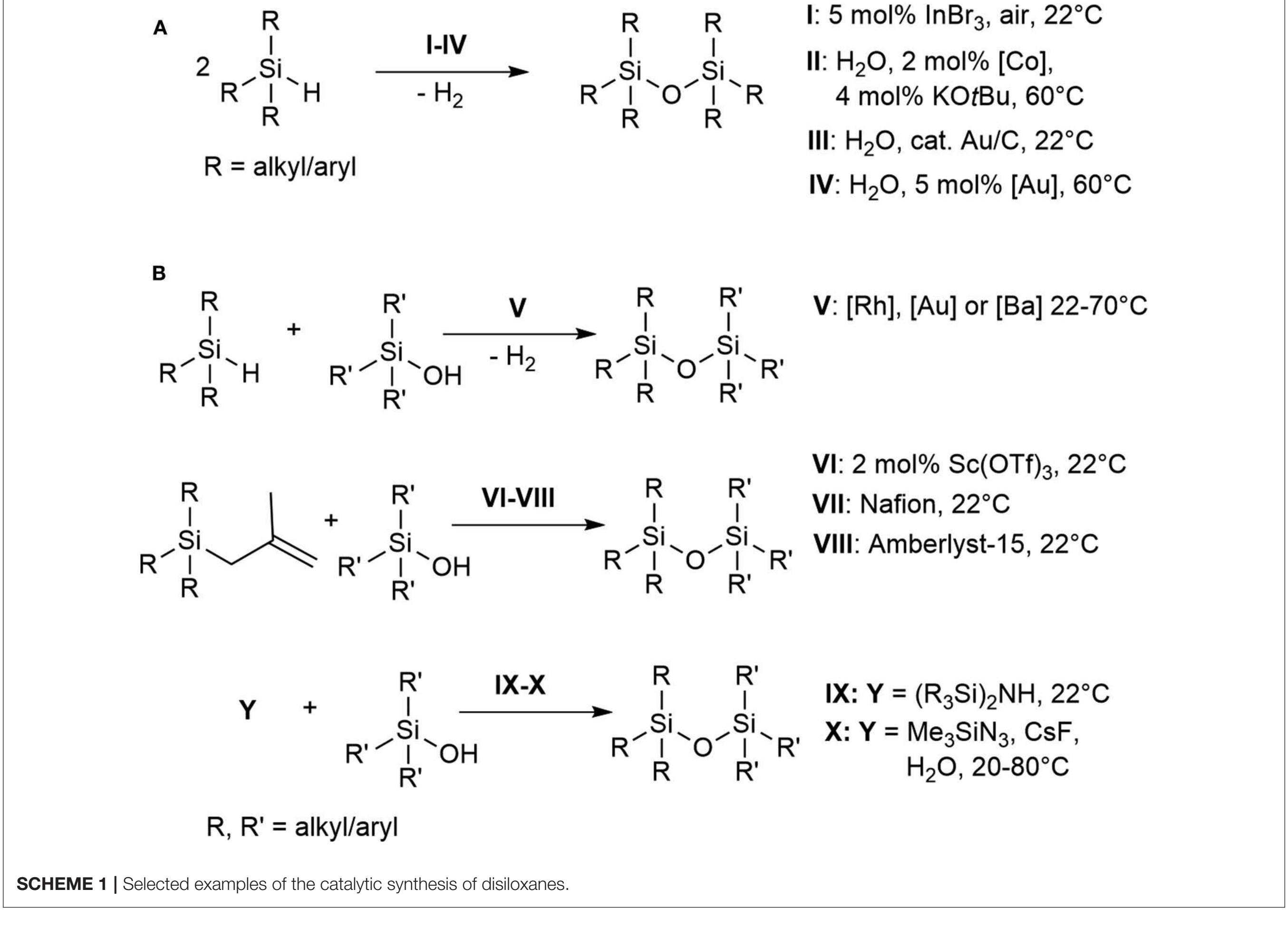

SCHEME 1 | Selected examples of the catalytic synthesis of disiloxanes.

preparation of siloxanes and hyperbranched siloxanes involving catalytic cross-coupling reactions of oxygen nucleophiles (e.g., alkoxysilanes, silanols, phenols, and ethers) with hydrosilanes (Kawakami et al., 2004; Chojnowski et al., 2005, 2006, 2008; Zhou and Kawakami, 2005; Shinke et al., 2007; Thompson and Davies, 2007; Cella and Rubinsztajn, 2008; Kurjata et al., 2009; Feghali and Cantat, 2014; Madsen et al., 2014; Zhang et al., 2014, 2020; Feghali et al., 2015; Laengert et al., 2017; Szawiola et al., 2017; Wu et al., 2017; Brook, 2018; Ai et al., 2019). Recently, Matsumoto and co-workers reported a sequence-controlled synthesis of oligosiloxanes via dehydrocarbonative coupling of alkoxysilanes and hydrosilanes, named the Piers-Rubinsztajn reaction, and also via hydrosilylation of carbonyl compounds using $B(C_6F_5)_3$ (Matsumoto et al., 2018). Several mechanistic studies have been demonstrated for the formation of siloxanes depending on the type of substrates and catalysts used (Brook, 2018; Pattanaik and Gunanathan, 2019). The standard Piers-Rubinsztajn reaction involves the condensation of a hydrosilane (R_3SiH) and alkoxysilane (R_3SiOR) to form a siloxane, with subsequent removal of an alkane, RH (R = alkyl/aryl). Knowledge of this mechanism has allowed for the design of controlled synthetic routes to polysiloxanes using $B(C_6F_5)_3$ as the catalyst (Chojnowski et al., 2005; Rubinsztajn and Cella, 2005; Cella and Rubinsztajn, 2008; Yi et al., 2018; Schneider et al., 2019). The strong affinity of $B(C_6F_5)_3$ with H_2O can lead to the formation of Brønsted acids which seems to not be a problem in terms of siloxane or polymer synthesis (Neumann et al., 2004; Chojnowski et al., 2005; Longuet et al., 2007). However, $B(C_6F_5)_3$ can form several complexes with H_2O which serve to remove the active catalyst from the reaction (Brook, 2018). In the presence of excess H_2O therefore, the Piers-Rubinsztajn reaction is not observed or leads to lower rate of reaction.

In this article, we report the synthesis of oligomeric siloxanes starting from hydrosilanes and tethered hydrosilanes using controlled amounts of H_2O. Specifically, we explored the possibility of replacing the $B(C_6F_5)_3$ catalyst with $(C_6F_5)_3B(OH_2)$ aimed at understanding the effect of the moisture stable $(C_6F_5)_3B(OH_2)$ catalyst on the selectivity, the recyclability and the mechanism of siloxane formation.

MATERIALS AND METHODS

All reactions and manipulations were performed under a nitrogen atmosphere in an MBraun Unilab 1200/780 glovebox or using conventional Schlenk techniques, unless otherwise specified. Dry solvents were obtained using a solvent purification system. Reagents were purchased from Sigma-Aldrich, AK Scientific, Arcos and TCI and used as received. $(C_6F_5)_3B(OH_2)$ (Beringhelli et al., 2001) was made by adding a stoichiometric amount of H_2O to $B(C_6F_5)_3$ followed by purification by sublimation. ^1H, ^{13}C, and ^{29}Si NMR spectra were recorded on a Bruker DPX-400 (400MHz) spectrometer. Chemical shifts for protons are reported in parts per million (ppm) downfield from tetramethylsilane and are referenced to residual protium in the NMR solvent (e.g., $CHCl_3$ = 7.26 ppm). Chemical shifts for carbon are reported in ppm downfield from $CDCl_3$ (77.3 ppm). Chemical shifts for silicon are reported in ppm downfield to the silicon resonance of tetramethylsilane (TMS δ 0.0). The silicon NMR resonances were determined with a DEPT pulse sequence. Data are represented as follows: chemical shift, multiplicity (app = apparent, br = broad, s = singlet, d = doublet, t = triplet, q = quartet, m = multiplet), coupling constants in Hertz (Hz), and integration. High resolution mass spectrometry measurements were made on a Bruker microTOF-QII mass spectrometer, equipped with a KD Scientific syringe pump, in positive ion ESI mode. Hard ionization mass spectrometry analysis was done on Agilent 7890A GC + 5975C EI-MS with Agilent auto-sampler. X-ray diffraction analysis of single crystals of **7a** and **8a** were performed on a Rigaku Oxford Diffraction XtaLAB-Synergy-S single crystal diffractometer with a PILATUS 200 K hybrid pixel array detector using Cu Kα radiation (**Supplementary Table 1**). The data was processed with the SHELX2016 (Sheldrick, 2015) and Olex2 (Dolomanov et al., 2009) software packages. All non-hydrogen atoms were refined anisotropically. Hydrogen atoms were inserted at calculated positions and refined with a riding model or without restrictions. **8a** was refined on a HKL5 dataset extracted from PLATON (Spek, 2003). Mercury 4.2.0 (Macrae et al., 2006) was used to visualize the molecular structures.

Intermolecular Reactions

Synthesis of Tertiary Disiloxanes, 3a-3c

Et_3SiOEt_3 (3a) and $PhMe_2SiOSiMe_2Ph$ (3b)

To a mixture of hydrosilane (Et_3SiH, **1a**, 5.0 mmol, 0.80 mL or $PhMe_2SiH$, **1b**, 5.0 mmol, 0.77 mL) and 0.1–5.0 mol% $(C_6F_5)_3B(OH_2)$, was added H_2O (2.5 mmol, 0.050 mL) while stirring at room temperature (22°C). The reaction was monitored using ^1H and $^{29}Si\{^1H\}$ NMR spectroscopy at specific time interval using an insert containing deuterated solvent. Yield: **3a**: 70.6%, **3b**: 94.0%.

3a (Sridhar et al., 2009; Jorapur and Shimada, 2012)

^1H NMR (400 MHz $CDCl_3$): δ 0.95–0.91 (t, CH_3, 6H), δ 0.55–0.49 (q, CH_2, 4H). $^{13}C\{^1H\}$ NMR (100.6 MHz, $CDCl_3$): δ 6.7 (s, CH_2), δ 6.4 (s, CH_3). $^{29}Si\{^1H\}$ NMR (79.5 MHz, $CDCl_3$): δ 8.9 ppm (s). GC-MS: cal'd: 246.1835 *m/z;* observed 246.1900 *m/z.*

3b (Jorapur and Shimada, 2012; Sawama et al., 2016)

^1H NMR (400 MHz $CDCl_3$): δ 7.57–7.36 (m, Ph, 10H), δ 0.35 (s, CH_3, 12H). $^{13}C\{^1H\}$ NMR (100.6 MHz, $CDCl_3$): δ 139.8, δ 133.0, δ 129.4, δ 127.7, δ 0.85 (s, CH_3). $^{29}Si\{^1H\}$ NMR (79.5 MHz, $CDCl_3$): δ 0.01 ppm (s). HRMS-ESI: $[C_{16}H_{22}OSi_2Na]^+$ = cal'd: 309.1101 *m/z;* observed 309.1091 *m/z.*

$Ph_3SiOSiPh_3$, 3c

To a mixture of Ph_3SiH (**1c**; 2.0 mmol, 0.26 g) and 0.1–5.0 mol% $(C_6F_5)_3B(OH_2)$ dissolved in 0.50 mL toluene-d_8, was added H_2O (1.0 mmol, 0.02 mL) while stirring at room temperature (22°C). The reaction was monitored using ^1H and $^{29}Si\{^1H\}$ NMR spectroscopy at specific time interval. Yield: 98.0%.

3c (Jorapur and Shimada, 2012)

^1H NMR (400 MHz $CDCl_3$): δ 7.49–7.24 (m, Ph, 30H). $^{13}C\{^1H\}$ NMR (100.6 MHz, $CDCl_3$): δ 135.5, δ 135.2, δ 129.8, δ 127.7.

$^{29}Si\{^1H\}$ NMR (79.5 MHz, $CDCl_3$): δ −18.6 ppm (s). HRMS-ESI: $[C_{36}H_{30}OSi_2Na]^+$ cal'd: 557.1733 *m/z;* observed 557.1701 *m/z.*

Synthesis of Secondary Oligosiloxanes, (Cyclo) 3d-3f, (Cyclo) 4e-4f, 5e

To a mixture of 4.0 mmol hydrosilane (0.52 mL Et_2SiH_2, **1d**; 0.55 mL $PhMeSiH_2$, **1e**; 0.76 mL Ph_2SiH_2, **1f**) and 0.1–5.0 mol% $(C_6F_5)_3B(OH_2)$, was added 2.0 mmol, 0.04 mL H_2O while stirring at room temperature (22°C). The reaction was monitored using ESI-MS at specific time interval. All products were filtered through Florisil to remove the catalyst using *n*-pentane or hexanes (10 ml) as eluent. ESI-MS: **3d (trimer)**: $[C_{14}H_{36}O_4Si_3Na]^+$ cal'd: 375.1819 *m/z*; observed 375.1812 *m/z*, **cyclo-3d (cyclic trimer)**: $[C_{13}H_{33}O_3Si_3Na]^+$ cal'd: 321.1737 *m/z*; observed 321.1731 *m/z*, **3e (trimer)**: $[C_{23}H_{30}O_4Si_3Na]^+$ cal'd: 477.1350 *m/z*; observed 477.1337 *m/z*, **4e (tetramer)**: $[C_{28}H_{34}O_5Si_4Na]^+$ cal'd: 585.1381 *m/z*; observed 585.1357 *m/z*, **5e (pentamer)**: $[C_{35}H_{42}O_6Si_5Na]^+$ cal'd: 721.1725 *m/z*; observed 721.1657 *m/z*, **cyclo-3f (cyclic trimer)**: $[C_{36}H_{30}O_3Si_3Na]^+$ cal'd: 617.1400 *m/z*; observed 617.1356 *m/z*, **cyclo-4f (cyclic tetramer)**: $[C_{48}H_{40}O_4Si_4Na]^+$ cal'd: 815.1901 *m/z*; observed 815.1837 *m/z.*

Intramolecular Reactions

Synthesis of Disilyl Precursors, 7a-7c

To an oven dried two neck round bottom flask purged with nitrogen was added magnesium turnings (12.0 mmol, 0.29 g), dry THF (5 mL) and diphenylchlorosilane (**7a**; 12.0 mmol, 2.3 mL) or dimethylchlorosilane (**7b, 7c**; 12.0 mmol, 1.3 mL). To this suspension was added 2-bromobenzylbromide (**6a;** 3.0 mmol, 0.75 g) or α,α'-dibromo-o-xylene (**6b**; 3.0 mmol, 0.79 g) dissolved in dry THF (10 mL) dropwise over a period of 15 min. The mixture was refluxed for 1 h and then stirred at 22°C overnight. The reaction mixture was quenched with saturated solution of $NaHCO_3$ (5 mL) and the aqueous layer was extracted with diethyl ether (3 × 10 mL). All the organic layers were combined and dried over Na_2SO_4. The crude product was obtained upon removal of solvents under vacuum.

(2-(diphenylsilyl)benzyl)diphenylsilane (7a)

The crude product was dissolved in *n*-pentane (20 mL) and the mixture was stored at −20°C overnight. Colorless crystals were filtered off and were washed with cold pentane (2 × 5 mL) to obtain the pure product in 72.3% yield.

^1H NMR (400 MHz $CDCl_3$): δ 7.45–6.97 (m, Ph, 24H), δ 5.53 (s, SiH, 1H), δ 4.8 (t, SiH, 1H), 2.8 (d, CH_2, 2H). $^{13}C\{^1H\}$ NMR (100.6 MHz, $CDCl_3$): δ 145.67, δ 137.16, δ 135.95, δ 135.38, δ 134.32, δ 133.58, δ 133.39, δ 131.36, δ 129.98, δ 129.66, δ 128.01, δ 127.89, δ 124.28, δ 23.06. $^{29}Si\{^1H\}$ NMR (79.5 MHz, $CDCl_3$): δ −13.70, δ −22.48 ppm. HRMS-ESI: $[C_{31}H_{28}Si_2Na]^+$ cal'd: 479.1626 *m/z*; observed: 479.1615 *m/z.*

(2-(dimethylsilyl)benzyl)diphenylsilane (7b)

The crude product was purified over silica gel column chromatography using hexanes as the eluent and was obtained as a colorless oil in 80.8% yield.

^1H NMR (400 MHz $CDCl_3$): δ 7.45–7.05 (m, Ph, 4H), δ 4.5 (sep, SiH, 1H), δ 3.9 (sep, SiH, 1H), 2.3 (d, CH_2, 2H), δ 0.3 (d, CH_3, 6H), δ 0.1 (d, CH_3, 6H). $^{13}C\{^1H\}$ NMR (100.6 MHz, $CDCl_3$): δ 146.04, δ 134.77, δ 129.34, δ 128.32, δ 123.85, δ 24.39, δ −3.06, δ −4.26. $^{29}Si\{^1H\}$ NMR (79.5 MHz, $CDCl_3$): δ −11.04, δ −21.63 ppm. HRMS-ESI: $[C_{11}H_{20}Si_2H]^+$ cal'd: 209.1181 *m/z*; observed: 209.1171 *m/z.*

1,2-bis((dimethylsilyl)methyl)benzene (7c)

The crude product was purified over silica gel column chromatography using hexanes as the eluent and was obtained as colorless oil in 52.5% yield.

^1H NMR (400 MHz $CDCl_3$): δ 6.99 (s, Ph, 4H), δ 4.0 (sep, SiH, 1H), δ 2.1 (d, CH_2, 2H), δ 0.1 (d, CH_3, 12H). $^{13}C\{^1H\}$ NMR (100.6 MHz, $CDCl_3$): δ 136.71, δ 129.19, δ 124.47, δ 21.61, δ −4.21. $^{29}Si\{^1H\}$ NMR (79.5 MHz, $CDCl_3$): δ−13.28 ppm. GC-MS: cal'd: 222.1260 *m/z;* observed: 222.1000 *m/z.*

Synthesis of Bridged Siloxanes, 8a-8c

1,1,3,3-tetraphenyl-3,4-dihydro-1H-2,1,3-benzoxadisiline (8a)

To a round bottom flask was added **7a** (1.0 mmol, 0.45 g) and 5.0 mol% $(C_6F_5)_3B(OH_2)$. The solids were dissolved in toluene (10 mL) and the reaction mixture was stirred at 90°C for 24 h. Toluene was removed under vacuum and the crude product was dissolved in hexanes (10 mL) which was then filtered through a Florisil pad with hexanes as eluent. Upon removal of volatiles the product was obtained as white solids. After recrystallization in ethyl acetate a pure crystalline product with 45.2% yield was obtained.

^1H NMR (400 MHz $CDCl_3$): δ 7.57–7.06 (m, Ph, 24H), δ 2.64 (s, CH_2, 2H). $^{13}C\{^1H\}$ NMR (100.6 MHz, $CDCl_3$): δ 145.04, δ 135.42, δ 135.14, δ 134.97, δ 134.31, δ 130.56, δ 130.48, δ 130.13, δ 130.02, δ 127.86, δ 124.63, δ 23.66. $^{29}Si\{^1H\}$ NMR (79.5 MHz, $CDCl_3$): δ −9.91, −14.11 ppm. HRMS-ESI: $[C_{31}H_{26}OSi_2Na]^+$ cal'd: 493.1419 *m/z*; observed: 493.1421 *m/z.*

1,1,3,3-tetramethyl-3,4-dihydro-1H-2,1,3-benzoxadisiline (8b)

To a vial was added 1.0 mol% $(C_6F_5)_3B(OH_2)$, 0.5 mL toluene and **7b** (1.0 mmol, 0.21 g). The reaction mixture was stirred for 3 h at 22°C. Toluene was then removed under reduced pressure and hexanes (3 mL) was added to the mixture. Upon Florisil filtration with hexanes as eluent and removal of volatiles the product was obtained as clear oil with 61.8% yield.

^1H NMR (400 MHz $CDCl_3$): δ 7.40–7.12 (m, Ph, 4H), δ 2.19 (s, CH_2, 2H), δ 0.38 (s, CH_3, 6H), δ 0.16 (s, CH_3, 6H). $^{29}Si\{^1H\}$ NMR (79.5 MHz, $CDCl_3$): δ 10.85, δ 3.66 ppm. HRMS-ESI: $[C_{11}H_{18}OSi_2H]^+$ cal'd: 223.0974 *m/z*; observed: 223.0925 *m/z.*

2,2,4,4-tetramethyl-1,2,4,5-tetrahydrobenzoxadisilepine (8c)

To a vial was added 1.0 mol% $(C_6F_5)_3B(OH_2)$, 0.5 mL toluene and **7c** (1.0 mmol, 0.22 g). The reaction mixture was stirred for 3 h at 22°C. Toluene was then removed under reduced pressure and hexanes (3 mL) was added to the mixture. Upon Florisil filtration with hexanes as eluent and removal of volatiles the product was obtained as clear oil with 30.6% yield.

^1H NMR (400 MHz $CDCl_3$): δ 7.03–6.95 (m, Ph, 4H), δ 2.16 (s, CH_2, 2H), δ 0.07 (s, CH_3, 12H). $^{13}C\{^1H\}$ NMR (100.6 MHz,

$CDCl_3$): δ 137.38, δ 129.35, δ 125.04, δ 27.48, δ 0.0. $^{29}Si\{^1H\}$ NMR (79.5 MHz, $CDCl_3$): δ 7.23 ppm. HRMS-ESI: $[C_{12}H_{20}OSi_2H]^+$ cal'd: 237.1130 *m/z*; observed: 237.1123 *m/z*.

Cross-Condensation Reactions

1:1 reaction of 1a and 1c

To a mixture of 1 equiv. **1a**, 1 equiv. **1c** and 5.0 mol% $(C_6F_5)_3B(OH_2)$ dissolved in 0.5 mL C_6D_6, was added 1.0 mmol, 0.02 mL H_2O. The reaction was stirred for 5 min at 22°C and was analyzed by ^1H and $^{29}Si\{^1H\}$ NMR spectroscopy.

1:1 reaction of 2a and 1b

A mixture of 1 equiv. **2a**, 1 equiv. **1b** and 5.0 mol% $(C_6F_5)_3B(OH_2)$ was stirred for 1 h at 22°C and was analyzed by ^1H and $^{29}Si\{^1H\}$ NMR spectroscopy.

1:1 reaction of 1b and 2b

A mixture of 1 equiv. **1b**, 1 equiv. **2b** and 5.0 mol% $(C_6F_5)_3B(OH_2)$ was stirred for 5 min at 22°C and was analyzed by ^1H and $^{29}Si\{^1H\}$ NMR spectroscopy.

Control Reactions

A mixture of silanol (Et_3SiOH, **2a**, 2.6 mmol, 0.40 mL or $PhMe_2SiOH$, **2b**, 2.6 mmol, 0.40 mL) and 0.1–0.5 mol% $(C_6F_5)_3B(OH_2)$ was stirred and allowed to react at room temperature (22°C). The reaction was monitored using ^1H and $^{29}Si\{^1H\}$ NMR spectroscopy at a specific time interval.

Catalyst Recycling Studies

3a

To 0.1–5.0 mol% $(C_6F_5)_3B(OH_2)$ was added 5.0 mmol, 0.80 mL Et_3SiH while stirring at room temperature (22°C). The reaction was monitored using ^1H NMR after 1 and 3 h. At the end of the 3 h period, each product from different catalyst loading was isolated by extraction with pentane while recovering back the $(C_6F_5)_3B(OH_2)$ catalyst used. The recovered catalyst at 1.0 mol% loading was recycled and re-used 4 times to give a total of 5 cycles and 5 isolated yields for $Et_3SiOSiEt_3$.

3b

To 0.1–5.0 mol% $(C_6F_5)_3B(OH_2)$ was added 2.0 mmol, 0.31 mL $PhMe_2SiH$ while stirring at room temperature (22°C). The reaction was monitored using ^1H NMR after 1 h. At the end of the 1 h period, each product from different catalyst loading was isolated by extraction with pentane. At 1.0 mol% catalyst loading, another 0.31 mL (2.0 mmol) of $PhMe_2SiH$ was added to the same vial. This procedure was done 4 times at 1 h intervals. The reported % yield at 1.0 mol% catalyst loading was the average of 5 cycles.

3c

To 0.1–5.0 mol% $(C_6F_5)_3B(OH_2)$ was added 1.0 mmol, 0.26 g Ph_3SiH, dissolved in 0.50 mL toluene, while stirring at room temperature (22°C). The reaction was monitored using ^1H NMR after 1 and 2 h. At the end of the 2 h period, each product from different catalyst loading was isolated by extraction with dichloromethane (5 mL). At 1.0 mol% catalyst loading, another 0.26 g (1.0 mmol) of Ph_3SiH dissolved in 0.50 mL toluene was added to the same vial. This procedure was done 4 times at a 2 h intervals. The reported % yield at 1.0 mol% catalyst loading was the average of 5 cycles.

RESULTS AND DISCUSSION

Intermolecular Synthesis of Oligosiloxanes Using a $(C_6F_5)_3B(OH_2)$ Catalyst

Three different types of tertiary hydrosilanes (Et_3SiH, **1a**; $PhMe_2SiH$, **1b**; and Ph_3SiH, **1c**) were reacted with varying equivalents of H_2O (0.0–1.0) and varying concentrations of catalyst (0.1–10.0 mol %), at 22°C to yield the corresponding disiloxane (**3a-c**; **Scheme 2**). For each completed reaction, the catalyst was removed by Florisil filtration. For **1a** and **1b**, the siloxane product was isolated by dissolving the reaction mixture in *n*-pentane to selectively precipitate out the $(C_6F_5)_3B(OH_2)$ catalyst. **1c** is a solid so the catalytic reactions were enabled by the addition of minimum amount of dry toluene (∼1 mL). The disiloxane products formed (**3a**-**3c**) from this synthetic route were isolated and confirmed by several characterization techniques in conjunction (**Supplementary Figures 1–28**) (Jorapur and Shimada, 2012). Generally, the complete conversion to disiloxane is much slower in the absence of H_2O and no reaction can be observed in the absence of the catalyst (**Table 1**). The transformation of neat **1b** to the corresponding disiloxane appeared to be the fastest and most facile at 0.1 mol% catalyst loading. This may be attributed to the fact that $(C_6F_5)_3B(OH_2)$ is quite soluble in **1b**.

The reaction of **1a** was slow at a low catalyst loading, 0.1 mol% $(C_6F_5)_3B(OH_2)$, in the presence of 0.5 eq H_2O. However, this allowed the for the detection of the silanol intermediate, Et_3SiOH, **2a**, along with the formation of the disiloxane, $Et_3SiOSiEt_3$, **3a** (**Supplementary Figures 6, 7**). After 3 h, the formation of both **2a** (δ_{Si} = 19.8 ppm) and **3a** (δ_{Si} = 8.9 ppm) was more evident with a significant amount of unreacted **1a** (δ_{Si} = 0.01 ppm). By contrast, the reaction was almost complete after 1 h when the catalyst loading was increased to 1.0 mol% $(C_6F_5)_3B(OH_2)$, with >99% conversion and the **3a** as the major product. There was no significant change observed when the same reaction was left to react further for 24 h (**Supplementary Figures 8, 9**). When the catalyst loading was further increased to 5.0 mol% $(C_6F_5)_3B(OH_2)$ the results were the same as those found at the 1.0 mol% catalyst loading. As suggested by the Piers-Rubinsztajn mechanism, the condensation of silanols to form oligo- or polysiloxanes occurs at relatively low catalyst concentration (Brook, 2018). A control reaction wherein **1a** was reacted with 1.0 eq H_2O in the absence of the catalyst gave no reaction, showing only the presence of unreacted **1a** by NMR spectroscopy. Similarly, no reaction was observed when **2a** was reacted with an equivalent of H_2O without a catalyst. These studies prove that both the conversion of **1a** to **2a** and the condensation step to **3a** require a catalyst (**Supplementary Figures 10, 11**).

Staring from a low catalyst loading of 0.1 mol% $(C_6F_5)_3B(OH_2)$ in the presence of 0.5 eq H_2O, the conversion of $PhMe_2SiH$, **1b**, to the corresponding disiloxane, **3b** (δ_{Si}

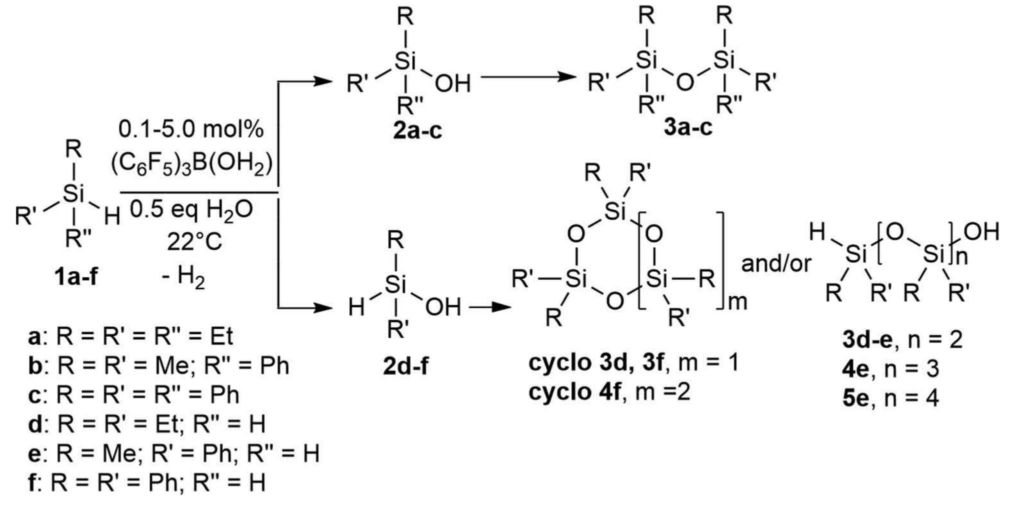

SCHEME 2 | Intermolecular synthesis of siloxanes using a $(C_6F_5)_3B(OH_2)$ catalyst.

TABLE 1 | Scope of substrates and products in the synthesis of disiloxanes, **3a-3c**.

Substrate	Catalyst, mol %	H_2O, equivalence	Reaction time, h	Major species present	Other species present	Yield, %
Et_3SiH	5.0	0.5	70	**3a**	–	71
1a	1.0	0.5	70	**3a**	–	73
	1.0	0.5	24	**3a**	–	72
	1.0	0.5	1	**3a**	–	69
	0.1	0.5	1	**1a**	**3a**, **2a**	*
	0.1	0.5	3	**1a**	**3a**, **2a**	*
	0.1	0.5	24	**1a**, **3a**	**2a**	*
	0.1	0.5	48	**3a**	**2a**	*
	0.0	1.0	24	No reaction		
$PhMe_2H$	5.0	0.5	70	**3b**	–	78
1b	1.0	0.2	1	**3b**	**1b**, **2b**	*
	1.0	0.2	3	**3b**	**1b**, **2b**	*
	1.0	0.2	72	**3b**	**1b**, **2b**	*
	1.0	Excess	1	**3b**	–	*
	1.0	Excess	24	**3b**	–	*
	0.5	0.5	1	**3b**	–	*
	0.5	0.5	3	**3b**	–	76
	0.1	0.5	1	**3b**	–	*
	0.1	0.5	3	**3b**	–	77
Ph_3SiH	5.0	0.0	70	**3c**	**3b**	*
1c	5.0	0.5	70	**3c**	–	75

% yield of **3a-3c was not determined as it was a mixture.*

= 0.01 ppm) was already evident after only 1 h reaction time. Even when the catalyst concentration was further increased to 0.5 and 5.0 mol%, the reaction proceeded in the same manner as when using a lower amount of catalyst (**Supplementary Figures 17, 18**). Decreasing the amount of H_2O to 0.2 eq at 1.0 mol% $(C_6F_5)_3B(OH_2)$ left some of the starting material, **1b**, and presence of the silanol, $PhMe_2SiOH$ (**2b**), was also observed (**Supplementary Figures 20, 21**). It can be inferred that the addition of H_2O plays an important role in the reaction, especially, in terms of the length of time needed to complete the reaction. Conversely, using an excess amount of H_2O hastened the reaction while using the same catalyst concentration of 1.0 mol% $(C_6F_5)_3B(OH_2)$. The reaction was observed to have been completed after 1 h (**Supplementary Figure 22**).

To further investigate the effect of reaction time and the necessity of H_2O, the direct synthesis of $Ph_3SiOSiPh_3$, **3c**, was conducted at 5.0 mol% $(C_6F_5)_3B(OH_2)$, for 70 h with and without

TABLE 2 | Scope of substrates and products in the synthesis of oligosiloxanes, **cyclo 3d, 3f**, **4f**, and **linear 3d-3e, 4e, 5e**.

Substrate	Catalyst, mol%	H_2O, equivalence	Reaction time, h	Major species present	Other (or minor) species present
Et_2SiH_2	2.0	1.0	1	**3d**	**cyclo 3d**
1d	2.0	1.0	6	**3d**	**cyclo 3d**
	2.0	1.0	24	**3d**	**cyclo 3d**
	2.0	1.0	48	**cyclo 3d**	**3d**
	2.0	0.0	96	**3d**	–
$PhMeSiH_2$	2.0	1.0	1	**3e**	–
1e	2.0	1.0	6	**3e**	–
	2.0	1.0	24	**3e, 4e**	**5e**
	2.0	1.0	48	**3e**, **4e**	**5e**
	2.0	0.0	96	**3e**	–
Ph_2SiH_2 **1f**	2.0	1.0	70	**cyclo 3f**	**cyclo 4f**

the addition of H_2O. It was observed that for reactions left for a longer period of time, the addition of H_2O seemed to be not necessary, and the presence of the catalyst $(C_6F_5)_3B(OH_2)$, alone is sufficient enough to yield the desired product. As previously observed with the other silanes, a mixture of Ph_3SiH (**1c**) with H_2O in the absence of the catalyst did not show any sign of a reaction (**Supplementary Figures 27, 28**).

Using the same protocol as for the tertiary silanes (**1a-c**), the reaction of secondary hydrosilanes (**1d-f**) was performed and generally resulted to the direct synthesis of oligomeric siloxanes with 3-5 repeat units identified based on ESI-MS. Three different secondary silanes were used: Et_2SiH_2, **1d**, $PhMeSiH_2$, **1e**, and Ph_2SiH_2, **1f.** Depending on the substrate used, the products were observed to be linear and/or cyclic siloxane chains (**Scheme 2**; **Supplementary Figures 29–31**). Furthermore, in the case of **1e** there was evidence of siloxanediol formation (Diemoz et al., 2016) indicating its role as an intermediate in the synthesis of the higher siloxanes under these conditions.

Similar to the synthesis of symmetrical disiloxanes, the reaction proceeded at a faster rate in the presence of H_2O. The reaction with **1e** gave mostly linear oligomers containing 3-5 repeat units, with a minor amount of oligosiloxanes containing 6-7 repeat units. The oligomerization of dialkylsilane, **1d**, resulted to both linear and cyclic products with 3 Si-O units, while the diarylsilane, **1f,** resulted to cyclic oligosiloxanes with $n = 3$ and 4. For **1d**, it is interesting to note that after 48 h it forms a cyclic species but if left for longer reverts back to the linear species (**Table 2**).

Intramolecular Synthesis of Tethered Siloxanes Using a $(C_6F_5)_3B(OH_2)$ Catalyst

We previously reported a preliminary study on the preparation of symmetrical naphthalene bridged disilanes with a Si-O-Si motif (Rabanzo-Castillo et al., 2019). Having success in forming linear siloxanes from tertiary and secondary silanes, it intrigued us to perform intramolecular reactions with catalytic amounts of $(C_6F_5)_3B(OH_2)$ to produce tethered and unsymmetrical siloxanes. In order to perform such reactions, disilyl precursors (**7a-c**) that resemble tertiary silanes having Si-H bonds were prepared using Grignard reactions from dibrominated bridge precursors (**6a-b**; **Scheme 3**). The synthesized disilyl tertiary silane precursors were obtained in high yields (**Supplementary Figures 32–44**) and were later subjected to intramolecular reactions with the catalyst under aerobic conditions to obtain the desired tethered siloxanes (**Supplementary Figures 45–57**), cyclic structures with 6-7 membered rings (**8a-c**; **Scheme 3**).

The intramolecular dehydrocoupling step was optimized for each of the disilyl tertiary silane precursors. **7a** ($\delta_{Si} = -13.7$, -22.5 ppm) is a solid therefore was dissolved in toluene prior to the intramolecular dehydrocoupling using 5.0 mol% $(C_6F_5)_3B(OH_2)$ at 90°C for 24 h. Under these conditions, the only product observed was **8a** ($\delta_{Si} = -9.9$, -14.1 ppm). The disilyl tertiary silane precursors **7b** ($\delta_{Si} = -11.0$, -21.6 ppm) and **7c** ($\delta_{Si} = -13.3$) are liquids and therefore were able to undergo intramolecular dehydrocoupling reactions without the addition of solvents, but the catalysis was more efficient with the addition of toluene along with 1.0 mol% $(C_6F_5)_3B(OH_2)$ at 22°C for 3 h, yielding **8b** ($\delta_{Si} = 10.9$, 3.7 ppm) and **8c** ($\delta_{Si} = 7.2$), respectively. The crude siloxanes (**8a-c**) were filtered through a Florisil pad to remove the catalyst. Although cyclic siloxanes are known to degrade when subjected to purification by silica gel column chromatography, compounds **8a-8c** could be purified by column chromatography, using hexanes as an eluent (Blackwell et al., 1999). The $^{29}Si\{^1H\}$ NMR chemical shifts of the purified product matched that of the filtered product suggesting that, in this case, the products do not degrade on silica gel (**Supplementary Figures 45–57**).

Single crystals were grown for compounds **7a** and **8a** by slow evaporation of pentane and ethyl acetate, respectively; the crystal structures were solved by single crystal X-ray diffraction (**Figure 1**; **Supplementary Table 1**). From the molecular structure of product **7a** it is evident that due to the steric bulk from the phenyl groups on the silyl substituents and the flexibility at C19, the Si-H bonds are quite far from each other. The two silicon atoms are 4.292 Å apart. The molecular structure

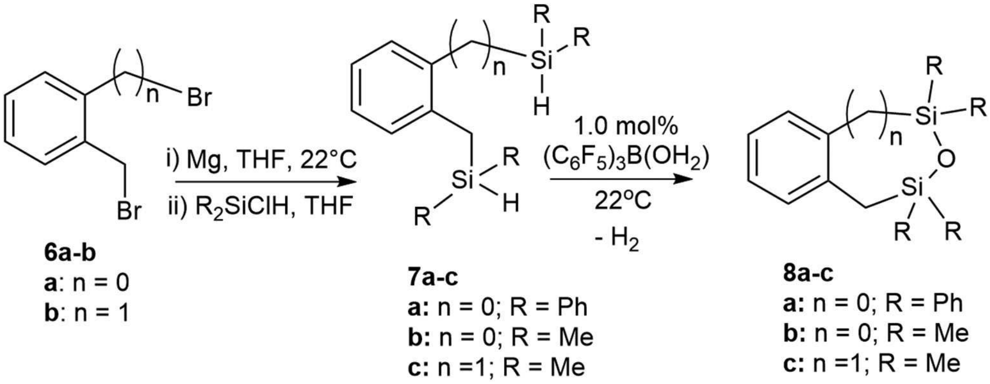

SCHEME 3 | Intramolecular synthesis of symmetric and asymmetric tethered siloxanes using a $(C_6F_5)_3B(OH_2)$ catalyst.

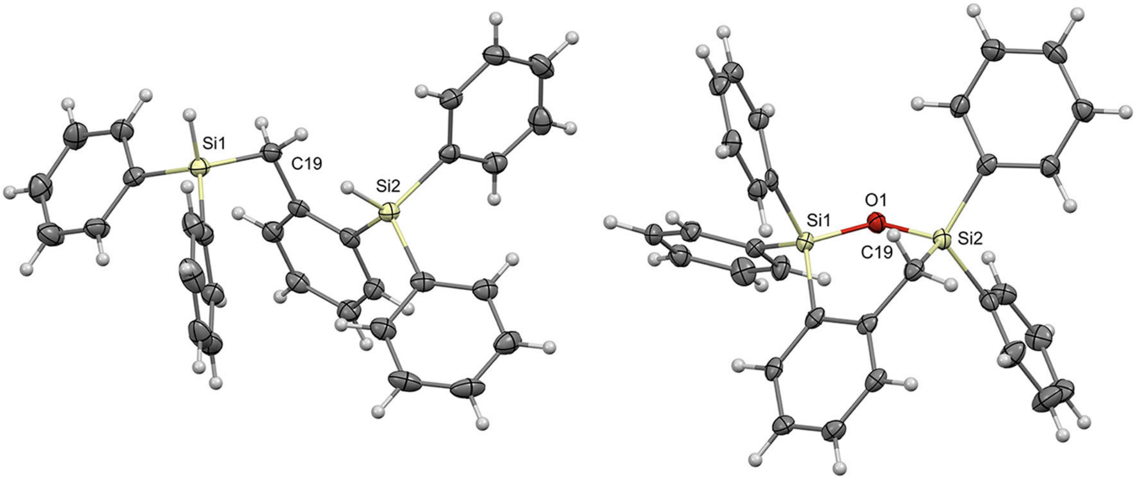

FIGURE 1 | Molecular structures of **7a (Left)** and **8a (Right)** with thermal ellipsoids drawn at the 50% probability level.

of **8a** shows that the newly formed 6-membered cyclic structure, containing the Si1-O1-Si2 bond, results in a slightly distorted boat shaped geometry with Si1 and C19 as the central two atoms. The distortion can be attributed to the presence of the Si-O-Si linkage and phenyl substituents lengthening the bonds through these atoms in addition to the wider Si-O-Si bond angle of 124.41°.

Mechanistic Considerations

Looking at the simplest system, using the tertiary silanes (**1a**-**c**), the mechanism of the catalysis was investigated. The reaction process involves the formation of the silanol intermediate and generation of either hydrogen gas or H_2O to give the disiloxanes, **3a-c**, depending on which pathway is operating (**route I** or **route II**; **Scheme 4**). It is important to note that the two pathways are experimentally distinct. Creation of **2** from **1** involves the loss of H_2. Similarly, with a 50% conversion to **2**, the silanol (**2**) can react with the hydrosilane (**1**) to form the disiloxane (**3**) with concomitant loss of H_2 in a dehydrocoupling reaction (**route I**; **Scheme 4**). However, if all of **1** becomes **2** (more likely under higher concentrations of H_2O), then the subsequent condensation of the silanols eliminates H_2O in a condensation reaction to form a disiloxane (**route II**; **Scheme 4**).

Kinetic studies were attempted to better probe the postulated mechanism, however, were not possible due to the difficulty in matching the experimental conditions by NMR spectroscopy. Moreover, each individual reactant (**1a**-**c**) gave reactions that were too fast with $(C_6F_5)_3B(OH_2)$. To elaborate the routes occurring, neat reactions of individual silanols (**2a**, **2b**), under the same reaction conditions of the hydrosilanes, were also performed. Hydrosilanes (**1**, R_3SiH) are said to be more susceptible to Brønsted acid-catalyzed reactions (Muzafarov, 2011) which is generally what was observed (**Table 3**). Interestingly, the addition of 0.5 eq. of H_2O increased the rate of reaction of **1a** to **3a**, from 50% conversion to >99% after 1 h, while the same addition of H_2O did not have an impact on the already rapid conversion of **1b** to **3b**. For the case of a catalytic reaction starting with Et_3SiOH, **2a**, the reaction took longer than the reaction starting with **1a** to reach completion (24 and 3 h, respectively). However, the same reaction starting

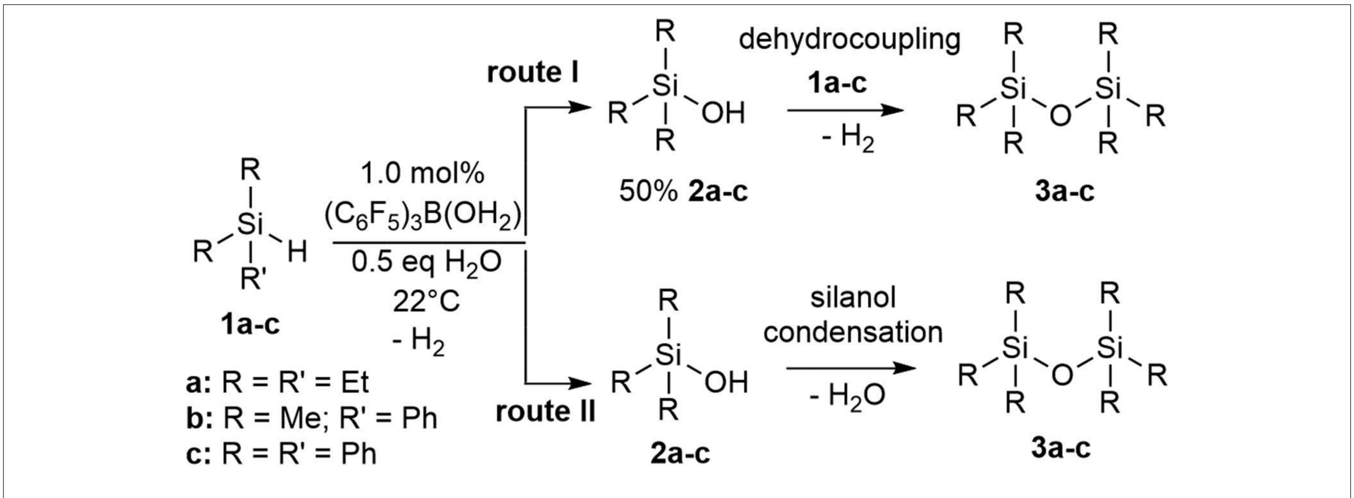

SCHEME 4 | Two potential routes to disiloxane from silane via silanol.

TABLE 3 | Comparative reactivities of SiH and SiOH groups in the presence of catalytic $(C_6F_5)_3B(OH_2)$.

$(C_6F_5)_3B(OH_2)$ +	Reaction time, h	Conversion, %
1a (in air)	1 h	50
1a (in air)	3 h	>99
1b (in air)	1 h	>99
1a (in air) + 0.5 eq H_2O	1 h	>99
1b (in air) + 0.5 eq H_2O	1 h	>99
2a (in air)	1 h	No reaction
2a (in air)	24 h	>99
2a (limited air)	24 h	No reaction
2b (in air)	1 h	>99
2b (limited air)	24 h	>99
1b + **2b** (in air)	Immediate	>99
1b + **2a** (in air)	1 h	>99

with $PhMe_2SiOH$, **2b**, proceeded to completion within an hour. Limiting air in the reactions starting with the silanol (e.g., **2a** and **2b**) only made a significant difference in the reaction rate for **2a**; **2b** was unaffected. When a 1:1 mixture of $PhMe_2SiH$, **1b**, and $PhMe_2SiOH$, **2b**, were reacted, a rapid exotherm and build-up of pressure was observed resulting to almost full conversion after only a few seconds (**Table 3**). These results suggest, not only that the reaction with **1b** is the most rapid in the series, but also, that both routes to form the disiloxane are possible under the catalytic conditions.

To elaborate on the relative rates of reaction for substrates **1a-c**, and to have a better indication of chemoselectivity, a cross-condensation reaction of a 1:1:1 mixture of Ph_3SiH (**1c**), Et_3SiH (**1a**), and H_2O was performed with 1 mol% catalyst loading. The reaction resulted in the rapid evolution of H_2 and was observed to reach completion soon after the addition of H_2O into the reaction mixture (**Supplementary Figures 58–61**). As expected, the reaction resulted to three different products—two homo-coupling products, $Ph_3SiOSiPh_3$ (**3c**) and $Et_3SiOSiEt_3$ (**3a**) and a cross-coupling product, $Ph_3SiOSiEt_3$. A crude estimate using the ^1H NMR spectrum of the product mixture revealed a ratio of 2.5 **3c:** 1 $Ph_3SiOSiEt_3$: 2 **3a**, instead of a 1:1:1 ratio which would be expected if the **1a** and **1c** reacted at the same rate. This deviation can be explained by the difference in kinetics and solubilities of the two reactants. **1c** alone and **1a** alone require 2 and 3 h reaction time, respectively, to reach full conversion, while **1b** is even more rapid at 1 h. To further confirm this claim, cross-condensation reaction between **1b** and **1a** (**Supplementary Figure 62**) resulted to **3b** and $PhMe_2SiOSiEt_3$ as the major products in a 1:6 ratio and, no **3a** was observed. Therefore, the reactivity to form disiloxanes (**3a-c**) from the three tertiary silane substrates under the catalytic conditions follows the trend **1b** > **1c** > **1a**.

Cross-coupling between $PhMe_2SiH$, **1b**, and Et_3SiOH, **2a**, on the other hand, resulted to a 1:1:1 ratio of **3b** to the cross product, $PhMe_2SiOSiEt_3$ to **3a**. In this case, both homo-coupling products were obtained along with the expected unsymmetrical cross-coupling product (**Supplementary Figures 63, 64**) and the ratio suggests that the difference in the aforementioned reactivity trend is mostly likely due to the rate determining formation of the silanol (**2**) from the silane (**1**), which is most sluggish for the conversion of **1a** to **2a**.

Monitoring the catalytic intermediates and the formation of silanol experimentally *in situ* in order to capture the impact of ppm-level changes of the substrates was challenging. Nevertheless, NMR tube reactions wherein 2.6 mmol each of **1b** and **2b** were reacted, separately, with 0.1 mol% of $(C_6F_5)_3B(OH_2)$. Experimentally, partial conversion to **2b** and **3b** after 4 h was observed with **1b**, which is significantly slower compared to the reaction performed with constant stirring. It is interesting to note that when using a hydrosilane (e.g., **1b**) as the starting material, the products that have been formed (i.e., **2b** and **3b**) after 4 h tend to revert back to $PhMe_2SiH$ after letting the reaction stand for a total of 96 h (**Supplementary Figure 65**). This indicates that the reaction is not quite as simple as implied, with reversibility at play along with the direct siloxane formation. In contrast, using the silanol (**2b**) as the starting material, full conversion was observed after 24 h and the product (**3b**) did not convert back to the silanol substrate after 96 h (**Supplementary Figure 66**).

In summary, the results obtained from cross-coupling and control reactions indicate that the prevalent mechanism is where the hydrosilane (R_3SiH) and silanol (R_3SiOH) undergo dehydrocoupling to yield the disiloxane product (**3**), but under high concentration regimes of some silanol substrates (e.g., as confirmed for **2b**) the silanol condensation route is possible. The postulated reaction mechanism, therefore, for the transformation is a modified Pier-Rubinsztajn reaction **(Scheme 5**). The process involves: i) the hydrolysis of Si-H to Si-OH using $(C_6F_5)_3B(OH_2)$ with subsequent release of H_2 gas, followed by ii) nucleophilic attack of silanol (**2**, R_3SiOH) to the hydrosilane (**1**, R_3SiH) to form a disiloxane and another equivalent of H_2 gas (**Scheme 5**).

In addition to the conversion of the three components (**1**, **2**, **3**) over time, the catalyst can have different interactions with the substrates (**1**, **2**) and H_2O that are present during the reaction. Decomposition of $(C_6F_5)_3B(OH_2)$ catalyst via B-C bond protonolysis is highly probable in strongly basic conditions and high temperatures (Bradley et al., 1996; Ashley et al., 2009; Scott et al., 2015). Generally, Frustrated Lewis Pairs (FLP's) demonstrate high sensitivity to moisture. The high Lewis acidity of $B(C_6F_5)_3$ leads to strong complexation with H_2O and deprotonation even with moderately strong bases can occur irreversibly (Bergquist et al., 2000). However, the method described in this article demonstrated moisture tolerance of the $(C_6F_5)_3B(OH_2)$ catalyst as it was conducted at room temperature, and due to the lack of any strong base in a reaction with a hydrosilane as the sole substrate.

Another way to view the direct synthesis of disiloxanes is through a non-conventional mechanism which features multiple catalytically relevant species and series of competitive reactions (**Scheme 6**). The formation of disiloxanes can be regarded as a Lewis acid-catalyzed reaction, a water-mediated or a silanol-mediated type of catalysis (Yu et al., 2018). In the Lewis acid catalysis (**Scheme 6**), the Si-H bond of the silane is activated by $B(C_6F_5)_3$ and then will further react with a silanol to produce the disiloxane with concomitant release of H_2. By contrast, hydrosilylation reactions catalyzed by $B(C_6F_5)_3$ are generally characterized by the formation of borane-silane complex (Parks and Piers, 1996; Parks et al., 2000; Rendler and Oestreich, 2008; Sakata and Fujimoto, 2013; Zhang et al., 2016; Cheng et al., 2018). Furthermore, several experimental and theoretical mechanistic studies have suggested that borane-catalyzed reactions of siloxanes are initiated by activation of the silane Si-H bond (Parks et al., 2000; Hog and Oestreich, 2009; Mewald and Oestreich, 2012; Sakata and Fujimoto, 2013; Mathew et al., 2017).

Since the $B(C_6F_5)_3$ catalyst has strong affinity with H_2O, the Lewis-acid mediated pathway (**Scheme 6**) is not enough on its own to describe the formation of the disiloxane. The reaction could also possibly proceed via a water-mediated catalytic cycle (**Scheme 6**). For this reaction pathway, R_3SiH is initially activated by the $(C_6F_5)_3B(OH_2)$ catalyst, which is in equilibrium with $B(C_6F_5)_3$ in the presence of H_2O. While $B(C_6F_5)_3$ is a potent Lewis acid $(C_6F_5)_3B(OH_2)$, can be regarded as a strong Brønsted acid (Bergquist et al., 2000). The Si-H activation step can lead to Lewis acidic silicon atom, which for this case then interacts with oxygen lone pair of the pre-formed silanol to generate **3** and eliminate H_2. One final catalytic possibility, under higher concentrations of silanol (**2**) is that it can mediate the catalysis. Here the silanol (**2**) interacts with $(C_6F_5)_3B(OH_2)$ catalyst via the oxygen atom which activates it toward a reaction with silane (**1**) to produce **3** and H_2 while regenerating the catalyst/silanol adduct (**Scheme 6**).

The observations from the control and competition reactions suggest that the water-mediated catalysis (**Scheme 6**) is the most probable catalytic pathway which will lead to the formation of disiloxane. Nonetheless, there also might be a competition between more than one catalytic cycle happening simultaneously or under different concentration regimes of substrates **1** (e.g., toward the start of the reaction) and **2** (e.g., toward full conversion to **3**). Therefore, this seemingly simple reaction may have an incredibly complex mechanism.

Catalyst Recycling Studies

Catalyst recycling, that is the reuse of the $(C_6F_5)_3B(OH_2)$ catalyst, was considered to demonstrate the efficiency and sustainability of the direct synthetic route to oligosiloxanes. For this purpose, all experiments were conducted with constant stirring to allow efficient removal of hydrogen gas and favor the formation of disiloxane product. The reactions were monitored by ^1H NMR spectroscopy to estimate the reaction time needed for each substrate to reach completion. From these studies, 3, 1 and 2 h reaction time was applied for Et_3SiH (**1a**), $PhMe_2SiH$ (**1b**) and Ph_3SiH (**1c**), respectively.

For $Et_3SiOSiEt_3$, **3a**, the catalyst was recovered conveniently as it settled at the bottom of the flask after the stirring was stopped. The product was isolated by addition of *n*-pentane followed by decantation using a cannula. Looking at catalyst loading (0.1–5.0 mol%) there was very little discrepancy in isolated yield over this range and the best TOF achieved was 167 h^{-1} with 0.1 mol% catalyst loading (**Figure 2**; **Supplementary Figure 67**; **Supplementary Table 2**). The dependence on catalyst loading for the reaction of **1b** to form $PhMe_2SiOSiMe_2Ph$, **3b**, is far less pronounced with the given experimental conditions allowing for an increase in TOF with a decrease in catalyst loading; 900 h^{-1} TOF was achieved at 0.1 mol% loading (**3b**, **Figure 2**; **Supplementary Figure 68**; **Supplementary Table 3**). The reaction was completed after 1 h as observed by ^1H NMR spectroscopy. In this case, the $(C_6F_5)_3B(OH_2)$ remained soluble even after the formation of **3b**. Therefore, due to the challenges of directly testing the catalyst recyclability on such a small scale (e.g., 0.1 mol% loading), the activity of the catalyst (at 1.0 mol% loading) was demonstrated by adding a constant amount of **1b** to the same flask every hour after testing the degree of completion by ^1H and ^{29}Si NMR spectroscopy. After 5 cycles, **3b** was isolated and the % yield for each trial was reported as the average of 5 cycles (94%). Similarly, using **1c** as the substrate, the reaction rate exhibited independence of catalyst loading with a TOF of 485 h^{-1} at 0.1 mol% loading (**3c**, **Figure 2**; **Supplementary Figure 69**;

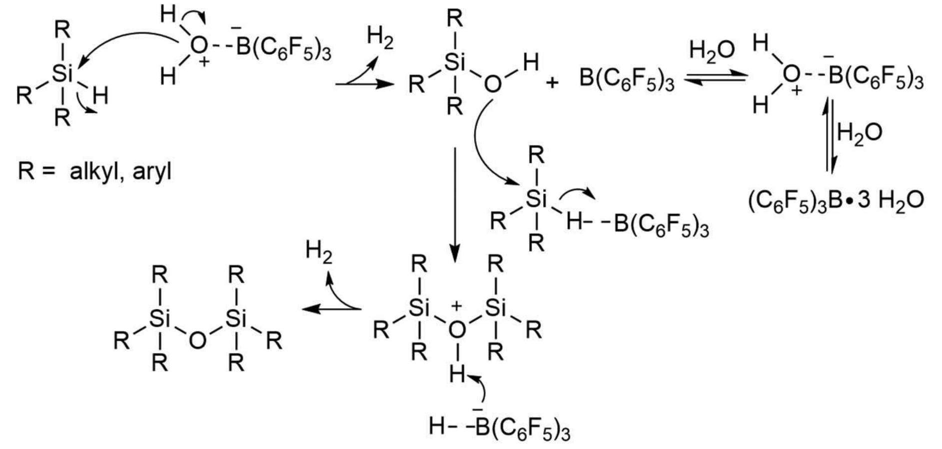

SCHEME 5 | Proposed mechanism for the catalytic formation of disiloxanes using $(C_6F_5)_3B(OH_2)$.

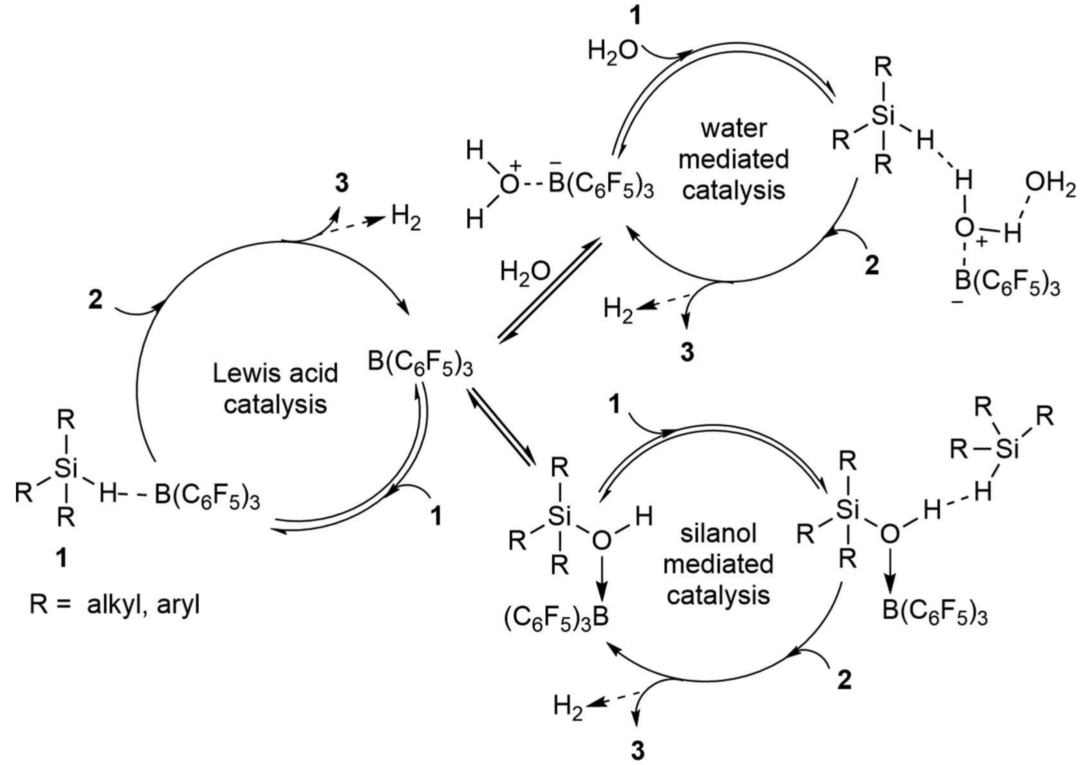

SCHEME 6 | A catalytic mechanism with multiple competing catalytic pathways to form disiloxanes.

Supplementary Table 4). However, the reaction required the addition of toluene to dissolve the two solids (**1c** and catalyst). Similar to the reaction with **1b**, given that the reaction was performed in a mmol scale, a constant volume of 3.0 M solution of **1c** in toluene was added sequentially to the same flask at 1.0 mol% catalyst loading. The product $Ph_3SiOSiPh_3$, **3c**, was again isolated collectively at the end of the fifth cycle (98%).

To demonstrate the recycling by separating the catalyst and product after each cycle, both 0.5 mol% and 1.0 mol% catalyst loadings of $(C_6F_5)_3B(OH_2)$ were chosen. The results showed that the activity of the catalyst for each cycle is almost the same (within experimental error) for up to five repeats (**Figure 3**). The volatility and solubility of the substrate plays an important role in facilitating the formation of the disiloxane product in excellent yields. Since the reactions were performed with constant stirring, it can be assumed that some of the Et_3SiH may have been lost prior to its conversion to product (see lower yield for **3a**, **Figure 2**). In addition, the solubility of the catalyst was

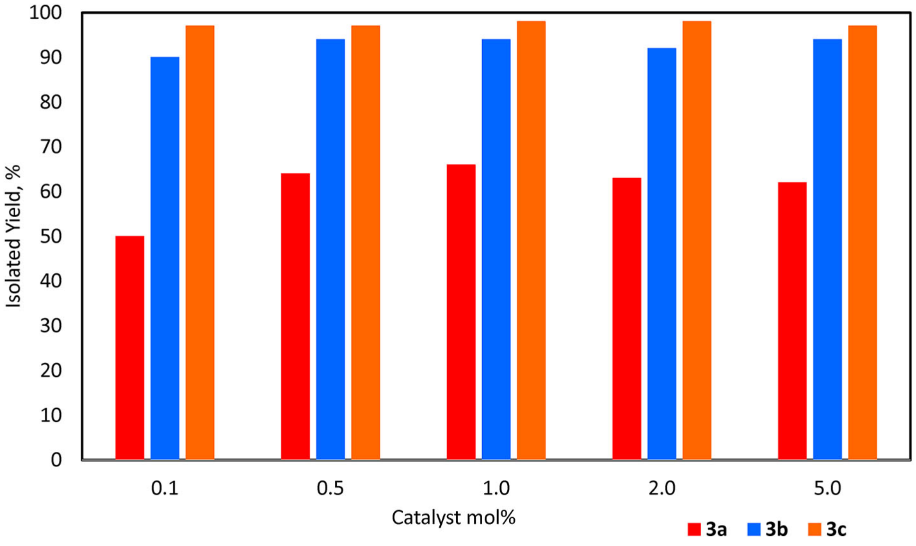

FIGURE 2 | Yields for **3a-c** with catalyst loadings 0.1–5.0 mol%.

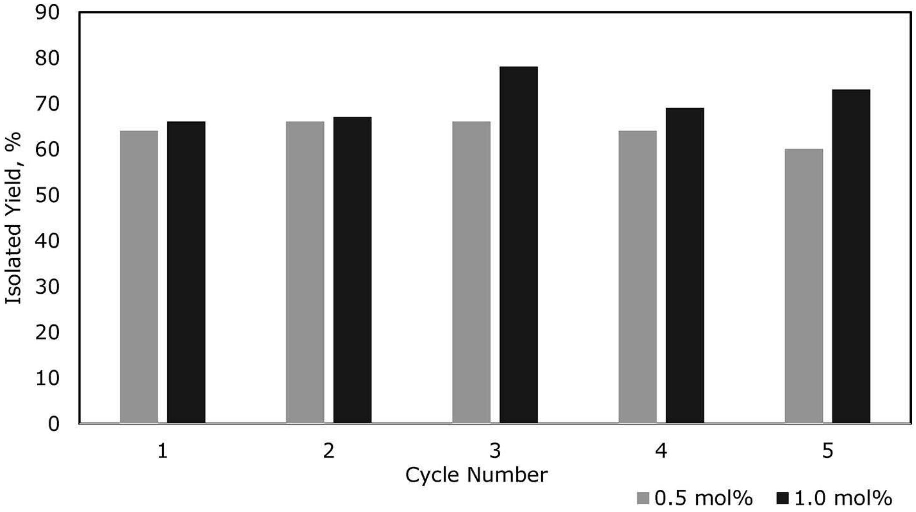

FIGURE 3 | Yields for **3a** over 5 cycles of recycling using 0.5 and 1.0 mol% catalyst loading.

enhanced in the presence of a solvent as compared to a neat reaction. Overall, these experiments successfully demonstrated the longevity of the $(C_6F_5)_3B(OH_2)$ catalyst and that it is possible to recycle it at least five times in reactions with the given substrates.

CONCLUSIONS

The study presented in this article has demonstrated an efficient route from secondary and tertiary hydrosilanes into the corresponding oligosiloxanes using a moisture-stable and recyclable $(C_6F_5)_3B(OH_2)$ catalyst through either an intermolecular or intramolecular reaction depending on the substrate. Multiple catalytically relevant species and a series of competitive reactions are probable when considering the mechanism involved for the direct synthesis of siloxanes from only hydrosilanes and water. A single catalytic pathway is simply not enough to describe the formation of the disiloxane. The experimental results gathered from control studies suggest that the most feasible route to disiloxanes is where the Si-H is partially converted to Si-OH followed by a heterodehydrocoupling reaction of Si-H/Si-OH. Moreover, the cross-coupling results show promise for the selective synthesis of unsymmetrical siloxanes under controlled conditions directly from silanes or using a mixture of silanes and silanols or alcohols and this will be the subject of future studies in our group. Nonetheless, given the wide range of hydrosilanes that are commercially available, this protocol should provide an easy route to a large variety of oligosiloxanes.

DATA AVAILABILITY STATEMENT

The datasets generated for this study can be found in the CCDC repository (1987430, 1987431) or are included in article/**Supplementary Material**.

AUTHOR CONTRIBUTIONS

KR-C and VK designed and performed the experiments under the supervision of EL. TS refined the crystal structures. KR-C and VK wrote the paper with editorial support from EL.

FUNDING

This work was supported by Royal Society of New Zealand, Marsden Fast Start Fund (16-UOA-042).

ACKNOWLEDGMENTS

The authors would like to acknowledge the School of Chemical Sciences at the University of Auckland for a doctoral scholarship (KR-C) as well as the Royal Society of New Zealand Marsden Fast-Start grant for providing financial support as well as a doctoral scholarship (VK). We thank Tatiana Groutso for collecting the single crystal X-ray diffraction data. We would also like to acknowledge the MacDiarmid Institute for financial support.

SUPPLEMENTARY MATERIAL

The Supplementary Material for this article can be found online at: https://www.frontiersin.org/articles/10.3389/fchem.2020.00477/full#supplementary-material

REFERENCES

Abele, R., Abele, E., Fleisher, M., Geinberga, S., and Lukevics, E. (2003). Novel fluoride ion mediated synthesis of unsymmetrical siloxanes under phase transfer catalysis conditions. *J. Organometal. Chem.* 686, 52–57. doi: 10.1016/S0022-328X(03)00286-9

Ai, L., Chen, Y., He, L., Luo, Y., Li S., and Xu, C. (2019). Synthesis of structured polysiloxazanes via a Piers–Rubinsztajn reaction. *Chem. Comm.* 55, 14019–14022. doi: 10.1039/C9CC07312D

Asao, N., Ishikawa, Y., Hatakeyama, N., Menggenbateer, Yamamoto, Y., Chen, M., et al. (2010). Nanostructured materials as catalysts: nanoporous-gold-catalyzed oxidation of organosilanes with water. *Angew. Chem. Int. Ed.* 49, 10093–10095. doi: 10.1002/anie.201005138

Ashley, A. E., Thompson, A. L., and O'Hare, D. (2009). Non-metal-mediated homogeneous hydrogenation of CO_2 to CH_3OH. *Angew. Chem. Int. Ed.* 48, 9839–9843. doi: 10.1002/anie.200905466

Bergquist, C., Bridgewater, B. M., Harlan, C. J., Norton, J. R., Friesner R. A., and Parkin, G. (2000). Aqua, alcohol, and acetonitrile adducts of Tris(perfluorophenyl)borane: evaluation of brønsted acidity and ligand lability with experimental and computational methods. *J. Am. Chem. Soc.* 122, 10581–10590. doi: 10.1021/ja001915g

Beringhelli, T., Maggioni, D., and D'alfonso, G. (2001). 1H and 19F NMR investigation of the reaction of $B(C_6F_5)_3$ with water in toluene solution. *Organometallics* 20, 4927–4938. doi: 10.1021/om010610n

Blackwell, J. M., Foster, K. L., Beck, V. H., and Piers, W. E. (1999). $B(C_6F_5)_3$-catalyzed silation of alcohols: a mild, general method for synthesis of silyl ethers. *J. Org. Chem.* 64, 4887–4892. doi: 10.1021/jo9903003

Bradley, D. C., Harding, I. S., Keefe, A. D., Motevalli, M., and Zheng, D. H. (1996). Reversible adduct formation between phosphines and triarylboron compounds. *J. Chem. Soc. Dalton Trans.* 3931–3936. doi: 10.1039/dt9960003931

Brinker, C. J., and Scherer, G. W. (1990). *Sol–Gel Science: The Physics and Chemistry of Sol–Gel Processing.* New York, NY: Academic Press.

Brook, M. A. (2018). New control over silicone synthesis using sih chemistry: the piers–rubinsztajn reaction. *Chem. Eur. J.* 24, 8458–8469. doi: 10.1002/chem.201800123

Cella, J., and Rubinsztajn, S. (2008). Preparation of polyaryloxysilanes and polyaryloxysiloxanes by $B(C_6F_5)_3$ catalyzed polyetherification of dihydrosilanes and bis-phenols. *Macromolecules* 41, 6965–6971. doi: 10.1021/ma800833c

Chauhan, B. P. S., Sarkar, A., Chauhan, M., and Roka, A. (2009). Water as green oxidant: a highly selective conversion of organosilanes to silanols with water. *Appl. Organomet. Chem.* 23, 385–390. doi: 10.1002/aoc.1528

Cheng, G. J., Drosos, N., Morandi, B., and Thiel, W. (2018). Computational study of $B(C_6F_5)_3$-catalyzed selective deoxygenation of 1,2-diols: cyclic and noncyclic pathways. *ACS Catal.* 8, 1697–1702. doi: 10.1021/acscatal.7b04209

Chojnowski, J., Fortuniak, W., Kurjata, J., Rubinsztajn, S., and Cella, J. A. (2006). Oligomerization of hydrosiloxanes in the presence of tris(pentafluorophenyl)borane. *Macromolecules,* 39, 3802–3807. doi: 10.1021/ma060080c

Chojnowski, J., Rubinsztajn, S., Cella, J. A., Fortuniak, W., Cypryk, M., Kurjata, J., et al. (2005). Mechanism of the $B(C_6F_5)_3$-catalyzed reaction of silyl hydrides with alkoxysilanes. Kinetic and spectroscopic studies. *Organometallics,* 24, 6077–6084. doi: 10.1021/om050563p

Chojnowski, J., Rubinsztajn, S., Fortuniak, W., and Kurjata, J. (2008). Synthesis of highly branched alkoxysiloxane–dimethylsiloxane copolymers by nonhydrolytic dehydrocarbon polycondensation catalyzed by tris(pentafluorophenyl)borane. *Macromolecules,* 41, 7352–7358. doi: 10.1021/ma801130y

Diemoz, K. M., Wilson, S. O., and Franz, A. K. (2016). Synthesis of structurally varied 1,3-disiloxanediols and their activity as anion-binding catalysts. *Chem Eur. J.* 22, 18349–18353. doi: 10.1002/chem.201604103

Dolomanov, O. V., Bourhis, L. J., Gildea, R. J., Howard, J. A. K., and Puschmann, H. (2009). OLEX2: a complete structure solution, refinement and analysis program. *J. Appl. Crystallogr.* 42, 339–341. doi: 10.1107/S0021889808042726

Feghali, E., and Cantat, T. (2014). Unprecedented organocatalytic reduction of lignin model compounds to phenols and primary alcohols using hydrosilanes. *Chem. Commun.* 50, 862–865. doi: 10.1039/C3CC47655C

Feghali, E., Carrot, G., Thuéry, P., Genre, C., and Cantat, T. (2015). Convergent reductive depolymerization of wood lignin to isolated phenol derivatives by metal-free catalytic hydrosilylation. *Energy Environ. Sci.* 8, 2734–2743. doi: 10.1039/C5EE01304F

Grubb, W. T. (1954). A rate study of the silanol condensation reaction at 25° in alcoholic solvents1. *J. Am. Chem. Soc.* 76, 3408–3414. doi: 10.1021/ja01642a014

Hog, D. T., and Oestreich, M. (2009). $B(C_6F_5)_3$-catalyzed reduction of ketones and imines using silicon-stereogenic silanes: stereoinduction by single-point binding. *Eur. J. Org. Chem.* 2009, 5047–5056. doi: 10.1002/ejoc.200900796

Hreczycho, G. (2015). An efficient catalytic approach for the synthesis of unsymmetrical siloxanes. *Eur. J. Inorg. Chem.* 2015, 67–72. doi: 10.1002/ejic.201402904

Hreczycho, G., Kucinski, K., Pawluć, P., and Marciniec, B. (2013). Catalytic synthesis of linear oligosiloxanes and germasiloxanes mediated by scandium trifluoromethanesulfonate. *Organometallics* 32, 5001–5004. doi: 10.1021/om400581g

Igarashi, M., Kubo, K., Matsumoto, T., Sato, K., Ando,W., and Shimada, S. (2014). Pd/C-catalyzed cross-coupling reaction of benzyloxysilanes with halosilanes for selective synthesis of unsymmetrical siloxanes. *RSC Adv.* 4, 19099–19102. doi: 10.1039/c4ra02126f

Ison, E. A., Corbin, R. A., and Abu-Omar, M. M. (2005). Hydrogen production from hydrolytic oxidation of organosilanes using a cationic oxorhenium catalyst. *J. Am. Chem. Soc.* 127, 11938–11939. doi: 10.1021/ja053860u

Jeon, M., Han, J., and Park, J. (2012). Transformation of silanes into silanols using water and recyclable metal nanoparticle catalysts. *ChemCatChem* 4, 521–524. doi: 10.1002/cctc.201100456

John, J., Gravel, E., Hagège, A., Li, H., Gacoin, T., and Doris, E. (2011). Catalytic oxidation of silanes by carbon nanotube–gold nanohybrids. *Angew. Chem. Int. Ed.* 50, 7533–7536. doi: 10.1002/anie.201101993

Jorapur, Y. R., and Shimada, T. (2012). An efficient method for the synthesis of symmetrical disiloxanes from alkoxysilanes using meerwein's reagent. *Synlett* 23, 1633–1638. doi: 10.1055/s-0031-1290668

Kawakami, Y., Li, Y., Liu, Y., Seino, M., Pakjamsai, C., Oishi, M., et al. (2004). Control of molecular weight, stereochemistry and higher order structure of siloxane-containing polymers and their functional design. *Macromol. Res.* 12, 156–171. doi: 10.1007/BF03218384

Kaźmierczak, J., and Hreczycho, G. (2018). Nafion as effective and selective heterogeneous catalytic system in O-metalation of silanols and POSS silanols. *J. Cat.* 367, 95–103. doi: 10.1016/j.jcat.2018.08.024

Kuciński, K., and Hreczycho, G. (2019a). A highly effective route to si-o-si moieties through *o*-silylation of silanols and polyhedral oligomeric silsesquioxane silanols with disilazanes. *ChemSusChem* 12, 1043–1048. doi: 10.1002/cssc.201802757

Kuciński, K., and Hreczycho, G. (2019b). O-metalation of silanols and POSS silanols over amberlyst-15 catalyst: a facile route to unsymmetrical siloxanes, borasiloxanes and germasiloxanes. *Inorg. Chim. Acta* 490, 261–266. doi: 10.1016/j.ica.2019.03.025

Kurihara, Y., Yamanoi, Y., and Nishihara, H. (2013). Pd-catalyzed synthesis of symmetrical and unsymmetrical siloxanes. *Chem. Comm.*, 49, 11275–11277. doi: 10.1039/c3cc46294c

Kurjata, J., Fortuniak, W., Rubinsztajn, S., and Chojnowski, J. (2009). $B(C_6F_5)_3$ catalyzed dehydrocarbon polycondensation of $PhSiH_3$ with (MeO)4Si as model polyfunctional comonomers in new route to hydrophobic silicone TQ resins. *Eur. Polym. J.* 45, 3372–3379. doi: 10.1016/j.eurpolymj.2009.10.004

Laengert, S. E., Schneider, A. F., Lovinger, E., Chen, Y., and Brook, M. A. (2017). Sequential functionalization of a natural crosslinker leads to designer silicone networks. *Chem. Asian J.* 12, 1208–1212. doi: 10.1002/asia.201700160

Lawson, J. R., and Melen, R. L. (2017). Tris(pentafluorophenyl)borane and beyond: modern advances in borylation chemistry. *Inorg. Chem.* 56, 8627–8643. doi: 10.1021/acs.inorgchem.6b02911

Le Coz, E., Kahlal, S., Saillard, J. Y., Roisnel, T., Dorcet, V., Carpentier J. F. et al. (2019). Barium siloxides and catalysed formation of Si-O-Si' motifs. *Chem. Eur. J.* 25, 13509–13513. doi: 10.1002/chem.201903676

Lee, M., Ko, S., and Chang, S. (2000). Highly selective and practical hydrolytic oxidation of organosilanes to silanols catalyzed by a ruthenium complex. *J. Am. Chem. Soc.* 122, 12011–12012. doi: 10.1021/ja003079g

Lee, Y., Seomoon, D., Kim, S., Han, H., Chang, S., and Lee, P. H. (2004). Highly efficient iridium-catalyzed oxidation of organosilanes to silanols. *J. Org. Chem.* 69, 1741–1743. doi: 10.1021/jo035647r

Liu, T., Yang, F., Li, Y., Ren, L., Zhang, L., Xu, K., et al. (2014). Plasma synthesis of carbon nanotube-gold nanohybrids: efficient catalysts for green oxidation of silanes in water. *J. Mater. Chem. A* 2, 245–250. doi: 10.1039/C3TA13693K

Longuet, C., Joly-Duhamel, C., and Ganachaud, F. (2007). Copolycondensation of regular functional silane and siloxane in aqueous emulsion using $B(C_6F_5)_3$ as a catalyst. *Macromol. Chem. Phys.* 208, 1883–1892. doi: 10.1002/macp.200700202

Macrae, C. F., Edgington, P. R., Mccabe, P., Pidcock, E., Shields, G. P., Taylor, R., et al. (2006). Mercury: visualization and analysis of crystal structures. *J. Appl. Crystallogr.* 39, 453–457. doi: 10.1107/S002188980600731X

Madsen, F. B., Javakhishvili, I., Jensen, R. E., Daugaard, A. E., Hvilsted, S., and Skov, A. L. (2014). Synthesis of telechelic vinyl/allyl functional siloxane copolymers with structural control. *Polym. Chem.* 5, 7054–7061. doi: 10.1039/C4PY00919C

Marciniec, B., Pawluć, P., Hreczycho, G., Macina, A., and Adalska, M. (2008). Silylation of silanols with vinylsilanes catalyzed by a ruthenium complex. *Tetrahedron Lett*. 49, 1310–1313. doi: 10.1016/j.tetlet.2007.12.091

Mathew, J., Eguchi, K., Nakajima, Y., Sato, K., Shimada, S., and Choe, Y.-K. (2017). Tris(pentafluorophenyl)borane-catalyzed reactions of siloxanes: a combined experimental and computational study. *Eur. J. Org. Chem.* 2017, 4922–4927. doi: 10.1002/ejoc.201700760

Matsumoto, K., Oba, Y., Nakajima, Y., Shimada, S., and Sato, K. (2018). One-pot sequence-controlled synthesis of oligosiloxanes. *Angew. Chem. Int. Ed.* 57, 4637–4641. doi: 10.1002/anie.201801031

Matsumoto, K., Shimada, S., and Sato, K. (2019). Sequence-controlled catalytic one-pot synthesis of siloxane oligomers. *Chem. Eur. J.* 25, 920–928. doi: 10.1002/chem.201803565

Matsuo, T., and Kawaguchi, H. (2006). From carbon dioxide to methane: homogeneous reduction of carbon dioxide with hydrosilanes catalyzed by zirconium–borane complexes. *J. Am. Chem. Soc.* 128, 12362–12363. doi: 10.1021/ja0647250

Mewald, M., and Oestreich, M. (2012). Illuminating the mechanism of the borane-catalyzed hydrosilylation of imines with both an axially chiral borane and silane. *Chem. Eur. J.* 18, 14079–14084. doi: 10.1002/chem.201202693

Mitsudome, T., Arita, S., Mori, H., Mizugaki, T., Jitsukawa, K., and Kaneda, K. (2008). Supported silver-nanoparticle-catalyzed highly efficient aqueous oxidation of phenylsilanes to silanols. *Angew. Chem. Int. Ed.* 47, 7938–7940. doi: 10.1002/anie.200802761

Mitsudome, T., Noujima, A., Mizugaki, T., Jitsukawa, K., and Kaneda, K. (2009). Supported gold nanoparticlecatalyst for the selective oxidation of silanes to silanols in water. *Chem. Commun.* 5302–5304. doi: 10.1039/b910208f

Muzafarov, A. M. (2011). *Advances in Polymer Science, Silicon Polymers.* Berlin: Springer-Verlag.

Neumann, B., Vincent, B., Krustev, R., and Müller, H. J. (2004). Stability of various silicone oil/water emulsion films as a function of surfactant and salt concentration. *Langmuir* 20, 4336–4344. doi: 10.1021/la035517d

Parks, D. J., Blackwell, J. M., and Piers, W. E. (2000). Studies on the mechanism of $B(C_6F_5)_3$-catalyzed hydrosilation of carbonyl functions. *J. Org. Chem.* 65, 3090–3098. doi: 10.1021/jo991828a

Parks, D. J., and Piers, W. E. (1996). Tris(pentafluorophenyl)boron-catalyzed hydrosilation of aromatic aldehydes, ketones, and esters. *J. Am. Chem. Soc.* 118, 9440–9441. doi: 10.1021/ja961536g

Pattanaik, S., and Gunanathan, C. (2019). Cobalt-catalyzed selective synthesis of disiloxanes and hydrodisiloxanes. *ACS Cataly.* 9, 5552–5561. doi: 10.1021/acscatal.9b00305

Piers, W. E. (2004). The chemistry of perfluoroaryl boranes. *Adv. Organomet. Chem.* 52, 1–76. doi: 10.1016/s0065-3055(04)52001-4

Rabanzo-Castillo, K. M., Hanif, M., Söhnel, T., and Leitao, E. M. (2019). Synthesis, characterisation and electronic properties of naphthalene bridged disilanes. *Dalton Trans.* 48, 13971–13980. doi: 10.1039/C9DT 03058A

Rendler, S., and Oestreich, M. (2008). Conclusive evidence for an SN_2-Si mechanism in the $B(C_6F_5)_3$-catalyzed hydrosilylation of carbonyl compounds: implications for the related hydrogenation. *Angew. Chem. Int. Ed.* 47, 5997–6000. doi: 10.1002/anie.200801675

Rubinsztajn, S., and Cella, J. A. (2005). A new polycondensation process for the preparation of polysiloxane copolymers. *Macromolecules* 38, 1061–1063. doi: 10.1021/ma047984n

Sakata, K., and Fujimoto, H. (2013). Quantum chemical study of $B(C_6F_5)_3$-catalyzed hydrosilylation of carbonyl group. *J. Org. Chem.* 78, 12505–12512. doi: 10.1021/jo402195x

Sawama, Y., Masuda, M., Yasukawa, N., Nakatani, R., Nishimura, S., Shibata, K., et al. (2016). Disiloxane synthesis based on silicon–hydrogen bond activation using gold and platinum on carbon in water or heavy water. *J. Org. Chem.* 81, 4190–4195. doi: 10.1021/acs.joc.6b00556

Schneider, A. F., Laidley, E., and Brook, M. A. (2019). Facile synthesis of Cx(AB)yCx triblock silicone copolymers utilizing moisture mediated living-end chain extension. *Macromol. Chem. Phys.* 220:1800575. doi: 10.1002/macp.201800575

Scott, D. J., Simmons, T. R., Lawrence, E. J., Wildgoose, G. G., Fuchter, M. J., and Ashley, A. E. (2015). Facile protocol for water-tolerant "frustrated lewis pair"-catalyzed hydrogenation. *ACS Catal.* 5, 5540–5544. doi: 10.1021/acscatal.5b01417

Sheldrick, G. (2015). SHELXT - integrated space-group and crystal-structure determination. *Acta Crystallogr. Sect. A* 71, 3–8. doi: 10.1107/S2053273314026370

Shimizu, K., Kubo, T., and Satsuma, A. (2012a). Surface oxygen-assisted pd nanoparticle catalysis for selective oxidation of silanes to silanols. *Chem. Eur. J.* 18, 2226–2229. doi: 10.1002/chem.201103088

Shimizu, K.-I., Shimura, K., Imaiida, N., and Satsuma, A. (2012b). Heterogeneous nickel catalyst for selective hydration of silanes to silanols. *J. Mol. Catal. A Chem.* 365, 50–54. doi: 10.1016/j.molcata.2012.08.007

Shinke, S., Tsuchimoto, T., and Kawakami, Y. (2007). Stereochemistry in Lewis acid-catalyzed silylation of alcohols, silanols, and methoxysilanes with optically active methyl(1-naphthyl)phenylsilane. *Silicon Chem.* 3, 243–249. doi: 10.1007/s11201-007-9026-y

Spek, A. (2003). Single-crystal structure validation with the program PLATON. *J. App. Cryst.* 36, 7–13. doi: 10.1107/S0021889802022112

Sridhar, M., Ramanaiah, B. C., Narsaiah, C., Kumara Swamy, M., Mahesh, B., and Kumar Reddy, M. K. (2009). An efficient and simple method for the preparation of symmetrical disiloxanes from hydrosilanes by Lewis acid-catalyzed air oxidation. *Tetrahedron Lett.,* 50, 7166–7168. doi: 10.1016/j.tetlet.2009.10.020

Szawiola, A. M., De Melo Souza, N., Lessard, B. H., and Bender, T. P. (2017). Phenoxylated siloxane-based polymers via the Piers–Rubinsztajn process. *Polym. Int.* 66, 1324–1328. doi: 10.1002/pi.5396

Tan, S. T., Kee, J. W., and Fan, W. Y. (2011). Catalytic hydrogen generation from the hydrolysis of silanes by ruthenium complexes. *Organometallics,* 30, 4008–4013. doi: 10.1021/om200256h

Thompson, J. L., and Davies, H. M. (2007). Enhancement of cyclopropanation chemistry in the silver-catalyzed reactions of aryldiazoacetates. *J. Am. Chem. Soc.* 129, 6090–6091. doi: 10.1021/ja069314y

Tsuchido, Y., Kanda, A., and Osakada, K. (2020). Gold (I) complexes with chloro(diaryl)silyl ligand. Stoichiometric reactions and catalysis for O-functionalization of organosilane. *Tetrahedron* 76:131076. doi: 10.1016/j.tet.2020.131076

Uchida, H., Kabe, Y., Yoshino, K., Kawamata, A., Tsumuraya, T., and Masamune, S. (1990). General strategy for the systematic synthesis of oligosiloxanes. Silicone dendrimers. *J. Am. Chem. Soc.* 112, 7077–7079. doi: 10.1021/ja00175a062

Wang, D., Klein, J., and Mejía, E. (2017). Catalytic systems for the cross-linking of organosilicon polymers. *Chem. Asian J.* 12, 1180–1197. doi: 10.1002/asia.201700304

Wu, C., Yu, J., Li, Q., and Liu, Y. (2017). High molecular weight cyclic polysiloxanes from organocatalytic zwitterionic polymerization of constrained spirocyclosiloxanes. *Polym. Chem.* 8, 7301–7306. doi: 10.1039/C7PY01499F

Yi, M., Chen, X., Wu, S., Ge, J., Zhou, X., and Yin, G. (2018). Fabrication of reactive poly(Phenyl-Substituted Siloxanes/Silsesquioxanes) with Si–H and alkoxy functional groups via the piers–rubinsztajn reaction. *Polymers* 10:1006. doi: 10.3390/polym10091006

Yu, Y., Zhu, Y., Bhagat, M. N., Raghuraman, A., Hirsekorn, K. F., Notestein, J. M., et al. (2018). Mechanism of regioselective ring-opening reactions of 1,2-epoxyoctane catalyzed by tris(pentafluorophenyl)borane: a combined experimental, density functional theory, and microkinetic study. *ACS Catal.* 8, 11119–11133. doi: 10.1021/acscatal.8b02632

Zhang, H., Xue, L., Li, J., and Ma, Q. (2020). Hyperbranched polycarbosiloxanes: synthesis by piers-rubinsztajn reaction and application as precursors to magnetoceramics. *Polymers* 12:672. doi: 10.3390/polym12030672

Zhang, J., Chen, Y., and Brook, M. A. (2014). Reductive degradation of lignin and model compounds by hydrosilanes. *ACS Sust. Chem. Eng.* 2, 1983–1991. doi: 10.1021/sc500302j

Zhang, Q., Fu, M. C., Yu, H. Z., and Fu, Y. (2016). Mechanism of boron-catalyzed N-alkylation of amines with carboxylic acids. *J. Org. Chem.* 81, 6235–6243. doi: 10.1021/acs.joc.6b00778

Zhou, D., and Kawakami, Y. (2005). Tris(pentafluorophenyl)borane as a superior catalyst in the synthesis of optically active Sio-containing polymers. *Macromolecules* 38, 6902–6908. doi: 10.1021/ma050329a

Conflict of Interest: The authors declare that the research was conducted in the absence of any commercial or financial relationships that could be construed as a potential conflict of interest.

frontiers in Chemistry

MINI REVIEW
published: 30 June 2020
doi: 10.3389/fchem.2020.00546

Hybrid Materials Based on Carbon Nanotubes and Nanofibers for Environmental Applications

Anastasiya G. Navrotskaya[1], *Darya D. Aleksandrova*[1], *Elena F. Krivoshapkina*[1], *Mika Sillanpää*[2,3,4]* and *Pavel V. Krivoshapkin*[1]*

[1] ChemBio Cluster, ITMO University, Saint Petersburg, Russia, [2] Institute of Research and Development, Duy Tan University, Da Nang, Vietnam, [3] Faculty of Environment and Chemical Engineering, Duy Tan University, Da Nang, Vietnam, [4] Faculty of Health, Engineering and Sciences, School of Civil Engineering and Surveying, University of Southern Queensland, Toowoomba, QLD, Australia

With the advances in material science, hybrid nanomaterials with unique mechanical, electrical, thermal and optical characteristics have been developed. Among them, hybrids based on filamentous forms of carbon, such as carbon nanotubes and carbon nanofibers, in combination with inorganic nanoparticles attract particular attention. Due to the structure and morphology, charge and energy transfer processes lead to synergistic effects that allow the use of less material with higher productivity. To clarify these issues, this review will summarize and discuss the relevant studies of the use of inorganic compounds of various chemical groups in modifying carbon nanomaterials for ecological applications.

Keywords: carbon nanotubes, carbon nanofibers, hybrid nanomaterials, inorganic nanoparticles, environmental application

Edited by:
Eugene A. Goodilin,
Lomonosov Moscow State University, Russia

Reviewed by:
Guanglin Xia,
Fudan University, China
Serguei Savilov,
Lomonosov Moscow State University, Russia

****Correspondence:***
Mika Sillanpää
mikaetapiosillanpaa@duytan.edu.vn
Pavel V. Krivoshapkin
krivoshapkin@scamt-itmo.ru

Specialty section:
This article was submitted to Nanoscience,
a section of the journal Frontiers in Chemistry

Received: *02 April 2020*
Accepted: *27 May 2020*
Published: *30 June 2020*

Citation:
Navrotskaya AG, Aleksandrova DD, Krivoshapkina EF, Sillanpää M and Krivoshapkin PV (2020) Hybrid Materials Based on Carbon Nanotubes and Nanofibers for Environmental Applications. Front. Chem. 8:546. doi: 10.3389/fchem.2020.00546

INTRODUCTION

Carbon based materials have a number of different properties, and today, are used in all areas of life, including industry, metallurgy, medicine, optics, and environmental protection. However, the rapid development of industries demands more advanced materials with new characteristics created for future uses. The solution was found in the creation of hybrid materials that not only combine the properties of individual components, but also lead to synergistic effects.

Briefly, hybrid materials (HMs) are a result of mixing chemically different components with the formation of interactions, such as Van der Waals, hydrogen bonding, weak electrostatic interactions or covalent bonds. When formed, HMs have a structure different from that of their component materials, but inherit some of their properties and functions. The important factor is the inner structure of the hybrid. By manipulating this aspect, we can control the physicochemical properties of the hybrid material. Combination of carbon nanomaterials (CNMs) with polymers and inorganic nanoparticles improves mechanical (Gomathi et al., 2005; Zhao et al., 2011; Dillon et al., 2015; Wu et al., 2017), electrical (Whitsitt and Barron, 2003; Hang et al., 2005; Ivnitski et al., 2008; Liang et al., 2012), thermal (Cui et al., 2011; Chen L. et al., 2014; Aghabozorg et al., 2016; Hameed et al., 2019), sorptive (Deng et al., 2005; Choi et al., 2010; Czech et al., 2015; Saud et al., 2015; Navrotskaya et al., 2019) and catalytic (Wu et al., 2009; Paula et al., 2011; Aazam, 2014; Kim et al., 2014) properties(Kumar et al., 2008; Wu et al., 2009; Cui et al., 2011; Dillon et al., 2015).

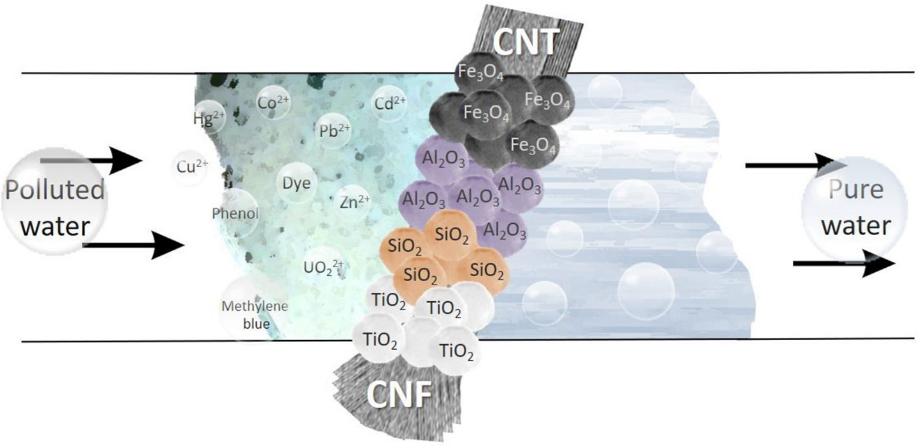

FIGURE 1 | Creation and application of hybrid materials.

Thus, currently there emerges an opportunity to modify CNMs with various nanomaterials using elements of the periodic table, namely metal and metal oxide nanoparticles and inorganic salts. In this context, this review summarizes recent progress in the fabrication and utilization of hybrid materials based on carbon nanomaterials and inorganic nanoparticles. It is especially worth noting that carbon structures, such as graphite, diamond, glassy carbon, graphene, amorphous powders, carbon fibrous materials, carbon nanofibers (CNFs), and carbon nanotubes (CNTs), are very interesting materials for research, development and large-scale production. One of the many advantages of CNTs and CNFs is their length to width ratio (>1,000), which results in a filamentous structure which translates to a high specific surface area (Wu et al., 2009; Paula et al., 2011; Aazam, 2014; Kim et al., 2014). In this regard, this review focuses solely on the advances of hybrid materials based on CNFs and CNTs for environmental applications, which distinguishes it from a number of works dedicated to carbon nanomaterials (**Figure 1**).

CARBON NANOMATERIALS

Carbon Nanotubes

Carbon nanotubes were first reported by Radushkevich and Lukyanovich in 1952 (Thakur and Thakur, 2016) and scientifically reported by Iijima in 1991 (Iijima, 1991). Carbon nanotubes are a seamless cylindrical graphene layer with half of a fullerene molecule at each end (Sarkar et al., 2018; Vashist et al., 2018a,b). CNTs are several nanometers in diameter, but several millimeters in length (Thakur and Thakur, 2016). Depending on the number of layers, CNTs can be single-walled (single-layer) (SWCNTs) or multi-walled (multi-layer) (MWCNTs) (Dai, 2002; Aqel et al., 2012; Das et al., 2014; Postnov et al., 2016). MWNTs are more attractive for widespread use as they are cheaper than SWCNTs (Aqel et al., 2012; Liu et al., 2013; Postnov et al., 2016; Thakur and Thakur, 2016). MWCNTs are made up of several concentric graphene pipes. Individual layers may be described as SWCNTs, which can be a semiconductor or metal. CNTs have a porous structure (Zeng et al., 2014; Chen et al., 2015; Zaytseva and Neumann, 2016).

Carbon nanofibers (CNFs) are filamentous nanomaterials that have mechanical and electrical properties similar to CNTs (Bergmann and Machado, 2015). There are, however, some key differences. Firstly, CNFs are not hollow. Also, the structure of CNFs can be described as graphene layers arranged perpendicularly or at an angle to the fiber axis (Klein et al., 2008; Mishakov et al., 2008; Feng et al., 2014; Yan et al., 2015). The most common CNF structures are "stack of coins" (or plane-parallel, "stacked"), "Christmas-tree structure" (or stack of cones, "fishbone," coaxial-conical), and "stack of cups" (or "lampshades," "bamboo") (Klein et al., 2008).

The similar structure of CNFs is due to their growing mechanism, which depends on the geometric characteristics of metal catalyst particles and the carbon source gas (Poveda and Gupta, 2016). CNFs are about several micrometers in length and have diameters ranging from 5 to 200 nm (Huang et al., 2010; Feng et al., 2014). Ballistic electron transport and tensile strength along the axis, as in diamond, are inherent characteristics of CNTs. CNFs, on the other hand, have higher reactivity and electron transfer through the sidewalls, which is important for functionalization and electrochemical application, respectively (Klein et al., 2008).

Purification and Functionalization of CNTs and CNFs

One of the stages of hybrid materials preparation is removing amorphous carbon, fullerenes, and metal catalyst particles from the CNFs and CNTs surface (Eder, 2010). There are several purification methods, each with its own advantages and disadvantages. Process efficiency should be the main criterion when choosing a purification method. It depends on the purity of the starting material, time and temperature of oxidation, pH and oxidizing agent. For example, carbon impurities can be removed via oxygen treatment, which is simply passing an H_2S and O_2 air mixture over the CNFs and CNTs. However, oxidation often results in broken surface tubes or fibers, especially when combined with ultrasonic and high-temperature processing. Oxidation via strong acids, such as HNO_3, H_2SO_4, another purification method, leads to broken surface tubes or fibers, as well as the formation of various functional groups. For the removal of metal catalyst particles without interfering with the carbon nanostructure, non-oxidizing acid treatment (for example HCl) is usually used. This leads to the fact that the metal nanoparticles move into the solution and leave the nanosystem. As an alternative to the above methods, high-temperature annealing in vacuum or inert gas can be performed. The processing temperature depends on the purpose and ranges from 600 to 2,000°C.

Much research has been dedicated to the surface functionalization of nanotubes for the creation of new materials with unique properties. This implies that CNTs are treated with different substances to form different functional groups on the surface (Thakur and Thakur, 2016). Covalent functionalization occurs when a covalent bond is formed between the carbon surface and the modifying agent. Functional groups can form at the end or on a sidewall of the nanotubes and nanofibers. For a single-walled carbon nanotube, this type of functionalization can lead to a shift in the electronic structure and thereby affect the conductivity. In the case of multi-walled carbon nanotubes, the internal electronic structure is preserved and new surface characteristics appear, which expands the possibilities of their application (Thakur and Thakur, 2016). In fact, covalent functionalization is carried out by organic molecules that interact with carboxyl groups after surface oxidation (Bright, 2000; Sahoo et al., 2010; Gao et al., 2012; Rabti et al., 2016).

Another type of functionalization—namely non-covalent functionalization—arises through Van der Waals forces and hydrogen bonding (Eder, 2010). Unlike covalent functionalization, it one does not lead to numerous surface defects or to any changes in the mechanical and conductive properties. In this case, modifying agents are various active substances and polymers that increase the solubility of CNTs in hydrophilic solvents and their dispersion in a polymer or ceramic matrix. Aromatic compounds (porphyrins, pyrenes) can also be included here due to π-π–interaction with the delocalized electron cloud of CNTs. The high curvature of CNTs determines reactivity connecting with π-orbital mismatch. The nanotube end, the fullerene hemispheres, are more reactive than the sidewalls. These properties can be used for the selective functionalization of CNTs.

Articles (Bright, 2000; Sahoo et al., 2010; Gao et al., 2012; Rabti et al., 2016) pay special attention to the positive influence of CNT surface modification. Through this process, the metal catalyst particles enter the solution in the form of salt and leave the nanosystem (Rao et al., 2007). In addition, the surface modification of carbon nanomaterials can lead to the formation of hydroxyl, carbonyl and carboxyl groups (Yang et al., 2009; Zawisza et al., 2012), and is most effectively achieved when the nanotubes (as sorbent) are oxidized using NaOCl, HNO_3 and $KMnO_4$ (Rao et al., 2007; Ihsanullah et al., 2016).

Carbon nanofibers can also be subjected to surface functionalization, but (unlike CNTs) their entire surface can be modified. CNFs activation by nitric acid or electrochemical oxidation can be used to form oxygen-containing groups without degradation of CNFs structure (Huang et al., 2010).

SYNTHESIS OF HYBRID MATERIALS

Inorganic hybrids based on CNTs and CNFs can be synthesized via *ex situ* and *in situ* methods. The first of these involves the separate preparation of the inorganic component in the desired size and morphology (usually spherical nanoparticles), then the attachment of this component to the carbon surface through covalent, non-covalent or electrostatic interactions. On the contrary, the *in situ* method involves the synthesis of an inorganic component in the presence of initial or functionalized CNTs and CNFs, on which the component grows in the form of particles, nanowires, or thin films (Eder, 2010). Filling the inside of a CNT with inorganic compounds from the gas or liquid phase is carried out by capillary forces based on condensation or wetting.

The valuable advantages of hybrid materials are the variety of synthesis routes and their relative simplicity. These materials can be obtained at low temperatures, through sol-gel and hydrothermal reactions, as well as in various morphologies, for example, in the form of three-dimensional structures, thin films or nanoparticles. The choice of methods for the synthesis of inorganic hybrids based on CNTs and CNFs and the degree of their synergistic effect depend on the type and purity of carbon materials, as well as their surface functionalization.

Sol-Gel Method

Sol-gel method is nowadays a common practice and can be said to be a comparatively new type of synthesis. This synthesis method results in the uniformed distribution of inorganic particles on the surface of the carbon nanomaterials. This process is diffusion-controlled, and the changing pH causes precursors to polymerize and form the inorganic particles. Different types of inorganic coatings can be created depending on the precursors used. For example, the hydrolysis of titanium isopropoxide resulted in a titanium dioxide matrix (Kim et al., 2011; Li et al., 2011; Hamid et al., 2014; Ge et al., 2015); iron (III) nitrate–iron (III) oxide matrix (Sun et al., 2005, 2018; Hassan et al., 2013; Wan et al., 2015); and also probably the creation of ZrO_2, HfO_2, and Ta_2O_5 oxide gels (Miller and Ko, 1996; Benad et al., 2018; Kiselev et al., 2019). Fixing elemental oxide on CNTs or CNFs surfaces changes hybrid materials characteristics.

Hydrothermal Treatment

Hydrothermal (and solvothermal) synthesis is conducted with a special piece of equipment called an autoclave under fixed pressure and temperature. Reagents are loaded into the autoclave then left in the oven for a period of time, allowing the reaction to take place without direct supervision (Byrappa and Adschiri, 2007; Yoshimura and Byrappa, 2008; Baruah and Dutta, 2009). During hydrothermal synthesis, aqueous solvents or mineralizers work under temperature and pressure to dissolve and recrystallize usual insoluble materials and decompose or recycle any waste material (Byrappa and Yoshimura, 2013). This process is carried out at high temperatures. As the precursors are the same as with the sol-gel synthesis method, hydrolysis is possible (Pirajno, 2009; Byrappa and Yoshimura, 2013). In this study, synthesized core-shell-structured carbon nanofiber (CNF)-titanate nanotubes (TiNT) by alkaline hydrothermal treatment. The CNF core could act as a support, and the TiO_2-decorated TiNT shell could act as a photocatalyst. The surface area increase as a result of the alkaline hydrothermal treatment may be responsible for the efficient photocatalytic activity of CNF-TiNTs (Kim et al., 2014; Kong et al., 2014; Guo et al., 2019).

Chemical Vapor Deposition (CVD) on Catalyst Nanoparticles

This method is often used in the semiconductor industry to obtain high clearing solid materials or thin films. Typically, during CVD, the substrate (catalyst) is placed in the precursor vapor and then the reaction produces the necessary substance. This process is used to obtain clean CNMs by making CNTs and CNFs then removing them from the nanoparticle-catalyst (substrate) surface (Bhat, 2006; Kumar and Ando, 2010; Prasek et al., 2011; Zhang et al., 2013; Bauman et al., 2017).

Nanomaterials can be used with the catalyst particles without separation. This resulting material is a hybrid. Here, catalyst particles act as both a substrate under the growing carbon nanomaterials, and as an arming dopant (Lee et al., 2002; Nessim, 2010). For use in ecology or the medical industry, catalysts must be non-toxic or must decrease the toxicity of carbon nanomaterials (Yu et al., 2011; Cendrowski et al., 2014; Chen J. et al., 2014).

In their publication, Cao et al. (2003) use this method to control the position and growth of CNTs (their length and direction) on the plane. Nanotube bridges connect samples of SiO_2 and demonstrate good electrical properties. It is important to note that SiO_2 neither coats CNTs nor decreases the conductivity. This method seems simple, inexpensive and controlled. Synthesized nanowires with dielectric shells present a new possibility for the effective and simple creation of high-pressure vertical broadband devices (Li et al., 2007).

Growing nanofibers on sphere nanoparticles leads to a significant increase in the fiber surface area. The reaction of growing CNTs decreases fiber strength, but the fiber module significantly increases, with compounds having grown CNTs fibers exhibiting significant improvement (up to 150%) in apparent shear strength in the transverse direction (Qian et al., 2010). The idea of hybridizing CNTs and Al_2O_3 is based on agglomeration prevention of CNTs due to Van der Waals interaction. Epoxide compounds with CNTs-Al_2O_3 demonstrate magnification >100% of compressive strength and Young's modulus (Zakaria et al., 2016). The introduction of nanocatalysts by this method is designed to improve the thermal properties of CNMs (Kumar et al., 2008; Ahmad et al., 2009, 2010).

Electrostatic Self-Assembly

This method is realized due to the interaction of the charged of particles on surface charged substrate, resulting in strong bond formation and uniformed distribution (Fang and Böhringer, 2008; Liu Y. et al., 2009; Olmedo et al., 2011; Choi et al., 2014). One-dimensional nanocomposite colloids are prepared through electrostatic self-assembly of CdTe nanocrystals on both carbon nanotubes (CNTs) and silica coated CNTs. The dense coverage of these linear nanoparticle assemblies minimizes the spacing between the nanocrystals, thereby facilitating efficient electron and energy transfer along the nanotubes (Grzelczak et al., 2006; Bogani et al., 2009; Liu Y. et al., 2009; Downes et al., 2015).

HYBRID MATERIALS FOR ENVIRONMENTAL APPLICATIONS

Hybrid carbon nanomaterials are used in many areas of our life, such as medicine, material science, and environmental concerns. These are not the only areas, but, due to the main properties of CNMs, the nanosystems would be most effective in the aforementioned fields due to the synergetic effect (**Table 1**). In the current climatic conditions, the environmental situation is such that there is a rising demand to protect the environment from toxic substances. Pollution, the release of harmful substances into the environment, is one of the results of the human lifestyle. The huge release of copper, mercury and other trace elements has produced a list of complex environmental problems. These materials are likely toxic to all living organisms. Highly sensitive and selective results show that these substances have received considerable attention in the last few years (Ghiasvand et al., 2020). Removal of these compounds is a mandatory step in protecting the environment. This topic has interested many scientists from around the world (Song et al., 2010; Ashrafi et al., 2014; Sareen et al., 2014; Zare et al., 2015).

The important area is removing divalent heavy metal ions Cu^{2+}, Zn^{2+}, Pb^{2+}, Cd^{2+}, Co^{2+} from aqueous solutions. Pure CNTs (Tofighy and Mohammadi, 2011) and CNFs (Zheng et al., 2014) can be used as sorption agents. Preference of adsorption onto the oxidized CNT sheets can be ordered as $Pb^{2+} > Cd^{2+} > Co^{2+} > Zn^{2+} > Cu^{2+}$ (Tofighy and Mohammadi, 2011). In the research of Asmaly et al. (2015), adsorption capacities increase in a row CNFs, untreated CNTs, CNFs-Fe_2O_3. The maximal sorption capacity has a material CNTs-Fe_2O_3. In their research Dr. Bagheri et al. propose a CNTs-magnetic SiO_2 compound for finding Cu^{2+} and Hg^{2+}, detectable even by human eyes (Li et al., 2007; Khani et al., 2010; Song et al., 2010; Bagheri et al., 2011; Ganjali et al., 2011). Because of its widespread use in modern society, copper poses serious environmental problems and is potentially toxic to all living organisms. Highly sensitive and selective detection of Cu^{2+} or Cu^{+} has received much attention in recent years.

The environmental impact of uranium and its associated health effects on humans has recently become a major concern—mainly due to the use of weakened uranium in armor-piercing bullets (Konstantinou et al., 2013). Radioactive uranium (VI) is weakened and loaded unto silver hydroxide nanoparticles—MWCNTs, which have been identified as an excellent adsorbent for the removal of UO_2^{2+} ion from aqueous solutions (Zare et al., 2015). In this technique, the application of an ultrasonic wave during the synthesis of these nanomaterials led to properties, such as high surface area; enhanced removal percentage and high adsorption capacity; a high number of active centers; and a large number of vacant, available reactive surface sites in addition to metallic or semi-metallic behavior necessary for removal of

TABLE 1 | Summary of the efficiency of various hybrid materials.

Hybrid material	Toxic substances	Sorption capacity	References
CNTs-Sb	Pb^{2+}, Cd^{2+}	37.50 ng/g, 0.34 μg/g	(Ashrafi et al., 2014)
CNTs-AgOH	UO_2^{2+}	140 mg/g	(Zare et al., 2015)
CNTs sheets	Pb^{2+}, Cd^{2+}, Co^{2+}, Zn^{2+}, Cu^{2+}	117.65, 92.59, 85.74, 74.63, 64.93 mg/g	(Tofighy and Mohammadi, 2011)
CNTs-Ni	Methylene blue	312 mg/g	(Jin et al., 2018)
CNTs-SiO_2/Al_2O_3	NaCl	6.5 mg/g	(Santos et al., 2018)
CNFs-Fe_2O_3, CNTs-Fe_2O_3	Phenol	1.684, 2.778 mg/g	(Asmaly et al., 2015)
CNTs-Cu-BDC MOFs	Bisphenol A	164.1 mg/g	(Ahsan et al., 2019)
BN/rCNT	S	43 mg/g	(Xia et al., 2019)
CNF-GnP	Methylene blue, Congo red	1178.5. and 585.3 mg/g	(Yu et al., 2020)
PHO-CNF	U (VI)	1550.0 mg/g	(Lehtonen et al., 2020)
Hybrid material	**Dye**	**Photocatalytic activity**	**References**
CNTs-TiO_2	Reactive Black 5	90%/15 min	(Hamid et al., 2014)
CNTs-TiO_2-SiO_2	Bisphenol A, carbamazepine	50%/30 min	(Czech and Buda, 2015)
CNFs-Fe_3O_4	Methylene blue, Rhodamine B (RhB)	95%/15 min	(Ren et al., 2012; Si et al., 2012)
CNFs-TiO_2-ZnO	Methylene blue	40%/15 min	(Pant et al., 2013)
CNTs-$PbBiO_2Br$	Ciprofloxacin	50%/30 min	(Wang B. et al., 2019)
CNTs-MoS_2/SnS_2	Cr (VI)	100%/90 min	(Dong et al., 2019)
CNTs-CoSnS	Rhodamine B	91.7%/80 min	(Jeyagopal et al., 2020)
CNFs-Cu	Chlortetracycline hydrochloride	68.2%/60 min	(Wang H. et al., 2019)

various toxic materials (Fasfous and Dawoud, 2012; Sun et al., 2012; Chen et al., 2013; Tan et al., 2015).

Photocatalytic or adsorptive removal of organic pollutants has often been based on the example of phenol, that propagates to other toxic, organic, aromatic poisons (Ren et al., 2012; Si et al., 2012; Asmaly et al., 2015; Tho et al., 2018). Also, it can be methylene blue (Kim et al., 2011; Yu et al., 2011; Saud et al., 2015; Yu et al., 2015; Tho et al., 2018), 4-chlorophenol (Liu H. et al., 2009; Ihsanullah et al., 2015; Zouzelka et al., 2016), Remazol Black Brilliant (Shakouri et al., 2016), visible-light photocatalytic activity in the degradation of Rhodamine B (RhB) (Shang et al., 2013; Jiang et al., 2015), bisphenol A and carbamazepine (Czech and Buda, 2015), acetaminophen (Czech and Buda, 2015). In the submitted article (Ivnitski et al., 2008) nanocomposite CNT-TiO_2/SiO_2 was synthesized using the sol-gel method. Up to a 2.2 eV decrease in the bandgap was observed in the resulting material. Composites containing 8 mass % CNT exhibited maximum photoactivity. This article (Whitsitt and Barron, 2003) illustrates the decreased toxicity of this material. There is no limit to a number of components for a potential hybrid material. For example, TiO_2/CCNFs (Graphene/carbon composite nanofibers) TiO_2/ZnO/CNFs, CdS/TiO_2/CNFs, Ag-AgI-TiO_2/CNFs in articles (Kim et al., 2012; Pant et al., 2013, 2014; Yu et al., 2015), respectively show multicomponent hybrid materials. The composites showed high adsorption and photocatalytic activity under irradiation due to the synergetic effect between high adsorption ability, good conductivity of CNMs, and extraordinary plasmonic effect of nanoparticles.

FUTURE DIRECTIONS AND CONCLUDING REMARKS

Today, the scientific community has obtained promising results in the filamentous carbon based hybrid materials area. Hybrid materials are unique in that their properties are not the sum of the properties of the individual components, but their synergy. The hybrid structure provides an additional degree of freedom, which when developing new materials can lead to the emergence of new or improved properties (conductivity, sorption, catalytic, mechanical, optical, and magnetic properties). Currently, the problem of environmental protection remains one of the most urgent in the world. Hybrids based on carbon nanotubes and carbon nanofibers in combination with inorganic (metal oxide) nanoparticles can potentially solve the problems of water and air pollution, and recycling. With them being highly efficient sorbents and photocatalysts, higher productivity can be seen using less material. Therefore, this area of the research has high potential in the development of high-performance materials. Meanwhile, future work toward obtaining the compatibility between carbon nanomaterials and functional nanomaterials is essential to advance the use of these hybrids in electronic, magnetic and environmental applications. Additionally, a better understanding of the key features of forming carbon based hybrids (including by functionalizing the carbon surface) will the development of novel protocols that can generate ideas for more affordable and reliable approaches to the production of advanced hybrid materials.

AUTHOR CONTRIBUTIONS

EK, PK, and MS conceptualized the manuscript and completed the text. DA and AN drafted the manuscript.

FUNDING

This work was financially supported by a grant from the Russian Foundation for Basic Research (project No. 18-29-19053_mk).

REFERENCES

Aazam, E. S. (2014). Visible light photocatalytic degradation of thiophene using Ag–TiO_2/multi-walled carbon nanotubes nanocomposite. *Ceramics Int.* 40, 6705–6711. doi: 10.1016/j.ceramint.2013.11.132

Aghabozorg, M. H., Rashidi, A., and Mohammadi, S. (2016). Experimental investigation of heat transfer enhancement of Fe_2O_3-CNT/water magnetic nanofluids under laminar, transient and turbulent flow inside a horizontal shell and tube heat exchanger. *Exp. Thermal Fluid Sci.* 72, 182–189. doi: 10.1016/j.expthermflusci.2015.11.011

Ahmad, I., Fay, M., Kennedy, M., and Zhu, Y. Q. (2009). "Interfacial investigations and mechanical properties of carbon nanotube reinforcing Al_2O_3 nanocomposites," in *ICCM International Conferences on Composite Materials* (Nottingham). doi: 10.1016/j.wear.2010.03.009

Ahmad, I., Unwin, M., Cao, H., Chen, H., Zhao, A., Kennedy, A., et al. (2010). Multi-walled carbon nanotubes reinforced Al_2O_3 nanocomposites: mechanical properties and interfacial investigations. *Compos. Sci. Technol.* 70, 1199–1206. doi: 10.1016/j.compscitech.2010.03.007

Ahsan, A., Jabbari, V., Islam, T., Turley, R. S., Dominguez, N., Kim, H., et al. (2019). Sustainable synthesis and remarkable adsorption capacity of MOF/graphene oxide and MOF/CNT based hybrid nanocomposites for the removal of bisphenol a from water. *Sci. Total Environ.* 673, 306–317. doi: 10.1016/j.scitotenv.2019.03.219

Aqel, A., Abou El-Nour, K. M. M., Ammarc, R. A. A., and Al-Warthan, A. (2012). Carbon nanotubes, science and technology part (I) structure, synthesis and characterisation. *Arab. J. Chem.* 5, 1–23. doi: 10.1016/j.arabjc.2010.08.022

Ashrafi, A. M., Cerovac, S., Mudrić, S., Guzsvány, V., Husáková, L., and Urbanová, I. (2014). Antimony nanoparticle-multiwalled carbon nanotubes composite immobilized at carbon paste electrode for determination of trace heavy metals. *Sensors Actuators B Chem.* 191, 320–325. doi: 10.1016/j.snb.2013.08.087

Asmaly, H. A., Abussaud, B., Ihsanullah, Saleh, T. A., Gupta, V. K., and Atieh, M. A. (2015). Ferric oxide nanoparticles decorated carbon nanotubes and carbon nanofibers: from synthesis to enhanced removal of phenol. *J. Saudi Chem. Soc.* 19, 511–520. doi: 10.1016/j.jscs.2015.06.002

Bagheri, H., Ayazi, Z., and Aghakhani, A. (2011). A novel needle trap sorbent based on carbon nanotube-sol–gel for microextraction of polycyclic aromatic hydrocarbons from aquatic media. *Anal. Chim. Acta* 683, 212–220. doi: 10.1016/j.aca.2010.10.026

Baruah, S., and Dutta, J. (2009). Hydrothermal growth of ZnO nanostructures. *Sci. Technol. Adv. Mater.* 10:013001. doi: 10.1088/1468-6996/10/1/013001

Bauman, Y., Mishakov, I., Vedyagin, A., Rudnev, A., Plyusnin, P., Shubin, Y., et al. (2017). Promoting effect of Co, Cu, Cr and Fe on activity of Ni-based alloys in catalytic processing of chlorinated hydrocarbons. *Topics Catal.* 60, 171–177. doi: 10.1007/s11244-016-0729-1

Benad, A., Jürries, F., Vetter, B., Klemmed, B., Hübner, R., Leyens, C., et al. (2018). Mechanical properties of metal oxide aerogels. *Chem. Mater.* 30, 145–152. doi: 10.1021/acs.chemmater.7b03911

Bergmann, C. P., and Machado, F. M. (2015). "Carbon nanomaterials as adsorbents for environmental and biological applications," in: *Carbon Nanostructures*, eds C. P. Bergmann and F. M. Machado (Cham: Springer International Publishing). doi: 10.1007/978-3-319-18875-1

Bhat, D. (2006). "Chemical vapor deposition," in *Coatings technology: fundamentals, testing, and processing techniques,* ed A. A. Tracton (CRC Press). doi: 10.1201/9781420044089.ch36

Bogani, L., Danieli, C., Biavardi, E., Bendiab, N., Barra, A.-L., Dalcanale, E., et al. (2009). Single-molecule-magnet carbon-nanotube hybrids. *Angew. Chem. Int. Ed.* 48, 746–750. doi: 10.1002/anie.200804967

Bright, W. (2000). Note. *Lang. Soc.* 29, 155–155. doi: 10.1017/S0047404500001044

Byrappa, K., and Adschiri, T. (2007). Hydrothermal technology for nanotechnology. *Prog. Crystal Growth Charac. Mater.* 53, 117–166. doi: 10.1016/j.pcrysgrow.2007.04.001

Byrappa, K., and Yoshimura, M. (2013). *Handbook of Hydrothermal Technology.* Waltham, MA: Elsevier. doi: 10.1016/B978-0-12-375090-7.00002-5

Cao, A., Baskaran, R., Frederick, M. J., Turner, K., Ajayan, P. M., and Ramanath, G. (2003). Direction-selective and length-tunable in-plane growth of carbon nanotubes. *Adv. Mater.* 15, 1105–1109. doi: 10.1002/adma.200304738

Cendrowski, K., Jedrzejczak, M., Peruzynska, M., Dybus, A., Drozdzik, M., and Mijowska, E. (2014). Preliminary study towards photoactivity enhancement using a biocompatible titanium dioxide/carbon nanotubes composite. *J. Alloys Compd.* 605, 173–178. doi: 10.1016/j.jallcom.2014.03.112

Chen, J., Luo, H., Shi, H., Li, G., and An, T. (2014). Anatase TiO_2 nanoparticles–carbon nanotubes composite: optimization synthesis and the relationship of photocatalytic degradation activity of acyclovir in water. *Appl. Catal. A Gen.* 485, 188–195. doi: 10.1016/j.apcata.2014.08.004

Chen, L., Youji, L., Peng, X., Ming, L., and Mengxiong, Z. (2014). Carbon nanotube embedded mesoporous titania pore-hole inorganic hybrid materials with high thermal stability, improved crystallinity and visible-light driven photocatalytic performance. *Microporous Mesoporous Mater.* 195, 319–329. doi: 10.1016/j.micromeso.2014.04.029

Chen, S., Hong, J., Yang, H., and Yang, J. (2013). Adsorption of uranium (VI) from aqueous solution using a novel graphene oxide-activated carbon felt composite. *J. Environ. Radioact.* 126, 253–258. doi: 10.1016/j.jenvrad.2013.09.002

Chen, Y.-P., Bashir, S., and Liu, J. (2015). "Carbon capture and storage," in *Advanced Nanomaterials and Their Applications in Renewable Energy*, eds J. L. Liu, and S. Bashir (Waltham, MA: Elsevier), 329–366. doi: 10.1016/B978-0-12-801528-5.00007-5

Choi, C. H., Chung, M. W., Kwon, H. C., Chung, J. H., and Woo, S. I. (2014). Nitrogen-doped graphene/carbon nanotube self-assembly for efficient oxygen reduction reaction in acid media. *Appl. Catal. B: Environ.* 144, 760–766. doi: 10.1016/j.apcatb.2013.08.021

Choi, W. S., Yang, H. M., Koo, H. Y., Lee, H.-J., Lee, Y. B., Bae, T. S., et al. (2010). Smart microcapsules encapsulating reconfigurable carbon nanotube cores. *Adv. Funct. Mater.* 20, 820–825. doi: 10.1002/adfm.200901739

Cui, W., Du, F., Zhao, J., Zhang, W., Yang, Y., Xie, X., et al. (2011). Improving thermal conductivity while retaining high electrical resistivity of epoxy composites by incorporating silica-coated multi-walled carbon nanotubes. *Carbon N. Y.* 49, 495–500. doi: 10.1016/j.carbon.2010.09.047

Czech, B., and Buda, W. (2015). Photocatalytic treatment of pharmaceutical wastewater using new multiwall-carbon nanotubes/TiO_2/SiO_2 nanocomposites. *Environ. Res.* 137, 176–184. doi: 10.1016/j.envres.2014.12.006

Czech, B., Buda, W., Pasieczna-Patkowska, S., and Oleszczuk, P. (2015). MWCNT–TiO_2-SiO_2 nanocomposites possessing the photocatalytic activity in UVA and UVC. *Appl. Catal. B Environ.* 162, 564–572. doi: 10.1016/j.apcatb.2014.07.035

Dai, H. (2002). Carbon nanotubes: opportunities and challenges. *Surf. Sci.* 500, 218–241. doi: 10.1016/S0039-6028(01)01558-8

Das, R., Abd Hamid, S. B., Ali, M. E., Ismail, A. F., Annuar, M. S. M., and Ramakrishna, S. (2014). Multifunctional carbon nanotubes in water treatment: the present, past and future. *Desalination* 354, 160–179. doi: 10.1016/j.desal.2014.09.032

Deng, Y., Deng, C., Yang, D., Wang, C., Fu, S., and Zhang, X. (2005). Preparation, characterization and application of magnetic silica nanoparticle functionalized multi-walled carbon nanotubes. *Chem. Commun.* 44:5548–5550. doi: 10.1039/b511683j

Dillon, F. C., Moghal, J., Koós, A., Lozano, J. G., Miranda, L., Porwal, H., et al. (2015). Ceramic composites from mesoporous silica coated multi-wall carbon nanotubes. *Microporous Mesoporous Mater.* 217, 159–166. doi: 10.1016/j.micromeso.2015.06.024

Dong, R., Zhong, Y., Chen, D., Li, N., Xu, Q., Li, H., et al. (2019). Morphology-Controlled Fabrication of CNT@MoS_2/SnS_2 nanotubes for promoting photocatalytic reduction of aqueous Cr (VI) under visible light. *J. Alloys Compd.* 784, 282–292. doi: 10.1016/j.jallcom.2019.01.032

Downes, R. D., Hao, A., Park, J. G., Su, Y.-F., Liang, R., Jensen, B. D., et al. (2015). Geometrically constrained self-assembly and crystal packing of flattened and aligned carbon nanotubes. *Carbon N. Y.* 93, 953–966. doi: 10.1016/j.carbon.2015.06.012

Eder, D. (2010). Carbon nanotube–inorganic hybrids. *Chem. Rev.* 110, 1348–1385. doi: 10.1021/cr800433k

Fang, J., and Böhringer, K. F. (2008). "Self-assembly," in *Comprehensive Microsystems*, eds Y. B. Gianchandani, O. Tabata, and H. P. Zappe (Amsterdam: Elsevier), 403–429. doi: 10.1016/B978-044452190-3.00018-5

Fasfous, I. I., and Dawoud., J. N. (2012). Uranium (VI) sorption by multiwalled carbon nanotubes from aqueous solution. *Appl. Surf. Sci.* 259, 433–440. doi: 10.1016/j.apsusc.2012.07.062

Feng, L., Xie, N., and Zhong, J. (2014). Carbon nanofibers and their composites: a review of synthesizing, properties and applications. *Materials (Basel).* 7, 3919–3945. doi: 10.3390/ma7053919

Ganjali, M. R., Alizadeh, T., Azimi, F., Larjani,.B., Faridbod, F., and Norouzi,. P. (2011). Bio-mimetic ion imprinted polymer based potentiometric mercury sensor composed of nano-materials. *Int. J. Electrochem. Sci.* 6, 5200–5208.

Gao, C., Guo, Z., Liu, J.-H., and Huang, X.-J. (2012). The new age of carbon nanotubes: an updated review of functionalized carbon nanotubes in electrochemical sensors. *Nanoscale* 4, 1948–1963. doi: 10.1039/c2nr11757f

Ge, Y., Zhu, J., Lu, Y., Chen, C., Qiu, Y., and Zhang, X. (2015). the study on structure and electrochemical sodiation of one-dimensional nanocrystalline TiO_2@C nanofiber composites. *Electrochim. Acta* 176, 989–996. doi: 10.1016/j.electacta.2015.07.105

Ghiasvand, A., Yazdankhah, F., and Paull, B. (2020). Heating-, cooling- and vacuum-assisted solid-phase microextraction (HCV-SPME) for efficient sampling of environmental pollutants in complex matrices. *Chromatographia* 83, 531–540. doi: 10.1007/s10337-020-03869-0

Gomathi, A., Vivekchand, S. R. C., Govindaraj, A., and Rao, C. N. R. (2005). Chemically bonded ceramic oxide coatings on carbon nanotubes and inorganic nanowires. *Adv. Mater.* 17, 2757–2761. doi: 10.1002/adma.200500539

Grzelczak, M., Correa-Duarte, M. A., Salgueiriño-Maceira, V., Giersig, M., Diaz, R., and Liz-Marzán, L. M. (2006). Photoluminescence quenching control in quantum dot–carbon nanotube composite colloids using a silica-shell spacer. *Adv. Mater.* 18, 415–420. doi: 10.1002/adma.200501523

Guo, H., Jiang, S., Wang, C., Li, S., Feng, J., and Sun, H. (2019). Carbonaceous nanofibers-titanium dioxide nanocomposites: synthesis and use as a platform for removal of dye pollutants. *J. Wuhan Univ. Technol. Mater. Sci. Ed.* 34, 303–307. doi: 10.1007/s11595-019-2051-9

Hameed, A., Mukhtar, A., Shafiq, U., Qizilbash, M., Khan, M. S., Rashid, T., et al. (2019). Experimental investigation on synthesis, characterization, stability, thermo-physical properties and rheological behavior of MWCNTs-Kapok seed oil based nanofluid. *J. Mol. Liq.* 277, 812–824. doi: 10.1016/j.molliq.2019.01.012

Hamid, S. B. A., Tan, T. L., Lai, C. W., and Samsudin, E. M. (2014). Multiwalled carbon nanotube/TiO_2 nanocomposite as a highly active photocatalyst for photodegradation of reactive black 5 dye. *Chin J. Catal.* 35, 2014–2019. doi: 10.1016/S1872-2067(14)60210-2

Hang, B. T., Watanabe, T., Eashira, M., Okada, S., Yamaki, J., Hata, S., et al. (2005). The electrochemical properties of Fe_2O_3-loaded carbon electrodes for iron–air battery anodes. *J. Power Sources* 150, 261–271. doi: 10.1016/j.jpowsour.2005.02.028

Hassan, M. S., Amna, T., Hwang, I. H., and Khil, M.-S. (2013). One-step facile construction of high aspect ratio Fe_3O_4 decorated CNFs with distinctive porous morphology: potential multiuse expectations. *Colloids Surf. B Biointerfaces* 106, 170–175. doi: 10.1016/j.colsurfb.2013.01.040

Huang, J., Liu, Y., and You, T. (2010). Carbon nanofiber based electrochemical biosensors: a review. *Anal. Methods* 2:202. doi: 10.1039/b9ay00312f

Ihsanullah, Abbas, A., Al-Amer, A. M., Laoui, T., Al-Marri, M. J., Nasser, M. S., et al. (2016). Heavy metal removal from aqueous solution by advanced carbon nanotubes: critical review of adsorption applications. *Separation Purif. Technol.* 157, 141–161. doi: 10.1016/j.seppur.2015.11.039

Ihsanullah, Asmaly, H. A., Saleh, T. A., Laoui, T., Gupta, V. K., and Atieh, M. A. (2015). Enhanced adsorption of phenols from liquids by aluminum oxide/carbon nanotubes: comprehensive study from synthesis to surface properties. *J. Mol. Liq.* 206, 176–182. doi: 10.1016/j.molliq.2015.02.028

Iijima, S. (1991). Helical microtubules of graphitic carbon. *Nature* 354, 56–58. doi: 10.1038/354056a0

Ivnitski, D., Artyushkova, K., Rincón, R. A., Atanassov, P., Luckarift, H. R., and Johnson, G. R. (2008). Entrapment of enzymes and carbon nanotubes in biologically synthesized silica: glucose oxidase-catalyzed direct electron transfer. *Small* 4, 357–364. doi: 10.1002/smll.200700725

Jeyagopal, R., Chen, Y., Ramadoss, M., Marimuthu, K., Wang, B., Li, W., et al. (2020). A Three-dimensional porous CoSnS@CNT nanoarchitecture as a highly efficient bifunctional catalyst for boosted OER performance and photocatalytic degradation. *Nanoscale* 12, 3879–3887. doi: 10.1039/C9NR09588H

Jiang, Z., Jiang, D., Yan, Z., Liu, D., Qian, K., and Xie, J. (2015). A New Visible Light Active Multifunctional ternary composite based on TiO_2-In_2O_3 nanocrystals heterojunction decorated porous graphitic carbon nitride for photocatalytic treatment of hazardous pollutant and H_2 evolution. *Appl. Catal. B Environ.* 170–171, 195–205. doi: 10.1016/j.apcatb.2015.01.041

Jin, L., Zhao, X., Qian, X., and Dong, M. (2018). Nickel nanoparticles encapsulated in porous carbon and carbon nanotube hybrids from bimetallic metal-organic-frameworks for highly efficient adsorption of dyes. *J. Colloid Interf. Sci.* 509, 245–253. doi: 10.1016/j.jcis.2017.09.002

Khani, H., Rofouei, M. K., Arab, P., Gupta, V. K., and Vafaei, Z. (2010). Multi-walled carbon nanotubes-ionic liquid-carbon paste electrode as a super selectivity sensor: application to potentiometric monitoring of mercury ion (II). *J. Hazard. Mater.* 183, 402–409. doi: 10.1016/j.jhazmat.2010.07.039

Kim, C. H., Kim, B.-H., and Yang, K. S. (2011). TiO_2 nanoparticles loaded on graphene/carbon composite nanofibers by electrospinning for increased photocatalysis. *Carbon N. Y.* 50, 2472–2481. doi: 10.1016/j.carbon.2012.01.069

Kim, C. H., Kim, B.-H., and Yang, K. S. (2012). Visible light-induced photocatalytic activity of Ag-containing TiO_2/carbon nanofibers composites. *Synthetic Metals.* 161, 1068–1072. doi: 10.1016/j.synthmet.2011.03.017

Kim, S., Kim, M., Kim, Y. K., Hwang, S.-H., and Lim, S. K. (2014). Core–shell-structured carbon nanofiber-titanate nanotubes with ednhanced photocatalytic activity. *Appl. Catal. B Environ.* 148–149, 170–176. doi: 10.1016/j.apcatb.2013.10.051

Kiselev, G. O., Kiseleva, A. P., Ilatovskii, D. A., Koshevaya, E. D., Nazarovskaia, D. A., Gets, D. S., et al. (2019). Upconversion metal (Zr, Hf, and Ta) oxide aerogels. *Chem. Commun.* 55, 8174–8177. doi: 10.1039/C9CC02452B

Klein, K. L., Melechko, A. V., McKnight, T. E., Retterer, S. T., Rack, P. D., Fowlkes, J. D., et al. (2008). Surface characterization and functionalization of carbon nanofibers. *J. Appl. Phys.* 103:061301. doi: 10.1063/1.2840049

Kong, J., Wei, Y., Zhao, C., Toh, M. Y., Yee, W. A., Zhou, D., et al. (2014). Growth of Rutile TiO_2 on the convex surface of nanocylinders: from nanoneedles to nanorods and their electrochemical properties. *Nanoscale* 6, 4352–4360. doi: 10.1039/C3NR04308H

Konstantinou, M., Demetriou, A., and Pashalidis, I. (2013). Adsorption of hexavalent uranium on dunite. *Glob. NEST J.* 9, 229–236. doi: 10.30955/gnj.000446

Kumar, L., Zhang, T., Du, G., Li, W., Wang, Q., Datye, A., et al. (2008). Thermal properties of CNT-alumina nanocomposites. *Compos. Sci. Technol.* 68, 2178–2183. doi: 10.1016/j.compscitech.2008.04.001

Kumar, M., and Ando, Y. (2010). Chemical vapor deposition of carbon nanotubes: a review on growth mechanism and mass production. *J. Nanosci. Nanotechnol.* 10, 3739–3758. doi: 10.1166/jnn.2010.2939

Lee, C. J., Park, J., and Yu, J. A. (2002). Catalyst effect on carbon nanotubes synthesized by thermal chemical vapor deposition. *Chem. Phys. Lett.* 360, 250–255. doi: 10.1016/S0009-2614(02)00831-X

Lehtonen, J., Hassinen, J., Kumar, A. A., Johansson, L.-S., Mäenpää, R., and Pahimanolis, N. (2020). Phosphorylated cellulose nanofibers exhibit exceptional capacity for uranium capture. *Cellulose.* doi: 10.1007/s10570-020-02971-8. [Epub ahead of print].

Li, X., Liu, Y., Fu, L., Cao, L., Wei, D., Wang, Y., et al. (2007). Synthesis and device integration of carbon nanotube/silica core–shell nanowires. *J. Phys. Chem. C* 111, 7661–7665. doi: 10.1021/jp0689417

Li, Z., Gao, B., Chen, G. Z., Mokaya, R., Sotiropoulos, S., and Li Puma, G. (2011). Carbon nanotube/titanium dioxide (CNT/TiO_2) core–shell nanocomposites with tailored shell thickness, CNT content and photocatalytic/photoelectrocatalytic properties. *Appl. Catal. B Environ.* 110, 50–57. doi: 10.1016/j.apcatb.2011.08.023

Liang, R.-P., Wang, Z.-X., Zhang, L., and Qiu, J.-D. (2012). A label-free amperometric immunosensor for alpha-fetoprotein determination based on highly ordered porous multi-walled carbon nanotubes/silica nanoparticles array platform. *Sensors Actuators B Chem.* 166–167, 569–75. doi: 10.1016/j.snb.2012.03.011

Liu, H., Li, J., Liu, X., and Jiang, S. (2009). A novel multiwalled carbon nanotubes bonded fused-silica fiber for solid phase microextraction–gas chromatographic analysis of phenols in water samples. *Talanta* 78, 929–935. doi: 10.1016/j.talanta.2008.12.061

Liu, X., Wang, M., Zhang, S., and Pan, B. (2013). Application potential of carbon nanotubes in water treatment: a review. *J. Environ. Sci.* 25, 1263–1280. doi: 10.1016/S1001-0742(12)60161-2

Liu, Y., Jiang, W., Li, S., and Li, F. (2009). Electrostatic self-assembly of Fe_3O_4 nanoparticles on carbon nanotubes. *Appl. Surf. Sci.* 255, 7999–8002. doi: 10.1016/j.apsusc.2009.05.002

Miller, J. B., and Ko, E. I. (1996). Acidic properties of silica-containing mixed oxide aerogels:preparation and characterization of zirconia–silica and comparison to titania–silica. *J. Catal.* 159, 58–68. doi: 10.1006/jcat.1996.0064

Mishakov, I., Buyanov, R., Zaikovskii, V., Strel'tsov, I., and Vedyagin, A. (2008). Catalytic synthesis of nanosized feathery carbon structures via the carbide cycle mechanism. *Kinetics Catal.* 49, 868–872. doi: 10.1134/S00231584080 60116

Navrotskaya, A. G., Krivoshapkina, E. F., Perovskiy, I. A., Bauman, Y. I., Mishakov, I. V., Vedyagin, A. A., et al. (2019). Synthesis and properties of carbon–metal oxide nanomaterials. *J. Sol-Gel Sci. Technol.* 92, 449–457. doi: 10.1007/s10971-019-04974-9

Nessim, G. D. (2010). Properties, synthesis, and growth mechanisms of carbon nanotubes with special focus on thermal chemical vapor deposition. *Nanoscale* 2, 1306–1323. doi: 10.1039/b9nr00427k

Olmedo, M., Wang, C., Ryu, K., Zhou, H., Ren, J., Zhan, N., et al. (2011). Carbon nanotube memory by the self-assembly of silicon nanocrystals as charge storage nodes. *ACS Nano* 5, 7972–7977. doi: 10.1021/nn202377f

Pant, B., Barakat, N. A. M., Pant, H. R., Park, M., Saud, P. S., Kim, J.-W., et al. (2014). Synthesis and photocatalytic activities of CdS/TiO2 nanoparticles supported on carbon nanofibers for high efficient adsorption and simultaneous decomposition of organic dyes. *J. Colloid Interf. Sci.* 434, 159–166. doi: 10.1016/j.jcis.2014.07.039

Pant, B., Pant, H. R., Barakat, N. A. M., Park, M., Jeon, K., Choi, Y., et al. (2013). Carbon nanofibers decorated with binary semiconductor (TiO_2/ZnO) nanocomposites for the effective removal of organic pollutants and the enhancement of antibacterial activities. *Ceramics Int.* 39, 7029–7035. doi: 10.1016/j.ceramint.2013.02.041

Paula, A. J., Stéfani, D., Souza Filho, A. G., Kim, Y. A., Endo, M., and Alves, O. L. (2011). Surface chemistry in the process of coating mesoporous SiO_2 onto carbon nanotubes driven by the formation of SiOC bonds. *Chem. A Eur. J.* 17, 3228–3237. doi: 10.1002/chem.201002455

Pirajno, F. (2009). *Hydrothermal Processes and Mineral Systems*. East Perth: Springer. doi: 10.1007/978-1-4020-8613-7

Postnov, V. N., Rodinkov, O. V., Moskvin, L. N., Novikov, A. G., Bugaichenko, A. S., and Krokhina, O. A. (2016). From carbon nanostructures to high-performance sorbents for chromatographic separation and preconcentration. *Russian Chem. Rev.* 8, 115–138. doi: 10.1070/RCR4551

Poveda, R. L., and Gupta, N. (2016). *Carbon Nanofiber Reinforced Polymer Composites. SpringerBriefs in Materials*. Cham: Springer International Publishing.

Prasek, J., Drbohlavova, J., Chomoucka, J., Hubalek, J., Jasek, O., Adam, V., et al. (2011). Methods for carbon nanotubes synthesis—review. *J. Mater. Chem.* 21:15872. doi: 10.1039/c1jm12254a

Qian, H., Bismarck, A., Greenhalgh, E. S., and Shaffer, M. S. P. (2010). Carbon nanotube grafted silica fibres: characterising the interface at the single fibre level. *Compos. Sci. Technol.* 70, 393–399. doi: 10.1016/j.compscitech.2009.11.014

Rabti, A., Raouafi, N., and Merkoçi, A. (2016). Bio(Sensing) devices based on ferrocene–functionalized graphene and carbon nanotubes. *Carbon N. Y.* 108, 481–514. doi: 10.1016/j.carbon.2016.07.043

Rao, G. P., Lu, C., and Su, F. (2007). Sorption of divalent metal ions from aqueous solution by carbon nanotubes: a review. *Separation Purif. Technol.* 58, 224–231. doi: 10.1016/j.seppur.2006.12.006

Ren, T., Si, Y., Yang, J., Ding, B., Yang, X., Hong, F., et al. (2012). Polyacrylonitrile/polybenzoxazine-based Fe_3O_4@carbon nanofibers: hierarchical porous structure and magnetic adsorption property. *J. Mater. Chem.* 22, 15919–15927. doi: 10.1039/c2jm33214k

Sahoo, N. G., Rana, S., Cho, J. W., Li, L., and Chan, S. H. (2010). Polymer nanocomposites based on functionalized carbon nanotubes. *Prog. Polym. Sci.* 35, 837–867. doi: 10.1016/j.progpolymsci.2010.03.002

Santos, C., Lado, J. J., García-Quismondo, E., Rodríguez, I. V., Hospital-Benito, D., Palma, J., et al. (2018). Interconnected metal oxide CNT fibre hybrid networks for current collector-free asymmetric capacitive deionization. *J. Mater. Chem. A* 6, 10898–10908. doi: 10.1039/C8TA01128A

Sareen, D., Kaur, P., and Singh, K. (2014). Strategies in detection of metal ions using dyes. *Coord. Chem. Rev.* 265, 125–154. doi: 10.1016/j.ccr.2014.01.015

Sarkar, B., Mandal, S., Tsang, Y. F., Kumar, P., Kim, K.-H., and Ok, Y. S. (2018). Designer carbon nanotubes for contaminant removal in water and wastewater: a critical review. *Sci. Total Environ.* 612, 561–581. doi: 10.1016/j.scitotenv.2017.08.132

Saud, P. S., Pant, B., Alam, A.-M., Ghouri, Z. K., Park, M., and Kim, H.-Y. (2015). Carbon quantum dots anchored TiO_2 nanofibers: effective photocatalyst for waste water treatment. *Ceramics Int.* 41, 11953–11959. doi: 10.1016/j.ceramint.2015.06.007

Shakouri, A., Heris, S. Z., Etemad, S. G., and Mousavi, S. M. (2016). Photocatalytic activity performance of novel cross-linked PEBAX copolymer nanocomposite on Azo dye degradation. *J. Mol. Liq*. 216, 273–283. doi: 10.1016/j.molliq.2016.01.008

Shang, M., Wang, W., Sun, S., Gao, E., Zhang, Z., Zhang, L., et al. (2013). The design and realization of a large-area flexible nanofiber-based mat for pollutant degradation: an application in photocatalysis. *Nanoscale* 5:5036. doi: 10.1039/c3nr00503h

Si, Y., Ren, T., Li, Y., Ding, B., and Yu, J. (2012). Fabrication of magnetic polybenzoxazine-based carbon nanofibers with Fe_3O_4 inclusions with a hierarchical porous structure for water treatment. *Carbon N. Y.* 50, 5176–5185. doi: 10.1016/j.carbon.2012.06.059

Song, Y., Qu, K., Xu, C., Ren, J., and Qu, X. (2010). Visual and quantitative detection of copper ions using magnetic silica nanoparticles clicked on multiwalled carbon nanotubes. *Chem. Commun.* 46, 6572–6574. doi: 10.1039/c0cc01593h

Sun, C., Chen, S., and Li, Z. (2018). Controllable synthesis of Fe_2O_3-carbon fiber composites via a facile sol-gel route as anode materials for lithium ion batteries. *Appl. Surf. Sci.* 427, 476–484. doi: 10.1016/j.apsusc.2017.08.070

Sun, Y., Yang, S., Sheng, G., Guo, Z., and Wang, X. (2012). The removal of U(VI) from aqueous solution by oxidized multiwalled carbon nanotubes. *J. Environ. Radioact.* 105, 40–47. doi: 10.1016/j.jenvrad.2011.10.009

Sun, Z., Yuan, H., Liu, Z., Han, B., and Zhang, X. (2005). A highly efficient chemical sensor material for H_2S: α-Fe_2O_3 nanotubes fabricated using carbon nanotube templates. *Adv. Mater.* 17, 2993–2997. doi: 10.1002/adma.2005 01562

Tan, L., Liu, Q., Jing, X., Liu, J., Song, D., Hu, S., et al. (2015). Removal of Uranium (VI) ions from aqueous solution by magnetic cobalt ferrite/multiwalled carbon nanotubes composites. *Chem. Eng. J.* 273, 307–315. doi: 10.1016/j.cej.2015.01.110

Thakur, V. K., and Thakur, M. K. (2016). *Chemical Functionalization of Carbon Nanomaterials: Chemistry and Applications.* Boca Raton, FL: CRC Press.

Tho, N. H., Thy, T. T. M., Dat, P. T., Minh, V. C., and Sang, N. X. (2018). Physical adsorption and photocatalytic activity of titanium dioxide nanotube and graphene oxide composite. *VNU J. Sci.* 34:4770. doi: 10.25073/2588-1140/vnunst.4770

Tofighy, M. A., and Mohammadi, T. (2011). Adsorption of divalent heavy metal ions from water using carbon nanotube sheets. *J. Hazard. Mater.* 185, 140–147. doi: 10.1016/j.jhazmat.2010.09.008

Vashist, A., Ajeet, K., Atul, V., Vidya, S., Ghosal, A., Gupta, Y. K., et al. (2018a). Advances in carbon nanotubes-hydrogel hybrids in nanomedicine for therapeutics. *Adv. Healthc. Mater.* 7:e1701213. doi: 10.1002/adhm.201701213

Vashist, A., Kaushik, A., Vashist, A., Sagar, V., Ghosal, A., Gupta, Y. K., et al. (2018b). Study of MgO transformation into MgF_2 in the presence of CF_2Cl_2. *J. Serbian Chem. Soc.* 82, 523–538. doi: 10.2298/JSC161020037V

Wan, Y., Yang, Z., Xiong, G., Guo, R., Liu, Z., and Luo, H. (2015). Anchoring Fe3O4 nanoparticles on three-dimensional carbon nanofibers toward flexible high-performance anodes for lithium-ion batteries. *J. Power Sources* 294, 414–419. doi: 10.1016/j.jpowsour.2015.06.057

Wang, B., Liu, G., Ye, B., Ye, Y., Zhu, W., Yin, S., et al. (2019). Novel CNT/$PbBiO_2Br$ hybrid materials with enhanced broad spectrum photocatalytic activity toward ciprofloxacin (CIP) degradation. *J. Photochem. Photobiol. A: Chem.* 382:111901. doi: 10.1016/j.jphotochem.2019.111901

Wang, H., Zhang, J., Yuan, X., Jiang, L., Xia, Q., and Chen, H. (2019). Photocatalytic removal of antibiotics from natural water matrices and swine wastewater via Cu(I) coordinately polymeric carbon nitride framework. *Chem. Eng. J.* 392:123638. doi: 10.1016/j.cej.2019.123638

Whitsitt, E. A., and Barron, A. R. (2003). Silica coated single walled carbon nanotubes. *Nano Lett.* 3, 775–778. doi: 10.1021/nl034186m

Wu, Z., Dong, F., Zhao, W., Wang, H., Liu, Y., and Guan, B. (2009). The fabrication and characterization of novel carbon doped TiO_2 nanotubes, nanowires and nanorods with high visible light photocatalytic activity. *Nanotechnology* 20:235701. doi: 10.1088/0957-4484/20/23/235701

Wu, Z., Gao, S., Chen, L., Jiang, D., Shao, Q., Zhang, B., et al. (2017). Electrically insulated epoxy nanocomposites reinforced with synergistic core-shell SiO_2 @MWCNTs and montmorillonite bifillers. *Macromol. Chem. Phys.* 218:1700357. doi: 10.1002/macp.201700357

Xia, D., Li, H., Huang, P., Mannering, J., Zafar,. U., Baker, D., et al. (2019). Boron-nitride/carbon-nanotube hybrid aerogels as multifunctional desulfurisation agents. *J. Mater. Chem. A* 7, 24027–24037. doi: 10.1039/C9TA06599G

Yan, Y., Miao, J., Yang, Z., Xiao, F.-X., Yang, H. B., Liu, B., et al. (2015). Carbon nanotube catalysts: recent advances in synthesis, characterization and applications. *Chem. Soc. Rev.* 44, 3295–3346. doi: 10.1039/C4CS00492B

Yang, S., Li, J., Shao, D., Hu, J., and Wang, X. (2009). Adsorption of Ni(II) on oxidized multi-walled carbon nanotubes: effect of contact time, PH, foreign ions and PAA. *J. Hazard. Mater.* 166, 109–116. doi: 10.1016/j.jhazmat.2008.11.003

Yoshimura, M., and Byrappa, K. (2008). Hydrothermal processing of materials: past, present and future. *J. Mater. Sci.* 43, 2085–2103. doi: 10.1007/s10853-007-1853-x

Yu, D., Bai, J., Liang, H., Wang, J., and Li, C. (2015). Fabrication of a novel visible-light-driven photocatalyst Ag-AgI-TiO_2 nanoparticles supported on carbon nanofibers. *Appl. Surf. Sci.* 349, 241–250. doi: 10.1016/j.apsusc.2015.05.019

Yu, W.-W., Zhang, Q.-H., Shi, G.-Y., Li, Y.-G., and Wang, H.-Z. (2011). Preparation of Pt-loaded TiO_2 nanotubes/nanocrystals composite photocatalysts and their photocatalytic properties. *J. Inorg. Mater.* 26, 747–752. doi: 10.3724/SP.J.1077.2011.00747

Yu, Z., Hu, C., Dichiara, A. B., Jiang, W., and Gu, J. (2020). Cellulose nanofibril/carbon nanomaterial hybrid aerogels for adsorption removal of cationic and anionic organic dyes. *Nanomaterials* 10:169. doi: 10.3390/nano10010169

Zakaria, M. R., Akil, H. M., Abdul Kudus, M. H., and Othman, M. B. H. (2016). Compressive properties and thermal stability of hybrid carbon nanotube-alumina filled epoxy nanocomposites. *Compos. B Eng.* 91, 235–242. doi: 10.1016/j.compositesb.2016.01.013

Zare, F., Ghaedi, M., Daneshfar, A., Agarwal, S., Tyagi, I., Saleh, T. A., et al. (2015). Efficient removal of radioactive uranium from solvent phase using AgOH–MWCNTs nanoparticles: kinetic and thermodynamic study. *Chem. Eng. J.* 273, 296–306. doi: 10.1016/j.cej.2015.03.002

Zawisza, B., Skorek, R., Stankiewicz, G., and Sitko, R. (2012). Carbon nanotubes as a solid sorbent for the preconcentration of Cr, Mn, Fe, Co, Ni, Cu, Zn and Pb prior to wavelength-dispersive X-ray fluorescence spectrometry. *Talanta* 99, 918–923. doi: 10.1016/j.talanta.2012.07.059

Zaytseva, O., and Neumann, G. (2016). Carbon nanomaterials: production, impact on plant development, agricultural and environmental applications. *Chem. Biol. Technol. Agric.* 3:17. doi: 10.1186/s40538-016-0070-8

Zeng, S., Baillargeat, D., Ho, H.-P., and Yong, K.-T. (2014). Nanomaterials enhanced surface plasmon resonance for biological and chemical sensing applications. *Chem. Soc. Rev.* 43, 3426–3452. doi: 10.1039/c3cs60479a

Zhang, Y., Zhang, L., and Zhou, C. (2013). Review of chemical vapor deposition of graphene and related applications. *Acc. Chem. Res.* 46, 2329–2339. doi: 10.1021/ar300203n

Zhao, X., He, X. D., Sun, Y., and Wang, L. D. (2011). Carbon nanotubes doped SiO_2/SiO_2-PbO double layer high emissivity coating. *Mater. Lett.* 65, 2592–2594. doi: 10.1016/j.matlet.2011.06.030

Zheng, Q., Cai, Z., and Gong, S. (2014). Green synthesis of polyvinyl alcohol (PVA)–cellulose nanofibril (CNF) hybrid aerogels and their use as superabsorbents. *J. Mater. Chem. A* 2, 3110–3118. doi: 10.1039/C3TA14642A

Zouzelka, R., Kusumawati, Y., Remzova, M., Rathousky, J., and Pauporté, T. (2016). Photocatalytic activity of porous multiwalled carbon nanotube-TiO_2 composite layers for pollutant degradation. *J. Hazard. Mater.* 317, 52–59. doi: 10.1016/j.jhazmat.2016.05.056

Conflict of Interest: The authors declare that the research was conducted in the absence of any commercial or financial relationships that could be construed as a potential conflict of interest.

frontiers in Chemistry

MINI REVIEW
published: 10 July 2020
doi: 10.3389/fchem.2020.00588

Promethium: To Strive, to Seek, to Find and Not to Yield

Veronika Elkina[1,2]* **and Mikhail Kurushkin**[2]

[1] School #197, Saint Petersburg, Russia, [2] Chemistry Education Research and Practice Laboratory, SCAMT Institute, ITMO University, Saint Petersburg, Russia

Promethium (Pm), element #61, got its name from the Greek Titan Prometheus, who stole fire from Zeus and passed it to people. The only element in the lanthanide series of the periodic table with no stable isotopes, Pm has found an impressive number of applications since its announcement in 1947 after World War II. Despite promethium having 38 known isotopes, ^{147}Pm is by far the most utilized and useful one. Promethium is used in long-life atomic batteries for satellites or space probes, satellite-to-submarine laser communication systems, "cosmic clocks" for the measurement of cosmic rays lifetime, monitoring of the changes in water content of citrus leaves caused by wetting and drying cycles in the soil, radiotherapy, and even for prevention of dandruff, to name but a few applications. During the Moon expeditions, Pm was used to illuminate instruments in the Apollo landing modules; currently it is used during preparations for long-term interplanetary missions (e.g., Mars) to simulate space conditions on Earth. This mini review offers a comprehensive illustration of promethium's history, synthesis techniques, properties, and its major applications in science, technology, and everyday life.

Keywords: power sources, portable x-ray sources, lasers, healthcare, illumination, measurements

Edited by:
Soumyajit Roy,
Indian Institute of Science Education and Research Kolkata, India

Reviewed by:
Mark Stoyer,
Lawrence Livermore National Laboratory (DOE), United States
Viktor Keskinov,
Saint Petersburg State Institute of Technology, Russia

Correspondence:
Veronika Elkina
veronikaelkinad@gmail.com

Specialty section:
This article was submitted to Inorganic Chemistry, a section of the journal Frontiers in Chemistry

Received: *23 January 2020*
Accepted: *08 June 2020*
Published: *10 July 2020*

Citation:
Elkina V and Kurushkin M (2020) Promethium: To Strive, to Seek, to Find and Not to Yield. Front. Chem. 8:588. doi: 10.3389/fchem.2020.00588

INTRODUCTION

Element #61 was originally called "prometheum", at the suggestion of the wife of one of its discoverers, in honor of the mythical hero Prometheus (Promethium, the New Name for Element 61, 1948), who stole fire from Zeus and passed it to people (Greenwood and Earnshaw, 1997a). The name was meant to emphasize not only the method of obtaining an element using nuclear fission energy, but also the threat of punishment to the instigators of war. According to Greek mythology, Zeus punished Prometheus by chaining him to a rock to be routinely tortured by an eagle (Cantrill, 2018). In 1950, the International Atomic Balance Commission gave element #61 its modern name "promethium," while all the old names, illinium (Harris et al., 1926), florence, cyclonium, and prometheum, were rejected.

Promethium (Pm) is well-known as the only element in the lanthanide series of the periodic table with no stable isotopes (Burke, 2019); it occurs in the Earth's crust in only tiny amounts in some uranium ores. It undergoes radioactive decay of two types: electron capture and negative beta emission (Greenwood and Earnshaw, 1997b). All the promethium, which might once have existed on the Earth when it formed, would have vanished within 10,000 years.

GRAPHICAL ABSTRACT | The hero of our mini review, spaceman Prometheus, with different accessories representing the versatility of promethium the element.

SYNTHETIC PROMETHIUM

Promethium, the final lanthanide to be added to the periodic table, acquired its undeniable evidence of existence in 1945 (a discovery which was not made public until 1947) by USA chemists Jacob Marinsky, Lawrence Glendenin and Charles Coryell (Guillaumont, 2019), who isolated the radioactive isotopes ^{147}Pm and ^{149}Pm from uranium fission products at Clinton Laboratories (TN, USA). The thermal neutron-induced fission of ^{235}U has a ^{147}Pm cumulative yield (CY) of 2.25% (England and Rider, 1994). This means for every 100 fissions of ^{235}U, there are 2.25 atoms of ^{147}Pm produced. The ^{149}Pm CY for thermal neutron-induced fission of ^{235}U is only 1.08%. Ion-exchange chromatography was later utilized in order to convincingly establish Pm's identification (McGill, 2000).

Key promethium isotopes are given in **Table 1**; their applications will be described throughout the main body of the present mini review.

To date, 38 different isotopes of Pm are known, ranging in half-life from <1 μs to 17.7(4) years (^{145}Pm) (May and Thoennessen, 2012; McLennan, 2018). For a detailed description of promethium isotopes that have been discovered to date, see (May and Thoennessen, 2012).

Fission products in nuclear fuel used to normally be the main source of ^{147}Pm (Broderick et al., 2019). Until the 1970s, Oak Ridge National Laboratory was rich with ^{147}Pm that had been obtained through a traditional method at Hanford, Washington (McLennan, 2018). Today, the Oak Ridge National Laboratory inventory is no longer storing promethium as the processing of nuclear fuel in the USA has been stopped, and there are no substantial sources of ^{147}Pm at present. Nevertheless, identically to ^{155}Eu and ^{171}Tm, there is an opportunity to produce ^{147}Pm by neutron capture of ^{146}Nd to ^{147}Nd, which β-decays to ^{147}Pm, through β^- decay of ^{147}Nd, its predecessor with a shorter half-life of nearly 11 d (Knapp, 2008).

MAIN PHYSICAL AND CHEMICAL PROPERTIES

In 1974, metallic promethium was reduced from promethium oxide with metallic thorium at 1,600°C with further distillation of promethium into a quartz dome. Using this method, the melting temperature and the phase transformation temperature of promethium were established: 1042 ± 5°C and 890 ± 5°C, respectively (Angelini and Adair, 1976). Promethium's boiling point is $\sim$3,000°C (McLennan, 2018).

The ionic radius of promethium is 110 pm (in 8-fold coordination), which is very similar to its neighboring elements, neodymium (112 pm) and samarium (108 pm) (McLennan, 2018). Hence, the close similarity in ionic radii and the same common oxidation state (+3) make it difficult to separate Pm from Nd and Sm (Balaram, 2019). When no stable isotopes exist, deductions regarding chemical properties may be drawn from known chemical surrogates (in case of promethium, other rare earth elements) (Radiological Contamination of the Oceans: Oversight Hearings Before the Subcommittee on Energy and the Environment of the Committee on Interior and Insular Affairs and House of Representatives, Ninety-fourth Congress, Second Session on Matters Pertaining to, 1976). The main Pm^{3+} compounds include: $Pm(OH)_3$ (light brown), Pm_2O_3 (yellow white), $PmCl_3$ (yellow), $Pm(NO_3)_2$ (pink), PmF_3, $Pm_2(C_2O_4)_3 \cdot 10H_2O$ and $Pm_2(SO_4)_3$ (Da and Jincheng, 2000; Sharma, 2001). Pm can also represent an oxidation state of +2. Thermodynamic properties of Pm^{2+} indicate that, similarly to $NdCl_2$ and $SmCl_2$, stable PmF_2, $PmCl_2$ and PmI_2 can also be obtained (Sharma, 2001).

POWER SOURCES

Promethium-147 is used in long-life atomic batteries (Flicker et al., 1964), in which small-scale promethium samples are inserted into a semiconductor matrix to transform their beta emission into electricity (Matheson, 1975). The mean beta energy of ^{147}Pm is 62 keV (Shao et al., 2017). Pm batteries can be used in cases where other kinds of batteries would be extremely heavyweight, e.g., satellites or space probes (Vl, 1956). Radioisotope batteries are usually either thermoelectric (containing Pu or Am) (Wiss et al., 2017) based on the heat generated from radioactive decay, or betavoltaic (alphavoltaic) based on electron/hole pair generation in a semiconductor (such as ^{147}Pm or other isotopes like tritium or ^{63}Ni) (Gale et al., 1975; Purdy, 1986; Spencer and Chandrashekhar, 2013; Murphy et al., 2019; Xue et al., 2019). Betavoltaic batteries, compared with thermoelectric batteries (Matheson, 1975), are characterized by a smaller size and a more reasonable price. Betavoltaics also have the characteristic of lower power or current (than thermoelectric or even Li-ion batteries for example) (Gale et al., 1975; Chandrashekhar et al., 2006, 2007; Olsen et al., 2012; Murphy et al., 2019). They are useful when low power is needed for periods of years. Unfortunately, their service period does not presently exceed ten years. Newest advances in the technology of betavoltaics, however, are expected to prolong the service period to fifteen years. For example, Betacel®, a betavoltaic battery, satisfies both corrosion and cremation fire standards and is suitable for clinical use (Spencer and Chandrashekhar, 2012) and in cardiac pacemakers (Smith et al., 1975; Purdy, 1986). Promethium-147 powered microbatteries with a lifetime of up to

TABLE 1 | Key promethium isotopes.

Isotope	Year of discovery	Author	Laboratory	References	Half-life	Main decay mode (Nuclear Data Center at KAERI Table of Nuclides, 2020)	Specific activity, TBq/g (Code of Federal Regulations Title 49, 2009, Transportation, Pt. 100-185, page 656, 2009)
^{142}Pm	1959	I. Gratot	Orsay	Gratot et al., 1959	40.5(5) s	e+	N/A
^{143}Pm	1952	V. Kistiakowsky	Berkeley	Kistiakowsky, 1952	265(7) d	EC	1.3×10^2
^{144}Pm	1952	V. Kistiakowsky	Berkeley		363(14) d	EC	9.2×10^1
^{147}Pm	1947	J.A. Marinsky	Oak Ridge	Marinsky et al., 1947	2.6234(2) yr	β-	3.4×10^1
^{149}Pm	1947	J.A. Marinsky	Oak Ridge		53.08(5) h	β-	1.5×10^4

5 years and an average power density of 5 mW/cm^3 are suitable candidates for implantable pacemakers (Gasper and Fester, 1975; Rosenkranz, 1975; Duggirala et al., 2007), where useful electrical power is converted from isotopic decay energy (Wheelwright and Fuqua, 1975; Greatbatch, 1980).

Despite its vast application in betavoltaic batteries, promethium can also be used in radioisotope thermoelectric generators to provide electricity for space probes (Choppin et al., 2013). Finally, promethium has also found its use as a direct lightly shielded isotopic heat source (Fullam and Van Tuyl, 1969; McNeilly and Roberts, 1969).

PORTABLE X-RAY SOURCES

Although promethium-147 has low gamma emission (Artun, 2017), it is a source of soft β-rays (Malson et al., 1980). Irradiation of heavy elements with β-particles generates X-ray radiation (Ellis-Davies et al., 1985; Labrecque et al., 1986), hence, promethium must be handled strictly according to safety regulations. X-ray radiation is generated when a particular beta emitter, ^{147}Pm (Sumiya et al., 1993; Llasat et al., 2017), interacts with certain d-elements like cobalt, iridium, rhodium, platinum, nickel, gold, and mixtures thereof. Radiation sources typically consist of a substrate having a non-radioactive metal surface, a metal layer of a radioactive isotope ^{147}Pm, and a non-radioactive metal with a high atomic number.

MEASUREMENTS

Based on promethium-147, a commonly used energy beta source, sensors have been developed that can measure films as thin as 2.54–5.08 μm (Sneller, 1979; Brown and Coats, 1981). For instance, Adaptive Technologies Industries, Inc. (ATI) offers a modern technique based on solid-state digital beta gauge, which allows achieving real-time measurements. In ATI gauges, β-particles attenuation is employed for thickness or mass measurement of materials including plastics, paper and metal. A radiation source and a radiation detector are the two main constituents of an ATI gauge. A bulk sample of Pm is placed above the investigated material and a detector is placed below. The detector counts the amount of radiation that passes through the material. If the metal sheet becomes too thin, more radiation passes through. The technique is also employed for coat and basis weight measurements (Typpo, 2000; How beta gauge works, 2019).

Promethium-147 as a radiation source is also used to determine the thickness of sour orange and sweet lime citrus leaves that are 10–40 mg/cm^2 thick. Interestingly, this β-ray gauging technique can also measure the changes in water content of leaves caused by wetting and drying cycles that occur in the soil (Bielorai, 1968). Alternatively, the isotopes ^{14}C and ^{204}Tl have also been used for various leaves mass thickness measurements (Takechi and Furudoi, 1970; Saini and Rathore, 1983). The attenuation of β-radiation from ^{147}Pm can be used in miniature probes for real-time measurements of dust suspension in the 0.1–2.0 kg/m^3 concentration range (Slezak and Buckius, 1983). Moreover, promethium-147 is used as an ionization source in electron-capture detectors for analyzing pesticides in water environments (Lubkowitz and Parker, 1971).

Another application of promethium as a pure electron-capture detector is the measurement of the mean confinement time of cosmic rays before their escape from the Galaxy (i.e., their lifetime), which is an important parameter in evaluating the sources and propagation of cosmic rays within the Galaxy. It is measured by comparing the cosmic-ray abundances of several Tc and Pm isotopes to those of neighboring, stable isotopes. The radioactive isotopes, which are most useful (^{143}Pm and ^{144}Pm) in "cosmic clocks," are those with decay times comparable to the confinement time (Drach and Salamon, 1987).

LASERS

Pm is applied in lasers that are used to communicate with submerged submarines (satellite-to-submarine laser communication systems or simply SLC). The fluorescence spectrum of Pm^{3+} is dominated by the transitions at nominally 933 and 1098 nm (Krupke et al., 1987), respectively. At room temperature, these manifolds are thermally unoccupied, a fact that enables four-level laser action at $T \approx 295$ K. The high efficiency of Pm lasers and operation at 919 nm make the Pm^{3+} ion suitable for use in fully solid-state SLC laser transmitters (Shinn et al., 1988). Solid-state promethium lasers have been reported to be pumped by 2-D diode arrays operating at 770 nm (McShea et al., 1988).

ILLUMINATION

Self-luminous sources of light for LCD watches that include a promethium-containing fluorescent layer are among the most widespread (Takami, 1980). Promethium, being usually found in the oxidized form, is not detrimental for the phosphor lattice and the material's luminosity decreases relatively slowly (Takami and Matsuzawa, 1981). Moreover, paints based on promethium isotopes, having a half-life about more than 2 years, are safer than radium alternatives. Promethium-147 is widely used not only as night lighting devices, but also as self-sustaining light sources by activating zinc sulfide phosphor with β-radiation of ^{147}Pm (Ravi et al., 2001). Another use of Pm is in phosphors for highlighting various labels without energy consumption. After the discovery of radioactivity, radium acted in this capacity until its harm was revealed. Promethium compounds, however, turned out to be harmless radioactive phosphors (Rafi and Rosli, 2018). Therefore, promethium found its place in fluorescent paints. The promethium compounds used to make the characteristic "medium spring green" (pale blue-green) (Emsley, 2011) glow are usually Pm_2O_3 or $Pm(OH)_3$ (Takami and Matsuzawa, 1981; Ravi et al., 2001; Rafi and Rosli, 2018). For example, promethium was used to illuminate instruments in the Apollo landing modules during the Moon expeditions (English et al., 1973).

HEALTHCARE

Sealed ^{147}Pm does not represent danger due to being easily shielded (Drumheller, 1968); contrariwise, improperly stored promethium becomes an environmental hazard.

The effect of promethium intake has been vastly studied on animals, including rats, rabbits, pigs, and dogs. When absorbed by rats, promethium is predominantly retained in the bones as well as in the tips of the villi of the distal small intestine of the gastrointestinal tract, with half the dose remaining a week after probing (Sullivan et al., 1984). More recent experiments on rats' skin illustrated the ways of the radionuclides penetration (Kassai et al., 2003). To identify the penetration of Pm^{3+} ions into the cell membrane, as well as the extracellular and cellular distribution of promethium, a study was conducted on the smooth muscle of the rabbit aorta. In the course of the study, it was found that significant amounts of promethium do not accumulate inside and are not excreted from the cells, but its distribution is properly described by desorption from fibers accessible from the surface (Weiss, 1996). When pig skin is exposed to surface doses of promethium (up to 10 krads), β-particles do not affect the nature of the dose dependence of the parameters of the epidermal basal cells (Zavialov et al., 1977). When absorbed by pigs, it has been shown that most of promethium is retained in the bones similarly to the results observed in case of rats (Sullivan et al., 1984). Five and a half months after beagles were exposed to Pm_2O_3 aerosols, promethium was found in the organs of dogs mainly in the lungs (44%), as well as in the skeleton (24%) and in the liver (22%) (Stuart, 1966).

Surprisingly, since early 80s little has been discovered regarding the effect promethium has on human organs; however, bone tissues are possible candidates (Metabolic data for promethium, 1981). Promethium-147 can be identified and analyzed in urine and feces using a simple co-precipitation technique, which applies mainly to the excrements of former employees of promethium processing plants (Berk and Moghissi, 1985). In the case of inhalation of promethium-containing luminous paints, most of it settles in the lungs, practically not excreted. A few days after inhalation due to phagocytosis, the activity is observed as "hotspots" in macrophages in bronchial epithelium and alveolar walls, mostly at the periphery of the lung lobes (Kraus, 1976). If swallowed, promethium-147 passes through the digestive tract without being absorbed into the walls of the lower large intestine; radiation doses can be measured by examining human feces (Vennart, 1967).

In medicine, promethium beta therapy can cure lumbosacral radiculitis (Purdy, 1986). At a Geneva hospital, ^{142}Pm was used in an *in vivo* generator for preclinical positron emission tomography (Beyer and Ruth, 2003). Promethium-149, in turn, as a medium-energy beta emitter, is a suitable radilolanthanide for receptor-targeted radiotherapy (Studer et al., 2019). A great advantage of ^{149}Pm is its low intensity emission of imageable γ-rays (286 keV), which provides *in vivo* tracking of the therapeutic dose (Hu et al., 2002).

Furthermore, promethium can prevent hair loss, promote hair regrowth and black hair formation as well as remove or even prevent dandruff (Kim and Choi, 2014).

CONCLUSIONS, OUTLOOK, AND OUTER SPACE

Here, we have summarized the history, synthesis techniques and the major applications of promethium. Although peak interest in Pm was in the 1980's, it has recently been receiving renewed attention: for instance, promethium is featured among strategic materials in the 2013 model year Ford Fiesta, Focus, Fusion and F-150 (Field et al., 2017).

The future research on Pm is expected to bring us into the outer space. Promethium is used as a prototype radiation source in attempts to simulate space conditions on Earth (Hellweg et al., 2007). Since cosmic radiation is identified as the most hazardous for the health of crew participating in long-term interplanetary missions (e.g., Mars), ^{147}Pm radiation is used in biological experiments aimed at determination of the allowed irradiation dose range of human embryonic kidney (HEK) cells survival (Hellweg et al., 2008).

In 2004, the possible identification of Pm in the spectra of HD 965 and HD 101065 was reported (Cowley et al., 2004). Recognition was based on statistical and traditional line-identification methods (Fivet et al., 2007). Promethium is also occasionally found as few atoms from uranium decay detected in the HR 465 star spectrum of Andromeda. The star is evidently manufacturing Pm on its surface, taking into account that no Pm isotope with a half-life longer than that of ^{145}Pm can exist. Thus, the elusive origin of Pm in outer space is yet to be explained (Emsley, 2011).

AUTHOR CONTRIBUTIONS

VE was responsible for literature search and analysis and initial draft preparation. MK was responsible for formulating the mini review objectives and finalizing the initial draft. Both authors contributed to the article and approved the submitted version.

ACKNOWLEDGMENTS

The authors acknowledge Diana Savchenko for the creation of a brilliant graphic abstract. The inspiration for the title was drawn from Alfred Tennyson's Ulysses poem (Tennyson, 1842).

REFERENCES

Angelini, P., and Adair, H. L. (1976). *Preparation of 147Pm Metal and the Determination of the Melting Point and Phase Transformation Temperatures.* Available online at: http://inis.iaea.org/search/search.aspx?orig_q=RN:08280872 (accessed June 06, 2020).

Artun, O. (2017). Investigation of the production of promethium-147 via particle accelerator. *Indian J. Phys.* 91:909. doi: 10.1007/s12648-0170997-z

Balaram, V. (2019). Rare earth elements: a review of applications, occurrence, exploration, analysis, recycling, and environmental impact. *Geosci. Front.* 10, 1285–1303. doi: 10.1016/j.gsf.2018.12.005

Berk, H. W., and Moghissi, J. W. (1985). Bioassay of radiopromethium. *Nucl. Chem. Waste Manag.* 5, 349–350. doi: 10.1016/0191-815X(85)90011-7

Beyer, G. J., and Ruth, T. J. (2003). The role of electromagnetic separators in the production of radiotracers for bio-medical research and nuclear medical application. *Nucl. Instruments Methods Phys. Res. Sect. B Beam Interact. with Mater. Atoms* 204, 694–700. doi: 10.1016/S0168-583X(03)00489-0

Bielorai, H. (1968). Beta-ray gauging technique for measuring leaf water content changes of citrus seedlings as affected by the moisture status in the soil. *J. Exp. Bot.* 19, 489–495. doi: 10.1093/jxb/19.3.489

Broderick, K., Lusk, R., Hinderer, J., Griswold, J., Boll, R., Garland, M., et al. (2019). Reactor production of promethium-147. *Appl. Radiat. Isot.* 144, 54–63. doi: 10.1016/j.apradiso.2018.10.025

Brown, J., and Coats, M. (1981). Improved accuracy in thin-film gaging. *Mod. Plast.* 58, 66–67.

Burke, M. (2019). Filling the promethium gap. *Chem. Ind.* 83:15.

Cantrill, S. (2018). Promethium puzzles. *Nat. Chem.* 10:1270. doi: 10.1038/s41557-018-0179-4

Chandrashekhar, M. V. S., Duggirala, R., Lal, A., and Spencer, M. G. (2007). "4H SiC beta-powered temperature transducer," *SENSORS, 2007 IEEE* (Atlanta, GA), 942–945. doi: 10.1109/ICSENS.2007.4388558

Chandrashekhar, M. V. S., Thomas, C. I., Li, H., Spencer, M. G., and Lal, A. (2006). Demonstration of a 4H SiC betavoltaic cell. *Appl. Phys. Lett.* 88, 1–3. doi: 10.1063/1.2166699

Choppin, G., Liljenzin, J.-O., Rydberg, J., and Ekberg, C. (2013). "Chapter 12 - The Origin of the Universe and Nucleosynthesis," in *Radiochemistry and Nuclear Chemistry (Fourth Edition)*, eds G. Choppin, J.-O. Liljenzin, J. Rydberg, and C. Ekberg (Oxford: Academic Press), 339–372. doi: 10.1016/B978-0-12-405897-2.00012-4

Code of Federal Regulations Title 49, Transportation, Pt. 100–185 (2009). Available online at: https://books.google.ru/books?id=x2U2QDLpwpIC&pg=PA656&lpg=PA656&dq=143pm+specific+activity&source=bl&ots=R8t1vvBkJk&sig=ACfU3U1fidnsusTnYtw5JLdIqzQGpvkovA&hl=ru&sa=X&ved=2ahUKEwi8zveFhbbpAhVuwqYKHcx3CUMQ6AEwCXoECAkQAQ#v=onepage&q=143pmspecificactivity&f=false (accessed June 06, 2020).

Cowley, C. R., Bidelman, W. P., Hubrig, S., Mathys, G., and Bord, D. J. (2004). On the possible presence of promethium in the spectra of HD∼101065 (Przybylski's star) and HD∼965. *Astron. Astrophys.* 419, 1087–1093. doi: 10.1051/0004-6361:20035726

Da, S., and Jincheng, L. (2000). *Cast Irons Containing Rare Earths*. Beijing: Tsinghua University Academic Treatise Available online at: https://books.google.ru/books?id=cJzNDgAAQBAJ&pg=PA33&lpg=PA33&dq=pm2o3$+$COLOUR&source$=$bl&ots$=$vTHEkf_Iqy&sig$=$ACfU3U1GwxJ5Pt4NWgJCTyRrAqUOUtO0nA&hl$=$ru&sa$=$X&ved$=$2ahUKEwjSiPjmorbpAhXE8qYKHaMWCTQQ6AEwBHoECAoQAQ#v=onepage&q=pm2o3COLOUR&f=false (accessed June 06, 2020).

Drach, J., and Salamon, M. H. (1987). Elemental technetium and promethium as cosmic-ray clocks. *Astrophys. J.* 319, 237–246. doi: 10.1086/165449

Drumheller, K. (1968). *Properties and Fabrication of Promethium Fuel Orms*. V 14, 156–170. Available online at: https://www.scopus.com/inward/record.uri?eid=2-s2.0-0014401099&partnerID=40&md5=ff361de862f3a049cd3f0bbe41408110 (accessed June 06, 2020).

Duggirala, R., Tin, S., and Lal, A. (2007). "3D silicon betavoltaics microfabricated using a self-aligned process for 5 Milliwatt/CC Average, 5 year lifetime microbatteries," in *IEEE*, 279–282. doi: 10.1109/SENSOR.2007.4300123

Ellis-Davies, G. C. R., Massey, S., and Malcolme-Lawes, D. J. (1985). Beta-induced fluorescence spectra of some aromatic systems. *J. Chem. Soc. Faraday Trans. 2 Mol. Chem. Phys.* 81, 581–590. doi: 10.1039/f29858100581

Emsley, J. (2011). *Nature's Building Blocks: An A-Z Guide to the Elements*. OUP Oxford Available online at: https://books.google.ru/books?id=dGZaDwAAQBAJ (accessed June 06, 2020).

England, T. R., and Rider, B. F. (1994). *LA-UR-94-3106 ENDF-349 Evaluation and Compilation of Fission Product Yields 1993*. Available online at: https://t2.lanl.gov/nis/publications/endf349.pdf (accessed June 06, 2020).

English, R. A., Benson, R. E., Bailey, J. V., and Barnes, C. M. (1973). *Protection Against Radiation*. Available online at: https://ntrs.nasa.gov/search.jsp?R=19730010172 (accessed June 06, 2020).

Field, F. R., Wallington, T. J., Everson, M., and Kirchain, R. E. (2017). Strategic materials in the automobile: a comprehensive assessment of strategic and minor metals use in passenger cars and light trucks. *Environ. Sci. Technol.* 51, 14436–14444. doi: 10.1021/acs.est.6b06063

Fivet, V., Quinet, P., Biémont, É., Jorissen, A., Yushchenko, A., and Eck, S. (2007). Transition probabilities in singly ionized promethium and the identification of Pm II lines in Przybylski's star and HR 465. *Mon. Not. R. Astron. Soc.* 380, 771–780. doi: 10.1111/j.1365-2966.2007.12118.x

Flicker, H., Loferski, J. J., and Elleman, T. S. (1964). Construction of a promethium-147 atomic battery. *IEEE Trans. Electron Devices* 11, 2–8. doi: 10.1109/T-ED.1964.15271

Fullam, H. T., and Van Tuyl, H. H. (1969). Promethium technology. A review. *Isot. Radiat. Technol.* 7, 207–221.

Gale, R. W., Glew, R. W., and Bryant, F. J. (1975). The electron-voltaic effect in CdS/Cu2S heterojunctions. *Solid. State. Electron.* 18, 839–844. doi: 10.1016/0038-1101(75)90004-0

Gasper, K. A., and Fester, K. E. (1975). "Cardiac pacemaker power sources," in *United States: Inst of Electrical and Electronics Engineers, Inc*. Available online at: http://inis.iaea.org/search/search.aspx?orig_q=RN:07237246 (accessed June 06, 2020).

Gratot, I., Le Pape, M., Olkowsky, J., and Ranc, G. (1959). Étude de quelques isotopes très déficients en neutrons du prométhéum et du samarium. *Nucl. Phys.* 13, 302–309. doi: 10.1016/0029-5582(59)90324-4

Greatbatch, W. (1980). Physiological stimulators and their power sources. *Med. Prog. Technol.* 7, 81–85.

Greenwood, N. N., and Earnshaw, A. (eds) (1997a). "1 - Origin of the Elements. Isotopes and Atomic Weights," in *Chemistry of the Elements*, 2nd Edn. Oxford: Butterworth-Heinemann, 1–19. doi: 10.1016/B978-0-08-030712-1.50004-1

Greenwood, N. N., and Earnshaw, A. (eds) (1997b). "30 - The Lanthanide Elements ($Z = 58–71$)," in *Chemistry of the Elements, 2nd Edn*. Oxford: Butterworth-Heinemann, 1227–1249. doi: 10.1016/B978-0-7506-3365-9.50036-5

Guillaumont, R. (2019). Completion and extension of the periodic table of elements beyond uranium. *Comptes Rendus Phys.* 20, 617–630. doi: 10.1016/j.crhy.2018.12.006

Harris, J. A., Yntema, L. F., and Hopkins, B. S. (1926). The element of atomic number 61; illinium. *Nature* 117, 792–793. doi: 10.1038/117792a0

Hellweg, C., Thelen, M., Arenz, A., and Baumstark-Khan, C. (2007). The German ISS-experiment cellular responses to radiation in space (CERASP): the effects of single and combined space flight conditions on mammalian cells. *Adv. Sp. Res.* 9, 1011–1018. doi: 10.1016/j.asr.2006.11.015

Hellweg, C. E., Baumstark-Khan, C., Spitta, L., Thelen, M., Arenz, A., Franz, M., et al. (2008). The space experiment CERASP: definition of a space-suited radiation source and growth conditions for human cells. *Acta Astronaut.* 63, 906–914. doi: 10.1016/j.actaastro.2008.03.006

How beta gauge works (2019). Available at: http://www.atigauge.com/how-html/ (accessed December 16, 2019).

Hu, F., Cutler, C. S., Hoffman, T., Sieckman, G., Volkert, W. A., and Jurisson, S. S. (2002). Pm-149 DOTA bombesin analogs for potential radiotherapy: *in vivo* comparison with Sm-153 and Lu-177 labeled DO3A-amide-βAla-BBN(7–14)NH2. *Nucl. Med. Biol.* 29, 423–430. doi: 10.1016/S0969-8051(02)00290-1

Kassai, Z., Koprda, V., Bauerová, K., Harangozó, M., Bendová, P., Bujnová, A., et al. (2003). Penetration of radionuclides across the skin: rat age dependent promethium permeation through skin *in vitro*. *J. Radioanal. Nucl. Chem.* 258, 669–672. doi: 10.1023/B:JRNC.0000011767.30604.96

Kim, S. H., and Choi, S. I. (2014). *Uses of Rare Earth Elements for Hair Improvement*. U.S. Patent No. 8715714B2. Available online at: https://patents.google.com/patent/US8715714B2/en

Kistiakowsky, V. (1952). Promethium isotopes. *Phys. Rev.* 87, 859–860. doi: 10.1103/PhysRev.87.859

Knapp, F. F. (2008). *Chromatographic Extraction With di(2-ethylhexyl)orthophosphric Acid for Production and Purification of Promethium-147.*

Kraus, W. (1976). Dosimetry in single lung cells by means of microautoradiographic activity measurements. *Phys. Med. Biol.* 21, 812–822. doi: 10.1088/0031-9155/21/5/010

Krupke, W. F., Shinn, M. D., Kirchoff, T. A., Finch, C. B., and Boatner, L. A. (1987). Promethium-doped phosphate-glass laser at 933 and 1098 nm. *Appl. Phys. Lett.* 51, 2186–2188. doi: 10.1063/1.98934

Labrecque, J. J., Rosales, P. A., and Mejías, G. (1986). Simultaneous determination of lanthanides by radioisotope x-ray fluorescence spectrometry based on characteristic K-radiation. *Anal. Chim. Acta* 188, 9–14. doi: 10.1016/S0003-2670(00)86024-9

Llasat, M., Rigo, T., and Villegas, J. (2017). "Techniques and Instruments to Aid in the Monitoring of Flood Events," in *Floods*, 91–113. doi: 10.1016/B978-1-78548-268-7.50006-7

Lubkowitz, J. A., and Parker, W. C. (1971). The utilization of promethium-147 as an ionization source in electron-capture detectors. *J. Chromatogr. A* 62, 53–61. doi: 10.1016/S0021-9673(01)96809-8

Malson, H. A., Honious, H. B., Moyer, S. E., and Janzow, E. F. (1980). *Radiation Sources and Process*. U.S. Patent No. 4197170A. Available online at: https://patents.google.com/patent/US4197170A/en

Marinsky, J. A., Glendenin, L. E., and Coryell, C. D. (1947). The Chemical Identification of Radioisotopes of Neodymium and of Element 61. *J. Am. Chem. Soc.* 69, 2781–2785. doi: 10.1021/ja01203a059

Matheson, W. E. (1975). "The Betavoltaic Pacemaker Power Source," in *Engineering in Medicine*, eds M. Schaldach and S. Furman (Berlin: Heidelberg: Springer), 401–424. doi: 10.1007/978-3-642-66187-7_25

May, E., and Thoennessen, M. (2012). Discovery of cesium, lanthanum, praseodymium and promethium isotopes. *At. Data Nucl. Data Tables* 98, 960–982. doi: 10.1016/j.adt.2011.09.005

McGill, I. (2000). "Rare Earth Elements," in *Ullmann's Encyclopedia of Industrial Chemistry* (American Cancer Society), 183–228. doi: 10.1002/14356007.a22_607

McLennan, S. M. (2018). "Promethium," in *Encyclopedia of Geochemistry: A Comprehensive Reference Source on the Chemistry of the Earth,* ed. W. M. White (Cham: Springer International Publishing), 1286. doi: 10.1007/978-3-319-39312-4_134

McNeilly, C. E., and Roberts, F. P. (1969). Thermal analysis of promethium oxalate. *Isot. Radiat. Technol.* 7, 24–27. Available at: https://www.scopus.com/inward/record.uri?eid=2-s2.0-0014562208&partnerID=40&md5=71d95784960c838ccaf40eb019ed1b41 (accessed June 06, 2020).

McShea, J. C., Petheram, J. C., Rosenberg, A., and Rosen, A. (1988). "High-power high-efficiency 2-D laser diode arrays for pumping solid-state lasers," in *Conference on Lasers and Electro-Optics* (Anaheim, CA: Optical Society of America), WB5. Available online at: http://www.osapublishing.org/abstract.cfm?URI=CLEO-1988-WB5 (accessed June 06, 2020).

Metabolic data for promethium (1981). *Ann. ICRP* 6, 58–60. doi: 10.1016/0146-6453(81)90102-0

Murphy, J. W., Voss, L. F., Frye, C. D., Shao, Q., Kazkaz, K., Stoyer, M. A., et al. (2019). Design considerations for three-dimensional betavoltaics. *AIP Adv.* 9:65208. doi: 10.1063/1.5097775

Nuclear Data Center at KAERI Table of Nuclides (2020). Available online at: http://atom.kaeri.re.kr/ (accessed May 15, 2020).

Olsen, L. C., Cabauy, P., and Elkind, B. J. (2012). Betavoltaic power sources. *Phys. Today* 65, 35–38. doi: 10.1063/PT.3.1820

Promethium, the New Name for Element 61 (1948). *Nature* 162:175. doi: 10.1038/162175a0

Purdy, D. L. (1986). "Nuclear Batteries for Implantable Applications," in *Batteries for Implantable Biomedical Devices*, ed. B. B. Owens (Boston, MA: Springer US), 285–352. doi: 10.1007/978-1-4684-9045-9_11

Radiological Contamination of the Oceans: Oversight Hearings Before the Subcommittee on Energy and the Environment of the Committee on Interior and Insular Affairs and House of Representatives, Ninety-fourth Congress, Second Session on Matters Pertaining to (1976). Available online at: https://books.google.ru/books?id=IofQAAAAMAAJ&pg=PA641&lpg=PA641&dq=chemical$+$surrogate$+$for$+$element$+$promethium&source=bl&ots=smeEJ-tYKz&sig=ACfU3U2Yv9uDgd8IgZRsi9oeIZRzJU8VYQ&hl=ru&sa=X&ved=2ahUKEwjugtLKmrbpAhUEwcQBHXDtC9gQ6AEwC3oECAYQAQ#v=onepage&q=chemicalsurrogateforelementpromethium&f=false (accessed June 06, 2020).

Rafi, N., and Rosli, A. (2018). The band structure of a rare earth element of Promethium (III) Oxide (Pm2O3) calculated using density functional theory. *J. Phys. Conf. Ser.* 1090:12005. doi: 10.1088/1742-6596/1090/1/012005

Ravi, S., Mathew, K. M., Seshadri, N. K., and Subramanian, T. K. (2001). Salient features in the preparation of promethium-147 activated zinc sulphide phosphor light sources. *J. Radioanal. Nucl. Chem.* 250, 565–568. doi: 10.1023/A:1017954701824

Rosenkranz, K. A. (1975). "Clinical Experience with Nuclear-Powered Pacemakers (Promethium-147)," in *Engineering in Medicine: Volume 1: Advances in Pacemaker Technology,* eds M. Schaldach and S. Furman (Berlin; Heidelberg: Springer Berlin Heidelberg), 503–529. doi: 10.1007/978-3-642-66187-7_31

Saini, B. C., and Rathore, T. R. (1983). Adaptation of beta-ray gauge technique for measurement of water deficit of intact rice leaves. *Biol. Plant.* 25, 326–330. doi: 10.1007/BF02878273

Shao, Q., Voss, L F., Murphy, J. M., Frye, C. D., Henderson, R. A., Stoyer, M. A., et al. (2017). "Accelerated aging in 4H-SiC as a betavoltaic semiconductor using an electron beam system," in *2017 IEEE Nuclear Science Symposium and Medical Imaging Conference (NSS/MIC)* (Atlanta, GA). doi: 10.1109/NSSMIC.2017.8532740

Sharma, B. K. (2001). *Nuclear and Radiation Chemistry*. Meerut: GOEL Publishing House. Available at: https://books.google.ru/books?id=L8mBZcaGUQAC&pg=PA145&lpg=PA145&dq=oxidation$+$state$+$promethium$+$%2B2&source=bl&ots=uwaPjq1xCP&sig=ACfU3U3GP8OHBzcF9olRDVviEPgSQ0RyUA&hl=ru&sa=X&ved=2ahUKEwiAgPjPnbbpAhUozqYKHQpNAa0Q6AEwDHoECCAQAQ#v=onepage&q=oxidationstatepromethium%2B2&f=false (accessed June 06, 2020).

Shinn, M. D., Krupke, W. F., Solarz, R. W., and Kirchoff, T. A. (1988). Spectroscopic and laser properties of Pm3+. *IEEE J. Quantum Electron.* 24, 1100–1108. doi: 10.1109/3.232

Slezak, S. E., and Buckius, R. O. (1983). Dust concentration measurement probe using beta attenuation. *Rev. Sci. Instrum.* 54, 618–625. doi: 10.1063/1.1137424

Smith, T. H., Greenborg, J., and Matheson, W. E. (1975). Benefit/risk analysis of cardiac pacemakers powered by betacel® Promethium-147 Batteries. *Nucl. Technol.* 26, 54–64. doi: 10.13182/NT75-A24404

Sneller, J. (1979). New sensors are starting a second revolution in extrusion control. *Mod Plast* 56, 40–43.

Spencer, M., and Chandrashekhar, M. V. S. (2012). *Betavoltaic Battery With a Shallow Junction and a Method for Making Same.* U.S. Patent No. 8153453B2. Available online at: https://patents.google.com/patent/US8153453

Spencer, M., and Chandrashekhar, M. V. S. (2013). *High Power Density Betavoltaic Battery*. U.S. Patent No. 8487392B2. Available online at: https://patents.google.com/patent/US8487392B2/en

Stuart, B. O. (1966). *Retention and Translocation of Inhaled Calcined Promethium Oxide in Beagle Dogs.* BNWL [reports]. U. S. At. Energy Comm., 70–72.

Studer, D., Heinitz, S., Heinke, R., Naubereit, P., Dressler, R., Guerrero, C., et al. (2019). Atomic transitions and the first ionization potential of promethium determined by laser spectroscopy. *Phys. Rev. A* 99, 62513. doi: 10.1103/PhysRevA.99.062513

Sullivan, M. F., Miller, B. M., and Goebel, J. C. (1984). Gastrointestinal absorption of metals (51Cr, 65Zn, 95mTc, 109Cd, 113Sn, 147Pm, and 238Pu) by rats and swine. *Environ. Res.* 35, 439–453. doi: 10.1016/0013-9351(84)90151-8

Sumiya, S., Hayashi, N., Katagiri, H., and Narita, O. (1993). A radioanalytical method for samarium-151 and promethium-147 in environmental samples. *Sci. Total Environ.* 130–131, 305–315. doi: 10.1016/0048-9697(93)90085-K

Takami, K. (1980). *Liquid Crystal Display Device.* U.S. Patent No. 4205522A. Available online at: https://patents.google.com/patent/US4205522

Takami, K., and Matsuzawa, T. (1981). *Self-Luminescent Light Source for Liquid Crystal Display Watch*. U.S. Patent No. 4285055A. Available online at: https://patents.google.com/patent/US4285055

Takechi, O., and Furudoi, Y. (1970). Water content and beta ray transmission of various leaves. *J. Agric. Meteorol.* 26, 1–3. doi: 10.2480/agrmet.26.1

Tennyson, A. (1842). *Poems*. London: Edward Moxon, Dover Street.

Typpo, P. M. (2000). *Nuclear Gauge for Measuring a Characteristic of Moving Sheet Material and Alignment Compensation.* U.S. Patent No. 6133578A. Available online at: https://patents.google.com/patent/US6133578

Vennart, J. (1967). The usage of radioactive luminous compound and the need for biological monitoring of workers. *Health Phys.* 13, 959–964. doi: 10.1097/00004032-196709000-00001

Vl (1956). Atomic batteries. *Sov. J. At. Energy* 1, 121–123. doi: 10.1007/BF01516325

Weiss, G. B. (1996). "Use of Lanthanum as a Tool to Delineate Calcium Mobilization Patterns in Smooth Muscle," in *Episodes from the History of the Rare Earth Elements*, ed C. H. Evans (Dordrecht: Springer Netherlands), 189–203. doi: 10.1007/978-94-009-0287-9_10

Wheelwright, E. J., and Fuqua, P. A. (1975). "Promethium and Plutonium as Fuels for Pacemaker Power Sources," in *Engineering in Medicine* (Berlin; Heidelberg: Springer), 383–400. doi: 10.1007/978-3-642-6618 7-7_24

Wiss, T., Freis, D., Griveau, J.-C., Popa, K., Vigier, J.-F., Somers, J., et al. (2017). "Investigation on the use of Americium Oxide for Space Power Sources: Radiation Damage Studies," in *E3S Web of Conferences*, ed F. A. (EDP Sciences). doi: 10.1051/e3sconf/20171605004

Xue, S., Tan, C., Kandlakunta, P., Oksuz, I., Hlinka, V., and Cao, L. R. (2019). Methods for improving the power conversion efficiency of nuclear-voltaic batteries. *Nucl. Instruments Methods Phys. Res. Sect. A Accel. Spectrometers, Detect. Assoc. Equip.* 927, 133–139. doi: 10.1016/j.nima.2019.01.097

Zavialov, A. P., Arefieva, Z. S., Nazarov, V. A., and Khryashcheva, L. A. (1977). Comparison of effects of β radiation from thallium 204 and promethium 147 on the skin of immature pigs. *Radiobiologiya* 17, 267–271. Available at: https://www.scopus.com/inward/record.uri?eid=2-s2.0-0017461687&partnerID=40&md5=8a806ac837794d0ded5aed1dbe353986 (accessed June 06, 2020).

Conflict of Interest: The authors declare that the research was conducted in the absence of any commercial or financial relationships that could be construed as a potential conflict of interest.

frontiers in Chemistry

ORIGINAL RESEARCH
published: 04 August 2020
doi: 10.3389/fchem.2020.00564

Indium Doping of Lead-Free Perovskite Cs_2SnI_6

Shodruz T. Umedov[1], **Anastasia V. Grigorieva**[1,2*], **Leonid S. Lepnev**[3], **Alexander V. Knotko**[1,2], **Koji Nakabayashi**[4], **Shin-ichi Ohkoshi**[4] and **Andrei V. Shevelkov**[2]

[1] Department of Materials Science, Lomonosov Moscow State University, Moscow, Russia, [2] Department of Chemistry, Lomonosov Moscow State University, Moscow, Russia, [3] Lebedev Physical Institute of the Russian Academy of Sciences, Moscow, Russia, [4] Department of Chemistry, School of Sciences, University of Tokyo, Tokyo, Japan

Structure and properties of an inorganic perovskite Cs_2SnI_6 demonstrated its potential as a light-harvester or electron-hole transport material; however, its optoelectronic properties are poorer than those of lead-based perovskites. Here, we report the way of light tuning of absorption and transport properties of cesium iodostannate(IV) Cs_2SnI_6 via partial heterovalent substitution of tin for indium. Light absorption and optical bandgaps of materials have been investigated by UV-vis absorption and photoluminescent spectroscopies. Low-temperature electron paramagnetic resonance spectroscopy was used to study the kind of paramagnetic centers in materials.

Keywords: perovskite photovoltaics, cesium iodostannate(IV), solid solution, Raman spectroscopy, optical characteristics

Edited by:
W. H. Eugen Schwarz,
University of Siegen, Germany

Reviewed by:
Thiti Bovornratanaraks,
Chulalongkorn University, Thailand
Lorenzo Malavasi,
University of Pavia, Italy

****Correspondence:***
Anastasia V. Grigorieva
anastasia@inorg.chem.msu.ru

Specialty section:
This article was submitted to
Inorganic Chemistry,
a section of the journal
Frontiers in Chemistry

Received: *15 February 2020*
Accepted: *02 June 2020*
Published: *04 August 2020*

Citation:
Umedov ST, Grigorieva AV, Lepnev LS, Knotko AV, Nakabayashi K, Ohkoshi S and Shevelkov AV (2020) Indium Doping of Lead-Free Perovskite Cs_2SnI_6. Front. Chem. 8:564. doi: 10.3389/fchem.2020.00564

INTRODUCTION

The efficiency of third-generation solar cells (SCs) based on materials with a perovskite structure is growing every year (Elumalai et al., 2016; Li et al., 2016; Powalla et al., 2018; Sani et al., 2018; Ajay et al., 2019). Such rapid success of using these materials in various fields of solar photovoltaics is due to their unique optoelectronic properties. Today, lead-based perovskite materials ($APbX_3$) are the most efficient in terms of converting solar radiation into electricity (Brandt et al., 2015; Dimesso et al., 2017; Yang et al., 2017; Zhu Z. et al., 2019), and it is caused by low binding energy of excitons, charge carrier mobility, long diffusion length, high absorption coefficient, and direct bandgap (Xiao and Yan, 2017; Deng et al., 2019). The theoretically calculated highest power conversion efficiency (PCE) (Shockley–Queisser limit) achieved by lead-based perovskite is 31.4% for $CH_3NH_3PbI_3$ (Wan-Jian et al., 2015) and the experimental efficiency (light converting efficiency) of SCs with this compound has exceeded 25% (Yang et al., 2017; Jeon et al., 2018; Powalla et al., 2018). However, the chemical and thermal stability of lead perovskites are not sufficiently well; moreover, lead is a toxic element (Kulbak et al., 2016; Wu Y. et al., 2017; Pisanu et al., 2019). These problems motivate finding new alternatives among lead-free materials with optimal optoelectronic characteristics (Hoefler et al., 2017; Fu, 2019; Pisanu et al., 2019). Instead of lead perovskites, materials with general formulas of ABX_3 [where A = $CH_3NH_3^+$, $HC(NH_2)_2^+$, or Cs^+, Rb^+, K^+; B = divalent inorganic cation; X = Cl, Br, I] and A_2BX_6 (where A and X the same cations and anions as in the case of ABX_3; B = tetravalent inorganic cations) are in focus for investigations (Huang and Lambrecht, 2013; Stoumpos et al., 2016; Cai et al., 2017; Ju et al., 2017). Among all lead-free compounds with the ABX_3 formula, cesium triiodostannate $CsSnI_3$ turned out to be the most promising material with good optoelectronic performance (Kumar et al., 2014, 2017; da Silva et al., 2015; Stoumpos et al., 2016). The first SCs based on Sn^{2+} perovskites had a very low efficiency (3×10^{-4}%−2%) (Chen et al., 2012; Kumar et al., 2014). Nevertheless, $CsSnI_3$ has excellent properties [optimal bandgap of 1.4 eV, higher theoretical short-circuit photocurrent (J_{SC}) density of 34.3 mA cm^{-2}, highest hole mobility ~585 cm^2 V^{-1} s^{-1} among p-type materials] for photovoltaic application as light harvesting or p-type semiconductor (Chung et al., 2012; Stoumpos et al., 2013). Thereby, the $CsSnI_3$ phase is still being actively studied (Song et al., 2018; Wijesekara et al., 2018; Pisanu et al., 2019) and the PCE of SCs based on it has achieved 5.03% (Wang Y. et al., 2019), but these results are still less satisfactory than those of $MAPbI_3$.

Another type of compounds are double perovskites, which are obtained by replacing the tetravalent cation B^{4+} and a vacancy in A_2BX_6 with the B^+/B^{3+} pair (where B^+ = Cu, Ag, Ga, In, Tl, etc.; B^{3+} = Sb, Bi etc.) so that the charge neutrality is preserved (Yin et al., 2019). According to Savory et al. (2016), the theoretical calculations show a PCE limit <8% for the double perovskite compound Cs_2AgBiX_6; however, higher PCE and suitable bandgaps have been predicted for other materials such as $Cs_2InSbCl_6$, $Cs_2AgInBr_6$, $Rb_2AgInBr_6$, and $Rb_2CuInCl_6$ (Zhao et al., 2017a,b). According to Xiao et al. (2019), the most promising double perovskites are based on cations such as Ag, In, Bi, and Sb (Greul et al., 2017; Wu C. et al., 2017; Gao et al., 2018; Liang and Gao, 2018; Fan et al., 2019; Igbari et al., 2019).

A promising lead-free non-toxic and stable perovskite-like material with a face-centered cubic cell is A_2SnX_6, where the tin atom is strongly covalently bonded and stabilizes the crystal lattice. Among all compounds in the A_2SnX_6 group, the Cs_2SnI_6 phase turned out to be a suitable material for photovoltaics (Cai et al., 2017; Maughan et al., 2018). Cesium iodostannate(IV) has promising optoelectronic properties (electron mobility up to 509 cm^2 V^{-1} s^{-1}; Guo et al., 2017; J_{SC} = 13.97 mA cm^{-2}; V_{OC} = 0.58 V; E_g = ~1.2 eV) (Kaltzoglou et al., 2016), which makes it a candidate as a light-harvesting material in SCs. Mixed cations $A^+((A_xA_{1-x})_2BX_6)$ (Ganesan et al., 2019) and anions $X^-(A_2B(X'_xX_{1-x})_6)$ (Lee et al., 2017; Ke et al., 2018; Yuan et al., 2019; Zhu W. et al., 2019) were considered to improve stability and properties of Cs_2SnX_6. Upon replacement of Cl^- by I^-, the optical absorption coefficient increases, the bandgap decreases, stability decreases, and the materials color changes from pale yellow (or white) to black. The Cs_2SnI_6 phase is also used as photodetectors (Han et al., 2019), for photoelectrochemical water splitting (Dang et al., 2019), as photocatalysts (Wang X.-D. et al., 2019), and the efficiency of the SCs based on it has reached ~11.2%. In this work, we have demonstrated the preparation of solid solutions based on Cs_2SnI_6 by doping with indium. Heterovalent substitution of tin (Sn^{4+} ionic radii 0.69 Å, Pauling electronegativity = 1.96) in the structure of Cs_2SnI_6 by indium (In^{3+} ionic radii 0.74 Å, Pauling electronegativity = 1.78) leads to the formation of solid solutions with improved optical properties. Here, for the $In^{3+} \rightarrow Sn^{4+}$ substitution, the difference in electronegativities of cations is 0.18 and the difference in ion sizes is 7.24%, which corresponds well to the Goldschmidt rule (Goldschmidt, 1926).

Recently, the new wave of enthusiasm among researchers has arrived from coming perspectives of nanocrystalline Cs_2SnI_6 phase and its derivatives for optoelectronics (Wang et al., 2016; Veronese et al., 2020). Because of this, development of nanochemistry of complex halides requires preliminary fundamental studies of phase equilibrium and analysis of optical and transport characteristics in polycrystalline materials.

EXPERIMENTAL SECTION

Syntheses of Materials

The sintering was carried out by solid-state sintering method in evacuated quartz ampules (RT pressure of $1.6 \cdot 10^{-2}$ Torr). The compositions were prepared by grinding cesium iodide CsI (Sigma-Aldrich 99.99%), tin iodide SnI_4 [direct synthesis from elementary tin ("Ruschim," 99.90+, O-1) and iodine in CCl_4 (purum, "Irea2000") with further purification by sublimation at 270°C], and elementary iodine (purum, "Reachim") and metallic indium ("Ruschim," 99.999%) with the stoichiometric mass ratios. The pristine Cs_2SnI_6 phase was obtained with the stoichiometric mass of CsI and SnI_4 (2:1). The mixtures were sealed in preliminarily dried quartz ampoules and heated with the rate of ~0.2°C/min to 300°C and then annealed at this temperature for 48 h. All samples were kept in double closed zip-lock bags in nitrogen.

All materials were characterized with powder XRD method for phase composition definition. We assumed that the obtaining materials have the composition related to the solid solutions $Cs_{2-x}Sn_{1-x}In_xI_{6-2x}$ based on Cs_2SnI_6 or $CsInI_4$ phases. The following chemical equation shows the phase composition and yield of the reaction products.

$$(2-x)\mathrm{CsI} + (1-x)\mathrm{SnI_4} + (x)\mathrm{In} + (1.5x)\mathrm{I_2} \rightarrow \mathrm{Cs_{2-x}Sn_{1-x}In_x}I_{6-2x} \quad (1)$$

Characterization Methods

The ampoules with samples were open right before the following analyses. The samples were transferred to the closely packed cells for further storing. XRD, Raman, and UV-vis measurements were performed in air for 15 min.

X-ray diffraction measurements (XRD) were performed on a Rigaku D/MAX 2500 diffractometer equipped with a rotating copper anode (Cu-Kα radiation) and operated at 45 kV and 250 mA from 5° to 80° in 2Θ; at the continuous scanning speed 5° min^{-1} with a measuring step of 0.02°. The experimental data were analyzed using WinXPow (database PDF2) to define the phase composition, and Jana2006 software was used for unit cell parameter calculations.

To analyze the optical properties, the samples were studied by diffuse reflection spectroscopy. One gram of each compound was placed in the cell of the spectrophotometer and pressed tightly with a quartz glass and then measured in the range of 1,400–200 nm with a scan step of 1 nm. UV-vis diffuse reflectance spectra were collected using a UV-vis spectrometer Lambda 950 (PerkinElmer). All measurements were performed at 298 K with a scanning rate of 2 nm/s using quartz glass as a reference. Reflectance (R) was converted to absorption (α) data in accordance with the Kubelka–Munk model: $\alpha/S = (1 - R)^2/(2 \cdot R)$. The optical energy bandgap (E_g) was acquired using a Tauc plot, the dependence of $(\alpha h\nu)^2$ on energy ($h\nu$).

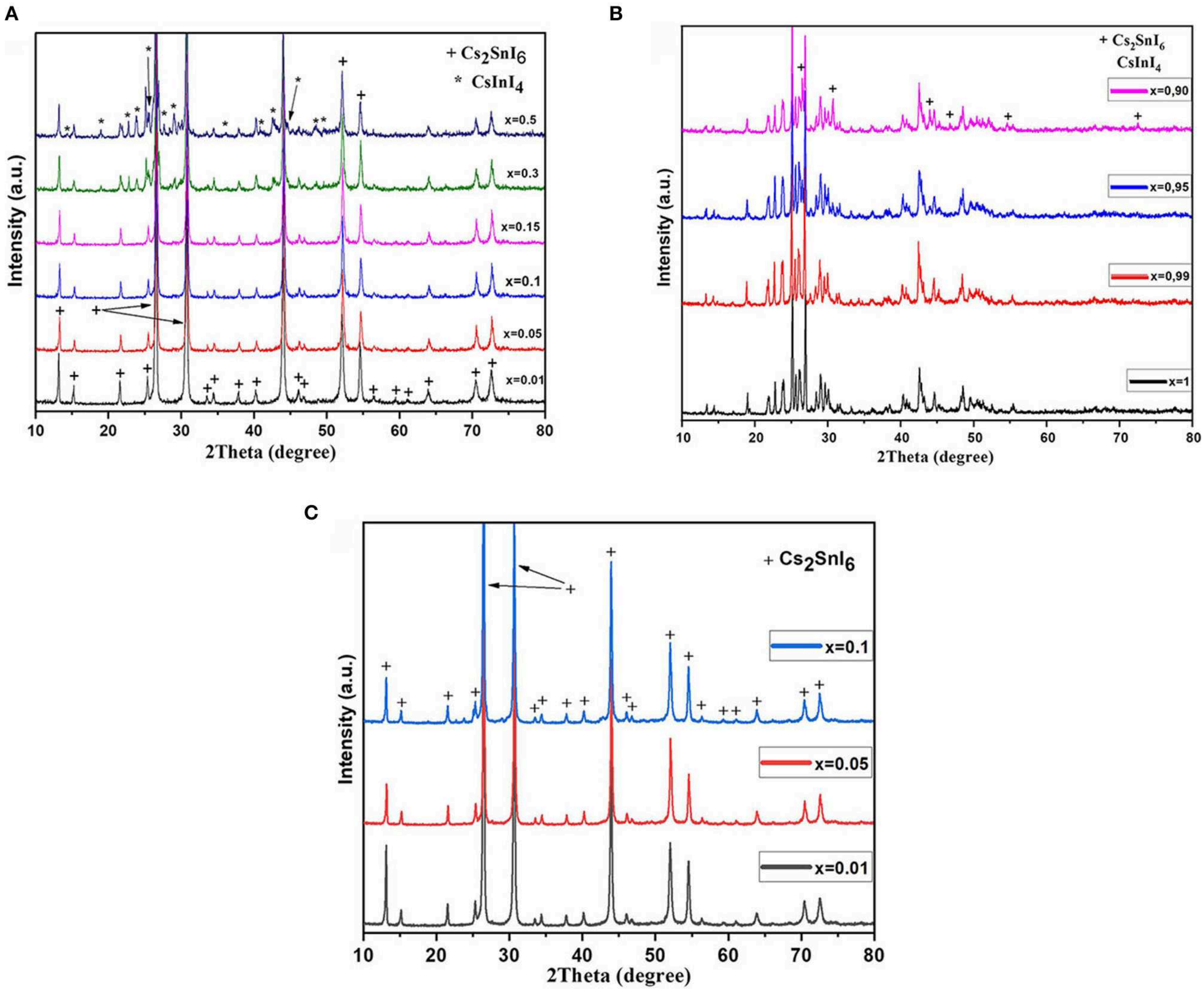

FIGURE 1 | (A) Powder XRD data for $Cs_{2-x}Sn_{1-x}In_xI_{6-2x}$ ($x = 0.01$–0.1) compounds. **(B)** XRD data of $Cs_{2-x}Sn_{1-x}In_xI_{6-2x}$ with high substitution rate x ($x = 0.9 - 1$). All unmarked reflections belong to the $CsInI_4$ phase. **(C)** XRD data of three samples with $x = 0.01$, 0.05, 0.1 ratio after a year of storage in air. "+" denotes Cs_2SnI_6 reflections, and "*" indicates reflections of $CsInI_4$.

TABLE 1 | XRD data for $Cs_{2-x}Sn_{1-x}In_xI_{6-2x}$ compositions.

Sample composition	Substitution rate *x*	Cell parameter *a*, Å	Unit cell volume *V*, Å^3	R_p	R_I
$Cs_{1.99}Sn_{0.99}In_{0.01}I_{5.98}$	0.01	11.6505 (6)	1581.4 (1)	13.66	5.52
$Cs_{1.95}Sn_{0.95}In_{0.05}I_{5.9}$	0.05	11.6541 (6)	1582.8 (1)	14.34	5.80
$Cs_{1.9}Sn_{0.9}In_{0.1}I_{5.8}$	0.10	11.6548 (3)	1583.1 (1)	15.91	6.32

Emission spectra were collected with a multichannel spectrometer S2000 (Ocean Optics) with a nitrogen LGI-21 ($\lambda_{ex} = 337$ nm) as an excitation source at 293 K and 77 K. All spectra were corrected for the wavelength response of the system. Additionally, the photoluminescence emission spectra of the sample $CsInI_4$ was investigated with a diode source of 365 nm.

EPR spectra were recorded using a X-band JES-FA200 (JEOL) spectrometer at the temperature of 294–4.2 K. The modulation frequency is 100 kHz and microwave frequencies are around 9.00 GHz. The samples are put in a quartz tube with an upper glass part, then purged by Ar gas and vacuum three times, and finally sealed in vacuum (about 20 Pa).

RESULTS AND DISCUSSION

As shown in **Figure 1A**, about 10% of tin atoms in the structure of Cs_2SnI_6 can be substituted by indium atoms. All reflections on the corresponding XRD patterns belong to the Cs_2SnI_6

with a cubic structure and space group F*m-3m*(225) (PDF2 file #73-330). Diffraction patterns for the compositions with x from 0 to 0.15 display a shift of the reflections toward lower 2θ upon increasing the substitution rate. The increase of the unit cell parameter a compared to pure Cs_2SnI_6 phase indicates a slight increase of the unit cell volume. According to the fact that the ionic radius of the In^{3+} (0.74 Å) is slightly larger than that of Sn^{4+} (0.69 Å), the cell volume increases. At higher substitution rates, x of 0.3 and 0.5, reflections of the $CsInI_4$ phase (PDF2 file #76-2101) with a monoclinic structure [P*21/c* (14) space group] are observed on diffraction patterns of the respective samples. The estimated cell parameters of the F-centered cubic Cs_2SnI_6 are given in **Table 1**. Such gentle change of the unit cell parameters is probably due to the formation of iodine vacancies in the anion sublattice.

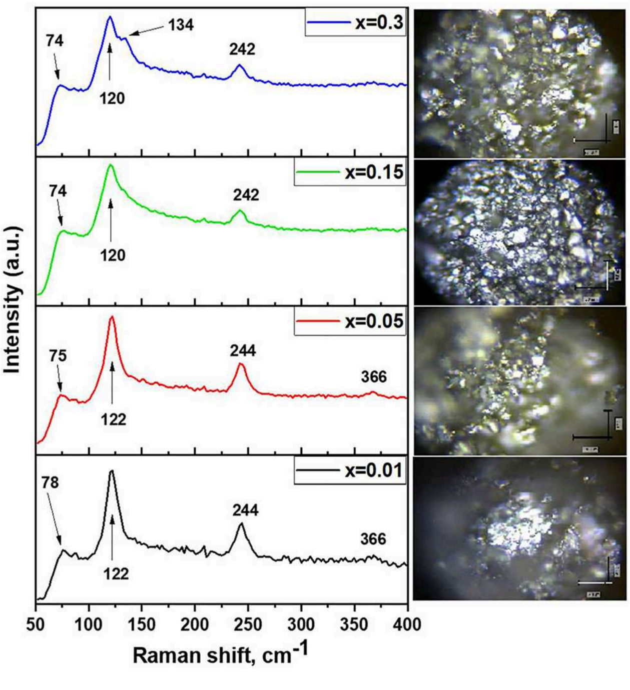

FIGURE 2 | Raman spectra of samples $Cs_{2-x}Sn_{1-x}In_xI_{6-2x}$ (x = 0.01–0.3) and their optical microscopy data.

Samples (polycrystalline powders) were stored in air under laboratory conditions for 1 year and investigated by powder XRD repeatedly during this period. According to the XRD results (**Figure 1**), the indium-substituted samples remain single-phase with the cubic Cs_2SnI_6 structure, while the pristine Cs_2SnI_6 phase (without doping) decomposed already after a month of storage into CsI and volatile SnI_4, which turned into SnO_2 as a result of hydrolysis. The stability of the substituted samples is probably due to the fact that indium with iodine form stronger ionic bonds than tin; therefore, the lattice of solid solutions is more stable than the pure phase lattice. At the same time, the sample with $x = 0.10$ has very weak reflections of admixture at 18.77°, 22.65°, and 23.66° in this XRD pattern. These reflections most probably belong to the $CsInI_4$ phase. For comparison, the strongest reflections of cesium iodide CsI should be at 22.87°, 32.56°, and 52.63°. The impurity is probably a result of the segregation process.

The samples of In-substituted Cs_2SnI_6 were studied by Raman spectroscopy. As can be seen from optical microscopy (**Figure 2**), the samples are homogeneous in appearance and all crystallites have a similar color. The spectra contain the strongest modes $\nu(A_{1g})$—122 cm^{-1}, $\nu(E_g)$—83 cm^{-1}, and $\delta(F_{2g})$—78 cm^{-1}, which are related to vibrations of $[SnI_6]^{2-}$ octahedra [namely, $\nu(A_{1g})$ is a symmetric stretching of Sn–X bonds; $\delta(F_{2g})$ is a X–Sn–X asymmetric bending]. Substitution of Sn^{4+} with In^{3+} resulted in shortening of M–I bonds and distortion of $[MI_6]^{2-}$ octahedrons. Since Cs_2SnI_6 perfectly absorbs the visible part of the spectrum, the excitation by a green laser (wavelength, 514.4 nm) excites second- and third-order harmonics at 244 and 366 cm^{-1} due to strong resonance. The relative shift of the lines relative to the theoretical ones in the direction of smaller or larger wave numbers is associated with a changing energy and lengths of the Sn–I bonds in the $[SnI_6]^{2-}$ octahedra. Substitution of tin by indium results in small "left shift" and broadening of $\nu(A_{1g})$, and $\delta(F_{2g})$ Raman modes show the increase of element–iodine bond length. Raman spectra of the In-doped Cs_2SnI_6 differ

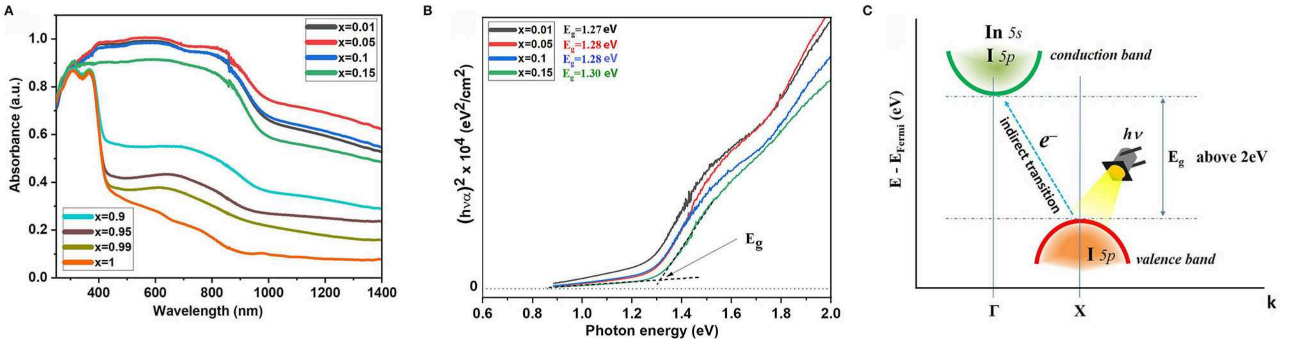

FIGURE 3 | (A) Optical absorption spectra of the samples $Cs_{2-x}Sn_{1-x}In_xI_{6-2x}$ (x = 0.01–1.0). **(B)** Tauc plot for Cs_2SnI_6-based compounds, and **(C)** scheme of the electronic band structure of $CsInI_4$.

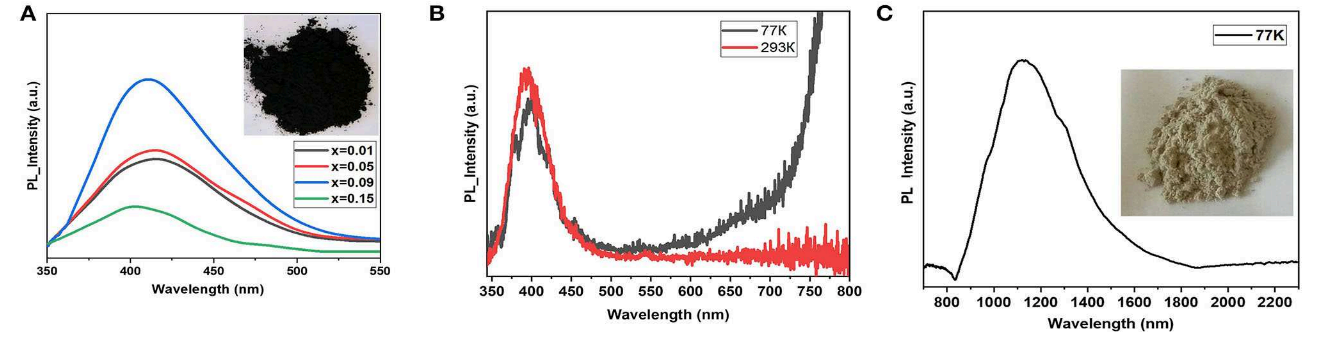

FIGURE 4 | Photoluminescence emission spectra of **(A)** the samples $Cs_{2-x}Sn_{1-x}In_xI_{6-2x}$ ($x = 0.01$–0.15) at 293 K, and **(B)** and **(C)** PL emission of pure phase $CsInI_4$ at 293 and 77 K in visible and infrared (IR) range, respectively.

also from the spectrum reported by Qui et al. for pure Cs_2SnI_6 (Qiu et al., 2017).

In the Raman spectrum of the two-phase sample $x = 0.3$, a band observed at 134 cm^{-1} corresponds to the vibration of the $[InI_4]^-$ tetrahedron. Namely, $\nu(A_{1g})$ is a symmetric stretching vibration of In–I bonds in $[InI_4]^-$ tetrahedral in $CsInI_4$ phase. Other vibration modes of $[InI_4]^-$ tetrahedra do not appear in the spectra. It was found that Raman spectrum of the $x = 0.15$ sample had an additional shoulder at 134 cm^{-1}. The possible reason for this is a fine and evenly distributed admixture of $CsInI_4$. Its XRD reflections do not present in diffractograms, but Raman spectroscopy revealed its presence as the surface admixture. Eventually, this admixture recrystallizes, leading to larger crystallites of cesium iodogallate.

The optical absorption spectra shown in **Figure 3** consist of two maxima (at ∼800 nm and at ∼600 nm). The materials absorb from the near infrared (from 1,000 nm) to ultraviolet (UV) (380 nm). The first local maximum (∼800 nm) is due to the transition of the electrons from the maximum of valence band (which is formed from I *5p* orbitals) to the minimum of conduction band formed by hybridized I *5p*–Sn *5s* orbitals. This transition is characteristic for all the samples excluding $x = 1$. The estimated bandgap energy grows slightly from 1.27 to 1.31 eV for the single-phase samples with $x = 0$–0.15 according to the corresponding Tauc plots (**Figure 3B**). The second peak in energy is approximately equal to the electron transfer energy from slightly hybridized I *5p*–Sn *5p* orbitals localized below the top of the valence band to hybridized I *5p*–Sn *5s* orbitals of the conduction band.

As the indium concentration in the composition of the materials increases, the content of the $CsInI_4$ phase increases, as can be seen from the XRD data, and this is manifested in the absorption spectrum of the sample $x = 0.5$ (∼370 nm). This absorption edge is approximately equal to ∼3.0 eV and relates to transitions in the electronic structure of the $CsInI_4$ phase (**Figure 3B**), namely, the electron transition from the I *5p* orbitals (top valence band) to the hybridized I *5p*–In *5s* orbitals (conduction band bottom). The experimental E_g differs from the calculated bandgap value presented in Persson (2016).

Figure 4A shows photoluminescence spectra of the samples. The C_2SnI_6 perovskite phase demonstrates rather moderate intensity of luminescence with the 337-nm (3.68 eV) excitation laser, while its In-doped analog shows an intensive violet band at 410 ± 10 nm. Its intensity increases with an increase in the doping level *x*. Weaker broad maxima in 450–480 nm regions are observed for the samples with lower substitution rate.

Most likely, the PL of the solid solutions $Cs_{2-x}Sn_{1-x}In_xI_{6-2x}$ ($x = [0; 0.1]$) corresponds to cascade relaxation of electrons from the high free levels (anti-bonding derivative of $Sn5p^0$ orbital) to the valence band (Xiao et al., 2015). It has been demonstrated that decrease of the temperature up to 77 K leads to devolution of the PL process. Such behavior is typical for materials with a gap slightly larger than the excitation laser wavelength. The visible photoluminescence in Cs_2SnI_6 phase is observed as a result of complex relaxation processes. The relaxation of the excited electron to the bottom of the conduction band occurs with visible luminescent process, and the following transition to the top of the valence band has a much lower energy than the observed PL process. Participation of deep levels originated from the point defects (V_I) and is another possible reason for the PL effect in the visible diapason (Maughan et al., 2018).

For comparison, the gray cesium iodoindate(III) shows intensive PL bands at 380 ± 10 nm and 400 ± 10 nm in the visible region and intensive PL process in IR diapason at 1,170 ± 20 nm (1.16 eV) (**Figures 4B,C**). The 380-nm (3.26 eV) band correlates with the experimental band gap transition above while the second maximum in the visible range probably corresponds to shallow defects or self-trapped exciton processes. Intensive IR photoluminescence also originates from self-defect in cesium iodoindate, but the deep level is attributed to deficiency in iodine sublattice.

It is remarkable that the electron spin resonance effect is more significant for the cesium iodostannate(IV) phase with doped indium than for the pure phase. The ESR spectra for the $Cs_{2-x}Sn_{1-x}In_xI_{6-2x}$ ($x = 0.01$, 0.05, 0.09, 0.9, and 1) shown

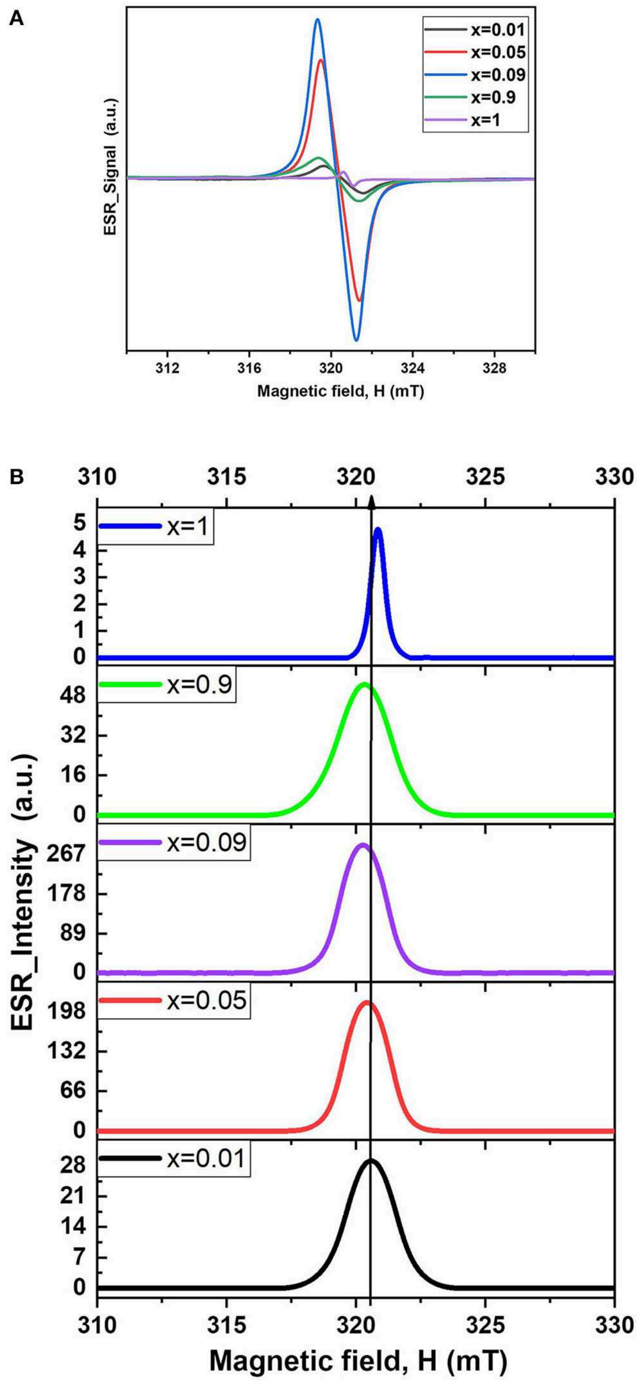

FIGURE 5 | ESR spectra of $Cs_{2-x}Sn_{1-x}In_xI_{6-2x}$ (with different ratio of *x*) at 4.2 K **(A)** in derivative form and **(B)** in integrated form.

TABLE 2 | ESR spectra characteristics.

Sample composition	Substitution rate *x*	Integration curve area	*g*-factor
$Cs_{1.99}Sn_{0.99}In_{0.01}I_{5.98}$	0.01	68.6	2.0045
$Cs_{1.95}Sn_{0.95}In_{0.05}I_{5.9}$	0.05	440.4	2.0051
$Cs_{1.9}Sn_{0.9}In_{0.1}I_{5.8}$	0.09	604.9	2.0054
$Cs_{1.1}Sn_{0.1}In_{0.9}I_{4.2}$	0.9	134	2.0065
$CsInI_4$	1	3.4	2.0029

in **Figure 5** demonstrate week shift of the resonance towards lower field values by the doping of indium from $x = 0.01$ to $x = 0.9$, resulting in the shift of the *g*-factor from 2.0045 to 2.0065. In the range of $x = 0.01$ to $x = 0.09$, the integral intensity of the ESR spectra grows up with increase of the substitution level *x* in the solid solution (**Table 2**), suggesting increment of the defects. The values of the *g*-factors and the areas calculated by the integration are given in **Table 2**. The spectra of the two-phase composition with *x* of 0.9 include less intensive and broad maximum at 321.2 mT. Probably, there could be an input shoulder related to the tin-doped cesium tetraiodoindate phase while the largest maximum corresponds to the spectrum of the solid solution $Cs_{2-x}Sn_{1-x}In_xI_{6-2x}$ saturated by In^{3+}. Lower ESR resonance in $CsInI_4$ phase, likely, attributed to lower defect concentration in cesium tetraiodoindate as a result of tetrahedral environment of indium and lower doping level.

CONCLUSIONS

The perovskite-like phase Cs_2SnI_6 forms substitution solid solutions, changing tin to indium, forming a substitution solid solution of about 10 at.% of dopant. Increase of the indium percentage leads to growth of ESR and photoluminescence effects for the material. The successful experience in heterovalent substitution of tin(IV) with elementary indium and iodine as precursors opens new challenges for "improving" the characteristics of cesium iodostannate for its application in photovoltaics or optoelectronic devices. Weak degradation of doped phase in comparison to pure Cs_2SnI_6 is a strong advantage of the new investigated materials. Analysis of optical properties has shown an increase of absorption coefficient of the material that originated from growth of occupancy in the valence band. The intensity of blue photoluminescence also grows with a substitution rate up to 15%.

DATA AVAILABILITY STATEMENT

All datasets generated for this study are included in the article/supplementary material.

AUTHOR CONTRIBUTIONS

SU: synthesis of the samples, Raman spectroscopy experiments and discussion, optical spectroscopy and discussion, ESR experiments. AG: PL spectroscopy and ESR spectroscopy data discussion, correction of the text, and funding. LL: PL spectroscopy experiments. AK: XRD measurements and discussion. KN: ESR experiments and correction of the text. SO:

ESR experiment discussion. AS: XRD discussion and correction of the text.

FUNDING

This project has been performed using the equipment and setups of the collective resource center of Moscow State University Technologies for synthesis of new nanostructured materials and their complex characterization. The reported study was funded by the Russian Foundation for Basic Research according to the research project N 19-03-00849_a.

ACKNOWLEDGMENTS

The authors are grateful to colleagues Dr. Tatyana A. Shestimerova, and Dr. Valery Yu. Verchenko (Lomonosov Moscow State University) for their assistance in XRD experiments.

REFERENCES

Ajay, K. J., Ashish, K., and Tsutomu, M. (2019). Halide perovskite photovoltaics: background, status, and future prospects. *Chem. Rev*. 119, 3036–3103. doi: 10.1021/acs.chemrev.8b00539

Brandt, R. E., Stevanović, V., Ginley, D. S., and Buonassisi, T. (2015). Identifying defect-tolerant semiconductors with high minority-carrier lifetimes: beyond hybrid lead halide perovskites. *MRS Commun*. 5, 265–275. doi: 10.1557/mrc.2015.26

Cai, Y., Xie, W., Ding, H., Chen, Y., Thirumal, K., Wong, L. H., et al. (2017). Computational study of halide perovskite-derived A_2BX_6 inorganic compounds: chemical trends in electronic structure and structural stability. *Chem. Mater*. 29, 7740–7749. doi: 10.1021/acs.chemmater.7b02013

Chen, Z., Wang, J. J., Ren, Y., Yu, C., and Shum, K. (2012). Schottky solar cells based on $CsSnI_3$ thin-films. *Appl. Phys. Lett*. 101:093901. doi: 10.1063/1.4748888

Chung, I., Song, J. H., Im, J., Androulakis, J., Malliakas, C. D., Li, H., et al. (2012). $CsSnI_3$: semiconductor or metal? High electrical conductivity and strong near-infrared photoluminescence from a single material. High hole mobility and phase-transitions. *J. Am. Chem. Soc*. 134, 8579–8587. doi: 10.1021/ja301539s

da Silva, E. L., Skelton, J. M., Parker, S. C., and Walsh, A. (2015). Phase stability and transformations in the halide perovskite $CsSnI_3$. *Phys. Rev. B* 91:144107. doi: 10.1103/PhysRevB.91.144107

Dang, T. C., Le, H. C., Pham, D. L., Nguyen, S. H., Nguyen, T. T. O., Nguyen, T. T., et al. (2019). Synthesis of perovskite Cs_2SnI_6 film via the solution processed approach: first study on the photoelectrochemical water splitting application. *J. Alloys Compd*. 805, 847–851. doi: 10.1016/j.jallcom.2019.07.122

Deng, J., Li, J., Yang, Z., and Wang, M. (2019). All-inorganic lead halide perovskites: a promising choice for photovoltaics and detectors. *J. Mater. Chem. C* 7, 12415–12440. doi: 10.1039/C9TC04164H

Dimesso, L., Das, C., Stöhr, M., and Jaegermann, W. (2017). Investigation of cesium tin/lead iodide ($CsSn_{1-x}Pb_xI_3$) systems. *Mater. Res. Bull*. 85, 80–89. doi: 10.1016/j.materresbull.2016.08.052

Elumalai, N. K., Mahmud, M. A., Wang, D., and Uddin, A. (2016). Perovskite solar cells: progress and advancements. *Energies* 861, 1–20. doi: 10.3390/en9110861

Fan, Q., McGee, G. V. B., Ma, J., Xu, Q., Pan, S., Peng, J., et al. (2019). Lead-free halide perovskite nanocrystals: crystal structures, synthesis, stabilities, and optical properties. *Angew. Chem. Int. Ed*. 59, 1030–1046. doi: 10.1002/anie.201904862

Fu, H. (2019). Review of lead-free halide perovskites as light-absorbers for photovoltaic applications: from materials to solar cells. *Solar Energy Mater. Solar Cells* 193, 107–132. doi: 10.1016/j.solmat.2018.12.038

Ganesan, R., Vinodhini, S. P., Balasubramani, V., Parthipan, G., Sridhar, T. M., Arulmozhi, M., et al. (2019). Tuning the band gap of hybrid lead free defect perovskite nano crystals for solar cell applications. *New J. Chem*. 43, 15258–15266. doi: 10.1039/C9NJ03902C

Gao, W., Ran, C., Xi, J., Jiao, B., Zhang, W., Wu, M., et al. (2018). High-quality Cs2AgBiBr6 double perovskite film for lead-free inverted planar heterojunction solar cells with 2.2 % efficiency. *ChemPhysChem* 19, 1696–1700. doi: 10.1002/cphc.201800346

Goldschmidt, V. M. (1926). Die Gesetze der Krystallochemie. *Naturwissenschaften* 14, 477–485.

Greul, E., Petrus, M. L., Binek, A., Docampo, P., and Bein, T. (2017). Highly stable, phase pure $Cs_2AgBiBr_6$ double perovskite thin films for optoelectronic applications. *J. Mater. Chem. A* 37, 5, 19972–19981. doi: 10.1039/C7TA06816F

Guo, F., Lu, Z., Mohanty, D., Wang, T., Bhat, I. B., Zhang, S., et al. (2017). A two-step dry process for Cs_2SnI_6 perovskite thin film. *Mater. Res. Lett*. 5, 540–546. doi: 10.1080/21663831.2017.1346525

Han, X., Liang, J., Yang, J.-H., Soni, K., Fang, Q., Wang, W., et al. (2019). Lead-free double perovskite Cs_2SnX_6: facile solution synthesis and excellent stability. *Small* 15:1901650. doi: 10.1002/smll.201901650

Hoefler, S. F., Trimmel, G., and Rath, T. (2017). Progress on lead-free metal halide perovskites for photovoltaic applications: a review. *Monatsh. Chem*. Chem. 2017, 148, 795–826. doi: 10.1007/s00706-017-1933-9

Huang, L.-,y., and Lambrecht, W. R. L. (2013). Electronic band structure, phonons, and exciton binding energies of halide perovskites $CsSnCl_3$, $CsSnBr_3$, and $CsSnI_3$. *Phys. Rev. B* 88:165203. doi: 10.1103/PhysRevB.88.165203

Igbari, F., Wang, Z.-K., and Liao, L.-S. (2019). Progress of lead-free halide double perovskites. *Adv. Energy Mater*. 9:1803150. doi: 10.1002/aenm.201803150

Jeon, N. J., Na, H., Jung, E. H., Yang, T.-Y., Lee, Y. G., Kim, G., et al. (2018). A fluorene-terminated hole-transporting material for highly efficient and stable perovskite solar cells. *Nat. Energy* 3, 682–689. doi: 10.1038/s41560-018-0200-6

Ju, M.-G., Chen, M., Zhou, Y., Garces, H. F., Dai, J., Ma, L., et al. (2017). Earth-abundant nontoxic titanium(IV)-based vacancy-ordered double perovskite halides with tunable 1.0 to 1.8 eV bandgaps for photovoltaic applications. *ACS Energy Lett*. 3, 297–304. doi: 10.1021/acsenergylett.7b01167

Kaltzoglou, A., Perganti, D., Antoniadou, M., Kontos, A. G., and Falaras, P. (2016). Stress tests on dye-sensitized solar cells with the Cs_2SnI_6 defect perovskite as hole-transporting material. *Energy Procedia* 102, 49–55. doi: 10.1016/j.egypro.2016.11.317

Ke, J. C.-R., Lewis, D. J., Walton, A. S., Spencer, B. F., O'Brien, P., Thomas, A. G., et al. (2018). Ambient-air-stable inorganic Cs_2SnI_6 double perovskite thin films via aerosol-assisted chemical vapour deposition. *J. Mater. Chem. A* 6, 11205–11214. doi: 10.1039/C8TA03133A

Kulbak, M., Gupta, S., Kedem, N., Levine, I., Bendikov, T., Hodes, G., et al. (2016). Cesium enhances long-term stability of lead bromide perovskite-based solar cells. *J. Phys. Chem. Lett*. 7, 167–172. doi: 10.1021/acs.jpclett.5b02597

Kumar, G. R., Kim, H.-J., Karupannan, S., and Prabhakar, K. (2017). Interplay between Iodide and tin vacancies in $CsSnI_3$ perovskite solar cells. *J. Phys. Chem. C* 121, 16447–16453. doi: 10.1021/acs.jpcc.7b06278

Kumar, M. H., Dharani, S., Leong, W. L., Boix, P. P., Prabhakar, R. R., Baikie, T., et al. (2014). Lead-free halide perovskite solar cells with high photocurrents realized through vacancy modulation. *Adv. Mater*. 26, 7122–7127. doi: 10.1002/adma.201401991

Lee, B., Krenselewski, A., Baik, S. I., Seidman, D. N., and Chang, R. P. H. (2017). Solution processing of air-stable molecular semiconducting iodosalts, $Cs_2SnI_{6-x}Br_x$, for potential solar cell applications. *Sustain. Energy Fuels* 1, 710–724. doi: 10.1039/C7SE00100B

Li, M. H., Yum, J. H., Moon, S. J., and Chen, P. (2016). Inorganic p-type semiconductors: their applications and progress in dye-sensitized solar cells and perovskite solar cells. *Energies*. 9:331. doi: 10.3390/en9050331

Liang, L., and Gao, P. (2018). Lead-free hybrid perovskite absorbers for viable application: can we eat the cake and have it too? *Adv. Sci*. 5:1700331. doi: 10.1002/advs.201700331

Maughan, A. E., Ganose, A. M., Almaker, M. A., Scanlon, D. O., and Neilson, J. R. (2018). Tolerance factor and cooperative tilting effects in vacancy-ordered double perovskite halides. *Chem. Mater*. 30, 3909–3919. doi: 10.1021/acs.chemmater.8b01549

Persson, K. (2016). *Materials Data on CsInI4 (SG:14) by Materials Project*. Berkeley, CA, 7. doi: 10.17188/1277593

Pisanu, A., Speltini, A., Quadrelli, P., Drera, G., Sangaletti, L., and Malavasi, L. (2019) Enhanced air-stability of Sn-based hybrid perovskites induced by dimethylammonium (DMA): synthesis, characterization, aging and hydrogen photogeneration of the $MA_{1--x}DMA_xSnBr_3$ system. *J. Mater. Chem. C* 7, 7020–7026. doi: 10.1039/C9TC01743G

Powalla, M., Paetel, S., Ahlswede, E., Wuerz, R., Wasserdorf, C. D., and Friedlmeier, T. M. (2018). Thin film solar cells exceeding 22% solar cell efficiency: an overview on $CdTe^-$, $Cu(In,Ga)Se^{2-}$, and perovskite-based materials. *Appl. Phys. Rev*. 5:041602. doi: 10.1063/1.5061809

Qiu, X., Cao, B., Yuan, S., Chen, X., Qiu, Z., Jiang, Y., et al. (2017). From unstable $CsSnI_3$ to air-stable Cs_2SnI_6: A lead-free perovskite solar cell light absorber with bandgap of 1.48eV and high absorption coefficient. *Solar Energy Mater. Solar Cells* 159, 227–234. doi: 10.1016/j.solmat.2016.09.022

Sani, F., Shafie, S., Lim, H., and Musa, A. (2018). Advancement on lead-free organic-inorganic halide perovskite solar cells: a review. *Materials* 11:E1008. doi: 10.3390/ma11061008

Savory, C. N., Walsh, A., and Scanlon, D. O. (2016). Can Pb-free halide double perovskites support high-efficiency solar cells? *ACS Energy Lett*. 1, 949–955. doi: 10.1021/acsenergylett.6b00471

Song, T.-B., Yokoyama, T., Longsdon, J., Wasielewski, M. R., Aramaki, S., and Kanatzidis, M. G. (2018). Piperazine suppresses self-doping in $CsSnI_3$ perovskite solar cells. *ACS Appl. Energy Mater*. 1, 4221–4226. doi: 10.1021/acsaem.8b00866

Stoumpos, C. C., Malliakas, C. D., and Kanatzidis, M. G. (2013). Semiconducting tin and lead iodide perovskites with organic cations: phase transitions, high mobilities, and near-Infrared photoluminescent properties. *Inorg. Chem*. 52, 9019–9038. doi: 10.1021/ic401215x

Stoumpos, C. C., Mao, L., Malliakas, C. D., and Kanatzidis, M. G. (2016). Structure–band gap relationships in hexagonal polytypes and low-dimensional structures of hybrid tin iodide perovskites. *Inorg. Chem*. 56, 56–73. doi: 10.1021/acs.inorgchem.6b02764

Veronese, A., Patrini, M., Bajoni, D., Ciarrocchi, C., Quadrelli, P., and Malavasi, L. (2020). Highly tunable emission by halide engineering in lead-free perovskite-derivative nanocrystals: The Cs_2SnX_6 (X = Cl, Br, Br/I, I) system. *Front. Chem*. 8:35. doi: 10.3389/fchem.2020.00035

Wang, A., Yan, X., Zhang, M., Sun, S., Yang, M., Shen, W., et al. (2016). Controlled synthesis of lead-free and stable perovskite derivative Cs_2SnI_6 nanocrystals via a facile hot-injection process. *Chem. Mater.* 28, 8132–8140. doi: 10.1021/acs.chemmater.6b01329

Wang, X.-D., Huang, Y.-H., Liao, J.-F., Jiang, J., Zhou, L., Zhang, X.-Y., et al. (2019). *In situ* construction of a Cs_2SnI_6 perovskite nanocrystal/SnS_2 nanosheet heterojunction with boosted interfacial charge transfer. *J. Am. Chem. Soc*. 141, 13434–13441. doi: 10.1021/jacs.9b04482

Wang, Y., Tu, J., Li, T., Tao, C., Deng, X., and Li, Z. (2019). Convenient preparation of $CsSnI_3$ quantum dots, excellent stability, and the highest performance of lead-free inorganic perovskite solar cells so far. *J. Mater. Chem. A* 7, 7683–7690. doi: 10.1039/C8TA10901J

Wan-Jian, Y., Ji-Hui, Y., Kang, J., Yan, Y., and Wei, S.-H. (2015). Halide perovskite materials for solar cells: a theoretical review. *J. Mater. Chem. A* 3, 8926–8942. doi: 10.1039/C4TA05033A

Wijesekara, A., Varagnolo, S., Dabera, G. D. M. R., Marshall, K. P., Pereira, H. J., and Hatton, R. A. (2018). Assessing the suitability of copper thiocyanate as a hole-transport layer in inverted $CsSnI_3$ perovskite photovoltaics. *Sci. Rep.* 8:15722. doi: 10.1038/s41598-018-33987-7

Wu, C., Zhang, Q., Liu, Y., Luo, W., Guo, X., Huang, Z., et al. (2017). The dawn of lead-free perovskite solar cell: highly stable double perovskite $Cs_2AgBiBr_6$ film. *Adv. Sci*. 5:1700759. doi: 10.1002/advs.201700759

Wu, Y., Xie, F., Chen, H., Yang, H., Su, H., Cai, M., et al. (2017). Thermally stable $MAPbI_3$ perovskite solar cells with efficiency of 19.19% and area over $1cm^2$ achieved by additive engineering. *Adv. Mater*. 29:1701073. doi: 10.1002/adma.201701073

Xiao, Z., Lei, H., Zhang, X., Zhou, Y., Hosono, H., and Kamiya, T. (2015). Ligand-hole in $[SnI_6]$ unit and origin of band gap in photovoltaic perovskite variant Cs_2SnI_6. *Bull. Chem. Soc. Jpn*. 88, 1250–1255. doi: 10.1246/bcsj.20150110

Xiao, Z., Song, Z., and Yan, Y. (2019). From lead halide perovskites to lead-free metal halide perovskites and perovskite derivatives. *Adv. Mater*. 31:1803792. doi: 10.1002/adma.201803792

Xiao, Z., and Yan, Y. (2017). Progress in theoretical study of metal halide perovskite solar cell materials. *Adv. Energy Mater*. 7:1701136. doi: 10.1002/aenm.201701136

Yang, W. S., Park, B. W., Jung, E. H., Jeon, N. J., Kim, N. C., Lee, D. U., et al. (2017). Iodide management in formamidinium-lead-halide–based perovskite layers for efficient solar cells. *Science* 356, 1376–1379. doi: 10.1126/science.aan2301

Yin, H., Xian, Y., Zhang, Y., Li, W., and Fan, J. (2019). Structurally-stabilizing and friendly-environmental triggers: double-metallic lead-free perovskites. *Solar RRL* 3:1900148. doi: 10.1002/solr.201900148

Yuan, G., Huang, S., Qin, S., Wu, X., Ding, H., and Lu, A. (2019). Structural, optical and thermal properties of $Cs_2SnI_{6-x}Br_x$ mixed perovskite solid solution. *Eur. J. Inorg. Chem*. 20, 2524–2529. doi: 10.1002/ejic.201900120

Zhao, X.-G., Yang, D., Sun, Y., Li, T., Zhang, L., Yu, L., et al. (2017b). Cu–In halide perovskite solar absorbers. *J. Am. Chem. Soc*. 139, 6718–6725. doi: 10.1021/jacs.7b02120

Zhao, X.-G., Yang, J.-H., Fu, Y., Yang, D., Xu, Q., Yu, L., et al. (2017a). Design of lead-free inorganic halide perovskites for solar cells via cation-transmutation. *J. Am. Chem. Soc*. 139, 2630–2638. doi: 10.1021/jacs.6b09645

Zhu, W., Yao, T., Shen, Y., Xu, W., Gong, B., Wang, Y., et al. (2019). *In situ* investigation of water interaction with lead-free all inorganic perovskite ($Cs_2SnI_xCl_{6-x}$). *J. Phys. Chem. C* 123, 14, 9575–9581. doi: 10.1021/acs.jpcc.9b00720

Zhu, Z., Li, N., Zhao, D., Wang, L., and Jen, A. K. Y. (2019). Improved efficiency and stability of Pb/Sn binary perovskite solar cells fabricated by galvanic displacement reaction. *Adv. Energy Mater.* 9:1802774. doi: 10.1002/aenm.201802774

Conflict of Interest: The authors declare that the research was conducted in the absence of any commercial or financial relationships that could be construed as a potential conflict of interest.

frontiers in Chemistry

MINI REVIEW
published: 12 August 2020
doi: 10.3389/fchem.2020.00630

Speciation of Uranium and Plutonium From Nuclear Legacy Sites to the Environment: A Mini Review

*Anna Yu. Romanchuk, Irina E. Vlasova and Stepan N. Kalmykov**

Department of Chemistry, Lomonosov Moscow State University, Moscow, Russia

The row of 15 chemical elements from Ac to Lr with atomic numbers from 89 to 103 are known as the actinides, which are all radioactive. Among them, uranium and plutonium are the most important as they are used in the nuclear fuel cycle and nuclear weapon production. Since the beginning of national nuclear programs and nuclear tests, many radioactively contaminated nuclear legacy sites, have been formed. This mini review covers the latest experimental, modeling, and case studies of plutonium and uranium migration in the environment, including the speciation of these elements and the chemical reactions that control their migration pathways.

Keywords: plutonium, uranium, migration, environment, speciation

Edited by:
W. H. Eugen Schwarz,
University of Siegen, Germany

Reviewed by:
Nail M. Shavaleev,
Independent Researcher, Ufa, Russia
Akitaka Ito,
Kochi University of Technology, Japan

***Correspondence:**
Stepan N. Kalmykov
stepan@radio.chem.msu.ru

Specialty section:
This article was submitted to
Inorganic Chemistry,
a section of the journal
Frontiers in Chemistry

Received: *15 March 2020*
Accepted: *17 June 2020*
Published: *12 August 2020*

Citation:
Romanchuk AY, Vlasova IE and Kalmykov SN (2020) Speciation of Uranium and Plutonium From Nuclear Legacy Sites to the Environment: A Mini Review. Front. Chem. 8:630. doi: 10.3389/fchem.2020.00630

INTRODUCTION

The discovery of the nuclear fissions of U-235 and Pu-239 led to the era of nuclear weapons development and nuclear energy production. The first national nuclear programs dealt with uranium separation from ore, U-235 enrichment, plutonium production, and fuel fabrication without considering the radiation safety and environmental protection. From the start of nuclear programs and up to the period of environmental awareness, 1940s to the 1980s, many nuclear sites were established worldwide that to this day are contaminated with uranium and plutonium (Rybalchenko et al., 2005; Novikov et al., 2006; Zachara et al., 2013). Every nuclear fuel production and waste reprocessing site in the 1940–1960s used surface or underground radioactive waste storage. Many countries adopted strategies for the remediation of contaminated sites, and in some cases, remediation has been started or even completed (Conradson et al., 2011). The speciation of radionuclides in contaminated sites has been studied, and recently new discoveries were made about the speciation of uranium and plutonium that were released into the environment as a result of accidents or in the course of daily operation. Sufficient time has passed since these sites were established to clarify the migration processes. Today, we have 60 years of data on nuclear test sites and 30 years of data on consequences of the Chernobyl nuclear power plant (NPP) accident. Analysis of these data may help us to better understand the environmental behavior of actinides.

We review the recent trends in the studies of the physics and chemistry of uranium and plutonium in the nuclear legacy sites and in laboratory experiments. **Figures 1**, **2** summarize the speciation of U and Pu and the migration pathways of U and Pu from the legacy sites into the environment.

URANIUM

Two main oxidation states of uranium, namely +4 and +6, exist under natural geochemical conditions. In aqueous solutions, uranium is mainly present in its most mobile form the uranyl cation $U^{VI}O_2^{2+}$, typically in the form of hydroxyl and carbonate complexes. The mobility

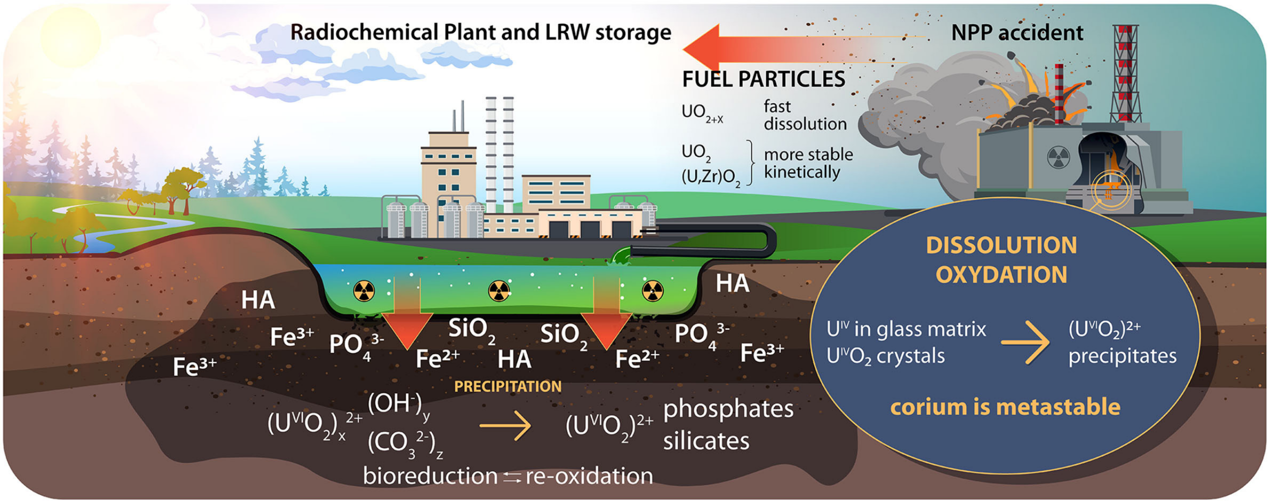

FIGURE 1 | U migration into the environment. NPP, nuclear power plant; LRW, liquid radioactive waste; HA, humic acid.

of uranium depends on the redox conditions and the presence of cations (Ca^{2+}, Fe^{2+}, and Fe^{3+}), anions (carbonate, phosphate, and sulfate), silica, natural rock-forming minerals, organic substances, and microorganisms (**Figure 1**). In a reducing environment (oxygen-free conditions of deep underground disposals in the presence of microorganisms), uranium can transform into a less mobile form, U(IV). However, U(IV) may easily reoxidize if the conditions change. At the same time, uranium could be kinetically stabilized in "hot" particles. For example, as a result of accidental fallout (e.g., the Chernobyl accident), kinetically stable fuel particles were released into the environment, in which U(IV) was mainly in the form of UO_2 (**Figure 1**).

For a long time, it was believed that pentavalent uranium does not occur in nature with a few exceptions since the cation $U^VO_2^+$ is unstable in aqueous solution due to its disproportionation into U^{IV} species and $U^{VI}O_2^{2+}$ (Arnold et al., 2009). In addition, a technical difficulty occurred in detecting pentavalent uranium in the samples. The latest U L_3 X-ray absorption spectroscopy (XANES) study demonstrates U^{VI} reduction to U^V in the presence of Fe^{II}/Fe^{III} oxides and oxy-hydroxides (Boland et al., 2014; Marshall et al., 2015). Three valence states of uranium, U(IV), U(V), and U(VI), could be distinguished via U M_4 edge high-energy resolution X-ray absorption spectroscopy (HERFD-XANES) in a sample with a U concentration range of 1,000–10,000 ppm (Pidchenko et al., 2017; Roberts et al., 2017). Therefore, U(V) should also be considered in the environment.

Immobilization of U

Uranium leakage from near-surface and surface liquid radioactive waste (LRW) storage facilities (**Figure 1**) as well as from underground deep disposals into permeable formations occurs mainly via the release of uranyl species. Moreover, in contaminated soils from the sites of uranium mining, milling and enrichment, uranium is also found mainly in the uranyl form. The mobility of hydroxo and carbonato uranyl complexes in aqueous systems is a severe problem for many nuclear legacy sites. The mechanisms of uranyl retention via sorption, incorporation, precipitation, and reduction, among other processes, are being studied under simulated natural and waste disposal conditions. In addition to laboratory modeling, the most effective strategies for U immobilization are identified via field tests and case studies.

The remediation of contaminated soils faces the problem of selecting a technical strategy. This is complicated by the factors that affect the behavior of uranium, which include the soil type, the mineral composition, the natural organic matter (OM), and the initial forms of uranium; see, for example Selvakumar et al. (2018) and references therein. In the case of uranium contamination of the vadose zone, especially in arid and semiarid climates, there are two main ways to prevent uranium from entering groundwater in quantities that exceed acceptable levels: by monitoring natural attenuation (e.g., through adsorption processes or radioactive decay) or by remedial actions (e.g., mass or mobility reduction of uranium) (Dresel et al., 2011). The Hanford site's natural-technological system is one of the most studied in terms of uranium behavior in the interactions of acidic, neutral, and alkaline wastes with deposits (Szecsody et al., 2013; Gartman et al., 2015). At two contaminated sites, Hanford 300A (Columbia River) and Rifle (Colorado River), subsurface uranium plumes have been examined following the surface excavation of contaminated materials (Zachara et al., 2013). The rate of the observed uranium decrease was much lower than expected at both sites. The mechanisms that control the plume persistence were considered. At the Hanford 300A site, U(VI) that is sorbed in the vadose zone enters the oxidizing aquifer during spring water excursion, and uranium release into the groundwater is controlled by kinetically limited surface complexation. At the Rifle site, U(IV) is slowly oxidized in the suboxic groundwater. The additional influx of U(VI) from the upper vadose zone is also controlled by surface complexation; however, its contribution is local, and it is not the dominant

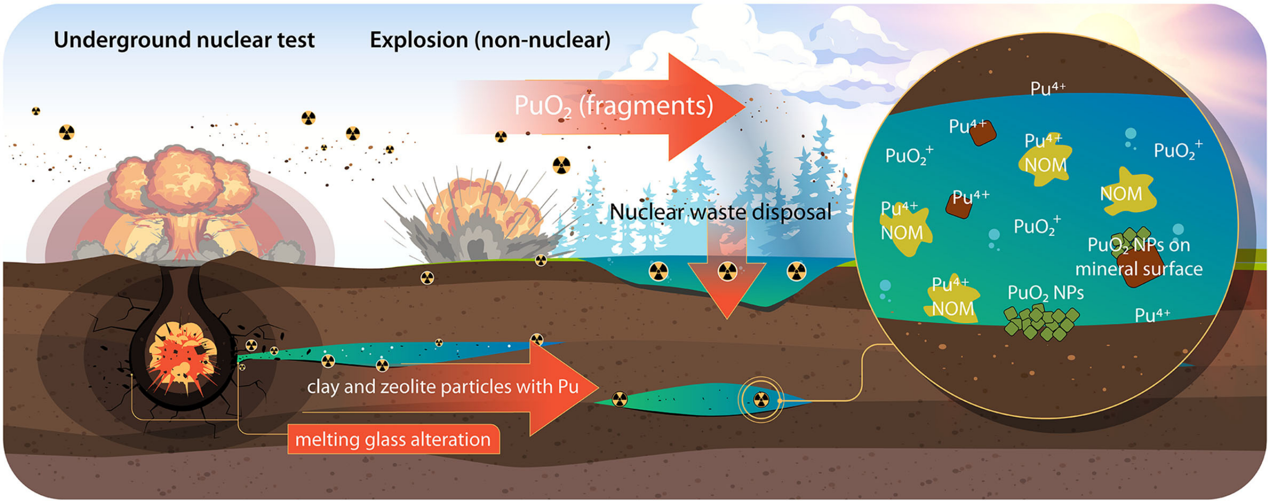

FIGURE 2 | Pu migration into the environment. NP, nanoparticle; NOM, natural organic matter.

mechanism of plume spreading. Thus, field studies show a wide variety of conditions and forms of uranium in real sites; hence, laboratory studies of the dependence of the uranium behavior on each of the environmental factors are required.

The behavior of uranyl in the presence of Ca^{2+} and CO_3^{2-} has been studied. At neutral pH and low concentrations ($<500\ \mu M$), U(VI) sorbs on the calcite surface with the formation of inner-sphere uranyl triscarbonate complexes, whereas at high U concentrations, U(VI) forms hydroxide/carbonato precipitates (Elzinga et al., 2004). The incorporation of uranium into the calcite and vaterite structure at the Ca^{2+} sites with aging was demonstrated in the case of at least a decimolar Ca concentration (Kelly et al., 2003, 2006; Niu et al., 2019). Experimental modeling of geological disposals under hyperalkaline calcite conditions at high U concentrations [at least $4.2\ \mu M$ U(VI)] demonstrated the precipitation of calcium uranate-type phases (Mace et al., 2013; Smith et al., 2015). At low U(VI) concentrations, the formation of liebigite-like $Ca_2UO_2(CO_3)_3$ surface complexes and binding to calcium silicate hydrates were confirmed. The difference in uranium behavior at low concentrations under neutral and high pH was observed; in the former case, the surface complexation dominates while, in the latter, uranium mainly precipitates (Smith et al., 2015). At the same time, it was demonstrated that U(VI) sorption on orthoclase and muscovite could be reduced by the presence of Ca^{2+} at a millimolar concentration at pH > 8 by up to 30% due to the formation of the neutral aqueous $Ca_2UO_2(CO_3)_3$ complex (Richter et al., 2016). The study of the ternary system of Ca^{2+}-U(VI)–CO_3^{2-} remains relevant because it covers diverse processes, such as the sorption, precipitation, and incorporation of uranium in the structure of calcium carbonate, which depend on the concentration of each member of the ternary system and the environment.

A study of the behavior of uranyl in the presence of clay minerals, one of the most common components of the environment, was conducted for U mill and mine tailing material from Saskatchewan, Canada (Schindler et al., 2015). The absorption of uranyl in the alteration zones of clay minerals and intergrowth of silicates and uranyl minerals were demonstrated along with processes of the nucleation of nanocrystals of uranyl-arsenates and silicates: cuprosklodowskite, $Cu[(UO_2)_2(SiO_3OH)_2](H_2O)_6$, and metazeunerite, $Cu[(UO_2)(AsO_4)_2](H_2O)_8$.

Iron oxides and oxyhydroxides appear to significantly change the behavior of uranium, and their effects continue to be studied as the new data raises new questions. Uranyl reduction to U(V) and incorporation into Fe(II/III) oxides and oxyhydroxides in cement leachates were studied under simulated geological disposal conditions at high pH (Marshall et al., 2014, 2015) and under neutral pH (Boland et al., 2014). The uranium sorption on ferrihydrite in the presence of natural organic matter (NOM) was investigated (Dublet et al., 2017), and it was shown that the effect on uranyl sorption depended on the pH and the type of NOM.

Research on uranium speciation at contaminated sites has been followed by work on the leaching, purification, and immobilization of uranium. Various approaches have been tested and revised, and recently, many laboratory studies and field tests have been conducted with the objective of evaluating the reliability of uranium retention.

There are two reliable mechanisms for the transformation of uranium from a mobile form to a solid phase in a field case: phosphate precipitation and reduction. Both are thoroughly investigated with site samples. The mobility of uranium, which is found in deposits as the relatively soluble carbonate and hydroxocomplexes, was found to be decreased by the introduction of polyphosphate solutions, thereby resulting in the precipitation of calcium uranyl phosphate (Mehta et al., 2016). Kanematsu et al. have studied uranium speciation in the solids that precipitated from synthetic acidic to neutral wastewaters in the presence and absence of dissolved silica and phosphate using U L_{III}-edge EXAFS. It was revealed that rapidly precipitated autenite [$Ca(UO_2)_2(PO_4)_2 \cdot 10–12(H_2O)$]-type and meta-ankoleite [$K_2(UO_2)_2(PO_4)_2 \cdot 6H_2O$]-type sheets transform into phosphuranylite [$K_2Ca(UO_2)_7(PO_4)_4(OH)_6 \cdot 6H_2O$]-type sheets after 30 days of reaction. This study proved that particle size, crystallinity, and composition of the precipitates control the thermodynamic and kinetic stability of uranyl solids in sediments that are impacted by acidic/neutral waste discharges (Kanematsu et al., 2014). The forms of uranium in a similar system, uranyl-silica-phosphate, were studied by Perdrial et al. In a phosphate-free system, uranium speciation was controlled initially by the precipitation of compreignacite [$K_2(UO_2)_6O_4(OH)_6 \cdot 8H_2O$]- and becquerelite [$Ca(UO_2)_6O_4(OH)_6 \cdot 8H_2O$]-like species. The subsequent removal of uranium coincided with that of silicon and the accumulation of boltwoodite [$(K, Na)(UO_2)_2O_4(HSiO_4)_2 \cdot 0.5(H_2O)$]-like species after 180 and 365 days. In the presence of PO_4^{3-}, meta-ankoleite [$K_2(UO_2)_2O_4(PO_4)_2 \cdot 6H_2O$]-like species exerted direct and strong control over U speciation (Perdrial et al., 2018). The dynamics of the precipitation–sorption-phase evolution in the uranyl-phosphate system at a pH of 6 in a several-week experiment was studied in the presence of goethite and mica to simulate the environment (Munasinghe et al., 2015). Chernikovite [$(H_3O)_2(UO_2)_2(PO_4)_2 \cdot 6(H_2O)$] was the first rapidly precipitated form in the experiments with U and P while partially hydrated (meta)autenite was formed only in the presence of goethite. The transition between phases was accelerated by sorption.

The bioavailability of uranium at near-surface contaminated sites is determined by the phosphate forms of uranyl, which are easily taken up by the plants (Edayilam et al., 2020). The complexity of the uranyl-phosphate system and its practical significance, highlighted in this review, support the necessity of its further study.

Emerson et al. proved the retardation of uranium on treatment with bases, such as sodium hydroxide, ammonium hydroxide, and ammonia gas, in the presence of various minerals and natural sediments from the Hanford site (Washington State, USA) (Emerson et al., 2018). The control of the pH with ammonia gas injection may be especially useful for vadose zone environments as it does not require the addition of liquids that would increase the flux toward the groundwater. The authors suggest that the likely mechanisms for the transfer of uranium from the aqueous to the solid phase are the formation of surface coatings, coprecipitation with carbonates, and adsorption.

Uranium and Organic Matter

Luo and Xu (2016) proved the key role of thiol groups in NOM. They are responsible for the bioremediation and immobilization of uranium when it enters the environment (soil, groundwater). Bioreduction, followed by reoxidation by oxygen, can sequestrate U via the formation of stable U-coated particles, as was shown by Li et al. (2019). The dual effects of microorganisms on the behavior of uranium (reduction or rapid reoxidation), along with biosorption, bioaccumulation, and biomineralization, are reviewed in Cumberland et al. (2016). Uncertainties that are associated with the oxidation state and mobility of uranium, which is influenced by microorganisms, on both the geological and molecular scales are reviewed in this work. Available information on the uranium-OM bond and the solubility of U-OM was collected and analyzed. During the biosorption of uranium by fungal cells, the oxidation state of uranium was unchanged while the uranium speciation did change (Günther et al., 2014). Extra- and intracellular phosphate groups are mainly responsible for uranium binding.

The interaction between uranium and NOM is especially important in wetlands. There are many examples of wetlands in which this interaction governs the partitioning (Kaplan et al., 2016, 2017; Koster van Groos et al., 2016; Mikutta et al., 2016; Schumann et al., 2017; Dublet et al., 2019; Stetten et al., 2020). One of the main characteristics of these places is the significant seasonal change. During the hot season, the wetlands become dry, and the oxidative conditions occur, while during the floods or even frozen season, the reductive conditions may change the uranium speciation. Examples around the world show all of these processes: oxidation/reduction together with precipitation/dissolution and sorption/complexation. Future research in this area could identify the relationship between the seasonal changes and the various parameters, such as the temperature, Eh, pH, [PO_4^{3+}], [NOM], microbial and plant community and uranium behavior.

Thermodynamic Modeling and Instrumental Techniques

Both the prediction of the uranium distribution in the environment and the selection of an efficient remediation strategy require the use of thermodynamic constants for reactions that involve U. The available databases for uranium (Grenthe et al., 1992; Guillaumont et al., 2003) lack many constants. In some cases, published constants differ significantly, and sometimes the data obtained are not in accordance with the current state of knowledge. The validation of available thermodynamic data and their refinement or the acquirement of new data are of substantial importance for investigating the behavior of uranium in nature. For example, thermodynamic data for the ternary complexation of calcium uranyl tricarbonate species $CaUO_2(CO_3)_3^{2-}$ and $Ca_2UO_2(CO_3)_3(aq)$ in the temperature range of 10–70°C were obtained in Jo et al. (2019) using time-resolved laser-induced fluorescence spectroscopy (TRLFS), ion-selective electrode potentiometry, and UV/vis adsorption spectroscopy. Thermodynamic modeling of uranium species and its comparison with the experimental data that were obtained via direct non-destructive methods is necessary to investigate of uranium behavior at the contaminated sites. The use of different databases for the same water composition leads to substantial differences in modeling as was shown by Mühr-Ebert et al. (2019). To clarify this, the researchers optimized the thermodynamic data using model calculations and laboratory tests by TRLFS, mass spectrometry, and extraction experiments under various model conditions (Mühr-Ebert et al., 2019).

The recent rapid development of spectrometric, microscopic, and other analytical methods enables us to better understand the processes that occur at the contaminated sites. Non-destructive techniques, such as scanning electron microscopy

(SEM) and transmission electron microscopy (TEM) with energy-dispersive X-ray analysis (EDX), are increasingly being used together with semidestructive secondary-ionization mass spectrometry (SIMS).

In addition to the classic methods, such as TRLFS, a highly sensitive method for the identification and detection of uranium species in solids and solutions is vibration spectroscopy, including infrared absorption and Raman scattering (Lu et al., 2018). The main advantage of these techniques is the possibility of *in situ* detection and the real-time monitoring of chemical reactions that involve uranium.

A combination of experiments and calculations in the identification of uranium species yields acceptable results. For example, five uranyl aqueous complexes under a fixed U conc. (10^{-5} M) over a wide pH range from 2 to 11 were identified from the TRLFS data with parallel factor analysis, UV excitation spectra (180–370 nm) and time-dependent density functional theory. The combination of experiment and theory confirmed the presence of the $[UO_2(H_2O)_5]^{2+}$ cation (aquo-complex 1:0) and the four hydroxo-complexes (1:1, 3:5, 3:7, and 1:3) (Drobot et al., 2015).

Synchrotron radiation X-ray techniques, such as X-ray fluorescence (XRF), diffraction (XRD), and absorption spectrometry (XAFS), especially with a submicron beam, provide information on the local molecular speciation (Kelly et al., 2006; Kanematsu et al., 2014; Smith et al., 2015). Recent study of the oxidation state of uranium and the structure of electronic orbitals using resonant inelastic X-ray scattering (RIXS) and HERFD-XANES measurements at the U L_{III} (Kvashnina et al., 2015), U M_{IV} (Kvashnina et al., 2013; Butorin et al., 2016) and Pu edges (Vitova et al., 2017; Kvashnina et al., 2019) give promising results for future applications. However, a significant limitation of these experimental methods is that the uranium concentrations, even at highly contaminated sites, are often below the detection limits of advanced analytical methods. Therefore, indirect destructive methods, such as sequential extraction and solvent extraction, remain the only available methods to obtain the information.

Uranium-containing phases were identified using advanced techniques in sludges from Hanford tanks (Peterson et al., 2018). The uranium concentration in radioactive waste is much higher than in the environment of the LRW storage. A limitation of this experimental approach is that in model systems, the uranium concentrations are 10^{-5}-10^{-7} mol/L while the uranium concentrations at contaminated sites are below the detection limits of advanced analytical methods. Even in studies in which XANES spectra for extremely low uranium concentrations were obtained (Zhang et al., 2016), the U content is about 40 ppm, which is not always the case for the contaminated soils. Few applications of advanced techniques for the identification of U species in the environment are available (Tayal et al., 2019). This research should be continued, but destructive analyses will inevitably have to be used to identify uranium partitioning in mobile fractions as they are often the only methods for determining the forms of uranium; see Qiao et al. (2012) and Skipperud et al. (2013).

Uranium in “Hot” Particles and Corium

In the case of accidental fuel fallout, such as the Chernobyl fallout, uranium enters the environment initially as U(IV) species, mainly as uranium dioxide, which is partially oxidized, and sometimes as mixed uranium-zirconium dioxide (UO_{2+x}, (U, Zr)O_2) (Pöml and Burakov, 2018; Shiryaev et al., 2018) (**Figure 1**). The solubility of these fuel particles depends more on the conditions of their formation than on the environment (Kashparov et al., 2019). The most kinetically stable are those (U,Zr)O_2 particles that were formed at the maximum temperature during an accident. UO_2 particles are less stable than (U,Zr)O_2 particles. The UO_{2+x} particles are the most soluble and the least stable. In addition to uranium, fuel particles contain fission products and transuranium elements and their behavior is associated with the behavior of the particles. According to the similarity of the chemical behaviors of Sr, Cs, and Am in the Polesie soils, these radionuclides bind to fuel particles (Bondarkov et al., 2011). For more than 30 years since the Chernobyl accident, we have traced the kinetics of the dissolution/destruction of fuel particles based on a large amount of statistical data (Beresford et al., 2016; Lecomte-Pradines et al., 2020).

Uranium can enter the environment in the form of uranium dioxide particles during an accidental discharge, such as the pollution of the Yenisei River (Bolsunovsky et al., 2017), and via regular technological influxes of liquid RW into storage pools, in which liquid RW accumulates in the bottom sediments and into sludge storage pools (Batuk et al., 2015).

A special form of uranium is corium, the molten zone of an emergency reactor. The lava-like fuel-containing materials that formed in the 4th Chernobyl NPP unit have been studied for a long time, and recently, additional analytical methods have become available to study the forms of radionuclides, such as uranium (Shiryaev et al., 2016; Burakov, 2019). The obtained data on the structures and the phase compositions of lava-like materials will facilitate the prediction of the kinetics of the mechanical destruction of “lava” and the development of best strategies for handling this type of radioactive waste, which will also be useful for handling the corium of the Fukushima Daiichi emergency reactors. Numerous core melt model studies have been conducted, and sacrificial materials have been selected (Veshchunov et al., 2008; Knebel et al., 2017).

PLUTONIUM

Plutonium can exist in four oxidation states: Pu(III), Pu(IV), Pu(V), and Pu(VI). These states can even exist simultaneously under suitable environmental conditions. The redox potentials for switching between the oxidation states are close to 1 V for many reactions, which creates a unique scenario in which multiple oxidation states can coexist in solution (Clark et al., 2005). The oxidation state of plutonium controls its reactivity and solubility. Pu(VI) and Pu(V) are more soluble in water than Pu(IV) and Pu(III). The most important reactions for the environmental plutonium behavior are sorption, complexation, precipitation, and colloid formation, on all of which the oxidation state has the most profound influence.

Far fewer studies have been published on the behavior of plutonium than on that of uranium in the environment.

Colloid Transport

The Pu migration in the environment was investigated at the Nevada National Security Site (NNSS), where 828 underground nuclear tests were conducted, and Pu was found in two aquifers, 1.3 km away from a nuclear test location (Kersting et al., 1999). Over 95% of the Pu in the groundwater well was associated with colloidal particles (mainly clays and zeolites). In recent years, the mechanism of the formation of these Pu species has been deeply clarified. It was found that alteration of the NNSS nuclear melt glass under hydrothermal conditions that likely occurred in the vicinity and aftermath of the underground nuclear explosion resulted in the formation of mineral colloids, which are similar to those that were reported in 1999, and plutonium was predominantly associated with them (Zavarin et al., 2019) (**Figure 2**). It was concluded that colloid-bound Pu was produced as a result of nuclear melt glass aging, which suggests that the local geochemistry of the test site may not be very important in the first stages of the migration. The authors attempted to describe the subsequent leaching of plutonium from these colloids. The results suggest that the hydrothermal conditions during colloid formation affect the Pu desorption rates from the colloids (Joseph et al., 2019). The desorption rates of Pu from the colloids that were formed at 140°C can be modeled based on the kinetics of Pu sorption/desorption onto montmorillonite at room temperature. The authors estimate that the half-life of Pu on colloids is on the order of 0.6–1.8 years (Begg et al., 2017). The Pu that is bound to zeolite and clay colloids at higher temperatures ($\geq$200°C) is more stable, and the desorption rate of Pu from these colloids is at least one order of magnitude slower than that for the colloids formed by leaching at a lower temperature.

The study of the colloid transport of Pu from Lake Karachay (PA "Mayak," Russia) (Novikov et al., 2006) found that a significant fraction of the plutonium is bound to colloids with a size $<$15 nm made of amorphous ferrihydrite. Many studies have been conducted on the sorption of plutonium onto mineral colloids to understand its transport. The plutonium sorption is complicated by redox reactions; hence, this topic remains open for discussion and study (Romanchuk et al., 2016b). Recently, it was found that Pu(IV) stabilization onto mineral surfaces may result in Pu surface precipitation in the form of PuO_2 nanoparticles (Kirsch et al., 2011; Romanchuk et al., 2013, 2016a; Schmidt et al., 2013; Zhao et al., 2016) (**Figure 2**). Therefore, the study of PuO_2 nanoparticles becomes increasingly important, and it is actively being conducted (Powell et al., 2011; Romanchuk et al., 2018; Kvashnina et al., 2019; Gerber et al., 2020).

The strong interaction of Pu with minerals and sediments results in stable association with no leaching is observed even after 32 years of aging (Emerson et al., 2019). In this study, solvent extraction of Pu that was bound with the surface for 3 days and for 32 years shows that the aging changes the speciation of Pu on the surface; however, the exact mechanism of the aging remains undefined. Understanding of the aging and of the stronger Pu binding with minerals or colloids is important for the prediction of Pu transport in the environment.

Plutonium and NOM

Most of the plutonium that was released into the environment during the Chernobyl accident was associated with uranium particles. The subsequent migration of this plutonium was controlled by the dissolution of these particles; see above. The plutonium concentration in the groundwater of the Chernobyl Exclusion Zone remains low (Bugai et al., 2020). However, these concentrations are much higher than those that are determined via simple calculations that apply the distribution coefficient (K_d) concept. A relatively low K_d of plutonium was obtained for the *in situ* experiments compared to the values that were reported for a batch. The mechanism of this overstated plutonium migration remains to be identified. It can most likely be explained by facilitated transport in the form of mobile colloids or of complexes with NOM, especially considering the local geochemistry. For example, (Levchuk et al., 2012) demonstrated using ultrafiltration that a large fraction of the plutonium in the groundwater of the "Red forest" (5 km from the Chernobyl NPP) is bound with low-molecular-weight NOM ($<$1 kDa) and humic and fulvic acids.

The influence of organic substances on plutonium migration has been discussed in other works (Zhao et al., 2011; Santschi et al., 2017; Lin et al., 2019). In the NNSS vadose zone, the water that was collected in a tunnel system had plutonium predominantly as an aqueous species, which was not bound with colloids (Zhao et al., 2011). It was found that more than 70% of the plutonium was complexed with dissolved organic matter and that its high content (15–19 mg/L) could be attributed to anthropogenic mining activity.

Another example of the influence of organic matter on the behavior of Pu was found in the Nishiyama reservoir (Nagasaki, Japan) (Lin et al., 2019). Nagasaki is the only city in the world where a Pu bomb was exploded. As a result, an area of 3–5 km^2 in Nagasaki was highly contaminated by 200 radioactive isotopes. Plutonium precipitated to the earth as a "black rain," which is a mixture of soot carbon and water. High levels of plutonium remain in the sediments of the Nishiyama reservoir. Most of the Pu in the sediments was preferentially bound to the organic matter that was stabilized by Fe oxides. The authors conclude that the chelation of Pu by the hydroxamate siderophores occurs in the sub-/surface soils, similar to the F-area of the Savannah River site and the Fukushima prefecture (Santschi et al., 2017). Santschi et al. proposed that Pu(IV) may become even more mobile than oxidized Pu(V/VI). As a result, Pu(IV) bound with organic matter can form mobile colloids, especially at higher pH. Therefore, NOM can immobilize or remobilize Pu depending on the pH. This effect should be considered in the migration modeling and should be studied further. The data on the influence of NOM on the interaction of Pu with minerals and sediments are limited.

Pu in "Hot" Particles

Synchrotron-based techniques, especially with microresolution, may help in the speciation of Pu-containing particles. A valuable example is the remediation of the Rocky Flats environmental technology site. A combination of XANES and EXAFS methods facilitated the detection of PuO_2-like particles in the soil (Conradson et al., 2011). These particles exhibit slow leaching with no production of secondary forms of plutonium. Thus, the remediation process could be made cheaper and easier.

Another example is a study of Pu-containing particles at the Taranaki site, which is in southern Australia, where 500 non-nuclear explosions were conducted in 1953–1963 (Ikeda-Ohno et al., 2016). Applying modern μ-XRF and μ-XANES techniques, the authors determined that the initial detonation of the weapon components resulted in the formation of PuO_2 particles that contain Pb. However, storage in the soil and the environmental reactions result in the precipitation or sorption on the surface of Pu particles. A core-shell structure with a Ca/Fe/U shell and a PuO_2 core were identified by the authors. These particles can be compared with the particles formed in the accidents in Palomeras (Spain) and Thule (Greenland). In each case, the accident occurred with a B-52 bomber. In Palomeras, a non-nuclear explosion of two weapons with subsequent fire resulted in the dispersion of Pu–U particles over a 2.30 km^2 area. In the Thule accident, a bomber crashed on the ice in the North Star Bay, 12 km west of Thule Air Base, due to a flight mission accident. This non-nuclear explosion also resulted in the dispersion of Pu–U particles in marine and terrestrial environments. The composition and properties of the particles in both accidents are similar (Lind et al., 2007). U and Pu oxide mixtures constitute the cores of the particles. The authors found that the oxidation state of U is predominately U(IV) with minor contributions from higher oxidation states (up to U_3O_8). Characterization of Pu shows it to be Pu(III)/Pu(IV), Pu(IV)/Pu(V), or a mixture of all three oxidation states. The particles in both accidents appear to be similar; however, their storage conditions differ. In the Thule accident, most of the particles were aged in a marine environment while a small fraction was aged in a terrestrial ecosystem that remains frozen for most of the year. In the Palomares accident, a terrestrial semi-desert ecosystem was mainly affected (Sancho and García-Tenorio, 2019). According to the leaching experiments (by 0.16 M HCl) of the EU-COMET project, the "hot" particles from the Thule sediment are more leachable than those from the Palomares soils (Vandenhove et al., 2017). These data demonstrate that the weathering of "hot" particles and their evolution over time may depend not only on the contamination scenario, but also on the storage conditions.

Pu in Waste Storage

A more complicated scenario is found in the radioactive waste disposal sites and in the pathways of migration from them. Many studies have been conducted on the temporary storage or disposal of liquid and solid radioactive wastes. The composition of the radioactive waste and the environmental conditions of disposal differ substantially from one disposal to another. Unfortunately, only a few of them are open for scientific discussion.

Recently, the migration of radionuclides from a legacy trench disposal site in eastern Australia was investigated (Payne et al., 2020). The authors studied the migration of actinides and fission products. It was found that mobilization of Pu from the trenches is related to complex interactions between the influx of oxidizing groundwater during rainfall and the subsequent extended period of reducing conditions. The microbial activity influences the distributions of actinides and other redox-sensitive elements, such as iron and manganese (Vázquez-Campos et al., 2017). The study shows seasonal changes in redox conditions, which can significantly change the migration of redox-sensitive actinides, especially Pu. The differences in seasonal changes in properties, such as the temperature and rainfall throughout the world may significantly affect the redox-sensitive migration of radionuclides.

The microbiological community, which plays a special role in these biogeochemical processes, should also be considered. The influence of the microbiological activity of radionuclide migration in groundwater was demonstrated (Kersting, 2013; Kato et al., 2020). The authors agree that the interaction of Pu with microorganisms results in a reduction, but other processes may also be involved, such as sorption onto cell surface, accumulation within the cells, biomineralization and complexation. The exact mechanism of the interaction and its influence on the Pu mobility is not clear. The interaction of Pu(V) and Pu(IV) with cells in the presence and absence of extracellular polymeric substances (EPS) was investigated (Boggs et al., 2016). It was found that the reduction of Pu(V) mostly occur in the interaction with EPS. In all studied systems, by the end of the reaction, the cells immobilize Pu on their surface. However, in other works, the reduction of Pu(IV) to Pu(III) on reaction with cells increased the mobility of the radionuclides (Xie et al., 2018).

OUTLOOK

The behavior of plutonium and uranium in the environment strongly depends on their source and the local geochemical conditions. In this mini review, we highlighted recent studies of the migration pathways of these radionuclides.

The research could be continued in two ways. First, the experiments under controlled laboratory conditions, which are supported by instrumental methods and calculations, may facilitate the identification of the mechanism of the reaction on the molecular level. This information is highly necessary. Thermodynamic modeling should accompany these experiments because reliable prediction of behavior of radionuclides in the environment remains impeded. In addition, long-term laboratory experiments should be conducted because aging often changes the pathways of these reactions.

Second is the characterization of environmental and the on-site experiments. Modern advanced techniques enable us to understand the chemistry of the migration at the molecular level even at the contaminated sites. However, in most cases, these methods are limited by the sensitivity. The differences between the contaminated sites means that more research should be conducted. This may facilitate the development of an economical, environmentally friendly, and sustainable solution of the remediation process.

AUTHOR CONTRIBUTIONS

AR and IV designed and wrote the review with input from SK regarding the conception and editing of the manuscript. All authors contributed to the article and approved the submitted version.

FUNDING

This work was supported by the Russian Science Foundation (Grant 19-73-20051).

REFERENCES

Arnold, P. L., Love, J. B., and Patel, D. (2009). Pentavalent uranyl complexes. *Coord. Chem. Rev.* 253, 1973–1978. doi: 10.1016/j.ccr.2009.03.014

Batuk, O. N., Conradson, S. D., Aleksandrova, O. N., Boukhalfa, H., Burakov, B. E., Clark, D. L., et al. (2015). Multiscale speciation of U and Pu at Chernobyl, Hanford, Los Alamos, McGuire AFB, Mayak, and Rocky Flats. *Environ. Sci. Technol.* 49, 6474–6484. doi: 10.1021/es506145b

Begg, J. D., Zavarin, M., and Kersting, A. B. (2017). Desorption of plutonium from montmorillonite: an experimental and modeling study. *Geochim. Cosmochim. Acta* 197, 278–293. doi: 10.1016/j.gca.2016.10.006

Beresford, N. A., Fesenko, S., Konoplev, A., Skuterud, L., Smith, J. T., and Voigt, G. (2016). Thirty years after the Chernobyl accident: what lessons have we learnt? *J. Environ. Radioact.* 157, 77–89. doi: 10.1016/j.jenvrad.2016.02.003

Boggs, M. A., Jiao, Y., Dai, Z., Zavarin, M., and Kersting, A. B. (2016). Interactions of plutonium with Pseudomonas sp. strain EPS-1W and its extracellular polymeric substances. *Appl. Environ. Microbiol.* 82, 7093–7101. doi: 10.1128/AEM.02572-16

Boland, D. D., Collins, R. N., Glover, C. J., Payne, T. E., and Waite, T. D. (2014). Reduction of U(VI) by Fe(II) during the Fe(II)-accelerated transformation of ferrihydrite. *Environ. Sci. Technol.* 48, 9086–9093. doi: 10.1021/es501750z

Bolsunovsky, A., Melgunov, M., Chuguevskii, A., Lind, O. C., and Salbu, B. (2017). Unique diversity of radioactive particles found in the Yenisei River floodplain. *Sci. Rep.* 7, 1–10. doi: 10.1038/s41598-017-11557-7

Bondarkov, M. D., Zheltonozhsky, V. A., Zheltonozhskaya, M. V., Kulich, N. V., Maksimenko, A. M., Farfán, E. B., et al. (2011). Assessment of the radionuclide composition of "hot Particles" sampled in the Chernobyl Nuclear Power Plant fourth reactor unit. *Health Phys.* 101, 368–374. doi: 10.1097/HP.0b013e31820dbc53

Bugai, D., Smith, J., and Hoque, M. A. (2020). Solid-liquid distribution coefficients (Kd-s) of geological deposits at the Chernobyl Nuclear Power Plant site with respect to Sr, Cs and Pu radionuclides: a short review. *Chemosphere* 242, 125175. doi: 10.1016/j.chemosphere.2019.125175

Burakov, B. E. (2019). "Lava-like materials formed and solidified during chernobyl accident," in *Comprehensive Nuclear Materials*, ed R. Konings (Amsterdam: Elsevier), 1–15. doi: 10.1016/B978-0-12-803581-8.11686-8

Butorin, S. M., Modin, A., Vegelius, J. R., Kvashnina, K. O., and Shuh, D. K. (2016). Probing chemical bonding in uranium dioxide by means of high-resolution X-ray absorption spectroscopy. *J. Phys. Chem. C* 120, 29397–29404. doi: 10.1021/acs.jpcc.6b09335

Clark, D. L., Hecker, S. S., Jarvinen, G. D., and Neu, M. P. (2005). "Plutonium," in *The Chemistry of the Actinide and Transactinide Elements*, eds L. R. Morss, N. M. Edelstein, J. Fuger (Dordrecht: Springer), 813–1264. doi: 10.1007/1-4020-3598-5_7

Conradson, S. D., Clark, D. L., Den Auwer, C., and Lezama-Pacheco, J. S. (2011). "X-ray absorption spectroscopy of plutonium particles at the Rocky Flats US Nuclear Weapons Production Site," in *Actinide Nanoparticle Research,* eds S. N. Kalmykov, and M. A. Denecke (Berlin: Springer-Verlag), 377–398. doi: 10.1007/978-3-642-11432-8_14

Cumberland, S. A., Douglas, G., Grice, K., and Moreau, J. W. (2016). Uranium mobility in organic matter-rich sediments: a review of geological and geochemical processes. *Earth-Sci. Rev.* 159, 160–185. doi: 10.1016/j.earscirev.2016.05.010

Dresel, P. E., Wellman, D. M., Cantrell, K. J., and Truex, M. J. (2011). Review: technical and policy challenges in deep vadose zone remediation of metals and radionuclides. *Environ. Sci. Technol.* 45, 4207–4216. doi: 10.1021/es101211t

Drobot, B., Steudtner, R., Raff, J., Geipel, G., Brendler, V., and Tsushima, S. (2015). Combining luminescence spectroscopy, parallel factor analysis and quantum chemistry to reveal metal speciation—a case study of uranyl(VI) hydrolysis. *Chem. Sci.* 6, 964–972. doi: 10.1039/C4SC02022G

Dublet, G., Lezama Pacheco, J., Bargar, J. R., Fendorf, S., Kumar, N., Lowry, G. V., et al. (2017). Partitioning of uranyl between ferrihydrite and humic substances at acidic and circum-neutral pH. *Geochim. Cosmochim. Acta* 215, 122–140. doi: 10.1016/j.gca.2017.07.013

Dublet, G., Worms, I., Frutschi, M., Brown, A., Zund, G., Bartova, B., et al. (2019). Colloidal size and redox state of uranium species in the porewater of a pristine mountain wetland. *Environ. Sci. Technol.* 53, 9361–9369. doi: 10.1021/acs.est.9b01417

Edayilam, N., Ferguson, B., Montgomery, D., Al Mamun, A., Martinez, N., Powell, B. A., et al. (2020). Dissolution and vertical transport of uranium from stable mineral forms by plants as influenced by the Co-occurrence of uranium with phosphorus. *Environ. Sci. Technol.* 54, 6602–6609. doi: 10.1021/acs.est.9b06559

Elzinga, E. J., Tait, C. D., Reeder, R. J., Rector, K. D., Donohoe, R. J., and Morris, D. E. (2004). Spectroscopic investigation of U(VI) sorption at the calcite-water interface. *Geochim. Cosmochim. Acta* 68, 2437. doi: 10.1016/j.gca.2003.09.023

Emerson, H. P., Di Pietro, S., Katsenovich, Y., and Szecsody, J. (2018). Potential for U sequestration with select minerals and sediments via base treatment. *J. Environ. Manag.* 223, 108–114. doi: 10.1016/j.jenvman.2018.06.012

Emerson, H. P., Kaplan, D. I., and Powell, B. A. (2019). Plutonium binding affinity to sediments increases with contact time. *Chem. Geol.* 505, 100–107. doi: 10.1016/j.chemgeo.2018.11.009

Gartman, B. N., Qafoku, N. P., Szecsody, J. E., Kukkadapu, R. K., Wang, Z., Wellman, D. M., et al. (2015). Uranium fate in Hanford sediment altered by simulated acid waste solutions. *Appl. Geochem.* 63, 1–9. doi: 10.1016/j.apgeochem.2015.07.010

Gerber, E., Romanchuk, A., Pidchenko, I., Amidani, L., Rossberg, A., Hennig, C., et al. (2020). The missing pieces of the PuO_2 nanoparticles puzzle. *Nanoscale*. doi: 10.1039/D0NR03767B. [Epub ahead of print].

Grenthe, I., Fuger, J., Konnings, R., Lemire, R. J., Muller, A., Nguyen-Trung Cregu, C., et al. (1992). "Chemical thermodynamics of uranium," in *Chemical Thermodynamics of Uranium,* eds. H. Wanner and I. Forest (Paris: OECD Nuclear Energy Agency).

Guillaumont, R., Fanghanel, T., Neck, V., Fuger, J., Palmer, D. A., Grenthe, I., et al. (2003). *Update on the Chemical Thermodynamics of Uranium, Neptunium, Plutonium, Americium and Technecium*. Amsterdam: OECD Nuclear Energy Agency.

Günther, A., Raff, J., Merroun, M. L., Roßberg, A., Kothe, E., and Bernhard, G. (2014). Interaction of U(VI) with Schizophyllum commune studied by microscopic and spectroscopic methods. *BioMetals* 27, 775–785. doi: 10.1007/s10534-014-9772-1

Ikeda-Ohno, A., Shahin, L. M., Howard, D. L., Collins, R. N., Payne, T. E., and Johansen, M. P. (2016). Fate of plutonium at a former nuclear testing site in Australia. *Environ. Sci. Technol.* 50, 9098–9104. doi: 10.1021/acs.est.6b01864

Jo, Y., Kirishima, A., Kimuro, S., Kim, H. K., and Yun, J II. (2019). Formation of $CaUO_2(CO_3)32$- and $Ca_2UO_2(CO_3)_3(aq)$ complexes at variable temperatures (10–70°C). *Dalt. Trans.* 48, 6942–6950. doi: 10.1039/C9DT01174A

Joseph, C., Balboni, E., Baumer, T., Treinen, K., Kersting, A. B., and Zavarin, M. (2019). Plutonium desorption from nuclear melt glass-derived colloids and implications for migration at the Nevada National Security Site, USA. *Environ. Sci. Technol.* 53, 12238–12246. doi: 10.1021/acs.est.9b03956

Kanematsu, M., Perdrial, N., Um, W., Chorover, J., and O'Day, P. A. (2014). Influence of phosphate and silica on U(VI) precipitation from acidic and neutralized wastewaters. *Environ. Sci. Technol.* 48, 6097–6106. doi: 10.1021/es4056559

Kaplan, D. I., Buettner, S. W., Li, D., Huang, S., Koster, P. G., Groos, V., et al. (2017). *In situ* porewater uranium concentrations in a contaminated wetland: effect of seasons and sediment depth. *Appl. Geochem.* 85, 128–136. doi: 10.1016/j.apgeochem.2016.11.017

Kaplan, D. I., Kukkadapu, R., Seaman, J. C., Arey, B. W., Dohnalkova, A. C., Buettner, S., et al. (2016). Iron mineralogy and uranium-binding environment in the rhizosphere of a wetland soil. *Sci. Total Environ.* 569, 53–64. doi: 10.1016/j.scitotenv.2016.06.120

Kashparov, V., Salbu, B., Levchuk, S., Protsak, V., Maloshtan, I., Simonucci, C., et al. (2019). Environmental behaviour of radioactive particles from chernobyl. *J. Environ. Radioact.* 208:106025. doi: 10.1016/j.jenvrad.2019.106025

Kato, K., Nagaosa, K., Kinoshita, T., Kastsuyama, C., Nazina, T., Ohnuki, T., et al. (2020). "Microbial ecological function in migration of radionuclides in groundwater," in *Behavior of Radionuclides in the Environment I*, eds K. Kato, A. Konoplev, and S. Kalmykov (Singapore: Springer), 1–35. doi: 10.1007/978-981-15-0679-6

Kelly, S. D., Newville, M. G., Cheng, L., Kemner, K. M., Sutton, S. R., Fenter, P., et al. (2003). Uranyl incorporation in natural calcite. *Environ. Sci. Technol.* 37, 1284–1287. doi: 10.1021/es025962f

Kelly, S. D., Rasbury, E. T., Chattopadhyay, S., Kropf, A. J., and Kemner, K. M. (2006). Evidence of a stable uranyl site in ancient organic-rich calcite. *Environ. Sci. Technol.* 40, 2262–2268. doi: 10.1021/es051970v

Kersting, A. B. (2013). Plutonium transport in the environment. *Inorg. Chem.* 52, 3533–3546. doi: 10.1021/ic3018908

Kersting, A. B., Efurd, D. W., Finnegan, D. L., Rokop, D. L., Smith, D. K., and Thompson, J. L. (1999). Migration of plutonium in groundwater at the Nevada Test Site. *Nature* 397, 56–59. doi: 10.1038/16231

Kirsch, R., Fellhauer, D., Altmaier, M., Neck, V., Rossberg, A., Fanghanel, T., et al. (2011). Oxidation state and local structure of plutonium reacted with magnetite, mackinawite, and chukanovite. *Environ. Sci. Technol.* 45, 7267–7274. doi: 10.1021/es200645a

Knebel, K., Bottomley, P. D. W., Rondinella, V. V., Lähde, A., and Jokiniemi, J. (2017). Characterisation of aerosols produced in a simulated severe nuclear accident using electron microscopy. *J. Aerosol Sci.* 106, 68–82. doi: 10.1016/j.jaerosci.2017.01.008

Koster van Groos, P. G., Kaplan, D. I., Chang, H., Seaman, J. C., Li, D., Peacock, A. D., et al. (2016). Chemosphere Uranium fate in wetland mesocosms: effects of plants at two iron loadings with different pH values. *Chemosphere* 163, 116–124. doi: 10.1016/j.chemosphere.2016.08.012

Kvashnina, K., Romanchuk, A., Pidchenko, I., Gerber, E., Trigub, A., Rossberg, A., et al. (2019). A novel meta-stable pentavalent plutonium solid phase on the pathway from aqueous Pu(VI) to PuO_2 nanoparticles. *Angew. Chem. Int. Ed.* 58, 17558–17562. doi: 10.1002/anie.201911637

Kvashnina, K. O., Butorin, S. M., Martin, P., and Glatzel, P. (2013). Chemical state of complex uranium oxides. *Phys. Rev. Lett.* 111, 1–5. doi: 10.1103/PhysRevLett.111.253002

Kvashnina, K. O., Kvashnin, Y. O., Vegelius, J. R., Bosak, A., Martin, P. M., and Butorin, S. M. (2015). Sensitivity to actinide doping of uranium compounds by resonant inelastic X-ray scattering at uranium L3 edge. *Anal. Chem.* 87, 8772–8780. doi: 10.1021/acs.analchem.5b01699

Lecomte-Pradines, C., Adam-Guillermin, C., Gashchak, S., Bradshaw, C., Copplestone, D., and Beresford, N. A. (2020). More than thirty years after the Chernobyl accident: what do we know about the effects of radiation on the environment? *J. Environ. Radioact.* 211, 2019–2021. doi: 10.1016/j.jenvrad.2019.106108

Levchuk, S., Kashparov, V., Maloshtan, I., Yoschenko, V., and Van Meir, N. (2012). Migration of transuranic elements in groundwater from the near-surface radioactive waste site. *Appl. Geochem.* 27, 1339–1347. doi: 10.1016/j.apgeochem.2012.01.002

Li, P. S., Wu, W. M., Phillips, D. H., Watson, D. B., Kelly, S., Li, B., et al. (2019). Uranium sequestration in sediment at an iron-rich contaminated site at Oak Ridge, Tennessee via. bioreduction followed by reoxidation. *J. Environ. Sci. China* 85, 156–167. doi: 10.1016/j.jes.2019.05.028

Lin, P., Xu, C., Kaplan, D. I., Chen, H., Yeager, C. M., Xing, W., et al. (2019). Nagasaki sediments reveal that long-term fate of plutonium is controlled by select organic matter moieties. *Sci. Total Environ.* 678, 409–418. doi: 10.1016/j.scitotenv.2019.04.375

Lind, O. C., Salbu, B., Janssens, K., Proost, K., García-León, M., and García-Tenorio, R. (2007). Characterization of U/Pu particles originating from the nuclear weapon accidents at Palomares, Spain, 1966 and Thule, Greenland, 1968. *Sci. Total Environ.* 376, 294–305. doi: 10.1016/j.scitotenv.2006.11.050

Lu, G., Haes, A. J., and Forbes, T. Z. (2018). Detection and identification of solids, surfaces, and solutions of uranium using vibrational spectroscopy. *Coord. Chem. Rev.* 374, 314–344. doi: 10.1016/j.ccr.2018.07.010

Luo, H. W., and Xu, F. (2016). Bioreduction and reoxidation of uranium enhanced by thiol functional groups in natural organic matter. *Chemosphere* 147, 20–24. doi: 10.1016/j.chemosphere.2015.12.092

Mace, N., Wieland, E., Dahn, R., Tits, J., and Sceinost, A. C. (2013). EXAFS investigation on U(VI) immobilization in hardened cement paste: influence of experimental conditions on speciation. *Radiochim. Acta* 101, 379–389. doi: 10.1524/ract.2013.2024

Marshall, T. A., Morris, K., Law, G., Mosselmans, W., Bots, P., Rberts, H., et al. (2015). Uranium fate during crystallization of magnetite from ferrihydrite in conditions relevant to the disposal of radioactive waste. *Miner. Mag.* 79, 1265–1274. doi: 10.1180/minmag.2015.079.6.02

Marshall, T. A., Morris, K., Law, G. T. W., Livens, F. R., Mosselmans, J. F. W., Bots, P., et al. (2014). Incorporation of uranium into hematite during crystallization from ferrihydrite. *Environ. Sci. Technol.* 48, 3724–3731. doi: 10.1021/es500212a

Mehta, V. S., Maillot, F., Wang, Z., Catalano, J. G., and Giammar, D. E. (2016). Effect of reaction pathway on the extent and mechanism of uranium(VI) immobilization with calcium and phosphate. *Environ. Sci. Technol.* 50, 3128–3136. doi: 10.1021/acs.est.5b06212

Mikutta, C., Langner, P., Bargar, J. R., and Kretzschmar, R. (2016). Tetra- and hexavalent uranium forms bidentate-mononuclear complexes with particulate organic matter in a naturally uranium-enriched Peatland. *Environ. Sci. Technol.* 50, 10465–10475. doi: 10.1021/acs.est.6b03688

Mühr-Ebert, E. L., Wagner, F., and Walther, C. (2019). Speciation of uranium: compilation of a thermodynamic database and its experimental evaluation using different analytical techniques. *Appl. Geochem.* 100, 213–222. doi: 10.1016/j.apgeochem.2018.10.006

Munasinghe, P. S., Elwood, M. E., Brooks, S. C., and Elwood, A. S. (2015). Dynamic interplay between uranyl phosphate precipitation, sorption, and phase evolution. *Appl. Geochem.* 58, 147–160. doi: 10.1016/j.apgeochem.2015.04.008

Niu, Z., Wei, X., Qiang, S., Wu, H., Pan, D., Wu, W., et al. (2019). Spectroscopic studies on U(VI) incorporation into $CaCO_3$: effects of aging time and U(VI) concentration. *Chemosphere* 220, 1100–1107. doi: 10.1016/j.chemosphere.2019.01.010

Novikov, A. P., Kalmykov, S. N., Utsunomiya, S., Ewing, R. C., Horreard, F., Merkulov, A., et al. (2006). Colloid transport of plutonium in the far-field of the Mayak Production Association, Russia. *Science.* 314, 638–641. doi: 10.1126/science.1131307

Payne, T. E., Harrison, J. J., Cendon, D. I., Comarmond, M. J., Hankin, S., Hughes, C. E., et al. (2020). Radionuclide distributions and migration pathways at a legacy trench disposal site. *J. Environ. Radioact.* 211, 106081. doi: 10.1016/j.jenvrad.2019.106081

Perdrial, N., Vázquez-Ortega, A., Wang, G., Kanematsu, M., Mueller, K. T., Um, W., et al. (2018). Uranium speciation in acid waste-weathered sediments: the role of aging and phosphate amendments. *Appl. Geochem.* 89, 109–120. doi: 10.1016/j.apgeochem.2017.12.001

Peterson, R. A., Buck, E. C., Chun, J., Daniel, R. C., Herting, D. L., Ilton, E. S., et al. (2018). Review of the scientific understanding of radioactive waste at the U.S. DOE Hanford Site. *Environ. Sci. Technol.* 52, 381–396. doi: 10.1021/acs.est.7b04077

Pidchenko, I., Kvashnina, K. O., Yokosawa, T., Finck, N., Bahl, S., Schild, D., et al. (2017). Uranium redox transformations after U(VI) coprecipitation with magnetite nanoparticles. *Environ. Sci. Technol.* 51, 2217–2225. doi: 10.1021/acs.est.6b04035

Pöml, P., and Burakov, B. (2018). Study of the redistribution of U, Zr, Nb, Tc, Mo, Ru, Fe, Cr, and Ni between oxide and metallic phases in the matrix of a multiphase chernobyl hot-particle extracted from a soil sample of the Western Plume. *Radiochim. Acta* 106, 985–990. doi: 10.1515/ract-2018-2957

Powell, B. A., Dai, Z., Zavarin, M., Zhao, P., and Kersting, A. B. (2011). Stabilization of plutonium nano-colloids by epitaxial distortion on mineral surfaces. *Environ. Sci. Technol.* 45, 2698–2703. doi: 10.1021/es1033487

Qiao, J., Hansen, V., Hou, X., Aldahan, A., and Possnert, G. (2012). Speciation analysis of 129I, 137Cs, 232Th, 238U, 239Pu and 240Pu in environmental soil and sediment. *Appl. Radiat. Isot.* 70, 1698–1708. doi: 10.1016/j.apradiso.2012.04.006

Richter, C., Müller, K., Drobot, B., Steudtner, R., Großmann, K., Stockmann, M., et al. (2016). Macroscopic and spectroscopic characterization of uranium(VI) sorption onto orthoclase and muscovite and the influence of competing Ca2+. *Geochim. Cosmochim. Acta* 189, 143–157. doi: 10.1016/j.gca.2016.05.045

Roberts, H. E., Morris, K., Law, G. T. W., Mosselmans, J. F. W., Bots, P., Kvashnina, K., et al. (2017). Uranium(V) incorporation mechanisms and stability in Fe(II)/Fe(III) (oxyhydr)oxides. *Environ. Sci. Technol. Lett.* 4, 421–426. doi: 10.1021/acs.estlett.7b00348

Romanchuk, A. Y., Kalmykov, S. N., Egorov, A. V., Zubavichus, Y. V., Shiryaev, A. A., Batuk, O. N., et al. (2013). Formation of crystalline $PuO_{2+x}\cdot nH_2O$ nanoparticles upon sorption of Pu(V,VI) onto hematite. *Geochim. Cosmochim. Acta* 121, 29–40. doi: 10.1016/j.gca.2013.07.016

Romanchuk, A. Yu., Kalmykov, S. N., Egorov, A. V., Zubavichus, Y. V., Shiryaev, A. A., Smirnov, E. A., et al. (2016a). Photoreduction of Pu(V,VI) by TiO_2. *Radiochim. Acta* 104, 843–851. doi: 10.1515/ract-2015-2494

Romanchuk, A. Y., Kalmykov, S. N., Kersting, A. B., and Zavarin, M. (2016b). Behaviour of plutonium in the environment. *Russ. Chem. Rev.* 85:995. doi: 10.1070/RCR4602

Romanchuk, A. Y., Plakhova, T. V., Egorov, A. V., Egorova, T. B., Dorovatovskii, P. V., and Zubavichus, Y. V. (2018). Redox-mediated formation of plutonium oxide nanoparticles. *Dalt. Trans.* 47, 11239–11244. doi: 10.1039/C8DT02396D

Rybalchenko, A. I., Pimenov, M. K., Kurochkin, V. M., Kamnev, E. N., Korotkevich, V. M., Zubkov, A. A., et al. (2005). Deep injection disposal of liquid radioactive waste in Russia, 1963-2002: results and consequences. *Dev. Water Sci.* 52, 13–19. doi: 10.1016/S0167-5648(05)52002-1

Sancho, C., and García-Tenorio, R. (2019). Radiological evaluation of the transuranic remaining contamination in Palomares (Spain): a historical review. *J. Environ. Radioact.* 203, 55–70. doi: 10.1016/j.jenvrad.2019.02.015

Santschi, P. H., Xu, C., Zhang, S., Schwehr, K. A., Grandbois, R., Kaplan, D. I., et al. (2017). Iodine and plutonium association with natural organic matter: a review of recent advances. *Appl. Geochemistry* 85, 121–127. doi: 10.1016/j.apgeochem.2016.11.009

Schindler, M., Legrand, C. A., and Hochella, M. F. (2015). Alteration, adsorption and nucleation processes on clay-water interfaces: mechanisms for the retention of uranium by altered clay surfaces on the nanometer scale. *Geochim. Cosmochim. Acta* 153, 15–36. doi: 10.1016/j.gca.2014.12.020

Schmidt, M., Lee, S. S., Wilson, R. E., Knope, K. E., Bellucci, F., Eng, P. J., et al. (2013). Surface-mediated formation of Pu(IV) nanoparticles at the muscovite–electrolyte interface. *Environ. Sci. Technol.* 47, 14178–14184. doi: 10.1021/es4037258

Schumann, R. R., Zielinski, R. A., Otton, J. K., Pantea, M. P., and Orem, W. H. (2017). Uranium delivery and uptake in a montane wetland, north-central Colorado, USA. *Appl. Geochem.* 78, 363–379. doi: 10.1016/j.apgeochem.2017.01.001

Selvakumar, R., Ramadoss, G., Mridula, P. M., Rajendran, K., Thavamani, P., Ravi N, et al. (2018). Challenges and complexities in remediation of uranium contaminated soils: a review. *J. Environ. Radioact.* 192, 592–603. doi: 10.1016/j.jenvrad.2018.02.018

Shiryaev, A. A., Vlasova, I. E., Burakov, B. E., Ogorodnikov, B. I., Yapaskurt, V. O., Averin, A. A., et al. (2016). Physico-chemical properties of Chernobyl lava and their destruction products. *Prog. Nucl. Energy* 92, 104–118. doi: 10.1016/j.pnucene.2016.07.001

Shiryaev, A. A., Vlasova, I. E., Yapaskurt, V. O., Burakov, B. E., Averin, A. A., and Elantyev, I. (2018). Forensic study of early stages of the Chernobyl accident: story of three hot particles. *J. Nucl. Mater.* 511, 83–90. doi: 10.1016/j.jnucmat.2018.09.003

Skipperud, L., Strømman, G., Yunusov, M., Stegnar, P., Uralbekov, B., Tilloboev, H., et al. (2013). Environmental impact assessment of radionuclide and metal contamination at the former U sites Taboshar and Digmai, Tajikistan. *J. Environ. Radioact.* 123, 50–62. doi: 10.1016/j.jenvrad.2012.05.007

Smith, K. F., Bryan, N. D., Swinburne, A. N., Bots, P., Shaw, S., Natrajan, L. S., et al. (2015). U(VI) behaviour in hyperalkaline calcite systems. *Geochim. Cosmochim. Acta* 148, 343–359. doi: 10.1016/j.gca.2014.09.043

Stetten, L., Lefebvre, P., Le, P., Mangeret, A., Blanchart, P., Merrot, P., et al. (2020). Experimental redox transformations of uranium phosphate minerals and mononuclear species in a contaminated wetland. *J. Hazard. Mater.* 384:121362. doi: 10.1016/j.jhazmat.2019.121362

Szecsody, J. E., Truex, M. J., Qafoku, N. P., Wellman, D. M., Resch, T., and Zhong, L. (2013). Influence of acidic and alkaline waste solution properties on uranium migration in subsurface sediments. *J. Contam. Hydrol.* 151, 155–175. doi: 10.1016/j.jconhyd.2013.05.009

Tayal, A., Conradson, S. D., Kanzari, A., Lahrouch, F., Descostes, M., and Gerard, M. (2019). Uranium speciation in weathered granitic waste rock piles: an XAFS investigation. *RSC Adv.* 9, 11762–11773. doi: 10.1039/C9RA00961B

Vandenhove, H., Muikku, M., Vives i Batlle, J., Søvik, Å., Lecomte-Pradines, C., Horemans, N. (2017). "COMET," in *Final Report of the European Commission Funded COMET-RATE Project*.

Vázquez-Campos, X., Kinsela, A. S., Bligh, M. W., Harrison, J. J., Payne, T. E., and Waite, T. D. (2017). Response of microbial community function to fluctuating geochemical conditions within a legacy radioactive waste trench environment. *Appl. Environ. Microbiol.* 83, 1–17. doi: 10.1128/AEM.00729-17

Veshchunov, M. S., Boldyrev, A. V., Shestak, V. E., and Mueller, K. (2008). Analysis of molten pool physico-chemical interactions and interpretation of the Phebus FP tests observations. *Nucl. Eng. Des.* 238, 1728–1742. doi: 10.1016/j.nucengdes.2007.10.015

Vitova, T., Pidchenko, I., Fellhauer, D., Bagus, P. S., Joly, Y., Pruessmann, T., et al. (2017). The role of the 5f valence orbitals of early actinides in chemical bonding. *Nat. Commun.* 8, 1–9. doi: 10.1038/ncomms16053

Xie, J., Liang, W., Lin, J., Zhou, X., and Li, M. (2018). Humic acids facilitated microbial reduction of polymeric Pu(IV) under anaerobic conditions. *Sci. Total Environ.* 610, 1321–1328. doi: 10.1016/j.scitotenv.2017.08.184

Zachara, J. M., Long, P. E., Bargar, J., Davis, J. A., Fox, P., Fredrickson, J. K., et al. (2013). Persistence of uranium groundwater plumes: contrasting mechanisms at two DOE sites in the groundwater-river interaction zone. *J. Contam. Hydrol.* 147, 45–72. doi: 10.1016/j.jconhyd.2013.02.001

Zavarin, M., Zhao, P., Joseph, C., Begg, J. D., Boggs, M. A., Dai, Z., et al. (2019). Hydrothermal alteration of nuclear melt glass, colloid formation, and plutonium mobilization at the Nevada National Security Site, U.S.A. *Environ. Sci. Technol.* 53, 7363–7370. doi: 10.1021/acs.est.8b07199

Zhang, L., Zhou, J., Zhang, J., Su, J., Zhang, S., Chen, N., et al. (2016). Extraction of local coordination structure in a low-concentration uranyl system by XANES. *J. Synchrotron Radiat.* 23, 758–768. doi: 10.1107/S1600577516001910

Zhao, P., Begg, J. D., Zavarin, M., Tumey, S. J., Williams, R., Dai, Z. R., et al. (2016). Plutonium(IV) and (V) Sorption to Goethite at sub-femtomolar to micromolar concentrations: redox transformations and surface precipitation. *Environ. Sci. Technol.* 50, 6948–6956. doi: 10.1021/acs.est.6b00605

Zhao, P., Zavarin, M., Leif, R. N., Powell, B. A., Singleton, M. J., Lindvall, R. E., et al. (2011). Mobilization of actinides by dissolved organic compounds at the Nevada Test Site. *Appl. Geochem.* 26, 308–318. doi: 10.1016/j.apgeochem.2010.12.004

Conflict of Interest: The authors declare that the research was conducted in the absence of any commercial or financial relationships that could be construed as a potential conflict of interest.

frontiers in Chemistry

MINI REVIEW
published: 02 October 2020
doi: 10.3389/fchem.2020.00724

Memristive TiO_2: Synthesis, Technologies, and Applications

Georgii A. Illarionov[1], *Sofia M. Morozova*[1], *Vladimir V. Chrishtop*[1], *Mari-Ann Einarsrud*[2] *and Maxim I. Morozov*[1]*

[1] *Laboratory of Solution Chemistry of Advanced Materials and Technologies, ITMO University, St. Petersburg, Russia,*
[2] *Department of Material Science and Engineering, NTNU Norwegian University of Science and Technology, Trondheim, Norway*

Titanium dioxide (TiO_2) is one of the most widely used materials in resistive switching applications, including random-access memory, neuromorphic computing, biohybrid interfaces, and sensors. Most of these applications are still at an early stage of development and have technological challenges and a lack of fundamental comprehension. Furthermore, the functional memristive properties of TiO_2 thin films are heavily dependent on their processing methods, including the synthesis, fabrication, and post-fabrication treatment. Here, we outline and summarize the key milestone achievements, recent advances, and challenges related to the synthesis, technology, and applications of memristive TiO_2. Following a brief introduction, we provide an overview of the major areas of application of TiO_2-based memristive devices and discuss their synthesis, fabrication, and post-fabrication processing, as well as their functional properties.

Keywords: TiO_2, memristor, nanoparticles, neuromorphic, electronic oxides

Edited by:
Eugene A. Goodilin,
Lomonosov Moscow State University, Russia

Reviewed by:
Dmitrii Petukhov,
Lomonosov Moscow State University, Russia
Olesya Kapitanova,
Lomonosov Moscow State University, Russia
Vadim G. Kessler,
Swedish University of Agricultural Sciences, Sweden

***Correspondence:**
Maxim I. Morozov
morozov@scamt-itmo.ru

Specialty section:
This article was submitted to Inorganic Chemistry, a section of the journal Frontiers in Chemistry

Received: *28 April 2020*
Accepted: *14 July 2020*
Published: *02 October 2020*

Citation:
Illarionov GA, Morozova SM, Chrishtop VV, Einarsrud M-A and Morozov MI (2020) Memristive TiO_2: Synthesis, Technologies, and Applications. Front. Chem. 8:724. doi: 10.3389/fchem.2020.00724

INTRODUCTION

Titanium dioxide (TiO_2) is a multifunctional semiconductor that exists in three crystalline forms: anatase, rutile, and brookite. Owing to an appropriate combination of physical and chemical properties, environmental compatibility, and low production cost, polycrystalline TiO_2 has found a large variety of applications and is considered to be a promising material for future technologies. One of the most distinctive physical properties of this material is its high photocatalytic activity (Nam et al., 2019); however, more recently it has attracted growing interest because of its resistive switching abilities (Yang et al., 2008).

The realization of neuromorphic resistive memory in TiO_2 thin films (Strukov et al., 2008) marked an important milestone in the search for bio-inspired technologies (Chua and Kang, 1976). Many research proposals urged a focus on memristivity as the common feature of two electrical models: (i) electromigration of point defects in titanium oxide systems (Baiatu et al., 1990; Jameson et al., 2007) and (ii) voltage-gated ionic channels in the membranes of biological neurons (Hodgkin and Huxley, 1952). In this regard, memristors functionally mimic the synaptic plasticity of biological neurons, and thus can be implemented in artificial and hybrid neural networks. This includes a new paradigm of future computing systems (Zidan, 2018) and biocompatible electronics such as biointerfaces and biohybrid systems (Chiolerio et al., 2017).

Currently, the development of TiO_2 memristors is associated with their use in modern highly technological applications, such as resistive random-access memory (RRAM), biohybrid systems, and sensors, as schematically shown in **Figure 1A**. In this mini-review, we briefly outline and summarize the key milestone achievements, as well as recent advances in the synthesis, fabrication, and application of TiO_2-based memristors. A special focus is placed on the relationships between the synthesis and deposition methods, the effects of post-synthesis treatment, and the resistive switching properties.

OXYGEN DEFICIENCY AND RESISTIVE SWITCHING MECHANISMS

The basic scenario of resistive switching in TiO_2 (Jameson et al., 2007) assumes the formation and electromigration of oxygen vacancies between the electrodes (Baiatu et al., 1990), so that the distribution of concomitant *n*-type conductivity (Janotti et al., 2010) across the volume can eventually be controlled by an external electric bias, as schematically shown in **Figure 1B**. Direct observations with transmission electron microscopy (TEM) revealed more complex electroforming processes in TiO_2 thin films. In one of the studies, a continuous Pt filament between the electrodes was observed in a planar Pt/TiO_2/Pt memristor (Jang et al., 2016). As illustrated in **Figure 1C**, the corresponding switching mechanism was suggested as the formation of a conductive nanofilament with a high concentration of ionized oxygen vacancies and correspondingly reduced Ti^{3+} ions. These ions induce detachment and migration of Pt atoms from the electrode via strong metal–support interactions (Tauster, 1987). Another TEM investigation of a conductive TiO_2 nanofilament revealed it to be a Magnéli phase Ti_nO_{2n-1} (Kwon et al., 2010). Supposedly, its formation results from an increase in the concentrations of oxygen vacancies within a local nanoregion above their thermodynamically stable limit. This scenario is schematically shown in **Figure 1D**. Other hypothesized point defect mechanisms involve a contribution of cation and anion interstitials, although their behavior has been studied more in tantalum oxide (Wedig et al., 2015; Kumar et al., 2016). The plausible origins and mechanisms of memristive switching have been comprehensively reviewed in topical publications devoted to metal oxide memristors (Yang et al., 2008; Waser et al., 2009; Ielmini, 2016) as well as TiO_2 (Jeong et al., 2011; Szot et al., 2011; Acharyya et al., 2014). The resistive switching mechanisms in memristive materials are regularly revisited and updated in the themed review publications (Sun et al., 2019; Wang et al., 2020).

APPLICATIONS

RRAM and the New Computing Paradigm

As they mimic the synapses in biological neurons, memristors became the key component for designing novel types of computing and information systems based on artificial neural networks, the so-called neuromorphic electronics (Zidan, 2018; Wang and Zhuge, 2019; Zhang et al., 2019b). Electronic artificial neurons with synaptic memristors are capable of emulating the associative memory, an important function of the brain (Pershin and Di Ventra, 2010). In addition, the technological simplicity of thin-film memristors based on transition metal oxides such as TiO2 allows their integration into electronic circuits with extremely high packing density. Memristor crossbars are technologically compatible with traditional integrated circuits, whose integration can be implemented within the complementary metal–oxide–semiconductor platform using nanoimprint lithography (Xia et al., 2009). Nowadays, the size of a Pt-TiOx-HfO2-Pt memristor crossbar can be as small as 2 nm (Pi et al., 2019). Thus, the inherent properties of memristors such as non-volatile resistive memory and synaptic plasticity, along with feasibly high integration density, are at the forefront of the new-type hardware performance of cognitive tasks, such as image recognition (Yao et al., 2017). The current state of the art, prospects, and challenges in the new brain-inspired computing concepts with memristive implementation have been comprehensively reviewed in topical papers (Jeong et al., 2016; Xia and Yang, 2019; Zhang et al., 2020). These reviews postulate that the newly emerging computing paradigm is still in its infancy, while the rapid development and current challenges in this field are related to the technological and materials aspects. The major concerns are the lack of understanding of the microscopic picture and the mechanisms of switching, as well as the unproven reliability of memristor materials. The choice of memristive materials as well as the methods of synthesis and fabrication affect the properties of memristive devices, including the amplitude of resistive switching, endurance, stochasticity, and data retention time.

Biointerfaces, Biomimicking, and Biohybrid Systems

The neuromorphic nature of the resistive switching in TiO_2 memristors has triggered a series of studies addressing their functional coupling with living biological systems. The common features of the electroconductive behavior of memristive and biological neural networks have been revised in terms of physical, mathematical, and stochastic models (Chua, 2013; Feali and Ahmadi, 2016). The memristive electronics was shown to support important synaptic functions such as spike timing-dependent plasticity (Jo et al., 2010; Pickett et al., 2013). Recently, a memristive simulation of important biological synaptic functions such as non-linear transmission characteristics, short-/long-term plasticity, and paired-pulse facilitation has been reported for hybrid organic–inorganic memristors using Ti-based maleic acid/TiO_2 ultrathin films (Liu et al., 2020). In relation to this, functionalized TiO_2 memristive systems may be in competition with the new generation of two-dimensional memristive materials such as WSe_2 (Zhu et al., 2018), MoS_2 (Li et al., 2018), MoS_2/graphene (Kalita et al., 2019), and other systems (Zhang et al., 2019a) with ionic coupling, ionic modulation effects, or other synapse-mimicking functionalities. Furthermore, the biomimetic fabrication of TiO_2 (Seisenbaeva et al., 2010; Vijayan and Puglia, 2019; Kumar et al., 2020) opens up new horizons for its versatile microstructural patterning and functionalizations.

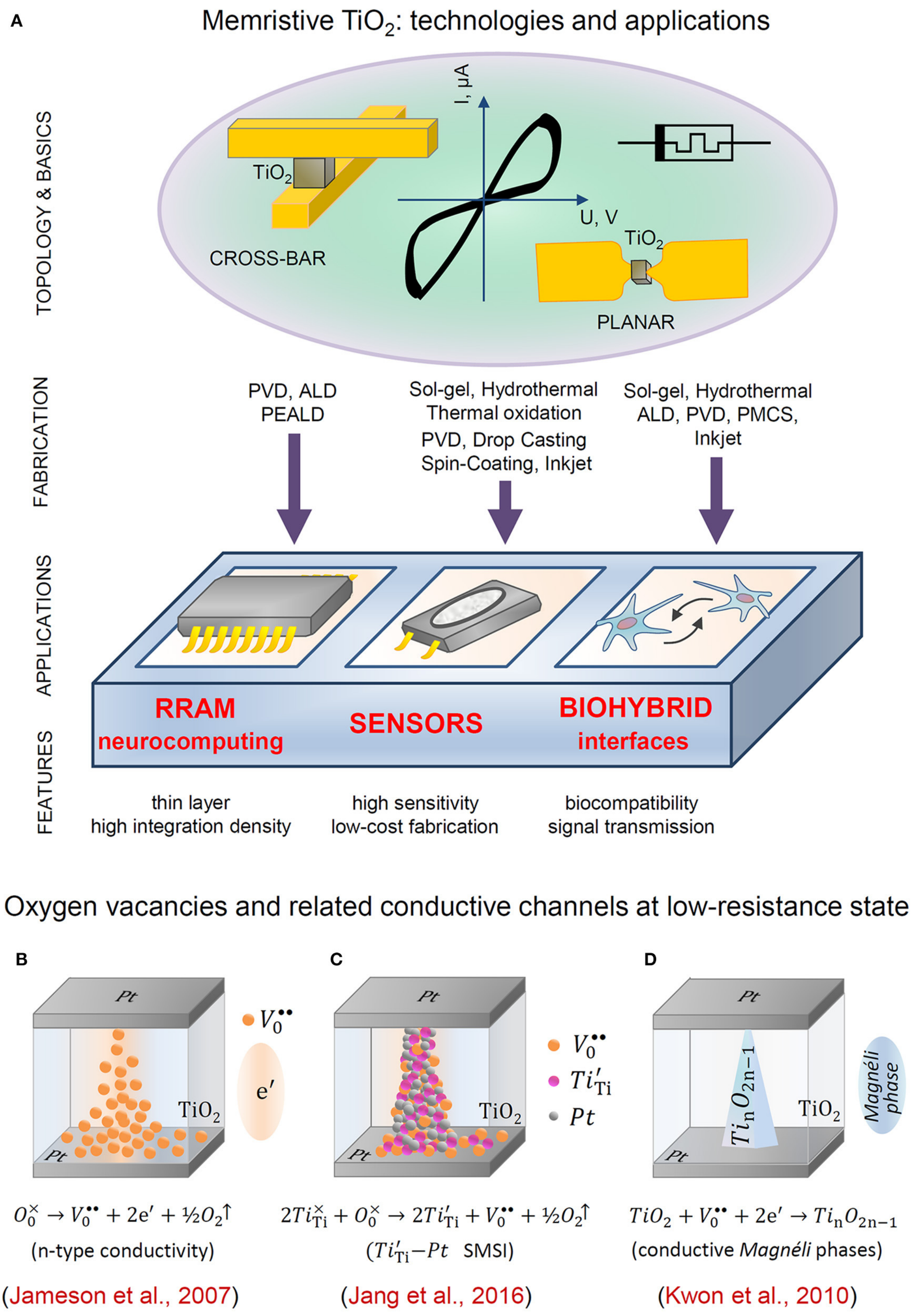

FIGURE 1 | (A) Technologies and applications of memristive TiO_2 thin films. **(B–D)** Formation of the conductive filament: **(B)** electromigration of oxygen vacancies inducing the *n*-type conductivity region; **(C)** detachment and migration of electrode metal atoms due to strong metal support interaction (SMSI); **(D)** formation of a conductive Magnéli phase.

The first study addressing the experimental convergence between *in vitro* spiking neurons and spiking memristors was attempted in 2013 (Gater et al., 2013). A few years later, Gupta et al. (2016) used TiO_2 memristors to compress information on biological neural spikes recorded in real time. In these *in vitro* studies electrical communication with biological cells, as well as their incubation, was investigated using multielectrode arrays (MEAs). Alternatively, TiO_2 thin films may serve as an interface material in various biohybrid devices. The bio- and neurocompatibility of a TiO_2 film has been demonstrated in terms of its excellent adsorption of polylysine and primary neuronal cultures, high vitality, and electrophysiological activity (Roncador et al., 2017). Thus, TiO_2 can be implemented as a nanobiointerface coating and integrated with memristive electronics either as a planar configuration of memristors and electrodes (Illarionov et al., 2019) or as a functionalization of MEAs to provide good cell adhesion and signal transmission. The known examples are electrolyte/TiO_2/Si(*p*-type) capacitors (Schoen and Fromherz, 2008) or capacitive TiO_2/Al electrodes (Serb et al., 2020). As a demonstration of the state of the art, an attempt at memristive interlinking between the brain and brain-inspired devices has been recently reported (Serb et al., 2020). The long-term potentiation and depression of TiO_2-based memristive synapses have been demonstrated in relation to the neuronal firing rates of biologically active cells. Further advancement in this area is expected to result in scalable on-node processors for brain–chip interfaces (Gupta et al., 2016). As of 2017, the state of the art of, and perspectives on, coupling between the resistive switching devices and biological neurons have been reviewed (Chiolerio et al., 2017).

Sensors

Apart from proximately neuromorphic technologies, TiO_2-based memristors have also found application in various sensors. The principle of memristive sensorics is based on the dependency of the resistive switching on various external stimuli. This includes recording of mechanical energy (Vilmi et al., 2016), hydrogen detection (Hossein-Babaei and Rahbarpour, 2011; Strungaru et al., 2015; Haidry et al., 2017; Vidiš et al., 2019), γ-ray sensing (Abunahla et al., 2016), and various fluidic-based sensors, such as sensors for pH (Hadis et al., 2015a) and glucose concentration (Hadis et al., 2015b). In addition, TiO_2 thin films may generate photoinduced electron–hole pairs, which give rise to UV radiation sensors (Hossein-Babaei et al., 2012). Recently, the biosensing properties of TiO_2-based memristors have been demonstrated in the detection of the bovine serum albumin protein molecule (Sahu and Jammalamadaka, 2019). Furthermore, this work has also demonstrated that the introduction of an additional graphene oxide layer may effectively prevent the growth of multidimensional and random conductive paths, resulting in a lower switching voltage, better endurance, and a higher resistance switching ratio. This opens up a new horizon for further functional convergence of metal oxides and two-dimensional memristive materials and interfaces (Zhang et al., 2019a).

SYNTHESIS AND FABRICATION

The functionality of TiO_2 memristors is largely related to the phase purity, phase structure, crystallinity, and defect structure. In turn, all these parameters depend on the synthesis method, fabrication processing, and post-fabrication treatment (Diebold, 2003; Chen and Mao, 2007; Goren et al., 2014). Most TiO_2 memristors consist of anatase or rutile because of the stability of these polymorphs. The formation of oxygen vacancies and concomitant *n*-type conductivity can be controlled at temperatures above 300°C (Hou et al., 2018).

The fabrication of a TiO_2 memristive device typically consists of (i) the synthesis of a nanostructured material, (ii) deposition of the functional layer, (iii) arrangement of the electrodes, and (iv) post-processing annealing at an elevated temperature under a suitable atmosphere. The first stage is required for traditional chemical synthesis routes, while the first two stages take place at the same time for physical deposition methods.

The choice of fabrication route is thus a trade-off in complexity, cost, scalability, desirable topology (film thickness and topological feature size of the electrode areas), threshold electroforming voltage (V_T), retention time, switching time, and the resistive switching ratio (R_{OFF}/R_{ON}). The main technological, topological, and exploitative characteristics of typical memristive devices are summarized in **Table 1** and will be reviewed in the following sections.

Synthesis

Chemical Approaches

Sol–gel

In this process, a liquid solution is converted into a viscoelastic gel phase. In the classical concept of sol–gel, the phase purity, size, and shape of synthesized TiO_2 nanoparticles are considered in relation to the hydrolysis and condensation reactions, the reactivity and concentration of the precursor (titanium alkoxide or $TiCl_4$), the solvent type, and the temperature (Cargnello et al., 2014). In addition, the early-stage processes such as nucleation, crystal growth, and aggregation (Teychené et al., 2020) may play a crucial role in the sol–gel synthesis of TiO_2 nanoparticles (Cheng et al., 2017). The memristive devices fabricated using the sol–gel method have various areas of application and operate at a threshold voltage ranging from ∼0.5 V (Abunahla et al., 2018) to 1.5 V (Vilmi et al., 2016; Hu et al., 2020) or higher (Illarionov et al., 2019) with a resistive switching ratio R_{OFF}/R_{ON} of 10^1-10^5 (**Table 1**). Thus, the functional parameters of these devices may be variable with respect to the morphology and purity of the sol–gel product, deposition method (see section Fabrication), and annealing conditions (see section Annealing and Electric Properties).

Thermal oxidation

Polycrystalline TiO_2 typically in the form of rutile can be obtained by thermal oxidation of a titanium layer at temperatures in the range 500–800°C (Cao et al., 2009). This method allows fabrication of TiO_2 films with thicknesses down to 4 nm (Park et al., 2011). Furthermore, thermal oxidation is a cost-efficient method that is compatible with standard RRAM

TABLE 1 | Overview of the structure and electrical properties of TiO$_2$-based memristors obtained by various synthesis methods.

Synthesis method	Deposition method (annealing temperature, time, and atmosphere)	Structure	Feature size*, μm^2 (TiO$_2$ phase)	Thickness, nm (particle size, nm)	V_T^{**}, V	R_{OFF}/R_{ON}	Application	Retention time, s (switching time, s)	Reference
Sol–gel	Spin coating (550°C, 10 h, air)	Cellular, Al/TiO$_2$/FTO	2×10^6 (anatase)	35	3.9	2×10^5	General	10^4 (N/D)	(Tao et al., 2020)
Sol–gel	Inkjet (200°C, 2 h, Air)	Planar, Au/TiO$_2$/Au	3 (anatase)	400 (7***)	∼4	∼20	Cell biology	N/D	(Illarionov et al., 2019)
Sol–gel	Drop casting (N/D)	Crossbar, Ag/TiO$_2$/Cu	4×10^6 (amorphous)	4.5×10^4	0.5	10^7	γ-ray sensor	4×10^4 (50 ÷ 360)	(Abunahla et al., 2018)
Sol–gel	Inkjet (150°C, 15 min, N$_2$)	Cellular, Ag/TiO$_2$/Ag/PET	3,600	10–160	∼1.5	500	Mechanical sensor	N/D	(Vilmi et al., 2016)
Sol–gel	Spin coating (500°C, 1 h, air)	Cells array, Al/TiO$_2$/FTO	2×10^5 (anatase)	100	∼1.8	>300	RRAM	10^4 (10)	(Hu et al., 2020)
Hydrothermal	Dip coating (450°C, 2 h, air)	Sandwiched, Ag/TiO$_2$/Al	N/D (anatase)	265	0.7	100	RRAM	N/D	(Dongale et al., 2014)
Hydrothermal	Dip coating (500°C, 3 h, air)	Sandwiched, Al/TiO$_2$/Ti	7.9×10^5 (anatase nanowires)	N/D	∼3	70	RRAM	10^4 (N/D)	(Xiao et al., 2017)
Hydrothermal	Dip coating (300°C, 2 h, air)	Sandwiched, Ag/TiO$_2$/FTO	1.3×10^7 (rutile + anatase, rutile)	7,000	1.2	>10	RRAM	4×10^6 (N/D)	(Irshad et al., 2019)
Solid state, 2D colloid	Dip coating	Crossbar, Al/TiO$_2$/Pt/Ti/SiO$_2$/Si	4	2	0.5 ÷ 1.5	10^6	RRAM	10^4 (20×10^{-9})	(Dai et al., 2017)
Thermal oxidation	–	Sandwiched, Ir/TiO$_2$/TiN	N/D	4	>1.5 (set)	∼100	RRAM	10^4 (10^{-7})	(Park et al., 2011)
Thermal oxidation	– (650°C, 1 h, air)	Cellular, Ti/TiO$_2$/Ti	∼3×10^6 (rutile)	400 (50)****	2	∼4	Humidity sensor	6×10^5 (∼10^{-2})	(Hossein-Babaei and Alaei-Sheini, 2016)
Anodizing	–	Cellular, Cu/TiO$_2$/Ti	4	8, 11, 29	–1.5	<80	RRAM	N/D	(Aglieri et al., 2018)
Anodizing	– (550°C, 1 h, N$_2$/H$_2$ 24/1)	Cells array, Pt/TiO$_2$/Ti	∼10^8	<100	<1	∼56	General	N/D	(Miller et al., 2010)
PVD, ALD	–	Crossbar, Pt/TiO$_2$/HfO$_2$/Pt	4×10^{-6}	7	∼1.8	450	RRAM, computing	120 (N/D)	(Pi et al., 2019)
PEALD	–	Crossbar, Al/TiO$_2$/Al	3,600 (amorphous)	13	2.1	>100	RRAM	N/D	(Jeong et al., 2010b)
PEALD	–	Crossbar, Pt/Ni/TiO$_2$/Al$_2$O$_3$/Pt	4,900 (amorphous)	12	∼0.5 ÷ 1.5	∼100	RRAM	N/D	(Jeong et al., 2010a)
PVD/RMS	– (600, 800°C, 3 h, air)	Crossbar, Pt/TiO$_2$/Pt	N/D (anatase)	2,000 (40–50)***	∼0.2 ÷ 1.0	< 6×10^5	H$_2$ sensor	N/D (5)	(Haidry et al., 2017)
PVD/RFS	– (400°C, 15 min, N$_2$)	Crossbar, Ni/TiO$_2$/Ni	1.1 (anatase)	10	∼0.8	10^4	RRAM	N/D	(Cortese et al., 2016)
PVD/RS	–	Cellular, Al/TiO$_2$/Au	100	50	0.5	12	General	N/D (10^{-3})	(Ghenzi and Levy, 2018)
PVD/RS	–	Crossbar, Pt/TiO$_2$/Pt/Cr	2.25, 9 (amorphous and anatase)	30 (10)***	∼0.5	∼100	RRAM	N/D	(Strachan et al., 2013)
PMCS	–	Planar, glass/TiO$_2$/Al	1.77×10^8 (rutile and anatase)	30	N/D	N/D	Bio-interface	N/D	(Roncador et al., 2017)
PLD	–	Cellular, Cu/TiO$_2$/Pt	1.26×10^5	100	∼0.2	∼3×10^3	RRAM	100 (250×10^{-9})	(Sahu et al., 2020)

*∼, estimated or recalculated values; *electrode area; **threshold voltage; ***by Scherrer equation; ****by SEM, scanning electron microscopy.*

2D, two-dimensional; ALD, atomic layer deposition; MRS, magnetron reactive sputtering; PEALD, plasma-enhanced atomic layer deposition; PVD, physical vapor deposition; RFS, radio frequency sputtering; R_{OFF}/R_{ON}, resistive switching ratio; RRAM, resistive random-access memory; RS, reactive sputtering; V_T, threshold electroforming voltage.

manufacturing technology (Acharyya et al., 2014). However, processing temperatures above 500°C might cause the formation of crystallographic line defects or microcracks.

Hydrothermal synthesis

This is defined as heterogeneous reactions in aqueous media under high pressure and temperature sufficient to dissolve and recrystallize materials that are insoluble in water under normal conditions (Byrappa and Yoshimura, 2001). Various metal alkoxides ($Ti(OR)_4$, $R = C_2H_5$, i-C_3H_7, C_4H_9) or $TiCl_4$ have been used as precursors (Oh et al., 2009; Zhang et al., 2011; Senthilkumar et al., 2013; Dongale et al., 2014; Irshad et al., 2019). In this process, temperatures up to 230°C and high pressures (around 200 bar) facilitate the formation of a crystalline product at relatively low temperatures (Dalod et al., 2017). The TiO_2-based materials obtained by this method show reasonable R_{OFF}/R_{ON} switching ratios of up to 100 (Dongale et al., 2014; Xiao et al., 2017), although higher values ($>10^4$) have also been reported (Senthilkumar et al., 2013). Additional control over the size and shape of TiO_2 particles can be achieved by means of a solvothermal approach (Dinh et al., 2009). Recently, this method has been successfully applied to obtain sub-10 nm TiO_2 nanoparticles that are capable of forming self-assembled monolayers and that possess resistive switching properties (Schmidt et al., 2017).

Electrochemical oxidation

Using an electrochemical method or anodizing, the oxidation of a titanium foil in an electrochemical cell provides nanostructures of TiO_2 (Yoo et al., 2013). With this method, the composition, thickness, and structure can be controlled by choosing an appropriate substrate, electrolyte, and electrochemical conditions. Only a few studies have addressed this method of fabricating TiO_2-based memristors (Miller et al., 2010; Yoo et al., 2013; Aglieri et al., 2018; Zaffora et al., 2018). Recently, promising advances in anodizing to form a compact topology of memristors (8–29 nm thickness and 4 μm^2 feature area) have been demonstrated (Aglieri et al., 2018). The method is relatively cheap and is typically performed at ambient temperature. However, precise control of film thickness and sensitivity to the type and surface of the substrate are major challenges.

Atomic layer deposition (ALD)

Chemical vapor-based deposition techniques are widely used in the fabrication of thin films. Ultrathin TiO_2 layers in memristive devices are usually fabricated by ALD or plasma-enhanced ALD (PEALD). In these methods, Ti-based precursors ($TiCl_4$, titanium alkoxides) are decomposed in the presence of an oxidizer (H_2O, O_3, or O_2) (Seo et al., 2011; Marichy et al., 2012). The PEALD process can be performed at relatively low substrate temperatures (Kwon et al., 2010). The methods allow very thin TiO_2 layers in the range of 7–13 nm to be formed (Jeong et al., 2010a,b) and are compatible with other fabrication techniques. Using a combination of ALD and other nanofabrication processes, a very small topological feature size of 4 nm^2 has been achieved for memristor crossbar arrays (Pi et al., 2019). The ALD methods are relatively costly, but provide high precision and thus scalability and reproducibility.

Physical Approaches

Physical vapor deposition (PVD)

These methods require the transfer and deposition of materials under vacuum. The post-processing annealing at 200–600°C may support adhesion and crystallization (Cortese et al., 2016; Haidry et al., 2017). The sputtered TiO_2 layers meet the criteria of the nanometer-range electronics industry (Strachan et al., 2013; Ghenzi and Levy, 2018) and therefore find application at an industrial level, especially in reproducible, long-lasting, and portable RRAM devices (Nickel et al., 2013). The methods are sensitive to contamination inside the chamber and require high power (Acharyya et al., 2014).

Pulsed microplasma cluster source (PMCS)

This technique forms supersonic pulsed beams of the metal oxide clusters and deposits them on a substrate. Deposition occurs at high energy and results in nanostructured thin films. The method was suggested for fabrication of TiO_2 memristors, as the nanocrystalline structure and porosity can be controlled by varying deposition parameters, while the growth can be performed at room temperature (Baldi et al., 2015). In addition to purely memristive applications, the method was also suggested for fabrication of biohybrid TiO_2 interfaces (Roncador et al., 2017) that demonstrated good properties for the growth and vitality of neuronal cell cultures and their electrical activity.

Fabrication

Thin-film fabrication implies depositing TiO_2 nanomaterials onto a substrate along with arrangement of the electrodes. In this section we briefly outline the most widely used techniques for fabrication of TiO_2 memristive devices.

Drop Casting

This is the simplest technology. Functional layers are formed by depositing drops of colloidal dispersions of TiO_2 onto a substrate using a syringe or pipette. The thickness of the TiO_2 layers obtained by this method typically ranges between 40 and 200 μm (Gale et al., 2014; Abunahla et al., 2018; De Carvalho et al., 2019). This thickness range does not match the usual topological features of RRAM memristors, although the method has recently been justified for various memristive sensors (Abunahla et al., 2016, 2018; Sahu and Jammalamadaka, 2019).

Spin Coating

This method is based on spinning of the substrate, which exploits an inertial force acting on the fixed substrate and an unfixed drop of slurry cast on top of it. Varying the viscosity of the slurry or solution and the rotation speed, the method may be adjusted to obtain TiO_2 thin films with thicknesses down to 35 nm (Tao et al., 2020). Thus, the method has been proposed for fabrication of RRAM (Hu et al., 2020).

Dip Coating

Dip coating is considered to be a high-quality and cost-efficient deposition method, if physical adsorption between the substrate and the adsorbate dispersed in a colloidal solution is adopted as a controllable process. In this way, memristive thin films comprising two-dimensional TiO_2 flakes with a thickness of ∼2 nm were obtained by dip coating. These films demonstrated distinctive properties such as a high resistive switching ratio, fast switching speed, and extremely low erase energy consumption (Dai et al., 2017).

Inkjet Printing

Inkjet printing is a cost-efficient fabrication method, especially for micro- and nanopatterning and laboratory-scale prototyping (Menard et al., 2007). The method has been applied for stretchable and flexible electronics (Nayak et al., 2019), including various TiO_2 memristive devices (Samardzić et al., 2015). Inkjet printers are used for automated drop casting and typically operate with a picoliter droplet volume and provide droplet deposition with 10–20 μm spatial resolution. The thickness of the film may be variable and usually exceeds 100 nm (Duraisamy et al., 2012), although a lower value of 80 nm has been reported recently (Salonikidou et al., 2019).

Annealing and Electric Properties

Annealing in reducing atmospheres affects the concentration of charged point defects and thus the resistive switching. Despite many experimental studies, including the post-fabrication thermal annealing stage (typically at 400–600°C) under vacuum (Schmidt et al., 2015), nitrogen (Seo et al., 2011; Cortese et al., 2016; Regoutz et al., 2016), argon (Nelo et al., 2013), or N_2 + H_2 (4–5%) gas mixtures (Yang et al., 2008; Miller et al., 2010), only a few studies have systematically addressed the effects of thermal treatment under various annealing atmospheres on the resistive switching behavior of TiO_2 memristive devices (Lai et al., 2013a,b; Nelo et al., 2013).

SUMMARY AND OUTLOOK

The current renaissance of the resistive switching phenomenon over the last 12 years has been intimately associated with studies on TiO_2 thin films that have often been addressed as prototype oxide memristors for many research applications. Numerous recent achievements highlighted in this mini-review demonstrate the rapid development of TiO_2-based memristors in various application fields, while the growing interest in these devices is seemingly far from saturation.

The major challenges of TiO_2 memristors have been outlined in several previous reviews and remain essentially unsolved. Technologically, the emerging properties of memristive systems concern the operational stochasticity, number of distinguishable states, switching energy, switching speed, endurance, retention, and feature size. Their relationship in various types of modern memristive systems has been comprehensively addressed in a recent topical review (Zhang et al., 2020). Besides the permanent technological issues of increasing the integration density and reducing the production costs, there are fundamental challenges in understanding the mechanisms of resistive switching in solids, which, in practice, limit the scalability and reproducibility of the memristive devices (Acharyya et al., 2014; Jeong et al., 2016; Zidan, 2018; Xia and Yang, 2019; Zhang et al., 2020). Despite the apparent simplicity of the metal–insulator–metal configuration, the mechanisms involved in the memristive electric performance are manifold and complex. Two types of electroforming processes, electronic (Shao et al., 2015) and ionic (Waser et al., 2009), play essential roles in the non-linearity and hysteresis of the voltage–current relationship. Thus, understanding the electron band structure of TiO_2 polymorphs (Scanlon et al., 2013), the defect structure (Bak et al., 2006), and the equilibrium relations with Magnéli phases (Padilha et al., 2016) are of key importance and should help to address the challenges at a theoretical level. In addition, many experimental studies have recently addressed tuning of the electric properties of TiO_2 memristors by choosing appropriate electrodes and an appropriate operating voltage regime or by affecting the phase ratio, defect structure, and microstructure of the synthesized materials using post-processing annealing under ambient or inert atmospheres (Goren et al., 2014; Schmidt et al., 2015; Cortese et al., 2016; Regoutz et al., 2016; Haidry et al., 2017; Tao et al., 2020). Thus, they have contributed to our understanding of the complex resistive switching phenomena in TiO_2. Meanwhile, only a few studies have systematically addressed the effect of thermal annealing at reduced oxygen partial pressures on the resistive and resistive switching properties of TiO_2 thin films (Lai et al., 2013a,b; Nelo et al., 2013). Seemingly, this issue also remains underexplored.

In view of the current trends and challenges of TiO_2-based memristors, we can expect an increasingly large role of chemical approaches to device fabrication, lowering of the production costs, rapid development of neuromorphic computing systems, and further convergence of artificial electronic neurons with biological cells based on TiO_2 thin films.

AUTHOR CONTRIBUTIONS

All authors listed have made a substantial, direct and intellectual contribution to the work, and approved it for publication.

FUNDING

The work was fulfilled with financial support from the Russian Science Foundation (Project no. 19-19-00433).

REFERENCES

Abunahla, H., Jaoude, M. A., O'Kelly, C. J., and Mohammad, B. (2016). Sol-gel/drop-coated micro-thick TiO_2 memristors for γ-ray sensing. *Mater. Chem. Phys.* 184, 72–81. doi: 10.1016/j.matchemphys.2016.09.027

Abunahla, H., Mohammad, B., Mahmoud, L., Darweesh, M., Alhawari, M., Jaoude, M. A., et al. (2018). Memsens: memristor-based radiation sensor. *IEEE Sens. J.* 18, 3198–3205. doi: 10.1109/JSEN.2018.2808285

Acharyya, D., Hazra, A., and Bhattacharyya, P. (2014). A journey towards reliability improvement of TiO_2 based resistive random access memory:

a review. *Microelectron. Reliab.* 54, 541–560. doi: 10.1016/j.microrel.2013.11.013

Aglieri, V., Zaffora, A., Lullo, G., Santamaria, M., Di Franco, F., Cicero, U. L., et al. (2018). Resistive switching in microscale anodic titanium dioxide-based memristors. *Superlattice. Microst.* 113, 135–142. doi: 10.1016/j.spmi.2017.10.031

Baiatu, T., Waser, R., and Härdtl, K. H. (1990). DC electrical degradation of perovskite-type titanates: III, a model of the mechanism. *J. Am. Ceram. Soc.* 73, 1663–1673. doi: 10.1111/j.1151-2916.1990.tb09811.x

Bak, T., Nowotny, J., and Nowotny, M. K. (2006). Defect disorder of titanium dioxide. *J. Phys. Chem.* 110, 21560–21567. doi: 10.1021/jp063700k

Baldi, G., Bosi, M., Giusti, G., Attolini, G., Berzina, T., Collini, C., et al. (2015). Optimization of synthesis protocols to control the nanostructure and the morphology of metal oxide thin films for memristive applications. *AIP Conf. Proc.* 1648:280002. doi: 10.1063/1.4912531

Byrappa, K., and Yoshimura, M. (2001). *Handbook of Hydrothermal Technology, a Technology for Crystal Growth and Materials Processing*. Norwich, NY: William Andrew Publishing.

Cao, X., Li, X., Yu, W., Zhang, Y., Yang, R., Liu, X., et al. (2009). Structural characteristics and resistive switching properties of thermally prepared TiO_2 thin films. *J. Alloy. Compounds* 486, 458–461. doi: 10.1016/j.jallcom.2009.06.175

Cargnello, M., Gordon, T. R., and Murray, C. B. (2014). Solution-phase synthesis of titanium dioxide nanoparticles and nanocrystals. *Chem. Rev.* 114, 9319–9345. doi: 10.1021/cr500170p

Chen, X., and Mao, S. S. (2007). Titanium dioxide nanomaterials: synthesis, properties, modifications, and applications. *Chem. Rev.* 107, 2891–2959. doi: 10.1021/cr0500535

Cheng, K., Chhor, K., and Kanaev, A. (2017). Solvent effect on nucleation-growth of titanium-oxo-alkoxy nanoparticles. *Chem. Phys. Lett.* 672, 119–123. doi: 10.1016/j.cplett.2017.01.059

Chiolerio, A., Chiappalone, M., Ariano, P., and Bocchini, S. (2017). Coupling resistive switching devices with neurons: state of the art and perspectives. *Front. Neurosci.* 11:70. doi: 10.3389/fnins.2017.00070

Chua, L. (2013). Memristor, Hodgkin-Huxley, and edge of chaos. *Nanotechnology* 24:383001. doi: 10.1088/0957-4484/24/38/383001

Chua, L. O., and Kang, S. M. (1976). Memristive devices and systems. *Proc. IEEE* 64, 209–223. doi: 10.1109/PROC.1976.10092

Cortese, S., Khiat, A., Carta, D., Light, M. E., and Prodromakis, T. (2016). An amorphous titanium dioxide metal insulator metal selector device for resistive random access memory crossbar arrays with tunable voltage margin. *Appl. Phys. Lett.* 108:033505. doi: 10.1063/1.4940361

Dai, Y., Bao, W., Hu, L., Liu, C., Yan, X., Chen, L., et al. (2017). Forming free and ultralow-power erase operation in atomically crystal TiO_2 resistive switching. *2D Materials* 4:025012. doi: 10.1088/2053-1583/aa598f

Dalod, A. R. M., Grendal, O. G., Skjærvø, S. L., Inzani, K., Selbach, S. M., Henriksen, L., et al. (2017). Controlling oriented attachment and *in situ* functionalization of TiO_2 nanoparticles during hydrothermal synthesis with APTES. *J. Phys. Chem. C* 121, 11897–11906. doi: 10.1021/acs.jpcc.7b02604

De Carvalho, R. C., Betts, A. J., and Cassidy, J. F. (2019). A simple nanoparticle-based TiO_2 memristor device and the role of defect chemistry in its operation. *J. Solid State Electrochem.* 23, 1939–1943. doi: 10.1007/s10008-019-04239-z

Diebold, U. (2003). The surface science of titanium dioxide. *Surf. Sci. Rep.* 48, 53–229. doi: 10.1016/S0167-5729(02)00100-0

Dinh, C. T., Nguyen, T. D., Kleitz, F., and Fo, T. O. (2009). Shape-controlled synthesis of highly crystalline titania nanocrystals. *ACS Nano* 3, 3737–3743. doi: 10.1021/nn900940p

Dongale, T. D., Shinde, S. S., Kamat, R. K., and Rajpure, K. Y. (2014). Nanostructured TiO_2 thin film memristor using hydrothermal process. *J. Alloy. Compounds* 593, 267–270. doi: 10.1016/j.jallcom.2014.01.093

Duraisamy, N., Muhammad, N. M., Kim, H. C., Jo, J. D., and Choi, K. H. (2012). Fabrication of TiO_2 thin film memristor device using electrohydrodynamic inkjet printing. *Thin Solid Films.* 520, 5070–5074. doi: 10.1016/j.tsf.2012.03.003

Feali, M. S., and Ahmadi, A. (2016). Realistic Hodgkin–Huxley axons using stochastic behavior of memristors. *Neural Process Lett.* 45, 1–14. doi: 10.1007/s11063-016-9502-5

Gale, E., Mayne, R., Adamatzky, A., and de Lacy Costello, B. (2014). Drop-coated titanium dioxide memristors. *Mater. Chem. Phys.* 143, 524–529. doi: 10.1016/j.matchemphys.2013.09.013

Gater, D., Iqbal, A., Davey, J., and Gale, E. (2013). "Connecting spiking neurons to a spiking memristor network changes the memristor dynamics," in *IEEE 20th International Conference on Electronics, Circuits, and Systems (ICECS)* (Abu Dhabi), 534–537. doi: 10.1109/ICECS.2013.6815469

Ghenzi, N., and Levy, P. (2018). Impact of sub-and supra-threshold switching in the synaptic behavior of TiO_2 memristors. *Microelectron. Eng.* 193, 13–17. doi: 10.1016/j.mee.2018.02.017

Goren, E., Ungureanu, M., Zaspe, R., Rozenberg, M., Hueso, L. E., Stoliar, P., et al. (2014). Resistive switching phenomena in TiO_x nanoparticle layers for memory applications. *Appl. Phys. Lett.* 105:143506. doi: 10.1063/1.4897142

Gupta, I., Serb, A., Khiat, A., Zeitler, R., Vassanelli, S., and Prodromakis, T. (2016). Real-time encoding and compression of neuronal spikes by metal-oxide memristors. *Nat. Commun.* 7, 1–16. doi: 10.1038/ncomms12805

Hadis, N. S. M., Manaf, A. A., and Herman, S. H. (2015a). "Characterization of R_{OFF}/R_{ON} ratio of fluidic based memristor sensor for pH detection," in *IEEE Regional Symposium on Micro and Nanoelectronics (RSM)* (Kuala Terengganu), 1–4. doi: 10.1109/RSM.2015.7354956

Hadis, N. S. M., Manaf, A. A., and Herman, S. H. (2015b). "Comparison on TiO_2 thin film deposition method for fluidic based glucose memristor sensor," in *IEEE International Circuits and Systems Symposium (ICSyS)* (Langkawi), 36–39. doi: 10.1109/CircuitsAndSystems.2015.7394060

Haidry, A. A., Ebach-Stahl, A., and Saruhan, B. (2017). Effect of Pt/TiO_2 interface on room temperature hydrogen sensing performance of memristor type Pt/TiO_2/Pt structure. *Sensor. Actuat. B Chem.* 253, 1043–1054. doi: 10.1016/j.snb.2017.06.159

Hodgkin, A. L., and Huxley, A. F. (1952). A quantitative description of membrane current and its application to conduction and excitation in nerve. *J. Physiol.* 117, 500–544. doi: 10.1113/jphysiol.1952.sp004764

Hossein-Babaei, F., and Alaei-Sheini, N. (2016). Electronic conduction in Ti/Poly-TiO_2/Ti structures. *Sci. Rep.* 6:29624. doi: 10.1038/srep29624

Hossein-Babaei, F., Lajvardi, M. M., and Boroumand, F. (2012). Large area Ag–TiO_2 UV radiation sensor fabricated on a thermally oxidized titanium chip. *Sensor. Actuat. A Phys.* 173, 116–121. doi: 10.1016/j.sna.2011.10.028

Hossein-Babaei, F., and Rahbarpour, S. (2011). Titanium and silver contacts on thermally oxidized titanium chip: Electrical and gas sensing properties. *Sol. State Electron.* 56, 185–190. doi: 10.1016/j.sse.2010.12.007

Hou, L., Zhang, M., Guan, Z., Li, Q., and Yang, J. (2018). Effect of annealing ambience on the formation of surface/bulk oxygen vacancies in TiO_2 for photocatalytic hydrogen evolution. *Appl. Surf. Sci.* 428, 640–647. doi: 10.1016/j.apsusc.2017.09.144

Hu, L., Han, W., and Wang, H. (2020). Resistive switching and synaptic learning performance of a TiO_2 thin film based device prepared by sol-gel and spin coating techniques. *Nanotechnology* 31:155202. doi: 10.1088/1361-6528/ab6472

Ielmini, D. (2016). Resistive switching memories based on metal oxides: mechanisms, reliability and scaling. *Semicond. Sci. Technol.* 31:063002. doi: 10.1088/0268-1242/31/6/063002

Illarionov, G. A., Kolchanov, D. S., Mukhin, I. S., Kuchur, O. A., Zhukov, M. V., Sergeeva, E., et al. (2019). Inkjet assisted fabrication of planar biocompatible memristors. *RSC Adv.* 9, 35998–36004. doi: 10.1039/C9RA08114C

Irshad, M. S., Abbas, A., Qazi, H. H., Aziz, M. H., Shah, M., Ahmed, A., et al. (2019). Role of point defects in hybrid phase TiO_2 for resistive random-access memory (RRAM). *Mater. Res. Exp.* 6:076311. doi: 10.1088/2053-1591/ab17b5

Jameson, J. R., Fukuzumi, Y., Wang, Z., Griffin, P., Tsunoda, K., Meijer, G. I., et al. (2007). Field-programmable rectification in rutile TiO_2 crystals. *Appl. Phys. Lett.* 91:112101. doi: 10.1063/1.2769961

Jang, M. H., Agarwal, R., Nukala, P., Choi, D., Johnson, A. T. C., Chen, I. W., et al. (2016). Observing oxygen vacancy driven electroforming in Pt-TiO_2-Pt device via strong metal support interaction. *Nano Lett.* 16, 2139–2144. doi: 10.1021/acs.nanolett.5b02951

Janotti, A., Varley, J. B., Rinke, P., Umezawa, N., Kresse, G., and Van de Walle, C. G. (2010). Hybrid functional studies of the oxygen vacancy in TiO_2. *Phys. Rev. B* 81:085212. doi: 10.1103/PhysRevB.81.085212

Jeong, D. S., Kim, K. M., Kim, S., Choi, B. J., and Hwang, C. S. (2016). Memristors for energy-efficient new computing paradigms. *Adv. Electron. Mater.* 2:1600090. doi: 10.1002/aelm.201600090

Jeong, D. S., Thomas, R., Katiyar, R. S., and Scott, J. F. (2011). Overview on the resistive switching in TiO2 solid electrolyte. *Integr. Ferroelect.* 124, 87–96. doi: 10.1080/10584587.2011.573726

Jeong, H. Y., Lee, J. Y., and Choi, S. Y. (2010a). Interface-engineered amorphous TiO_2-based resistive memory devices. *Adv. Funct. Mater.* 20, 3912–3917. doi: 10.1002/adfm.201001254

Jeong, H. Y., Lee, J. Y., Ryu, M. K., and Choi, S. Y. (2010b). Bipolar resistive switching in amorphous titanium oxide thin film. *Phys. Status Solidi Rapid Res. Lett.* 4, 28–30. doi: 10.1002/pssr.200903383

Jo, S. H., Chang, T., Ebong, I., Bhadviya, B. B., Mazumder, P., and Lu, W. (2010). Nanoscale memristor device as synapse in neuromorphic systems. *Nano Lett.* 10, 1297–1301. doi: 10.1021/nl904092h

Kalita, H., Krishnaprasad, A., Choudhary, N., Das, S., Dev, D., Ding, Y., et al. (2019). Artificial neuron using vertical MoS2/graphene threshold switching memristors. *Sci. Rep.* 9:53. doi: 10.1038/s41598-018-35828-z

Kumar, S., Graves, C. E., Strachan, J. P., Grafals, E. M., Kilcoyne, A. L. D., Tyliszczak, T., et al. (2016). Direct observation of localized radial oxygen migration in functioning tantalum oxide memristors. *Adv. Mater.* 28, 2772–2776. doi: 10.1002/adma.201505435

Kumar, S. N., Suvarna, P. R., Babu Naidu, C. K., Banerjee, P., Ratnamala, A., and Manjunatha, H. (2020). A review on biological and biomimetic materials and their applications. *Appl. Phys. A* 126:445. doi: 10.1007/s00339-020-03633-z

Kwon, D. H., Kim, K. M., Jang, J. H., Jeon, J. M., Lee, M. H., Kim, G. H., et al. (2010). Atomic structure of conducting nanofilaments in TiO_2 resistive switching memory. *Nat. Nanotechnol.* 5, 148–153. doi: 10.1038/nnano.2009.456

Lai, C. H., Chen, C. H., and Tseng, T. Y. (2013a). Resistive switching behaviour of sol-gel deposited TiO_2 thin films under different heating ambience. *Surf. Coat. Technol.* 231, 399–402. doi: 10.1016/j.surfcoat.2012.05.045

Lai, C. H., Liu, C. Y., Hsu, C. H., Lee, Y. M., Lin, J. S., and Yang, H. (2013b). Effect of firing atmosphere and bottom electrode on resistive switching mode in TiO_2 thin films. *Thin Solid Films.* 529, 430–434. doi: 10.1016/j.tsf.2012.09.025

Li, D., Wu, B., Zhu, X., Wang, J., Ryu, B., Lu, W. D., et al. (2018). MoS_2 memristors exhibiting variable switching characteristics towards bio-realistic synaptic emulation. *ACS Nano.* 12, 9240–9252. doi: 10.1021/acsnano.8b03977

Liu, C., Cao, Y. Q., Wu, D., and Li, A. D. (2020). Simulation of biologic synapse through organic-inorganic hybrid memristors using novel Ti-based maleic acid/TiO_2 ultrathin films. *IEEE Electron Dev. Lett.* 41, 155–158. doi: 10.1109/LED.2019.2956282

Marichy, C., Bechelany, M., and Pinna, N. (2012). Atomic layer deposition of nanostructured materials for energy and environmental applications. *Adv. Mater*. 24, 1017–1032. doi: 10.1002/adma.201104129

Menard, E., Meitl, M. A., Sun, Y., Park, J. U., Shir, D. J. L., Nam, Y. S., et al. (2007). Micro- and nanopatterning techniques for organic electronic and optoelectronic systems. *Chem. Rev.* 107, 1117–1160. doi: 10.1021/cr050139y

Miller, K., Nalwa, K. S., Bergerud, A., Neihart, N. M., and Chaudhary, S. (2010). Memristive behavior in thin anodic titania. *IEEE Electron Dev. Lett.* 31, 737–739. doi: 10.1109/LED.2010.2049092

Nam, Y., Lim, J. H., Ko, K. C., and Lee, J. Y. (2019). Photocatalytic activity of TiO_2 nanoparticles: a theoretical aspect. *J. Mater. Chem. A* 7, 13833–13859. doi: 10.1039/C9TA03385H

Nayak, L., Mohanty, S., Nayak, S., and Ramadoss, A. (2019). A review on inkjet printing of nanoparticle inks for flexible electronics. *J. Mater. Chem. C* 7, 8771–8795. doi: 10.1039/C9TC01630A

Nelo, M., Sloma, M., Kelloniemi, J., Puustinen, J., Saikkonen, T., Juuti, J., et al. (2013). Inkjet-printed memristor: printing process development. *Jpn. J. Appl. Phys.* 52:05DB21. doi: 10.7567/JJAP.52.05DB21

Nickel, J. H., Strachan, J. P., Pickett, M. D., Schamp, C. T., Yang, J. J., Graham, J. A., et al. (2013). Memristor structures for high scalability: non-linear and symmetric devices utilizing fabrication friendly materials and processes. *Microelectron. Eng.* 103, 66–69. doi: 10.1016/j.mee.2012.09.007

Oh, J. K., Lee, J. K., Kim, S. J., and Park, K. W. (2009). Synthesis of phase-and shape-controlled TiO_2 nanoparticles via hydrothermal process. *J. Ind. Eng. Chem.* 15, 270–274. doi: 10.1016/j.jiec.2008.10.001

Padilha, A. C. M., Raebiger, H., Rocha, A. R., and Dalpian, G. M. (2016). Charge storage in oxygen deficient phases of TiO_2: defect Physics without defects. *Sci. Rep*. 6:28871. doi: 10.1038/srep28871

Park, J., Jung, S., Lee, J., Lee, W., Kim, S., Shin, J., et al. (2011). Resistive switching characteristics of ultra-thin TiO_x. *Microelectron. Eng.* 88, 1136–1139. doi: 10.1016/j.mee.2011.03.050

Pershin, Y. V., and Di Ventra, M. (2010). Experimental demonstration of associative memory with memristive neural networks. *Neural Netw*. 23, 881–886. doi: 10.1016/j.neunet.2010.05.001

Pi, S., Li, C., Jiang, H., Xia, W., Xin, H., Yang, J. J., et al. (2019). Memristor crossbar arrays with 6-nm half-pitch and 2-nm critical dimension. *Nat. Nanotechnol.* 14, 35–39. doi: 10.1038/s41565-018-0302-0

Pickett, M. D., Medeiros-Ribeiro, G., and Williams, R. S. (2013). A scalable neuristor built with Mott memristors. *Nat. Mater.* 12, 114–117. doi: 10.1038/nmat3510

Regoutz, A., Gupta, I., Serb, A., Khiat, A., Borgatti, F., Lee, T. L., et al. (2016). Role and optimization of the active oxide layer in TiO_2-based RRAM. *Adv. Funct. Mater*. 26, 507–513. doi: 10.1002/adfm.201503522

Roncador, A., Jimenez-Garduño, A. M., Pasquardini, L., Giusti, G., Cornella, N., Lunelli, L., et al. (2017). Primary cortical neurons on PMCS TiO_2 films towards bio-hybrid memristive device: A morpho-functional study. *Biophys. Chem.* 229, 115–122. doi: 10.1016/j.bpc.2017.04.010

Sahu, D. P., and Jammalamadaka, S. N. (2019). Detection of bovine serum albumin using hybrid TiO_2 + graphene oxide based Bio–resistive random access memory device. *Sci. Rep.* 9:1614. doi: 10.1038/s41598-019-52522-w

Sahu, V. K., Das, A. K., Ajimsha, R. S., and Misra, P. (2020). Low power high speed 3-bit multilevel resistive switching in TiO_2 thin film using oxidisable electrode. *J. Phys. D Appl. Phys.* 53:225303. doi: 10.1088/1361-6463/ab7acb

Salonikidou, B., Yasunori, T., Le Borgne, B., England, J., Shizuo, T., and Sporea, R. A. (2019). Toward fully printed memristive elements: a-TiO_2 electronic synapse from functionalized nanoparticle ink. *ACS Appl. Electron. Mater.* 1, 2692–2700. doi: 10.1021/acsaelm.9b00701

Samardzić, N., Mionić, M., Dakić, B., Hofmann, H., Dautović, S., and Stojanović, G. (2015). Analysis of quantized electrical characteristics of microscale TiO_2 ink-jet printed memristor. *IEEE Trans. Electron Dev.* 62, 1898–1904. doi: 10.1109/TED.2015.2421283

Scanlon, D. O., Dunnill, C. W., Buckeridge, J., Shevlin, S. A., Logsdail, A. J., Woodley, S. M., et al. (2013). Band alignment of rutile and anatase TiO_2. *Nat. Mater.* 12, 798–801. doi: 10.1038/nmat3697

Schmidt, D. O., Hoffmann-Eifert, S., Zhang, H., La Torre, C., Besmehn, A., Noyong, M., et al. (2015). Resistive switching of individual, chemically synthesized TiO_2 nanoparticles. *Small* 11, 6444–6456. doi: 10.1002/smll.201502100

Schmidt, D. O., Raab, N., Noyong, M., Santhanam, V., Dittmann, R., and Simon, U. (2017). Resistive switching of sub-10 nm TiO_2 nanoparticle self-assembled monolayers. *Nanomaterials* 7:370. doi: 10.3390/nano7110370

Schoen, I., and Fromherz, P. (2008). Extracellular stimulation of mammalian neurons through repetitive activation of Na^+ channels by weak capacitive currents on a silicon chip. *J. Neurophysiol.* 100, 346–357. doi: 10.1152/jn.90287.2008

Seisenbaeva, G. A., Moloney, M. P., Tekoriute, R., Hardy-Dessources, A., Nedelec, J. M., Gun'ko, Y. K. et al. (2010). Biomimetic synthesis of hierarchically porous nanostructured metal oxide microparticles - potential scaffolds for drug delivery and catalysis. *Langmuir* 26, *9809*—9817. doi: 10.1021/la1000683

Senthilkumar, V., Kathalingam, A., Kannan, V., Senthil, K., and Rhee, J. K. (2013). Reproducible resistive switching in hydrothermal processed TiO_2 nanorod film for nonvolatile memory applications. *Sensor. Actuat. A* 194, 135–130. doi: 10.1016/j.sna.2013.02.009

Seo, K., Kim, I., Jung, S., Jo, M., Park, S., Park, J., et al. (2011). Analog memory and spike-timing-dependent plasticity characteristics of a nanoscale titanium oxide bilayer resistive switching device. *Nanotechnology* 22:254023. doi: 10.1088/0957-4484/22/25/254023

Serb, A., Corna, A., George, R., Khiat, A., Rosci, F., Reato, M., et al. (2020). Memristive synapses connect brain and silicon spiking neurons. *Sci. Rep.* 10:2590. doi: 10.1038/s41598-020-58831-9

Shao, X. L., Zhou, L. W., Yoon, K. J., Jiang, H., Zhao, J. S., Zhang, K. L., et al. (2015). Electronic resistance switching in the Al/$TiO_{(x)}$/Al structure for forming-free and area-scalable memory. *Nanoscale* 7:11063–11074. doi: 10.1039/C4NR06417H

Strachan, J. P., Yang, J. J., Montoro, L. A., Ospina, C. A., Ramirez, A. J., Kilcoyne, A. L. D., et al. (2013). Characterization of electroforming-free titanium dioxide memristors. *Beilstein J. Nanotechnol.* 4, 467–473. doi: 10.3762/bjnano.4.55

Strukov, D. B., Snider, G. S., Stewart, D. R., and Williams, R. S. (2008). The missing memristor found. *Nat. Lett.* 453, 80–83. doi: 10.1038/nature06932

Strungaru, M., Cerchez, M., Herbertz, S., Heinzel, T., El Achhab, M., Schierbaum., et al. (2015). Interdependence of electroforming and hydrogen incorporation in nanoporous titanium dioxide. *Appl. Phys. Lett.* 106:143109. doi: 10.1063/1.4917034

Sun, W., Gao, B., Chi, M., Xia, Q., Yang, J. J., Qian, H., et al. (2019). Understanding memristive switching via *in situ* characterization and device modeling. *Nat. Commun.* 10:3453. doi: 10.1038/s41467-019-11411-6

Szot, K., Rogala, M., Speier, W., Klusek, Z., Besmehn, A., and Waser, R. (2011). TiO_2 – a prototypical memristive material *Nanotechnology* 22:254001. doi: 10.1088/0957-4484/22/25/254001

Tao, D. W., Chen, J. B., Jiang, Z. J., Qi, B. J., Zhang, K., and Wang, C. W. (2020). Making reversible transformation from electronic to ionic resistive switching possible by applied electric field in an asymmetrical Al/TiO_2/FTO nanostructure. *Appl. Surf. Sci.* 502:144124. doi: 10.1016/j.apsusc.2019.144124

Tauster, S. J. (1987). Strong metal-support interactions. *Acc. Chem. Res.* 20:389–394. doi: 10.1021/ar00143a001

Teychené, S., Rodriguez-Ruiz, I., and Ramamoorthy, R. K. (2020). Reactive crystallization: from mixing to control of kinetics by additives. *Curr. Opin. Colloid Interface Sci.* 46, 1–19. doi: 10.1016/j.cocis.2020.01.003

Vidiš, M., Plecenik, T., Moško, M., Tomašec, S., Roch, S., Satrapinskyy, L., et al. (2019). Gasistor: a memristor based gas-triggered switch and gas sensor with memory. *Appl. Phys. Lett.* 115:093504. doi: 10.1063/1.5099685

Vijayan, P. P., and Puglia, D. (2019). Biomimetic multifunctional materials: a review. *Emerg. Mater.* 2, 391–415. doi: 10.1007/s42247-019-00051-7

Vilmi, P., Nelo, M., Voutilainen, J. V., Palosaari, J., Pörhönen, J., Tuukkanen, S., et al. (2016). Fully printed memristors for a self-sustainable recorder of mechanical energy. *Flex. Print. Electron.* 1:025002. doi: 10.1088/2058-8585/1/2/025002

Wang, J. R., and Zhuge, F. (2019). Memristive synapses for brain-inspired computing. *Adv. Mater. Technol.* 4:1800544. doi: 10.1002/admt.201800544

Wang, Z., Wu, H., Burr, G. W., Hwang, C. S., Wang, K. L., Xia, Q., et al. (2020). Resistive switching materials for information processing. *Nat. Rev. Mater.* 5, 173–195. doi: 10.1038/s41578-019-0159-3

Waser, R., Dittmann, R., Staikov, G., and Szot, K. (2009). Redox-based resistive switching memories – nanoionic mechanisms, prospects, and challenges. *Adv. Mater.* 21, 2632–2663. doi: 10.1002/adma.200900375

Wedig, A., Luebben, M., Cho, D. Y., Moors, M., Skaja, K., Rana, V., et al. (2015). Nanoscale cation motion in TaO x, HfO x and TiO x memristive systems. *Nat. Nanotechnol.* 11, 67–74. doi: 10.1038/nnano.2015.221

Xia, Q., Robinett, W., Cumbie, M. W., Banerjee, N., Cardinali, T. J., Yang, J. J., et al. (2009). Memristor-CMOS hybrid integrated circuits for reconfigurable logic. *Nano Lett.* 9, 3640–3645. doi: 10.1021/nl901874j

Xia, Q., and Yang, J. J. (2019). Memristive crossbar arrays for brain-inspired computing. *Nat. Mater.* 18, 309–323. doi: 10.1038/s41563-019-0291-x

Xiao, M., Musselman, K. P., Duley, W. W., and Zhou, N. Y. (2017). Resistive switching memory of TiO_2 nanowire networks grown on Ti foil by a single hydrothermal method. *Nano-Micro Lett.* 9:15. doi: 10.1007/s40820-016-0116-2

Yang, J. Y., Pickett, M. D., Li, X., Ohlberg, D. A. A., Stewart, D. R., and Williams, S. (2008). Memristive switching mechanism for metal/oxide/metal nanodevices. *Nat. Nanotech.* 3, 429–433. doi: 10.1038/nnano.2008.160

Yao, P., Wu, H., Gao, B., Eryilmaz, S. B., Huang, X., Zhang, W., et al. (2017). Face classification using electronic synapses. *Nat. Commun.* 8:15199. doi: 10.1038/ncomms15199

Yoo, J., Lee, K., Tighineanu, K., and Schmuki, P. (2013). Highly ordered TiO_2 nanotube-stumps with memristive response. *Electrochem. Commun.* 34, 177–180. doi: 10.1016/j.elecom.2013.05.038

Zaffora, A., Macaluso, R., Habazaki, H., Valov, I., and Santamaria, M. (2018). Electrochemically prepared oxides for resistive switching devices. *Electrochim. Acta* 274, 103–111. doi: 10.1016/j.electacta.2018.04.087

Zhang, F., Gan, X., Li, X., Wu, L., Gao, X., Zheng, R., et al. (2011). Realization of rectifying and resistive switching behaviors of TiO_2 nanorod arrays for nonvolatile memory. *Electrochem. Solid State Lett.* 14:H422. doi: 10.1149/1.3617442

Zhang, L., Gong, T., Wang, H., Guo, Z., and Zhang, H. (2019a). Memristive devices based on emerging two-dimensional materials beyond graphene. *Nanoscale* 11, 12413–12435. doi: 10.1039/C9NR02886B

Zhang, T., Yang, K., Xu, X., Cai, Y., Yang, Y., and Huang, R. (2019b). Memristive devices and networks for brain-inspired computing. *Phys. Status Solidi RRL* 13:1900029. doi: 10.1002/pssr.201900029

Zhang, Y., Wang, Z., Zhu, J., Yang, Y., Rao, M., Song, W., et al. (2020). Brain-inspired computing with memristors: challenges in devices, circuits, and systems. *Appl. Phys. Rev.* 7:011308. doi: 10.1063/1.5124027

Zhu, J., Yang, Y., Jia, R., Liang, Z., Zhu, W., Rehman, Z. U., et al. (2018). Ion gated synaptic transistors based on 2D van der waals crystals with tunable diffusive dynamics. *Adv. Mater.* 30:1800195. doi: 10.1002/adma.201800195

Zidan, M. A. (2018). The future of electronics based on memristive systems. *Nat. Electron.* 1, 22–29. doi: 10.1038/s41928-017-0006-8

Conflict of Interest: The authors declare that the research was conducted in the absence of any commercial or financial relationships that could be construed as a potential conflict of interest.

frontiers in Chemistry

MINI REVIEW
published: 02 November 2020
doi: 10.3389/fchem.2020.550625

Perovskite Puzzle for Revolutionary Functional Materials

Nikolai Belich[1], Natalia Udalova[1], Anna Semenova[1], Andrey Petrov[1], Sergey Fateev[1], Alexey Tarasov[1,2] and Eugene Goodilin[1,2*]

[1] Department of Materials Science, Lomonosov Moscow State University, Moscow, Russia, [2] Department of Chemistry, Lomonosov Moscow State University, Moscow, Russia

Widely spread crystal lattices of perovskites represent a natural flexible platform for chemical design of various advanced functional materials with unique features. An interplay between chemical bonding, defects and crystallochemical peculiarities makes the perovskite structure a "LEGO designer" utilizing natural features of chemical elements of the renowned Mendeleev's Periodic Table (PTE) celebrating its 150-year anniversary. In this mini-review, crystal chemistry and bonding features, physical and functional properties, preparation methods and tuning functional properties with periodicity "tools" of the PTE will be exemplified for legendary families of high-temperature superconductive cuprates, colossal magnetoresistive manganites and hybrid lead halides for a new generation of solar cells.

Keywords: perovskites, superconductivity, magnetoresistance, photovoltaics, copper, manganese, perovskite solar cells, lead halides

Edited by:
Zhong Jin,
Nanjing University, China

Reviewed by:
Yanlin Song,
Institute of Chemistry (CAS), China
Yulia Gorbunova,
NS Kurnakova Institute of General and Inorganic Chemistry (RAS), Russia

****Correspondence:***
Eugene Goodilin
goodilin@inorg.chem.msu.ru

Specialty section:
This article was submitted to Inorganic Chemistry, a section of the journal Frontiers in Chemistry

Received: *09 April 2020*
Accepted: *28 August 2020*
Published: *02 November 2020*

Citation:
Belich N, Udalova N, Semenova A, Petrov A, Fateev S, Tarasov A and Goodilin E (2020) Perovskite Puzzle for Revolutionary Functional Materials. Front. Chem. 8:550625. doi: 10.3389/fchem.2020.550625

INTRODUCTION

The perovskite lattice (**Figure 1**) represents one of the most common motifs of solid phases and, also, is quite typical for the famous families of advanced functional materials including photocatalysis, electrocatalysts and fuel cell components, insertion cathodes of chemical power sources, high—temperature superconductors, multyferroics, magnetic and magnetoresistive materials, materials for solar cell energy and photoluminescence (Ahn et al., 2004; Haugan et al., 2004; Gao et al., 2010; Du et al., 2011, 2013; Jiang et al., 2012; Osterloh, 2013; Frost et al., 2014; Song et al., 2015; De Roo et al., 2016; Weidman et al., 2016; Hwang et al., 2017, 2019; Wang et al., 2019; Hao et al., 2020). At the same time only three families of perovskite-based functional materials have attracted major interest in view of prospects in developing mass-production technologies and practical applications.

Colossal **M**agneto**R**esistive (CMR) manganites (**Figure 1b**) were discovered in the 1950's (Van Santen and Jonker, 1950; Volger, 1954) and rediscovered in the 1990's (von Helmolt et al., 1993). In 2007, a Nobel Prize in Physics was awarded for the same effect observed in layered heterostructures demonstrating the Giant MagnetoResistance based on the fundamentally important effect of control of electron scattering by spin polarization (Fert et al., 1995). **H**igh–**T**emperature **S**uper **C**onducting (HTSC) cuprates (**Figure 1c**) have been found in 1986 (Bednorz and Müller, 1986) and have been awarded next year with the Nobel Prize in Physics which is one of a total of six Nobel Prizes for superconductivity. The most recent high-impact perovskites (**Figure 1a**) have been suggested for **P**erovskite **P**hotovoltaics presented solely by **H**ybrid **L**ead **H**alides applied for solar cells in 2009 by Tsutomi Miyasaka (Kojima et al., 2009), developed further in 2012 by Michael Grätzel with

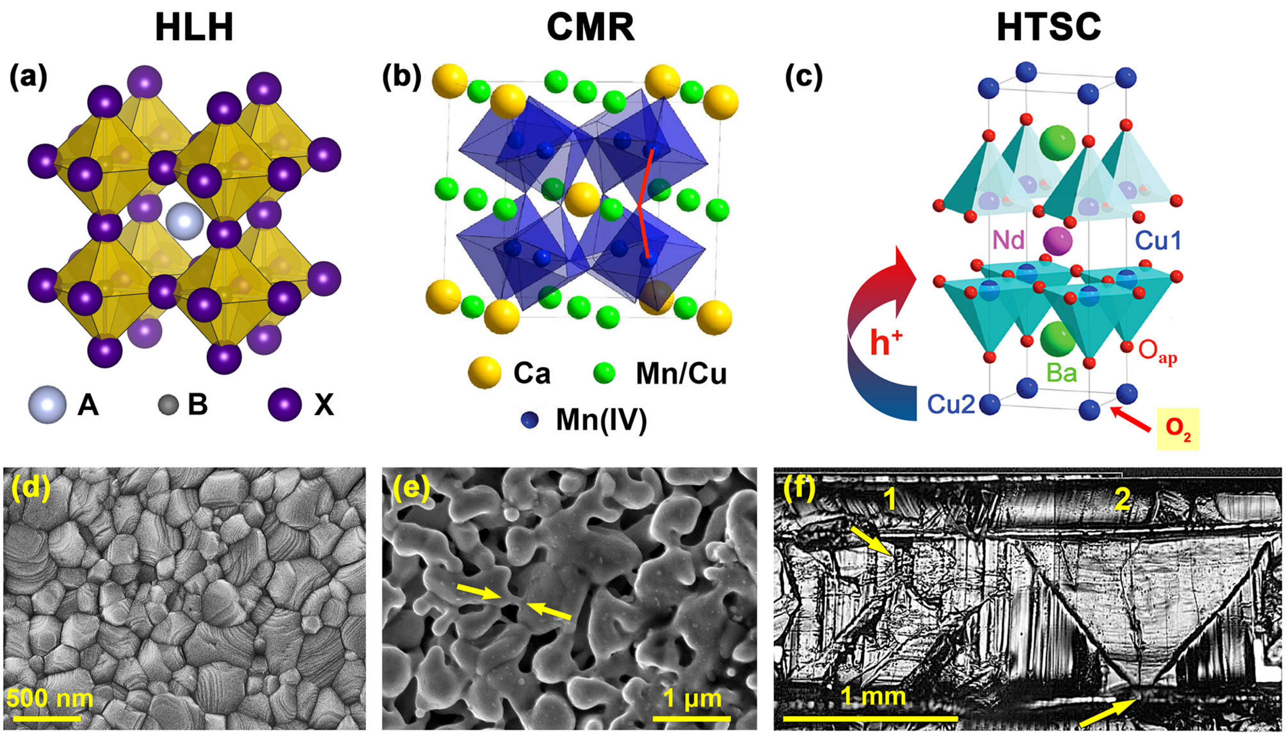

FIGURE 1 | Crystal structures **(a,b,c)** and, respectively, typical morphologies from a top view of films or coatings of solution–derived HLH perovskites **(d)**, ASP—deposited CMR manganites **(e)** and melt—processed HTSC cuprates **(f)**. The A, B, X for the structure of HLH perovskite **(a)** represent a large inorganic or organic cation (A), lead (B) and halogen (X), respectively. The structure of CMR manganites **(b)** is shown for a special family of the CaCu$_3$Mn$_4$O$_{12}$ solid solution. The HTSC is represented by the most famous family of REE-barium cuprates (NdBa$_2$Cu$_3$O$_{6+x}$), the arrow symbolizes the hole (h$^+$) transfer from Cu(2) ions in the charge reservoir to Cu(1) in superconducting plains. The white arrows show intergrain necks **(e)** or nucleation sites of crystallization for two adjacent millimeter–sized HTSC grains on a graphotexturing substrate **(f)**. Note, the morphology shown for CMR manganites is not acceptable for HLH or HTSC perovskites while the HLH microstructure would not be suitable for HTSCs.

essential works known from Henry Snaith, Nam-Gyu Park, and others (Grätzel, 2014; Park et al., 2016; Eperon et al., 2017; Li et al., 2017, 2018; Gao et al., 2018; Leijtens et al., 2018; Snaith and Hacke, 2018; Fu et al., 2019; Nayak et al., 2019). They represent a new generation of solar cell materials overcoming easily the records of DSSC devices with chemically stable and quite effective tetrapyrolic sensitizers and approaching closely the best values of effectiveness of silicon (Bottari et al., 2010; Li and Diau, 2013; Mathew et al., 2014; Martynov et al., 2019; Abdulaeva et al., 2020).

These families of perovskite-like materials represent three conceptually different areas of materials research for advanced electronics and alternative energy. The unique behavior of these materials originates of chemical element features composing the phases, different metal—non-metal bonds resulting in different target physical properties and demanding, in turn, quite special optimal morphologies of the materials under the question (**Figure 1**). The latter, obviously, can be achieved by material-specific production techniques being the limiting factors of the materials implementation. It is risky to compare all these almost dissimilar materials (**Table 1**) but there is the only valuable aspect of such a story that is closely related to the key chemical approaches utilized for enhancing their optimal morphologies. This material—related analysis seems to be useful for a rational design and future progress in preparation techniques toward the development of the perovskite—based devices with record characteristics. This purpose is highlighted in the current mini-review to shape the research directions of prospective chemical preparation routes based on the PTE peculiarities of the respective elements.

STRUCTURAL FEATURES OF PEROVSKITES vs. COMPOSING ELEMENT PECULIARITIES

None of the discussing materials demonstrate ideal ABX$_3$ perovskite structures where A—a larger central cation, B—a smaller cation octahedrally surrounded by X anions (**Figure 1**). Moreover, different HTSC, CMR, HLH families and homologs, intergrown or none-perovskite structures are well-known (Zhang et al., 1996; Tretyakov and Goodilin, 2000; Tretyakov et al., 2004; Attfield, 2011; Lee et al., 2014; Ovcharov et al., 2019). However, their "classical" representatives are stack to the simplest perovskite lattice (**Table 1**, **Figure 1**). HTSC cuprates and CMR

TABLE 1 | Basic features of HTMC cuprates, CMR manganites and HLH solar perovskites in comparison.

Features	HTSC cuprate perovskites	CMR manganite perovskites	Solar/hybrid lead halide perovskites
Key chemical elements configuration, ion size and framework bonding	Cu—O (d/p) Cu: [Ar]3d^{10}4s^{1} O: [He]2s^{2}2p^{4} 68–71 pm for Cu(III)—Cu(I) 126 pm for O^{2-}	Mn—O (d/p) Mn: [Ar]3d^{5}4s^{2} O: [He]2s^{2}2p^{4} 67–72 pm for Mn(IV)—Mn(III) 126 pm for O^{2-}	Pb—I (s/p, p/p) Pb: [Xe]4f^{14}5d^{10}6s^{2}6p^{2} I: [Kr]4d^{10}5s^{2} 5p^{5} 133 pm for Pb(II) 206 pm for I^{-}
Functional properties	Superconductivity Diamagnetic	Magnetoresistance Magnetic semiconductor / metallic	Photoeffect Semiconductor
Carriers	Hole pairs (bosons, BCS pairs)	Electrons (spin–polarized)	Hole–electron pairs (excitons)
Metal oxidation state(s)	Mixed +2/+3	Mixed +3/+4	Fixed +2
Conduction path	Flat CuO$_2$ sheets (doped from charge reservoir)	Lined Mn–O–Mn chains (double exchange etc.)	Pb–I–Pb chains ("redox")
Point defects	Disordered and ordered oxygen vacancies, cation antisites, homo- and heterovalent substitution in both cation and anion sublattices	Disordered oxygen vacancies, cation antisites, homo- and heterovalent substitution in both cation and anion sublattices	Mostly homovalent substitution in either cation or anion sublattices, iodine vacancies
Deviation from stoichiometry ratio	Large for oxygen, much smaller for the larger central cations and copper (wide range for proper substitutions)	Small for both oxygen and cations (wide range for proper substitutions)	Iodine stoichiometry (still unclear) (wide range for proper substitutions)
Carrier generation	Oxidation	Heterovalent substitutions	Light absorption
Local distortions	Jahn–Teller effect, ion mismatch	Jahn–Teller effect, ion mismatch	Ion mismatch
Microstructure required	Biaxial texturing, large grains, clean boundaries, no weak links	Intergrain tunneling (other requirements are not essential)	No pinholes, no charge traps at grain boundaries, large grains are better, no texture is required
Whiskers	Exist, no need	Exist, no need	Exist, possibly useful
Applications	Large grain ceramics, epitaxial thin films, heterostructures	Thin films, polycrystalline coatings	Polycrystalline thin films, heterostructures, quantum dots, single crystals
Best processing	Melt techniques (LAP, MTG, LPP, PDMG, IMC, GPM, CGMG, SLMG, PMP, TPP, GEORGE, QMG, OCMG, MPMG, QDR) and thin films (ASP/CVD/MOCVD/PVD/RaBiTS)	Ceramic sintering, thin films (CVD/MOCVD/PVD/ASP)	Thin films (solution/precipitation, CVD/PVD/ASP, RP-MAGIC)
Spinodal decomposition	Known, useful for pinning	Known, useless	Known, under study

LAP, liquid assisted processing (crystallization or recrystallization with traces of melt); MTG, melt textured growth (melting and cooling process under constant pO$_2$); LPP, liquid phase processing (melting and stepwise cooling); PDMG, platinum doped melt growth; IMC, isothermal melt crystallization (melting and crystallization by pO$_2$ variation under constant temperature); GPM, gas pressure method (crystallization under elevated partial pressure of oxygen); CGMG, constant gradient melt growth (crystallization along the concentrational/spatial gradient of REE); SLMG, solid liquid melt growth (melting and cooling process of fine mixture of powders under constant pO$_2$); PMP, powder melt process; TPP, two powder process; GEORGE, GEometrically-ORganized-Growth-Evaluation (crystallization along the geometrically created concentrational / spatial gradient of REE); QMG, quench melt growth; OCMG, oxygen controlled melt growth; MPMG, melt powder melt growth; QDR, quenched directional recrystallization; RP-MAGIC, reactive polyiodide melt assisted growth through in situ conversion; (MO) CVD, (metal-organic) chemical vapor deposition; PVD, physical vapor deposition; ASP, aerosol spray pyrolysis.

manganites, according to the Pearson's formalism[1], are the compounds of hard acids (cations) from the d-block (Cu and Mn) and a hard base O^{2-} from the p-block. On the contrary, the lead halide perovskites are composed from a soft acid Pb^{2+} and a soft base I^{-} from the p-block of PTE. These combinations result in phases which are more stable but different. The hard acid–hard base compounds with stronger interactions of smaller non-polarizable ions in the lattice exist in air up to the temperatures of ca. 1000 (HTSC)–1,300°C (CMR) while the HLH soft acid–soft base perovskites with large polarizable ions do not survive, expectedly, above 120–150°C but easily form solutions and adducts with various donor solvents (Fateev et al., 2018) thus presenting the most attractive solvent-based deposition technologies of solar cell production (Park, 2016). HLH is a unique compound family made of the heaviest and the largest non-radioactive elements of PTE.

HTSC cuprates (**Figure 1c**) and CMR manganites (**Figure 1b**) are mixed—valent phases with a large non-stoichiometry of X—anion for HTSC or A—cation in the case of CMR phases (Tretyakov and Goodilin, 2000; Pomerantseva et al., 2004; Tretyakov et al., 2004). The HLH perovskites demonstrate a moderate or small X-site non-stoichiometry and, formally, fixed oxidation states of lead and halogens. The mixed-valent states of HTSC cuprates and CMR manganites are achieved by

---

[1] Pearson, 1963; species with larger radii, corresponding smaller charge states and higher polarizability of chemical elements reduce the lattice energy of solid phases and their dependent "thermal stability."

means of two chemically different approaches. Oxygen nonstoichiometry is the major factor used for oxidation of the HTSC phases with molecular oxygen (**Figure 1**) and that leads to an increase of the copper oxidation state, for example, from +1/+2 for $REEBa_2Cu_3O_6$ (REE—Rare Earth Elements) to +2 and exotic Cu(III) for $REEBa_2Cu_3O_7$ (Shiohara and Goodilin, 2000; Tretyakov and Goodilin, 2000). CMR manganites use heterovalent doping of the A—cation rather than varying oxygen content to provide the needed balance of Mn(III) / Mn(IV) in the structure. Normally, the B—site substitution, especially heterovalent, provides no drastic improvement of functional properties and, often, deteriorates them. For example, <1–5 at % of Zn, Mg, and other elements substituting copper in $REEBa_2Cu_3O_7$ lead to a half reduction of the superconductivity transition temperature, similar substitutions of manganese in CMR manganites are also risky, have no linear dependence on their concentration and normally are not effective for properties improvements. For HLH (**Figure 1a**), lead substitution with tin, bismuth etc. usually results in decreasing functional parameters while the X-site substitution with mixed halide ions is often useful for fine tuning of the physical and thermodynamic properties. The X-site substitution, even heterovalent (like fluorine), is applied rarely to tune the properties of HTSCs and CMR materials but it could not be considered as primary method of their target chemical modifications.

The A-site cation plays an important but a secondary role. The A-cation usually affects no physical properties but it is primarily needed to stabilize the structure electrostatically and geometrically since the ionic radii of this cation is counted in the famous Goldshmidt tolerance factor predicting the overall structure stability. Noticeably, a 12–13% decrease of the REE size due to the lanthanide contraction effect results in the $REEBa_2Cu_3O_7$ melting temperature falling by about 120°C (Shiohara and Goodilin, 2000), from 1,085°C (Nd) down to 965°C (Yb); this effect is much weaker for mixed REE–AEE CMR manganites (AEE—Alkali Earth Elements). In the case of HLH, the largest purely inorganic cation in the PTE, Cs^+, seems to be still too small to solely stabilize the HLH perovskite structure near room temperature thus demanding a larger cation, such as methylammonium and formamidinium (Travis et al., 2016). The latter makes the HLH perovskites belong to the hybrid, organic–inorganic, phases and therefore this feature entirely changes their chemical properties and preparation techniques. A further increase of the A-cation size or changing its geometry produces low-dimensional HLH phases with complex structures (Smith et al., 2018); thus a set of available cations to form the HLH perovskites is quite limited. The consequences of the asymmetry of such a "hybrid" cation include local structural distortions and, for some solid solutions, a possibility of spinodal decomposition which is useless for the HLH perovskites. Oppositely, the spinodal decomposition is a remarkable phenomenon for the A-site substituted solid solutions based on the HTSC cuprates (Petrykin et al., 2000; Shiohara and Goodilin, 2000) since the demixing generates compositional nanofluctuations acting as effective pinning centers and thus resulting in record critical currents under magnetic fields. A more complex structure of HTSCs and CMR manganites could also yield antisites in the structure of perovskites resulting in the preparation "prehistory" effects (Petrykin et al., 2000). In the case of HLH perovskites, a mixture of various A-cations are routinely applied for the entropy-driven stabilization (Yi et al., 2016).

The framework of corner-sharing octahedra BX_6 of the perovskites generates the main application-related properties of these materials (Tretyakov et al., 2004). In this contest, The Jahn–Teller effect, being quite typical for Mn^{3+} and Cu^{2+}, causes frustrated structures, spin waves for manganites (Pomerantseva et al., 2004) or result in drastic structural distortions for HTSCs. In the case of $REEBa_2Cu_3O_7$, the structure (**Figure 1c**) is composed of three perovskite-like oxygen deficient intergrown blocks (Shiohara and Goodilin, 2000; Tretyakov and Goodilin, 2000). The two of them containing barium and empty oxygen vacancies near copper ($Cu(1)O_2$—$BaO_{(ap)}$—$Cu(2)O_x$) operate as charge reservoirs accumulating holes upon copper oxygenation and oxygen content growth, $V_O{}^{**} + 1/2\ O_2 = O_O{}^X + 2\ h^*$. It is a direct representation of the Jahn–Teller effect that there is no octahedra with copper and oxygen in this structure but, instead, Cu(1) is included into flat superconducting (SC) planes CuO_2 and have a five-fold pyramidal coordination counting also the "apical" oxygen $O_{(ap)}$ in the BaO "layer." The second type of copper, Cu(2), possesses a two-fold linear coordination for the tetragonal oxygen-disordered $REEBa_2Cu_3O_6$ compound or rhombs for the superconducting $REEBa_2Cu_3O_7$ orthorhombic phase with ordered residual oxygen vacancies. The central CuO_2-REE–CuO_2 block contains two flat superconducting planes and REE^{3+} cations. Upon oxygenation, holes are concentrated in the charge reservoir blocks and are transferred then to the superconducting plains CuO_2 by shifting the apical oxygen $O_{(ap)}$ from Cu(2) toward Cu(1). A critical concentration of holes in the SC plains gives bosons, the BCS pairs, if cooled below a SC critical temperature T_c. Actually, such a crystal architecture makes HTSCs cuprates highly anisotropic layered compounds originated of perovskites.

The flatter the SC plains, the higher T_c of HTSCs, otherwise overlapping the d-orbitals of Cu(1) and p-orbitals of oxygen is deteriorated. In the case of CMR manganites and HLH perovskites, no deep modifications of the perovskite motif are observed (Tretyakov et al., 2004). Moreover, the Mn–O–Mn chains in the structure of CMR phases (**Figure 1b**) have to be linear with the angle between Mn^{3+}, O^{2-} and Mn^{4+} close to 180° for effective overlapping of the respective d_{Mn} and p_O orbitals corresponding each other by symmetry (Babushkina et al., 1998; Pomerantseva et al., 2004). Due to the antiferromagnetic, double exchange in these linear fragments, electrons may transfer from Mn^{3+} to Mn^{4+} via the linking oxygen. To reduce the electrical resistance of the phase, the electron carriers should be correlated or spin–polarized by an external magnetic field in different parts of CMR manganite and grains which results in the negative magnetoresistance effect. The overlapping of the s, p-orbitals of iodine and lead in HLH semiconducting phases also provides effective pathways for charge transfer however both hole and electron carriers are generated by the photovoltaic effect utilizing electron density redistribution between the s- and p–orbitals of Pb^{2+} and p–orbitals of I^- within the Pb-I-Pb framework

(**Table 1**). The HLH phases seem to be mostly "tolerant" to various defects (Meggiolaro et al., 2018) as not typical for classical semiconductors. Among others, the HLH perovskites seem to be the chemically and physically simplest phases (**Figure 1a**) with no peculiarities caused by defect ordering, heterovalent substitution or spin-correlated phenomena. The noted peculiarities of the discussed frameworks pre-determine, to a large extent, both the morphology and production schemes of the final materials and devices.

MORPHOLOGIES, MICROSTRUCTURES AND RELEVANT PROCESSING TECHNIQUES

Nowadays, the perovskite-like phases under discussion are mostly used as 2D polycrystalline materials (thin films and heterostuctures) with already rare inventions of their 3D ceramic or single crystalline forms. As a polycrystalline matter for advanced practical applications, each of the materials requires its own optimal combination of general morphological parameters like crystalline grain size, orientation, thickness, uniformity and the organization of intergrain boundaries since the required different morphologies of the materials ensure the achievement of record functional properties. All the HTSCs, CMR and HLH materials are prominent in low-current applications, sensing devices and smart circuits for information technologies, communication, and microelectronics. HTSCs and CMR materials are involved in applications as magnetic field sensors, in both the cases, the artificial or natural organization of grain boundaries play an extraordinary role. The most known and the most magnetic field sensitive devices are SQUID magnetometers and tomographs utilizing the quantum Josephson's effect for a special gap / boundary architecture within a superconductor (Colclough et al., 1987). CMR materials for spintronics utilize artificial junctions to operate with spin-polarized carriers created by a magnetic field in spin valves and other elements of spintronics (Yang et al., 2019); in the simple case of magnetic sensors, grain boundaries within CMR manganites play a major role for target variation of electrical conductivity. It should be noted that, oppositely, multiple grain boundaries play a negative role for HTSCs even in those low-current applications. HLH semiconducting materials demonstrate a photovoltaic effect leading to generation of carriers for conversion of solar energy into electricity (Grätzel, 2014; Chen et al., 2017; Eperon et al., 2017). In such a case, grain boundaries are not a positive factor since they could quench and trap the carriers reducing the operational effectiveness although they are not really used for the control of a transport current. Vice versa, HLH materials can effectively generate light by converting electrical energy in light-emitting devices and quantum dots under low voltages and low currents (De Roo et al., 2016; Fu et al., 2019). HTSCs are the only type of materials in this group requiring high current applications demanded for industrial transport of electricity, industrial current limiters or generation of record magnetic fields in energy generation or transport systems (Bednorz, 2019; Dong et al., 2019).

Thus, HTSCs, CMR manganites, HLH perovskites demand three different approaches to achieve a proper morphology (**Figure 1**). For important devices utilizing these three perovskites, thin films, heterostructures or sandwiched structures have to be deposited (Zhang et al., 1996; Shiohara and Goodilin, 2000; Tretyakov and Goodilin, 2000; Tretyakov et al., 2004; Snaith and Hacke, 2018). CMR manganites (Pomerantseva et al., 2004) operate with a relative change of resistance under applied magnetic fields and this demands lateral transport of weak electrical currents while intergrain boundaries become highly important due to the effect of tunneling magnetoresistance (TMS). This means that CMR manganites would require a uniform thickness of the films but not necessarily their single crystallinity, polycrystalline CMR films seem to have some advantages thus this type of perovskites post the weakest requirements to their microstructure (**Figure 1e**). HTSC cuprate films below 1 μm in thickness, preserving the epitaxial control over the biaxial texturing, are necessary for spreading a lateral critical current for long distances (RABiTS tapes, rolling-assisted-biaxially-textured-substrate, and other "second generation" HTSCs) but its values exceed a fantastic level of 10^7 A/cm^2 which is achievable by no other known materials. Under such a large current, non-uniformity of any kind or "weak links" between the grains result immediately in "hot spots" with huge local overheating leading finally to thermal destruction of the films. Therefore, HTSCs are extraordinarily sensitive to their microstructure demanding, at least, large grain and biaxially textured (epitaxial) films with clean grain boundaries, fully transparent for large values of electric current below T_c (**Figure 1f**). The HLH perovskites remain comparatively tolerant to microstructural requirements and occupy a position in between CMR and HTSC materials since they demand, due to an extraordinary large extinction coefficient, only 100–300 nm thin and uniform light absorbing layers with no pin holes to prevent shunting the circuit. This is demanded by the typical operational geometry of the new generation of solar cells with movement of negative and positive charge carriers across the sandwiched layers owing to the photovoltaic effect. The mean grain size of HTSC films would exceed millimeters (**Figure 1f**), the same typical parameter for CMR films falls into the submillimeter range (Pomerantseva et al., 2004). In contrast, HLH films with the best optoelectronic properties (**Figure 1d**) possess the grains of micrometer sizes and demand no perfect in-plain orientation although such films should contain no carrier traps at the boundaries (Zhang et al., 2016; Shlenskaya et al., 2018).

No real applications are known so far for single crystals of the noted perovskites although their effective grown techniques are developed successfully (Goodilin et al., 1997, 1998; Shiohara and Goodilin, 2000; Zhumekenov et al., 2018). Probably, some of them seem to be prospective for light-emitting devices, photodetectors and X-ray detectors (Wei and Huang, 2019; Murali et al., 2020). As for whiskers, they are not usually single crystalline, probably pseudomorphic (Petrov et al., 2017b), and are not yet involved in real applications.

HTSCs stand along among this group because of the second application domain related to large grain textured ceramics for industry like magnetic transport levitation, motors and generators (Tretyakov et al., 2004). In such ceramics, the same principle of biaxial texturing remains as in the case of HTSC thin films. Additionally, pinning centers of SC Abrikosov's vortexes are required for the ceramics however they are self-generated due to the developed processing schemes discussed below. At the same time, thin film solutions related to the so-called second generation of HTSCs are being developed to replace almost all high-current bulk materials.

Special requirements of achieving optimal morphologies lead to the wide elaboration of preparation techniques of these families of perovskite-related materials. In particular, thin film deposition and soft chemistry approaches are not unique and well-developed for all the discussing perovskite systems including, generally, different thermal, electron beam evaporation, laser ablation, CVD or MOCVD approaches, sol-gel and spin-coating techniques, aerosol spray pyrolysis, even graphoepitaxy; freeze drying is effective for preparation of some type of precursor particles (Tretyakov and Goodilin, 2000; Goodilin et al., 2002; Tretyakov et al., 2004; Gao et al., 2018; Snaith and Hacke, 2018; Nayak et al., 2019). Thin film deposition is quite complicated, but is already well-established, for the second generation of flexible tapes of HTSCs since this procedure includes unavoidably the metallic substrate texturing, coating with several buffer layers with precisely controlled microstructures followed by epitaxial growth of HTSC film, shunting and protective layers. The complexity of this procedure for finely tuned morphologies gave birth to special modifications of film deposition techniques like IBAD (ion beam assisted deposition) or ISD (inclined substrate deposition). Compared to that, HLH film deposition is much simpler and includes routine stages of deposition without controlling epitaxy relations. The specificity of those scale—up procedures for HLH is the ability to use nearly room temperatures and common solvents within the "wet" techniques like slot—die, blade-, spin-coating, ink–jet printing, screen printing etc (Li et al., 2018). Those methods have been surely tested for HTSC but they showed lower effectiveness compared to CVD or PVD because of much stricter requirement to the microstructure and higher phase conversion temperatures.

Solvent-deposition techniques of functional films seem to be oversimplified by common thinking however they are rather complicated by the phenomena of new phase formation, phase transformation, mass and heat transfer in terms of solvent evaporation, decomposition of intermediate hydrates and hydrolysis products (HTSC, CMR) or complex solvent adducts (HLH) resulting often in loosing morphological, chemical uniformity, shrinkage, crack formation etc (Petrov et al., 2017c; Shlenskaya et al., 2018). This all leads to the successful search for novel solvent-free, for example, melt-based, preparation approaches. Only two families of the perovskites utilize effectively melt preparation techniques—HTSCs and HLHs (**Figure 1**). In the first case, melt preparation is one of the basic and well-developed approaches (**Table 1**) while HLH phases have demonstrated such a potential only recently (Petrov et al., 2017a; Turkevych et al., 2019).

HTSCs undergo peritectic decomposition which can be exemplified for $REEBa_2Cu_3O_7$ as "melting": $REEBa_2Cu_3O_7 = REE_2BaCuO_5 + L + O_2$ where L–melt containing Cu(I) and Cu(2), REE_2BaCuO_5–a properitectic phase (Shiohara and Goodilin, 2000; Tretyakov and Goodilin, 2000). The reversal transformation depends on heat transfer, oxygen partial pressure and REE concentration in the melt. The latter is quite important because the melt is barium- and Cu(I)- rich and REE_2BaCuO_5 particles is the only source of REE. It actually gives no heterogeneous nucleation sites, as might be expected, it is proven that REE_2BaCuO_5, instead, provides a higher REE^{3+} content in the vicinity of the properitectic particles leading to homogeneous nucleation of $REEBa_2Cu_3O_7$. Such a mechanism has direct consequences in terms of appearing several groups of melt processing (**Table 1**). All of these methods are already finally developed and therefore this system gives a full set of possible examples of effective melt preparation routes. In particular, most of the methods utilize, expectedly, melting and cooling regimes. Another group applies an isothermal controllable variation of pO_2, as a volatile component, to crystallize the melt. Finally, some methods apply a spatial gradient of REE to provide the needed biaxial texture of HTSCs. The size distribution of the properitectic phase seems to be quite important since it determines the key morphological features of melt—processed large grain HTSC ceramics as well as the generation of effective pinning centers for type II superconductors. Therefore a special degree of freedom is used to vary this parameter closely connected with shifting the precursors toward more non-equilibrium states, in particular, by replacing the final product $REEBa_2Cu_3O_7$ undergoing melting by imitators of the quenched peritectic melt, like REE_2BaCuO_5 and Cu(II) cuprate mixtures, or REE_2O_3 and Cu(I) cuprite mixtures, as observed upon decomposition of the $REEBa_2Cu_3O_7$ phase at 1,300–1,400°C and quenching (Tretyakov et al., 2004). The best methods already known for HTSCs melt processing (**Table 1**) utilize both, the shift to non-equilibrium mixtures and the controllable change of pO_2 (Tretyakov and Goodilin, 2000).

It is hard to expect that the HLH perovskites will undergo the same complex evolution of melt processing techniques since this family requires much simpler microstructures with no biaxial texturing, inclusions of secondary phases or large grains. At the same time, at least two analogous approaches are already suggested thus manifesting a start of development of HLH melt processing as a trend. Unfortunately, HLHs undergo irreversible decomposition with loosing highly volatile components like iodine and methylamine upon melting (Boyd et al., 2019). In this contest, traditional melt processing, even despite of comfortable melting points around 140–170°C is not applicable. At the same time, an excess of iodine or methylamine forms a self-flux - the room-temperature melts allowing crystallization of HLH perovskites from those liquids (Chen et al., 2017; Petrov et al., 2019). The recently developed and quite promising RP—MAGIC approach (**Table 1**) utilizes reactionary polyiodide melts (RPM) to convert thin layers of metallic lead to form a uniform film of light absorbing HLH: $Pb + MAI_3 = MAPbI_3$ (Turkevych et al., 2019). The driving force of this "chemical" crystallization process is that this is not an equilibrium system and has a huge difference in chemical potentials of components between the contacting phases. The chemical transformation of lead into a chemically compatible phase PbI_2 results in its dissolution in RPM followed by crystallization of the HLH perovskite from supersaturated RPM since it is dictated by the driving force of the first stage of the lead interaction with RPM. Actually, this much resembles the most effective protocol of HTSC melt processing (OCMG, Tretyakov and Goodilin, 2000), starting from the REE_2O_3 phase incompatible with an admixture of Cu(I) barium cuprite which is transformed upon heating in liquid converting REE_2O_3 into the REE_2BaCuO_5 compatible phase followed by its dissolution in the cuprate melt under cooling to crystallize finally the $REEBa_2Cu_3O_7$ HTSC (Tretyakov et al., 2004). Thus, the philosophy of preparation of new functional materials is common enough for different perovskites under the question with deviations naturally connected with chemical features predicted by the element's position in PTE.

CONCLUSIONS AND PERSPECTIVES

The families of promising perovskite materials discussed in this review have achieved quite different stages of implementation and practical applications. Despite the earliest discovery of CMR manganites, their applications are postponed for years because of their too narrow possible use in spintronics which is still not competitive with current trends in modern electronics. Expectations to use the CMR materials as wide-spread and fast magnetic sensors are moderate since SQUID devices outperform the manganites to a large extent. The remaining area of manganite applications is still connected with multiferroic systems and possible devices based on these multifunctional materials. HTSCs have achieved the heights of first industrial applications in superconducting electronics like SQUID and magnetic medical tomographs or industrial fault current limiters based on the second generation HTSC tapes, all after about 30 years beyond the HTSC discovery. There are a few already successful pilot projects of HTSC applications in transport systems like Maglev trains, propulsion ships and even small air craft jet systems. At the same time, a huge area of future applications of HTSCs is thinkable in megascience magnetic systems like synchrotrons, adroid colliders and thermonuclear plasma traps. However, the cost and operation stability issues still do not allow for the replacement of low temperature intermetallic superconductors. The frontier HLH solar cells and efficient light emitting devices, tandem power generating systems are the current challenges for science and engineering of hybrid perovskites with important remaining problems of stability and scaling up approaches. At the same time, their simpler architecture, chemistry and morphological requirements allow us to believe that these perovskites will come into commercial use much sooner compared to the other two families of perovskites, at least it is a prediction to optimistically believe.

AUTHOR CONTRIBUTIONS

EG prepared and wrote the manuscript draft. All authors added textual and reference information and approved the manuscript submission after mutual discussion.

FUNDING

This work was supported by Russian Science Foundation (project No. 19-73-30022).

ACKNOWLEDGMENTS

The authors thank S. Lee, E. Pomerantseva, V. Ivanov, and D. Itkis for fruitful discussions.

REFERENCES

Abdulaeva, I. A., Birin, K. P., Bessmertnykh-Lemeune, A., Tsivadze, A., and Gorbunova, Y. G. (2020). Heterocycle-appended porphyrins: synthesis and challenges. *Coord. Chem. Rev*. 407:213108. doi: 10.1016/j.ccr.2019.213108

Ahn, K. H., Lookman, T., and Bishop, A. R. (2004). Strain-induced metal-insulator phase coexistence in perovskite manganites. *Nature* 428, 401–404. doi: 10.1038/nature02364

Attfield, J. P. (2011). Chemistry and high temperature superconductivity. *J. Mater. Chem*. 21, 4756–4764. doi: 10.1039/c0jm03274c

Babushkina, N. A., Belova, L. M., Gorbrnko, O. Y., Kaul, A. R., Bosak, A. A., Ozhogin, V. I., et al. (1998). Metal–insulator transition induced by oxygen isotope exchange in the magnetoresistive perovskite manganites. *Nature* 391, 159–161. doi: 10.1038/34380

Bednorz, G. (2019). Georg Bednorz. *Nat. Rev. Mater*. 4, 292–293. doi: 10.1038/s41578-019-0104-5

Bednorz, J. G., and Müller, K. A. (1986). Possible highT c superconductivity in the Ba–La–Cu–O system. *Zeitschrift fur Phys. B Condens. Matter*. 64, 189–193. doi: 10.1007/BF01303701

Bottari, G., de la Torre, G., Guldi, D. M., and Torres, T. (2010). Covalent and noncovalent phthalocyanine–carbon nanostructure systems: synthesis, photoinduced electron transfer, and application to molecular photovoltaics. *Chem. Rev*. 110, 6768–6816. doi: 10.1021/cr900254z

Boyd, C. C., Cheacharoen, R., Leijtens, T., and McGehee, M. D. (2019). Understanding degradation mechanisms and improving stability of perovskite photovoltaics. *Chem. Rev*. 119, 3418–3451. doi: 10.1021/acs.chemrev.8b00336

Chen, H., Ye, F., Tang, W., He, J., Yin, M., Wang, Y., et al. (2017). A solvent- and vacuum-free route to large-area perovskite films for efficient solar modules. *Nature* 550, 92–95. doi: 10.1038/nature23877

Colclough, M. S., Gough, C. E., Keene, M., Muirhead, C. M., Thomas, N., Abell, J. S., et al. (1987). Radio–frequency SQUID operation using a ceramic high–temperature superconductor. *Nature* 328, 47–48. doi: 10.1038/328047a0

De Roo, J., Ibanez, M., Geiregat, P., Nedelcu, G., Walravens, W., Maes, J., et al. (2016). Highly dynamic ligand binding and light absorption coefficient of cesium lead bromide perovskite nanocrystals. *ACS Nano* 10, 2071–2081. doi: 10.1021/acsnano.5b06295

Dong, F., Huang, Z., Hao, L., Xu, X., Jin, Z., and Shao, N. (2019). An on–board 2G HTSC magnets system with cooling–power–free and persistent–current operation for ultrahigh speed superconducting maglevs. *Sci. Rep.* 9:11844. doi: 10.1038/s41598-019-48136-x

Du, Y., Wang, X., Chen, D., Yu, Y., Hao, W., Cheng, Z., et al. (2013). Manipulation of domain wall mobility by oxygen vacancy ordering in multiferroic $YMnO_3$. *Phys. Chem. Chem. Phys.* 15, 20010–20015. doi: 10.1039/c3cp52892h

Du, Y., Wang, X. L., Chen, D. P., Dou, S. X., Cheng, Z. X., Higgins, M., et al. (2011). Domain wall conductivity in oxygen deficient multiferroic $YMNO_3$ single crystals. *Appl. Phys. Lett*. 99:252107. doi: 10.1063/1.3671393

Eperon, G., Hörantner, M., and Snaith, H. (2017). Metal halide perovskite tandem and multiple-junction photovoltaics. *Nat. Rev. Chem.* 1:0095. doi: 10.1038/s41570-017-0095

Fateev, S. A., Petrov, A. A., Khrustalev, V. N., Dorovatovskii, P. V., Zubavichus, Y. V., Goodilin, E. A., et al. (2018). Solution processing of methylammonium lead iodide perovskite from γ-butyrolactone: crystallization mediated by solvation equilibrium. *Chem. Mater*. 30, 5237–5244. doi: 10.1021/acs.chemmater.8b01906

Fert, A., Grünberg, P., Barthélémy, A., Petroff, F., and Zinn, W. (1995). Layered magnetic structures: interlayer exchange coupling and giant magnetoresistance. *J. Magn. Magn. Mater*. 140–144, 1–8. doi: 10.1016/0304-8853(94)00880-9

Frost, J. M., Butler, K. T., Brivio, F., Hendon, C. H., van Schilfgaarde, M., and Walsh, A. (2014). Atomistic origins of high-performance in hybrid halide perovskite solar cells. *Nano Lett.* 14, 2584–2590. doi: 10.1021/nl500390f

Fu, Y., Zhu, H., Chen, J., et al. (2019). Metal halide perovskite nanostructures for optoelectronic applications and the study of physical properties. *Nat. Rev. Mater*. 4, 169–188. doi: 10.1038/s41578-019-0080-9

Gao, P., Bin Mohd Yusoff, A. R., and Nazeeruddin, M. K. (2018). Dimensionality engineering of hybrid halide perovskite light absorbers. *Nat. Commun.* 9:5028. doi: 10.1038/s41467-018-07382-9

Gao, X. S., Rodriguez, B. J., Liu, L. F., Birajdar, B., Pantel, D., Ziese, M., et al. (2010). Microstructure and properties of well-ordered multiferroic Pb(Zr, Ti)O_3/$CoFe_2O_4$ nanocomposites. *ACS Nano* 4, 1099–1107. doi: 10.1021/nn9012934

Goodilin, E., Kambara, M., Umeda, T., and Shiohara, Y. (1997). Solubility of neodymium in copper-rich oxide melts in air and growth of $Nd_{1-x}Ba_{2-x}Cu_3O_z$ solid solution single crystals. *Phys. C* 289, 37–50. doi: 10.1016/S0921-4534(97)01596-7

Goodilin, E., Oka, A., Wen, J. G., Shiohara, Y., Kambara, M., and Umeda, T. (1998). Twins and related morphology of as-grown neodymium-rich $Nd_{1+x}Ba_{2-x}Cu_3Oz$ crystals. *Phys. C* 299, 279–300. doi: 10.1016/S0921-4534(97)01808-X

Goodilin, E. A., Reddy, E. A., Noudem, J. G., Tarka, M., and Schmitz, G. J. (2002). Texture formation in melt-solidified yba2cu3oz thick films by artificial surface reliefs. *J. Cryst. Growth* 241, 512–534. doi: 10.1016/S0022-0248(02)01320-9

Grätzel, M. (2014). The light and shade of perovskite solar cells. *Nat. Mater.* 13, 838–842. doi: 10.1038/nmat4065

Hao, M., Bai, Y., Zeiske, S., Ren, L., Liu, J., Yuan, Y., et al. (2020). Ligand-assisted cation–exchange engineering for high–efficiency colloidal $Cs_{1-x}FA_xPbI_3$ quantum dot solar cells with reduced phase segregation. *Nat. Energy* 5, 79–88. doi: 10.1038/s41560-019-0535-7

Haugan, T., Barnes, P. N., Wheeler, R., Meisenkothen, F., and Sumption, M. (2004). Addition of nanoparticle dispersions to enhance flux pinning of the $YBa_2Cu_3O_{7-x}$ superconductor. *Nature* 430, 867–870. doi: 10.1038/nature02792

Hwang, J., Feng, Z., Charles, N., Wang, X. R., Lee, D., Stoerzinger, K. A., et al. (2019). Tuning perovskite oxides by strain: electronic structure, properties, and functions in (electro)catalysis and ferroelectricit. *Mater. Today* 31, 100–118. doi: 10.1016/j.mattod.2019.03.014

Hwang, J., Rao, R. R., Giordano, L., Katayama, Y., Yu, Y., and Shao-Horn, Y. (2017). Perovskites in catalysis and electrocatalysis. *Science* 358, 751–756. doi: 10.1126/science.aam7092

Jiang, J., Li, Y. Y., Liu, J. P., Huang, X. T., Yuan, C. Z., and Lou, X. W. (2012). Recent advances in metal oxide-based electrode architecture design for electrochemical energy storage. *Adv. Mat*. 24, 5166–5180. doi: 10.1002/adma.201202146

Kojima, A., Teshima, K., Shirai, Y., and Miyasaka, T. (2009). Organometal halide perovskites as visible-light sensitizers for photovoltaic cells. *J. Am. Chem. Soc.* 131, 6050–6051. doi: 10.1021/ja809598r

Lee, S., Petrykin, V., Molodyk, A., Samoilenkov, S., Kaul, A., Vavilov, A., et al. (2014). Development and production of second generation high T_c superconducting tapes at superOx and first tests of model cables. *Supercond. Sci. Technol.* 27:044022. doi: 10.1088/0953-2048/27/4/044022

Leijtens, T., Bush, K. A., Prasanna, R., and McGehee, M. D. (2018). Opportunities and challenges for tandem solar cells using metal halide perovskite semiconductors. *Nat. Energy* 3, 828–838. doi: 10.1038/s41560-018-0190-4

Li, L.-L., and Diau, E. W.-G. (2013). Porphyrin-sensitized solar cells. *Chem. Soc. Rev*. 42, 291–304. doi: 10.1039/C2CS35257E

Li, W., Wang, Z., Deschler, F., Gao, S., Friend, R. H., and Cheetham, A. K. (2017). Chemically diverse and multifunctional hybrid organic–inorganic perovskites. *Nat. Rev. Mater.* 2:16099. doi: 10.1038/natrevmats.2016.99

Li, Z., Klein, T. R., Kim, D. H., Yang, M., Berry, J. J., van Hest, M. F. A. M., et al. (2018). Scalable fabrication of perovskite solar cells. *Nat. Rev. Mater*. 3:18017. doi: 10.1038/natrevmats.2018.17

Martynov, A. G., Safonova, E. A., Tsivadze, A. Y., and Gorbunova, Y. G. (2019). Functional molecular switches involving tetrapyrrolic macrocycles. *Coord. Chem. Rev*. 387, 325–347. doi: 10.1016/j.ccr.2019.02.004

Mathew, S., Yella, A., Gao, P., Humphry-Baker, R., Curchod, B. F. E., Ashari-Astani, N., et al. (2014). Dye-sensitized solar cells with 13% efficiency achieved through the molecular engineering of porphyrin sensitizers. *Nat. Chem.* 6, 242–247. doi: 10.1038/nchem.1861

Meggiolaro, D., Motti, S. G., Mosconi, E., Barker, A. J., Ball, J., Andrea Riccardo Perini, C., et al. (2018). Iodine chemistry determines the defect tolerance of lead-halide perovskites. *Energy Environ. Sci.* 11, 702–713. doi: 10.1039/C8EE00124C

Murali, B., Kolli, H. K., Yin, J., Ketavath, R., Bakr, O. M., and Mohammed, O. F. (2020). Single crystals: the next big wave of perovskite optoelectronics. *ACS Mater. Lett*. 2, 184–214. doi: 10.1021/acsmaterialslett.9b00290

Nayak, P. K., Mahesh, S., Snaith, H. J., and Cahen, D. (2019). Photovoltaic solar cell technologies: analysing the state of the art. *Nat. Rev. Mater.* 4, 269–285. doi: 10.1038/s41578-019-0097-0

Osterloh, F. E. (2013). Inorganic nanostructures for photoelectrochemical and photocatalytic water splitting. *Chem. Soc. Rev.* 42, 2294–2320. doi: 10.1039/C2CS35266D

Ovcharov, A. V., Degtyarenko, P. N., Chepikov, V. N., Vasiliev, A. L., Gavrilkin, S. Y., Karateev, I. A., et al. (2019). Microstructure and superconducting properties of high-rate PLD–derived $GdBa_2Cu_3O_{7-\delta}$ coated conductors with $BaSnO_3$ and $BaZrO_3$ pinning centers. *Sci. Rep*. 9:15235. doi: 10.1038/s41598-019-51348-w

Park, N., Grätzel, M., Miyasaka, T., Zhu, K., and Emery, K. (2016). Towards stable and commercially available perovskite solar cells. *Nat. Energy* 1:16152. doi: 10.1038/nenergy.2016.152

Park, N.-G. (2016). Methodologies for high efficiency perovskite solar cells. *Nano Converg*. 3:15. doi: 10.1186/s40580-016-0074-x

Pearson, R. G. (1963). Hard and soft acids and bases. *J. Am. Chem. Soc*. 85, 3533–3539. doi: 10.1021/ja00905a001

Petrov, A. A., Belich, N. A., Grishko, A. Y., Stepanov, N. M., Dorofeev, S. G., Maksimov, E. G., et al. (2017a). A new formation strategy of hybrid perovskites via room temperature reactive polyiodide melts. *Mater. Horiz*. 4, 625–632. doi: 10.1039/C7MH00201G

Petrov, A. A., Fateev, S. A., Zubavichus, Y. V., Dorovatovskii, P. V., Victor, N., Zvereva, I. A., et al. (2019). Methylammonium polyiodides: remarkable phase diversity of the simplest and low-melting alkylammonium polyiodide system. *J. Phys. Chem. Lett*. 10, 5776–5780. doi: 10.1021/acs.jpclett.9b02360

Petrov, A. A., Pellet, N., Seo, J.-Y., Belich, N. A., Kovalev, D. Y., Shevelkov, A. V., et al. (2017b). New insight into the formation of hybrid perovskite nanowires via structure directing adducts. *Chem. Mater*. 29, 587–594. doi: 10.1021/acs.chemmater.6b03965

Petrov, A. A., Sokolova, I. P., Belich, N. A., Peters, G. S., Dorovatovskii, P. V., Zubavichus, Y. V., et al. (2017c). Crystal structure of DMF-intermediate phases uncovers the link between $CH_3NH_3PbI_3$ morphology and precursor stoichiometry. *J. Phys. Chem. C* 121, 20739–20743. doi: 10.1021/acs.jpcc.7b08468

Petrykin, V. V., Goodilin, E. A., Hester, J., Trofimenko, E. A., Kakihana, M., Oleynikov, N. N., et al. (2000). Structural disorder and superconductivity suppression in $NdBa_2Cu_3O_z$ (z similar to 7). *Phys. C* 340, 16–32. doi: 10.1016/S0921-4534(00)00368-3

Pomerantseva, E. A., Itkis, D. M., Goodilin, E. A., Noudem, J. G., Lobanov, M. V., Greenblatt, M., et al. (2004). Homogeneity field and magnetoresistance of the Ca(Mn, $Cu)_7O_{12}$ solid solution prepared in oxygen. *J. Mater. Chem*. 14, 1150–1156. doi: 10.1039/b313570e

Shiohara, Y., and Goodilin, E. A. (2000). "Single crystal growth for science and technology," in *Handbook on the Physics and Chemistry of Rare-Earths (Special Volumes on High Temperature Rare Earth Superconducrors), Vol. 30*, eds K. A. Gschneidner, Jr., L. Etring, and M. B. Maple (Amsterdam: Elsevier Science Publishers), 154. doi: 10.1016/S0168-1273(00)30006-X

Shlenskaya, N. N., Belich, N. A., Gratzel, M., Goodilin, E. A., and Tarasov, A. B. (2018). Light-induced reactivity of gold and hybrid perovskite as a new possible degradation mechanism in perovskite solar cells. *J. Mater. Chem. A* 6, 1780–1786. doi: 10.1039/C7TA10217H

Smith, M. D., Crace, E. J., Jaffe, A., and Karunadasa, H. I. (2018). The diversity of layered halide perovskites. *Annu. Rev. Mater. Res*. 48, 111–136. doi: 10.1146/annurev-matsci-070317-124406

Snaith, H. J., and Hacke, P. (2018). Enabling reliability assessments of pre-commercial perovskite photovoltaics with lessons learned from industrial standards. *Nat. Energy* 3, 459–465. doi: 10.1038/s41560-018-0174-4

Song, J., Li, J., Li, X., Xu, L., Dong, Y., and Zeng, H. (2015). Quantum dot light-emitting diodes based on inorganic perovskite cesium lead halides ($CsPbX_3$). *Adv. Mater*. 27, 7162–7167. doi: 10.1002/adma.201502567

Travis, W., Glover, E. N. K., Bronstein, H., Scanlon, D. O., and Palgrave, R. G. (2016). On the application of the tolerance factor to inorganic and hybrid halide perovskites: a revised system. *Chem. Sci*. 7, 4548–4556. doi: 10.1039/C5SC04845A

Tretyakov, Y. D., and Goodilin, E. A. (2000). Chemical principles of the metall-oxide superconductors preparation. *Russian Chem. Rev*. 69, 3–40. doi: 10.1070/RC2000v069n01ABEH000526

Tretyakov, Y. D., Goodilin, E. A., Peryshkov, D. V., and Itkis, D. M. (2004). Structural and microstructural features of functional materials based on cuprates and manganites. *Russian Chem. Rev*. 73, 954–973. doi: 10.1070/RC2004v073n09ABEH000920

Turkevych, I., Kazaoui, S., Belich, N. A., Grishko, A. Y., Fateev, S. A., Petrov, A. A., et al. (2019). Strategic advantages of reactive polyiodide melts for scalable perovskite photovoltaics. *Nat. Nanotechnol*. 14, 57–63. doi: 10.1038/s41565-018-0304-y

Van Santen, J. H., and Jonker, G. H. (1950). Electrical conductivity of ferromagnetic compounds of manganese with perovskite structure. *Physica* 16, 599–600. doi: 10.1016/0031-8914(50)90104-2

Volger, J. (1954). Further experimental investigations on some ferromagnetic oxidic compounds of manganese with perovskite structure. *Physica* 20, 49–66. doi: 10.1016/S0031-8914(54)80015-2

von Helmolt, R., Wecker, J., Holzapfel, B., Schultz, L., and Samwer, K. (1993). Giant negative magnetoresistance in perovskitelike La2/3Ba1/3MnOx ferromagnetic films. *Phys. Rev. Lett*. 71, 2331–2333. doi: 10.1103/PhysRevLett.71.2331

Wang, L., Xu, K., Cui, W., Lv, D., Wang, L., Ren, L., et al. (2019). Monolayer epitaxial heterostructures for selective visible-light-driven photocatalytic NO oxidatiion. *Adv. Funct. Mater*. 29:1808084. doi: 10.1002/adfm.201808084

Wei, H., and Huang, J. (2019). Halide lead perovskites for ionizing radiation detection. *Nat. Commun*. 10:1066. doi: 10.1038/s41467-019-08981-w

Weidman, M. C., Seitz, M., Stranks, S. D., and Tisdale, W. A. (2016). Highly tunable colloidal perovskite nanoplatelets through variable cation, metal, and halide composition. *ACS Nano* 10, 7830–7839. doi: 10.1021/acsnano.6b03496

Yang, W., Shi, Q., Miao, T., Li, Q., Cai, P., Liu, H., et al. (2019). Achieving large and nonvolatile tunable magnetoresistance in organic spin valves using electronic phase separated manganites. *Nat. Commun*. 10:3877. doi: 10.1038/s41467-019-11827-0

Yi, C., Luo, J., Meloni, S., Boziki, A., Ashari-Astani, N., Grätzel, C., et al. (2016). Entropic stabilization of mixed A-cation ABX 3 metal halide perovskites for high performance perovskite solar cells. *Energy Environ. Sci*. 9, 656–662. doi: 10.1039/C5EE03255E

Zhang, W., Eperon, G. E., and Snaith, H. J. (2016). Metal halide perovskites for energy applications. *Nat. Energy* 1:16048. doi: 10.1038/nenergy.2016.48

Zhang, W., Goodilin, E. A., and Hellstrom, E. E. (1996). Composition studies for Ag-sheathed $Bi_2Sr_2CaCu_2O_8$ conductors processed in 100% O_2. *Supercond. Sci. Technol*. 9, 211–217. doi: 10.1088/0953-2048/9/3/014

Zhumekenov, A. A., Saidaminov, M. I., and Bakr, O. M. (2018). "Perovskite single crystals: synthesis, properties and devices," in *World Scientific Handbook of Organic Optoelectronic Devices*, eds J. Huang and Y. Yuan (Singapore: World Scientific Publishing Co Pte Ltd.), 241–283. doi: 10.1142/9789813239494_0008

Conflict of Interest: The authors declare that the research was conducted in the absence of any commercial or financial relationships that could be construed as a potential conflict of interest.

frontiers in Chemistry

REVIEW
published: 06 January 2021
doi: 10.3389/fchem.2020.00813

Understanding Periodic and Non-periodic Chemistry in Periodic Tables

Changsu Cao[1]*, **René E. Vernon**[2]*, **W. H. Eugen Schwarz**[1,3]* and **Jun Li**[1,4]*

[1] Department of Chemistry, Tsinghua University, Beijing, China, [2] Charles Sturt University, Wagga Wagga, NSW, Australia, [3] Department of Chemistry, University of Siegen, Siegen, Germany, [4] Department of Chemistry, Southern University of Science and Technology, Shenzhen, China

Edited by:
Salah S. Massoud,
University of Louisiana at Lafayette,
United States

Reviewed by:
Marta Elena Gonzalez Mosquera,
University of Alcalá, Spain
Edwin Charles Constable,
University of Basel, Switzerland

***Correspondence:**
Changsu Cao
changsuc@126.com
orcid.org/0000-0002-2437-6825
René E. Vernon
rene@webone.com.au
orcid.org/0000-0003-0108-6646
W. H. Eugen Schwarz
eugen.schwarz@uni-siegen.de
orcid.org/0000-0001-8730-1508
Jun Li
junli@tsinghua.edu.cn
orcid.org/0000-0002-8456-3980

Specialty section:
This article was submitted to
Inorganic Chemistry,
a section of the journal
Frontiers in Chemistry

Received: 05 April 2020
Accepted: 03 August 2020
Published: 06 January 2021

Citation:
Cao C, Vernon RE, Schwarz WHE and
Li J (2021) Understanding Periodic
and Non-periodic Chemistry in
Periodic Tables. Front. Chem. 8:813.
doi: 10.3389/fchem.2020.00813

The chemical elements are the "conserved principles" or "kernels" of chemistry that are retained when substances are altered. Comprehensive overviews of the chemistry of the elements and their compounds are needed in chemical science. To this end, a graphical display of the chemical properties of the elements, in the form of a Periodic Table, is the helpful tool. Such tables have been designed with the aim of either classifying real chemical substances or emphasizing formal and aesthetic concepts. Simplified, artistic, or economic tables are relevant to educational and cultural fields, while practicing chemists profit more from "chemical tables of chemical elements." Such tables should incorporate four aspects: **(i)** typical valence *electron configurations of bonded atoms* in chemical compounds (instead of the common but chemically atypical ground states of free atoms in physical vacuum); **(ii)** at least three basic chemical properties (*valence number, size, and energy* of the valence shells), their joint variation across the elements showing principal and secondary periodicity; **(iii)** elements in which the $(sp)^8$, $(d)^{10}$, and $(f)^{14}$ *valence shells become closed and inert under ambient chemical conditions*, thereby determining the "fix-points" of chemical periodicity; **(iv)** *peculiar elements at the top and at the bottom* of the Periodic Table. While it is essential that Periodic Tables display important trends in element chemistry we need to keep our eyes open for unexpected chemical behavior in ambient, near ambient, or unusual conditions. The combination of experimental data and theoretical insight supports a more nuanced understanding of complex periodic trends and non-periodic phenomena.

Keywords: chemical elements, chemical properties, electron configurations, orbital energies, orbital radii, periodic tables, relativistic effects, superheavy elements

INTRODUCTION

Two to one-and-half centuries ago, authors of chemistry books and chemistry teachers such as Leopold Gmelin (Gmelin, 1843), Lothar Meyer (Meyer, 1864), Dmitri Mendeleev (Mendeleev, 1869b) and Viktor von Richter (Von Richter, 1875) felt the need for an ordered arrangement of the increasing number of elements. They addressed this need with the help of two-dimensional tables for groups of elements. Within half a century, with more or less delay depending on the author, Periodic Tables of elements entered most chemistry books and lecture rooms (Kaji et al., 2015; Robinson, 2019).

Then, during the past hundred years, students learned general and inorganic chemistry, and later practiced these through Periodic-Table colored glasses, rationalized by atomic structure theory. Thus, modern chemistry developed not only along the lines of easily available and practically useful chemicals, but also with effectively blinkered expectations according to the Periodic Table (Keserü et al., 2014; Pye et al., 2017; Llanos et al., 2019; Restrepo, 2019a,b). Under such circumstances, misunderstandings of the Periodic Table happen easily, and unexpected chemistry is overlooked. Some compounds or chemical preparation methods were thought to be non-existent or impossible. Therefore, we analyze the following points: the general principles of empirical periodicity; their objective physical background; deviations from expected periodicity; misrepresentations or misinterpretations of periodicity; and unexpected trends in chemistry. These points are illustrated with examples. Before the (sub)sections we present the inferences according to our own viewpoints, as *take-home messages in italicized text*. The general conclusions are presented in the last, summarizing section.

THE EMERGENCE OF NATURALLY 2-DIMENSIONAL TABLES OF CHEMICAL ELEMENTS

Chemical elements are the basic, abstract entities conserved in chemical transformations of real substances. The many allotropic 'elementary substances' (carbon as diamond, graphite, graphenes, nanotubes, fullerenes, etc., for example) are composed of a single 'abstract element' only. The IUPAC suggests using the word 'element' as a homonym for both. Common Periodic Tables are mnemonics for the trends of the meta-properties of the chemical elements under common conditions, useful in practical chemistry and in chemical education. The chemical ordinal number Z of an element in the Periodic Table is equal to the physical cardinal number of Z electrons in the neutral atom around its nucleus of the same charge number Z.

History

Chemistry is the art, craft, and science of modifying matter, hopefully improving materials for the benefits of humanity. Most chemical materials are used *under ambient conditions*, which is the most important aspect of chemistry for us humans. Different chemical behaviors under astrochemical or geochemical conditions may be relevant in other contexts (Esteban et al., 2004; McSween and Huss, 2010; Misra, 2012; Dong et al., 2015; Yamamoto, 2017; White, 2018; Rahm et al., 2019) and may suggest differently designed Periodic Tables.

Various notions of 'origins,' 'principles,' or 'elements' of the material world have been developed since antiquity. By the term 'chemical element' we are referring to an immutable something (a conservation principle in the physical sense) that is preserved in chemical transmutations from one chemical material to another. Our present understanding has arisen since the late eighteenth century. Even now there are still open questions (Ghibaudi et al., 2013; Scerri and Ghibaudi, 2020). The concept of an element has three basic aspects. Until the advent of the Renaissance and Enlightenment in sixteenth century Europe, elements were regarded in all developed cultures as carriers of directly observable qualities. This concept has survived only with a secondary bearing. For example, atomic weight and atomic volume were instrumental in the early development of Periodic Tables by Mendeleev and Meyer. And the density of an element, given by atomic weight divided by atomic volume, influences the observable densities of the compounds of that element.

However, the rational and enlightened Greek philosophy of the period two to one-half millennia ago was unique in human conceptual development. Sage thinkers suggested, for example, two atomistic concepts of the elements. Demokritos, Epikouros, and Titus Lucretius Carus wrote of conserved particles, forming compounds that induce the observations in our senses. Lucretius discussed many examples of natural experiences from daily life, craftsmen and doctors, and similar ideas still form the basis of present chemical atomism. Platon developed the first speculative "mathematical sub-atomic theory" that was known to the inventors of quantum mechanics and in this sense survives in modern subatomic physics (Heisenberg, 1959; Von Weizsäcker, 1971, 1985; Stückelberger, 1979; Grimes, 1983; Metzger, 1983).

Anyway, the concept of *one abstract conserved chemical element* should always and explicitly be distinguished from the *many* allotropes and phases of *real transformable elementary substances*, consisting of a single abstract element only (Van Spronsen, 1969; Scerri, 2007, 2020; Cao et al., 2019). For example, we distinguish between carbon as the abstract element found in carbon dioxide (CO_2) and such allotropic forms of phases of pure carbon as diamond, graphite, the many different graphenes, nanotubes and fullerenes, and amorphous soot. At present more than a hundred (i.e., 118) elements, are known, without a gap.

The modern concept of conserved elements in chemical reactions was put into reality in the 'chemical revolution' by a network of scientists in Paris around the couple of Antoine-Laurent de Lavoisier and Marie-Anne Pierrette Paulze, a decade ahead of the cultural and political revolution in France (Ihde, 1964; Brock, 1992; Scerri, 2007, 2020). When the first half-hundred elements had been discovered around 1820, the need for *a systematic ordering and a classification* (Leal and Restrepo, 2019) became pressing. An early two-dimensional arrangement of elements was propagated in Leopold Gmelin's Handbooks (e.g., Gmelin, 1843), based purely on qualitative chemical experiences.

At the very first international scientific congress at Karlsruhe in 1860, Cannizzaro promoted older physico-chemical concepts, which permitted the change-over *from qualitative to quantitative criteria*. First, the elements could be linearly ordered according to the unique semi-empirical atomic weight numbers, instead of the partial ordering with the help of purely empirical equivalent weights, or of compounds' densities. Second, the elements could be classified into similarity groups, on the basis of oxidation and valence numbers (Meyer, 1864) or unique sum formulas (Mendeleev, 1869a), and atomic volume values (Meyer, 1870), in addition to general qualitative chemical experience (Scerri, 2007, 2020; Gade, 2019).

On the basis of the Geiger-Marsden-Rutherford experiments of atomic scattering of α- and β-particles in the years of 1908 to 1913, Rutherford concluded (first in 1911) that atoms consist of a tiny massive center of *positive charge of ca. half its mass* *number*, and a surrounding cloud of a respective number of negative electrons. Van den Broek, a scientifically interested amateur immediately suggested the nuclear charge and electron number should be a bit smaller and equal to the element number in the Periodic Table. Thereby he attached a well-defined physical meaning to this so-far, somewhat arbitrary, chemical number. This development inspired Moseley in his experimental X-ray spectroscopic work on the elements. He could prove that the chemically motivated order of elements cobalt < nickel has a physical basis, while the average atomic weights *(A)* of the elements from the earth's crust (which have a somewhat accidental origin in cosmic and geochemical history) increase in the opposite order, nickel *(A* = 58.7) to cobalt *(A* = 58.9). Later, also the order of argon *(A* = 39.95) < potassium *(A* = 39.1) and of tellurium *(A* = 127.6) < iodine *(A* = 126.9) was verified (Da Costa Andrade, 1958; Scerri, 2007, 2020).

While Moseley's work was at first purely empirical, Bohr's invention of his atomic model in 1913 allowed Moseley to verify van den Broek's hypothesis. The elements became ordered according to the *physically based chemical element number Z*, which is the nuclear charge and electron number of the elemental atoms. Both enter the equations of time-independent quantum-mechanics, thereby physically determining 'static' chemistry, say at the lowest order Born-Oppenheimer approximation. Further, *Z* correlates approximately with the atomic weight *A* as ensued during cosmic history. *A* enters the time-dependent equations, thereby determining 'kinetic' chemistry and rotational and vibrational spectroscopies. The change from the "chemically corrected empirical *A*" to the "basic, theoretical *Z*" was a conceptual change in two senses. (i) The fuzzy combination of atomic weight, maximum oxidation state and chemical similarities to linearly order the elements in the most probable manner was replaced by the unique, integer, direct experimentally-based element number *Z* with a physical (nuclear charge number) and a chemical meaning (electron number). (ii) The question for missing entries, which had caused so much uncertainness, could be answered once for all.

Structure of Periodic Tables

The chemical periodicity of the elements is triggered by the closure of atomic valence shells with a supervening orbital energy gap that is comparatively large compared to primary bonding energies and thermodynamic conditions in ambient conditions of pressure p and temperature T. A significant fraction of the variation of chemical behavior of the abstract elements at common conditions can be simulated by just two 'main factors,' consistent with the two-dimensional topology of common rectangular Periodic Tables, with the noble gases at the borders. A large part of the periodic structure will fade away at higher than common p and T, while at low T and p the diversity of chemistry increases as various new molecules can survive and, while there are fewer thermally induced reactions, a novel chemistry can be enabled by designed binding. The Periodic Rule is specific for the selected field of chemistry such as at ambient human (or planetary core, or cosmic space) conditions.

One of the various types of Periodic Table designs is the 'short form,' an example being displayed in **Figure 1**. In 1870, the elements with a yellow foreground were known. The *chemical periodicity* is mainly connected to the large change of chemical character from the halogens (fluorine to iodine) in group VII (or 17) through the noble gases in group VIII (or 18/0) to the

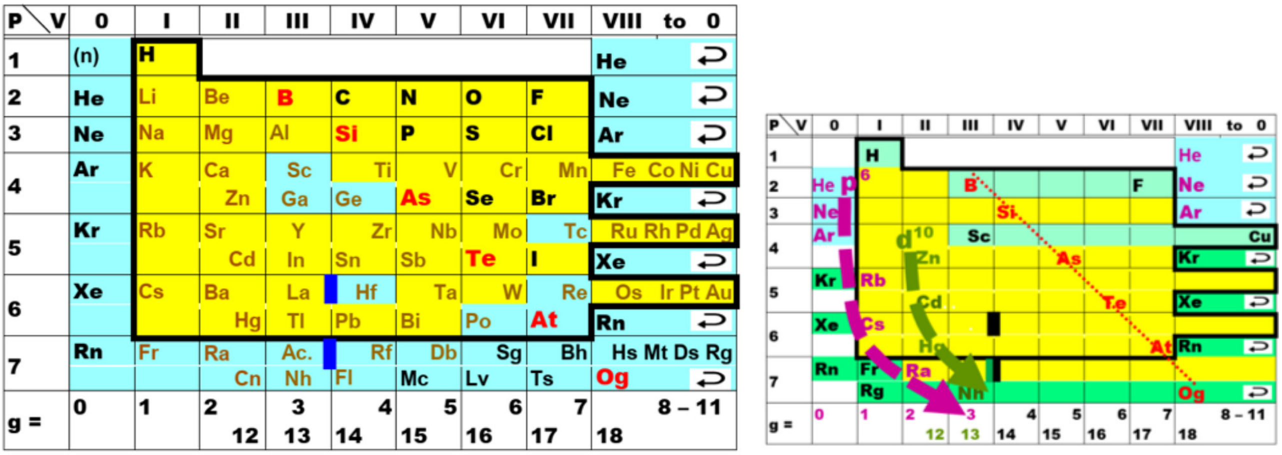

P \ V	0	I	II	III	IV	V	VI	VII	VIII to 0
1	(n)	H							He ↩
2	He	Li	Be	B	C	N	O	F	Ne ↩
3	Ne	Na	Mg	Al	Si	P	S	Cl	Ar ↩
4	Ar	K	Ca	Sc	Ti	V	Cr	Mn	Fe Co Ni Cu
			Zn	Ga	Ge	As	Se	Br	Kr ↩
5	Kr	Rb	Sr	Y	Zr	Nb	Mo	Tc	Ru Rh Pd Ag
			Cd	In	Sn	Sb	Te	I	Xe ↩
6	Xe	Cs	Ba	La	▮ Hf	Ta	W	Re	Os Ir Pt Au
			Hg	Tl	Pb	Bi	Po	At	Rn ↩
7	Rn	Fr	Ra	Ac.	▮ Rf	Db	Sg	Bh	Hs Mt Ds Rg
			Cn	Nh	Fl	Mc	Lv	Ts	Og ↩
g =	0	1	2 12	3 13	4 14	5 15	6 16	7 17	8 – 11 18

P \ V	0	I	II	III	IV	V	VI	VII	VIII to 0
1		H							He ↩
2	He			B				F	Ne ↩
3	Ne				Si				Ar ↩
4	Ar			Sc					Cu
			Zn			As			Kr ↩
5	Kr	Rb							
			Cd				Te		Xe ↩
6	Xe	Cs			▮				
			Hg					At	Rn ↩
7	Rn	Fr	Ra		▮				
		Rg		Nh					Og ↩
g =	0	1	2 12	3 13	4 14	5 15	6 16	7 17	8 – 11 18

FIGURE 1 | Periodic Table of elements in the 'short' form, as rather common during the early decades. The noble gases are here displayed twice, at the left and right borders, to underline the spiral topology of the natural system. P = number of the period, V = valence number of the group, g = modern group number. Elements known in the early 1860s are displayed within the bold frame on a yellow foreground. **(Left)** The then unknown elements are on an aqua foreground. The lanthanoids and actinoids are indicated by bold deep-blue bars (only six of the 30 were known: La, Ce, Er, Tb; Th, U). The approximate divide (bold red letters) between the more metallic (in brown) and the more non-metallic elements (in black). **(Right)** The small table highlights two points of chemical relevance. (i) Both, the well-known elements with a light green foreground toward the top of the table (H; B-F; Sc-Cu), and the more or less well-known elements with a darker green foreground toward the bottom (Kr, Xe, Rn, Og; Fr; Rg-Og) show rather 'unique' properties. (ii) The pivots of periodicity are the closures of the p^6 shells of the elements in lilac (He, Ne, Ar, Rb, Cs, Ra) and of the d^{10} shells of the elements in olive (Zn, Cd, Hg, Nh). The shell closure shifts to the right toward the bottom of the table, for p^6 from group 0 to 3, and for d^{10} from group 12 to 14, as indicated by the bold bent dashed arrows.

alkali metals (lithium to cesium) in group I (or 1). As we now know, the halogens have a compact, strongly electron-attracting (electronegative) open valence p-shell.[1] This becomes a closed core shell, fully occupied and chemically inert, for the alkali metals, which in addition have a new, diffuse, weakly electron-binding (electropositive) open valence s-shell, with *a large energy gap* between the $(n-1)$p and ns shells (Longuet-Higgins, 1957; Wang and Schwarz, 2009).

The noble gases were discovered in the 1890s (Ar was isolated in 1894, He in 1895, Ne, Kr, Xe in 1898). In principle they could be easily incorporated into the Periodic Table. Meyer's table of 1864 had columns for valences 4, 3, 2, 1 of the electronegative elements (for the C, N, O, F groups), and for valences 1, 2 of the electropositive elements (for the alkali and alkaline earth metals), but with no in-between zero valence. (Known elements B, Al, Y, La with valence 3 appeared too diverse to place them together into the equivalent of present groups 3 and 13.) Not everyone was convinced that the concept of zero-valence elements forming only elementary substances would make any sense. On the other hand, Mendeleev's tables since 1869 had eight transition groups, but only seven main groups (**Figure 1**), despite the gaps in the series of atomic weights between the halogens and alkali metals being large enough to insert (or not) a new group of elements. Yet, it took some time, and Mendeleev for instance did not accept the incorporation of the noble gases before 1900 (Scerri, 2007, 2020).

A somewhat less pronounced periodic jump occurs when the $(n-1)$d valence shell of the transition elements (in the nine transition groups from 3 to 11, with many colorful, multivalent, magnetic compounds from group 4 onward; see e.g., Grochala, 2020) becomes a filled and chemically inert $(n-1)d^{10}$ core shell from the zinc group-12 onward.

During the times when only the yellow foreground elements in **Figure 1** were known, and during the following decades when noble-gas chemistry was unknown, and when only a little chemistry of a few elements in period 7 was known, a strong conviction emerged in the chemical community, which has survived to the present day, namely: *The periodic trends in the upper part of the periodic system are valid in general*. However, we now know that the lighter elements with small principal quantum numbers of their valence shells have well-separated orbital energy bands and well-separated electron density shells in space (Jørgensen, 1969; Levine, 1970; Kohout and Savin, 1996), and can be well and easily approximated by the non-relativistic approximation of quantum theory, with negligible spin-orbit coupling. This no longer holds for the heavier atoms. Therefore, it is unrealistic to extrapolate Periodic Tables linearly and vertically down into the region of high Z (up to several hundred or even $> 1{,}000$; see e.g., Karol, 2002; Rath, 2018). In particular, the lynchpins of periodicity cannot be presumed to move vertically down the common designs of Periodic Tables as indicated in **Figure 1**, right.

Three important aspects were well-highlighted in some of the earlier tables (**Figures 2**, **3**) but have unfortunately become less fashionable. **(i)** Periodicity means the repeated recurrence of properties along a coherent array; this can be underlined by repeating the border-line elements on the right and left borders. **(ii)** The first element H-$1s^1$ cannot be categorically assigned to any group, neither to group 1 with 1 valence electron, nor to group 17 with 1 hole in the valence shell, nor to group 14 with half-filled valence shell, nor to more exotic suggestions such as group 3.[2] Therefore, H is sometimes positioned on top of the whole table. **(iii)** Conversely, the light group-2 elements Be, Mg can be related to both the heavy group-2 (Ca etc.) or group-12 (Zn etc.) elements; and the light group-3 elements B and Al can be related to both the medium-heavy group-3 (Sc, Y) or group-13 (Ga etc.) elements, and Y can be related to the heavy group-3 (La, Ac) or group-3' (Lu, Lr) elements (see also **Figure 4**). While active chemists usually investigate the comprehensive group, there are authors who prefer to classify the border-case elements in a rigorous unique manner (Luchinskii and Trifonov, 1981; Jensen, 1982, 2003, 2015; Grochala, 2018; Petruševski and Cvetković, 2018; Chandrasekara et al., 2019; Kurushkin, 2020; Rayner-Canham, 2020; Scerri, 2020; Vernon, 2020b). Anyhow, the bifurcations in the Periodic System are a basic aspect of empirical chemical periodicity (Bayley, 1882; Carnelley, 1886; Thomsen, 1895; Bohr, 1922; Hackh, 1924; Von Antropoff, 1926; Clark, 1933, 1950; Shchukarev, 1954).

The topology of printed pages suggests a two-dimensional *display of the system of elements* in 'paper format', as initiated by Guyton de Morveau (Guyton de Morveau, 1782); Dumas (Dumas, 1828); Döbereiner (Döbereiner, 1829); and Gmelin (Gmelin, 1843). Since chemistry is much richer than any flatland projection, already Gmelin hoped that a three-dimensional matrix of elements would allow for a deeper insight into the structure of the chemistry of the elements. In the first documented periodic arrangement of all known elements, Béguyer de Chancourtois (Béguyer de Chancourtois, 1862/3) drew the one-dimensional array of elements, ordered by atomic weights, as a helix on the two-dimensional surface of a physical cylinder, embedded in our three-dimensional space. This display exhibited some of the similarities of the elements, and the smooth variation as well as jumps in their properties under ambient chemical conditions, both along the array and 'orthogonal' to it. Later inventors of Periodic Tables cut, so to speak, this cylindrical

---

[1] We apply the word *atomic 'shell'* for a single one-electron level such as $np^3/_2$, and also for energetically adjacent sets of levels such as np, or $(n-1)$dns, or $n$sp. Note: orbitals with non-vanishing angular momentum such as p ($\ell = 1$) or d ($\ell = 2$) are energetically split by relativistic spin-orbit coupling into two separate $\ell \pm ½$ spinor levels (see footnote 5). This phenomenon becomes qualitatively significant for the chemistry of the lower part of the periodic table. In particular, np is split into two separate levels np½ and $np^3/_2$.

[2] The anomalous properties of hydrogen are due to its unique valence shell consisting of a single symmetric orbital, and to its unique core of a naked nucleus without inner screening electrons. The naked proton easily attaches itself to the nearest electron pair. Unlike the alkali metal (A) compounds, which can often be described as containing A^+ units, hydrogen always tends to complete its $1s^2$ valence shell, with H^+ rarely appearing in realistic descriptions. Hydrogen exhibits similarities with lithium in particular, because of the small $1s^2$ core of the 2nd period elements. Both hydrogen and lithium exhibit a significant *covalent* chemistry with slightly electronegative partners, while for compounds with strongly electronegative elements, the model of *ionic* interactions works well. Hydrogen atoms can stand in for alkali metal atoms in many alkali metal compounds. Hydrogen is also capable of forming alloy-like hydrides, featuring *metallic* bonding, with several transition metals.

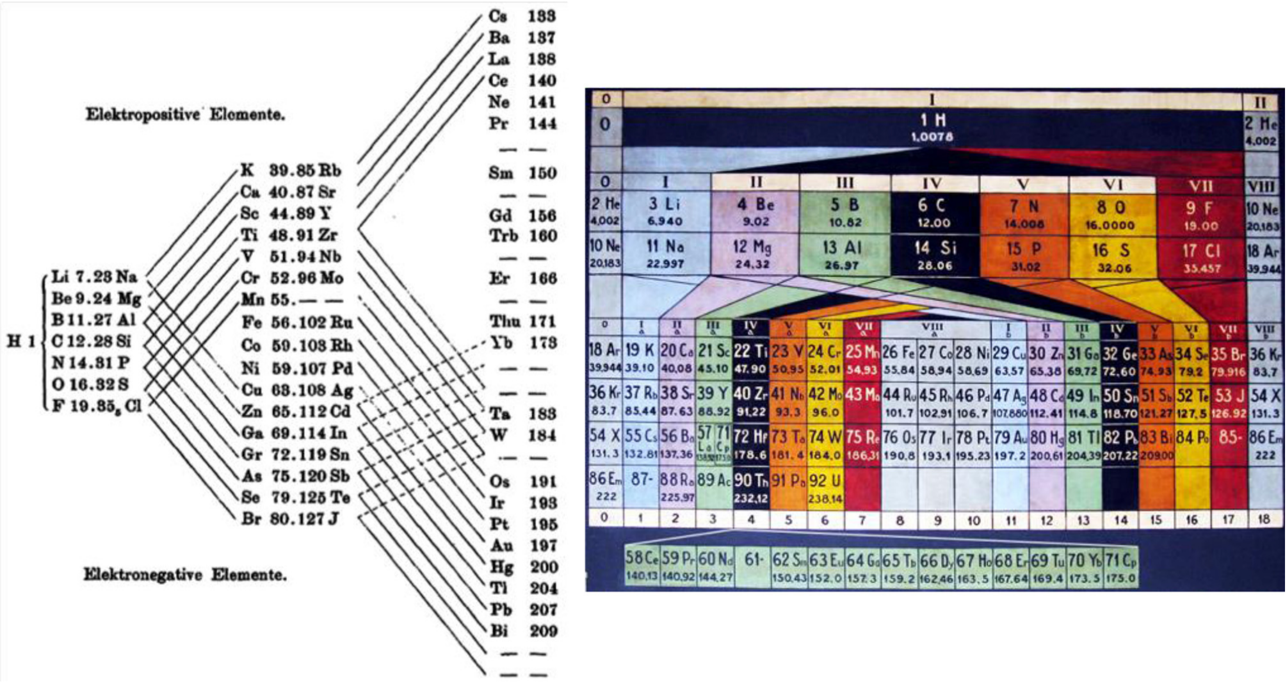

FIGURE 2 | Early bifurcating Periodic Tables explicitly showing (i) the smooth trends of properties along the array of elements (from the alkali metals through the intermediate elements to the halogens), (ii) the jumps (from the halogens to the next alkali metals), and (iii) the bifurcating similarities of elements of the main and transition groups. H is positioned at the central starting point, chemical sensibly without group assignment. **(Left)** An early, bifurcating triangular table, yet without the noble gases (source: Thomsen, 1895, p. 192). **(Right)** Design of Von Antropoff (Von Antropoff, 1926), as presented in the renovated lecture hall of the University of Barcelona (source: private photo by Claudi Mans: Mans i Teixidó, 2008).

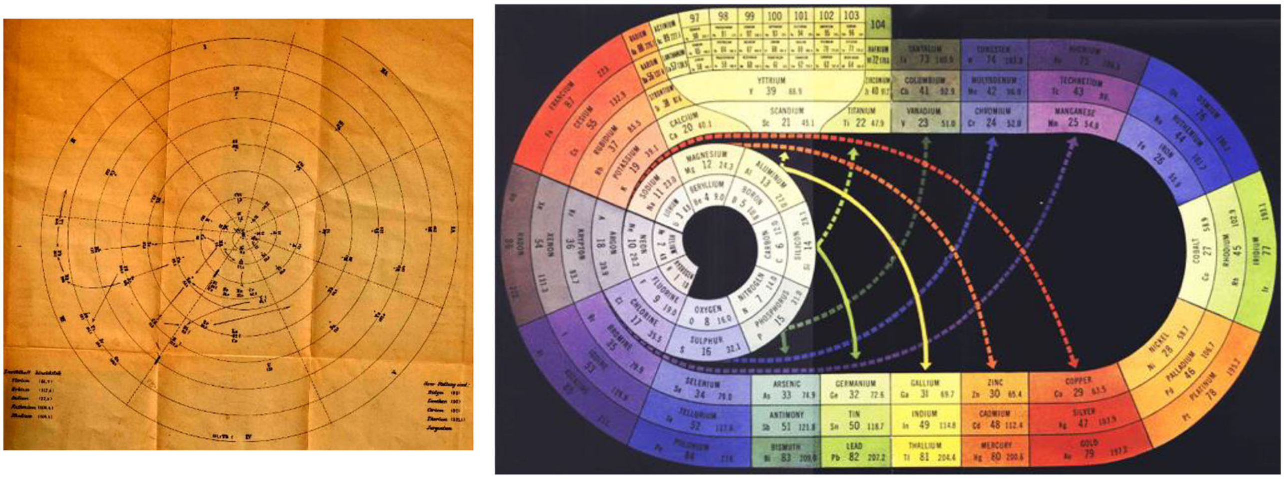

FIGURE 3 | Early spiral tables stressing both the continuity of the array of elements and the bifurcation of the chemical similarity classes, as an alternative to **Figure 2**. **(Left)** Following Béguyer de Chancourtois (1862/3), the spiral of Baumhauer (source: Baumhauer, 1870, leaflet at the end). **(Right)** The spiral (with bifurcations) of Clark (1933, 1949, 1950) with the noble gases at the middle left (in gray) and the f-block in the boron-aluminum–scandium-yttrium group at the top left (in yellow, each f-series after La and Ac is split up into two septets: 4f in Ce$^{(IV,III)}$-Gd^{III}, Tb$^{(IV,III)}$-Lu^{III} and 5f in Th^{IV}-Cm$^{(IV,III)}$, Bk$^{(IV,III)}$-Lr^{III}), source: Clark (1949).

bent surface at different points, in order to obtain flat printable tables. A cut between the halogens and the alkali-metals, where the largest change of chemical behavior occurs, became the most favored one, at least among practicing chemists. When the noble gases were discovered, they were placed between the halogens and the alkali metals, either to the right of the halogens, or the left of the alkali metals, or both. According to each author's preferences, different rectangular (**Figures 1**, **2**, **4**, **6**) or spiral

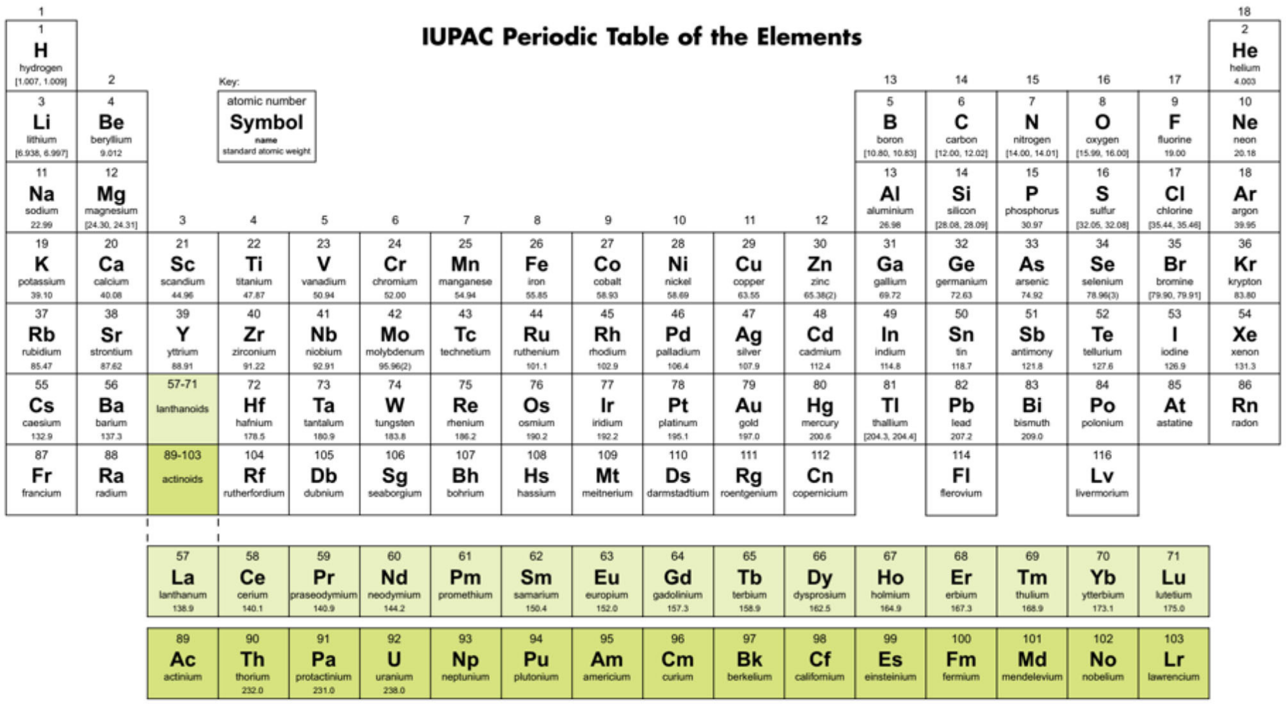

IUPAC Periodic Table of the Elements

Key:
atomic number
Symbol
name
standard atomic weight

1	2	3	4	5	6	7	8	9	10	11	12	13	14	15	16	17	18
1 H hydrogen [1.007, 1.009]																	2 He helium 4.003
3 Li lithium [6.938, 6.997]	4 Be beryllium 9.012											5 B boron [10.80, 10.83]	6 C carbon [12.00, 12.02]	7 N nitrogen [14.00, 14.01]	8 O oxygen [15.99, 16.00]	9 F fluorine 19.00	10 Ne neon 20.18
11 Na sodium 22.99	12 Mg magnesium [24.30, 24.31]											13 Al aluminium 26.98	14 Si silicon [28.08, 28.09]	15 P phosphorus 30.97	16 S sulfur [32.05, 32.08]	17 Cl chlorine [35.44, 35.46]	18 Ar argon 39.95
19 K potassium 39.10	20 Ca calcium 40.08	21 Sc scandium 44.96	22 Ti titanium 47.87	23 V vanadium 50.94	24 Cr chromium 52.00	25 Mn manganese 54.94	26 Fe iron 55.85	27 Co cobalt 58.93	28 Ni nickel 58.69	29 Cu copper 63.55	30 Zn zinc 65.38(2)	31 Ga gallium 69.72	32 Ge germanium 72.63	33 As arsenic 74.92	34 Se selenium 78.96(3)	35 Br bromine [79.90, 79.91]	36 Kr krypton 83.80
37 Rb rubidium 85.47	38 Sr strontium 87.62	39 Y yttrium 88.91	40 Zr zirconium 91.22	41 Nb niobium 92.91	42 Mo molybdenum 95.96(2)	43 Tc technetium	44 Ru ruthenium 101.1	45 Rh rhodium 102.9	46 Pd palladium 106.4	47 Ag silver 107.9	48 Cd cadmium 112.4	49 In indium 114.8	50 Sn tin 118.7	51 Sb antimony 121.8	52 Te tellurium 127.6	53 I iodine 126.9	54 Xe xenon 131.3
55 Cs caesium 132.9	56 Ba barium 137.3	57-71 lanthanoids	72 Hf hafnium 178.5	73 Ta tantalum 180.9	74 W tungsten 183.8	75 Re rhenium 186.2	76 Os osmium 190.2	77 Ir iridium 192.2	78 Pt platinum 195.1	79 Au gold 197.0	80 Hg mercury 200.6	81 Tl thallium [204.3, 204.4]	82 Pb lead 207.2	83 Bi bismuth 209.0	84 Po polonium	85 At astatine	86 Rn radon
87 Fr francium	88 Ra radium	89-103 actinoids	104 Rf rutherfordium	105 Db dubnium	106 Sg seaborgium	107 Bh bohrium	108 Hs hassium	109 Mt meitnerium	110 Ds darmstadtium	111 Rg roentgenium	112 Cn copernicium		114 Fl flerovium		116 Lv livermorium		

57 La lanthanum 138.9	58 Ce cerium 140.1	59 Pr praseodymium 140.9	60 Nd neodymium 144.2	61 Pm promethium	62 Sm samarium 150.4	63 Eu europium 152.0	64 Gd gadolinium 157.3	65 Tb terbium 158.9	66 Dy dysprosium 162.5	67 Ho holmium 164.9	68 Er erbium 167.3	69 Tm thulium 168.9	70 Yb ytterbium 173.1	71 Lu lutetium 175.0
89 Ac actinium	90 Th thorium 232.0	91 Pa protactinium 231.0	92 U uranium 238.0	93 Np neptunium	94 Pu plutonium	95 Am americium	96 Cm curium	97 Bk berkelium	98 Cf californium	99 Es einsteinium	100 Fm fermium	101 Md mendelevium	102 No nobelium	103 Lr lawrencium

FIGURE 4 | A Periodic Table in 'medium long' form, as suggested by the IUPAC until the end of 2015; see also the IUPAC Recommendations 2005 (Connelly et al., 2005: the Red Book III). H is positioned in group 1, He in group 18, and the f-block of 15 members still positioned so that the early members appear below their chemical relatives from the d-block (Sc, Y → La, Ac; Ti-Hf → Ce, Th; Cr-W → U; etc.). Source: IUPAC (2015).

(**Figure 3**) or more complex graphics, flat or bent or conical or multi-connected, two-parametric tables were designed (Quam and Battell Quam, 1934; Van Spronsen, 1969; Mazurs, 1974; Scerri, 2007, 2020; Stewart, 2007, 2010; Imyanitov, 2016).

Arrangements of the elements were also suggested that are genuinely three-dimensional, that is three-parametric, not simply two-parametric ones embedded in a three-dimensional space. Conceptually there are differences between bent, variously connected two-dimensional objects such as cylindrical or spherical surfaces (e.g., cyclopolyacene, Möbius-cyclopolyacene, fullerene), three-dimensional crystal lattices and structures such as those of the zeolites. Displayed on flat paper, three-dimensional arrangements appear rather complicated, and have so far hardly impressed the chemical community. There may be good reason. Namely, comprehensive analyses of a huge number of properties of the elements and their compounds revealed just two dominant "Main Factors" and a rather large number of minor factors (Sneath, 2000; Restrepo et al., 2006; Leach, 2013).[3] The two Main Factors, which are mixtures of electronegativity, valency, molar density, metallicity, acidity etc. simulate a significant part of the variation of the properties of the compounds of each element. Earlier work by Godovikov and Hariya (1987) continuing on Shchukarev's surveys (Shchukarev, 1969, 1977) had already produced a remarkable mapping of the broad contours of the periodic system of elements' properties, using just two criteria, an electric (ionization potential) and a spatial one (orbital radii, with a strong correlation, in periodic mapping terms, to electron affinity).

Thus, a *2-dimensional display of the elements appears naturally appropriate*, bearing in mind such periodicity is largely confined to the common conditions in our laboratories, industries and daily life. The general applicability of a simple and general *Periodic Rule* will progressively fade away, if applied to matter under more extreme conditions (as viewed from the anthropocentric standpoint). The so-called Periodic Law is a contingent rule that happens to hold in chemistry under 'human' conditions. Its importance in chemistry is comparable to the basic laws in physics, but its epistemological status is not comparable (Hettema and Kuipers, 1988).

Length of Periodic Tables

An important condition for the emergence of periodicity of chemical behavior under ambient conditions is a well-structured atomic orbital level scheme, in particular with gaps, above 1s and 2p to 6p. This quantum-mechanical phenomenon determines the period lengths of 2, 8, 8, 18, 18, 32. At the bottom of common Periodic Tables, four changes happen together, accidentally: (i) The high number Z of electrons occupy orbitals with high principal quantum numbers n, with small energy gaps. (ii) The value of the Coulomb coupling constant causes different screenings of the

---

[3] Sneath referred to two composite factors, which may be labeled *reactivity* (broadly related to oxidation potentials and electronegativity), and *metallicity*. Restrepo's two factors were (only) for binary compounds of the elements and their stoichiometries. Leach (also: Leach, 1999–2020) confirmed the importance of electronegativity as a basic elemental property, noting its strong correlation with numerous atomic parameters, physical, and chemical.

s, p, d, and f orbitals by the large atomic cores that smooth out the shell structure at large Z. (iii) The actual value of the fine structure constant causes additional orbital splitting of qualitative chemical relevance via spin-orbit coupling at the bottom of the table. (iv) The actual values of the coupling constants of particle physics let the nuclear lifetimes decrease at the end of the second 32-period to values below the time limit required for the existence of a chemical substance.

Where does the *chemical system of elements end?* Physicists consider atomic nuclei as representatives of elements, and they require that the particle clusters forming a nuclear complex stay together longer than the fly-by time of ca. 10^{-23} s. On the other hand, the existence of bulk chemical stuff requires longevity of the nuclei. Lifetimes τ below a year (ca. $10^{7.5}$ s) will quickly cause crystal structure defects and thermo-dynamic modification. Beneficial uses approach their end, and only a few quick experiments of molecular gas-phase or surface or tracer chemistry are possible for the elements (longest isotopic lifetimes τ in parentheses): radon $_{86}$Rn ($\tau \approx 4$ days), astatine $_{85}$At ($\tau \approx 1/3$ day), and francium $_{87}$Fr ($\tau \approx 1/3$ min); and for the late actinoids and the early transactinoids (super-heavy transition elements) up to dubnium $_{105}$Db (Eka-Ta) with lifetimes of hours.[4] But for the late super-heavy transition elements seaborgium $_{106}$Sg (Eka-W) to copernicium $_{112}$Cn (Eka-Hg) with lifetimes of minutes to seconds, and for the super-heavy p-block elements nihonium $_{113}$Nh (Eka-Tl, $\tau \approx 10$ s) to oganesson $_{118}$Og (Eka-Rn, $\tau < 1$ ms), ultra-fast reaction-kinetics and spectroscopy come to their limits. The joint IUPAC/IUPAP definition of a chemical element is a lifetime of $\tau \geq 10^{-14}$ s, which may be long enough for most nuclei to reach their own ground state and also to collect their atomic electrons (Wapstra, 1991). This sounds fine for nuclear and atomic physicists, though not for molecular and solid state physicists, not to speak of chemists. Accidentally in period 7, both the lifetime of the elements becomes too short from the chemical point of view, and the chemical periodicity of the electronic valence shells changes, so that period 7 represents the bottom end of the chemical periodic system (Ball, 2019).

EMPHASIS OF STANDARD PERIODICITY: SIMPLIFIED MODELS FOR ABUNDANT CHEMISTRY

The first groups of elements were recognized on qualitative chemical grounds, after the first few dozen of elements had been discovered. Quantitative values of valence, redox potential and atomic volumes (~radii[3]) established the scientific soundness of the empirically emerged Periodic Rule for chemistry under ambient conditions. The finally successful physical rationalization of the Periodic Rule was initiated by Bohr's (semi-)classical atomic model, just a century ago. The main periodic repetition of chemical properties occurs for the series of elements with n(s,p) valence shells. For periods 4 to 7, series of elements with (n−1)d or (n−2)f, (n−1)d valence shells appear embedded in the n(s,p) series. This yields the factual ns|(n−2)f|(n−1)d|np structure of the actual chemical periods, as an accidental by-product caused by the simple-structured physical theory, when applied to the complex field of chemistry. The series of blocks in the Periodic Table does not indicate a general order of atomic orbital energetic levels, which varies with Z and ionic charge of the atoms.

The Periodic Rule

The acceptance of the "*Periodic Rule*" (**Figures 1–4**) by the chemical community was not automatic (Gordin, 2004, 2019; Scerri, 2007, 2020). For some chemists of the time, the property-variations appeared fortuitous or partly unimpressive. However, Meyer's graphic display of periodicity of numerical atomic volumes (Meyer, 1870), and Mendeleev's correct predictions of various properties of unknown elements and their compounds by interpolation in the table (Mendeleev, 1869a; Mendelejeff, 1871: predictions on scandium, gallium, germanium—in the center of **Figure 1**—experimentally verified between 1875 and 1886) appeared convincing to the community (Scerri, 2007, 2020; Stewart, 2019). A theoretical breakthrough was achieved by Bohr and Coster (1923) with their (semi-)classical atomic model that reproduced the spectroscopic data of hydrogen and cationic helium (He^+) exactly, and paved the way for a qualitative *physical rationalization of various chemical trends* (Schwarz, 2013).

From then on, in principle, the energies *and* radii (proportional to $\sqrt[3]{\text{volumes}}$; see Biltz, 1934) of the atomic valence *and* outer-core shells could be utilized to explain chemistry. Atomic energy levels were available from decades of atomic spectroscopy (Moore, 1949 et seq.) and atomic distances from the emerging field of X-ray crystallography (Lima-de-Faria, 1990). The new quantum mechanics of Schrödinger and Dirac was applied to *chemically unbound atoms* and reviewed by Condon and Shortley (1935). Since then it was easy to acquire basic knowledge of (i) the mixing of single-electronic $n\ell j$ spinor-orbital[5] configurations in many-electronic

---

[4] For convenience, the yet less common *symbols of the super-heavy elements* are listed here. From $Z = 113$ to 118, the group numbers (in bold) of (f)d/sp elements happen to be just $g = Z{-}100$:

Group	**(3)/11**	**(3)/12**	**3/13**	**4/14**	**5/15**	**6/16**	**7/17**	**8/18**	**9/1**	**10/2**
(f)d block	$_{101}$Md	$_{102}$No	$_{103}$Lr	$_{104}$Rf	$_{105}$Db	$_{106}$Sg	$_{107}$Bh	$_{108}$Hs	$_{109}$Mt	$_{110}$Ds
sp block	$_{111}$Rg	$_{112}$Cn	$_{113}$Nh	$_{114}$Fl	$_{115}$Mc	$_{116}$Lv	$_{117}$Ts	$_{118}$Og	$_{119}$Uue	$_{120}$Ubn

[5] We apply the following *nomenclature conventions for orbitals*;

"*Space-orbital*": An *orbital* is a one-electron function in 3-dimensional space, $\phi(\boldsymbol{r})$, real or complex. Examples of p-shell ϕ are $p_{m=0} = p_z \sim z$, $p_{m=+1} = (p_x + i \cdot p_y)/\sqrt{2} \sim x + i \cdot y$. "~" means "proportional to."

"*Spin-orbital*": Means $\phi(\boldsymbol{r})\cdot\alpha$ or $\phi(\boldsymbol{r})\cdot\beta$, where α and β indicate electrons with the same α or β spin everywhere in space. "α spin-up," often symbolized by ↑, means an angular momentum vector with component +½ (in atomic units ħ) along the chosen reference axis, usually called *z*. The *x,y* component of the spin vector is $\sqrt{2}$ times larger. The angle of the spin vector with the reference axis is the 'magic angle' $\arccos\sqrt{1/3} \approx 54.7^{\circ} > 45^{\circ}$. An α spin-up points more to the side than up, ↗ or ↖! Since an angular momentum is of type $\boldsymbol{r} \times \boldsymbol{p}$, and the Heisenberg uncertainty principle holds for products of $\boldsymbol{r}$ and $\boldsymbol{p}$, $\Delta\boldsymbol{r}\Delta\boldsymbol{p} \geq \mathbf{1}\cdot\hbar/2$, orbital and spin angular momenta in 3-dimensional space have only 2 well-defined components. That is, in microscopic quantum-mechanical 3-dimensional reality, we cannot graphically describe an angular-momentum vector by a 3-component arrow, for sure not by a vertical arrow, but only, for instance, by a cone specified by the 2 parameters of height and opening angle. Then, a two-electronic spin-singlet state may be represented by anti-parallel arrows, e.g., ↗↙, while the three states of a spin-triplet may be symbolized by, for instance ↖↗, ↘↗, ↙↘. *(continued)* systems, (ii) the spin-orbit mixed orbitals in the dominant (leading) configuration, and (iii) the spin-orbit-coupling that may be neglected in non-relativistic approximate atomic *nℓ* position-orbitals (good for the lighter elements). The plethora of atomic spectral data was liberated from the data graveyard and chemically usefully interpreted (Herzberg, 1937).

s,p vs. d,f Shells

The energies (and radii) of the outer s and p valence shells of the elemental atoms form pairs, smoothly varying along the series of elements. This gives rise to the sp block of main-group elements with smoothly increasing electronegativity and decreasing atomic radii. The chemical periodicity is fixed by the large jump of elemental properties under ambient chemical conditions, when the 1s or nsp (n = 2, 3, 4, 5, 6) shell becomes filled and inert, with a new loosely bound valence shell above a large energy gap at the beginning of the new period. Due to better shielding from nuclear attraction by the sp core electrons, the (n−1)d and (n−2)f shells however vary in steps along the series of elements. They fall below the sp valence band after group 2 or 3 and give rise to the transition block of d and df elements of groups 3 to 11, embedded in the sp block. In the heavier periods, divalent main group elements appear twice, with an empty d^0 Rydberg[6] shell in group 2 and a filled d^{10} core shell in group 12.

The *smooth and parallel variation of the atomic one-electron s- and p-levels vs. the stepwise variation of the d- and f-levels, and the changing order of s and p vs. d and f* was known (in principle) since Bohr and Coster (Bohr and Coster, 1923). Bohr's (semi-)classical model concepts worked approximately even for the interpretation of the observed many-electronic atomic levels. A quarter century later, after WW2, atomic structure quantum calculations became routine. *All orbital energy levels and orbital radii* for all free neutral atoms were published by various groups. We mention a few of these groups here: Latter (Latter, 1955), Herman and Skillman (Herman and Skillman, 1963), Gombás (Gombás and Szondy, 1970), Fricke and Waber (Fricke and Waber, 1971), Desclaux (Desclaux, 1973). They found their way into few textbooks on physical chemistry, such as Glasstone (Glasstone, 1946 seq.), quantum chemistry, such as Levine (Levine, 1970), or the Periodic Table, such as Mazurs (Mazurs, 1974). (It is recommended to check the original papers cited by Mazurs as his reproductions often were 'artistically' redrawn).

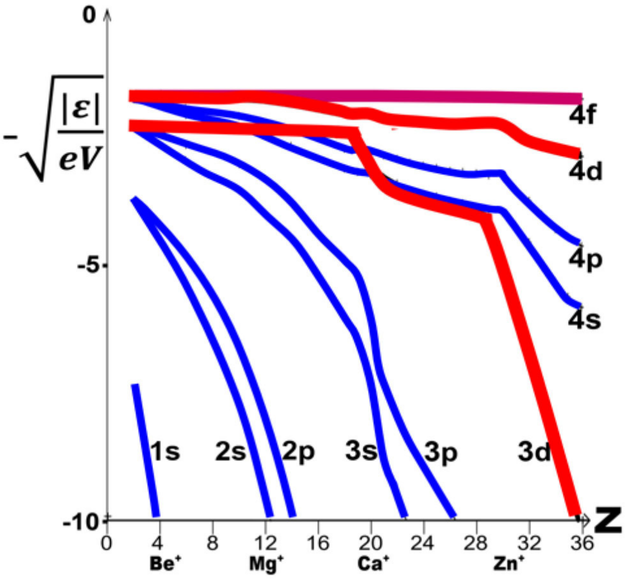

FIGURE 5 | Atomic one-electron energies **|ε|** for 1s to 4f orbitals, vs. element number ***Z***. **|ε|** is defined as the experimental atomic second ionization energy (correlating with the metals' chemistries), configuration-averaged[7] and displayed as **$\sqrt{|\varepsilon/eV|}$,** which corresponds to $Z_{\mathrm{eff}}/n_{\mathrm{eff}}$ (data from NIST: NIST Team, 2019). Note the smooth and nearly parallel decline of the *n*s and *n*p energies (in blue) vs. the more stepwise decline of the *n*d energies (in red) for increasing *Z* (and at higher **Z** also of the *n*f energies, not shown here).

The *n*s and *n*p orbitals have rather similar energies. For increasing element number *Z*, they stabilize smoothly together, with secondary kinks occurring when a new inner subshell becomes occupied (**Figure 5**). Since the d and f orbitals are well-shielded from nuclear attraction by the s and p core electrons, their energy levels at first hardly vary with increasing Z. For the noble gases and alkali metals in groups 0 and 1 of period *n*, there is a large energy gap between the outer closed $(n{-}1)p^6$ core shell and the next *n*s, *n*p valence shells. The (*n*−1)d levels [and for the heaviest elements also the (*n*−2)f levels] are even higher in energy, but then 'collapse' from far above to just below the *n*s, *n*p pair (Goeppert Mayer, 1941; Connerade, 1991; Schwarz, 2010b; Cao et al., 2019). The varying order of canonical one-electron energy levels ε[7] along the periods of elements (**Figure 5**) is described by the following relations (1) to (4), where the symbol ≪ indicates atomic orbital energy differences so large that the lower level remains inert under ambient chemical conditions and

---

"*Spinor-orbital*": In the real, relativistic world, the one-electron states are represented by spinors, consisting of two complex orbitals for the α and β contributions, $\phi_\alpha(\boldsymbol{r})\cdot\alpha + \phi_\beta(\boldsymbol{r})\cdot\beta$. For instance, the spin-orbit coupled ground-state of a p-electron may be described by spinor-orbital $p_x\cdot\beta+i\cdot p_y\cdot\beta+p_z\cdot\alpha$, or by its Kramer's mate $p_x\cdot\alpha-i\cdot p_y\cdot\alpha-p_z\cdot\beta$. Both p½ spinor-orbitals and any mixture of them has a spherically symmetric density distribution.

[6] *Rydberg orbitals* are diffuse orbitals around an atom (or molecule), forming a series like the hydrogen-like orbitals with increasing quantum number *n*, their energies converging toward the ionization energy *IE* as $IE - Z_{\mathrm{eff}}^2/(n{-}\delta_{\mathrm{eff}})^2$ (in Rydberg energy units). They are too diffuse to contribute to local chemical bonds. This Rydberg must not be mixed up with the same name, more recently introduced by Weinhold and Landis (2005) in the framework of so-called natural bond orbital analysis for core and valence shell basis set remainder/garbage.

[7] *Orbital energy* ε is here defined as the negative atomic one-electron ionization energy. An atomic open shell configuration with $\ell > 0$ may give rise to several to several hundred different energy levels, with a spread of several or many eV for neutral atoms (1 eV ≈ 10^5 J/mol), and even more for cations (Wang et al., 2006; Schwarz, 2010b). Simplest example: the p^2 valence configuration of group 14 elements has 15 states at five energy levels with a spread of ca. 200 (Si, Ge, Sn) to 260 (C) to 350 (Pb) kJ/mol. Note: It is an inappropriate chemical habit of specifying individual energies by only giving the originating electronic configuration without any *LSJp,i* state assignment. On the other hand, configurational average energies are more relevant anyway for chemical bonding than the somewhat "accidental" individual atomic ground state energies. Therefore we here define the orbital energies ε with respect to the configurational averages, which can be derived with the help of some theory, from spectroscopic observations or quantum computations.

will NOT ionize, form dative bonds, or hybridize with the next higher valence-active level(s):

Relation	Groups	Order of atomic one-electron energies	Comments
(1)	0, 1	$\varepsilon[(n-1)p] \ll \varepsilon[ns] < \varepsilon[np] \ll \boldsymbol{\varepsilon[(n\text{-}1)d]}$	d-orbital collapse begins
(2)	2	$\varepsilon[(\mathrm{n}-1)p] \ll \varepsilon[ns] < \boldsymbol{\varepsilon[(n-1)d]} < \varepsilon[np]$	here the ($n+\ell$, n) rule happens to apply
(3)	3–11	$\varepsilon[(n-1)p] \ll \boldsymbol{\varepsilon[(n-1)d]} < \varepsilon[ns] < \varepsilon[np]$	element series of hardly varying ε values
(4)	12–18	$\varepsilon[(n-1)p] < \boldsymbol{\varepsilon[(n-1)d]} \ll \varepsilon[ns] < \varepsilon[np]$	second step of d-orbital collapse

DIFFERENT REPRESENTATIONS OF PERIODICITY: CHEMICAL NARRATIVES

From Correct Quantum Chemistry to Chemical Facts

A large body of chemistry can be logically rationalized qualitatively, and theoretically simulated quantitatively, with the help of sufficiently digested quantum physics. Atoms and even more so molecules are rather complex systems with a pattern of observable properties that exhibits some coarse structure that is advantageous to be exploited in practice, with the help of fact-adapted Periodic Tables. For pedagogic introductions into the field of chemistry, 'impressive' and more simplistic (though yet pragmatically fact-adapted) designs may be most useful. Important points for chemistry are that chemically unbound neutral atoms in a vacuum may differ from chemically bound atoms in compounds, and that the energetic order of s,p vs. d,f valence orbitals changes after group 2 or 3, keeping the large orbital energy gap above closed noble-gas shells.

Remarkable trends of chemical thought on several related issues in the present context emerged in the chemical community as accepted narratives during the past decades. Conceptually as well as in reality, the series of unperturbed neutral atoms in a vacuum can be obtained by stepwise adding a proton (and some neutrons) to the atomic nucleus, and simultaneously a 'differentiating' electron to the atomic shells. The leading electron configuration[8] from which the physical ground *state* with the lowest energy *level* of the chemically non-bonded atom derives, depends in an involved manner on the Coulomb, exchange, and spin-coupling interactions of the many electrons in the atom (Condon and Shortley, 1935). Which leading orbital occupation scheme dominates in the ${}^{M}L^{P}_{J,i}$ ground level (M = spin multiplicity; L = total orbital angular momentum; J = total orbital + spin angular momentum; P = parity; i = parentage) depends in some cases on energy differences (Moore, 1949 et seq.) as small as thermal energies, while chemical bond interaction energies are up to several hundred times larger. Therefore, which electronic orbital configuration dominates in a free atomic ground states is a complicated issue (Schwarz, 2010b), the result being listed in the textbooks to train the memory. On the other hand, which configuration(s) dominate in chemically bonded atoms is a rather different issue, but plays a major role in chemistry; its understanding might be useful for chemists.

The simply structured physical laws of quantum mechanics, when applied to many-electron atoms (or even to chemical molecules) lead to a rather complicated set of results. Madelung (1936) mentioned an empirical finding that gave rise to an 'idealized' rule, how he called it, which reproduced the leading configurations of the outermost orbitals in the special field of *ground states of neutral free atoms* of all main-group elements, and of ca. 2/3 of the transition elements. A useful qualitative rule (here for vacuum spectroscopy of non-bonded atoms) should work, however, in at least 90 per cent of cases (Schultz, 2010).

When quantum mechanical concepts were absorbed by a broader chemical community in the middle of the twentieth century, a narrative evolved and was taken over by physicists, educators and philosophers, when they gave thought to the system of chemical elements. Namely, Madelung's ($n+\ell$, n) rule was given a new interpretation (Scerri, 2007, 2020; Schwarz and Rich, 2010). Originally, atomic spectroscopists used the ($n+\ell$, n) rule to memorize which 'differentiating' orbitals become additionally occupied in *free neutral atoms*, when element number Z increases stepwise. Chemical educators however applied it to the *chemically more interesting case of the various ions of a given element Z* with a stepwise increase of number of valence electrons. It is a pity that the ($n+\ell$, n) rule usually fails when d and f orbitals are involved. Concerning the heavier p elements, the order of orbital energies corresponds to $(n-1)d^{10}$-core < ns^2 np^{g-12}, while the ($n+\ell$, n) rule assumes the inverted order $ns^2 < (n-1)d^{10}$ np^{g-12}. Concerning the d elements, the ($n+\ell$, n) rule fails to reproduce the leading[8] configurations of the series of neutral free atoms in some cases, and of the series of oxidation states of a given d element in most cases.[9]

---

[8] A '*leading configuration*' is one with comparatively large weight: The quantum mechanical state a of an n-electron system is described by a wavefunction $\Psi_a(x_1,\ldots, x_\mathrm{n})$, depending on all $i = 1$ to n electronic position-spin coordinates x_i. Ψ_a can be expressed as an infinite sum of configurations of Pauli-antisymmetrized products of n spin(or)-orbitals (see footnote 5) each from 'complete' orbital set $\{\phi_r(x_\mathrm{i}),\ r = 1 \text{ to } \infty\}$. There are basically three cases. (I) "The single-configuration model works": one can find some set of n orbitals $\{\phi_q,\ q = 1 \text{ to } n\}$ so that just one orbital configuration well approximates the wave-function, $\Psi_a \approx \mathrm{A}\{\Pi\phi_q(x_i),\ q{=}1\text{-}n,\ i{=}1\text{-}n\}$; despite the same number of electrons, the two different concepts must not be mixed up. (II) "The state is strongly correlated": several configurations d are needed for any acceptable approximation of $\Psi_a \approx \Sigma_d\, c_d{\cdot}\mathrm{A}\{\Pi\phi_{ad}(x_i)\}$; typical examples are the two-configurational Be atom $1s^22s^2$ and $1s^22p^2$ (Watson, 1960), or the transition metal complexes of high oxidation state such as the permanganate ion MnO_4^- (Buijse and Baerends, 1990). Note: in both cases the set of orbitals can be mixed and transformed to another equivalent set, e.g., local or delocal orbitals (Autschbach, 2012). (III) "The orbital model breaks down": the wavefunction Ψ cannot be reasonably approximated by any short sum Σ_d. This happens frequently when an electron is ionized from the lower part of a valence or core band such as for $N_2^+(2s\sigma g^{-1})$ or $Ca^+(2s^{-1})$ (Cederbaum et al., 1977).

[9] *The ($n+\ell$, n) rule applied* to the series of cations Z^{+q} of a given element Z (here chromium) up to the neutral atom Z^0, is contrasted with the leading configurations

A further change of meaning was the interpretation of (n+ℓ, n) as reproducing a *universal energetic order of the atomic orbitals*. There are two aspects to such an interpretation. First, there is no universal energetic order. An important basic fact of the electronic structure of atoms is that the orbital energy order varies significantly with Z and also with the ionic charge [see relations (1–4); **Figure 5**; and footnote 9]. That was known, in principle, a century ago (Bohr and Coster, 1923). Further, an oversimplified 'strict' Aufbau rule (then called principle) is sometimes postulated that excludes the simultaneous occupation of energetically slightly different orbitals, something that is common in transition metal complex compounds of the weak ligand field type (Ballhausen, 1962).[10]

Eventually, the difference of *free atoms in space*, and of *bonded atoms in compounds*, was discarded. However, free atoms in vacuum have ample space around them. The diffuse ns Rydberg orbitals (see footnote 6) with weak e-e repulsion are energetically favorable in comparison to the compact (n−1)d orbitals. In molecules, however, the extended ns orbitals are energetically destabilized by Pauli repulsion of the occupied shells of the bonded ligand atoms (Wang et al., 2006), except for hydrides where the proton has no occupied core shells. A special case are the metals, where the crystal structure with high coordination numbers allows for delocalized valence bands, which support diffuse ns orbital occupation. A useful rule of thumb is that the leading configuration of a transition metal ion of oxidation state $+q$, Z^{+q}, in group g of the periodic table, may be approximated by $(n-1)\mathrm{d}^{g-q}$ (Ballhausen, 1962; Jørgensen, 1969). The effectively neutral atoms in metals have the approximate configuration $(n-1)\mathrm{d}^{g-1}n\mathrm{s}^1$, while effectively negatively charged transition metal atoms in respective complexes have the leading (see foonote 8) configuration $(n-1)\mathrm{d}^{g-1}n\mathrm{s}^2$.

This common knowledge of transition metal chemistry has yet not entered the common chemical textbooks, which explicitly or implicitly teach that the electronic structure of unbound atoms in physical vacuum is an optimal paradigm for the electronic structure of bonded atoms in chemical compounds (Millikan, 1982; Schwarz, 2010b). In a famous article at the centenary of the Periodic Table, Löwdin (Löwdin, 1969) asked "the question at what degree of ionization the energy rule has become changed". Since Madelung's rule holds for a significant fraction of the series of neutral free atoms, and the chemical (n+ℓ, n) rule for a small fraction of the series of differently charged ions of a given atom,[8] any so-called proof in the more recent literature must appear problematic (e.g., Wong, 1979; Meek and Allen, 2002; Thyssen and Ceuleman, 2017; Kholodenko and Kauffman, 2019).

In their early searches for a periodic system, Meyer (Meyer, 1864, 1870) and Mendeleev (Mendeleev, 1869a,b; Mendelejeff, 1871) had cut the helical array of elements (**Figure 3**, right) at different places. In later years, the most common convention became cutting between the p-block halogens and the s-block alkali metals. It is there, where the largest variations of the pseudo-periodic chemical properties of elements occur. Examples of this convention are the 'short' table in **Figure 1**, and the nowadays more common 'medium' tables with 18 groups as in **Figure 4** (with the f-block under the main table, a clever alternative to a 'long' table with 32 groups, printable on common paper format). **Figure 4** was suggested (though not prescribed) by the IUPAC (the "Red Book" by: Connelly et al., 2005; IUPAC's archives: IUPAC, 2015).

Other options are the cut before or inside or after the d-block, so that the 'pivots of periodicity,' and the groups with dominant valence −1, 0, +1, show up somewhere in the middle of the table (Meyer, 1864; Mendeleev, 1869a). Before the discovery of the noble gases, there was no group with zero valence between −1 (halogens) and +1 (alkali metals); the void of chemical elements without any valence activity appeared natural and acceptable to the former chemists.

The (n+ℓ, n) rule assumes, for the values $n+\ell = 1$ to 8 in the Periodic Table, a rather atypical orbital energy order, where the steps of n+ℓ are indicated by '$\ll$':

$$(5)\quad 1s \ll 2s \ll 2p < 3s \ll 3p < 4s \ll 3d < 4p < 5s \ll 4d < 5p < 6s \ll 4f < 5d < 6p < 7s \ll 5f < 6d < 7p < 8s$$

Relation (5) maps onto the periodic table design of **Figure 6**, with 8 periods up to Z = 120, being called the Janet *Left Step Periodic Table* (LSPT; Janet, 1930; Scerri, 2007, 2020; Stewart, 2010, 2020). The LSPT looks particularly 'elegant' and 'symmetric' with regularly arranged s, p, d, f blocks. The LSPT is obtained by cutting the periodic spiral in the left middle of the sp block, i.e., after the open $(\mathrm{sp})^2$ shells, and then shifting hydrogen and helium (with closed $1\mathrm{s}^2$ shell) above lithium and beryllium. The simple

---

of the ground states of the respective cations, either unbound in physical vacuum, or bound in chemical compounds:

	Cr^{+6}	Cr^{+5}	Cr^{+4}	Cr^{+3}	Cr^{+2}	Cr^{+1}	Cr^0
Atomic ions according to the (n+ℓ, n) rule:	$1s^2$-$3p^6$	**$4s^1$**	**$4s^2$**	**$3d^14s^2$**	**$3d^24s^2$**	**$3d^34s^2$**	**$3d^44s^2$**
Real free atomic cations in physical vacuum:	$1s^2$-$3p^6$	**$3d^1$**	**$3d^2$**	**$3d^3$**	**$3d^4$**	**$3d^5$**	**$3d^54s^1$**
Real bound atoms in chemical compounds:	$1s^2$-$3p^6$	**$3d^1$**	**$3d^2$**	**$3d^3$**	**$3d^4$**	**$3d^5$**	**$3d^6$**∗

∗The delocalized metallic valence bands give rise to some s orbital occupation of the transition metals, also an electronic surplus on formal metallic anions. However, the d- and f-block elements in the vast majority of metal complexes, and all the heavier p-block elements have the (n-1)d energetically below the ns orbital, violating the (n+ℓ, n) rule.

[10] *The crystal-field-MO or ligand-field model* well explains the chemistry and spectroscopy of transition metal compounds. The Lewis-basic pair-donating ligands form covalent-dative bonds with the d shell of the metal atom, which may back-donate d pairs if the ligands have low empty acceptor orbitals. A good approximation for the valence shell of a transition metal ion of formal charge q from element group g is by electron configuration d^{g-q}. Note that the s shell plays hardly any role in real chemistry of d elements except for free or metallic or anionic d atoms. The highest occupied and lowest unoccupied orbitals of the complexes, responsible for redox and substitution reactions and optical effects, usually have significant d metal character. One distinguishes weak-field high-spin complexes with several near-degenerate singly-occupied d-type orbitals, and strong-field low-spin complexes (most common for the heavier d elements) with occupied lower d-type orbitals and unoccupied higher d-type orbitals above a gap.

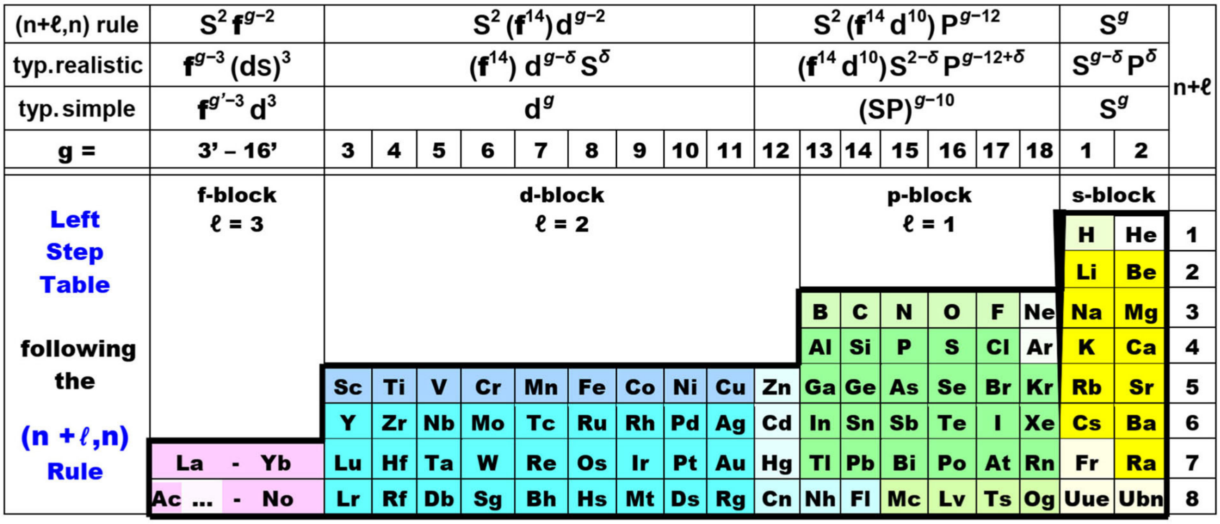

(n+ℓ,n) rule	$S^2 f^{g-2}$	$S^2 (f^{14}) d^{g-2}$									$S^2 (f^{14} d^{10}) P^{g-12}$							S^g		n+ℓ
typ.realistic	$f^{g-3} (ds)^3$	$(f^{14})\, d^{g-\delta} S^{\delta}$									$(f^{14} d^{10}) S^{2-\delta} P^{g-12+\delta}$							$S^{g-\delta} P^{\delta}$		
typ. simple	$f^{g'-3} d^3$	d^g									$(SP)^{g-10}$							S^g		
g =	3' – 16'	3	4	5	6	7	8	9	10	11	12	13	14	15	16	17	18	1	2	
Left Step Table following the (n +ℓ,n) Rule	f-block ℓ = 3	d-block ℓ = 2										p-block ℓ = 1						s-block		
																		H	He	1
																		Li	Be	2
												B	C	N	O	F	Ne	Na	Mg	3
												Al	Si	P	S	Cl	Ar	K	Ca	4
		Sc	Ti	V	Cr	Mn	Fe	Co	Ni	Cu	Zn	Ga	Ge	As	Se	Br	Kr	Rb	Sr	5
		Y	Zr	Nb	Mo	Tc	Ru	Rh	Pd	Ag	Cd	In	Sn	Sb	Te	I	Xe	Cs	Ba	6
	La - Yb	Lu	Hf	Ta	W	Re	Os	Ir	Pt	Au	Hg	Tl	Pb	Bi	Po	At	Rn	Fr	Ra	7
	Ac … - No	Lr	Rf	Db	Sg	Bh	Hs	Mt	Ds	Rg	Cn	Nh	Fl	Mc	Lv	Ts	Og	Uue	Ubn	8

FIGURE 6 | The elegant "Left Step" periodic table, following the canonized "(*n*+ℓ, *n*) rule," see relation (5) below.
—1st line at the top: Madelung's "idealized" occupations of the s, p, d, f (ℓ = 0, 1, 2, 3) valence shells in many *neutral unbound* free atoms in physical vacuum, taken over by the chemical community as the (*n*+ℓ, *n*) rule for less or more *polar-bonded* atoms in chemical compounds.
—2nd line: typ. realistic = ℓ-occupations of typical, *bonded* atoms in real chemical compounds, where the case-dependent population parameter is mostly $0 < \delta < 1$.
—3rd line: typ. simple = simplified approximate chemical valence configuration of typical bonded atoms.
—4th line: **g** = group number = number of chemically active electrons in the valence shell of largely neutral atoms bonded at ambient conditions (modulo 10).
—Colored block castes of elements: s—yellow, p—green, d—blue, f—lilac.
Notes on variant backgrounds:
—(a) Ac … : some early actinoids Pa to Pu (and possibly Th and Am) are chemically quite different from their lanthanoid counterparts (Ce)-Pr-Nd-Pm-Sm-(Eu). Conversely, Ac and the heavier actinoids Cm to Lr are quite similar to their lanthanoid counterparts La and Gd to Lu, and to Sc and Y.
—(b) The 3d elements Sc to Cu are special in forming high- and low-spin, or weak- and strong-field, complexes with ligands from the left and right part, respectively, of the spectro-chemical series, while the 4d and 5d elements usually only form low-spin strong-field complexes with any ligands.
—(c) Elements Zn-Hg of group 12 have closed d^{10} shells and are better regarded as members of the sp block.
—(d) The 2p series B-F is unique with the 2s and 2p orbitals of comparable spatial extension and a strong tendency for sp hybridization.
—(e) H and He are unique with having no extended atomic core and no other orbital energetically nearby 1s.
—(f) He, Ne, Ar have well-closed $1s^2$, $2p^6$, $3p^6$ shells, respectively, at most forming complexes with weak secondary bonds, i.e., they have no 'real chemistry' under ambient conditions. In contrast, Be etc., and Kr etc. form primary bonds under ambient chemical conditions.
—(g) The superheavy elements at the end of the bottom row feature peculiarities: Cn, Nh, Fl are predicted to have a chemically active d shell under ambient conditions. Fl, Mc, Ts, Og have comparably inert $7s½^2$ (and $7p½^2$) pairs.
—(h) Fr, Og, Uue, Ubn are predicted to have unusual valence-active $(n-1)p^3/^4_2 ns^{0-2}$ shells, i.e., no closed p^6 noble-gas shell.

outer shape of the LSPT may be useful in introductory chemistry courses (Kurushkin, 2017). While the assumed systematic valence electron configurations of the rule (1st line in **Figure 6**) differ quite a bit w.r.t. to orbital order and orbital occupation from *real chemically bonded atoms* (2nd line; see also **Figure 8**), the graphic nevertheless appears useful to display the chemical trends. However, it must be noted that for the heavy p-block elements, the $(n+\ell,\ n)$ rule shifts the occupied $(n-2)f^{14}$ and $(n-1)d^{10}$ shells in between the $ns^{2-\delta}$ and $np^{g-12+\delta}$ valence shells, while the observed energetic order is $(n-2)f \ll (n-1)d \ll ns < np$. Concerning the d-block, in the vast majority of cases there is no ns^2 shell below the $(n-1)d^{g-2}$ shell, but a weakly occupied *ns* shell somewhat above (except for negatively charged transition metal atoms with approximate ns^2 occupation, and for metallic phases with neutral metal atoms and approximate ns^1 occupation).

The zinc-group 12 is also special (Jensen, 2003), since d^{10} is no longer valence-active, but behaves as an inert core shell. These "d-block" elements behave chemically as typical s-block members. The yet unconfirmed case of mercury tetrafluoride (HgF_4) is no counter-argument, since it is labile under standard conditions (Wang et al., 2007; Jensen, 2008; Rooms et al., 2008; Ghosh and Conradie, 2016; Gao et al., 2019; Lin et al., 2020). Finally, for the f-block, the dominant valence-bonding shell is (*n*–1)d; the (*n*–2)f falls deeper into the atomic core, the higher the effective positive charge on the atom becomes; as a rule of thumb, the f contributes to covalent bonding only in some cases of Ce(4f5d) and for Pa to Pu (5f6d), while the *ns* shell only weakly contributes to bonding, as in the other d-elements.

Various clarifying comments are necessary (legend of **Figure 6**) when looking from the viewpoint of the $(n+\ell,\ n)$ rule onto the behavior of *real chemical elements*. Admittedly, this holds partially also for other designs of Periodic Tables (such as in **Figures 1–5**). To explain the chemistry of the elements, one must consider not only the correct leading (see foonote 8) valence configuration, but also the correct configuration of the occupied core shells, and not only the orbital energies but also the orbital radii. For instance, the valance *n*s orbitals are very diffuse (see footnote 6) at the beginning of a period (or at the very end of the LSPT) so that they play little role for covalent overlap interactions. The positioning of a closed-shell element (such as He-1s^2) above an open-shell (such as Be-2(sp)^2) has no basis in chemistry or quantum mechanics.

From Partial Aspects of Reality to Created Patterns

The chemical trends along the Z-line of elements are non-linear and of different characters. The regular grid of periodic tables is adapted to the wish for a well-ordered presentation, but curtails the chemical facts. The common IUPAC Table is already half-way between realistic aim-dependent presentations of some details of the natural System of Elements and the idealization of a desired overall appearance of a symbol for the System in the form of a Periodic Table.

We had noted the two points before that different chemical behaviors are relevant in *different contexts* such as under 'common' or astrochemical or geochemical conditions, and that some chemists prefer to classify *borderline cases* in either this or that rigorous, unique manner. Combined with the *fuzzy nature of chemistry* (Syropoulos, 2020), this may lead to futile disputes, including those over the Periodic Table (Schwerdtfeger et al., 2020). Chemistry has all sorts of fuzzy definitions such as chemical periodicity or chemical bonding or hydrogen bonding etc. Rather than a black or white categorization, the IUPAC definition of a *hydrogen bond* (Arunan et al., 2011) suggests the strategy that classification is more reliable and less open to controversy, the greater the number of given criteria is satisfied. The range of *metalloids* on the metal to non-metal divide (**Figure 1**, right; Vernon, 2013) or the representation of *groups 3 and 13* including the f-block are further examples. Such issues are less disputed in practical chemistry.

Several theoretically oriented chemists argue that chemistry loses its basic ingredients (i.e., techniques useful to handle a complex field) and becomes like physics (which is adapted to handle the simple basic structures of reality). Some argue in favor of different practices, while others argue against any fuzzy concepts including those that have proven useful in previous times for classifying the nearly continuous distribution of observations, with few borderline cases remaining. However, some scholars do not like ambiguous borderline cases. It is our experience that many young students expect that a teacher should have a simple answer to any (complicated) problem.

No such loss of chemical richness is warranted. Jones (2010) cogently summarized the situation: "Scientists need not lose sleep over the hard cases. As long as a classification system is beneficial to *economy of description*, to *structuring knowledge* [italics added] and to our understanding, and hard cases constitute a small minority, then keep it. If the system becomes less than useful, then scrap it and replace it with a system based on different shared characteristics." In the case of hydrogen and helium, for example, we agree with the suggestion of Schwerdtfeger et al. (2020): "Although hydrogen and helium are clearly separate from the rest of the PTE, almost every chemist agrees that we can leave these elements in their current place in the PTE, *keeping their distinctive quantum nature in mind* [italics added]."

In another sense, the problematic cases can be regarded as addressing philosophical issues that border on what a periodic table tries to represent. What you get from your Periodic Table is what you put in, unlike the nature-given Periodic System. The learning is to consider how many insights and how much understanding could be gained from appreciating these different stepping stones including, but not limited to, the fundamental and important nature of inanimate matter. The takeaway is to explain some relevant context to readers, colleagues, and students.

- The so-called IUPAC Table (**Figure 4**) is more of a chemistry-focused Pragmatic Table.
- The form with lutetium instead of lanthanum in group 3 is more of an Idealized Table, instead of a Pragmatic Table with "no need to lose sleep" (Scerri, 2020).
- In a Solid-State Physicist's Table, both lanthanum and lutetium, as 5d metals, go under yttrium (Vosko and Chevary, 1993).
- In the electronegativity-focused Pauling Table (Pauling, 1953), group 3 is boron, aluminum, scandium, yttrium, lanthanum, and actinium.
- Aluminum over scandium is more of a Metallurgist's Table (Habashi, 2009).
- Geochemical Tables (McSween and Huss, 2010; Railsback, 2018) emphasize property trends important for the earth scientist, i.e., they give up the beauty of symmetrized arrangements in favor of irregular chemical facts. Some tables define the carbon-silicon group as containing titanium, zirconium, hafnium rather than the standard set of germanium, tin, lead.
- In the Astronomer's Tables (Esteban et al., 2004; McSween and Huss, 2010; Yamamoto, 2017), hydrogen and helium are the only non-metals and all the other elements are labeled as metals.
- In a Superconductivity Periodic Table, group 2 is split into: barium and radium; calcium, strontium, and ytterbium; group 12 is beryllium, magnesium, zinc, cadmium, and mercury (Wittig, 1973).
- A periodic table with hydrogen over boron makes for a nice Designer Table (Luchinskii and Trifonov, 1981).

The basis of element grouping may be a (sometimes unspecified) selection of facts, or a preset and appealing pattern useful in education or promotion.

ATYPICAL PERIODICITIES

At Top and Bottom

The chemistry of elements is richer than being satisfactorily pictured in a table. The individuality of elements from the same similarity group is most pronounced at the top, where the number of valence orbitals is small (one 1s, four 2sp) and the orbital energies and radii form bands with gaps. At the bottom of the periodic table, these distinctions become washed out. That is due to both the non-relativistic increase of the density of states and different *screening effects, and the relativistic orbital shifts and splittings energy- and radii-wise.*

Already Gmelin (Gmelin, 1843) and Mendeleev (Mendeleev, 1869a,b; Mendelejeff, 1871) had noted that the lightest elements of the similarity groups exhibit somewhat peculiar chemical behaviors. Mendeleev labeled the elements of the second period the typical ones (типические элементы, sometimes translated as representative elements), and we today call groups 13, 14 etc. the boron, carbon etc. groups. Biron (Biron, 1915) recognized a zig-zag behavior down the main-group elements with similar extrema in periods 2, 4, and 6, and called it secondary periodicity. Jørgensen (Jørgensen, 1969) and Shchukarev (Shchukarev, 1977) discussed the peculiarity of the first element of any group of the periodic system in great detail and related it to the comparatively *small radii of orbitals without radial nodes*: 1s (hydrogen), 2p (boron to fluorine), 3d (scandium to copper), and 4f (cerium et seq.). Kutzelnigg (Kutzelnigg, 1984) explained the special behavior of the light 2p main-group elements as due to the similar extensions of the 2s and 2p valence orbitals, which supports sp hybridization. In contrast, the p-valence shells of the heavier p-block elements are significantly more extended than the respective s-valence shells, which is beneficial for pure σ(p) bond formation. Shchukarev (Shchukarev, 1977) in the 'East' named the feature of the radial nodelessness of the (n,ℓ=n-1) valence orbitals *kaino-symmetric* (kainos = new), while Pyykkö (Pyykkö, 1979a,b) in the "West" introduced the term *primo-genic* (primus = first). The basic relevance of the radii of the atomic valence orbitals was later discussed in review articles (e.g., Kaupp, 2006), but hardly entered the chemical textbook scene (an example of where it did: Huheey et al., 2014).

When Z increases, kainosymmetric orbitals with new primogenic ℓ-values become occupied above the noble-gas core shells [$1s^2$ and $1s^2$-$(n-1)p^6$] at energies $\varepsilon_{n\ell} = -(Z_{\text{eff}}/n_{\text{eff}})^2$. At the beginning of period n with just a few valence electrons, the value of n_{eff} can be modeled by $n_{\text{eff}} = [n - \delta_{\text{screen}} + \ell(\ell+1)/6]$, where δ_{screen} is the screening of the nuclear attraction of the ns valence shell by the noble-gas core. For $\ell = 0$ and 1, i.e., $\ell(\ell+1)/6 = 0$ and 1/3, the valence s and p shells appear nearly together after the noble-gas shell closure. d and in particular f with $\ell = 2$ and 3 appear later corresponding to $\ell(\ell+1)/6 = 1$ and 2, meaning that (n**−2**)f and (n–**1**)d appear nearly together with (n–**0**) (s,p). Because of the quantum constraint $\ell \leq n-$ **1**, new electronic shells in screened atomic Coulomb potentials appear in double-steps. Therefore, there are two periods each of length 8 for 2sp and 3sp, of length 18 for 3d4sp and 4d5sp, and of length 32 for 4f5d6sp and 5f6d7sp. Apparently, there is no physical-chemical reason for two ns periods before the first $(sp)^8$ period, except the desire for more symmetry and beauty in the generated Periodic Table (Jensen, 1986). The appearance of the kainosymmetric 2p, 3d, and 4f shells every second period causes the secondary periodicity with the scandoid and lanthanoid contractions of the effective atomic bond radii. Many parameters of the elements and their atoms derived from the individual chemical observations can be approximated as expansions in terms of the number of ℓ-valence electrons (Imyanitov, 2019a,b) and in terms of $1/Z = Z^{-1}$ (Layzer, 1959), at least within non-relativistic quantum chemistry.

However, the real world behaves quantum-relativistically. The errors of the non-relativistic approximation are conventionally called the "relativistic corrections," which can be expressed by expansions in terms of powers of Z^2 (e.g., Schwarz, 2010a). Consequently, it is difficult to make reliable predictions on the chemistry of the heavy elements with high Z, i.e., with increasingly larger terms of Z^2, Z^4, etc., by *extra*polation from the region of the lighter "non-relativistic" elements. In contrast, *inter*polations within the region of the lighter half of the elements, say in the first five periods up to $Z = 54$ (xenon), are easily successful, as Mendeleev had demonstrated. Below we will draw attention to some basic though empirically un-expectable chemical phenomena of the heavy elements in the 7th period, on the basis of the few chemical observations and quantum-chemical calculations (e.g., Nash, 2005; Pyykkö, 2012a,b; Pershina, 2015; Schädel, 2015; Türler et al., 2015; Türler, 2016; Düllmann, 2017; Giuliani et al., 2019; Trombach et al., 2019).

The chemically most relevant trends due to the 'relativistic corrections' are (Schwarz, 2010a; Pyykkö, 2012a):

(i) The ns-levels are energetically stabilized and spatially contracted, with the $(n-1)d^{5}/_{2}$ – ns½ and $(n-1)p^{3}/_{2}$ – ns½ gaps being reduced.

(ii) The p-levels are also stabilized and contracted, and strongly spin-orbit-split, so that the np½ spinor level is also contracted and stabilized toward the ns½ level; but the sp hybridization is hampered because of the complex structure of the p½ spinor.[4]

(iii) The $p^{3}/_{2}$ valence shell is destabilized, therefore the p½ – $p^{3}/_{2}$ gap is increased and the gap between the $p^{3}/_{2}$ to the next s½ is decreased.

(iv) Due to the orbital angular momentum of quantum numbers ℓ = 2 and 3, there emerges a significant centrifugal force $\sim\ell(\ell+1)/2r^3$. Therefore, the d and f orbitals do not strongly penetrate the inner atomic core shells and are better shielded from the nuclear attraction due to the relativistic sp contraction of the s and p type shells. There results an 'indirect' destabilization of d and f shells, whereby the $(n-1)d^{5}/_{2}$ – ns½ gap is further reduced (see also above).

Orbital Energies and Radii at the Bottom

At the bottom of the periodic table, relativistic orbital changes become qualitatively relevant for chemical thermodynamics. The gap between the $(n-1)p^{3}/_{2}$ noble-gas core shell and the s-metallic valence shell decreases. In the early actinoid series, 5f and 6d can hybridize. The (n+ℓ,n) rule may hold for the first time in the 6d series. The level pattern of $6d^{3}/_{2}$ – $6d^{5}/_{2}$ – 7s½ – 7p½ – $7p^{3}/_{2}$ – 8s½ at the middle and end of the 7th period changes qualitatively, suggesting a different chemistry and change of periodicity at the end of the 7th period and the start of the hypothetical but practically meaningless 8th period.

Because of the large relativistic spin-orbit coupling in the heavy elements, it becomes mandatory to consider the spin-orbit coupled spinor-orbitals (see footnote 5). Only for lighter elements, the picture of space-orbitals with different spins is an acceptable approximation. It is sufficient for instance for the comparatively weak spin-orbit induced "heavy-atom" corrections to "spin-forbidden" transitions in spectroscopy and in kinetics. Every element has a different core and a different valence shell (Figure 12 of: Cao et al., 2019), which together determine the chemical behavior in a physically lawful, though effectively rather complex manner. A general understanding of the system of chemical elements can be obtained by an analysis of the trends of the energies and radii of the outer-core and valence shells. The inner core and the outer Rydberg shells, which are important in XUV and UV spectroscopies, are less relevant for genuine chemistry and will not be considered here.

In **Figure 7**, we display the energy levels ε of selected atoms of period 7 from 'alkali metal' francium ($_{87}$Fr, group 1) to 'noble gas' oganesson (group18) (see footnote 4), with two representative elements for each block, namely $_{90}$Th and $_{102}$No (Eka-Yb) for the f-block, $_{106}$Sg and $_{110}$Ds (Eka-Pt) for the d-block, and $_{114}$Fl (Eka-Pb) and $_{118}$Og for the p-block. In order to show both weakly and strongly bound shells in the same graphic, we apply a square-root scale $\gamma = -\sqrt{|\varepsilon/\mathrm{eV}|} \sim Z_{\mathrm{eff}}/n_{\mathrm{eff}}$. The horizontal dashed line at $\gamma = -4$ is near to the value of the O^0-2p shell. Electronegative ligands such as oxygen, fluorine or chlorine would form homopolar bonds with atomic shells having $\gamma \approx -4$ [provided the overlap conditions are favorable and the number of valence electrons does not require filling the antibonding companion level(s)]. More or less electronegative ligands will lead to polarized covalences, where the charge transfer is partially counter-balanced by lowering/raising the ε values of the positively/negatively charged atoms, respectively.

In **Figure 8**, both the one-electron orbital energies and radial-density-maxima of the outer-core and the valence shells are shown, for atoms down a representative group of the s-block (group 2; for comparison the closely related group 12 is also displayed), the f-block [the central $f^7(ds)^3$ elements]; the d-block (middle group 7); and the $p_{1/2,3/2}$ block (middle group 15). The devised states in a model of independent electrons in the mean field of a many-particle atom or molecule are characterized by the positional and spin distributions in three-dimensional space. The spin-orbit coupling for states of spatial angular momentum ℓ in a central field causes energy and radial changes approximately proportional to $c_\ell \cdot \ell(\ell+1)$. The spin-orbit splitting increases quadratically with angular momentum ℓ, but the prefactor c_ℓ typically varies as ℓ^{-3}, because the radial spin-orbit coupling strength decreases with ℓ because increasing ℓ keeps the electron away from the atomic center where the coupling is largest. Consequently, in a given energy-shell of the atom, the spin-orbit effect is counter-intuitively the larger the smaller the orbital angular momentum is, that is, largest for the p-shell. The common space-orbital model with p_x, p_y, and p_z is no longer qualitatively correct for the "super-heavy elements" (SHE), but must be replaced by the spinor-orbital model. In **Figure 8**, the spin-orbit splittings of the energies ($\gamma \sim \sqrt{-\varepsilon}$) and radii ($\boldsymbol{r}_{\max}$) of the p-shells – both the outer-core and valence shells – are formidable for all heavy atoms, while the d and f splittings are less pronounced.

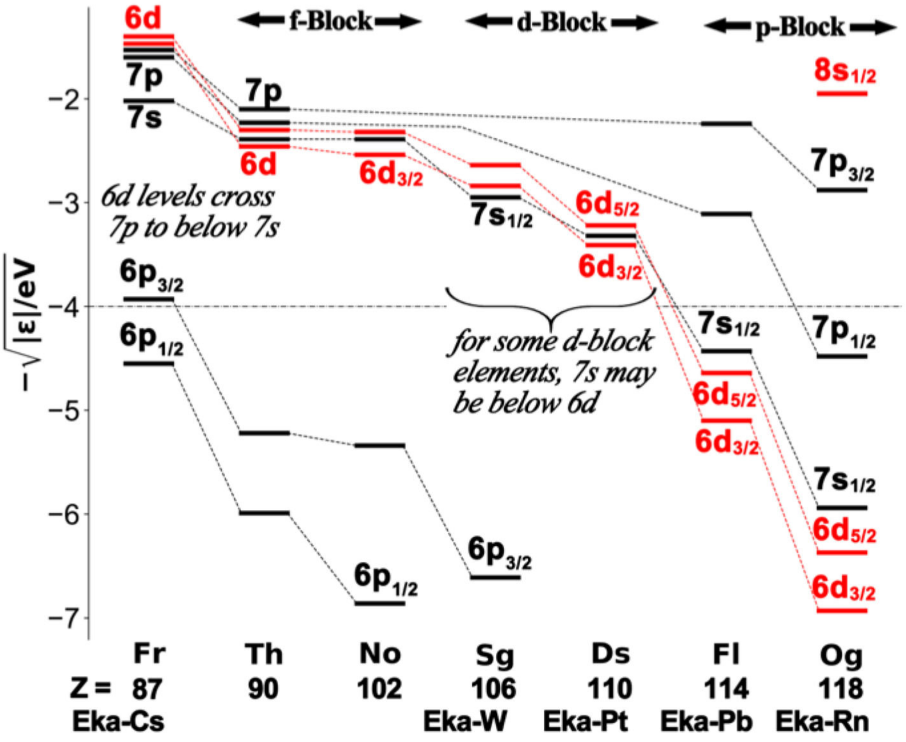

FIGURE 7 | Atomic one-electron energies of the outer-core and the valence shells, displayed as $-\sqrt{|\varepsilon/\mathrm{eV}|}$, over the lowest period 7 of the system of elements from francium to oganesson, at the Dirac-Fock level of approximation.

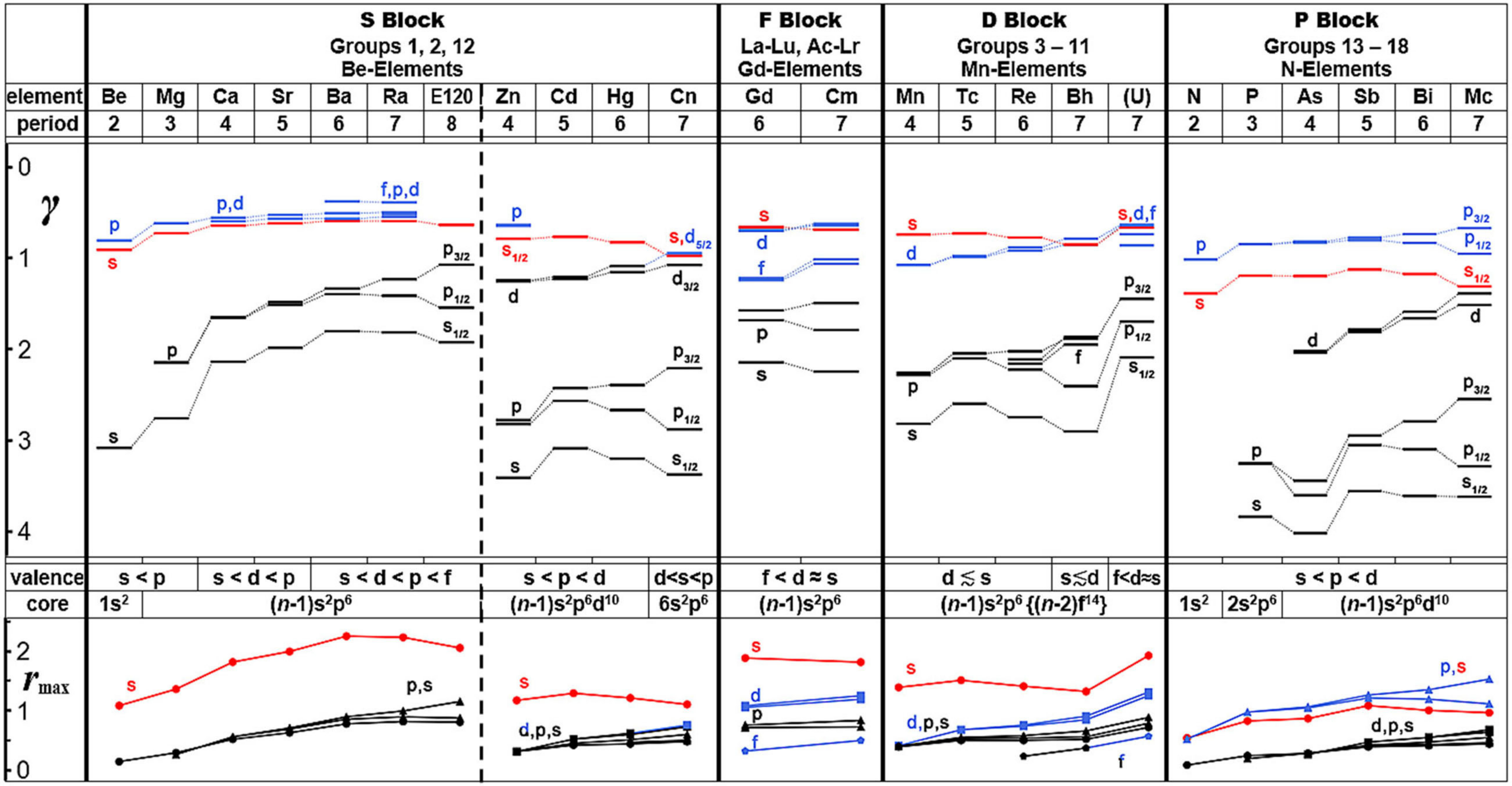

FIGURE 8 | Energies and radii of atomic shells of main and transition group elements, governing their chemistries (representative, light to heavy members, from the s and p blocks, and from the d and f blocks) from atomic Dirac-Fock computations. *Upper part:* Energetic order of the chemical valence shells (top: s in red; p, d, f in blue) and of the outer core shells (bottom: in black) in terms of parameter $\gamma = \sqrt{|\varepsilon/\mathrm{Ry}|} = Z_{\mathrm{eff}}/n_{\mathrm{eff}}$, where ε is the orbital energy, corresponding to the experimental single-electronic ionization energy (in units of Rydberg Ry = 13.6 eV or 1313 kJ/mol). *Lower part:* Radial density maxima $r_{\max}$ of the atomic shells, in Å (color code of valence and core shells as above).

Now, which bonding patterns of the elements of the 7th period may be expected against this background? In the following subsections, we will individually discuss the heavier members of: the s-block (groups 1–2); the early d-block including the f elements (groups 3–5); the later d-block (groups 6–11); the $s_{1/2}p_{1/2}$ block (groups 12–14); and those of the $p_{3/2}$ block (groups 15–18).

THE BLOCKS

The s-Block Elements

The heaviest elements of groups 1 and 2, $_{87}$Fr, $_{119}$Uue, and $_{120}$Ubn, are predicted as similar to the middle s-block elements. However, they may behave in a Janus-faced manner depending on the conditions, i.e., like typical low-valent s-block elements or very differently like penta- and hexa-valent heavy p-block elements.

Upon increasing the element number of a noble gas with outer closed shell $1s^2$, $2p^6$, $3p^6$, …, the additional electrons in the respective alkali and alkaline earth metals of periods $n = 2$, 3, 4, … are accommodated in the rather *diffuse* $(n\mathrm{sp})^2$ valence shell (with the option of some $(n\text{-}1)$d admixture from period $n = 4$ onward (Woolman et al., 2018; Li et al., 2019; Fromm, 2020). The s-block elements appear strictly mono- and di-valent under common conditions. While the ionic compounds have a formally empty valence shell, the partially covalent complexes and organometallic compounds as well as the metallic phases exhibit non-negligible s-p(d) occupation, and orbital mixing due to the small *n*s-*n*p or *n*s-*n*p-(*n*-1)d energy gaps. In particular, Be and Mg are *n*s(p) valence-active, while Ca, Sr and Ba are *n*s(*n*-1)d valence active (Fernández et al., 2020).

From the quantum-theoretical as well as from the chemical-empirical points of view, there is an objective qualitative difference between the alkaline-earth-metal and helium atoms, since He has a rather compact, closed $(1s)^2$ shell (without any appreciable p admixture). Helium remains zero-valent even under pressure, such as in the cubic inclusion compounds $[Na_2^+ (e_2)^{2-} He^0]$ or $[Na_2^+ (O)^{2-} He^0]$, where formally $He(1s^2)^0$ and $(1s^2)^{2-}$ or $O(2p^6)^{2-}$ respectively are inserted into the voids between the Na^+ ions of a new pressure-induced structure of Na (Dong et al., 2015, 2017; Rahaman et al., 2018; Zou et al., 2020). Depending on the chosen partitioning of the atoms in molecules and crystals, the obtained effective charges are $Na^{+(1-\delta)}$, $(e_2$ or $O)^{-(2-\eta)}$ and $He^{(2\delta-\eta)}$ with small numbers δ and η. For $(2\delta - \eta)$ $>$ or $<$ 0, narratively oriented chemists may postulate bonding attractions of the chemically inactive He, either of ionic He^+-O^- or He^--Na^+, or of covalent $He^{+\gamma} \rightarrow O^{-\gamma}$ or $He^{+\gamma} \rightarrow Na^{-\gamma}$ type. This is a nice example of the different views within and between the Two Cultures.[11]

Figure 8 shows just a little variation of the s valence shell energies and radii for the s-block members, with flat extrema at period **6**, of ionization potential, electron affinity, electronegativity and effective atomic radii. Elements $_{119}$Uue (Eka-Fr) and $_{120}$Ubn (Eka-Ra) in period **8** were accordingly predicted to resemble the lighter homologs in period **4** (Türler and Pershina, 2013; Pershina, 2015; Chemey and Albrecht-Schmitt, 2019). One must consider however that the *n*s shells of these heavier elements, in particular of the heavier alkali metals, are spatially very diffuse, yielding only weak overlap interactions with small differences among each other, but differing from the group 12 elements.

For the heaviest elements, however, the highest core level $(n{-}1)p_{3/2}^4$ moves up into an energy range typical for strongly electronegative elements, and becomes radially less compact (**Figures 7**, **8**). Fricke and Waber (Fricke and Waber, 1971; Fricke, 1975) had already speculated about raised valences of elements $_{119}$Uue and $_{120}$Ubn. In more recent years, computations and experiments up to the megabar range have established the stability of alkali and alkaline-earth polyhalides under high pressure met inside the planets (Dong et al., 2015, 2017; Zhu et al., 2015; Goesten et al., 2017; Miao et al., 2017; Luo et al., 2018; Lin et al., 2019; Rahm et al., 2019). Under standard conditions polyfluorides CsF_n and BaF_n are at most metastable, with a decay barrier that may render their temporary stability possible under standard pressure only at exotically low temperatures (see e.g., Rogachev et al., 2015; Vent-Schmidt et al., 2015). This also holds for HgF_4 (Wang et al., 2007; Jensen, 2008; Rooms et al., 2008; Ghosh and Conradie, 2016; Gao et al., 2019; Lin et al., 2020).

Apparently, cesium, barium and mercury from period 6 are borderline cases, and it may well be that the heavier homologs francium, radium, ($_{112}$Copernicium), and $_{119}$Uue, $_{120}$Ubn, behave no longer as typical alkali and alkaline-earth elements but form higher-valent complexes similar to those of the late heavy p-block elements such as $[SbF_6]^-$ or TeF_6, stable in ambient conditions. Explicit molecular calculations by Cao et al. (2019) indicate thermodynamic *stability* of $[Fr(V)\,F_6]^-$, $[Uue(V)\,F_6]^-$ and $[Ubn(VI)\,F_6]^0$ under *standard* conditions against loss of F_2, for instance

$$(6)\quad [Uue(V)\,F_6]^- \nrightarrow [Uue(IV)\,F_5]^- + \tfrac{1}{2}\,F_2 \nrightarrow$$

$$[Uue(III)\,F_4]^- + F_2 \nrightarrow \ldots.$$

As indicated in **Figure 1**, right, the $(n{-}1)p^6$ shell is chemically inert under ambient conditions in periods $n = 3$ and 4 from group-0 elements neon and argon onward. But $(n{-}1)p^6$ is still chemically active in krypton and xenon. $(n{-}1)p^6$ becomes an inactive noble-gas core shell in periods $n = 5$ and 6 only from group 1 elements rubidium and cesium onward. The $(n{-}1)p^6$ shell becomes inert in period $n = 7$ from group 2 element radium onward, while in period $n = 8$ it is apparently active even in group 2 element $_{120}$Ubn.

The theoretically predicted unexpected behavior of francium, $_{119}$Uue and $_{120}$Ubn, i.e., being poly-valent and forming polyhalide complexes, has hardly any direct practical-chemical consequences. The lifetimes of all francium isotopes are shorter than 1/3 h. In the real lab, only single francium compound

---

[11] *The Two Cultures* of science and art were defined by physical chemist and novelist C.P. Snow in 1956/1959 (Snow, 1962). We interpret them as the fact and rationality; and the narrative and opinion based human endeavors (science & technology vs. humanities & social sciences). They become integrated in chemistry, for instance when periodic tables are designed on chemical properties for chemical education by the technique of the arts. Chemically different elements He and Be are positioned in Periodic Table 6 above to obtain a regular outer shape with elements therein classified according to the graphical similarly of the conventional symbols He-$1s^2$ and Be-$2s^2$, independent of the different quantum-mechanical meanings.

molecules in a beam in vacuum, or on a surface, or in a matrix, or in chemically related compounds doped with tracer amounts of francium, could be investigated by 'quick' researchers. $_{119}$Uue and $_{120}$Ubn are the next elements to be synthetized in the coming decades and are expected with lifetimes far below a ms. The chemistry of possible compounds of such chemically 'non-existing' elements is yet relevant as they form reference points for the varying chemical trends between the upper and lower ends of any group in the chemically finite Periodic Table.

In summary, the 'noble gas core shell' is inert under ambient conditions for the three light noble gases helium, neon, (argon), but chemically active for the three heavier congeners krypton, xenon, radon, and also for oganesson being predicted a semi-metallic semi-conductor (Mewes et al., 2019a); with an expected bandwidth of 1.5 eV, Og could even have a metallic appearance. Of course this would only be true if the short-lived nuclei would live very much longer.

The Heavy Early d-Block Elements Including the f-Block

The two sets of group-3 to group-4 elements, lanthanum to hafnium, and actinium to rutherfordium, are typical early (n−1)d-elements with a little admixture of ns. From cerium (group 4') to ytterbium (group 2'), and from protactinium (group 5') to nobelium (group 2'), some valence electrons can be variably stored in the "f-cellar" of the atomic cores. In addition 4f contributes to chemical bonding for cerium (and praseodymium) and 5f contributes to bonding for protactinium to plutonium (and americium, groups 8' and 9').

The most important theoretical aspect here is the non-uniform spatial contraction and energetic stabilization of the 4f5d shells vs. the 6sp shells, and of 5f6d vs. 7sp, as functions of the element number Z and the effective charge q of the atom in a compound: $\varepsilon(Z, q)$ and $r(Z, q)$. The 'comparatively simple' $\varepsilon(Z)$ behavior of 4sp vs. 3d was sketched in **Figure 5**. In the first two groups, the $(n-1)$d and $(n-2)$f shells are high-energy, diffuse Rydberg levels, hardly contributing to bonding in the majority of cases (Ji et al., 2015; see however: Levy and Hargittai, 2000; Wu et al., 2018a,b), which changes from group 3 onward.

How to define the f-block (i.e., including, or not, lanthanum and actinium or lutetium and lawrencium, or both pairs) within the series of early d-block elements is a still ongoing, standpoint-oriented controversy of philosophical, though of little chemical relevance (Edelstein et al., 2010; Morss et al., 2010; Pyykkö, 2019; Vernon, 2020b). Covalent contributions to the bonds of all these elements are dominantly based on the $(n-1)$d orbital overlap interactions. In period 6, the energy and radius of the 4f shell lends itself to additional covalent bond contribution in Ce(III) and in a few praseodymium compounds (Dolg and Moossen, 2015; Moossen and Dolg, 2016; Zhang et al., 2016; Hu et al., 2017; Smiles et al., 2020). Elsewise, the 4f level is too contracted, sitting inside the atomic core with outer $(n-1)p^6$ shell (**Figure 8**), but can store electrons thereby changing the oxidation state, the number of d-valence electrons and the ionic core radius (Dognon, 2014, 2017; Liu et al., 2017; Pathak et al., 2017; Lu et al., 2019). In particular, the bond-oriented σ and π components of the f-shell can better contribute to overlap-binding, while the δ and ϕ components remain more contracted. The *n*s orbital is still dominantly Rydberg-like, see $\boldsymbol{r}_{\max}$ in **Figure 8**.

Due to the radial node effect (meaning the correlation of small radius and no radial node of atomic orbitals, reviewed by Kaupp: Kaupp, 2006; Huheey et al., 2014; Wang et al., 2020), the 5f contraction along the series of elements occurs more slowly than 4f, so that f still contributes to the covalence of protactinium, uranium, neptunium and plutonium, and in special cases of thorium (potentially) and americium, too, as a rule of thumb (Morss et al., 2010; Neidig et al., 2013; Ortu et al., 2016; Liu et al., 2017; Vitova et al., 2017; Wilson et al., 2018). From the common chemical empirical point of view, the elements thorium, protactinium, uranium, neptunium, and plutonium are more akin to the lighter outer transition elements hafnium, tantalum, tungsten, rhenium, and osmium, than to their officially homologous inner transition elements cerium, praseodymium, neodymium, promethium, and samarium. Indeed, during the first century of periodic tables, i.e., until Glen Seaborg (Seaborg, 1946), the early actinoids resided in the d-block.

Also at the second beginning of the series of 5d and 6d elements (lutetium and lawrencium), the $(n-1)$d and *n*s orbitals play the dominant role. An interesting example of 6d-chemistry is lawrencium (Xu and Pyykkö, 2016). Despite the recent excitement that the spin-orbit coupled ground state of the chemically unbound free lawrencium atom is of p-type, $^2\mathrm{P}^{\mathrm{o}}_{1/2}$ $(5f^{14}6d^0 7s^2 7p^1)$, the chemistries of Lu and Lr are found to be of typical f^{14}-contracted d(s) type.

The Later d-Block Elements

The d-elements of periods 6 and 7 appear rather similar at first glance. However, the $6d^5/_2$ shell becomes relativistically scalar and spin-orbit destabilized and expanded, while the 7s½ shell is stabilized and contracted so that the (n+ℓ,n) rule of the chemical textbooks appears to hold for the first time in the d-block. This causes various changes in the bonding details. The 3d and 6d series differ from the pair of 4d and 5d series.

The di-metallic molecules M_2 in periods 4, 5, and 6 have a comparatively large number of bonding orbitals derived from the ligand-overlapping $(n-1)$d-shells. The *n*s orbitals play only a little role except when the electropositive metal atoms carry small or negative changes. As an example, the di-tungsten molecule may be symbolized by Lewis formula $|W{\equiv}W|$ and leading electron configuration $(\sigma_d^2\ \sigma_s^2\ \pi_d^4\ \delta_d^4)$, with four bonding molecular orbitals σ_d, σ_s, and π_d, and hardly any bonding orbitals δ_d (Many authors in the literature count the basically non-bonding δ orbitals as bonding, to get a higher bond order, see: Roos et al., 2007; Ruiperez et al., 2011; Li Manni et al., 2012; Sun et al., 2013; Singh et al., 2016; Chen et al., 2017). In the heaviest dimers, however, because of the $(n-1)$d-*n*s inversion in period 7 (**Figures 7**, **8**), some $(n-1)$d-type molecular orbital is replaced by an *n*s-type orbital. As a result, the di-seaborgium molecule is to be represented by Lewis formula $|\underline{\mathrm{Sg}}{\equiv}\mathrm{Sg}| \leftrightarrow |\mathrm{Sg}{\equiv}\underline{\mathrm{Sg}}|$ with leading electron configuration $(\sigma_s^2\ \pi_d^4\ \sigma_d^2\ \sigma_s^*2\ \delta_{d3/2}^2)$, where the non-bonding $\delta_{d5/2}^2$ pair is replaced by the antibonding molecular orbital σ_s^*. Thereby the bond order (now only three) and the vibrational force constant are reduced and the bond length is increased. Similar changes occur for all dimers of periods 6 and 7 from groups 4 to 8 (Wang et al., 2016).

In the case of the coinage metal dimers M_2 from group 11 (Cu_2, Ag_2, Au_2), the M–M single bond is due to interaction of $\sigma_{(n-1)d,ns}$ valence-hybrids between the polarized M-$(n-1)d^{10}$ closed shell cores. In Rg_2 however, the upper antibonding σ_{u-6d}^*2 orbital has changed its character due to the relativistic $6d^5/_2$ destabilization and 7s½ stabilization to dominantly $\sigma_{u,7s}^*2$ type, with remarkable changes of force constant, bond energy and charge and pair density distributions (Li et al., 2018).

Increased relevance of the *n*s valence orbital has also been verified in quantum calculations of various complexes of the period-7 transition elements such as $[MO_4]^{0,q-}$ and its thio-analogs $[MS_4]^{0,q-}$ (Huang et al., 2016, 2017; Hu et al., 2018). At the end of the d-series, the $6d_{5/2}$ shell is still energetically high enough to supply all electrons to form Rg-F bonds in $Rg^{7+}(6d_{3/2}^4\ 6d_{5/2}^0\ 7s_{1/2}^0)F_7$ while stoichiometric AuF_7 is still $Au^{5+}F_5{\cdot}F_2$ (Himmel and Riedel, 2007; Conradie and Ghosh, 2019).

The Early p-Block Elements, Including Group 12

The d-shell becomes chemically inert from group 12 onward. Only under exotic conditions can the d^{10} shell of mercury be oxidized, while this is predicted as easily possible in period 7 for copernicium, and possibly for nihonium. On the other hand, the 6s and 6p1/2 shells are remarkably stable for mercury, thallium and lead, and even more so for the heavier homologs, leading to an inert $6d^{10}7s^2$ core for flerovium.

As in the case of the s-block, scholars usually focus on aspects known from the upper part of the periodic table, that is, here on the *n*s and *n*p valence shells. Then, for the heavy members, only the relativistic stabilization and contraction of the $ns_{1/2}$ and $np_{1/2}$ shells (**Figures 7**, **8**) are discussed, whilst the destabilization and expansion of the upper $(n-1)d_{5/2}$ core shell is rarely considered. Zinc, cadmium and mercury, with beryllium and magnesium as their precursors, are divalent throughout, which also holds for the XM–MX compounds of beryllium (I) through mercury (I). On the other hand, higher valent species have sometimes been reported such as apparent zinc (III) complexes with a broken $3d^{10}$ shell, but were not generally accepted (Schlöder et al., 2012).

However, mercury (IV) compounds with broken $5d^{10}$ shell have been reported (albeit not yet confirmed) under cryogenic conditions or high pressure and were supported quantum-chemically (Wang et al., 2007; Botana et al., 2015; Miao et al., 2017; Gao et al., 2019; Pravica et al., 2019). Yet, mercury should not be included among the common transition elements, since all these higher-valent compounds are quite unstable in ambient conditions (Jensen, 2008).

The elements of groups 12 to 14 in period 7, namely copernicium, nihonium and flerovium (with lifetimes in the range of seconds) have electron configurations $(6d_{5/2}^4\ 7s^2\ 7p_{1/2}^{0-2})$. As elementary substances, copernicium would be a volatile metallic noble liquid similar to mercury, and flerovium would be a volatile, rather noble metal (Yakushev et al., 2014; Schädel, 2015; Steenbergen et al., 2017; Mewes et al., 2019b). Little is known of their chemistry. Small molecules of low valency such as CnO, NhH, or FlF_2 are similar to their lighter homologs, typically with slightly reduced bond strength (Liu et al., 2002; Demidov and Zaitsevskii, 2014, 2015).

An extreme chemical impact of scalar and spin-orbit relativistic effects occurs for the voltage of the mercury cell and in particular in lead batteries (Ahuja et al., 2011; Zaleski-Ejgierd and Pyykkö, 2011). Higher valences in period 7 were investigated by Ghosh and Conradie (2016). While HgF_4 is at most meta-stable, the $(n-1)d_{5/2}$ level of copernicium is sufficiently destabilized and the $ns_{1/2}$ sufficiently stabilized, so that CnF_4 becomes stable as D_{4h}-$Cn^{4+}(6d_{5/2}^4\ 7s^0)\ F_4$. In general, spin-orbit coupling weakens existing covalent bonding, because ligand field effects and spin-orbit effects perturb each other (Hafner et al., 1981), while here it induces bonding. A similar mechanism works six elements further, where the p-shell closure is delayed due to the destabilized $(n\text{-}1)p_{3/2}$ level and the stabilized $ns_{1/2}$ level, as described above. The d-shell closure happens in period 7 for flerovium, the $6d_{5/2}$ and $7s_{1/2}$ levels having moved down in energy (**Figure 7**). Eventually the 6d shell has become chemically inert, and the 7s-reluctant/inert-pair effect has grown. Consequently flerovium no longer has a raised valence as observed for roentgenium (VII) vs. gold (V), for copernicium (IV) vs. mercury (II) and possibly for nihonium (V) vs. thallium (III), but has instead the lowered valence of flerovium (II) vs. PbF_4 (Ghosh and Conradie, 2016).

The Late p-Block Elements

The light elements O, F, Ne with core-like $2s^2$ shell are strongly electronegative with low valences 2, 1, 0; all heavier late p-elements are less electronegative but with higher valences 5 to 7 of the nsp shell. The superheavy members $_{115}Mc$ to $_{118}Og$ are more electropositive with rather stable 7s½²7p½² and an active $7p^3/_2$ valence shell without a large gap to 8s½. Little is known, but unusual chemistry is to be expected.

The heavy elements of groups 15 to 18 have dominant valence electron configurations $(np_{3/2})^{1-4}$, while the $np_{1/2}^2$ and in particular the $ns_{1/2}^2$ shells become more and more core-like. The first ionization potential, the electron affinity, and consequently the electronegativity too, of $_{115}$Mc-$7p_{3/2}^1$ and $_{116}$Lv-$7p_{3/2}^2$ are remarkably small (livermorium has also a small second ionization potential). The moscovium mono-halides have a strongly ionic character (Borschevsky et al., 2015; Santiago and Haiduke, 2020). The elements below the metal-non-metal divide in **Figure 2**-right are of a metallic character. The p-series in period 7 is mostly metallic, with astatine expected to be a metal (Hermann et al., 2013) and last member oganesson is either a semiconductor (Mewes et al., 2019a) or a metalloid, depending on one's definition (Vernon, 2013), or a metal (Gong et al., 2019). Trombach et al. (2019) has summarized the sparse chemical speculations, based on pronounced reluctant-pair and spin-orbit coupling effects.

THE PERIODIC TABLE AS A BLINKER AS WELL AS AN EYE-OPENER

There is a long history in chemistry about substances and reactions regarded as possible or impossible, according to powerful stories in journals and text-books. They emerged because periodicity expectations and other theoretical models excluded, precluded or prescribed them, and they were advanced by earlier accidentally unsuccessful experimental efforts causing accepted narratives in the community. This is another example of how heavily empirical observations and non-observations are theory-laden in positive and negative senses. Many compounds are metastable under ambient conditions, but only very specific synthetic routes yield them with low internal energy so that they will not decay over the activation barrier as soon as they are formed. These cases need to be distinguished from basically instable compounds that can only be kept near 0 K and if separated from other molecules (such as in cold noble gas matrices, or in the vacuum of mass spectrometers, or in molecular beams), or that are forced together by high pressures. One may construct a Periodic Table for the classification of (meta)stable compounds, or of unstable compounds at low T, or of unstable compounds hold together by high p. The properties of the elements of a group may appear more similar, if compared under more different and exotic conditions.

Blinkered Expectations Finally Verified

Group 18: Noble Gas Compounds

The unsuccessful attempts in the early twentieth century to prepare noble gas compounds were reviewed by Chernick (1963) and by Laszlo and Schrobilgen (1988). The inertness of the noble gases "was preached so dogmatically wherever chemistry was taught that few chemists would spend their time trying to produce *impossible compounds."* The trends of valence at the ends of the 2nd vs. the later periods (namely 0 for Ne vs. 8 for Ar, Kr, Xe) are not consistent within the noble-gas group, and later turned out as unreliable (valences under ambient conditions are 0 for He and Ne; 1 and 2 for the border cases Ar and Kr; 6 or 8 for Xe; smaller for Rn; see Lozinšek et al., 2020; Rohdenburg et al., 2020). Partially correct experimental trials in the late 1920s and predictions by Pauling in the early 1930s were only reproducibly realized in the early 1960s. Extrapolations in the Periodic Table of both possibilities and impossibilities sometimes go wrong.

Group 17: Halogen Oxoacids

Similarly, while the perchlorates and periodates and their acids were long known, over a century passed between the first record of unsuccessful attempts to prepare *perbromic acid* (Watts, 1863) and its synthesis by Appelman in 1968 (see: Appelman, 1973). Greenwood and Earnshaw (Greenwood and Earnshaw, 1984 seq.; in particular 1998) later wrote that "The quest for perbromic acid and perbromates and the various reasons adduced for their apparent 'non-existence' make fascinating and salutary reading" including Pauling's and others' mispredictions (Herrell and Gayer, 1972). Another example is *hypofluorous acid.* In contrast to the customary heavier halogen oxyacids and their salts, no oxyacids of fluorine were known for a longtime. Thus, "chemists had pretty well-convinced themselves that no oxyacids of fluorine were ever likely to be isolated … [on the basis] of straightforward thermodynamic arguments." Only in 1971, HOF was isolated as a chemical compound by Studier and Appelman (see: Appelman, 1973) and also LiOF as a molecule by Andrews and Raymond (1971).

Group 16: Chalcogen Chains

The heavier chalcogens from sulfur onward are known to form chains such as –S–S–S– etc. Concerning oxygen, only the monoxides $_{/}\mathrm{O}_{\backslash}$, peroxides $_{/}\mathrm{O{-}O}^{/}$, and ozonides $-\mathrm{O}^{/}\mathrm{O}^{\backslash}\mathrm{O}$- (inorganic salts of O^-, O^{2-}, O_2^-, O_2^{2-}, O_3^- and organic compounds) are well-known. However, the simple hydrogen trioxide, H_2O_3, already proposed by Berthelot (1880), was prepared in 1994 (Cerkovnik and Plesničar, 1993) and found to be metastable below −40°C. The tetroxide, H_2O_4, was suggested by Mendeleev in 1895 and characterized below −125°C (Levanov et al., 2011). Cryogenic conditions enable the realization of chemists' fantasies.

Group 15: Pentachlorides, and Chains

The existence of penta-halides of P and Sb in contrast to N, As, and Bi was one of the grounds for Biron (1915) to develop the concept of secondary vertical periodicity. Several explanations were subsequently put forward. Eventually Seppelt (1976, 1977) synthesized $AsCl_5$ by irradiating a mixture of $AsCl_3$ and liquid Cl_2 with UV light at −105°C. However, $AsCl_5$ decomposes at temperatures above −50°C. Single molecules NF_5 and NCl_5 are less stable even near 0 K, if at all (Bettinger et al., 1998). This is another case for the floating borderline between common environmental and exotic conditions at low T (or high p). *Polynitrogen:* Long-known small inorganic and organic polynitrogen compounds are the azides, containing the energetic anionic N_3^- and radicalic $^\bullet N_3$ species. The synthesis of higher nitrogen polymers as HEDMs (High Energy Density Materials) was unsuccessful for many decades, thus most chemists doubted during a century that such allotropic species of nitrogen could exist. Finally, the pentazonium chain cation N_5^+ was synthesized by Christe et al. (1999), and a cyclic aromatic N_5^- pentazolate compound by Zhang et al. (2017). The elementary substances of the group 15 elements P to Bi are solid polymers under ambient conditions, while until recently nitrogen was only known as a dimeric gas. Predicted polymeric 'black nitrogen' phases are now established at high pressures and temperatures (Cheng et al., 2020; Ji et al., 2020; Laniel et al., 2020). The lightest member of group 15 is not that different, if very different conditions are compared.

Group 14: Oxoacids

Oxidation state IV is most common among group 4 and 14 elements, such as in the ubiquitous carbonates and silicates. Yet in 2012, Jespersen et al. (2012, p. 167, 180) wrote that "carbonic acid is too unstable to be isolated as a pure compound." Pure carbonic acid had been isolated and characterized since 1990. It was even possible to sublime and re-condense the solid. While the activation barrier of the exothermic monomolecular decay, $H_2CO_3 \rightarrow CO_2 + H_2O$, is as large as 2 eV, the process becomes auto-catalyzed by the water molecules (Hage et al., 1998; Loerting et al., 2000; Abramson et al., 2018).

Transition Groups 3–13

Lothar Meyer failed in the early 1860s (Meyer, 1864) with the chemical grouping of what we now call the transition elements. The vertical, horizontal, diagonal etc. similarity patterns are complex, and Mendeleev's success was bought by restraining the chemical view. The IUPAC (2012) and Connelly et al. (2005) defines the transition elements as the ones whose atoms may have a partially occupied d shell in their compounds, i.e., the nine groups 3–11. Group 3 elements have formally a d^1 shell only in less common oxidation state II (Meyer, 2014), and group 11 element silver has an incomplete d^8 shell only in less common oxidation state III. In contrast to the transition elements, the d-block elements are usually defined as comprising the 10 groups 3–12, where group 12 elements Zn, Cd, Hg have a closed d^{10} shell under ambient conditions. The inner transition elements are the 15 lanthanoids La to Lu and the 15 actinoids Ac to Lr, where the first ones (La, Ac) have an empty and chemically hardly active f^0 shell, and the last ones (Lu, Lr) have a closed and chemically hardly active f^{14} shell.

Groups 1 and 2: Higher Valences

As mentioned in the subsection on the s-block elements, the heavier alkali metals can be multiply oxidized under high pressure. It has been theoretically predicted that Fr may behave as a typical mono-valent s-block element, but also as a polyvalent p-block element, breaking the Periodic Rule under ambient conditions. The art of synthesis that finally decides about the expected and unexpected gaps mentioned above, has here still to achieve the definitive answers.

Periodically Unexpected Facts Finally Accommodated

Only a fraction of the properties of the elements can be highlighted in any simplistic structure of Periodic Tables. Chemical handicrafts, scientific practice and theory only 'incidentally' discover the non-periodic physical and chemical properties of the elements, including the fuzzy end of the Periodic Table.

Non-metal Diversity vs. Vertical Similarity Classification

Aside from the noble gases and the halogens, the remaining nonmetals are often regarded as being too solitary and diverse to be discussed holistically in vertical groups (**Figure 9**). Metals can be gauged by their low values of electronegativity (or ionization energy and electron affinity; Yoder et al., 1975) *and* by the appearance of comparably diffuse orbitals in their atomic valence shells leading to broad metallic orbital bands, which result in the typical properties of metallic substances and the near-continuous variety of metallic elements. For the nonmetals Zuckerman and Nachod opined (Steudel, 1977) that "The marvelous variety and infinite subtlety of the non-metallic elements, their compounds, structures and reactions, is not sufficiently acknowledged in the current teaching of chemistry." In fact the pre-halogen non-metals share more distinctive properties than any other class of elements. While the noble gases, as elemental substances, can be characterized by their invisibility and torpidity, and the halogens by their variegated appearance and acridity, the non-metallic pre-halogen elements exhibit the following characteristics: (i) being sandwiched between the strongly electronegative halogen nonmetals and the 'weakly (non)metallic' metalloids, their physical and chemical character is overall 'moderately non-metallic'; (ii) the elemental substances have a semi-metallic

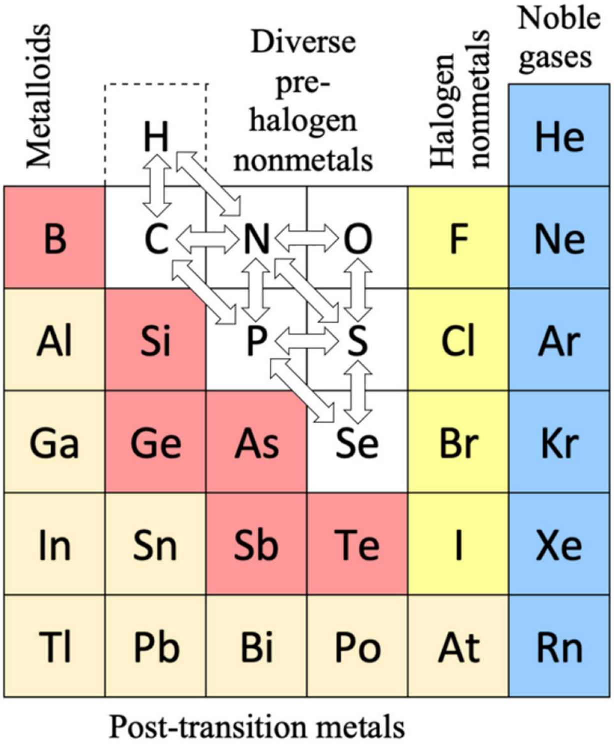

FIGURE 9 | Periodic table extract, showing the non-metallic elements: the groups of noble-gases (blue) and halogens (yellow), and the pre-halogen non-metals including H (white), which are chemically quite diverse, with pronounced vertical, horizontal and diagonal relationships[1] as recorded in the literature (Vernon, 2020). (No attempt is made here to quantify the strengths of the arrowed relations, nor are any cross-class relations considered). The post-transition metals (beige) and the "mysterious" metalloids (red) in between; Vernon (2013) are also displayed. Hydrogen (see footnote 2) in the dashed box, with 1s^1 configuration, has one electron, one hole, and a half-filled shell, with intermediate electronegativity (EN); it is often placed above the alkali metals with one valence electron but low EN; sometimes above the halogens with one valence hole but high EN; rarely (here, compare **Figure 2**, Cronyn, 2003) above carbon with half-filled (2sp)^4 shell and inter-mediate EN; and very rarely above boron which, like hydrogen, has one unpaired valence electron and very similar EN (Luchinskii and Trifonov, 1981).

---

[1] Many different stoichiometries and structures are known for each pair. For example, the nitrogen-oxygen pair with small electronegativity difference forms about two dozen of neutral and ionic molecular species $N_1O_4^q$ to $N_4O_1^q$. Among the less familiar ones are the peroxo-nitrate and ortho-nitrate anions $N(O)_2(O_2)^{1-}$ and NO_4^{3-}, the trinitramide $N(NO_2)_3$, a possible rocket propellant (Lucien, 1958; Schulz et al., 1993; Goldstein and Czapski, 1998; Rahm et al., 2011; Anusha et al., 2018), and nitrosyl-azide ON-N_3, a pale yellow solid stable below −50°C.

[graphitic carbon, black phosphorus (the most stable form under ambient conditions, now easily prepared by Tiouitchi et al., 2019), selenium] or colored (sulfur) or colorless (hydrogen, nitrogen, and oxygen) appearance and possess a brittle comportment if in solid phase (including N under high pressure: Cheng et al., 2020; Ji et al., 2020; Laniel et al., 2020); (iii) they show an overall tendency to form covalent compounds featuring localized and catenated bonds as chains, rings, and layers; (iv) in light of their relatively small atomic radii and sufficiently low ionization energy values, a capacity to form interstitial and refractory compounds (West, 1931; Goldschmidt, 1967; Glasson and Jayaweera, 1968; Wulfsberg, 2000); (v) prominent geological, biochemical (beneficial and toxic), organocatalytic, and energetic aspects (Akerfeldt and Fagerlind, 1967; Hutzinger, 1980; Dalko and Moisan, 2004; Nancharaiah and Lens, 2015; Vernon, 2020a).

Metalloids as In-Between Elements

The different chemistry of all metals in s-, f-, d-, and p-blocks, and that of the "typical" non-metals from the upper-right p-block has largely been appreciated since the advent of modern chemistry. On ontological grounds, anything not metal-like is a non-metal, and this would include the metalloids found in the p-block (Oderberg, 2007). Since the metalloids (Halb-Metall in German) behave predominantly as chemically weak non-metals, the question arises: should we treat them simply in the class of otherwise nondescript nonmetals (Newth, 1894; Friend, 1914); or as a class *sui generis*. This is a typical example of the dependence of classification on the particular context, for instance whether Po, At or Rn shall be counted among the metalloids (Stein, 1985; Hermann et al., 2013). Concerning electric properties, the two metalloids germanium and silicon enabled the establishment of the semi-conductor industry in the 1950s and the development of solid-state electronics from the early 1960s (Vernon, 2013). Remarkable is the 'diagonal' range, overlaying the dominantly vertical structure of the chemical similarity groups, which however is not that unique in consideration of the diagonal relationship between the 2nd and 3rd periods (Edwards and Sienko, 1983; Greenwood and Earnshaw, 1984 seq.), the knight's move relationships (Rayner-Canham, 2020), and the 'ᒪ' behavior of the closure of the p^6 and d^{10} shells (**Figure 1**, right).

Metallic Superconductivity at liquid-helium cooling temperatures and normal pressures was accidentally discovered in 1911 by Kamerlingh-Onnes for the metal that he could get in most pure form, Hg (Van Delft and Kes, 2010). In the following 75 years, many complex pure and doped substances were discovered that exhibit superconductivity within ca. 30 K; this appeared as an upper limit according to the Bardeen-Cooper-Schrieffer (BCS) theory. High-Temperature Superconductivity (HTS) seemed impossible, and pushing the temperature higher was the stuff of fantasy. The discovery of HTS in 1986 came as an unexpected surprise. Since then many complex $M^{III}M^{II}$-cuprate materials such as $(Y,La)Ba_2Cu_3O_7$ or $TlBaCaCu_{1.5}O_5$ have been discovered that become superconducting at liquid-nitrogen cooling temperatures (Kleiner and Buckel, 2016; Mangin and Rémi Kahn, 2017). Also materials becoming HTS under high pressure, including H_2S, were found. Serendipity was of great relevance, while periodic trends of the two or three metallic partners in the copper oxides and the iron pnictides were just of partial help (Nipan et al., 2000; Kitazawa, 2012).

An End of the Periodic Table, Facts and Fantasy

Numerological arguments on the number and arrangement of elements in the periods led E. Q. Adams (1911) to the early supposition that elements of atomic weight greater than ca. 256 would not exist. In modern-day terms this equates to elements $Z < 100$ with lifetimes $\tau > 1$ year, simple numbers Adams could not have dreamed of. Only astatine, radon, and francium are shorter-lived than $_{100}$fermium with $\tau \lesssim$ ¼ year. $_{99}$Es and $_{100}$Fm are the heaviest elements, which have been investigated in macroscopic quantities (Morss et al., 2010). For these heavy elements, bulk specimens such as crystals for x-ray structure analysis become quickly radiation damaged and may even evaporate. Accidentally, Adams' logically unfounded guess appears reasonable for today's practicing chemist. Remarkably, extrapolations of the non-relativistic structure of the periodicity of the upper part of the table into the region of 'non-existing' Z values of hundreds or thousands, violating published results on electronic structure of atoms up to the 170s (e.g., Pyykkö, 2011), are still published until these days.

SUMMARY AND CONCLUSIONS

Physicists noted that the set of universal natural constants is fine-tuned within a narrow range. Thereby it allowed for the big-bang cosmic history, with the formation of a System of Elements of specific abundances, the formation of our sun and earth with a 'habitable' temperature-pressure range for some time period, allowing for life and the development of brains that can understand the big-bang cosmic history, with an *anthropocentric view of semantic consistency*.

Conservation principles are basic in physics. Modern scientific chemistry began with Lavoisier's law of the conservation of mass in chemical reactions. In chemistry the basic *conserved abstract entities are the elements*. The chemical element number Z is the physical *natural linear ordering parameter*, where Z determines the nuclear charge number and the atomic electron number in neutral chemical species; Z also determines all terms in the quantum-chemical Hamiltonian. As far as we know, the chemical elements behave strictly according to relativistic quantum theory. No indication of a theoretical defect is known at present concerning the simulation and explanation of chemistry under common conditions in this physical framework (Pyykkö, 2012a,b; Hettema, 2017; Schwerdtfeger et al., 2020). Of course there are many unsolved technical problems of solving the physical equations correctly. However, simplifying *ad-hoc* rules (such as the Periodic Rule, sometimes called the 'Periodic law') may show 'exceptions from reality.' Further, the electronic behavior of heavy-element systems at *the bottom of the present Periodic Table* causes deviations from the apparent periodicity that is showing up for the lighter elements. Accidentally also the nuclear lifetimes decrease at the bottom of the present Periodic Table so that there would anyway be no chemistry in the common sense in an extended table.

Chemistry is dominantly governed by the behavior of the valence-active electrons with orbital energies significantly above those of the atomic core shells. Every element differs from the other by *different core and/or valence shells*. Since the complicated effective screened potentials in atomic ions Z^{q+} deviate appreciably from the symmetric hydrogenic Coulomb potential, there appear *large orbital energy gaps above just filled* $1s^2$*,* $2p^6$ *to* $5p^6$ *or* $6p^6$*, and* $3d^{10}$ *to* $5d^{10}$ *shells*. The gaps vary along the Z-row and with effective atomic charge $q+$, therefore a fuzzy repetition of elemental qualities occurs at various steps of ΔZ. This causally complex phenomenon of chemical periodicity exhibits a somewhat *accidental structural symmetry*. Different aspects can be graphically highlighted. Various Periodic Tables for use in chemistry display aspects of our chemical knowledge, mostly referring to *common environmental conditions*.

Only a section of our chemical experiences can be approximately represented by a two-dimensional table, either flat or bent or split. The full chemical space is high dimensional. But the variations of several important chemical properties of the elements, in particular valence and maximum oxidation numbers (Riedel and Kaupp, 2009; Higelin and Riedel, 2017), effective atomic radii, electronegativity and metallicity, along the periods and down the groups are significantly correlated among each other (Kornilov, 1965), so that *a two-dimensional display is particularly knowledge-economic*.

Incorporating fashionable and exciting experiences under cryogenic or high-pressure conditions such as in outer space or inside the earth adds to the irregularities in the two-dimensional tabular projections, 'deformed' into a regular grid. The complex variation of chemical behavior of the elements at the top and bottom of the periodic system gives some clues and insight on chemistry under non-standard conditions, at very low temperatures or very high pressures. In the chemical sciences a pragmatic view of reality may result in Periodic Tables that are different from the dogmatic tables advocated in the meta-sciences.

The more or less approximate repetition of chemical properties along the array of elements ordered by their ordinal numbers Z is coupled to the closure and stabilization of the valence shells upon increasing Z. The s valence shell at the beginning of a period changes to the d(s) valence shell of the transition elements. The d valence shells in the two lowest periods are not drastically changed upon $(f)^{14}$ shell filling (except for the lanthanoid and actinoid contractions, and d-f mixing for the early actinoids Pa to Pu). Upon $(d)^{10}$ shell closure, the valence shell changes over to s(p) and then to (s)p type. The biggest change of orbital symmetry, energy, and radius of the valence shell occurs upon the *(sp)*^{8} *shell closure, which determines the periodicity*, its fix points and the property jumps from the halogens to the noble gases to the alkali metals.

Simplification is inherent in any periodic table. Yet the basic electronic outer-core and valence shells should be represented qualitatively correctly, concerning the relevant shell types, their electronic populations (see second line of **Figure 6**), *energies and radii* (see **Figures 7**, **8**), which are both needed to understand the chemistry of the elements. If one wants to explain the structure of the Periodic System with the help of the orbital model, *two rules are inevitable for the orbital orders* in period n: for groups 0 and 1 $(n{-}1)p^6 < ns < np < (n{-}1)d < (n{-}2)f$; the nearly inverted rule for the majority of groups 4 or 5 to 18, $(n{-}1)p^6 < (n{-}2)f < (n{-}1)d < ns < np$; in between the d and f orbital collapses occur. *Free atoms in a physical vacuum and bonded atoms in chemical substances* are different objects. An atomic shell is chemically active under common conditions, if of intermediate energy and of intermediate radius. *Diffuse Rydberg orbitals* (see footnote 6) are important in atomic and molecular spectroscopy, they have some relevance for metallic band formation, but they are less important for covalent bonding. Conversely, *the 4f and later 5f orbitals are too small* in general, in the majority of cases, for covalent interaction [except for cerium, praseodymium, and thorium (?) to americium, in particular] but their energies are sufficient to support variable oxidation states.

First order rules or approximations can map the broad contours of the situation in chemistry. That said, the primogenic-kainosymmetric peculiarities at the top of the periodic system, the horizontal and vertical pseudo-periodicities over its body, and the modifications at the bottom due to both larger n and ℓ values and relativity, create a subtle and nuanced richness of chemistry that may not necessarily be encompassed by simple generalizations. Further experimental-chemical and theoretical-computational researches into the behavior of the full plethora of compounds of the elements remains required (Restrepo, 2018 has estimated the number of energetically stable chemical compounds as $>10^{60}$, while chemists have so far explored only a negligible fraction of this huge chemical space), such as those that will follow in this issue.

AUTHOR CONTRIBUTIONS

All authors have written the manuscript and are responsible for the content.

FUNDING

This work was financially supported by the National Natural Science Foundation of China (Grant Nos. 21590792, 91645203, and 21433005).

ACKNOWLEDGMENTS

WHES thanks for hospitality at Tsinghua Beijing and Siegen Universities. Discussions with R. Berger, S. Druzhinin, G. Frenking, E. A. Goodilin, R. Jones, M. Kaupp, M. V. Kurushkin, M. Leach, C. Mans, S. Riedel, E. Scerri, P. Schwerdtfeger, P. Stewart and the reviewers are gratefully acknowledged.

REFERENCES

Abramson, E. H., Bollengier, O., Brown, J. M., Journaux, B., Kaminsky, W., and Pakhomova, A. (2018). Carbonic acid monohydrate. *Am. Mineral.* 103, 1468–1472. doi: 10.2138/am-2018-6554

Adams, E. Q. (1911). A modification of the periodic table. *J. Am. Chem. Soc*. 33, 684–688. doi: 10.1021/ja02218a004

Ahuja, R., Blomqvist, A., Larsson, P., Pyykkö, P., and Zaleski-Ejgierd, P. (2011). Relativity and the lead-acid battery. *Phys. Rev. Lett*. 106:018301. doi: 10.1103/PhysRevLett.106.018301

Akerfeldt, S., and Fagerlind, L. (1967). Selenophosphorus compounds as powerful cholinesterase inhibitors. *J. Med. Chem*. 10, 115–116. doi: 10.1021/jm00313a032

Andrews, L., and Raymond, J. I. (1971). Matrix infrared spectrum of of and detection of LiOF. *J. Chem. Phys*. 55, 3078–3086. doi: 10.1063/1.1676549

Anusha, M. B., Shivanna, N., Kumar, G. P., and Anilakumar, K. R. (2018). Efficiency of selected food ingre-dients on protein efficiency ratio, glycemic index and *in vitro* digestive properties. *J. Food Sci. Technol*. 55, 1913–1921. doi: 10.1007/s13197-018-3109-y

Appelman, E. H. (1973). Nonexistent compounds - two case histories. *Acc. Chem. Res*. 6, 113–117. doi: 10.1021/ar50064a001

Arunan, E., Desiraju, G. R., Klein, R. A., Sadlej, J., Scheiner, S., Alkorta, I., et al. (2011). Definition of the hydrogen bond. *Pure Appl. Chem*. 83, 1637–1641. doi: 10.1351/PAC-REC-10-01-02

Autschbach, J. (2012). Orbitals: some fiction and some facts. *J. Chem. Educ*. 89, 1032–1040. doi: 10.1021/ed200673w

Ball, P. (2019). On the edge of the periodic table. *Nature* 565, 552–555. doi: 10.1038/d41586-019-00285-9

Ballhausen, C. J. (1962). *Introduction to Ligand Field Theory*. New York, NY: McGraw-Hill.

Baumhauer, H. (1870). *Die Beziehungen Zwischen dem Atomgewichte und der Natur der Chemischen Elemente*. Braunschweig: Vieweg.

Bayley, T. (1882). On the connection between the atomic weight and the chemical and physical properties of elements. *Phil. Mag. Ser*. 13, 26–37. doi: 10.1080/14786448208627140

Béguyer de Chancourtois, A. E. (1862/3). *Vis Tellurique*. Paris (See: Leach, 1999–2020).

Berthelot, M. (1880). Compt. *Rend* 90:656.

Bettinger, H. F., Von, R., Schleyer, P., and Schaefer, H. F. III. (1998). NF$_5$ - viable or not? *J. Am. Chem. Soc*. 120, 11439–11448. doi: 10.1021/ja9813921

Biltz, W. E. (1934). *Raumchemie der Festen Stoffe*. Leipzig: Voss.

Biron, E. V. (1915). The phenomenona of secondary periodicity (in Russian). *Zh. Russ. Fiz. Khim. Obshch*. 47, 964–988.

Bohr, N. (1922). *Drei Aufsätze über Spektren und Atombau*. Braunschweig: Vieweg.

Bohr, N., and Coster, D. (1923). Röntgenspektren und periodisches system der elemente. *Z. Phys*. 12, 342–374. doi: 10.1007/BF01328104

Borschevsky, A., Pasteka, L. F., Pershina, V., Eliav, E., and Kaldor, U. (2015). Ionization potentials and electron affinities of the superheavy elements 115–117 and their sixth-row homologues Bi, Po, and At. *Phys. Rev. A* 91:020501. doi: 10.1103/PhysRevA.91.020501

Botana, J., Wang, X.-L., Hou, C.-J., Yan, D.-D., Lin, H.-Q., Ma, Y., et al. (2015). Mercury under pressure acts as a transition metal: calculated from first principles. *Angew. Chem. Int. Ed*. 54, 9280–9283. doi: 10.1002/anie.2015 03870

Brock, W. H. (1992). *The Fontana History of Chemistry*. London: Harper Collins.

Buijse, M. A., and Baerends, E.-J. (1990). Analysis of nondynamic correlation in the metal-ligand bond - pauli repulsion and orbital localization in MnO$_4$-. *J. Chem. Phys*.? 93,? 4129–4141. doi: 10.1063/1.458746

Cao, C.-S., Hu, H.-S., Li, J., and Schwarz, W. H. E. (2019). Physical origin of chemical periodicities in the system of elements. *Pure Appl. Chem*. 91, 1969–1999. doi: 10.1515/pac-2019-0901

Carnelley, T. (1886). Suggestions as to the cause of the periodic Law, and the nature of the chemical elements. *Chem. News* 53, 157–159, 169–172, 183–186, 197–200.

Cederbaum, L. S., Schirmer, J., Domcke, W., and Von Niessen, W. (1977). Complete breakdown of quasi-particle picture for inner valence-electrons. *J. Phys. B* 10, L549–L553. doi: 10.1088/0022-3700/10/15/001

Cerkovnik, J., and Plesničar, B. (1993). Characterization and reactivity of hydrogen trioxide (HOOOH), a Reactive intermediate formed in the low-temperature ozonation of 2-ethylanthrahydroquinone. *J. Am. Chem. Soc*. 115, 12169–12170. doi: 10.1021/ja00078a067

Chandrasekara, A., Joshib, M., and Ghanty, T. K. (2019). On the position of La, Lu, Ac and Lr in the periodic table: a perspective. *J. Chem. Sci*. 131:122. doi: 10.1007/s12039-019-1713-7

Chemey, A. T., and Albrecht-Schmitt, T. E. (2019). Evolution of the periodic table through the synthesis of new elements. *Radiochim. Acta* 107, 771–801. doi: 10.1515/ract-2018-3082

Chen, Y., Hasegawa, J.-Y., Yamaguchi, K., and Sakaki, S. (2017). A coordination strategy to realize a sextuply-bonded complex. *Phys. Chem. Chem. Phys*. 19, 14947–14954. doi: 10.1039/C7CP00871F

Cheng, P., Yang, X., Zhang, X., Wang, Y., Shuqing Jiang, S.-Q., and Goncharov, A. F. (2020). Polymorphism of polymeric nitrogen at high pressures. *J. Chem. Phys*. 152:244502. doi: 10.1063/5.0007453

Chernick, C. L. (1963). Chemical compounds of the noble gases. *Rec. Chem. Progr*. 24, 139–155.

Christe, K. O., Wilson, W. W., Sheehy, J. A., and Boatz, J. A. (1999). N$_5^+$: a novel homoleptic poly-nitrogen ion as a high energy density material. *Angew. Chem. Int. Ed*. 38, 2004–2009.

Clark, J. D. (1933). A new periodic chart. *J. Chem. Educ*. 10, 675–677. doi: 10.1021/ed010p675

Clark, J. D. (1949). Table of the elements. *Life Mag*. 16, 82–83.

Clark, J. D. (1950). A modern periodic chart of chemical elements. *Science* 111, 661–663. doi: 10.1126/science.111.2894.661

Condon, E. U., and Shortley, G. H. (1935). *The Theory of Atomic Spectra*. London: Cambridge University Press.

Connelly, N. G., Hartshorn, R. M., Damhus, T., and Hutton, A. T. (2005). *Nomenclature of Inorganic Chemistry - IUPAC Recommendations 2005 (Red Book III)*. Cambridge: Royal Society of Chemistry.

Connerade, J. P. (1991). Orbital collapse in extended homologous sequences. *J. Phys. B* 24, L109–L115. doi: 10.1088/0953-4075/24/5/001

Conradie, J., and Ghosh, A. (2019). Theoretical search for the highest valence states of the coinage metals: roentgenium heptafluoride may exist. *Inorg. Chem*. 58, 8735–8738. doi: 10.1021/acs.inorgchem.9b01139

Cronyn, M. W. (2003). The proper place for hydrogen in the Periodic Table. *J. Chem. Educ*. 80, 947–951. doi: 10.1021/ed080p947

Da Costa Andrade, E. N. (1958). The birth of the nuclear atom. *Proc. R. Soc. Lond. A* 244, 437–455. doi: 10.1098/rspa.1958.0053

Dalko, P. I., and Moisan, L. (2004). In the golden age of organocatalysis. *Angew. Chem. Int. Ed*. 43, 5138–5175. doi: 10.1002/anie.200400650

Demidov, Y., and Zaitsevskii, A. (2015). A comparative study of molecular hydroxides of element 113 (I) and its possible analogs: *Ab initio* electronic structure calculations. *Chem. Phys. Lett*. 638, 21–24. doi: 10.1016/j.cplett.2015.08.017

Demidov, Y. A., and Zaitsevskii, A. V. (2014). Simulation of chemical properties of superheavy elements from the island of stability. *Rus. Chem. Bul. Int. Ed*. 63, 1647–1655. doi: 10.1007/s11172-014-0650-3

Desclaux, J. P. (1973). Relativistic dirac-fock expectation values for atoms with Z = 1 to Z = 120. *At. Data Nucl. Data Tabs* 12, 311–406. doi: 10.1016/0092-640X(73)90020-X

Döbereiner, J. W. (1829). Versuch zu einer gruppierung der elementaren stoffe nach ihrer analogie. *Poggendorffs Ann. Phys. Chem*. 15, 301–315. doi: 10.1002/andp.18290910217

Dognon, J.-P. (2014). Theoretical insights into the chemical bonding in actinide complexes. *Coord. Chem. Rev*. 266–267, 110–122. doi: 10.1016/j.ccr.2013.11.018

Dognon, J.-P. (2017). Electronic structure theory to decipher the chemical bonding in actinide systems. *Coord. Chem. Rev*. 344, 150–162. doi: 10.1016/j.ccr.2017.02.003

Dolg, M., and Moossen, O. (2015). Cerium oxidation state and covalent 4f-orbital contributions in the ground state of bis(eta(8)-pentalene)cerium. *J. Organomet. Chem*. 794, 17–22. doi: 10.1016/j.jorganchem.2015.05.063

Dong, X., Oganov, A. R., Goncharov, A. F., Stavrou, E., Lobanov, S., Saleh, G., et al. (2017). A stable compound of helium and sodium at high pressure. *Nat. Chem*. 9, 440–445. doi: 10.1038/nchem.2716

Dong, X., Oganov, A. R., Qian, G., Zhou, X.-F., Zhu, Q., and Wang,. H.-T. (2015). How do chemical properties of the atoms change under pressure? *arXiv preprint* arXiv: 1503.00230.

Düllmann, C. E. (2017). Studying chemical properties of the heaviest elements. *Nucl. Phys. News* 27, 14–20. doi: 10.1080/10619127.2017.1280333

Dumas, J.-B. A. (1828). *Traité de Chimie Appliquée aux art,* Vol. 1. Paris: Béchet.

Edelstein, N. M., Fuger, J., Katz, J. J., and Morss, L. R. (2010). "Summary and comparison of properties of the actinide and transactinide elements," in *The Chemistry of the Actinide and Transactinide Elements*, eds L. R. Morss, N. Edelstein, J. Fuger, and J. J. Katz (Dordrecht: Springer), 1753–1835.

Edwards, P. P., and Sienko, M. J. (1983). On the occurrence of metallic character in the periodic table of the elements. *J. Chem. Educ.* 60, 691–696. doi: 10.1021/ed060p691

Esteban, C., García López, R. J., Herrero, A., and Sánchez, F. (2004). *Cosmochemistry: The Melting Pot of the Elements*. Cambridge: Cambridge University Press.

Fernández, I., Holzmann, N., and Frenking, G. (2020). The valence orbitals of the alkaline-earth atoms. *Chemistry* 26, 14194–14210. doi: 10.1002/chem.202002986

Fricke, B. (1975). Superheavy elements. A prediction of their chemical and physical properties. *Struct. Bond*. 21, 89–144. doi: 10.1007/BFb0116498

Fricke, B., and Waber, J. T. (1971). Theoretical predictions of the chemistry of superheavy elements. continuation of the periodic table up to Z=184. *Actin. Rev*. 1, 433–485.

Friend, J. N. (1914). *A Text-Book of Inorganic Chemistry, Vol. 1*. London: Charles Griffin.

Fromm, K. M. (2020) Chemistry of alkaline earth metals: it is not all ionic and definitely not boring! *Coord. Chem. Rev*. 408:213193. doi: 10.1016/j.ccr.2020.213193

Gade, L. H. (2019). Chemical valency: its impact on the proposal of the periodic system and some thoughts about its current significance. *Struct. Bond*. 181, 59–80. doi: 10.1007/430_2019_40

Gao, C., Hu, S.-X., Han, H.-X., Guo, G.-N., Suo, B.-B., and Zou, W.-L. (2019). Exploring the electronic structure and stability of HgF_6: exact 2-component (X2C) relativistic DFT and NEVPT2 studies. *Comput. Theor. Chem*. 1160, 14–18. doi: 10.1016/j.comptc.2019.05.007

Ghibaudi, E., Regis, A., and Roletto, E. (2013). What do chemists mean when they talk about elements? *J. Chem. Educ*. 90, 1626–1631. doi: 10.1021/ed3004275

Ghosh, A., and Conradie, J. (2016). The valence states of copernicium and flerovium. *Eur. J. Inorg. Chem*. 18, 2989–2992. doi: 10.1002/ejic.201600146

Giuliani, S. A., Matheson, Z., Nazarewicz, W., Olsen, E., Reinhard, P.-G., Sadhukhan, J., et al. (2019). Colloquium: superheavy elements: oganesson and beyond. *Rev. Mod. Phys*. 91:011001. doi: 10.1103/RevModPhys.91.011001

Glasson, D. R., and Jayaweera, S. A. A. (1968). Formation and reactivity of nitrides I. Review and introduction. *J. Appl. Chem.* 18, 65–77. doi: 10.1002/jctb.5010180301

Glasstone, S. (1946 seq.). *Textbook of Physical Chemistry*. New York, NY: Van Nostrand.

Gmelin, L. (1843). *Handbuch der Chemie*, *3rd Edn, Vol*. 1. Heidelberg: Karl Winter.

Godovikov, A. A., and Hariya, Y. (1987). The connection between the properties of elements and compounds, mineralogical-crystallochemical classification of elements. *J. Fac. Sci. Hokkaido Univ. Ser. IV* 22, 357–385.

Goeppert Mayer, M. (1941). Rare-earth and transuranic elements. *Phys. Rev*. 60, 184–187. doi: 10.1103/PhysRev.60.184

Goesten, M. G., Rahm, M., Bickelhaupt, F. M., and Hensen, E. J. M. (2017). Cesium's off-the-map valence orbital. *Angew. Chem. Int. Ed*. 56, 9772–9776. doi: 10.1002/anie.201704118

Goldschmidt, H. J. (1967). *Interstitial Alloys*. London: Butterworths.

Goldstein, S., and Czapski, G. (1998). Formation of peroxynitrate from the reaction of peroxynitrite with CO_2: evidence for carbonate radical. *J. Am. Chem. Soc*. 120, 3458–3463. doi: 10.1021/ja9733043

Gombás, P., and Szondy, T. (1970). *Solutions of the Simplified Self-Consistent Field for All Atoms of the Periodic System of Elements from Z=2 to Z=92*. London: Hilger.

Gong, S., Wu, W., Wang, F. Q., Liu, J., Zhao, Y., Shen, Y.-H., et al. (2019). Classifying superheavy elements by machine learning. *Phys. Rev. A* 99:022110. doi: 10.1103/PhysRevA.99.022110

Gordin, M. D. (2004). *A Well-Ordered Thing: Dmitrii Mendeleev and the Shadow of the Periodic Table*. New York, NY: Basic Books.

Gordin, M. D. (2019). Ordering the elements. *Science* 363, 471–473. doi: 10.1126/science.aav7350

Greenwood, N. N., and Earnshaw, A. (1984). *Chemistry of the Elements*. Oxford: Pergamon.

Grimes, R. N. (1983). Letter on: chemistry a la plato. *Mosaic* 14:37.

Grochala, W. (2018). On the position of helium and neon in the periodic table of elements. *Found. Chem*. 20,191–207. doi: 10.1007/s10698-017-9302-7

Grochala, W. (2020). Watch the colors: or about qualitative thinking in chemistry. *Found. Chem*. doi: 10.1007/s10698-020-09369-1

Guyton de Morveau, L. B. (1782). Sur les dénominations chymiques, la necéssité d'en perfectionner le système et le régles pour y parvenir. *J. Phys. Hist. Nat. Arts* 19, 370–382.

Habashi, F. (2009). Metals: typical and less typical, transition and inner transition. *Found. Chem*. 12, 31–39. doi: 10.1007/s10698-009-9069-6

Hackh, I. W. D. (1924). *Das Synthetische System der Atome*. Hamburg: Hephaestos.

Hafner, P., Habitz, P., Ishikawa, Y., Wechsel-Trakowski, E., and Schwarz, W. H. E. (1981). Quasi-relativistic model-potantial approach. Spin-orbit effects on energies and geometries of several di- and tri-atomic molecules. *Chem. Phys. Lett*. 80, 311–315. doi: 10.1016/0009-2614(81)80115-7

Hage, W., Liedl, K. R., Hallbrucker, A., and Mayer, E. (1998). Carbonic acid in the gas phase and its astrophysical relevance. *Science* 279, 1332–1335. doi: 10.1126/science.279.5355.1332

Heisenberg, W. (1959). *Physik und Philosophie.* Stuttgart: Hirzel.

Herman, F., and Skillman, S. (1963). *Atomic Structure Calculations*. Upper Saddle River, NJ: Prentice-Hall.

Hermann, A., Hoffmann, R., and Ashcroft, N. W. (2013). Condensed astatine: monatomic and metallic. *Phys. Rev. Lett.* 111:116404. doi: 10.1103/PhysRevLett.111.116404

Herrell, A. Y., and Gayer, K. H. (1972). The elusive perbromates. *J. Chem. Educ*. 49, 583–586. doi: 10.1021/ed049p583

Herzberg, G. (1937). *Atomic Spectra and Atomic Structure*. New York, NY: Prentice Hall.

Hettema, H. (2017). *The Union of Chemistry and Physics*. Cham: Springer International.

Hettema, H., and Kuipers, T. A. F. (1988). The periodic table – its formalization, status, and relation to atomic theory. *Erkenntnis* 28, 387–408.

Higelin, A., and Riedel, S. (2017). "High oxidation states in transition metal fluorides," in *Progress in Fluorine Science, Modern Synthesis Processes and Reactivity of Fluorinated Compounds,* eds H. Groult, F. R. Leroux, and A. Tressaud (Amsterdam: Elsevier), 561–586.

Himmel, D., and Riedel, S. (2007). After 20 years, theoretical evidence that "AuF_7" is actually $AuF_5 \cdot F_2$. *Inorg. Chem*. 46, 5338–5342. doi: 10.1021/ic700431s

Hu, S.-X., Jian, J.-W., Su, J., Wu, X., Li, J., and Zhou, M.-F. (2017). Pentavalent lanthanide nitride-oxides: NPrO and NPrO− complexes with N≡Pr triple bonds. *Chem. Sci*. 8, 4035–4043. doi: 10.1039/C7SC00710H

Hu, S.-X., Li, W.-L., Lu, J.-B., Bao, J. L., Yu, H. S., Truhlar, D. G., et al. (2018). On the upper limits of oxidation states in chemistry. *Angew. Chem. Int. Ed*. 57, 3242–3245. doi: 10.1002/anie.201711450

Huang, W., Jiang, N., Schwarz, W. H. E., Yang, P., and Li, J. (2017). Diversity of chemical bonding and oxidation states in MS_4 molecules of group 8 elements. *Chem. Eur. J*. 23, 10580–10589. doi: 10.1002/chem.201701117

Huang, W., Xu, W. H., Schwarz, W. H. E., and Li, J. (2016). On the highest oxidation states of metal elements in MO_4 molecules (M = Fe, Ru, Os, Hs, Sm, and Pu). *Inorg. Chem*. 55, 4616–4625. doi: 10.1021/acs.inorgchem.6b00442

Huheey, J. E., Keiter, E. A., and Keiter, R. L. (2014). "Inorganic chemistry: principles of structure and reactivity, 5th Edn," in *Periodizität und Fortgeschrittene Aspekte der Chemischen Bindung,* eds R. German, C. H. Steudel, and M. Kaupp (Berlin: Walter de Gruyter).

Hutzinger, O. (ed.). (1980) *The Handbook of Environmental Chemistry. Vol. 1-A. The Natural Environment and the Biogeochemical Cycles*. Berlin: Springer.

Ihde, A. J. (1964). *The Development of Modern Chemistry*. New York, NY: Harper and Row.

Imyanitov, N. S. (2016). Spiral as the fundamental graphic representation of the periodic law. Blocks of elements as the autonomic parts of the periodic system. *Found. Chem*. 18, 153–173. doi: 10.1007/s10698-015-9246-8

Imyanitov, N. S. (2019a). Does the period table appear doubled? Two variants of division of elements into two subsets. Internal and secondary periodicity. *Found. Chem*. 21, 255–284. doi: 10.1007/s10698-018-9321-z

Imyanitov, N. S. (2019b). Periodic law: new formulation and equation description. *Pure Appl. Chem*. 91, 2007–2021. doi: 10.1515/pac-2019-0802

IUPAC (2012) *Compendium of Chemical Terminology – Gold's Book*. Version 2.3.2 2012-08-19. Available online at: goldbook.iupac.org/

IUPAC (2015). *Periodic Table – Archives (1999–2018)*. Available online at: iupac.org/wp-content/uploads/2015/09/ IUPAC_Periodic_Table-1May13.pdf

Janet, C. (1930). *Concordance de 1'Arrangement Quantique de Base Électrons Planétaires des Atomes avec la Classification Scalariforme Hélicoïdale des Éléments Chimiques*. Beauvais; Imp. Dept. de l'Oise.

Jensen, W. B. (1982). The positions of lanthanum (actinium) and lutetium (lawrencium) in the periodic table. *J. Chem. Educ*. 59, 634–636. doi: 10.1021/ed059p634

Jensen, W. B. (1986). Classification, symmetry and the periodic table. *Comp. Math. Appl. B* 12, 487–510. doi: 10.1016/B978-0-08-033986-3.50038-0

Jensen, W. B. (2003). The place of zinc, cadmium, and mercury in the periodic table. *J. Chem. Educ*. 80, 952–961. doi: 10.1021/ed080p952

Jensen, W. B. (2008). Is mercury now a transition element? *J. Chem. Educ*. 85, 1182–1183. doi: 10.1021/ed085p1182

Jensen, W. B. (2015). The positions of lanthanum (actinium) and lutetium (lawrencium) in the periodic table: an update. *Found. Chem*. 17, 23–31. doi: 10.1007/s10698-015-9216-1

Jespersen, N. D., Brady, J. E., and Hyslop, A. (2012). *Chemistry: The Molecular Nature of Matter,* 6th Edn. New York, NY: John Wiley.

Ji, C., Adeleke, A. A., Yang, L., Wan, B., Gou, H., Yao, Y., et al. (2020). Nitrogen in black phosphorus structure. *Sci. Adv*. 6:eaba9206. doi: 10.1126/sciadv.aba9206

Ji, W.-X., Xu, W., Schwarz, W. H. E., and Wang, S.-G. (2015). Ionic bonding of lanthanides, as influenced by d- and f-atomic orbitals, by core–shells and by relativity. *J. Comput. Chem*. 36, 449–458. doi: 10.1002/jcc.23820

Jones, B. W. (2010). *Pluto: Sentinel of the Outer Solar System*. Cambridge: Cambridge University Press.

Jørgensen, C. K. (1969). *Oxidation Numbers and Oxidation States*. Berlin: Springer.

Kaji, M., Kragh, H., and Palló, G. (2015). *Early Responses to the Periodic System*. Oxford: Oxford University Press.

Karol, P. J. (2002). The mendeleev-seaborg periodic table: through Z = 1138 and beyond. *J. Chem. Educ*. 79, 60–63. doi: 10.1021/ed079p60

Kaupp, M. (2006). The role of radial nodes of atomic orbitals for chemical bonding and the periodic table. *J. Comput. Chem*. 2006, 320–325. doi: 10.1002/jcc.20522

Keserü, G. M., Soós, T., and Kappe, C. O. (2014). Anthropogenic reaction parameters – the missing link between chemical intuition and the available chemical space. *Chem. Soc. Rev*. 43, 5387–5399. doi: 10.1039/C3CS60423C

Kholodenko, A. L., and Kauffman, L. H. (2019). How the modified Bertrand theorem explains regularities of the periodic table I. From conformal invariance to Hopf mapping. *arXiv preprint* arXiv:190605278.

Kitazawa, K. (2012). Superconductivity: 100th anniversary of its discovery and its future. *Jpn. J. Appl. Phys*. 51:010001. doi: 10.7567/JJAP.51.010001

Kleiner, R., and Buckel, W. (2016). *Superconductivity. An Introduction, 3rd Edn*. Weinheim: Wiley-VCH.

Kohout, M., and Savin, A. (1996). Atomic shell structure and electron numbers. *Int. J. Quant. Chem*. 60, 875–882.

Kornilov, I. I. (1965). Recent developments in metal chemistry. *Russ. Chem. Rev*. 34, 31–46. doi: 10.1070/RC1965v034n01ABEH001403

Kurushkin, M. (2017). Building the periodic table based on the atomic structure. *J. Chem. Educ*. 94, 976–979. doi: 10.1021/acs.jchemed.7b00242

Kurushkin, M. (2020). Helium's placement in the periodic table from a crystal structure viewpoint. *IUCr J*. 7, 577–578. doi: 10.1107/S2052252520007769

Kutzelnigg, W. (1984). Chemical bonding in higher main group elements. *Angew. Chem. Int. Ed*. 23, 272–295. doi: 10.1002/anie.198402721

Laniel, D., Winkler, B., Fedotenko, T., Pakhomova, A., Chariton, S., Milman, V., et al. (2020). High-pressure polymeric nitrogen allotrope with the black phosphorus structure. *Phys. Rev. Lett*. 124:216001. doi: 10.1103/PhysRevLett.124.216001

Laszlo, P., and Schrobilgen, G. J. (1988). One or several pioneers - the discovery of noble-gas compounds. *Angew. Chem. Int. Ed*. 100, 1479–489. doi: 10.1002/anie.198804791

Latter, R. (1955). Atomic energy levels for the thomas-fermi and thomas-fermi-dirac potential. *Phys. Rev*. 99, 510–519. doi: 10.1103/PhysRev.99.510

Layzer, D. (1959). On a screening theory of atomic spectra. *Ann. Phys*. 8, 271–296. doi: 10.1016/0003-4916(59)90023-5

Leach, M. R. (1999–2020). *Internet Database of Periodic Tables*. Available online at: www.meta-synthesis.com/webbook/35_pt/pt_database.php (accessed Octocber, 10 2020).

Leach, M. R. (2013). Concerning electronegativity as a basic elemental property and why the periodic table is usually represented in its medium form. *Found. Chem*. 15, 13–29. doi: 10.1007/s10698-012-9151-3

Leal, W., and Restrepo, G. (2019). Formal structure of periodic system of elements. *Proc. R. Soc. A* 475:20180581. doi: 10.1098/rspa.2018.0581

Levanov, A. V., Sakharov, D. V., Dashkova, A. V., Antipenko, E. E., and Lunin, V. V. (2011). Synthesis of hydrogen polyoxides H_2O_4 and H_2O_3 and their characterization by Raman spectroscopy. *Eur. J. Inorg. Chem*. 2011, 5144–5150. doi: 10.1002/ejic.201100767

Levine, I. N. (1970). *Quantum Chemistry*. Boston, MA: Allyn and Bacon, Pearson.

Levy, J. B., and Hargittai, M. (2000).Unusual dimer structures of the heavier alkaline earth dihalides: a density functional study. *J. Phys. Chem. A* 104, 1950–1958. doi: 10.1021/jp994339n

Li Manni, G., Dzubak, A. L., Mulla, A., Brogden, D. W., Berry, J. F., and Gagliardi, L. (2012). Assessing metal–metal multiple bonds in Cr–Cr, Mo–Mo, and W–W compounds and a hypothetical U–U compound: a quantum chemical study comparing DFT and multireference methods. *Chem. Eur. J*. 18, 1737–1749. doi: 10.1002/chem.201103096

Li, H.-R., Lu, X.-Q., Ma, Y.-Y., Mu, Y.-W., Lu, H.-G., Wu, Y.-B., et al. (2019). $K(CO)^-$ and $Rb(CO)^-$: cube-like alkali octacarbonyls satisfying the 18-electron rule. *J. Cluster Sci*. 30, 621–626. doi: 10.1007/s10876-019-01521-y

Li, W.-L., Lu, J.-B., Wang, Z.-L., Hu, H.-S., and Li, J. (2018). Relativity-induced bonding pattern change in coinage metal dimers M_2 (M = Cu, Ag, Au, Rg). *Inorg. Chem*. 57, 5499–5506. doi: 10.1021/acs.inorgchem.8b00438

Lima-de-Faria, J. (1990). *Historical Atlas of Crystallography*. Dordrecht: Kluwer.

Lin, J.-Y., Du, X., Rahm, M., Yu, H., Xu, H.-Y., and Yang, G.-C. (2020). Exploring the limits of transition-metal fluorination at high pressures. *Angew. Chem. Int. Ed*. 59, 9155–9163. doi: 10.1002/anie.202002339

Lin, J.-Y., Du, X., and Yang, G.-C. (2019). Pressure-induced new chemistry. *Chin. Phys. B* 28:106106. doi: 10.1088/1674-1056/ab3f91

Liu, J.-B., Chen, G. P., Huang, W., Clark, D. L., Schwarz, W. H. E., and Li, J. (2017). Bonding trends across the series of tricarbonatoactinyl anions [(AnO2)(CO3)3]4– (An = U–Cm): the plutonium turn. *Dalton Trans*. 46, 2542–2550. doi: 10.1039/C6DT03953G

Liu, W.-Y., Van Wüllen, C., Wang, F., and Li, L.-M. (2002). Spectroscopic constants of MH and M_2 (M=Tl, E113, Bi, E115): direct comparisons of four- and two-component approaches in the framework of relativistic density functional theory. *J. Chem. Phys*. 116, 3626–3634. doi: 10.1063/1.1446026

Llanos, E. J., Wilmer, W., Luu, D. H., Jost, J., Stadler, P. F., and Restrepo, G. (2019). Exploration of the chemical space and its three historical regimes. *Proc. Nat. Acad. Sci. U.S.A*. 116, 12660–12665. doi: 10.1073/pnas.1816039116

Loerting, T., Tautermann, C., Kroemer, R. T., Kohl, I., Hallbrucker, A., Mayer, E., et al. (2000). On the surprising kinetic stability of carbonic acid H_2CO_3. *Angew. Chem. Int. Ed*. 39, 892–894.

Longuet-Higgins, H. C. (1957). A periodic table. *J. Chem. Educ*. 34, 30–31. doi: 10.1021/ed034p30

Löwdin, P.-O. (1969). Some comments on the periodic system of the elements. *Int. J. Quantum Chem*. 3S, 331–334. doi: 10.1002/qua.560030737

Lozinšek, M., Mercier, H. P. A., and Schrobilgen, G. J. (2020). Mixed Noble-Gas Compounds of Krypton(II) and Xenon(VI); $[F_5Xe(FKrF)AsF_6]$ and $[F_5Xe(FKrF)_2AsF_6]$. *Angew. Chem. Int. Ed*. 26, 8935–8950. doi: 10.1002/anie.202014682

Lu, E.-L., Sajjad, S., Berryman, V. E. J., Wooles, A. J., Kaltsoyannis, N., and Liddle, S. T. (2019). Emergence of the structure-directing role of f-orbital overlap-driven covalency. *Nat. Commun*. 10:634. doi: 10.1038/s41467-019-08553-y

Luchinskii, G. P., and Trifonov, D. N. (1981). "Some problems of chemical elements classification and the structure of the periodic system (in Russian)," in *Uchenie o Periodichnosti. Istoriya i Sovremennoct* (Moscow: Nauka), 200–220.

Lucien, H. W. (1958). The preparation and properties of nitrosyl azide. *J. Am. Chem. Soc*. 80, 4458–4460. doi: 10.1021/ja01550a004

Luo, D.-, Wang, Y.-, Yang, G.-, and Ma, Y. (2018). Barium in high oxidation states in pressure-stabilized barium fluorides. *J. Phys. Chem. C* 122, 12448–12453. doi: 10.1021/acs.jpcc.8b03459

Madelung, E. (1936). *Die Mathematischen Hilfsmittel des Physikers*, 3rd Edn. Berlin: Springer.

Mangin, P., and Rémi Kahn, R. (2017). *Superconductivity. An Introduction*. Cham:Springer International.

Mans i Teixidó, C. (2008). Available online at: emp-web-72.zetcom.ch/eMP/eMuseumPlus?service=ExternalInterface&module=collection&objectId=305andviewType=detailView (accessed October 10, 2020).

Mazurs, E. G. (1974). *Graphic Representations of the Periodic System During One Hundred Years*. Tuscaloosa, AL: University of Alabama Press.

McSween, H., and Huss, Y. G. R. (2010). *Cosmochemistry*. Cambridge: Cambridge University Press.

Meek, T. L., and Allen, L. C. (2002). Configuration irregularities: deviations from the madelung rule and inversion of orbital energy levels. *Chem. Phys. Lett*. 362, 362–364. doi: 10.1016/S0009-2614(02)00919-3

Mendeleev, D. (1869a). Sootnoshenie svoist s atomnym vesom elementov. *Zh. Russ. Fis. Khim. Obshch*. 1, 60–77.

Mendeleev, D. (1869b). *Osnovy Khimii*, Vol. 1. Sankt-Peterburg: Demakov.

Mendelejeff, D. (1871). Die periodische Gesetzmäßigkeit der chemischen elemente. *Ann. Chem. Pharm. Suppl*. 8, 133–229.

Metzger, N. (1983). Chemistry a la plato. *Mosaic* 14, 26–32.

Mewes, J.-M., Jerabek, P., Smits, O. R., and Schwerdtfeger, P. (2019a). Oganesson is a semiconductor: on the relativistic band-gap narrowing in the heaviest noble-gas solids. *Angew. Chem. Int. Ed*. 58, 14260–14264. doi: 10.1002/anie.201908327

Mewes, J.-M., Smits, O. R., Kresse, G., and Schwerdtfeger, P. (2019b). Copernicium: a relativistic noble liquid. *Angew. Chem. Int. Ed*. 58, 17964–17968. doi: 10.1002/anie.201906966

Meyer, G. (2014). All the lanthanides do it and even uranium does oxidation state +2. *Angew. Chem. Int. Ed*. 53, 3550–3551. doi: 10.1002/anie.201311325

Meyer, L. (1864). *Die Modernen Theorien der Chemie und ihre Bedeutung für die Chemische Statistik*. Leipzig: Maruschke and Berendt.

Meyer, L. (1870). Die natur der chemischen elemente als function ihrer atomgewichte. *Ann. Chem. Pharm. Suppl*. 7, 354–364.

Miao, M.-, Botana, J., Pravica, M., Sneed, D., and Park, C. (2017). Inner-shell chemistry under high pressure. *Jpn. J. Appl. Phys*. 56:05FA10. doi: 10.7567/JJAP.56.05FA10

Millikan, R. C. (1982). Why teach the electron configuration of the elements as we do? *J. Chem. Educ*. 59, 757–757. doi: 10.1021/ed059p757

Misra, K. C. (2012). *Introduction to Geochemistry: Principles and Applications*. Oxford: Wiley-Blackwell.

Moore, C. E. (1949). *Atomic Energy Levels*, *Vol*. I, II, III. Washington, DC: NBS.

Moossen, O., and Dolg, M. (2016). Assigning the cerium oxidation state for CH_2CeF_2 and $OCeF_2$ based on multireference wave function analysis. *J. Phys. Chem. A* 120, 3966–3974. doi: 10.1021/acs.jpca.6b03770

Morss, L. R., Edelstein, N. M., and Fuger, J. (eds.) (2010) *The Chemistry of the Actinide and Transactinide Elements.* Dordrecht: Springer.

Nancharaiah, Y. V., and Lens, P. N. L. (2015). Ecology and biotechnology of selenium-respiring bacteria. *Microbiol. Mol. Biol. Rev*. 79, 61–80. doi: 10.1128/MMBR.00037-14

Nash, C. S. (2005). Atomic and molecular properties of elements 112, 114, and 118. *J. Phys. Chem. A* 109, 3493–3500. doi: 10.1021/jp050736o

Neidig, M. L., Clark, D. L., and Martin, R. L. (2013). Covalency in f-element complexes. *Coord. Chem. Rev*. 257, 394–406. doi: 10.1016/j.ccr.2012.04.029

Newth, G. S. (1894). *A Text-Book of Inorganic Chemistry*. London: Longmans, Green and Co.

Nipan, D., Kol'tsova, T. N., Ochertyanova, L., and Bel'skii, N. K. (2000). On the history of the discovery of oxide high-temperature superconductors. *Rus. J. Inorg. Chem*. 45, 1319–1321. doi: 10.1002/chin.200103225

NIST Team (2019). *NIST Standard Reference Database 78*. Available online at: physics.nist.gov/physrefdata/asd/levels_form.html, and nist x-ray transition energies database. physics.nist.gov/physrefdata/xraytrans/ html/search.html

Oderberg, D. S. (2007). *Real Essentialism*. London: Routledge.

Ortu, F., Formanuik, A., Innes, J. R., and Mills, D. (2016). New vistas in the molecular chemistry of thorium: low oxidation state complexes. *Dalton Trans*. 45, 7537–7549. doi: 10.1039/C6DT01111J

Pathak, A. K., Paudyal, D., Mudryk, Y., and Pecharsky, V. K. (2017). Role of 4f electrons in crystallographic and magnetic complexity. *Phys. Rev. B* 96:064412. doi: 10.1103/PhysRevB.96.064412

Pauling, L. (1953). *General Chemistry: An Introduction to Descriptive Chemistry and Modern Chemical Theory*. San Francisco, CA: Freeman.

Pershina, V. (2015). Electronic structure and properties of superheavy elements. *Nucl. Phys. A* 944, 578–613. doi: 10.1016/j.nuclphysa.2015.04.007

Petruševski, V. M., and Cvetković, J. (2018). On the 'true position' of hydrogen in the periodic table. *Found. Chem*. 20, 251–260. doi: 10.1007/s10698-018-9306-y

Pravica, M., Schyck, S., Harris, B., Cifligu, P., Kim, E., and Billinghurst, B. (2019). Fluorine chemistry at extreme conditions: possible synthesis of HgF_4. *Papers Phys*. 11:110001. doi: 10.4279/pip.110001

Pye, C. R., Bertin, M. J., Lokey, R. S., Gerwick, W. H., and Linington, R. G. (2017). Retrospective analysis of natural products provides insights for future discovery trends. *Proc. Nat. Acad. Sci. U.S.A.* 114, 5601–5606. doi: 10.1073/pnas.1614680114

Pyykkö, P. (1979a). Secondary periodicity in the periodic system. *J. Chem. Res. S* 11, 380–381.

Pyykkö, P. (1979b). Dirac-fock one-centre calculations Part 8. The $^1\Sigma$ States of ScH, YH, LaH, AcH, TmH, LuH and LrH. *Phys. Scripta* 20, 647–651. doi: 10.1088/0031-8949/20/5-6/016

Pyykkö, P. (2011). A suggested periodic table up to $Z \leq 172$, based on dirac–fock calculations on atoms and ions. *Phys. Chem. Chem. Phys*. 13, 161–168. doi: 10.1039/C0CP01575J

Pyykkö, P. (2012a). Relativistic effects in chemistry: more common than you thought. *Annu. Rev. Phys. Chem*. 63, 45–64. doi: 10.1146/annurev-physchem-032511-143755

Pyykkö, P. (2012b). The physics behind chemistry and the periodic table. *Chem. Rev*. 112, 371–384. doi: 10.1021/cr200042e

Pyykkö, P. (2019). An essay on periodic tables. *Pure Appl. Chem*. 91, 1959–1967. doi: 10.1515/pac-2019-0801

Quam, G. N., and Battell Quam, M. (1934). Types of graphic classifications of the elements. *J. Chem. Educ. 11*, 288–297. doi: 10.1021/ed011p288

Rahaman, Z., Ali, L., and Rahman, A. (2018). Pressure-dependent mechanical and thermodynamic properties of newly discovered cubic Na_2He. *Chin. J. Phys*. 56, 231–237. doi: 10.1016/j.cjph.2017.12.024

Rahm, M., Cammi, R., Ashcroft, N. W., and Hoffmann, R. (2019). Squeezing all elements in the periodic table: electron configuration and electronegativity of the atoms under compression. *J. Am. Chem. Soc*. 141, 10253–10271 doi: 10.1021/jacs.9b02634

Rahm, M., Dvinskikh, S. V., Furó, I., and Brinck, T. (2011). Experimental detection of trinitramide, $N(NO_2)_3$. *Angew. Chem. Int. Ed*. 50, 1145–1148. doi: 10.1002/anie.201007047

Railsback, L. B. (2018). "The earth scientist's periodic table of the elements and their ions," in *Mendeleev to Oganesson: A Multidisciplinary Perspective on the Periodic Table*, eds E. Scerri and G. Restrepo (New York, NY: Oxford University Press), 206–218.

Rath, M. C. (2018). Periodic table of elements revisited for accommodating elements of future years. *Curr. Sci*. 115, 1644–1647. doi: 10.18520/cs/v115/i9/1644-1647

Rayner-Canham, G. (2020). *The Periodic Table: Past, Present, Future.* Singapore: World Scientific.

Restrepo, G. (2018). "Poorly explored chemical spaces and the challenges for chemistry," in *ISPC-SS in Bristol, 16th July*.

Restrepo, G. (2019a). Challenges for the periodic systems of elements: chemical, historical and mathematical perspectives. *Chem. Eur. J*. 25, 15430–15440. doi: 10.1002/chem.201902802

Restrepo, G. (2019b). Compounds bring back chemistry to the system of chemical elements. *Substantia* 3, 115–124. doi: 10.13128/Substantia-739

Restrepo, G., Llanos, E. J., and Mesa, H. (2006). Topological space of the chemical elements and its properties. *J. Math. Chem*. 39, 401–416. doi: 10.1007/s10910-005-9041-1

Riedel, S., and Kaupp, M. (2009). The highest oxidation states of the transition metal elements. *Coord. Chem. Rev*. 253, 606–624. doi: 10.1016/j.ccr.2008.07.014

Robinson, A. E. (2019). Chemical pedagogy and the periodic system. *Centaurus* 2019, 1–19. doi: 10.1111/1600-0498.12229

Rogachev, A. Y., Miao, M. S., Merino, G., and Hoffmann, R. (2015). Molecular CsF_5 and CsF_2^+. *Angew. Chem. Int. Ed*. 54, 8275–8278. doi: 10.1002/anie.201500402

Rohdenburg, M., Azov, V. A., and Warneke, J. (2020). New perspectives in the noble gas chemistry opened by electrophilic anions. *Front. Chem.* 8:8580295. doi: 10.3389/fchem.2020.580295

Rooms, J. F., Wilson, A. V., Harvey, I., Bridgeman, A. J., and Young, N. A. (2008). Mercury–fluorine interactions: a matrix isolation investigation of Hg. . .F_2, HgF_2 and HgF_4 in argon matrices. *Phys. Chem. Chem. Phys*. 10, 4594–4605. doi: 10.1039/b805608k

Roos, B. O., Borin, A. C., and Gagliardi, L. (2007). Reaching the maximum multiplicity of the covalent chemical bond. *Angew. Chem. Int. Ed*. 46, 1469–72. doi: 10.1002/anie.200603600

Ruiperez, F., Ugalde, J. M., and Infante, I. (2011). Electronic structure and bonding in heteronuclear dimers of V, Cr, Mo, and W: a CASSCF/CASPT2 study. *Inorg. Chem*. 50, 9219–9229. doi: 10.1021/ic200061h

Santiago, R. T., and Haiduke, R. L. A. (2020). Determination of molecular properties for moscovium halides (McF and McCl). *Theoret. Chem. Acc*. 139:60. doi: 10.1007/s00214-020-2573-4

Scerri, E. (2020). Recent attempts to change the periodic table. *Phil. Trans. A Math. Phys. Eng*. 378:20190300. doi: 10.1098/rsta.2019.0300

Scerri, E., and Ghibaudi, E. (2020) *What is a Chemical Element?* A Collection of Essays by Chemists, Philosophers, Historians, and Educators. New York, NY: Oxford University Press.

Scerri, E. R. (2007). *The Periodic Table. Its Story and Its Significance*. Oxford; New York, NY: Oxford University Press.

Schädel, M. (2015). Chemistry of the superheavy elements. *Philos. Trans. R. Soc. A* 373:20140191. doi: 10.1098/rsta.2014.0191

Schlöder, T., Kaupp, M., and Riedel, S. (2012). Can zinc really exist in its oxidation state +III? *J. Amer. Chem. Soc*. 134, 11977–11979. doi: 10.1021/ja3052409

Schultz, E. (2010). Reflections catalyzed by an assault on a favorite principle. *J. Chem. Educ*. 87, 472–473. doi: 10.1021/ed800164k

Schulz, A., Tornieporth-Oetting, I. C., and Klapötke, T. M. (1993). Nitrosyl azide, N_4O, an intrinsically unstable oxide of nitrogen. *Angew. Chem. Int. Ed*. 32, 1610–1612. doi: 10.1002/anie.199316101

Schwarz, W. H. E. (2010a). "An introduction to relativistic quantum chemistry," in *Relativistic Methods for Chemists*, eds M. Maria Barysz and Y. Ishikawa (Dordrecht: Springer), 1–98.

Schwarz, W. H. E. (2010b). The full story of the electron configurations of the transition elements. *J. Chem. Educ*. 87, 444–448. doi: 10.1021/ed8001286

Schwarz, W. H. E. (2013). 100th Anniversary of bohr's model of the atom. *Angew. Chem. Int. Ed*. 52, 12228–12238. doi: 10.1002/anie.201306024

Schwarz, W. H. E., and Rich, R. L. (2010). Theoretical basis and correct explanation of the periodic system: review and update. *J. Chem. Educ*. 87, 435–443. doi: 10.1021/ed800124m

Schwerdtfeger, P., Smits, O. R., and Pyykkö, P. (2020). The periodic table and the physics that drives it. *Nat. Rev. Chem*. 4, 359–380. doi: 10.1038/s41570-020-0195-y

Seaborg, G. T. (1946). The transuranium elements. *Science* 104, 379–386. doi: 10.1126/science.104.2704.379

Seppelt, K. (1976). Arsenic pentachloride, $AsCl_5$. *Ang. Chem. Int. Ed*. 15, 377–378.? doi: 10.1002/anie.197603771

Seppelt, K. (1977). Arsenic pentachloride, $AsCl_5$. *Z. Anorg. Allg. Chem*. 434, 5–15.? doi: 10.1002/zaac.19774340101

Shchukarev, S. A. (1954). The periodic law of D. I. mendeleev as a basic concept in modern chemistry. *J. Gen. Chem*. 24, 595–603.

Shchukarev, S. A. (1969). Similarity and difference in the elements lying on the horizontal, vertical, and diagonal sections of D. I. mendeleev's table in the light of electronic theory. *Rus. J. Inorg. Chem*. 14, 1374–1382.

Shchukarev, S. A. (1977). New views on the theory of D. I. mendeleev's system. I. periodicity in the stratigraphy of atomic electronic shells in the system, and the concept of kainosymmetry. II. prospects in the theory of the periodicity and rhythmics. *J. Gen. Chem*. 47, 227–238, 449–459.

Singh, V., Dixit, M., Kosa, M., Major, D. T., Levi, E., and Aurbach, D. (2016). Is it true that the normal valence-length correlation is irrelevant for metal-metal bonds? *Chem. Eur. J*. 22, 5269–5276. doi: 10.1002/chem.201504161

Smiles, D. E., Batista, E. R., Booth, C. H., Clark, D. L., Keith, J. M., Kozimor, S. A., et al. (2020). The duality of electron localization and covalency in lanthanide and actinide metallocenes. *Chem. Sci*. 11, 2796–2809. doi: 10.1039/C9SC06114B

Sneath, P. H. A. (2000). Numerical classification of the chemical elements and its relation to the periodic system. *Found. Chem*. 2, 237–263. doi: 10.1023/A:1009933705492

Snow, C. P. (1962). *The Two Cultures and the Scientific Revolution*. London: Cambridge University Press.

Steenbergen, K. G., Mewes, J. M., Pasteka, L. F., Gaggeler, H. W., Kresse, G., Pahl, E., et al. (2017). The cohesive energy of superheavy element copernicium determined from accurate relativistic coupled-cluster theory. *Phys. Chem. Chem. Phys*. 19, 32286–32295. doi: 10.1039/C7CP07203A

Stein, L. (1985). New evidence that radon is a metalloid element: ion-exchange reactions of cationic radon. *J. Chem. Soc. Chem. Commun*. 1985, 1631–1632. doi: 10.1039/c39850001631

Steudel, R. (1977). *Chemistry of the Non-metals: With an Introduction to Atomic Structure and Chemical Bonding*. English eds by F. C. Nachod and J. J. Zuckerman. Berlin: Walter de Gruyter.

Stewart, P. J. (2007). A century on from dmitrii mendeleev: tables and spirals. *Found. Chem*. 9, 235–245. doi: 10.1007/s10698-007-9038-x

Stewart, P. J. (2010). Charles janet: unrecognized genius of the periodic system. *Found. Chem*. 12, 5–15. doi: 10.1007/s10698-008-9062-5

Stewart, P. J. (2019). Getting it right is not equivalent to getting it wrong. *Found. Chem*. 21, 145–146. doi: 10.1007/s10698-018-9316-9

Stewart, P. J. (2020). From telluric helix to telluric remix. *Found. Chem*. 22, 3–14. doi: 10.1007/s10698-019-09334-7

Stückelberger, A. (1979). *Antike Atomphysik*. München: Heimeran.

Sun, Z., Schaefer, H. F. III, Xie, Y.-, Liu, Y., and Zhong, R. (2013). Does the metal-metal sextuple bond exist in the bimetallic sandwich compounds $Cr_2(C_6H_6)_2$, $Mo_2(C_6H_6)_2$ and $W_2(C_6H_6)_2$? *Mol. Phys*. 111, 2523–2535. doi: 10.1080/00268976.2013.798434

Syropoulos, A. (2020). On vague chemistry. *Found. Chem*. 22. doi: 10.1007/s10698-020-09383-3

Thomsen, J. (1895). Systematische gruppierung der chemischen elemente. *Z. Anorg. Chem*. 9, 190–193. doi: 10.1002/zaac.18950090115

Thyssen, P., and Ceuleman, A. (2017). *Shattered Symmetry: Group Theory from the Eightfold Way to the Periodic Table*. Oxford: Oxford University Press.

Tiouitchi, G., Ait Ali, M., Benyoussef, A., Hamedoun, M., Lachgar, A., Benaissa, M., et al. (2019). An easy route to synthesize high-quality black phosphorus from amorphous red phosphorus. *Mater. Lett*. 236, 56–59. doi: 10.1016/j.matlet.2018.10.019

Trombach, L., Ehlert, S., Grimme, S., Schwerdtfeger, P., and Mewes, J.-M. (2019). Exploring the chemical nature of super-heavy main-group elements by means of efficient plane-wave density-functional theory. *Phys. Chem. Chem. Phys*. 21, 18048–18058. doi: 10.1039/C9CP02455G

Türler, A. (2016). Advances in chemical investigations of the heaviest elements. *EPJ Web Conf*. 131:07001. doi: 10.1051/epjconf/201613107001

Türler, A., Eichler, R., and Yakushev, A. (2015). Chemical studies of elements with $Z \geq 104$ in gas phase. *Nucl. Phys. A* 944, 640–689. doi: 10.1016/j.nuclphysa.2015.09.012

Türler, A., and Pershina, V. (2013). Advances in the production and chemistry of the heaviest elements. *Chem. Revs*. 113, 1237–1312. doi: 10.1021/cr3002438

Van Delft, D., and Kes, P. (2010). The discovery of superconductivity. *Phys. Today* 63, 38–43. doi: 10.1063/1.3490499

Van Spronsen, J. W. (1969). *The Periodic System of Chemical Elements. A History of the First Hundred Years*. Amsterdam: Elsevier.

Vent-Schmidt, T., Brosi, F., Metzger, J., Schlöder, T., Wang, X.-F., Andrews, L., et al. (2015). Fluorine-rich fluorides: new insights into the chemistry of polyfluoride anions. *Angew. Chem. Int. Ed*. 54, 8279–8283. doi: 10.1002/anie.201502624

Vernon, R. E. (2013). Which elements are metalloids? *J. Chem. Educ*. 90, 1703–1707. doi: 10.1021/ed3008457

Vernon, R. E. (2020a). Organizing the metals and nonmetals. *Found. Chem*. 22. doi: 10.1007/s10698-020-09356-6

Vernon, R. E. (2020b). The location and composition of group 3 of the periodic table. *Found. Chem*. 22. doi: 10.1007/s10698-020-09384-2

Vitova, T., Pidchenko, I., Fellhauer, D., Bagus, P. S., Joly, Y., Pruessmann, T., et al. (2017). The role of the 5f valence orbitals of early actinides in chemical bonding. *Nat. Commun*. 8:16053. doi: 10.1038/ncomms16053

Von Antropoff, A. (1926). Eine neue form des periodischen systems der elemente. *Z. Angew. Chem*. 39, 722–725. doi: 10.1002/ange.19260392304

Von Richter, V. (1875). *Kurzes Lehrbuch der Anorganischen Chemie*. Bonn: Max Cohen.

Von Weizsäcker, C. F. (1971). *Die Einheit der Natur*. München: Hanser, Von Weizsäcker, C. F. (1985). *Aufbau der Physik*. München: Hanser.

Vosko, S. H., and Chevary, J. A. (1993). Prediction of a further irregularity in the electron filling of subshell: Lu^- $[Xe]4f^{14}5d^16s^26p^1$ and its relation to the group IIIB anions. *J. Phys. B* 26, 873–887.

Wang, S.-G., and Schwarz, W. H. E. (2009). Icon of chemistry: the periodic system of chemical elements in the new century. *Angew. Chem. Int. Ed*. 48, 3404–3415. doi: 10.1002/anie.200800827

Wang, S. G., Qiu, Y. X., Fang, H., and Schwarz, W. H. E. (2006). The challenge of the so-called electron configurations of the transition metals. *Chem. Eur. J*. 12, 4101–4114. doi: 10.1002/chem.200500945

Wang, X.-F., Andrews, L., Riedel, S., and Kaupp, M. (2007). Mercury is a transition metal: the first experimental evidence for HgF_4. *Angew. Chem. Int. Ed*. 46, 8371–8375. doi: 10.1002/anie.200703710

Wang, Y.-L., Hu, H.-S., Li, W.-L., Wei, F., and Li, J. (2016). Relativistic effects break periodicity in group 6 diatomic molecules. *J. Am. Chem. Soc*. 138, 1126–1129. doi: 10.1021/jacs.5b11793

Wang, Z.-L., Hu, H.-S., Von Szentpály, L., Stoll, H., Fritzsche, S., Pyykkö, P., et al. (2020). Why are elements B to F so unique: valence orbital radii depend on electron kinematics in differently screened atomic potentials. *Chem. Eur. J*. 26. doi: 10.1002/chem.202003920

Wapstra, A. H. (1991). Criteria that must be satisfied for the discovery of a new chemical element to be recognized. *Pure Appl. Chem*. 63, 879–886. doi: 10.1351/pac199163060879

Watson, R. E. (1960). Approximate wave functions for atomic be. *Phys. Rev*. 119, 170–177. doi: 10.1103/PhysRev.119.170

Watts, H. A. (1863). *A Dictionary of Chemistry and the Allied Branches of other Sciences*, Vol. 1. London: Longman.

Weinhold, F., and Landis, C. R. (2005). *Valency and Bonding*. Cambridge: Cambridge University Press.

West, C. J. A. (1931). *Survey of American Chemistry*. New York, NY: Chemical Catalog Company.

White, W. M. (ed.) (2018) *Encyclopedia of Geochemistry*. Cham: Springer.

Wilson, R. E., De Sio, S., and Vallet, V. (2018). Protactinium and the intersection of actinide and transition metal chemistry. *Nat. Commun*. 9:622. doi: 10.1038/s41467-018-02972-z

Wittig, J. (1973). The pressure variable in solid state physics: what about 4f-band superconductors? *Adv. Solid State Phys*. 13, 375–396.

Wong, D. P. (1979). Theoretical justification of madelung's rule. *J. Chem. Educ*. 56, 714–717. doi: 10.1021/ed056p714

Woolman, G., Robinson, V. N., Marqués, M., Loa, I., Ackland, G. J., and Hermann, A. (2018) Structural and electronic properties of the alkali metal incommensurate phases. *Phys. Rev. Mater*. 2:053604. doi: 10.1103/PhysRevMaterials.2.053604

Wu, X., Zhao, L., Jiang, D., Fernández, I., Berger, R., Zhou, M., et al. (2018b). Barium as honorary transition metal in action: experimental and theoretical study of $Ba(CO)^+$ and $Ba(CO)^-$. *Angew. Chem. Int. Ed*. 57, 3974–3980. doi: 10.1002/anie.201713002

Wu, X., Zhao, L., Jin, J., Pan, S., Li, W., Jin, X., et al. (2018a). Observation of alkaline earth complexes $M(CO)_8$ ($M =$ Ca, Sr, or Ba) that mimic transition metals. *Science* 361, 912–916. doi: 10.1126/science.aau0839

Wulfsberg, G. (2000). *Inorganic Chemistry*. Sausalito, CA: University Science Books.

Xu, W.-H., and Pyykkö, P. (2016). Is the chemistry of lawrencium peculiar? *Phys. Chem. Chem. Phys*. 18, 17351–17355. doi: 10.1039/C6CP02706G

Yakushev, A., Gates, J. M., Turler, A., Schadel, M., Dullmann, C. E., Ackermann, D., et al. (2014). Superheavy element flerovium (element 114) is a volatile. *Metal. Inorg. Chem*. 53, 1624–1629. doi: 10.1021/ic4026766

Yamamoto, S. (2017). *Introduction to Astrochemistry*. Tokyo: Springer Japan.

Yoder, C. H., Suydam, F H., and Snavely, F. A. (1975). *Chemistry*, *2nd Edn*. New York, NY: Harcourt Brace Jovanovich, 78.

Zaleski-Ejgierd, P., and Pyykkö, P. (2011). Relativity and the mercury battery. *Phys. Chem. Chem. Phys*. 13, 16510–16512. doi: 10.1039/c1cp21738k

Zhang, C., Sun, C., Hu, B., Yu, C., and Lu, M. (2017). Synthesis and characterization of the pentazolate anion cyclo-N_5^- in $(N_5)_6(H_3O)_3(NH_4)_4Cl$. *Science* 355, 374–376. doi: 10.1126/science.aah3840

Zhang, Q.-N., Hu, S.-X., Qu, H., Su, J., Wang, G.-J., Lu, J.-B., et al. (2016). Pentavalent lanthanide compounds: formation and characterization of praseodymium(V) oxides. *Angew. Chem. Int. Ed*. 55, 6896–6900. doi: 10.1002/anie.201602196

Zhu, Q., Oganov, A. R., and Zeng, Q. (2015). Formation of stoichiometric CsF_n compounds. *Sci. Rep*. 5:7875. doi: 10.1038/srep07875

Zou, Z. B., Wu, R. Q., and Zhao, Y. F. (2020). Na_2HeO: a possible helium compound from first-principles study. *Int. J. Comput. Mater. Sci. Eng*. 9:2050001. doi: 10.1142/S2047684120500013

Conflict of Interest: The authors declare that the research was conducted in the absence of any commercial or financial relationships that could be construed as a potential conflict of interest.

Advantages of publishing in Frontiers

OPEN ACCESS
Articles are free to read
for greatest visibility
and readership

FAST PUBLICATION
Around 90 days
from submission
to decision

HIGH QUALITY PEER-REVIEW
Rigorous, collaborative,
and constructive
peer-review

TRANSPARENT PEER-REVIEW
Editors and reviewers
acknowledged by name
on published articles

Frontiers
Avenue du Tribunal-Fédéral 34
1005 Lausanne | Switzerland

Visit us: www.frontiersin.org
Contact us: info@frontiersin.org | +41 21 510 17 00

REPRODUCIBILITY OF RESEARCH
Support open data
and methods to enhance
research reproducibility

DIGITAL PUBLISHING
Articles designed
for optimal readership
across devices

FOLLOW US
@frontiersin

IMPACT METRICS
Advanced article metrics
track visibility across
digital media

EXTENSIVE PROMOTION
Marketing
and promotion
of impactful research

LOOP RESEARCH NETWORK
Our network
increases your
article's readership